SLAC-R-885
November 2007

Papers from U.S. Department of Energy Science Undergraduate Laboratory Internship Program (SULI)

Editors: S.E. Rock and M. Woods

SLAC-R-885

Prepared for the Department of Energy
under contract number DE-AC02-76SF00515

Printed in the United States of America. Available from the National Technical Information Service, U.S. Department of Commerce, 5285 Port Royal Road, Springfield, VA 22161.

SLAC-TN-07-029

Fast Track Finding in the ILC's Silicon Detector, SiD01

David E. Baker

Office of Science, Science Undergraduate Laboratory Internship Program

Carnegie Mellon University

Stanford Linear Accelerator Center

Stanford, CA

August 24, 2007

Prepared in partial fulfillment of the requirement of the Office of Science, Department of Energy's Science Undergraduate Laboratory Internship under the direction of Norman Graf in the Linear Collider Detector Department at the Stanford Linear Accelerator Center.

Participant: _____

Signature

Research Advisor: _____

Signature

Work supported in part by US Department of Energy contract DE-AC02-76SF00515

Abstract

A fast track finder is presented which, unlike its more efficient, more computationally costly $O(n^3)$ time counterparts, tracks particles in $O(n)$ time (for n being the number of hits). Developed as a tool for processing data from the ILC's proposed SiD detector, development of this fast track finder began with that proposed by Pablo Yepes in 1996 [1] and adjusted to accommodate the changes in geometry of the SiD detector. First, space within the detector is voxellated, with hits assigned to voxels according to their r, φ, and η coordinates. A hit on the outermost layer is selected, and a "sample space" is built from the hits in the selected hit's surrounding voxels. The hit in the sample space with the smallest distance to the first is then selected, and the sample space recalculated for this hit. This process continues until the list of hits becomes large enough, at which point the helical circle in the x, y plane is conformally mapped to a line in the x', y' plane, and hits are chosen from the sample spaces of the previous fit by selecting the hits which fit a line to the previously selected points with the smallest χ^2. Track finding terminates when the innermost layer has been reached or no hit in the sample space fits those previously selected to an acceptable χ^2. Again, a hit on the outermost layer is selected and the process repeats until no assignable hits remain. The algorithm proved to be very efficient on artificial diagnostic events, such as one hundred muons scattered at momenta of 1 GeV/c to 10 GeV/c. Unfortunately, when tracking simulated events corresponding to actual physics, the track finder's efficiency decreased drastically (mostly due to signal noise), though future data cleaning programs could noticeably increase its efficiency on these events.

Table of Contents

Introduction

After the BaBar experiment, the last particle physics experiment at SLAC, has been completed, particle physicists will need a new tool to study high-energy physics and lepton interactions. The proposed tool is the International Linear Collider (ILC), to be 40 km long and collide positron/electron (e^+/e^-) pairs at energies of up to 1 TeV. This device is expected to implement innovative methods of e^+/e^- storage, beam acceleration, and particle detection. One proposed detector is the "SiD" model, which replaces layers of drift chambers or scintillating material with silicon panels measured on the micrometer scale. These silicon panels would be able to resolve the location of a particle hit on its surface to five micrometers, resulting in a highly improved digital tracking mechanism.

The SiD model consists of five finely-faceted vertex detector layers surrounding the immediate vicinity of collisions, followed by some number of tracker barrels: layers of silicon paneling outside the vertex detector meant to track particles moving through the collider's magnetic field. This study is intended to investigate algorithms which would identify corresponding particle hits through the vertex detector and tracker barrels, and reconstruct particle tracks. Secondary considerations of the study would include optimizing the accuracy of the tracking algorithm with respect to the number of tracker barrels and the cost of the device.

The "fast track finder" of Dr. Pablo Yepes [1] was used as a launching point for this study. It is already an efficient algorithm, and the one developed here implements the same methods: the space of the detector is voxellated, with hits in each voxel stored together in data structures. A hit on the outermost layer is then selected, and the closest hit on the second-outermost layer found (with the assumption that in the outermost layer, hit density is small enough that these two hits must be associated). Because charged particles in a magnetic field move in helices, and it is computationally easier to fit lines than circles, hit coordinates are conformally mapped into a "feature space," which maps circles in the real space into lines. A linear projection between the two points is then used to estimate the locations of associated points on inner layers. When enough points have been assigned to a track, cuts can be made on χ^2 fits to lines in feature space and circles in real space to determine which tracks probably belong to particles. This process is repeated until all in-range hits have been assigned to tracks to a desirable level of accuracy.

Challenges in the adaptation of the tracker include tracking particles through the decreased number of tracker barrel layers (detectors outfitted with drift chambers commonly have many more layers of tracking material) as well as reconstructing tracks that decayed outside the vertex detector, such as the decay products of neutral hadrons. With computing power freed due to a decreased number of hits, more rigorous methods of predicting the location of corresponding hits can be integrated into the algorithm, resulting in an increase in accuracy without suffering a loss of efficiency.

Data for testing the algorithm was generated by running Monte Carlo simulations, designed to replicate the detector's geometry and magnetic field. Debugging was done using single-particle or few-particle events, the physics of which was not relevant to the detector, while efficiency studies used these events and actual simulations of the intended e^+/e^- collisions at 500 GeV and 1 TeV. Tracks produced by the algorithm could be compared to the Monte Carlo data for the event, and the differences between the opening angle, distance of closest approach, and curvature, of the reconstructed tracks against the tracks generated by Monte Carlo tracks could be used to measure the algorithm's efficiency.

Materials

The Silicon Detector over which this tracker was implemented had two parts: a vertex detector and a tracker barrel. The vertex detector consists of silicon wafers with 20 μm pixel readout, arranged in five cylindrical layers concentric about the beam line at the interaction point. The tracker barrel consists of five more layers of similarly arranged silicon strips, spaced much more widely in radius than those in the tracker barrel. The dimensions of the vertex cylinders and tracker barrel cylinders are given in tables 1.a and 1.c, respectively. The vertex detector and tracker barrel are each outfitted with four disks lying perpendicular to the detectors' cylindrical axes. Dimensions of these disks are given in tables 1.b and 1.d, respectively. To track particles moving in the forward or backward direction, each disk in the vertex detector is covered with forward-facing silicon wafers, again with 20 μm pixel readout. Each disk in the tracker barrel is covered in two layers of elongated silicon sensor strips, set at an angle from one another so that different strips overlap.

Collisions in the vertex detector produce jets of particles flying outward through the detector's magnetic field. As a charged particle passes through a layer of silicon, a signal is read

into positron sensors on an attached chip which can resolve the position of the hit on the silicon plate to 5 μm [2]. This provides, for each event, a set of three-coordinate points, each of which represents the location where a charged particle crossed a silicon wafer. Particles then pass through the outer tracker barrels, which make more (albeit less-precise) measurements of particle location. In the outer tracker endcap disks, the intersection area of two activated strips provides the three dimensional space point of the particle which activated them.

Procedure

The sample data used consisted of Monte Carlo simulations, which matched the geometry of the detector and the energies specific to the ILC [3], which was read in to the program through a Java Analysis Studio (JAS3) driver. The space of the detector was then digitally divided into equally-sized voxels in the r, φ, η[1] coordinates (the size of which depended on hard-coded parameters within the program) and each voxel was assigned a list of the hits whose coordinates fell within its domain. The algorithm began by randomly selecting a hit on the outermost populated layer and building a 'sample space' about that point. The sample space consisted of all the hits which fell into voxels immediately about the selected point. For instance, if the selected point was within the i^{th} layer, j^{th} φ and k^{th} η voxel, (hereafter labeled r_i, φ_j, η_k), the sample space would be filled with the hits assigned to all the voxels with the labeled by

$$\begin{array}{ccc} r_{i+n}, \varphi_{j-1}, \eta_{k-1} & r_{i+n}, \varphi_{j}, \eta_{k-1} & r_{i+n}, \varphi_{j+1}, \eta_{k-1} \\ r_{i+n}, \varphi_{j-1}, \eta_{k} & r_{i+n}, \varphi_{j}, \eta_{k} & r_{i+n}, \varphi_{j+1}, \eta_{k} \\ r_{i+n}, \varphi_{j-1}, \eta_{k+1} & r_{i+n}, \varphi_{j}, \eta_{k+1} & r_{i+n}, \varphi_{j+1}, \eta_{k+1} \end{array}$$

Here, n ranges from $1 \leq n \leq N$, where N was left as a parameter of the program. Since hit density on the outermost layers is significantly smaller than hit density on the innermost layers, the simplest way to connect a hit with the first was to select the most proximal hit in the sample space of the first. Here, the “most proximal hit” was the hit with the smallest distance d to the hit previously selected, where for two hits j and k, d was defined by

$$d_{jk} = |r_j - r_k| \times (|\varphi_j - \varphi_k| + |\eta_j - \eta_k|)$$

The algorithm constructed tracks in this way until a certain number of hits had been assembled. (The exact number left as a parameter in the program, though since three coplanar hits are required to uniquely define a circle, there had to be at least three.)

1 Here, r is the distance orthogonal to the beam line, φ is the angle in the plane orthogonal the beam line, and η is the pseudorapidity, $\eta = -\ln [\ \tan(\theta/2)\ ]$, which (at these energies) is well approximated by $\eta = -3z / (\ |z| + r\ )$.

Once the track was large enough, the hits in the track were to be fit to a circle in the x, y plane, and points could be chosen from the sample space by choosing whichever best fits this circle. Since fitting points to a circle is computationally difficult, the following conformal mapping:

$$x' = \frac{x - x_0}{r^2}, \quad y' = \frac{y_0 - y}{r^2}, \quad \text{where} \quad r^2 = (x - x_0)^2 + (y - y_0)^2,$$

was implemented, which defines a one-to-one mapping from circles that lie on the point (x_0, y_0) in real (x, y) space to lines through the origin in feature (x', y') space (see Figure 1). Once enough hits on the outermost layers were selected, each hit on the track and in the sample space was transformed, taking the x and y coordinates of the first hit as x_0 and y_0. The next hit was selected by iterating through the hits in the sample space of the previous hit and selecting the hit which, when appended to the list of hits already discovered, provided the line in feature space with the smallest χ^2 value. This hit was then added to the track, and the sample space recalculated from its location. The process repeated until either the innermost layer had been reached or the sample space for the last hit found was empty. If the set of hits collected met certain criteria[2], the hits in the track were permanently removed from the sample space, and the purity and fitting properties of the track evaluated.

Analysis & Results

To measure the efficiency of the detector, hits in the Monte Carlo simulations which corresponded to the same particles were assembled as tracks. Both the found tracks and the Monte Carlo tracks were fit to helices as circles in the x, y plane and lines in the s, z plane (where s is the arc-length about the helix), and each such helix was uniquely defined by five parameters:

- d_0, the distance of closest approach of the closest hit to the circle of the helix in the x, y plane
- φ_0, the azimuthal angle of the momentum of the particle at the point of closest approach
- Ω, or $1/R$, where R is the radius of curvature of the circle in the x, y plane
- z_0, the z position of the track at the distance of closest approach from some reference point
- $\tan \lambda$ is the slope, ds/dz, of the helix in the s, z plane, defined from the momentum $\vec{p}$ by

2 These criteria were variable and based on parameters hard-coded into the program. Often, cuts were made on the number of hits found, the χ^2 values of linear fits in feature space, and circular fits in real space. In this analysis, we required nothing but the number of hits on the track be greater than seven.

$$\tan\lambda = \frac{p_z}{\sqrt{p_x^2 + p_y^2}}.$$

(For more information on helical track parameters, as well as how they are calculated, see [5].) Since the values of d_0 and z_0 could change drastically depending on which hit the finder concluded its search on, the analysis of this track finder focused on the parameters φ_0, Ω, and λ.[3]

The track finder was tested on an artificial data set consisting of 1,000 events of 100 muons, scattered at momenta varying from 1 GeV/c to 10 GeV/c. Of the 1,000 events, all were processed in under one second (see Figure 2) with a mean processing time of 300 milliseconds. The 'efficiency' of the track finder at a given momentum is defined as the number of tracks found by the track finder in a given momentum range (subject to a purity cut[4]) divided by the number of findable tracks in that momentum range. The efficiency of the track finder is plotted for the 1,000 events of 100 scattered muons in Figure 3. As can be seen in the histogram, in the 1 GeV/c momentum range, the efficiency was greater than one, which indicates the discovery of many fake tracks. The track finder seems to be most efficient in the momentum range about 2.0 GeV/c, where the efficiency is nearly 1. This is curious, because we would expect higher momentum particles, the motion of which is more linear, to be tracked more easily than lower momentum particles, the motion of which is more helical.

Unfortunately, when run on Monte Carlo simulations of physically relevant events, these results could not be replicated. For instance, when run on 100 simulated τ^+/τ^- collisions (with six resultant jets), though each event was processed in under 1 second, with an average processing time of 404 milliseconds, the efficiency of the tracker rarely exceeded 0.3 (see Figure 4).

Conclusion

The fast track finder presented here proved to track particles with considerable efficiency, operating at speeds hundreds, or even thousands, of times faster than track finders which work in $O(n^3)$ time. It will undoubtedly prove to be a very beneficial tool to have at hand for fast data processing and data mining after the ILC comes online.

Curiously, this track finder's performance differs from most others in that it shows greater efficiency at tracking low momentum particles, which move as helices, than high momentum

[3] In the author's opinion, Ω is the most important parameter, since it maps directly onto the particle's momentum.

[4] We define "purity" as the greatest number of hits on a track belonging to a single particle divided by the number of hits on the track. In this analysis, we required the purity of findable tracks to be greater than 0.75.

particles, the motion of which is much more linear. Since most other track finders track high momentum particles more efficiently, it would be interesting to study the cause of this track finder operating well in the low regime. If this effect could be replicated in other track finders,

Though this track finder performed well on clean sets of sample data, its performance was found to be lacking on events simulating actual physics. Background noise, such as ionized electrons from the silicon plates being registered as hits, low momentum particles, and daughter particles created outside the vertex tracker, confused the track finder. This interference caused the finder to track as many as four times the number of particles in the event. Since programs which will find and remove such interference are under development by members of the SiD Tracking team, we can conclude that further studies of this algorithms' efficiency should be conducted when it can be run in tandem with such data processing algorithms. The ability to track actual events with the speed and efficiency exhibited by the track finder on the artificial data could prove to be indispensible for processing data from modern detectors.

References

[1] P. Yepes, *"A fast track pattern recognition,"* Nuclear Instruments & Methods in Physics Research A 380 (1996) pp. 582-585.

[2] Silicon Detector (v1) for the Linear Collider at the SLAC Confluence
http://confluence.slac.stanford.edu/display/ilc/sid01

[3] Anonymous FTP for the Linear Collider at the SLAC Confluence
ftp://ftp-lcd.slac.stanford.edu/lcd/ILC/

[4] T. Ferbel, *"Techniques and Concepts of High-Energy Physics,"* St. Croix (1988), pp. 407 – 499

[5] T. Krämer, *"Track Parameters in LCIO,"* LC-DET-2006-004 (2006)

Vertex Layer	Radius (cm)	Length (cm)
1	1.46 cm	± 6.25 cm
2	2.26 cm	± 6.25 cm
3	3.54 cm	± 6.25 cm
4	4.80 cm	± 6.25 cm
5	6.04 cm	± 6.25 cm

Vertex Disk	Radius (cm)	Dist (z, cm)
1	1.4 cm	± 7.21 cm
2	1.6 cm	± 9.05 cm
3	1.8 cm	± 12.19 cm
4	2.0 cm	± 17.03 cm

Table 1.a (above): radius and length along the cylindrical axis of the silicon layers in the vertex detector.

Table 1.b (below): the dimensions of the vertex endcap disks, where "dist" measures the extant distance from the assumed interaction point (at the origin). Each disk has an outer radius of 7.1 cm.

Tracker Layer	Radius (cm)	Length (cm)
1	21.8 cm	± 55.8 cm
2	46.8 cm	± 82.5 cm
3	71.8 cm	± 108.3 cm
4	96.8 cm	± 134.7 cm
5	121.8 cm	± 160.6 cm

Tracker Disk	Radius (cm)	Dist (z, cm)
1	49.4 cm	± 85.5 cm
2	74.7 cm	± 111.4 cm
3	99.9 cm	± 137.8 cm
4	125.0 cm	± 163.6 cm

Table 1.c (above): radius and length along the cylindrical axis of the barrel layers in the outer tracker.

Table 1.d (below): the dimensions of the tracker barrel endcap disks, as in Table 1.b. Each disk has an inner radius of 20.7 cm and a second layer of sensors 0.40 cm further from the origin than the given "dist".

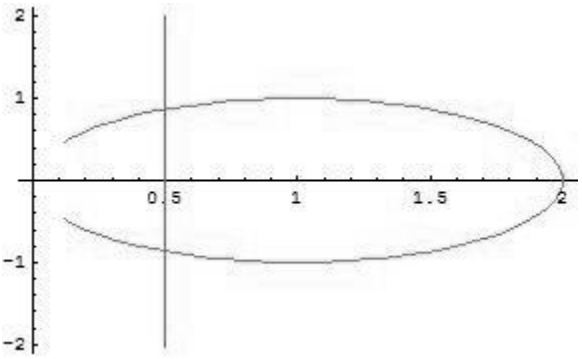

Figure 1: A parametric plot of the given conformal transformation, mapping the line $x = 1$, $y = t$ to the ellipse $x = 2\cos(t)$, $y = \sin(t)$.

For $w = x' + iy'$, $z = x + iy$, and $w(z) = z^{-1}$,

$$w = x' + iy' = \frac{1}{z} = \frac{1}{x + iy}.$$

Multiplying the numerator and denominator by the denominator's complex conjugate,

$$x' + iy' = \frac{1}{x + iy}\left(\frac{x - iy}{x - iy}\right) = \frac{x - iy}{x^2 + y^2}.$$

Matching real and imaginary parts, we have

$$x' = \frac{x}{\quad} \qquad y' = \frac{-y}{\quad}$$

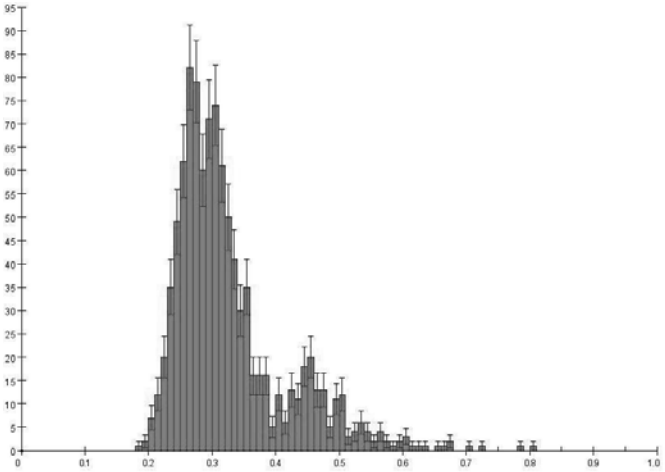

Figure 2: A histogram of the time taken to track each of the thousand artificial events, where the *y*-axis is measured in units of "seconds."

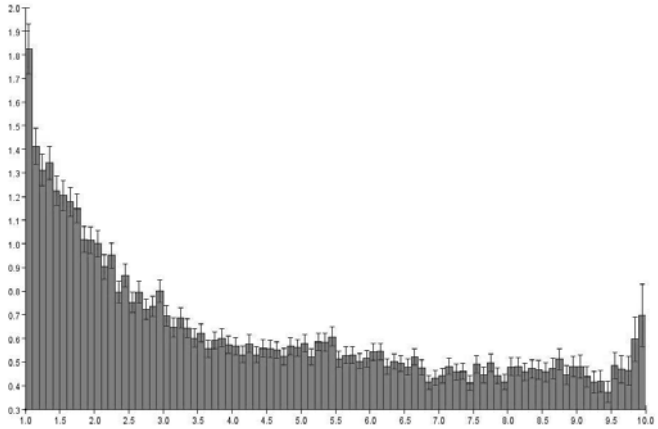

Figure 3: A histogram of the track finder's 'efficiency,' as previously defined, over the range (on the *y*-axis) of 1 GeV/c to 10 GeV/c.

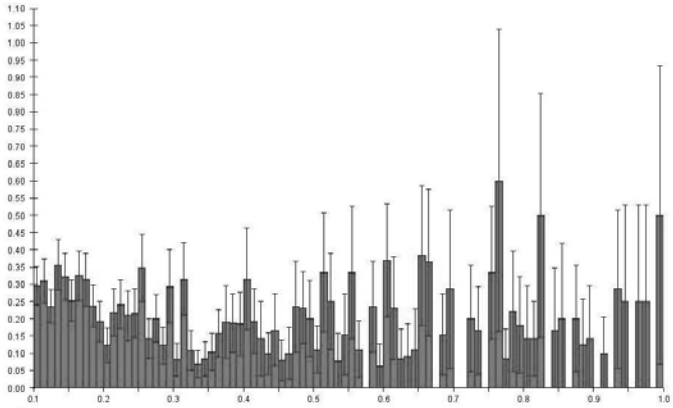

Figure 4: A histogram of the track finder's 'efficiency,' as previously defined, over 100 simulated τ^+/τ^- collisions, each with six jets.

SLAC-TN-07-010
August 2007

Measuring Strain Using X-Ray Diffraction

James Belasco

Office of Science, SULI Program

Villanova University

Stanford Linear Accelerator Center

Menlo Park, CA

August 17, 2007

Prepared in partial fulfillment of the requirements of the Office of Science, U.S. Department of Energy Science Undergraduate Laboratory Internship (SULI) Program under the direction of Dr. Michael Woods at the Stanford Linear Accelerator Center.

Participant: _____
Signature

Research Advisor: _____
Signature

Work supported in part by US Department of Energy contract DE-AC02-76SF00515

Table of Contents

Abstract

Measuring Strain Using X-Ray Diffraction. JAMES BELASCO (Villanova University, Villanova, PA, 19085) APURVA MEHTA (Stanford Linear Accelerator Center, Menlo Park, CA, 94025)

Determining the strain in a material has often been a crucial component in determining the mechanical behavior and integrity of a structural component. While continuum mechanics provides a foundation for dealing with strain on the bulk scale, how a material responds to strain at the very local level—the understanding of which is fundamental to the development of a cohesive framework for the behavior of strained material—is still not well understood. One of the critical components in determination of the behavior of materials under strain at a local scale is an understanding how global average deformation, as a response to an externally applied load, gets distributed locally. This is critical and very poorly understood for a polycrystalline materials—the material of choice for a large variety of structural components. We studied this problem for BCC iron using x-ray diffraction. By using a nanocrystalline iron sample and taking x-ray diffraction patterns at different load levels and at different rotation angles, a complete 2^{nd} rank strain tensor was determined for the three sets of crystallites with three distinct crystallographic orientations. The determination of the strain tensors subsequently allowed the calculation of the elastic modulus along each crystallographic plane. When compared to measured values from single crystal for the corresponding crystal orientations, the data from our polycrystalline sample demonstrated a higher degree of correlation to the single crystal data than expected. The crystallographic planes demonstrated a high degree of anisotropy, and therefore, to maintain displacement continuity, there must be a secondary mode of strain accommodation in a regime that is conventionally thought to be purely elastic.

Introduction

Every successful major bridge builder for half a century has used continuum mechanics to analyze the response of materials to strain. However, while continuum mechanics can model the deformation of materials at large scales, at the very local scale materials invariably deform and fail, (even in large structures failure is often initiated by a single crack). At the very local scale, materials are not the homogeneous and isotropic structures continuum mechanics assumes them to be, but instead are composed of an anisotropic arrangement of discreet atoms and molecules. Thus, a more complete understanding of mechanical behavior is necessary to reconcile the discrepancy between the two views of the behavior of materials as they are subjected to stress.

The two types of strain, classified as plastic, or irreversible strain, and elastic, or reversible strain, produce two different types of perturbations in the lattice structure of a material. Elastic strain causes a stretching in the lattice bonds while plastic strain results in dislocation and motion of slip-bands. The ideal method for measuring such changes is X-ray diffraction, which produces a distinctly different pattern for the two different types of strains. Elastic strain, which is the primary focus of this paper, alters the spacing of the crystalline lattice and therefore results in shifting of the diffraction peaks [2]. Thus, as a sample is strained along a particular axis, X-ray diffraction patterns can be taken that will elucidate the deformation in the lattice structure. Using BCC iron, a ring pattern can be obtained that can be mathematically analyzed to generate the full second order strain tensor. These tensors thereby indicate the particular deformation of the sample under strain as it responds along multiple axes. By calculating the strain tensors for each of the three diffraction rings of iron, the (110), (200), and (211), (each of which corresponds to

a different crystallographic orientation) and comparing them to one another the deformation of the crystallites with those crystallographic orientations can be determined. Ultimately, the elastic modulus of each lattice plane can be calculated through an analysis of the change in the strain level for increasing load levels.

Materials and Methods

Sample Preparation

BCC iron samples with a thickness of 13.5 microns were prepared for x-ray diffraction by cutting them into dog bone shapes that were then inserted into a displacement controlled tensile rig. The dog bone shape is used to facilitate purely tensile loading and limit the amount of out of plane strain in the material

Data collection Procedure

X-ray diffraction patterns (see Figure 1) were taken with a set wavelength of 0.975 Å as the prepared iron samples were rotated from 0 degrees to + 45 degrees with a diffraction pattern taken every 9 degrees. To study the elastic deformation, the sample was strained to the onset of plastic deformation (the plastic strain limit taken to be that determined by traditional continuum mechanics sources) and the diffraction patterns were taken at set intervals as the sample was unloaded, to ensure that at least under conventional mechanics model the subsequent deformation is purely elastic. Patterns were taken at five separate load levels as well as at the initial zero load level.

Pattern Analysis

An unstrained lattice produces a diffraction pattern with circular rings. When a sample is under elastic tensile stress, the lattice spacing elongates in the direction of the applied load and contracts in the orthogonal directions. This results in an elliptical

distortion of the diffraction rings. The eccentricity of these ellipses directly corresponds to how the sample has deformed under strain. In order to analyze the nature of this ellipse, the 2-D diffraction images were converted to diffraction coordinates (Q, chi) from pixel positions using Fit2D. Fit2D itself was calibrated for specific measurements using LaB_6 samples that have standardized diffraction parameters. The eccentricity of the ellipse and the resulting magnitude of all the six independent components of the 2nd rank strain tensor were determined from this converted data by the procedure outlined below.

Strain Tensor Determination

The change in ellipticity of a diffraction ring under load is seen as a noticeable fluctuation (termed "wiggle") in the normally straight line of the Q vs. chi polar plot (see Figure 2). Using a program developed in MATLAB®, a Gaussian fit was used to determine the location of the high intensity points of the wiggle (Figure 3), the magnitude of the intensity, and the width of the intensity curve. The resulting Q and chi coordinates of the intensity peaks were then transformed into the psi and phi coordinates used in the standard $\sin^2\Psi$ technique [1]. These calculated values were then used to generate the coefficients for the strain tensors equation according to:

$$\varepsilon_{\Phi} = \varepsilon_{11}\cos^2\Phi\sin^2\psi + \varepsilon_{22}\sin^2\Phi\sin^2\psi + \varepsilon_{33}\cos^2\psi + \varepsilon_{12}\sin 2\Phi\sin^2\psi + \varepsilon_{23}\sin\Phi\sin 2\psi + \varepsilon_{13}\cos\Phi\sin 2\psi \quad (1)$$

Where: $\varepsilon_{\Phi\psi} = \dfrac{d_{\Phi\psi} - d_0}{d_0}$ (2)

And the change in d is the displacement of the sample as it stretches under strain. For each load level, the MATLAB® program takes data from all the diffraction patterns as output by Fit2D and then uses the collective data points from each strain level in a least-squares fit, weighted by widths provided by the intensity curves, to solve for the second

order strain tensors (ε_{ij}) as well as generate the error values for each calculated tensor. This process was then repeated for each of the three diffraction rings produced by BCC iron.

Results

The strain tensor data for each ring at each load level was tabulated (see Table 4,5,6) and for each ring the calculated strain tensor in the ε_{22} direction (the load axis of the dog bone sample which will demonstrate the most dramatic stain) was plotted in Origin against the stress at each load level as demonstrated in Figure 4. Assuming the elastic deformation is linear with stress and strain, a linear fit of the strain data was taken for each ring. The slope of this fit provided the elastic modulus along each crystallographic direction.

The theoretical values for the elastic modulus along each of the crystallographic planes of the BCC iron were calculated using:

$$\frac{1}{E} = s_{11} - 2[(s_{11} - s_{12}) - \tfrac{1}{2}s_{44}](l_1^2 l_2^2 + l_2^2 l_3^2 + l_1^2 l_{31}^2) \quad (4)$$

Where l_1, l_2, l_3 are the direction cosines for the particular lattice plane as given in Table 1, and the s values are the stiffness constants specific to a given material, shown in Table 2 for iron.

These values are compared to the single crystal values for the elastic modulus in the chosen crystallographic directions in Table 3.

Discussion

The tabulated values for the strain tensor data demonstrate what is expected in terms of sample deformation along particular axes. As the strain increases in the ε_{22} direction, the

strain values in the ε_{33} become negative as would be expected from a material elongating in one direction while contracting in the other direction.

The data as plotted in the ε_{22} graph produces a pretty good linear fit, providing credible elastic modulus values along the different crystallographic directions. The error bars on the individual points, while present, are too small to be noticeable demonstrating a high confidence in the method developed for obtaining strain from 2D diffraction pattern. However, the plotted ε_{22} data sets and fitted lines do not have intercepts at zero because their location on the y-axis depends on the particular unstrained lattice spacing (d0). The data was manually shifted closer to the origin to compensate for the inaccurate estimation of d0 values. Ideally the actual d0 value could be determined by analyzing calibration parameters. In any case, the shifted data does not impact the calculation of the elastic modulus for the different lattice directions.

The measured values for the elastic modulus along the three crystallographic directions are surprisingly dissimilar from each other, and similar to the single crystal values. In fact, the measured value for the (211) plane is exceptionally close to the single crystal value. Rather than exhibiting the behavior expected by continuum mechanics—including the averaging out of strain values as the material was stretched—such a correlation indicates that in the polycrystalline sample used the strain is distributed along the different crystallographic directions in highly anisotropic manner. Thus, although the sample is polycrystalline, the high anisotropy of the crystallographic orientations of iron has a large effect as the sample reacts to stress.

Such a conclusion is problematic because this high anisotropy would seem to indicate that the crystalline structure would deform differently in the same direction depending on

crystallographic orientation resulting in discontinuities between grains in the material, if they are not accommodated by a secondary mode of strain distribution. But the loading procedure utilized is supposed to result in purely elastic – single mode deformation. Certainly continuum mechanics is proven on a larger scale, and the degree of anisotropy demonstrated indicates that more research must be done to determine by what mechanism crystalline structures distribute strain to accommodate the anisotropy observed here while still demonstrating elasticity.

Acknowledgements

This project was performed at the Stanford Linear Accelerator Center in Palo Alto, California. I would like to thank the U.S. Department of Energy for providing the funding and facilities for the Summer Undergraduate Laboratory Internship (SULI) program in which I was allowed to participate. I would also like to thank my mentor, Apurva Mehta, for his guidance, support, and expertise as well as David Bronfenbrenner who worked with me throughout this project.

References

[1] I.C. Noyan, J.B Cohen. *Residual Stress: Measurement by Diffraction and Interpretation.* New York: Springer-Verlag, 1987, pp. 117-120

[2] B.E. Warren. *X-Ray Diffraction*. New York: Dover Publications, 1969, pp. 102-115

[3] Viktor Hauk. *Structural and Residual Stress Analysis by Nondestructive Methods*. New York: Elsevier, 1997. pp. 135-150

[4] Richard W. Hertzberg. *Deformation and Fracture Mechanics of Engineering Materials.* New York: Wiley, 1995. pp.10-16.

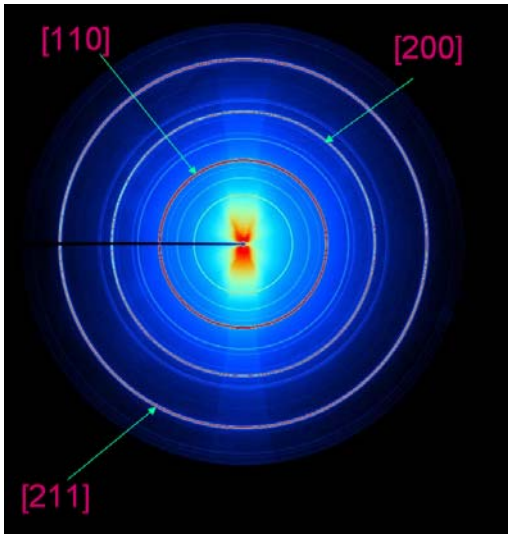

Figure 1. Diffraction pattern for BCC iron highlighting the three analyzed rings.

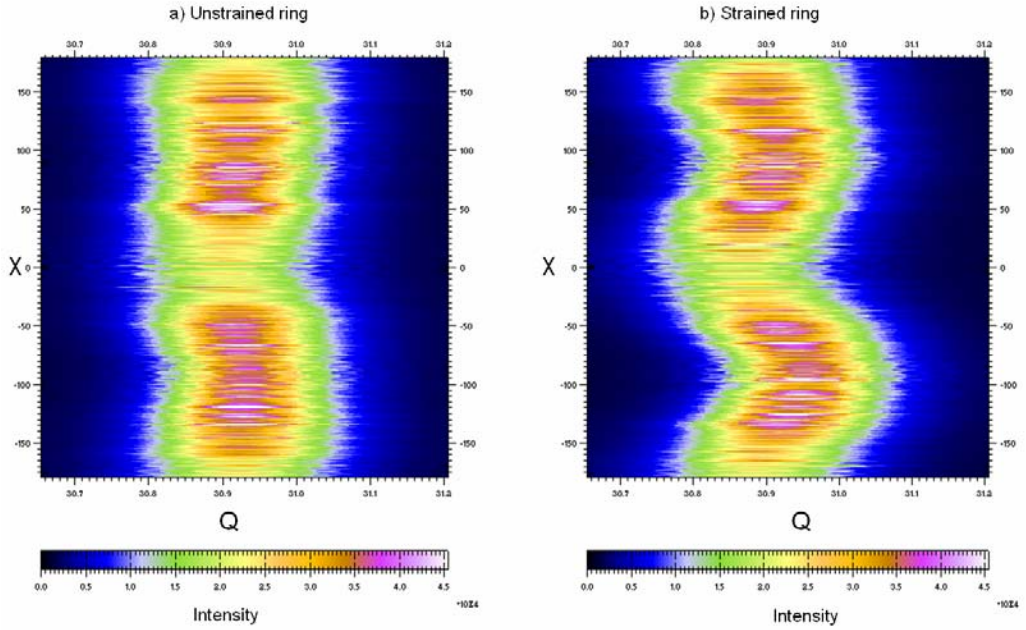

Figure 2. Results of Fit2D coordinate transformation of diffraction pattern to Q/chi space. a) the transformed pattern of an unstrained sample b) the pattern from a strained sample

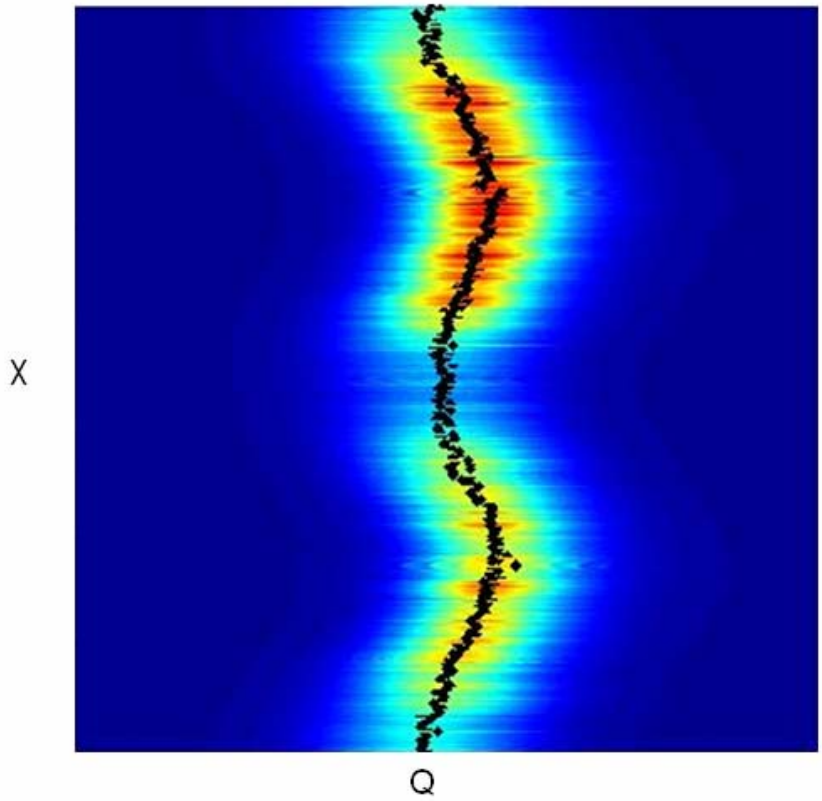

Figure 3. Plot of high intensity points as determined by Gaussian fit for each chi value

Direction	l_1	l_2	l_3
[200]	1	0	0
[110]	$1/\sqrt{2}$	$1/\sqrt{2}$	0
[211]	$2/\sqrt{6}$	$1/\sqrt{6}$	$1/\sqrt{6}$

Table 1. Direction Cosines

a) Established Values

	Elastic Modulus (GPa)
110	210
200	125
211	210

b) Measured Values

	Elastic Modulus (GPa)
110	177 ±11
200	152 ±6
211	207 ±9

Table 3. Established values for Elastic Modulus of single crystal iron

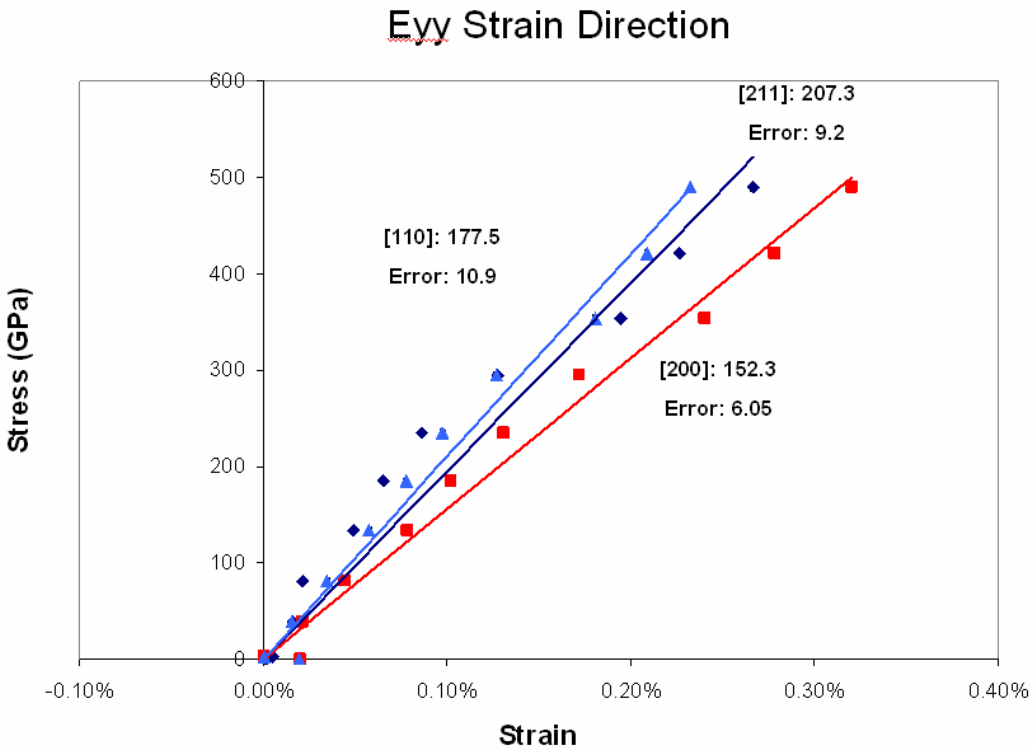

Figure 4. Stress-strain plot for each crystallographic plane along the principle loading direction.

Comment [DJB1]: Parenthesis when talking about planes, brackets when talking about direction.

	Load Level (GPa)										
[110]	490.37	420.74	353.33	295.56	234.81	184.44	134.07	80.74	39.26	2.22	0.00
exx	-1.18E-04	2.05E-05	3.04E-05	-4.26E-04	-5.77E-04	-5.32E-04	-7.20E-04	-3.95E-04	-3.62E-05	-2.70E-04	2.32E-04
exx error	4.80E-05	4.92E-05	5.55E-05	7.67E-05	5.54E-05	5.29E-05	6.04E-05	5.24E-05	3.70E-05	3.85E-05	2.67E-05
exy	-8.45E-05	-2.97E-05	-2.01E-05	1.69E-05	-1.58E-04	-2.54E-05	7.13E-05	-2.00E-05	9.06E-05	4.88E-05	4.34E-05
exy error	1.30E-05	1.34E-05	1.51E-05	1.73E-05	1.51E-05	1.44E-05	1.64E-05	1.43E-05	1.00E-05	1.04E-05	7.22E-06
exz	-3.31E-04	-8.40E-05	-9.45E-05	-2.20E-04	6.48E-06	-5.76E-05	-1.74E-04	-1.59E-05	-2.37E-04	-3.45E-04	4.21E-05
exz error	1.97E-05	2.01E-05	2.27E-05	2.32E-05	2.27E-05	2.17E-05	2.47E-05	2.15E-05	1.52E-05	1.58E-05	1.10E-05
eyy	2.67E-03	2.26E-03	1.94E-03	1.27E-03	8.62E-04	6.54E-04	4.85E-04	2.13E-04	1.61E-04	4.93E-05	1.71E-05
eyy error	9.15E-06	9.43E-06	1.06E-05	1.23E-05	1.07E-05	1.02E-05	1.16E-05	1.01E-05	7.08E-06	7.37E-06	5.10E-06
eyz	3.24E-06	2.52E-06	-6.48E-07	4.88E-06	-3.19E-05	-1.09E-05	9.19E-06	-1.48E-05	1.10E-06	1.48E-05	-3.35E-05
eyz error	7.73E-06	7.95E-06	8.96E-06	9.44E-06	8.98E-06	8.57E-06	9.75E-06	8.49E-06	5.97E-06	6.21E-06	4.31E-06
ezz	-4.14E-04	-4.79E-04	-3.95E-04	-7.17E-04	-6.72E-04	-5.99E-04	-4.74E-04	-3.70E-04	-2.99E-04	-1.78E-04	-5.91E-05
ezz error	1.01E-05	1.03E-05	1.17E-05	1.23E-05	1.16E-05	1.11E-05	1.27E-05	1.10E-05	7.78E-06	8.09E-06	5.61E-06

Table 4. Calculated strain tensors for the [110] crystallographic plane

	Load Level (GPa)										
[200]	490.37	420.74	353.33	295.56	234.81	184.44	134.07	80.74	39.26	2.22	0.00
exx	0.003015	0.003054	0.003064	0.002529	0.002578	0.002708	0.002544	0.002703	0.002788	0.00263	0.003075
exx error	4.61E-05	5.52E-05	5.45E-05	8.73E-05	5.41E-05	5.19E-05	5.22E-05	5.05E-05	5.05E-05	5.07E-05	2.24E-05
exy	-2.39E-05	-2.24E-05	-2.32E-05	6.59E-06	-9.68E-05	-2.18E-05	3.49E-05	-2.56E-05	3.64E-05	3.06E-05	7.10E-05
exy error	1.33E-05	1.20E-05	1.19E-05	1.34E-05	1.19E-05	1.14E-05	1.14E-05	1.11E-05	1.10E-05	1.11E-05	6.51E-06
exz	-2.77E-04	4.09E-06	-3.60E-05	-8.97E-05	-5.15E-06	-9.56E-06	-9.18E-05	-1.82E-06	-2.78E-05	-8.72E-05	9.73E-05
exz error	2.05E-05	1.86E-05	1.83E-05	2.01E-05	1.82E-05	1.75E-05	1.75E-05	1.70E-05	1.70E-05	1.70E-05	9.97E-06
eyy	6.05E-03	5.63E-03	5.25E-03	4.56E-03	4.15E-03	3.86E-03	3.63E-03	3.29E-03	3.06E-03	2.85E-03	3.05E-03
eyy error	1.34E-05	1.30E-05	1.28E-05	1.66E-05	1.28E-05	1.23E-05	1.23E-05	1.20E-05	1.19E-05	1.20E-05	6.54E-06
eyz	2.50E-05	1.74E-05	1.50E-05	8.12E-06	-1.68E-05	-8.79E-06	-9.11E-06	-2.23E-05	-1.28E-05	-1.10E-05	-3.98E-05
eyz error	1.00E-05	8.83E-06	8.72E-06	9.64E-06	8.69E-06	8.33E-06	8.35E-06	8.10E-06	8.08E-06	8.13E-06	4.93E-06
ezz	2.49E-03	2.51E-03	2.67E-03	2.46E-03	2.55E-03	2.67E-03	2.83E-03	2.95E-03	3.05E-03	3.13E-03	3.10E-03
ezz error	1.33E-05	1.22E-05	1.20E-05	1.55E-05	1.20E-05	1.15E-05	1.15E-05	1.12E-05	1.11E-05	1.12E-05	6.45E-06

Table 5. Calculated strain tensors for the [200] crystallographic plane

	Load Level (GPa)										
	490.37	420.74	353.33	295.56	234.81	184.44	134.07	80.74	39.26	2.22	0.00
exx	1.37E-03	9.70E-04	9.75E-04	6.98E-04	6.36E-04	7.36E-04	7.84E-04	7.32E-04	7.48E-04	6.51E-04	8.11E-04
exx error	4.04E-05	2.76E-05	2.56E-05	3.03E-05	2.22E-05	2.36E-05	2.45E-05	2.41E-05	1.89E-05	2.06E-05	1.25E-05
exy	3.39E-05	-8.06E-06	-5.91E-06	1.09E-05	-4.34E-05	2.87E-07	3.96E-05	-6.03E-07	3.94E-05	3.72E-05	6.85E-05
exy error	9.60E-06	6.56E-06	6.09E-06	5.07E-06	5.28E-06	3.95E-06	4.08E-06	4.03E-06	4.47E-06	4.89E-06	2.95E-06
exz	-2.15E-04	9.99E-07	-1.51E-05	-4.03E-05	5.34E-06	-1.29E-05	-3.97E-05	-9.72E-07	-1.51E-05	-4.40E-05	2.75E-05
exz error	1.46E-05	9.93E-06	9.21E-06	7.48E-06	7.97E-06	5.81E-06	6.03E-06	5.93E-06	6.80E-06	7.43E-06	4.49E-06
eyy	2.32E-03	2.09E-03	1.80E-03	1.27E-03	9.72E-04	7.75E-04	5.75E-04	3.45E-04	1.55E-04	0.00E+00	1.95E-04
eyy error	1.36E-05	9.32E-06	8.64E-06	8.53E-06	7.50E-06	6.65E-06	6.88E-06	6.78E-06	6.37E-06	6.96E-06	4.19E-06
eyz	3.63E-05	1.37E-05	1.26E-05	5.30E-06	-6.92E-06	-4.61E-06	-4.19E-06	-1.09E-05	-1.28E-06	1.63E-06	-2.49E-05
eyz error	8.61E-06	5.88E-06	5.45E-06	4.53E-06	4.72E-06	3.53E-06	3.65E-06	3.60E-06	4.01E-06	4.39E-06	2.64E-06
ezz	2.31E-04	3.30E-04	4.53E-04	2.72E-04	3.38E-04	4.53E-04	5.55E-04	6.42E-04	6.95E-04	7.54E-04	7.00E-04
ezz error	1.24E-05	8.42E-06	7.81E-06	7.87E-06	6.76E-06	6.12E-06	6.33E-06	6.24E-06	5.75E-06	6.29E-06	3.77E-06

Table 6. Calculated strain tensors for the [210] crystallographic plane

SLAC-TN-07-021

Electromagnetic Interference from the ILC Beams

LaVonda N. Brown
Office of Science, Science Undergraduate Laboratory Internship Program

Norfolk State University, Norfolk

Stanford Linear Accelerator Center
Menlo Park, California

August 17, 2007

Prepared in partial fulfillment of the requirement of the Office of Science, Department of Energy's Science Undergraduate Laboratory Internship under the direction of Gary Bower in the CEF Scientific Staff Department at Stanford Linear Accelerator Center.

Participant: _____
Signature

Research Advisor**:** _____
Signature

Work supported in part by US Department of Energy contract DE-AC02-76SF00515

TABLE OF CONTENTS

ABSTRACT

Electromagnetic Interference from the ILC Beams. LAVONDA BROWN (Norfolk State University, Norfolk, VA 23504) GARY BOWER (Stanford Linear Accelerator, Menlo Park, CA 94025).

Electromagnetic interference is an emerging problem of the future. This investigation analyzed the data collected from airborne radiation waves that caused electronic devices to fail. This investigation was set up at SLAC in End Station A and the data collected from the electromagnetic waves were received from antennas. In order to calibrate the antennas it required a signal generator to transmit the signals to the antenna and a digital oscilloscope to receive the radiation waves from the other antenna. The signal generator that was used was only able to generate signals between 1 and 1.45 GHz; therefore, the calibrations were not able to be completed. Instead, excel was used to create a curve fitting for the attenuation factors that were already factory calibrated. The function from the curve fitting was then used to extend the calibrations on the biconical and yagi antennas. A fast Fourier Transform was then ran in Matlab on the radiation waves received by the oscilloscope; in addition, the attenuation factors were calculated into the program to show the actual amplitudes of these radiation waves. For future research, the antennas will be manually calibrated and the results will be reanalyzed.

1. INTRODUCTION

Electromagnetic interference (EMI) is caused by the airborne radiation of an electric or magnetic field in a circuit [5]. For example, a disturbance on a television set due to lightening is the result of EMI. Since the 1970's high energy physicists worldwide have had a concern with EMI affecting detector electronic devices [5]. After recent research done here at the Stanford Linear Accelerator Center (SLAC) and experiments testing EMI, physicists found that airborne electromagnetic waves were in fact causing of these electronic devices to fail.

Within the past 15 years, the number of radio frequency emission sources that have entered society have increased dramatically [6]. Personal computers, digital pagers, hand-held radios, cellular phones, and wireless input devices have all become more common in the modern environment. Being that these devices are so efficient, electronic mechanisms and wireless technologies will not diminish; in fact greater uses are foreseen [6].

Although these devices provide many benefits, they also create a greater opportunity for increased EMI with devices. It is important that engineers realize the extent of danger these devices can create with complex interactions. Handling this emerging problem should be recognized as a major concern for the medical community since it involves the use of many different electronic devices [6].

We investigated the disruption of electronics by accelerator beam generated EMI. This investigation was being conducted at SLAC in the End Station A (ESA) beam line. The beam generated EMI source is a 2 inch long ceramic gap section of the beam pipe. The beam from the Linac is pulsed at 10 Hz into ESA with bunch charges. In the 1990's

when the SLD detector was taking data at the SLC linear collider at SLAC, a problem with the electronics occurred. A work around was created, but the original problem was never understood. In this investigation, we used the same electronic module from the SLD detector that failed.

There were three different antennas used in this investigation: the log periodic (yagi), the biconical, and the diode. All of these pick up signals with different frequencies. The biconical is calibrated for 30-330 MHz, the yagi is calibrated for 650-4000 MHz, and the diode is calibrated for approximately 20 GHz and higher. The diode is the newest antenna and is sensitive to higher frequencies. The antennas measured the electromagnetic waves that the beam produced. The antennas give off a signal when the EMI hits it, and it was important to calibrate these signals in order to calculate its strength [7]. My focus was to calibrate the yagi between 30-330 MHz by using the biconical, and to calibrate the biconical between 650-4000 MHz by using the yagi as a reference. One antenna will be the transmitter of the signal while the other antenna will be the receiver.

It is essential to calibrate the antennas because radiation waves lose amplitude as it transfers from the beam to the oscilloscope [7]. Attenuation factors are used to calculate the actual amplitude of the radiation waves at the instant it leaves the beam. Antenna attenuation factor is not a constant; it is different for different frequencies of signals. This means the recorded signal has to be broken down into its component frequency parts so each frequency can be calibrated [7]. This is one of the reasons we do the Fourier analysis.

I performed a Fourier analysis of the EMI radiation. The EMI signal produced by the beam is picked up by the antennas and recorded on a digital oscilloscope. I then did a

Fourier analysis of the signal by decomposing these waves down into a number of different sine waves with different frequencies and amplitudes. I did this by using Matlab software [4]. Later in the investigation, I wanted to try applying more sophisticated techniques such as wavelet and Frog analysis, but there was not enough time to do so [3].

2. MATERIALS AND METHODS

In this investigation, we measured the amount of EMI that would cause an electronic device to fail. The airborne radiation waves from the EMI were analyzed through the three antennas: the yagi, the biconical, and the diode. We had to turn the beam off multiple times and make many accesses into ESA. During the accesses the antennas were moved around a ceramic gap. Restarting the beam usually took approximately 20 minutes and once it was turned off, one must wait 20 minutes to reenter in order to avoid harmful radiation. One run took approximately 45 minutes so it was extremely important to use time wisely during this investigation.

The beam generated EMI signals were picked up by the antennas and read on the digital oscilloscope. I then analyzed these radiation waves on Matlab by feeding the data into the system in the form of data points. Once I performed a fast Fourier transform on these radiation waves, I then calculated the attenuation factors into the results. By doing so, I found the amplitude and the dominating frequency of the radiation waves that made up these signals.

Once I gathered all my data, I then analyzed it by calibrating the yagi and the biconical antennas. I first gathered the materials which included the Tektronix Digital Phosphor Oscilloscope which has a Windows based interface. In addition, we needed a

Hewlett Packard Synthesized CW Generator which produced a signal for the antennas to calibrate. This signal generator only produces signals between 1 and 20 GHz; therefore, we only can calibrate the biconical from1-4GHz using the yagi as the transmitter (since yagi is already calibrated from 650-4000MHz).

I also needed two 20 foot cables which connected each antenna to either the oscillator or signal generator. A 1.3 foot cable was needed to connect the signal generator directly to the oscillator in order to test the voltage loss. A Fluke 87-True RMS Multimeter was used to insure that the cables were in good shape and had no electrical shorts.

After the materials were gathered, I set up the experiment in ESA as it appears in Figure 1. The yagi was connected to the signal generator and it transmitted signals to the biconical. The biconical was connected to the oscilloscope. I sent different frequencies to the yagi and recorded the data that the biconical produced onto the oscilloscope. After the calibrations were completed, I was then able to analyze the data collected from the fast Fourier Transform.

3. RESULTS

During the calibration of the biconical, I found that the biconical was most sensitive at a 70˚ angle from its original position. Therefore, I gathered all my data with it at this angle. I was only able to calibrate the biconical between 1 and 1.45 GHz because the signal generator was unable to extend any further (Table 1). I was unable to calibrate the yagi anymore than it already is because I could not locate a signal generator in the range of 30-650 MHz. Therefore, I was forced to use the factory calibrations; I extended

my calibrations using a curve fitting on the factory calibrations in excel. Figure 2 shows the biconical's extended calibration and Figure 3 shows the yagi's extended calibration.

Figure 4 shows the airborne radiation the oscilloscope measured from the beam pipe. I ran a fast Fourier analysis on the biconical data and figure 5 shows the data. Figure 6 shows the data of the FFT ran on the yagi.

4. DISSCUSSION AND CONCLUSION

I was not able to fully calibrate the biconical or the yagi antenna. Because of this, I was force to use excel to extend the calibrations by performing a curve fitting. These calibrations are not necessarily correct, but for now they will have to suffice. The biconical and yagi's calibrations still need to be extended for future studies.

I successfully ran an FFT on the calibrated radiation waves. I had hoped to see similar calibrated FFT graphs from the yagi and biconical antennas, but that was not the case. In an ideal world, one would suspect that if two antennas are measuring airborne radiation at the same location, that they would show the same electromagnetic waves. For this reason, the investigation still requires more study. Hopefully once the calibrations are done, the FFT's will resemble one another and will prove that the antennas are in fact receiving the same electromagnetic waves.

5. ACKNOWLEDGEMENTS

The research was done the summer of 2007 in End Station A and Building 751 at SLAC. A warm thanks to my mentor Gary Bower who assisted me dramatically throughout the summer. I would also like to thank Nick Sinev for his assistance. A special thanks to the Department of Energy, Office of Science, and SLAC for creating, funding, and organizing this undergraduate program.

6. REFERENCES

[1] A.D. Oliver, A.W. Rudge, K. Milne, and P. Knight, *The Handbook of Antenna Design.* Peregrinus, 1982.

[2] Brigham, E. Oran, *The Fast Fourier Transform and its Applications.* Prentice-Hall, 1988.

[3] Debnath, Lokenath, *Wavelet Transforms and their Applications.* Birkhauser, 2002.

[4] Duane Hanselman and Bruce Littlefield, *Mastering Matlab 7.* Pearson Education, 2005.

[5] "Electromagnetic Interference." Encarta Encyclopedia. http://encarta.msn.com/dictionary_1861689690/electromagnetic_interference.html.

[6] "Electromagnetic Interference: Causes and Concerns in the Health Care Environment." Institute of Biomedical Engineering Technology. http://ibet.asttbc.org/emi.htm.

[7] Jasik, Henry, *Antenna Engineering Handbook.* McGraw-Hill, 1961.

FIGURES:

(a)

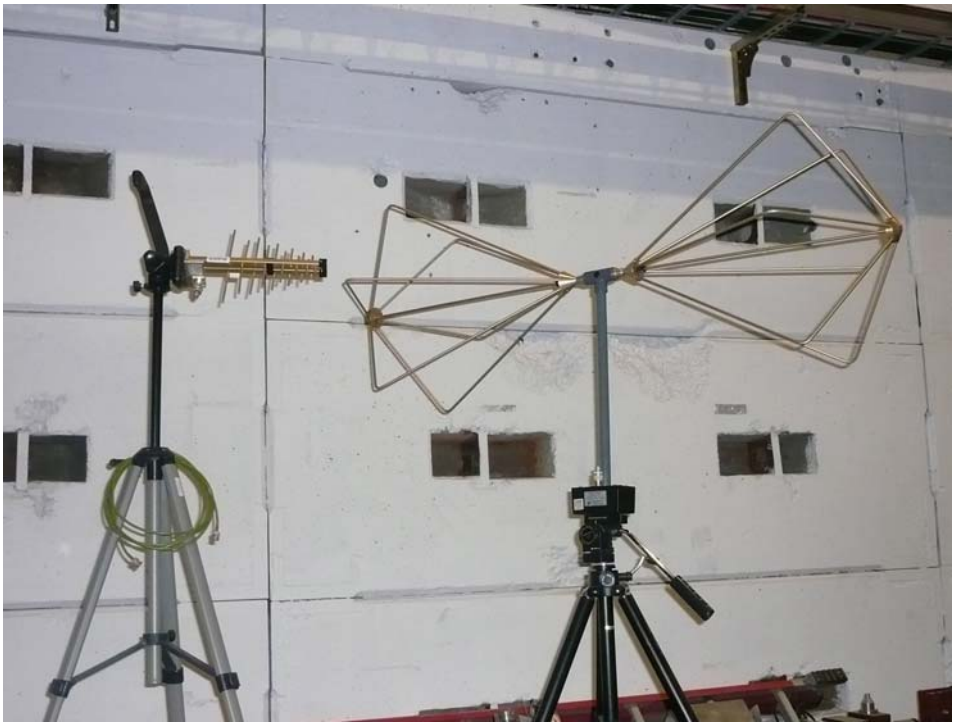

(b)

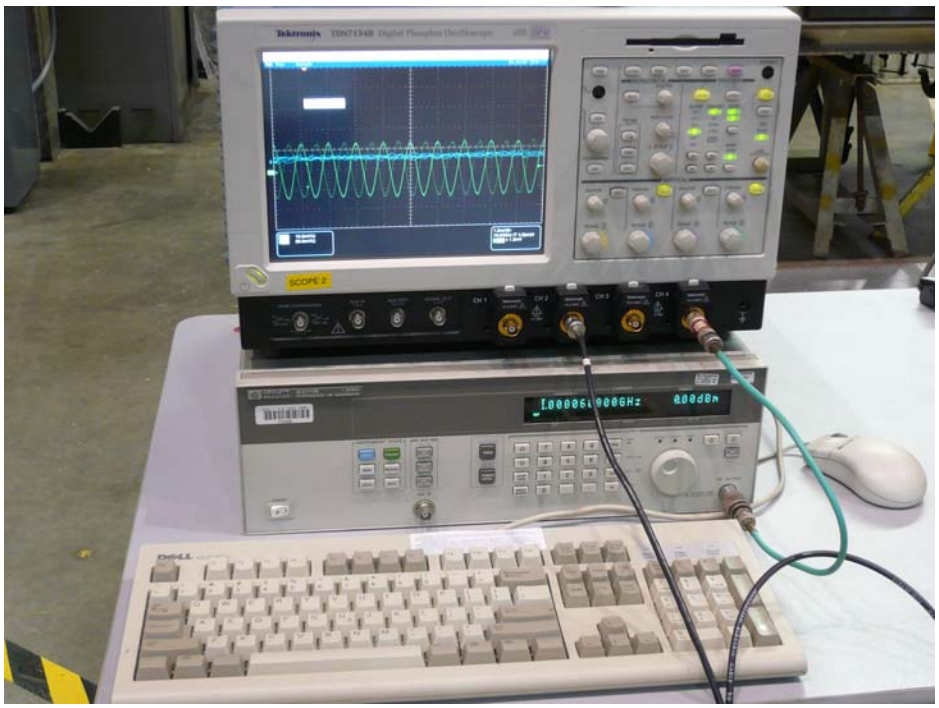

Figure 1: The general setup for the biconical calibration. (a) Left: The yagi. Right: The biconical. (b) The oscilloscope on top of the signal generator.

(a)

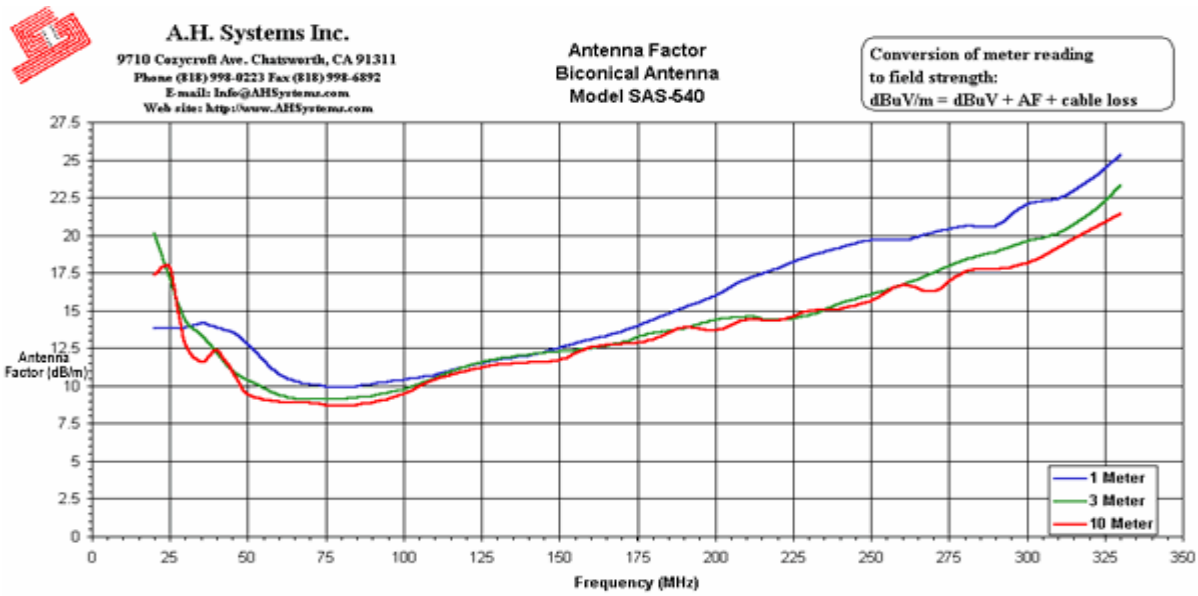

(b)

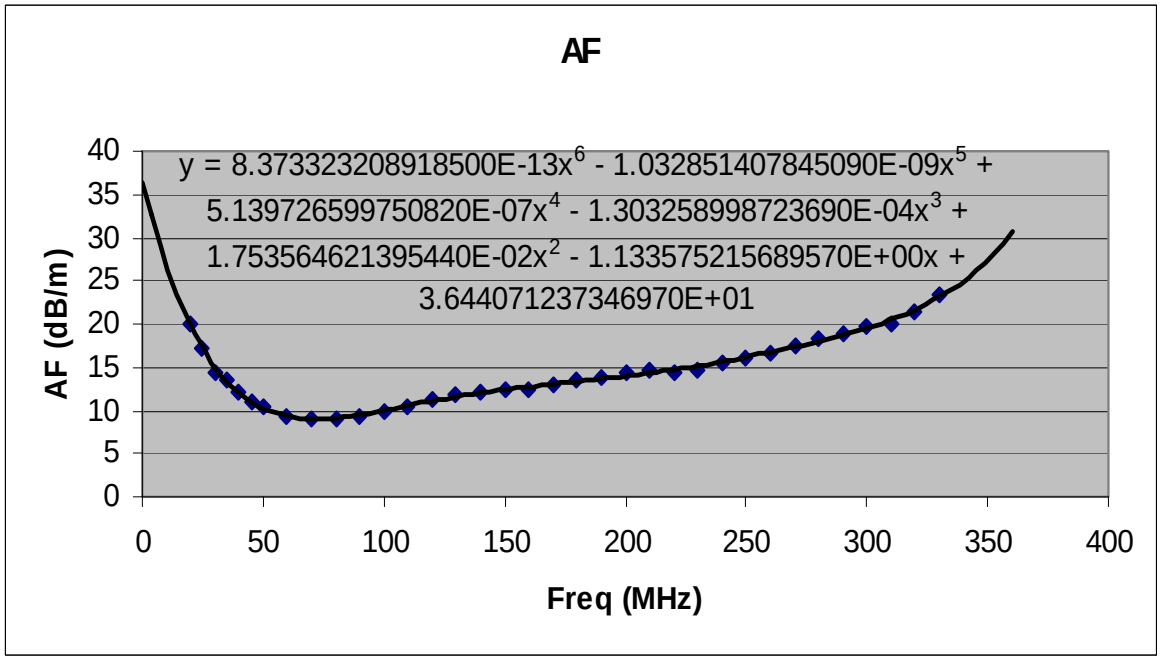

Figure 2: (a) The factory calibrated attenuation factors for the biconical. (b) The curve fitting of the factory calibrations on excel.

(a)

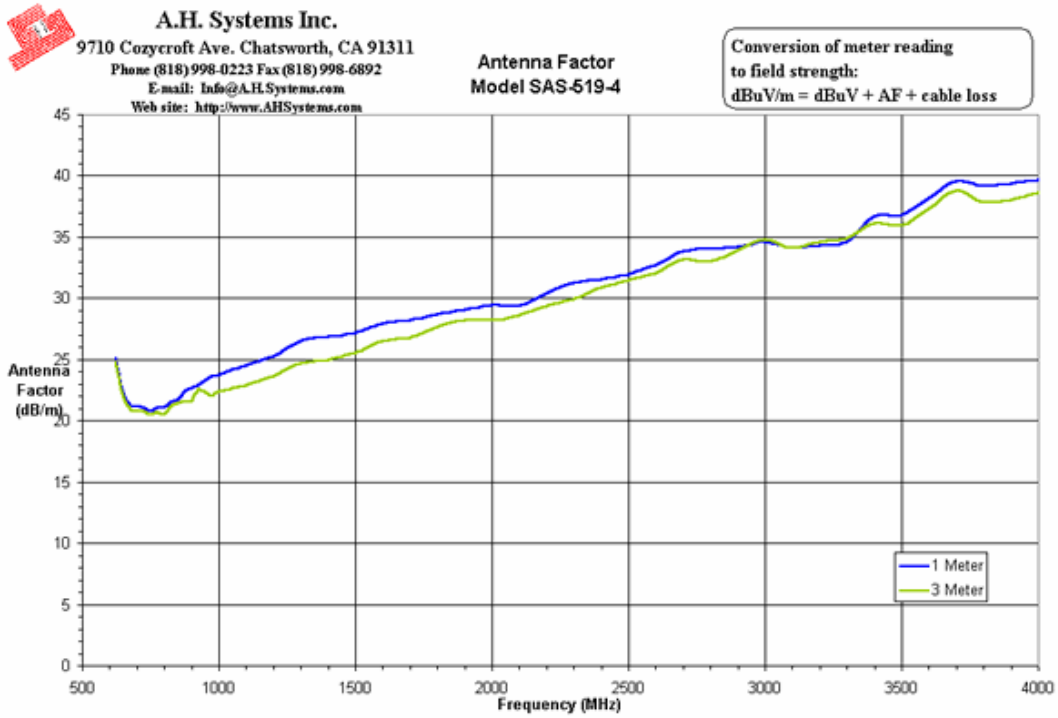

(b)

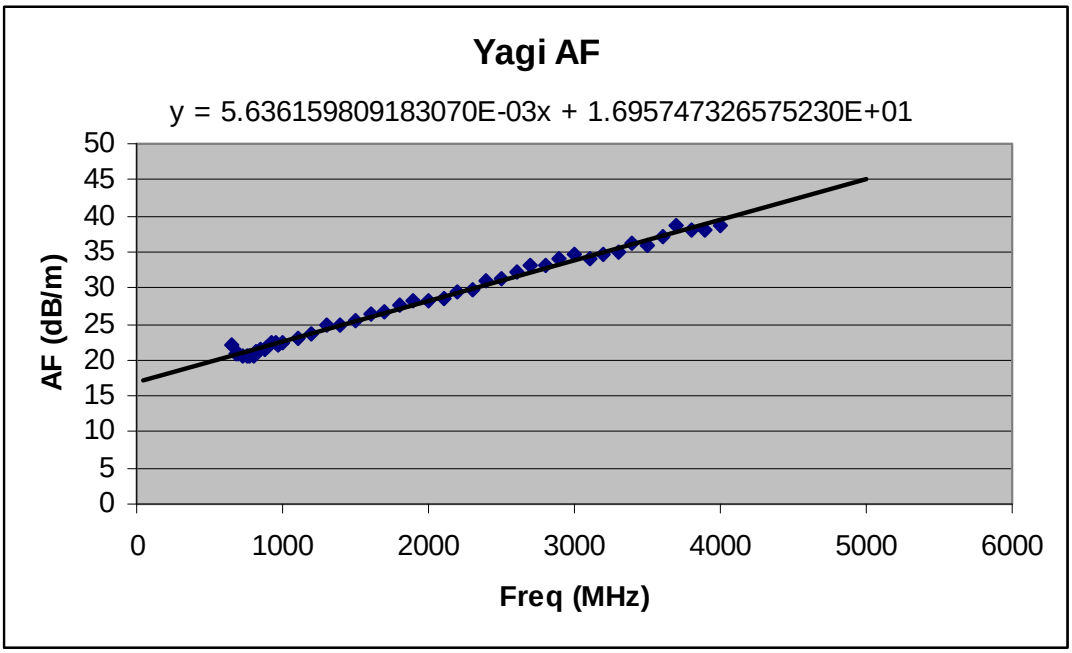

Figure 3: (a) The factory calibrated attenuation factors for the yagi. (b) The curve fitting of the factory calibrations on excel.

(a)

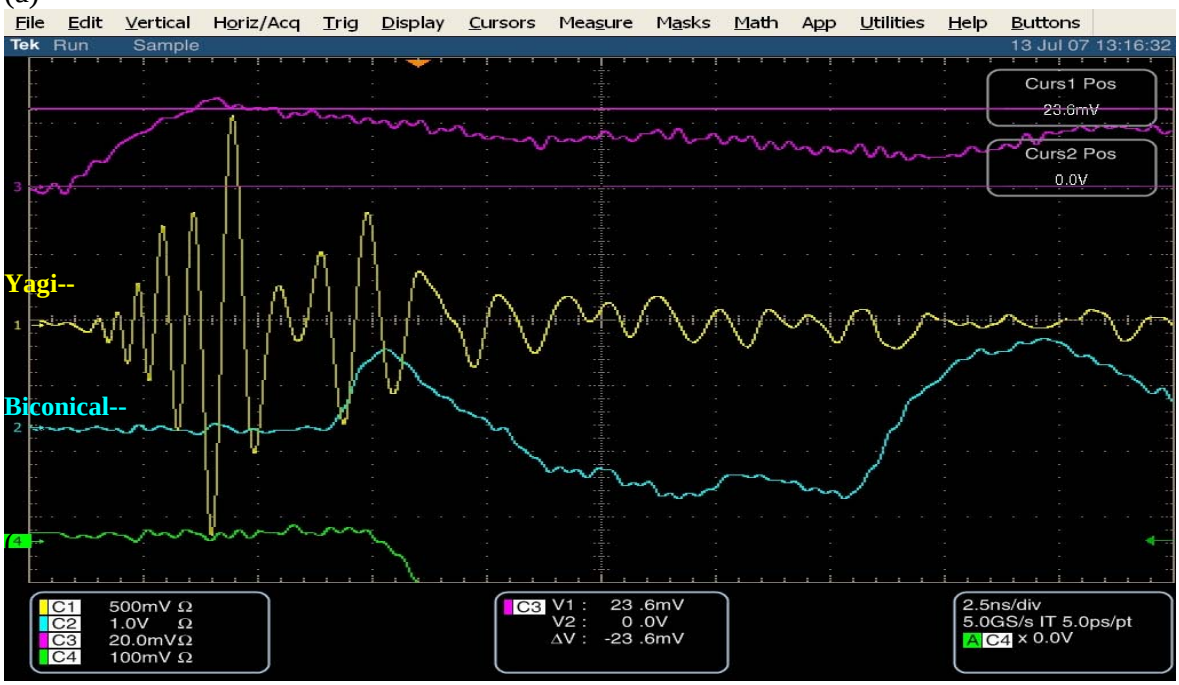

b)

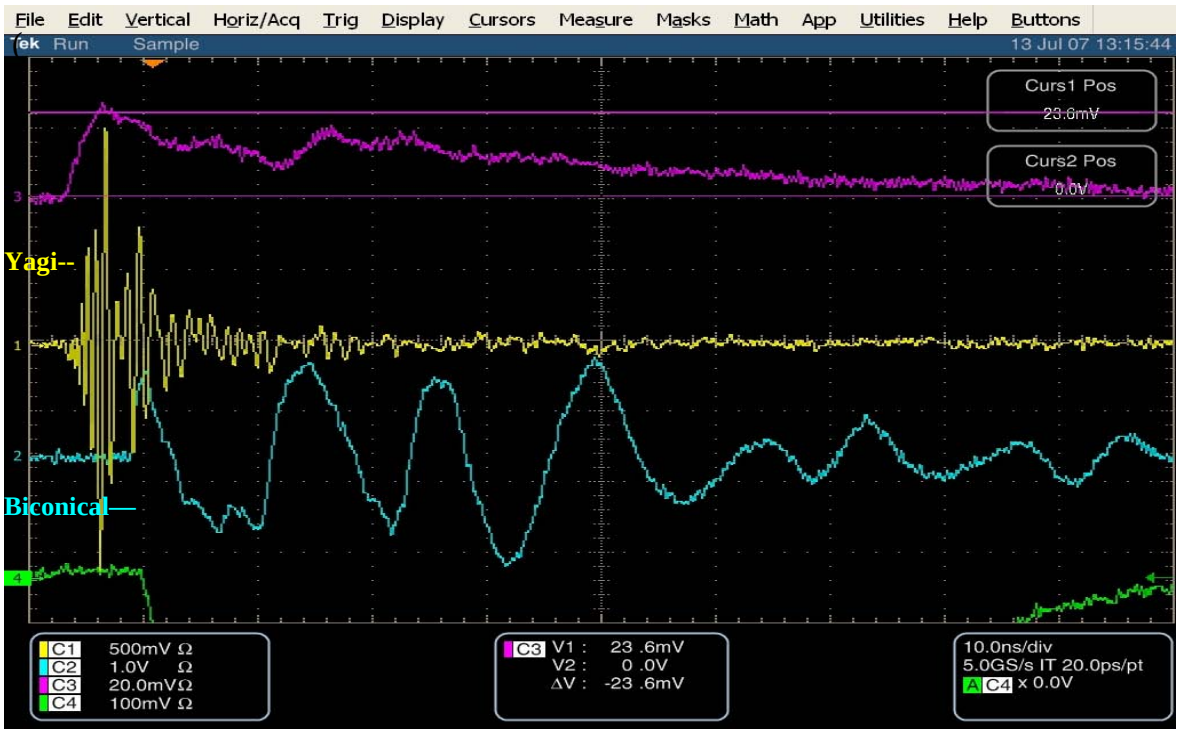

Figure 4: The data collected from the oscilloscope when measuring the radiation waves from the beam. (a) Data collected over a 25 nanosecond period. (b) Data collected over a 100 nanosecond period.

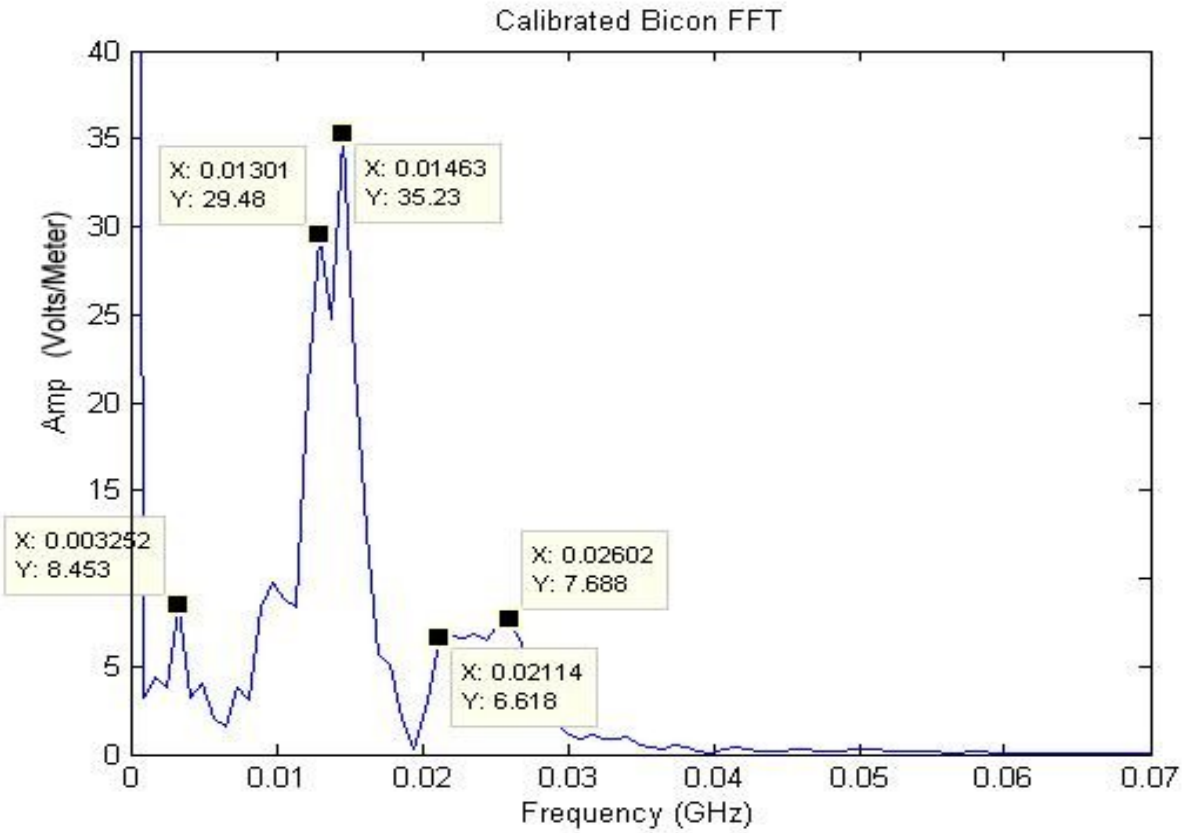

Figure 5: The calibrated FFT of the biconical radiation waves that were projected onto the oscilloscope from Figure 4.

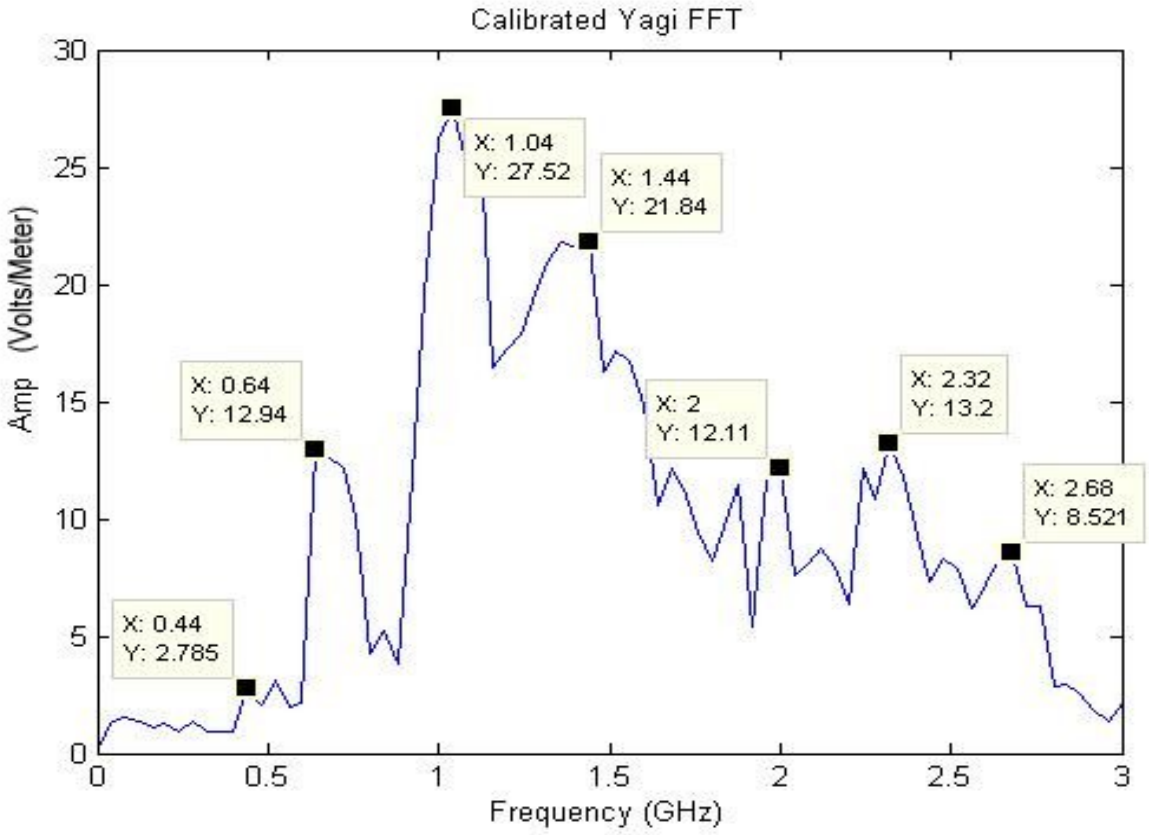

Figure 6: The calibrated FFT of the yagi radiation waves that were projected onto the oscilloscope from Figure 4.

TABLES:

Biconical

Frequency (GHz)	Amplitude (mV)
1	36
1.15	30
1.3	17
1.45	11.5

Table 1: The data collected from the biconical calibrations.

Crystallographic studies of two bacterial antibiotic resistance enzymes: Aminoglycoside Phosphotransferase (2'')-Ic and GES-1 β-lactamase

Laura Byrnes

Office of Science, Science Undergraduate Laboratory Internship (SULI)

Rensselaer Polytechnic Institute

Stanford Linear Accelerator Center

Menlo Park, CA

August 24, 2007

Prepared in partial fulfillment of the requirements of the Office of Science, Department of Energy's Science Undergraduate Laboratory Internship under the direction of C. Smith in the Basic Sciences Division at the Stanford Linear Accelerator Center.

Participant: _____
Signature

Research Advisor: _____
Signature

Work supported in part by US Department of Energy contract DE-AC02-76SF00515

Table of Contents

ABSTRACT

Crystallographic studies of two bacterial antibiotic resistance enzymes: Aminoglycoside Phosphotransferase (2'')-Ic and GES-1 β-lactamase. LAURA BYRNES (Rensselaer Polytechnic Institute, Troy, NY 12180) CLYDE SMITH (Stanford Linear Accelerator Center, Menlo Park, CA 94025)

Guiana Extended-Spectrum-1 (GES-1) and Aminoglycoside phosphotransferase (2'')-Ic (APH(2'')-Ic) are two bacteria-produced enzymes that essentially perform the same task: they provide resistance to an array of antibiotics. Both enzymes are part of a growing resistance problem in the medical world. In order to overcome the ever-growing arsenal of antibiotic-resistance enzymes, it is necessary to understand the molecular basis of their action. Accurate structures of these proteins have become an invaluable tool to do this. Using protein crystallography techniques and X-ray diffraction, the protein structure of GES-1 bound to imipenem (an inhibitor) has been solved. Also, APH(2'')-Ic has been successfully crystallized, but its structure was unable to be solved using molecular replacement using APH(2'')-Ib as a search model. The structure of GES-1, with bound imipenem was solved to a resolution of 1.89Å, and though the inhibitor is bound with only moderate occupancy, the structure shows crucial interactions inside the active site that render the enzyme unable to complete the hydrolysis of the β-lactam ring. The APH(2'')-Ic dataset could not be matched to the model, APH(2'')-Ib, with which it shares 25% sequence identity. The structural information gained from GES-1, and future studies using isomorphous replacement to solve the APH(2'')-Ic structure can aid directly to the creation of novel drugs to combat both of these classes of resistance enzymes.

Introduction

For almost as long as bacteria have existed, they have waged wars against each other using an arsenal of chemicals which attack specific cellular processes necessary for their survival. In turn, it was necessary to have some way of preventing these chemicals from harming their maker, as well as have a defense against the antibiotics produced by other bacteria. In this way, antibiotic resistance was born and has advanced (with help from humans) to where it is today. Two such resistance proteins are the subject of this study. Protein crystallographic analysis is used to understand these types of proteins' enzymatic mechanisms, with the ultimate goal of creating novel drugs which will either deactivate these enzymes or bypass their action completely.

The general class of β-lactamases has been a part of antibiotic resistance since the beginning of the wide-spread use of antibiotics. The more recent arrival of extended-spectrum β-lactamases (ESBLs) has added to this problem. One of the most recent families of ESBLs to be discovered is the Guiana Extended-Spectrum (GES) family [1]. The protein sequence of the GES proteins has significant differences from other β-lactamases of the same class [2]. The classification of "extended-spectrum" resistant β-lactamases refers to the fact that they are able to hydrolyze (deactivate) the type of β-lactam antibiotics designed to resist hydrolysis by β-lactamases identified previously, often referred to as "last resort" antibiotics. The β-lactam family of antibiotics, which include the penicillins, cephalosporins, carbapenems, and monobactams, act by disabling cell-wall biosynthesis proteins, namely transpeptidases, which are responsible for the construction and modification of a peptidoglycan layer surrounding the cell membrane [3]. The way in which β-lactamases affect the action of these types of antibiotics is by hydrolyzing the β-lactam ring structure. Within the β-lactamase family, there are four

classes: A, B, C, and D [4]. The GES family is a class A β-lactamase, and is further classified as a third generation carbapenemase. The general structure of carbapenems is shown in Figure 1. The protein of interest in this study, GES-1, shows strong activity against most carbapenems, with some exceptions such as imipenem (structure shown in Figure 1) and specific inhibitors clavulanic acid, tazobactam, and sulfobactam [2]. The interesting part about its resistance profile is that while it is inhibited by imipenem, two other point mutants, namely GES-2 and GES-5, show 100-fold and 400-fold increases respectively in hydrolysis of imipenem [5]. The results of this structural study will aim to answer the question as to why these point mutants show such drastic differences in their activity towards imipenem.

Aminoglycosides are a second type of antibiotic used in medicine today. This class of antibiotics inhibits bacterial growth by binding to ribosome active sites, thereby halting protein synthesis [6]. With this second type of antibiotic comes a separate class of resistance enzymes. In general, they are called transferases, as they catalyze the transfer of a specific functional group to the antibiotic, thereby deactivating it. Aminoglycoside phosphotransferases (APH) are one member of this family of enzymes. APH enzymes transfer a phosphate to a particular hydroxyl group of the aminoglycoside antibiotic in an ATP-mediated fashion [7]. There are many isoforms of APH proteins, each classified by which hydroxyl group they phosphorylate (identified by a number in parenthesis), and the type of antibiotics they show activity against. For example, the enzyme in this study, APH(2’’)-Ic, phosphorylates the 2’’ hydroxyl of gentamicin, kanamycin, and tobramycin (see Figure 2 for some example structures). Of the APH enzymes, three others have had their crystal structures solved, including APH(2’’)-Ib, APH(3’)-IIa and APH(3’)-III [6, 8]. Several variants were used to attempt to grow crystals for this protein, including the wild-type and several mutants (two single and one double), with and without nucleotide (GTP) bound. By

working out the conditions for crystallizing APH(2'')-Ic, though the structure was unable to be solved with molecular models, this study will aid in speeding up the process for future studies using alternative techniques (e.g. isomorphous replacement) for solving its structure.

Materials and Methods

Protein crystallization

For all of the APH(2'')-Ic variants, initial coarse screens were performed using commercially available sparse-matrix screens (Crystal Screens I and II, Hampton Research) using the sitting drop method. One condition from Crystal Screen I [30% PEG 4000, 0.1M Tris HCl pH 8.5, at 15°C] resulted in crystals for F108L, wild-type, and double mutant variants (all bound GTP). Further fine screening of the F108L mutant using the hanging drop method resulted in crystals suitable for diffraction. Crystals grew as clusters of thin plates in 2μL drops containing protein in 25mM HEPES buffer (pH 7.6), 1mM DTT, and 1mM Mg_2GTP, at a protein concentration of 8.8 mg/ml. The drops with the three crystals used for data analysis contained a 1:1 mixture of protein to solution, one in 20% and two in 23% PEG 4000, all with 0.25M $MgCl_2$, and 0.1M Tris HCl (pH 8.5), with the first (20% PEG) grown at 15°C and the other two (23% PEG) grown at 22°C for 3 days before harvesting. In addition, later fine screening using the wild-type protein produced similar crystals (flat and clustered), in conditions which included 23-25% PEG 4000, 0.2M $MgCl_2$, 0.1M Tris HCl (pH 8.5), at 22°C.

Data collection and processing

The data previously collected for the imipenem-bound GES-1 protein was processed

using MOSFLM [9], and merged and scaled with SCALA [10] from the CCP4 suite of programs [11]. Data collection statistics can be found in Table 1.

Data from the APH(2'')-Ic crystals were collected at BL11-1 at the Stanford Synchrotron Radiation Laboratory (SSRL). The crystals used were flash frozen in liquid nitrogen before data collection. Earlier data analysis showed the crystals belonged to the monoclinic C2 space group, with unit cell parameters a = 81.77Å, b = 54.28Å, c = 77.42Å, and β = 108.97°. The calculated Matthews coefficient was 2.38Å/Da, indicating one molecule in the asymmetric unit. Additional data collection statistics can be found in Table 1.

Molecular replacement and refinement

Molecular replacement of GES-1 (bound imipenem) was carried out using COOT [12], utilizing the previously solved GES-1 structure [5] as the starting model. Refinements were done using the program REFMAC [13], as part of the CCP4 software, using data between 20- and 1.89-Å. A random five percent of the data set was left out as a test set (for the calculation of R_{free}). After 10 rounds of refinements, the R-factor and R_{free} converged to 15.8 and 21.9% respectively.

Molecular replacement of APH(2'')-Ic was carried out using the program MOLREP [14], using the previously solved structure of APH(2'')-Ib as a search model. The two proteins share about 25% sequence identity, and the model was modified so as to replace the unconserved residues with alanine. The CCP4 software was used for all calculations.

Results:

Structural Determination of APH(2’’)-1c

Starting from the initial screenings, several of the APH(2’’)-Ic variants exhibited fast-formed, spiky crystal formation early on in a solution containing 30% PEG 4000, 0.2M $MgCl_2$, and 0.1M Tris HCl (pH 8.5) at 15°C from Crystal Screen I. Initial tests provided proof that the crystals were indeed protein, and thereafter fine screening to refine crystal formation began. Numerous conditions were tested to slow down crystal formation, and the best results arose from the lower PEG concentrations, the same pH, and similar or slightly higher salt concentrations. Tests on temperature as a factor gave mixed results, with 4°C giving no useful crystals, 15°C resulting in the several useful crystals, and 22°C giving fewer, but better formed crystals. Large crystals formed as several flat sheets stuck together at a point, and when mounting these crystals, the sheets separated fairly easily and could be mounted individually. Useful datasets were collected from three crystals, one with 20% PEG 4000 (grown at 15°C) and two with 23% PEG 4000 (grown at 22°C), all with 0.1M Tris HCl (pH8.5) and 0.25M $MgCl_2$. So far there is no indication as to which, if any, dataset will yield the best results in finding the structure.

The APH(2’’)-Ic crystals, namely the F108L mutant, belongs to the space group C2, with one molecule in the asymmetric unit. Efforts to solve the three-dimensional structure using APH(2’’)-Ib have so far failed to give a reasonable solution to the structure.

Using the wild-type APH(2’’)-Ic, fine screening of the crystallization conditions resulted in crystals comparable in quality to those used to collect datasets from in the mutant. These conditions included 23, 24, and 25% PEG 4000, 0.2M $MgCl_2$, and 0.1M Tris HCl (pH 8.5), at 22°C. Datasets have not yet been taken from these crystals, as the synchrotron was not in service.

Inhibitor-binding studies with GES-1 β-lactamase

The data was fit using the previously solved GES-1 structure. Some refinement statistics are given in Table 2. The active site residues that are proposed to interact with the inhibitor are present, including Ser64, Lys67, Glu98, and Glu161. The imipenem molecule showed moderate (~65%) occupancy for the active site, with the other fraction occupied by a sulfate group (a solvent molecule). Several features are still visible, including covalent bonding between Ser64 side chain oxygen and the imipenem C7 atom, with a bond length of 1.40Å. The hydrolytic water molecule is also present, but only at lower occupancy (<40%) and forms a hydrogen bonding interaction with oxygen 62 of imipenem and Glu161.

Discussion and Conclusion:

The solved structure of GES-1 with bound imipenem sheds some light on the reason for the differences in activity between GES-1 and the other GES proteins discovered later. GES-1, although showing the characteristic active site disulfide bond of the carbapenemase-hydrolyzing β-lactamases, is incapable of hydrolyzing imipenem, a typical carbapenem antibiotic, and is in fact inhibited by this molecule. It has been shown that two point mutants of GES-1, Gly165Asn (called GES-2) and Gly165Ser (GES-5) [15, 16] have significant activity against imipenem. Although the imipenem molecule was bound with only ~65% occupancy, several interactions between the inhibitor and the active site residues were present. In the refined structure, covalent bonding between imipenem and Ser64 of GES-1 is clearly observed, giving rise to an acyl-enzyme intermediate which is the first step in the hydrolysis of the β-lactam ring. In addition, there are several hydrogen bonding interactions with other active site residues. A few of these hydrogen bonding partners are shown in Figure 3. Additionally, the hydrolytic water molecule is

present in the active site, and has hydrogen bonding partners which include the imipenem and the side chains of Ser64 and Glu161. However, the hydrolytic water molecule, which plays a crucial role in completing the hydrolysis of the β-lactam ring, shows less than 40% occupancy for its site above the hydroxyethyl moiety of the imipenem molecule. This result suggests that the reason for the decrease in GES-1 catalytic activity against imipenem could be due to the fact that the essential hydrolytic water is not held tightly and is therefore not optimally positioned for attack on the acyl-enzyme intermediate. On the other hand, GES-2 and GES-5, having the point mutations G165N and G165S, respectively, provide an additional hydrogen bonding partner for the hydrolytic water. In these enzymes, the hydrolytic water molecule may be held in the correct position to facilitate hydrolysis of the acyl-enzyme. Future structural studies using GES-2 and GES-5 bound imipenem are necessary to provide further evidence for this explanation.

The APH(2'')-Ib model has so far proved to be an insufficient search model for molecular replacement against the APH(2'')-1c dataset. In the APH(2'')-Ib structure, the alpha domain is somewhat disordered, which suggests that the APH(2'')-Ic alpha domain could also be disordered or have a different orientation. Perhaps because of this, the model could not yield a reasonable fit to the data. Further studies using protein bound with 8-bromo-ATP, multiple isomorphous replacement experiments, or the preparation and crystallization of selenomethionine-substituted wild-type APH(2'')-Ic may provide ways around this problem.

Acknowledgements:

This research was conducted at the Stanford Linear Accelerator Center. I would like to express my gratitude to my mentor, Clyde Smith, for sharing his expertise, patience, and attention during my short time here. Thank you also to the U.S. Department of Energy for the

unique opportunity of participating in the SULI program, one of the most useful learning experiences I've ever been privileged to take part in. Finally, I'd like to acknowledge and thank Apurva Mehta, who took time out of his busy work schedule to meet with a group of other SSRL summer students and me to help us gain a deeper understanding of the research we participated in.

References:

[1] G. F. Weldhagen, "GES: an Emerging Family of Extended Spectrum Beta-Lactamases", Clinical Microbiology Newsletter, Vol. 28, No. 19, 145-149, Oct. 2006

[2] L. Poirel, I. Le Thomas, T. Naas, A. Karim, and P. Nordmann, "Biochemical Sequence Analysis of GES-1, a Novel Class A Extended-Spectrum β-Lactamase, and the Class 1 Integron In52 from *Klebsiella pneumoniae*", in Antimicrobial Agents and Chemotherapy, Vol 44, No. 3, pp. 622-632, Mar. 2000

[3] P. A. Bradford, "Extended-Spectrum β-Lactamases in the 21st Century: Characterization, Epidemiology, and Detection of this Important Resistance Threat", Clinical Microbiology Reviews, Vol. 14, No. 4, pp 933-951, 2001

[4] W. Sougakoff, G. L'Hermite, L. Pernot, T. Naas, V. Guillet, P. Nordmann, V. Jarlier, and J. Delettre, "Structure of the imipenem-hydrolyzing class A β -lactamase SME-1 from *Serratia marcescens*", Acta Crystallographica D, Vol. 58, Part 2, pp. 267-274

[5] C. A. Smith, M. Caccamo, K. A. Kantardjieff, and S. Vakulenko, "Structure of GES-1 at atomic resolution: insights into the evolution of carbapenemase activity in the class A extended-spectrum β-lactamases", Acta Crystallographica D, Vol. 63, Part 9, pp 982-992, 2007

[6] D. Nurizzo, S. C. Shewry, M. H. Perlin, S.A. Brown, J. N. Dholakia, R. L. Fuchs, T. Deva, E. N. Baker, and C. A. Smith, "The Crystal Structure of Aminoglycoside-3'-Phospho-transferase-IIa, and Enzyme Responsible for Antibiotic Resistance", Journal of Molecular Biology, Vol. 327, pp 491-506, Jan. 2003

[7] C. A. Smith and E. N. Baker, "Aminoglycoside Antibiotic Resistance by Enzymatic Deactivation", Current Drug Targets – Infectious Disorders, Vol. 2, pp 143-160, 2002

[8] W. C. Hon, G. A. McKay, P. R. Thompson, R. M. Sweet, D. S. C. Yang, G. D. Wright, and A. M. Berghuis, "Structure of an enzyme required for aminoglycoside antibiotic resistance reveals homology to eukaryotic protein kinases", Cell Vol. 89, pp 887-895.

[9] Leslie, A.G.W., “Recent changes to the MOSFLM package for processing film and image plate data “, Joint CCP4 + ESF-EAMCB Newsletter on Protein Crystallography, No. 26, 1992

[10] P.R. Evans, “Scala”, Joint CCP4 and ESF-EACBM Newsletter 33, pp 22-24, 1997

[11] Collaborative Computational Project, "The CCP4 Suite: Programs for Protein Crystallography", Acta Crystallographica D, Vol. 50, Part 4, pp 760-763, 1994

[12] P. Emsley and K. Cowtan, “Coot: Model-Building Tools for Molecular Graphics”, Acta Crystallographica D - Biological Crystallography, Vol. 60, pp 2126-2132, 2004

[13] G. N. Murshudov, A. A. Vagin, and E.J. Dodson, “Refinement of Macromolecular Structures by the Maximum-Likelihood Method”, Acta Crystallographica D, Vol. 53, Part 3, pp 240-255, 1997

[14] A.Vagin, A.Teplyakov, “MOLREP: an automated program for molecular replacement” J. Appl. Cryst., 30, 1022-1025, 1997

[15] L. Poirel, G. F. Weldhagen, T. Naas, C. De Champs, M. G. Dove, P. Nordmann, “GES-2, a Class A β-Lactamase from *Pseudomonas aeruginosa* with Increased Hydrolysis of Imipenem”, Antimicrobial Agents and Chemotherapy, Vol. 45, No. 9 pp 2598-2603, Sept. 2001

[16] I. K. Bae, Y. N. Lee, S. H. Jeong, S. G. Hong, J. H. Lee, S. H. Lee, H. J. Kim, H. Youn, “Genetic and biochemical characterization of GES-5, an extended-spectrum class A β-lactamase from *Klebsiella pneumoniae*”, Diagnostic Microbiology and Infectious Disease, Vol. 58, Issue 4, pp 465-468, Aug. 2007

Tables and Figures:

Table 1: Data Collection Statistics for imipenem-GES-1 and APH(2")-Ic

	Imipenem-GES-1	APH(2")-Ic
Space group	$P2_1$	C2
Unit cell parameters (Å)	a=42.796, b=81.192, c=71.892, β=102.18°	a=82.4 , b=54.2, c=77.0, β=108.8°
Resolution (Å)	20-1.89	2.15
Unique reflections	38, 545	14, 484
Total reflections	872,781	377, 107
R_{merge} (%)	10.8	9.4
Completeness (%)	99.96	97.1
I/σ_I (%)	5.1	6.4

Table 2: Refinement Statistics for imipenem-GES-1

Resolution range (Å)	20.0 – 1.89
Number of protein residues	266
Number of waters	547
Average B value:	15.837
R-factor/R_{free} (%)	15.8 / 21.9
rmsd bond lengths (Å)	0.015
rmsd angles (°)	1.614

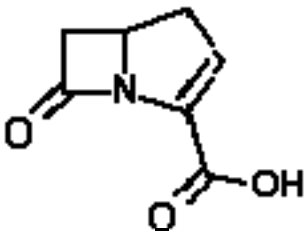

General structure

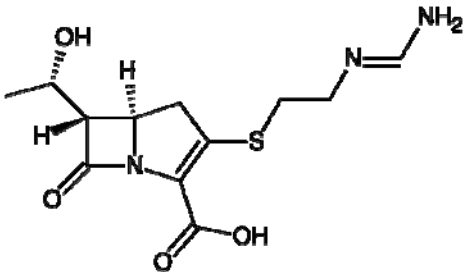

Imipenem

Figure 1: Chemical structures of carbapenems.

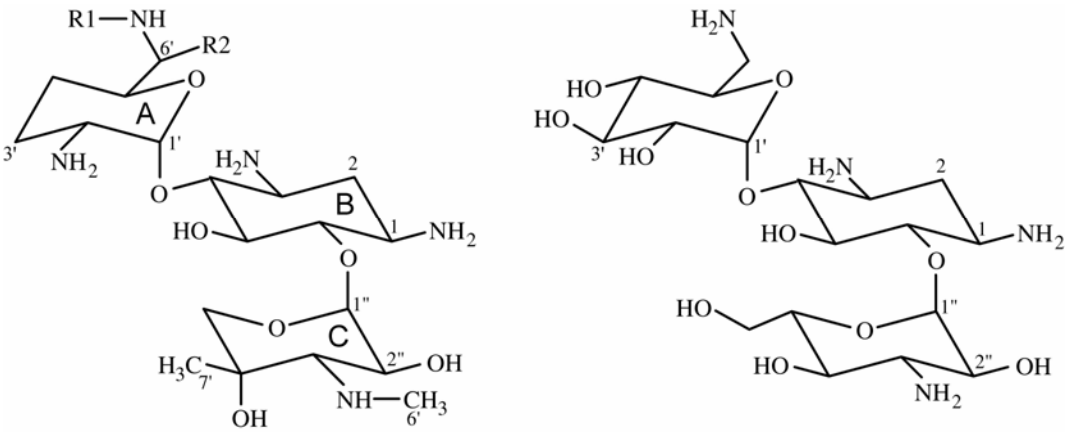

Gentamicin Kanamycin

Figure 2: Chemical structures of some aminoglycosides.

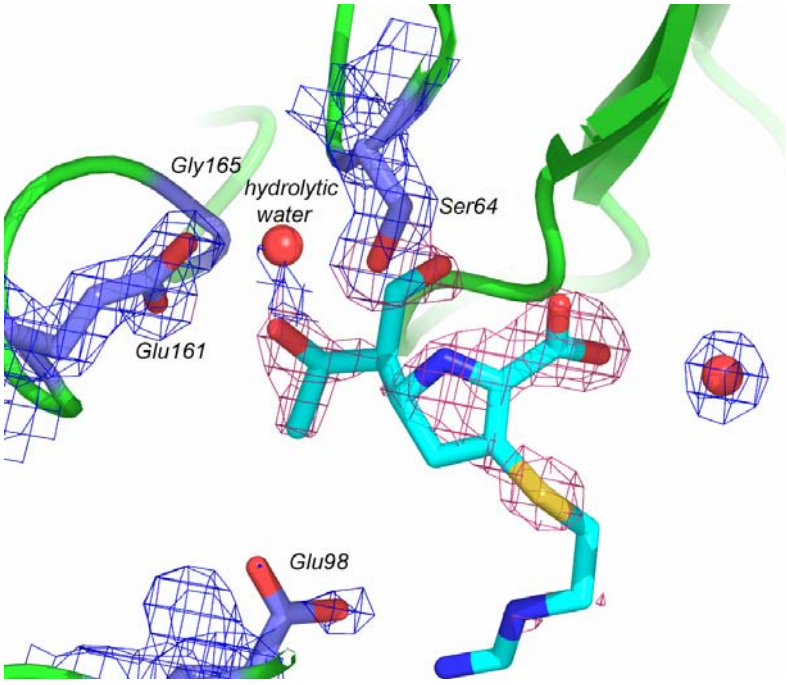

Figure 3: Electron density map of GES-1 active site, bound imipenem. Active site residues and water molecules are shown with blue electron density, while the inhibitor (imipenem) has its electron density shown in pink. $2F_o$-F_c density maps are shown.

SLAC-TN-07-008
August 2007

Surveying and Mapping for a Localized GIS

India S. Calhoun

Office of Science, Science Undergraduate Laboratory Internship Program

Savannah State University

Stanford University

Stanford Linear Accelerator Center

Menlo Park, California

Prepared in partial fulfillment of requirements of the Office of Science, U. S. Department of Energy Science Undergraduate Laboratory Internship (SULI) Program under the direction of Brian Fuss in the Alignment Engineering Group (AEG) of the Metrology Department at the Stanford Linear Accelerator Center.

Participant: _____
Signature

Research Advisor: _____
Signature

Work supported in part by US Department of Energy contract DE-AC02-76SF00515

Table of Contents

ABSTRACT

Surveying and Mapping for Localized GIS. INDIA S.CALHOUN (Savannah State University, Savannah, GA 31414) BRIAN FUSS (Stanford Linear Accelerator Center Menlo Park, CA 94309)

The Alignment Engineering Group (AEG) is responsible for an extensive array of alignment and positioning activities at the Stanford Linear Accelerator Center (SLAC). In particular, the location of accelerator components using specialized tools and data adjustment procedures are the center mission(s) of the group. My established goals for this project are to accurately measure a set of buildings known as Forte Apache to produce a 3-dimensional CAD drawing that will be used to create a 2-dimensional Geographic Information Systems (GIS). Computer Aided Design (CAD) is the use of a wide range of computer-based tools that assist engineers, architects and other design professionals in their design activities [5]. Overall, in the project, I will construct a 2-dimensional GIS that can be used to analyze relationships between features.

INTRODUCTION

Geographic Information Systems (GIS) are tools which are used for making and using spatial information. GIS can be defined as a computer-based system to aid in the collection, maintenance, storage, analysis, output, and distribution of spatial data and information. [1]. In this project, Geographic Information Systems will play a vital role allowing mapped objects to be identified using queries. Surveying data is collected using GPS and a TotalStation. From the raw surveying data, a map is created that will be used for the GIS. More specifically, the positions of some buildings at SLAC will be measured using GPS. Surveying is one of the vital factors in creating an accurate GIS. Surveying deals primarily with geometric measurements on the earth's surface, the computation of derived quantities, such as coordinates, area, and the representation of numerical data in geographical form, such as in plans or maps [4].

GPS is known as the Global Positioning System, "which is a worldwide radio-navigation system formed from a constellation of satellites and their ground stations" [2]. With the GPS surveying at SLAC, the GPS instruments use these satellites as reference points to calculate positions accurate to a matter of centimeters. GPS equipment is used to aid the surveying tools for accurate measurements which will later be recorded and used as points in the 2D/3D drawing.

The program with the imported data for which my drawing will be created is called MicroStation TriForma V8 2004 Edition. MicroStation TriForma is a computer application for the building design, management and construction industry [2] [3]. It provides the essential tool(s) to design projects in 3D. TriForma is a complete 3D application that can model a project in plan view as well as isometric and perspective views. Plan view meaning "a view looking down from above at a horizontal plane located in a position of interest" or flat view [3]. Isometric view means visually represents three-dimensional objects and perspective view is "a view of a three-dimensional image that portrays height, width, and depth" [3]. This program supplies volume elements or forms to build a 3D model. A form can be line-based to add walls, or shape-based to add floor slabs, columns, or roof planes [2] [3]. MicroStation TriForma helps visualization for this project by allowing the creation of a 3D representation of a set of buildings at SLAC.

Once the objects are added to the CAD model, the resulting information on the positions of the buildings will be used to create a Geographic Information System using MicroStation Geographics that can then help with queries such as what buildings are affected by power outages at SLAC. The information is directly usable from the CAD data that was measured using GPS and the TotalStation.

Surveying is one of the vital factors in creating a GIS due to it providing accurate spatial information. GIS and GPS speculation is becoming even more valuable as it helps the planning for the purchase of hardware and software. “It is a new science that is used to design future information systems and will expand into new fields and application areas” [5].

METHODS and MATERIALS

It is assumed that all equipment listed is used. First, we measured control points with GPS. Then, we set up two tripods; one with a reflector, the second with the TotalStation 1105 and the third tripod with a 360 degree Prism. The locations around the buildings are known as Miho Control Point (MCP) 1, MCP 2 and MCP3 respectively. These points are designated markers for the project. They consist of a nail in the ground which indicates the center of the control point. In setting up the tripods, we have to make certain that the middle leg of the back sight tripod is on the center of the nail. An accurate way of centering the tripods is to adjust the bubble level to the center of a circle; this is located on the TotalStation. Then, we can measure the different corners of the buildings. Later, we will use the coordinates as data to import into the computer's database. Various tools were used to make the necessary measurements. The Allegro Field PC is an electronic device that stores the input data that is exported from the TCRA 1105 Plus [8].

The 1105 is known as a TotalStation. The TCRA Plus is robotic, which means it is programmed to create data that would aid in measuring the distance between each survey point as well as, building points. However, a data collector was used to compile all information gained from surveying. Also, I used a GPH1 reflector and 360

degree Prism were used to assist the TotalStation with sights to lower building corners that could not be seen or were difficult to measure. For the GIS, MicroStation and MicroStation Geographics programs were used for the graphical interface in addition, for the 3D drawings. Microsoft Access was the database used to store attributes data of the features (see Section 7).

RESULTS

Tables 1 and 2 illustrate the text data which are the survey point coordinates of each of the three buildings that were measured through surveying. The values indicate the coordinate position of corners of the buildings. Northeast (NE), Northwest (NW), Southeast (SE) and Southwest (SW) refer to the particular corner of each building; while T and B refer to the top or bottom position respectively (see Tables 1 & 2). In addition, the buildings' name is represented by B as the first part of the name. In Table 2, are survey points and the coordinate measurements for the control points. These are used to draw an accurate CAD drawing of the area. Table 3 displays GIS queries for thematic mapping and topology analysis. Thematic mapping categorizes feature types by various colors. Topology analysis examines relationships of features [9]. This project allowed three new buildings to be added to the growing AEG base map.

DISCUSSION and CONCLUSION

In order to design an efficient GIS, the first basic goal is to get accurate measurements (locations) of the buildings. By gaining this information it was vital to use surveying equipment, such as the TotalStation along with the reflector and 360 degree prism. Collecting this data was essential for setting the foundations in drawing a 3 dimensional picture. It was necessary that the coordinates and measurements be exact so that GIS topological queries will be accurate. Along with this, a key factor for creating a 3D version of data was the use of MicroStation TriForma.

With MicroStation TriForma, I was able to import data from the surveying equipment into the computer's database. As the information was received, survey points could be processed into making accurate positions to form the foundation of the buildings. I used existing GIS data from the Alignment Engineering Group's project known as AEGis. This allowed me to add my buildings to the existing database and map. The GIS also allowed me to post queries that in turn gave me the results required to relate the buildings to other results in the GIS. There were eight queries that were used and worked efficiently (see Table 3). The results of each query were represented by various colors. In Figure 2, an example of a query result for a thematic map including a legend. After the completion of the buildings in MicroStation TriForma, they were

added to the AEGis. There was no analysis that went wrong. The buildings are located southeast of the Computer Building (SCS) and west of the Cryogenics Laboratory. In conclusion, my purpose was to assist the Alignment Engineering Group to create a GIS that will, in the near future, store and use surveying data for measurements that will allow scientists to also use themselves.

REFERENCES

[1] P. Bolstad, GIS Fundamentals: A First Text on Geographic Information Systems, United States of America: Eider Press, 2002.

[2] MicroStation TriForma User's Guide, Bentley System, 1999.

[3] MicroStation Fundamentals Multi-Discipline Exercise Workbook, Orem, UT, Professional Software Solutions, Incorporated, 2004.

[4] W. Faig and H. Kahmen, Surveying, Berlin; New York: de Gruyter, 1988.

[5] K. Clarke, Getting Started with Geographic Information Systems 4th Ed., Upper Saddle River, NJ: Pearson Education, Incorporated, 2003.

[6] http://www-group.slac.stanford.edu/met/Align/GIS/AEGis_Report.pdf

[7] http://www-group.slac.stanford.edu/met/Align/GIS/GIS.html

[8] Private Communication: Michael Rogers, Surveyor with SLAC Alignment Engineering Group, 2007.

[9] M. Matias, B. Fuss and C. LeCocq, "SLAC MicroStation Geographics Study", Version 1.0, Menlo Park, CA: Stanford Linear Accelerator Center, 2007, pp. 4-15

ACKNOWLEDGEMENTS

This research was conducted at the Stanford Linear Accelerator Center. I would like to take this opportunity to give special thank you to Mr. Alonzo Baker for introducing me to the SULI Program, Mr. Brian Fuss, my mentor for all his hard work, dedication, and commitment to bettering my understanding of this project. Mrs. Miho Matias, for her patience, kindness as well as showing me the fundamentals of MicroStation TriForma and GIS. To Mrs. Catherine LeCocq, for allowing me to work within her group. The Alignment Engineering Group for all of their hospitality. To my fellow SLACERS, it was a pleasure meeting you and thanks for making me feel special. Lastly, the United States Department of Energy Office of Science for this amazing opportunity to participate in the SULI Program.

Tables

Building Name-Position	X Coordinate (m)	Y Coordinate (m)	Z Coordinate (m)
B281-NWB	1849256.7822	603143.7332	90.2950
B281-NEB	1849274.3111	603149.1609	90.2950
B281-SEB	1849276.4570	603142.1609	90.2950
B281-SWB	1849258.9281	603136.8031	90.2950
B281-NWT	1849256.7822	603143.7332	93.2127
B281-NET	1849274.3111	603149.1609	93.2127
B281-SET	1849276.4570	603142.2307	93.2127
B281-SWT	1849258.9281	603136.8031	93.2127
B282-SWB	1849262.9585	603123.7186	90.2828
B282-SEB	1849280.4913	603129.1299	90.2828
B282-NEB	1849278.3480	603136.0743	90.2828
B282-NWB	1849260.8152	603130.6631	90.2828
B282-SWT	1849262.9585	603123.7186	93.2160
B282-SET	1849280.4913	603129.1299	93.2160
B282-NET	1849278.3480	603136.0743	93.2160
B282-NWT	1849260.8152	603130.6631	93.2160
B283-NWB	1849276.2989	603149.7645	89.6423
B283-SWB	1849281.7995	603132.3070	89.6423
B283-SEB	1849292.1681	603135.5740	89.6423
B283-NEB	1849286.6675	603153.0315	89.6423
B283-NWT	1849276.2989	603149.7645	92.8623
B283-SWT	1849281.7995	603132.3070	92.8623
B283-SET	1849292.1681	603135.5740	92.8623
B283-NET	1849286.6675	603153.0315	92.8623

Table 1 Surveying points of angle/position measurements of buildings.

Survey Points Name	X Coordinate (m)	Y Coordinate (m)	Z Coordinate(m)
MCP1	1849279.488	603161.261	88.989
MCP2	1849305.078	603157.163	88.525
MCP3	1849256.949	603133.204	89.799
MCP4	1849245.151	603149.309	89.985
MCP5	1849295.372	603122.043	92.645
MCP6	1849264.333	603115.563	92.669

Table 2. Indicates survey control point's coordinates in meters on the XYZ scale.

List of GIS Queries
1. SELECT * FROM BUILDINGS WHERE Type = 'Office'
2. SELECT * FROM BUILDINGS WHERE Type = 'Laboratory'
3. SELECT * FROM BUILDINGS WHERE Type = 'Service'
4. SELECT * FROM BUILDINGS WHERE Type = 'Fire Station'
5. SELECT * FROM BUILDINGS WHERE Type = 'Utility'
6. SELECT * FROM BUILDINGS WHERE Type = 'Utility'
7. SELECT * FROM BUILDINGS WHERE Type = 'Gate'
8. SELECT * FROM BUILDINGS WHERE Type = 'Cooling Tower'

Table 3. Queries used in the GIS portion of this project.

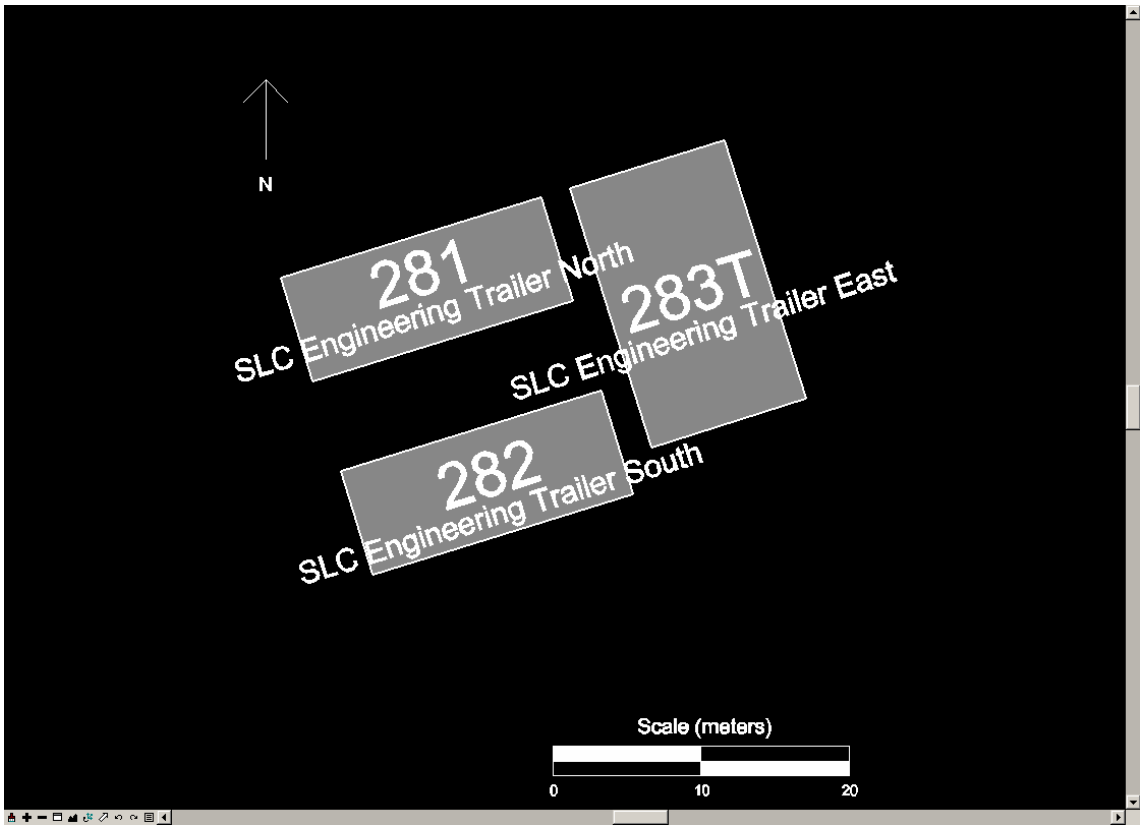

Figure 1. Query results of building type = “offices”**.**

Figure 2. Query result showing a thematic map of various building types.

SLAC-TN-07-022

Characterizing the Noise Performance of the K*PiX* ASIC Readout Chip

Jerome Kyrias Carman

Office of Science, Science Undergraduate Laboratory Internship (SULI)

Cabrillo College

Stanford Linear Accelerator Center

Stanford, CA

August 28, 2007

Prepared in partial fulfillment of the requirements of the Office of Science, Department of Energy's Science Undergraduate Laboratory Internship under the direction of Timothy Knight Nelson at the Stanford Linear Accelerator Center.

Participant: _____

Signature

Research Advisor: _____

Signature

Work supported in part by US Department of Energy contract DE-AC02-76SF00515

ABSTRACT

Characterizing the Noise Performance of the K*PiX* ASIC Readout Chip. JEROME KYRIAS CARMAN (Cabrillo College, Aptos, CA 95062) TIMOTHY KNIGHT NELSON (Stanford Linear Accelerator Center, Stanford, CA 94025)

K*PiX* is a prototype front-end readout chip designed for the Silicon Detector Design Concept for the International Linear Collider (ILC). It is targeted at readout of the outer tracker and the silicon-tungsten calorimeter and is under consideration for the hadronic calorimeter and muon systems. This chip takes advantage of the ILC timing structure by implementing pulsed-power operation to reduce power and cooling requirements and buffered readout to minimize material. Successful implementation of this chip requires optimal noise performance, of which there are two measures. The first is the noise on the output signal, previously measured at $1500e^-$, which is much larger than the anticipated $500e^-$. The other is the noise on the trigger logic branch, which determines where thresholds must be set in order to eliminate noise hits, thus defining the smallest signals to which the chip can be sensitive. A test procedure has been developed to measure the noise in the trigger branch by scanning across the pedestal in trigger threshold and taking self-triggered data to measure the accept rate at each threshold. This technique measures the integral of the pedestal shape. Shifts in the pedestal mean from injection of known calibration charges are used to normalize the distribution in units of charge. The shape of the pedestal is fit well by a Gaussian, the width of which is determined to be $2480e^-$, far in excess of the expected noise. The variation of the noise as a function of several key parameters was studied, but no significant source has been clearly isolated. However, several problems have been identified that are being addressed or are under further investigation. Meanwhile, the techniques developed here will be critical in ultimately verifying the performance goals of the K*PiX* chip.

INTRODUCTION

The proposed International Linear Collider (ILC), in contrast to the Large Hadron Collider (LHC), presents a benign environment for detector components since e^+e^- collisions produce events with relatively few background processes resulting in a much lower data rate and a mild radiation environment. This feature allows for the study of many processes that are buried underneath vast amounts of data produced in hadronic collisions, enabling detailed investigations of the Higgs sector and any new physics such as supersymmetry or extra dimensions that may be revealed by the LHC. While this optimal environment, combined with the high energies of ILC, presents an enticing opportunity for the study of rare high energy physics events, delivering on this promise presents numerous detector design challenges. In particular, detector performance requirements include precise momentum resolution for charged tracks and successful implementation of the "particle flow" calorimetry concept[1] via a highly granular calorimeter design.

Currently there are four proposed detector designs[1], one of which is referred to as the Silicon Detector (SiD) Concept. This concept utilizes all-silicon tracking, a silicon-tungsten electromagnetic calorimeter, and a single 5T solenoid (see Figure 1). A silicon sensor readout chip called KPiX is currently being developed for use in the outer tracker and the silicon-tungsten calorimeter. This device is also being considered for use in the hadronic calorimeter and the muon system. KPiX utilizes a number of state-of-the-art ideas to accommodate ILC physics requirements.

A key feature of the ILC is that e^- and e^+ beams are delivered in 1ms "trains" consisting of 2652 particle bunches, with each bunch separated by 369ns. These trains are repeated at a rate of 5Hz providing 199ms of quiet time between trains. This feature allows a "pulsed power" [2] concept which only runs the analog components of the KPiX chip during each train. Successful implementation of pulsed power operation reduces power consumption

by two orders of magnitude compared with continuous readout. This allows a simpler air cooled design and significant material reduction in comparison to liquid cooled detectors. Meanwhile, the low cross-section for e^+e^- collisions at the ILC results in very low per-channel occupancies in the outer detectors. Therefore, a small number of readout buffers per channel are capable of holding all data generated by all collisions in each bunch train. Implementation of buffered readout in K*PiX* via storage of signals in four bunch-tagged analog buffers followed by digitization and readout between trains results in further simplification. This is because lack of noise from digitization and readout during the trains allows the chip to be bump-bonded directly to the face of an active sensor, eliminating additional material usually required to isolate the sensor from the readout chip.

The K*PiX* chip is in an early prototyping phase and much testing and debugging remains [2] in order to understand its behavior and refine the design to achieve optimal performance. This paper presents an analysis of the analog front end of prototype version 4 of the K*PiX* chip. There are many features which work in concert to balance the need for high bandwidth during acquisition with the requirement of low noise occupancy in the storage buffers. In particular, the threshold trigger logic is critical to this task as it is responsible for selecting signals and rejecting noise. The studies presented characterize the noise in the trigger branch through a carefully designed test procedure and attempt to isolate noise sources by studying its dependence on key parameters.

MATERIALS AND METHODS

The K*PiX Chip*

K*PiX* is a multi-channel readout chip designed to amplify, shape, buffer, and digitize input signals from a silicon sensor. Each individual channel consists of an analog block connected to a digital block, both of which communicate through an address register block. The main

components of the analog section consist of a transconductance amplifier, a signal pulse shaper, reset and trigger logic, and four capacitive storage buffers. In the digital section, the signals in the analog buffers are converted to digital values via a Wilkinson analog-to-digital converter (ADC) and are read out through differential low-voltage digital signal lines. The trigger branch, which decides which events to store in the buffers, is of particular interest here as it must be optimized to provide high efficiency for real signals while minimizing the probability of storing noise hits throughout an entire bunch train. Since the expected event signals are quite small, typically 22,000e^-, and may be distributed across two or more channels, the noise at the trigger stage must be low in order to efficiently select them without storing random noise during the long (1ms) acquisition cycle.

In order to accurately calibrate the K*PiX* chip a set of four 200fF calibration capacitors are integrated on-chip to inject signals of known charge. A digital-to-analog converter (DAC) applies a known voltage to these capacitors according to a digital input value, therefore storing a known charge which is placed on the input of a specified channel at a specified time. This feature is crucial for calibrating the charge corresponding to both an output ADC count and a trigger threshold DAC step.

To minimize charge buildup within the analog circuitry the K*PiX* includes a periodic channel reset. The threshold trigger logic consists of a pre-trigger discriminator designed to delay the onset of the channel reset in order to allow the pulse shaper enough time to build a possible signal. Since a reduced shaper bandwidth generally results in an improved signal-to-noise ratio (S/N), the pre-trigger attempts to balance a high acquisition rate with a long integration time. In practice the pre-trigger threshold value should be set somewhere between the noise pedestal and the trigger threshold. If a signal reaches the pre-trigger threshold value, channel reset is delayed and the signal is given a chance to reach the trigger threshold value, in which case the signal is stored.

The charge amplifier of the K*PiX* chip can amplify a signal via three different gain

modes. Low gain utilizes a 10pF feedback capacitor, normal gain a 400fF feedback capacitor, and double gain a pair of 400fF capacitors. The intention is to use normal gain to allow sufficient amplification of low charge signals from minimum ionizing particles (MIPs), with logic included to automatically switch to low gain when the signal is large enough to approach ADC saturation as will be the case for large showers in the silicon-tungsten calorimeter. Double-gain mode reduces noise due to reference voltage fluctuations on the chip for best performance with small signals, as will be the case in the tracker. An additional amplifier is included which, when enabled, inverts the voltage polarity of the inputs. The purpose of this is to allow for readout of different types of sensors, such as the gas electron multipliers (GEMs) being considered for the SiD HCal. This amplifier also features twice the gain of the normal gain mode of the primary amplifier.

In all tests a silicon sensor is wire-bonded to the K*PiX* chip which is attached to a daughter board (see Figure 2) connected to version 2 of a K*PiX* test board. This test board is connected via USB to a computer from which various programs are used to operate the chip and process the data collected. The K*PiX* chip, daughter board and test board are located inside an aluminum box which both acts as a Faraday cage and keeps the sensor optically isolated. Analog and digital voltages (AVDD and DVDD) are both set at 2.5V which is provided by regulators operating from an external Power Designs TP340 power supply set at 7.5V. Eight 9V batteries supply a noise-free 72V bias to the silicon strip sensor.

Analysis Software

A program called `thresh_scan` was developed to scan K*PiX* over a range of trigger and pre-trigger threshold values to allow the measurement of the trigger accept rate at each threshold. Data is taken without calibration charge injected in order to measure the bare pedestal, and with various calibration pulses of known charge in order to establish the charge equivalence of the threshold values. Calibration pulses are chosen to be close to the upper tail of the bare

pedestal to minimize uncertainties due to possible non-linearities in the calibration pulses or threshold settings. All tests look at a single channel, usually channel 0, since the K*PiX* bus traces leading to this channel are the least likely to be susceptible to cross talk from other channels because of their physical location.

This program utilizes the timing sequence shown in Figure 3 by repeating the sequence numerous times at each threshold to minimize statistical errors. The two significant bunch crossing times referred to in most tests are shown; bunch crossing 1254 and 2564. These times correlate to a delay of four bunch crossings after the threshold trigger logic enable time of 1250 where the bare pedestal is measured, and a delay of four bunch crossings after the calibration strobe injection time of 2560. The delay between action and sample time is expected and these choices of bunch number are largely arbitrary.

A number of programs were developed to analyze the data generated by the `thresh_scan` program. The `thresh_scan_plot` program is used to observe the general location of the noise and calibration pulse pedestals in threshold DAC steps. The `thresh_stime_hist` program is used to display a histogram of trigger times which spans the length of a single bunch train to help identify the correct timing for the threshold scan. The recorded samples are plotted with respect to the specific bunch crossing at which they occur. Figure 4 shows an example.

The key piece of analysis software is the `thresh_stime_plot` program which plots the accept rate of the trigger as a function of threshold. For the bare pedestal, the rate at which samples appear in the first buffer at time 1254 is plotted as a function of threshold. The resulting s-shaped curve is the integral of the bare pedestal, the width of which is a measurement of the critical noise in the trigger branch. This plot is divided by the total number of samples taken at each threshold in order to calculate the fraction of the pedestal that lies above a given threshold. The errors on these fractions are calculated according to Bayesian binomial errors which are asymmetric near zero and one. Errors associated with threshold DAC values are set to zero as these are discrete voltage values and ideally have

no uncertainty. Using the MINUIT fitting package, the Gaussian cumulative distribution function is fitted to the data to extract the associated mean and one-standard-deviation errors. To express the noise in terms of equivalent noise charge (ENC) the plot at bunch crossing 2564 is considered for multiple calibration charges. The relative shift in the mean value of the resulting s-curves correspond to a single DAC step in the calibration pulse (see Figure 5). Since the charge of a calibration pulse is known, a plot of the mean threshold value as a function of charge can be made (see Figure 8), the slope of which is used to convert threshold DAC steps into units of charge.

To compare the noise at the trigger branch with that from the ADC, the `calib_dist` program is used. Noise is measured by repetitively injecting the same calibration pulse voltage and force triggering the chip to store the resulting distribution, the width of which measures the noise. The ADC gain is measured by injecting a range of known calibration pulses. The `calib_dist_plot` program utilizes this data to plot the ADC gain as function ADC counts versus charge. The noise is plotted as the distribution of samples versus ADC counts.

RESULTS

The noise of the bare pedestal and the threshold DAC gain are measured in normal gain mode with the pre-trigger function disabled by setting it equal to the trigger threshold at each step. The Gaussian cumulative distribution function fits the data well as shown in Figure 6. Taken together with the threshold gain in DAC/fC shown in Figure 8, the one-sigma noise is $2480e^-$ as summarized in Table 1. For comparison, the noise at the ADC is estimated to be $1500e^-$ from the forced-trigger distribution shown in Figure 7, with ADC counts converted to charge using the gain curve of Figure 9. All results are for channel 0, but are typical for other channels.

These measurements are repeated in several different configurations in an attempt to understand the noise sources as summarized in Table 1. First, the noise is measured with the inverted amplifier enabled to compare the noise when the gain of the amplifier is doubled. This results in a noise measurement of $4680e^-$. Second, the noise is measured with the channel reset disabled, since recent literature suggests that a periodic reset may be a significant noise source in such designs [3]. The periodic reset is disabled by setting the pre-trigger threshold significantly below the bare pedestal. The threshold trigger enable time is decreased to bunch crossing 50 and the calibration strobe is injected at bunch crossing 56 to avoid charge buildup due to lack of reset from affecting the results. The magnitude of the measured noise reveals a slight relative increase to 1.056 threshold DAC steps. However, this result is somewhat inconclusive since the chip refused to trigger on the calibration pulses and the measurement of threshold gain could not be verified. The reason for this is not known.

An additional experiment looks at the affect of lowering the analog and digital voltage from 2.5V to 1.8V. A different K*PiX* chip, running at lower voltage and without an attached sensor, was used and found to have a noise of $1170e^-$ as shown in Table 1. The sensor, with a capacitance of less than 10 pF, should not significantly change the chip behavior, but results are inconclusive since this chip was found to be damaged while attempting to run at 2.5V as a cross-check.

Another test investigates a longer shaper differentiation time, which is accomplished by changing the shaper bias with a 100MΩ resistor on the test board. This test resulted in very similar noise behavior, as shown in Table 1. However, the measured gain, which should have changed significantly due to this modification, remained the same contrary to expectation.

DISCUSSION AND CONCLUSIONS

The expected noise from the ADC for the configuration under test is less than $500e^-$ and the noise in the trigger branch should be similar. While the $1500e^-$ noise measurement from the ADC motivated the investigation of the trigger branch, the fact that the noise there is much larger still, $2480e^-$, is surprising since it was thought that the ADC itself was responsible. Instead, it appears there is at least one unexpected source of noise. Since uncorrelated noise adds in quadrature, these sources dominate the overall noise performance. The first significant result is therefore the fact that the shape of the pedestal is accurately represented by a Gaussian distribution, indicating that these unknown sources are random rather than systematic.

One possibility that would affect both the ADC output and the trigger branch is that the noise performance of the front-end amplifier driving both is much worse than expected. In this case, the factor-of-two gain change from operating in inverted mode would not alter the noise measurement. Another possibility is that there are fluctuations in the voltage references for the trigger threshold and the Wilkinson ADC, which would reduce the apparent noise in electrons by a factor of two in inverted mode. Thus, the result showing that the noise in inverted mode is larger, $4680e^-$, is puzzling and may indicate an additional problem with the inverted amplifier. Another method for performing this test was attempted utilizing the double gain feature of the primary amplifier to eliminate the inverter from the signal path. However, the double gain feature proved to be unstable in the current K*PiX* version. This test is a clear priority for future revisions of the chip.

Analysis of the affect of the periodic channel reset was inconclusive. While the noise measurement of 1.056 threshold DAC steps is similar and therefore inspires confidence in the channel reset design, the lack of a successful calibration measurement casts doubt on this result, since the chip was not designed to be operated in this mode. Further investigation is

required to understand the underlying cause of this behavior and fully eliminate the periodic reset as a noise source.

Interestingly, results of the AVDD and DVDD voltage settings of 1.8V, in addition to the different shaper bias results, while both inconclusive, may indicate issues with the pulse shaper. Given the significant role of the shaper in determining the performance of the trigger branch, development of additional tests to isolate shaper characteristics may well lead to answers to some of the questions raised here. Meanwhile, significant revisions to the operation of the shaper are being planned to eliminate possible issues that may relate to these observations.

Results of this project indicate that the noise performance of the trigger branch of the current K*PiX* prototype is insufficient for its primary mission in readout of the Si-W calorimeter and outer tracker of the SiD detector, since it will not be possible to trigger on minimum ionizing signals from the silicon sensors without accepting noise hits at a rate that will fill the readout buffers. This is a key result and indicates the need to further study the problem until a solution is found. Additional tests have established no clear evidence of noise produced by any of the expected sources, so an explanation of the characteristic noise of $2500e^-$ remains unresolved. Comparisons with data taken on a similar test setup at the University of Oregon have been generally consistent when analyzed with these methods. It is anticipated that the techniques developed here will be vital in continued efforts to isolate these issues and to establish that adequate performance has been achieved by future revisions of the K*PiX* chip, the next generation of which is currently in production.

ACKNOWLEDGMENTS

I would like to thank the U.S Department of Energy for sponsoring my stay at the Stanford Linear Accelerator Center through the Summer Undergraduate Laboratory Internship pro-

gram. I would like to thank my mentor, Timothy Knight Nelson, who was extremely helpful, patient and encouraging throughout my internship. Many thanks to Ryan Herbst for providing the equipment and software required for these experiments, and for answering my many questions. Dietrich Freytag was also a wonderful help through his invaluable insights and suggestions. I would also like to thank the K*PiX* group including Martin Breidenbach and David Strom for including me in the many discussions and meetings that occurred during my internship, and the SiD group including Richard Partridge for providing a broader scope of how the K*PiX* technology fits in with the detector concept. Lastly, I would like to thank Michael Woods, Stephen Rock, and Farah Rahbar for organizing the many wonderful lectures, tours, and unique informal discussions which made my stay at SLAC an invaluable experience.

REFERENCES

[1] International Linear Collider Global Design Effort and World Wide Study Groups, "International Linear Collider Reference Design Report: Volume 4, Detectors," August 2007. [Online]. Available: http://www.desy.de/~behnke/dcr/Detector/DCR.pdf

[2] SiD Tracking Group, "Sid Tracker R&D Report," pp. 26–28. [Online]. Available: http://0-www-sid.slac.stanford.edu.ilsprod.lib.neu.edu/Documents/Tracking_review.pdf

[3] A. E. Gamal and H.-S. P. Wong, Private Communication.

FIGURES

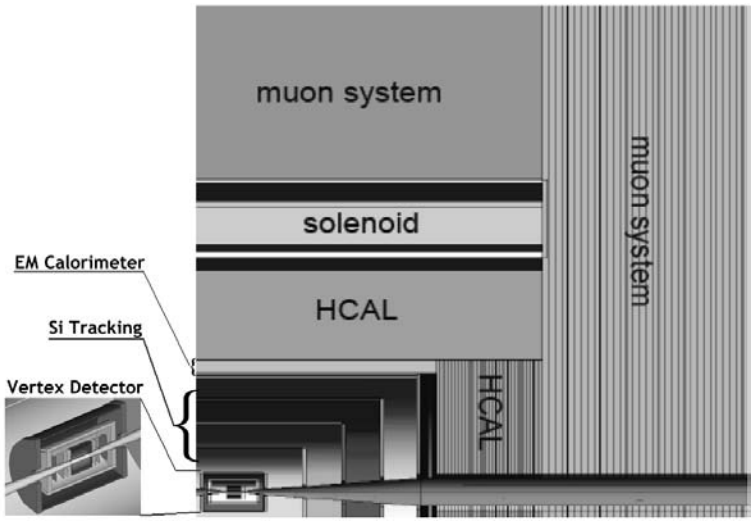

Figure 1: Cross section of the SiD detector design. Use of the K*PiX* chip for readout is planned or under consideration for every detector component shown except for the vertex detector.

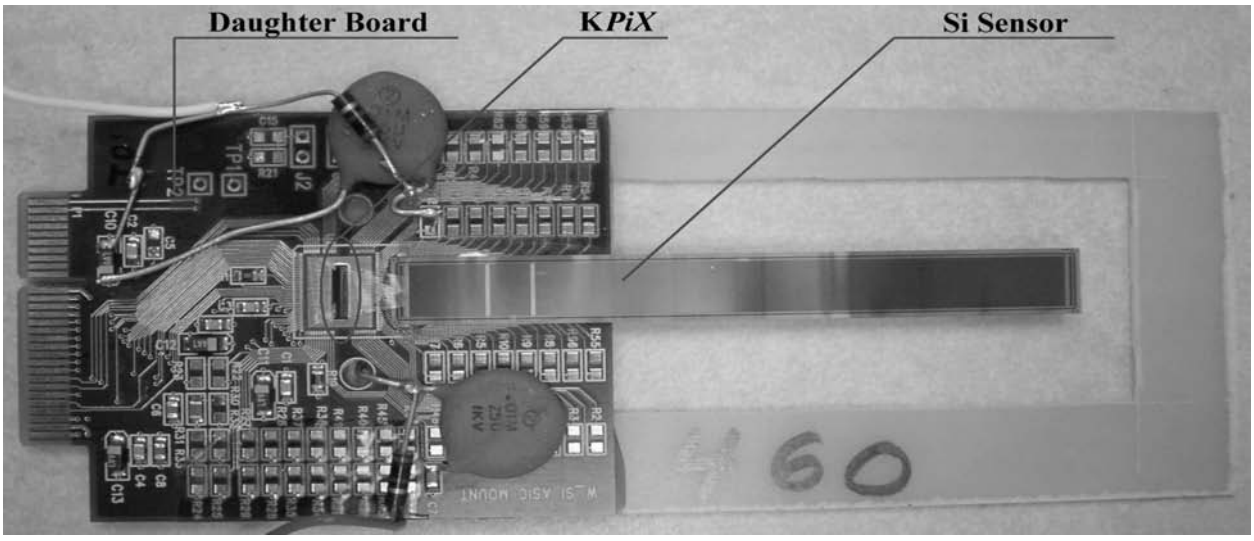

Figure 2: Image of a 64-channel K*PiX* mounted to a daughter board and wire-bonded to a spare silicon microstrip sensor from CDF Layer 00.

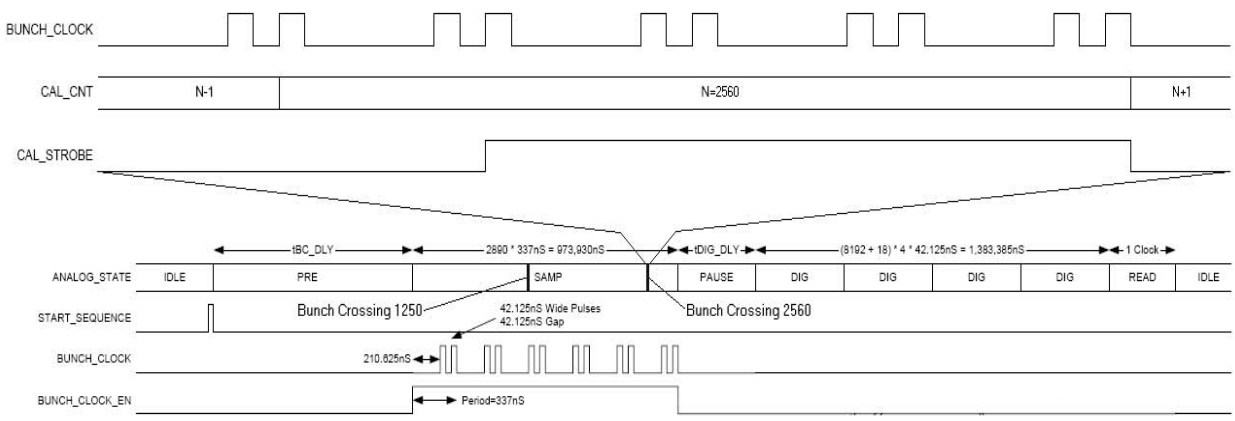

Figure 3: The K*PiX* analog timing sequence with a detailed schematic of a calibration pulse. Shown are the trigger threshold logic enable time of bunch crossing 1250, and the calibration pulse injection time of 2560.

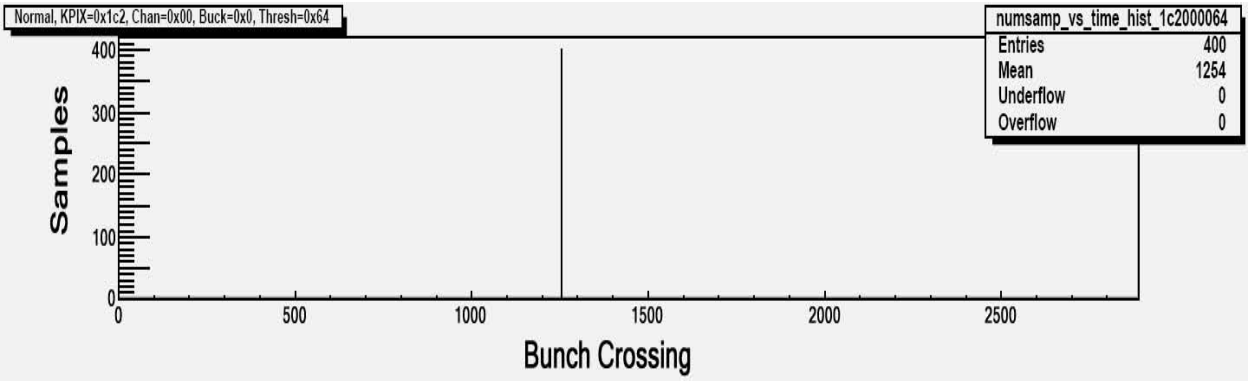

Figure 4: Time line plot in bunch crossings at a particular threshold value for one test iteration. This shows the time at which samples were stored in the first buffer for channel 0. At low thresholds, all samples are noise hits, which occur four bunch crossings after the trigger logic is enabled.

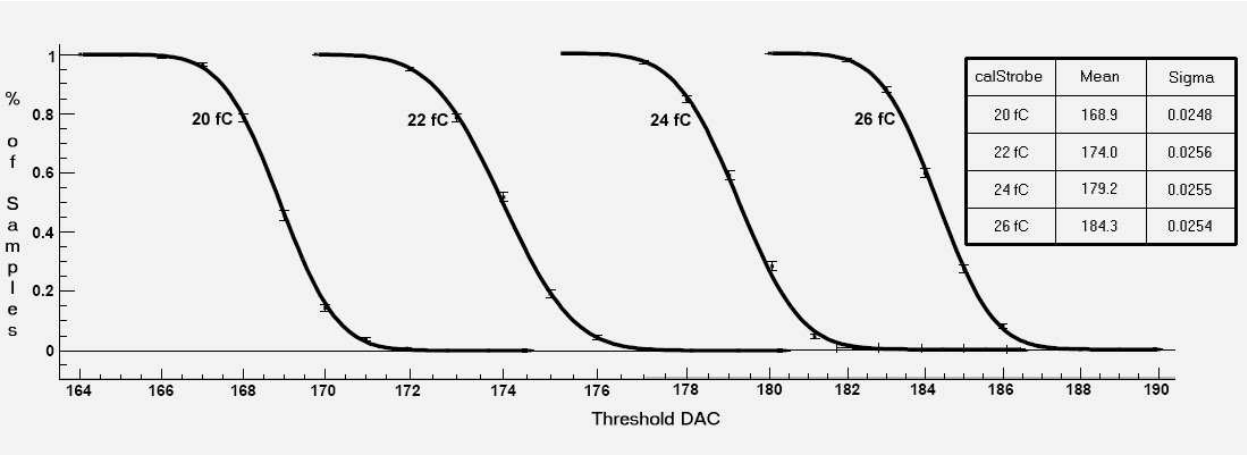

Figure 5: Plot of pedestal shifts in threshold with increasing calibration charge. The shifts are used to calibrate the charge corresponding to a threshold DAC step.

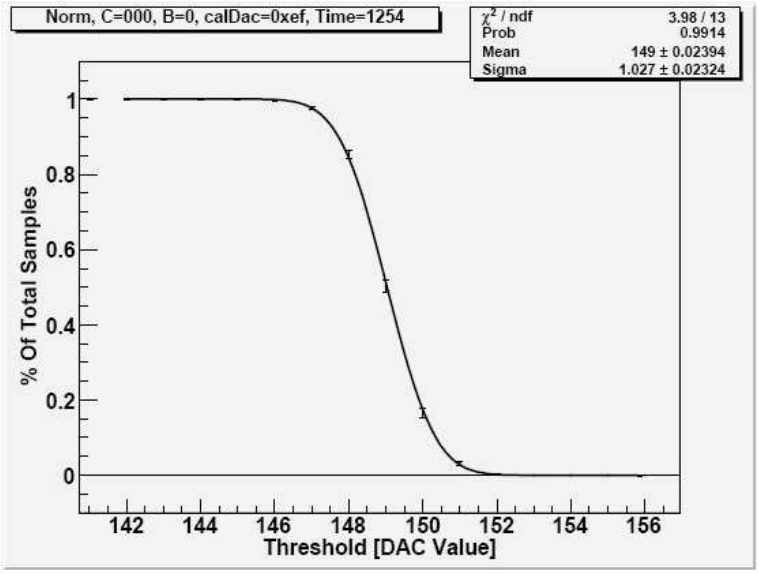

Figure 6: Noise measurement in threshold DAC steps at the trigger threshold logic in positive polarity mode for channel 0. Sigma is the one standard deviation noise, and the mean is the mean value of the pedestal.

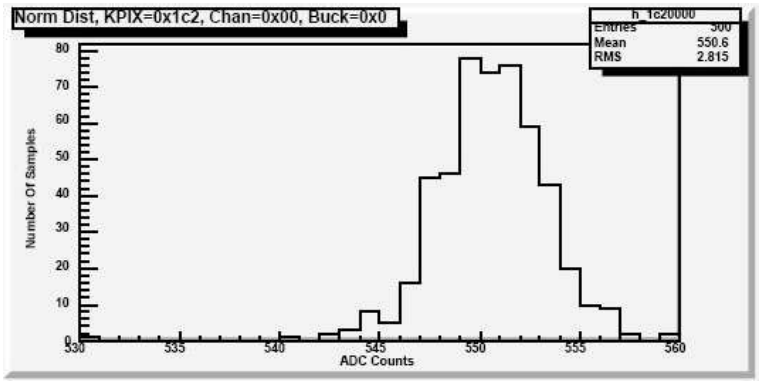

Figure 7: Noise measurement in ADC counts at the ADC for positive polarity mode for channel 0. RMS value is the one standard deviation noise, and the mean is the mean value of the pedestal.

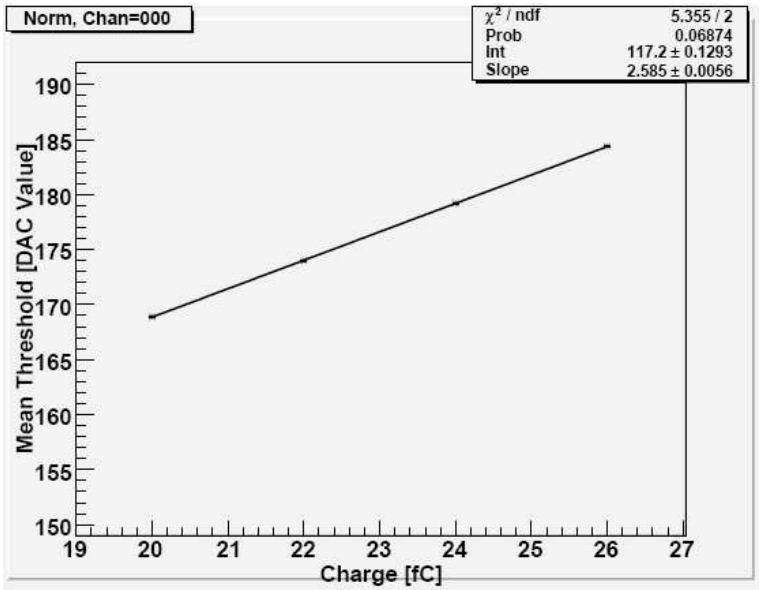

Figure 8: Results of a threshold DAC calibration test. The slope is the conversion factor from threshold DAC counts to calibration DAC counts, which are of known charge.

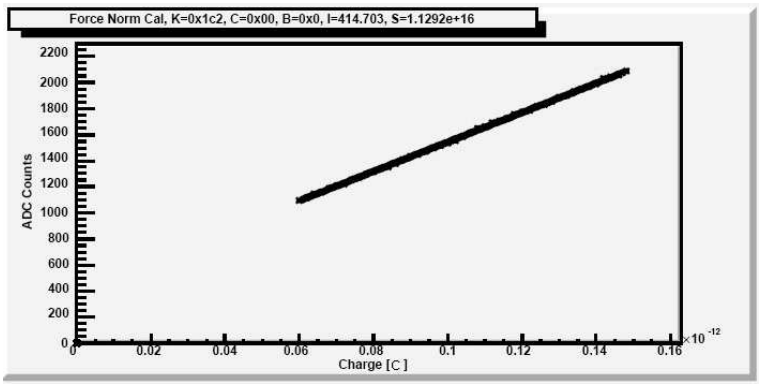

Figure 9: Results of an ADC count calibration test. The slope is the conversion factor from ADC counts to calibration DAC counts, which are of known charge.

TABLES

Experiment	1σ [DAC]	Gain [DAC/fC]	Noise [e^-]
Baseline Measurement	1.027 ± 0.023	2.585 ± 0.006	2480 ± 55.8
Inverted Amplifier	2.919 ± 0.039	3.894 ± 0.008	4680 ± 63.2
Periodic Reset	1.056 ± 0.036	Not Measured	≈2500 (using gain of 2.585)
1.8V AVDD and DVDD	0.610 ± 0.024	3.242 ± 0.008	1170 ± 46.3
100MΩ Shaper Bias	1.102 ± 0.120	2.528 ± 0.047	2720 ± 301

Table 1: Summary of noise and gain results at the trigger branch.

SLAC-TN-07-012
August 2007

Characterizing surface layers in Nitinol using x-ray photoelectron spectroscopy

Rebecca Christopfel

Office of Science, Science Undergraduate Laboratory Internship (SULI)

Western Washington University

Stanford Linear Accelerator Center

Menlo Park, CA

August 17, 2007

Prepared in partial fulfillment of the requirements of the Office of Science, U.S. Department of Energy Science Undergraduate Laboratory Internship (SULI) Program under the direction of Dr. Apurva Mehta at Stanford Synchrotron Radiation Laboratory (SSRL) Stanford Linear Accelerator Center

Participant: _____
Signature

Research Advisor: _____
Signature

Work supported in part by US Department of Energy contract DE-AC02-76SF00515

Table of Contents

ABSTRACT

Characterizing surface layers in Nitinol using x-ray photoelectron spectroscopy. REBECCA CHRISTOPFEL (Western Washington University, Bellingham WA 98225) APURVA MEHTA (Stanford Linear Accelerator Center, SSRL, Menlo Park, CA 94025).

Nitinol is a shape memory alloy whose properties allow for large reversible deformations and a return to its original geometry. This nickel-titanium alloy has become a material used widely in the biomedical field as a stent to open up collapsed arteries. Both ambient and biological conditions cause surface oxidation in these devices which in turn changes its biocompatibility. Depending on the type and abundance of the chemical species on or near the surface, highly toxic metal ions can leak into the body causing cell damage or even cell death. Thus, biocompatibility of such devices is crucial. By using highly surface sensitive x-ray photoelectron spectroscopy to probe the surface of these structures, it is possible to decipher both layer composition and layer thickness. Two different samples, both of which were mechanically polished with one then exposed to a phosphate buffered saline solution to mimic the chemical properties of blood, were investigated. It was found that the latter sample had a slightly thicker oxide layer and more significantly a phosphate layer very near the surface suggesting toxic metal components are well contained within the sample. These are considerable indications of a biocompatible device.

INTRODUCTION

The equiatomic nickel-titanium alloy (Nitinol) is an advanced material which is finding more and more use as a biomedical device. It is critical from a medical perspective that a foreign body implant is biocompatible. Understanding the nature of the surface oxide layers on these devices helps determine the biocompatibility and thus the usability of such materials. Biocompatibility is “the ability of a material to perform with an appropriate host response in a specific application” [1]. A device under investigation is tested both *in vitro*

and *in vivo* to examine the degree of toxicity of the devices to cells of the material. Materials that are not biocompatible induce many complications in the body. Specifically, corrosion of metals can create toxic metal ions inducing cell death [2]. In the case of Nitinol, nickel and nickel compounds are the components that are at the center of toxicity concerns.

In this experiment the NiTi alloy being tested is used to manufacture stents to be placed in the human body to open collapsed arteries. Several different alloys whose production processes vary are being tested to better understand the surface oxidation that occurs and what affects said events can have when implanted.

By probing the surface of these metallic structures we can determine the composition e.g. the abundance of titanium vs. titanium oxide and nickel vs. nickel oxide. The technique used is x-ray photoelectron spectroscopy (XPS), which involves irradiating a material with x-rays while measuring the kinetic energy and number of emitted photoelectrons. The binding energy of the core electron is then determined as the difference of the incident x-ray energy and the kinetic energy of the photoelectron. Analyzing the position and intensity of peaks allows determination of the amount of different chemical species in the material. Escape depth of electrons from a material is very small ~1-2 nm and is strongly dependant on the kinetic energy, therefore by either varying the energy of the incident photon (and thus the kinetic energy) and/or changing the angle of incidence, we can determine the location of the identified species as a function of depth from the surface. We will use these techniques to understand the character of the oxidation/corrosion layer on NiTi when exposed to different chemical environments including a liquid that mimics the chemical properties of blood.

MATERIAL AND METHODS

The samples of interest in this experiment include two different Nitinol substrates. Nitinol is a shape memory alloy, SMA, in that it remembers its geometry. Assuming it

undergoes some deformation from its original crystalline structure, it has the ability to regain its original geometry when heated or cooled. The property that enables such processes is the superelasticity of a material, i.e. the amount of strain a material can handle before the atomic structure is permanently altered.

Both samples were mechanically polished, a process that strips away surface materials. Each of the samples were polished with 320, 400, 600, 800, and 1200 grit alumina paper. This was followed by cleaning with acetone (10 min), and then distilled water (10 min) in an ultrasonically agitated bath [3]. One of the samples was then soaked in a Phosphate-buffered saline solution that consists of 0.154 M NaCl, 0.0003 M Na_2HPO_4 and 0.004 M KH_2PO_4 (pH 7.4), and PBS with an addition of 0.0013 M $CaCl_2$ [4]. This solution acts as a liquid that mimics the chemical properties of blood, enabling a determination of the biocompatibility of such devices.

Measurements were carried out at beam line 5-1 at SSRL. The end-station is equipped with two interconnecting UHV chambers with operation pressure in the low 10^{-11} Torr range. One chamber is dedicated to surface preparation and contains an ion gun for ample sputtering, mass spectrometer for residual gas analysis and thermal desorption spectroscopy (TDS), pulsed gas dosing system and LEED-optics. The other chamber, dedicated to core level spectroscopies, houses a hemispherical SES-100 electron analyzer (VG-Scienta) and a multi-channel plate partial electron yield detector as well as a collimated beam gas-doser regulated by the backing pressure at the backside of an array of multi-channel plates.

The sample rod allows for mounting of several different samples at the same time, both mounted to have a grazing incident angle of the photon beam to the sample of about 5° or less. The sample rod can be rotated around the photon beam axis allowing for variation of the escape angle of the electron and therefore variation of escape depth. The manipulator onto

which the sample rod is attached is equipped with computer controlled stepper motors for easy alignment in the spectroscopy chamber, sample scanning procedures and transport between the two chambers [3].

Samples were irradiated with x-rays at a known energy of approximately 1100 eV. The detector and sample orientation was varied to provide information about the structure and chemistry of the sample, namely depthos the various surface structures and chemical species. The rod and affixed sample was rotated such that the detector was at 0, 18, 48, 60 and 70 degrees from the surface normal of the sample.

An overview scan was taken at the beginning of each of the detector/sample orientations to ensure an appropriate scan range of the different species. Depending on the resolution of the spectrum, each energy range was swept by the x-ray beam for a certain number of frames, whereby the length of the sample is scanned by the beam, and the intensity of each spectra are summed. Intensities and corresponding kinetic energies are recorded. (Figure 1).

RESULTS ANS DISCUSSION

To come up with a physical model of the speciation and location of said species that exist on the surface of Nitinol, a theoretical model is first called upon. To excite core electrons sufficient incident energy is required. The intensity of photoelectrons collected by the detector than becomes a function of this incident photon flux and combination of parameters associated with the irradiated material as well as the detector position and geometry. Thus, an equation for number of counts for a given layer of finite thickness is given by

$$S(\alpha,\beta) = I_{\circ}[e^{-\frac{\mu d}{\cos\beta}}(\frac{h}{\cos\beta})Df\,]e^{-\frac{d}{\lambda\cos\alpha}}St \qquad (1)$$

Where α = angle of detector with respect to surface normal of sample, β = angle of incident x-ray, $I_\circ$ = intensity , μ_x = property of incident x-ray traveling through material which depends on energy of photon and material, d = depth, h = width of area probed by x-ray, D = concentration of species, f = rate at which electrons are ejected from sample (cross section), λ = function of material that depends on KE of electron and material in which it propagates, S = detector geometry and t = time.

Under some constraints and by making some assumptions [6], a signal to signal ratio of peaks whose energies are very close allows for elimination of many of the unknowns and can provide a qualitative model of the structure by locating surface and near surface layers with respect to one another.

$$\frac{S^1}{S^2} = Ce^{-\frac{1}{\lambda\cos\alpha}(d_1-d_2)} \qquad (2)$$

where C is a collection of constants and parameters whose values do not depend on detector angle α while d_1 and d_2 are depths of a certain species from the surface of the sample. By taking the natural log of Eq. (2) we get a linear relationship where the natural log of the signal ratio depends on inverse $\cos\alpha$.

$$\ln\left(\frac{S^1}{S^2}\right) = \ln(C) - \frac{1}{\cos\alpha}\left(\frac{d_1 - d_2}{\lambda}\right) \qquad (3)$$

The line has a y-intercept equal to $\ln(C)$ and a slope equal to -$\left(\frac{d_1 - d_2}{\lambda}\right)$. Thus, when the natural log of the signal ratio is plotted against inverse $\cos\alpha$, the length $d_1 - d_2$ can be calculated and the distance between two different species in a sample is estimated. The value for λ, the inelastic mean free path of electrons in a sample, is known and assumed to be the same for species whose energies are very close. A large positive slope implies that the depth of species relative to the surface species is very deep, while a small positive slope implies a

species closer to the reference species, but still below it. A negative slope implies a species above the reference. If we pick a reference species, say alumina, which we assume is remnant from the mechanical polishing and therefore very near the surface and determine the depth of the other layers with respect to that, we can get a reasonable picture of the composition of surface layers.

The signal is determined by finding the area under the peaks of a given spectra. Theory tells us that purely metallic peaks occur at lower binding energies and will therefore have higher kinetic energies. Oxidized peaks, whose valence electrons are paired with an oxygen molecule, have more tightly bound core electrons and thus a higher binding energy. The peaks were fit with a series of curves which had a small and fixed amount of Lorentzian component and a large variable Gaussian component. See Figure 1. The widths, energies and areas under the various peaks for the samples listed in a certain energy range are listed in Table 1. Our data shows multiple peaks for a given core level and therefore imply surface layers contain species with various oxidation levels, including the stable oxidation states of titanium oxide, TiO_2 and nickel oxide, NiO, as well as partially oxidized Ni peaks. The number of peaks becomes evident in the fitting process; however the identification of all peaks has not been possible, and further investigation and an alternative experimental approach is needed for completion. To come up with helpful information regarding the structure of these two samples, specific signal to signal ratios were taken, metallic peak to a sum of the oxidized peaks—or more generally, a reference peak to a series of other peaks, at multiple angles. See Figures 2 and 4 and Table 2. Lines are fit to the data points and structural information about the composition of the mechanically polished sample and the mechanically polished sample exposed to the PBS solution is revealed. Comparisons between samples can then be made. See Figures 3 and 5.

By analyzing the slopes of these lines from a series of different spectra it is possible to formulate a layer by layer model (see Figure 6) of each of the samples without necessarily knowing the composition of each layer or the arrangement of the constituents between layers. Regardless, an understanding of the configuration of oxide layers can help determine the biocompatibility of these devices.

The mechanically polished sample appears to have a thicker oxide layer than that of the one exposed to the PBS solution. However, the different forms of nickel oxides are further from the bulk material suggesting they are closer to the surface in the mechanically polished sample.

CONCLUSION

From both qualitative and quantitative analysis, our data agrees with what chemistry and physics predict. The mechanically polished sample and the mechanically polished sample in solution have an approximate 5 nm surface to substrate thickness. This was determined by comparing the surface alumina signal to that of metallic titanium whose depth is associated with that of the Nitinol substrate. From there, the signal to signal ratios allowed for depth analysis of each of the species we identified. In both samples, the majority of the 5 nm thickness was titanium oxide, with some metallic nickel and nickel oxide very near the base of this titanium oxide. However the sample that was treated with the PBS solution also appeared to have a slightly thicker titanium oxide layer, and also included a phosphate layer near the surface, but below the alumina. An exciting conclusion from this analysis is the fact that the phosphorous lies above the oxide very near the surface. This implies that the oxide on the mechanically polished sample is impenetrable by PBS (and thus other bodily fluids) as well as thick enough to contain the potentially harmful metallic nickel and nickel oxide ions from leaking into the body.

AKNOWLEDGEMENTS

Portions of this research were carried out at the Stanford Synchrotron Radiation Laboratory, a national user facility operated by Stanford University on behalf of the U.S. Department of Energy. I would like to thank the Department of Energy for providing such an exciting and rewarding experience. The directors of the SULI program here at SLAC have made this experience both comfortable and highly enjoyable. I would also like to thank Zhi Liu, a staff scientist at SLAC, for his consistent support, sense of humor and knowledge. Finally, sincere thanks to Apurva Mehta who simultaneously challenged and enabled me to successfully complete this project. It was an honor to work under the stewardship of such distinguished people.

References:

[1] Ratner, Buddy D., et al. *Biomaterials Science: An Introduction to Materials in Medicine*. Academic Press: San Diego, 1996.

[2] Lim, Issel A., *Biocompatibilty of Stent Materials.* MURJ. 11, 34 (2004)

[3] Private Communication with Valeska Schroeder

[4] V. Schroeder, A. Mehta, A. R. Pelton, and P. Pianetta. *An Investigation of the Passive Film on Nitinol in Simulated Biological Fluids*

[5] Anderson, K. *"Structure, Bonding and Chemistry of Water and Hydroxyl on Transition Metal Surfaces"* PhD Thesis, Stockholm University, Sweden, 2006

[6] Assumptions made include: keeping incident photon beam at a fixed angle; peaks are very close together in energy such that the elastic mean free path for each species in a given spectra is the same; layers are very thin and homogeneous.

TABLES and FIGURES

Phospahte (P2p)	Peak0	Peak1	Peak2
MPPBS			
AREA			

Ti3p_MPPBS.fil	p0 938.753	p1 941.919	p2 945.379
0 deg	5.46E+05	7.48E+05	9.16E+05
18 deg	5.79E+05	7.79E+05	9.79E+05
48 deg	3.33E+05	4.48E+05	6.88E+05
60 deg	2.01E+05	2.73E+05	5.18E+05
70 deg	91258	1.28E+05	3.48E+05
ENERGY			
Ti3p_MPPBS.fil	p0 938.753	p1 941.919	p2 945.379
0 deg	938.7615	941.9441	945.3409
18 deg	938.8604	942.0377	945.4329
48 deg	938.8463	942.03	945.4292
60 deg	938.765	941.9416	945.3619
70 deg	938.753	941.9194	945.3792
GAUSS			
Ti3p_MPPBS.fil	p0 938.753	p1 941.919	p2 945.379
0 deg	0.7627	0.7926	1.092
18 deg	0.7777	0.7951	1.087
48 deg	0.7661	0.7834	1.09
60 deg	0.7554	0.7894	1.064
70 deg	0.7637	0.7843	1.075

Table 1. Data from phosphate (P2p) energy range, including area under various peaks, energy, and Gaussian width.

	MP	MPPBS	KE (avg.)	Lambda (nm)	Thickness (MP)	Thickness (MPPBS)
Ni3p						
Al2p:Ni3p(1/2)	1.9943	1.9701	1020	2	3.9886	3.9402
Al2p:Ni3p(3/2)	2.0072	1.7247	1020	2	4.0144	3.4494
Al2p:Ti3s	1.5122	0.5418	1020	2	3.0244	1.0836
Ti3s:Ni3p	0.4856	1.2927	1020	2	0.9712	2.5854
Ni2p						
metallic:partially	-0.6162	4.3377	233	0.8	-0.49296	3.47016
metallic:oxidized	-0.4214	-2.4838	233	0.8	-0.33712	-1.98704
partially:oxidized	0.1949	-6.8217	233	0.8	0.15592	-5.45736
Ti3p						
metal:oxide	-0.6549	-1.8966	1047	2	-1.3098	-3.7932
Ti2p					0	
metal:oxide	-0.1296	-0.5714	626	1.4	-0.18144	-0.79996
O1s						
oxide:hydroxide	0.5425	1.0021	555	1.2	0.651	1.20252
P2p						
p3:p1		0.431	950	1.8		0.7758
p3:p2		0.415	950	1.8		0.747
p2:p1		0.016	950	1.8		0.0288
TiO:p3		-0.549		1.9		-1.0431

Table 1. Left column describes the signal to signal ratio that was taken. Columns 2 and 3 give the slope of the best fit line. Lambda is the inelastic mean free path of the electron. The product of the slope and lambda yields thickness separation between said species in nanometers.

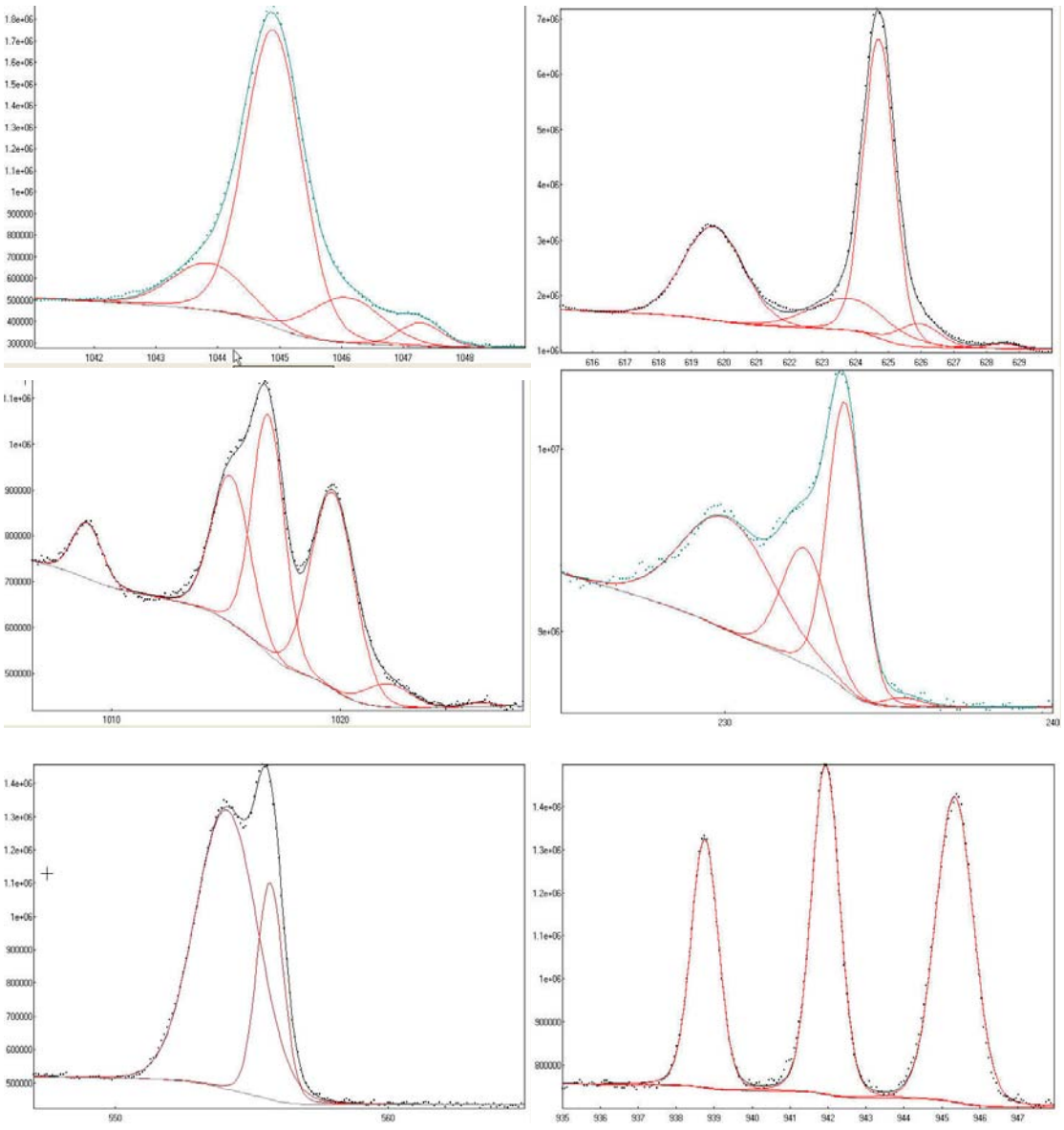

Figure 1. Spectra and fitted peaks for the six energy ranges. From left to right, top to bottom: Ti3p, Ti2p, Ni3p, Ni2p, O1s and P2p.

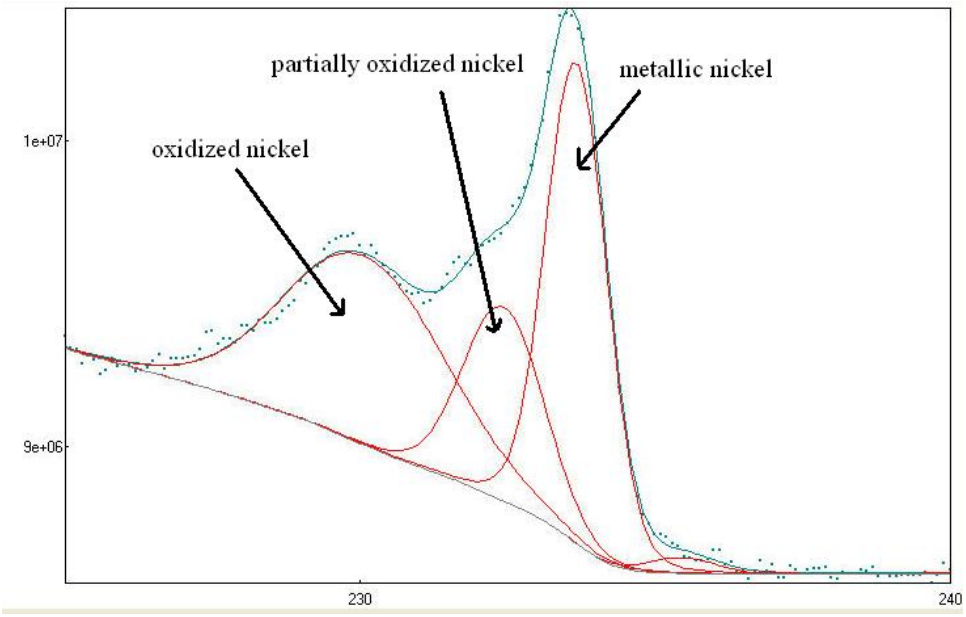

Figure 2. Example of curve fitting and labeled peaks for mechanically polished Ni2p spectra at 18 degrees.

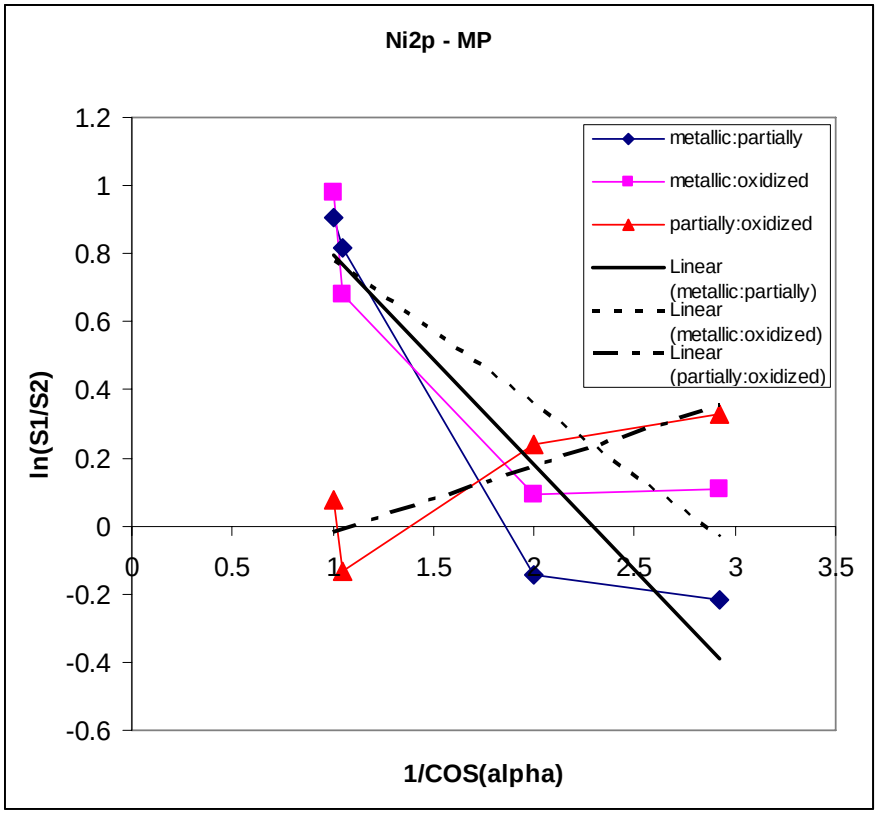

Figure 3. Best fit lines and equations for mechanically polished Ni2p scan data

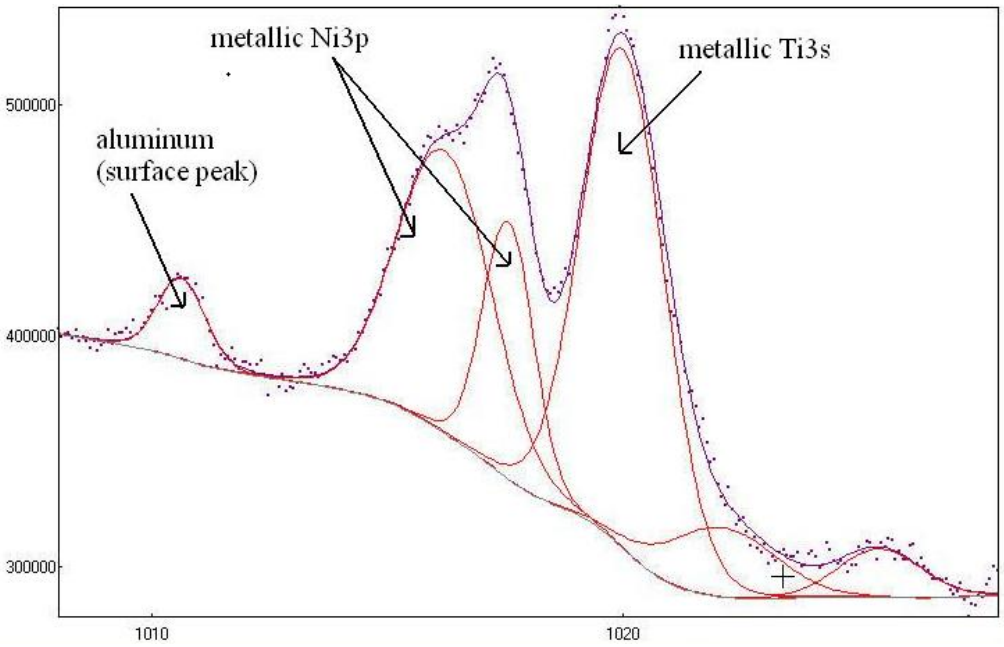

Figure 4. Example of curve fitting and labeled peaks for mechanically polished Ni3p spectra at 60 degrees.

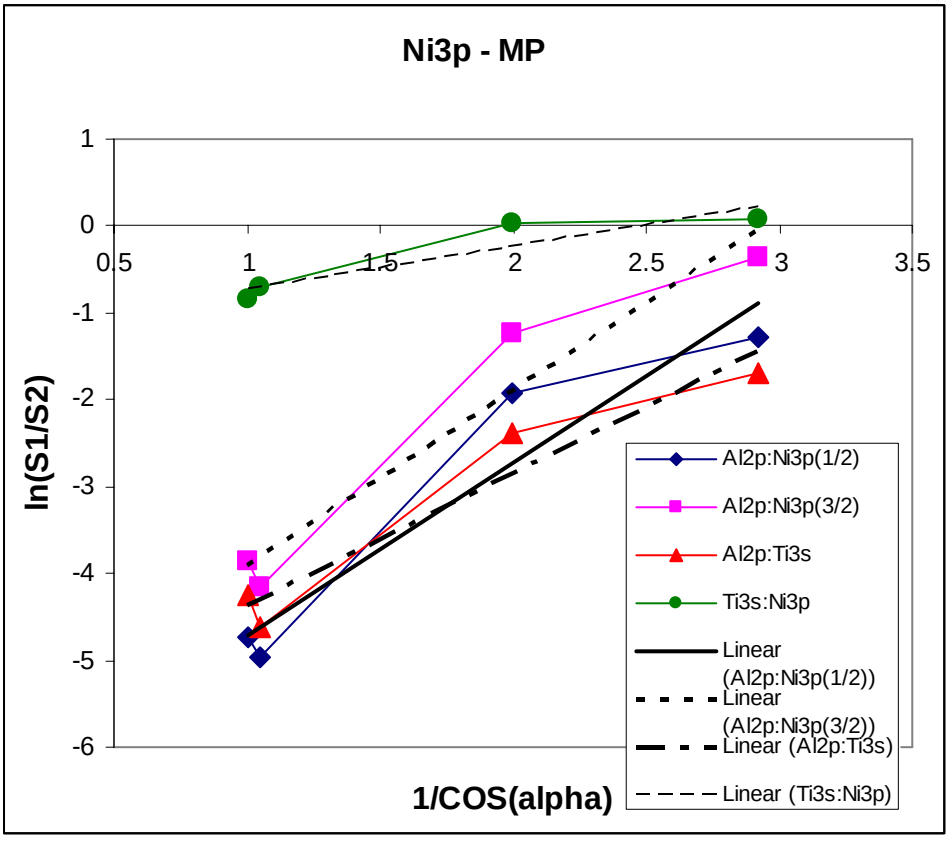

Figure 5. Best fit lines and equations for mechanically polished Ni3p scan data

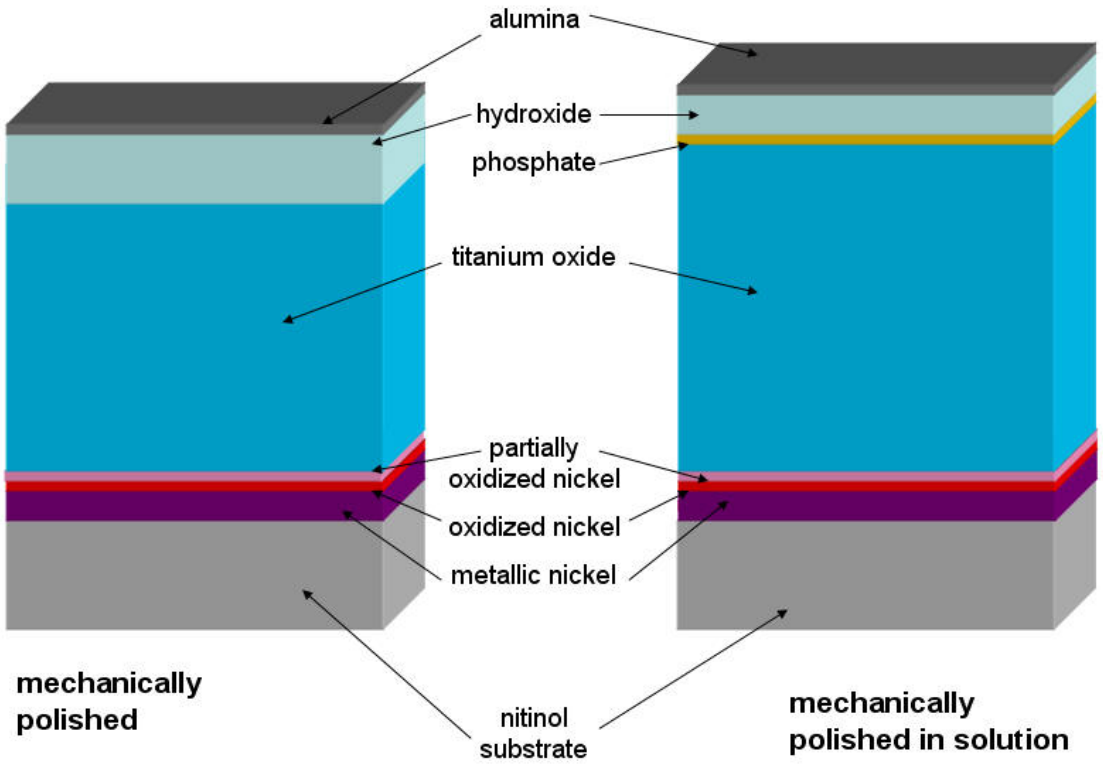

Figure 6. Schematic model of mechanically polished sample and mechanically polished in PBS solution

SLAC-TN-07-023

Study of K_S Production With The *BABAR* Experiment

Thomas J. Colvin

Office of Science, Science Undergraduate Laboratory Internship (SULI)

The Ohio State University

Stanford Linear Accelerator Center

Stanford, CA

August 24, 2007

Prepared in partial fulfillment of the requirements of the Office of Science, Department of Energy's Science Undergraduate Laboratory Internship under the direction of Jochen Dingfelder at the BaBar, Stanford Linear Accelerator Center.

Participant: _____

Signature

Research Advisor: _____

Signature

Work supported in part by US Department of Energy contract DE-AC02-76SF00515

TABLE OF CONTENTS

ABSTRACT

Study of K_S Production With The *BABAR* Experiment. THOMAS J. COLVIN (The Ohio State University, Columbus OH, 43210) JOCHEN DINGFELDER (BaBar, Stanford Linear Accelerator Center, Stanford, CA 94025)

We study the inclusive production of short-lived neutral kaons (K_S) with the *BABAR* experiment at the Stanford Linear Accelerator Center. The study is based on a sample of 383 million $B\overline{B}$ pairs produced in e^+e^- collisions at the $\Upsilon(4S)$ resonance, in which one B meson has been fully reconstructed. We select a clean sample of K_S mesons and compare kinematic spectra for data and simulation. We find that the simulation overestimates the total production rate of K_S and we see differences in the shape of the K_S momentum spectra. We derive correction factors for different momentum intervals to bring the simulation into better agreement with the observed data.

INTRODUCTION

The *BABAR* experiment [1] at the Stanford Linear Accelerator Center (SLAC) studies the decays of B mesons, which are bound states of a b-quark and a light quark. Its goals are studying CP-violation in the B system and the properties of the electroweak interaction, as well as measurements of rare B-meson decays and much more. SLAC operates as a B meson factory, producing B and $\overline{B}$ meson pairs from e^+e^- collisions that are tuned to the $\Upsilon(4S)$ resonance ($e^+e^- \rightarrow \Upsilon(4S) \rightarrow B\overline{B}$). In addition to the actual data taken from *BABAR*, there are also computer simulations which model the production of particles from collisions as well as modeling their reconstruction and identification in the detector. The simulations allow us to better understand the data that *BABAR* physically takes. Thus, we wish to ensure that the simulation is as accurate as possible. It is the goal of this study to examine the production of neutral kaons with *BABAR* and to compare the simulated data with the actual data, look for discrepencies, and suggest corrections to the simulation.

Neutral kaons come in two physically observable states, which are symmetric or anti-symmetric superpositions of K^0 and $\bar{K}^0$. One state is long-lived, the other short-lived. The neutral kaons with the longer lifetime are called K-longs (K_L) and have a mean lifetime of 51.2 ns [2]. Those with the shorter lifetime are called K-shorts (K_S) and they have a mean lifetime of 89.6 ps [2]. It is the specific focus of this study to investigate the production rates and kinematic spectra of the K_S particle from decaying B mesons.

Since we are only interested in looking at K_S particles which come from B decays, events in the data with a $B\overline{B}$ pair in them are selected by "tagging" one of the B mesons. Having received data that contain only tagged events, we then want to obtain a clean sample of the K_S which are reconstructed through their decays into $\pi^+\pi^-$ pairs. This involves removing the noise generated by combinatorial errors in the reconstruction of the B and K_S decays, as well as removing the remaining noise from non-$B\overline{B}$ events. With this clean sample, we can then confidently study the rate of production and the spectra of K_S. Various points

of interest are the momentum, and angular distributions, as well as the decay length and lifetime of K_S. Any discrepancies in these distributions between the computer simulation and the actual data taken are reflections of faults in the simulation. After correcting for the known shortcomings in the reconstruction efficiency of the K_S, the problems must then lie in the simulated production of the particles.

While the main goal of the study is to measure and understand the production of K_S and to improve the computer simulations, the findings have a broader applicability. K_L mesons are produced at the same rate as K_S and a study of K_S production thus allows us to draw direct conclusions in K_L production. K_L mesons escape the *BABAR* detector without completely depositing their energy and are rarely fully detected. This poses a serious problem, for instance, when trying to reconstruct B decays with a neutrino in the final state. Neutrinos leave no traces in the detector whatsoever and they can only be inferred from missing momentum and energy in the event. Since the K_L particles leave the detector carrying some energy with them, they obscure the amount of missing energy and momentum that would otherwise be attributed to the neutrinos. Thus, knowing how many K_S particles are in a sample will indicate how many K_L particles are expected as well, thereby allowing one to correct for their effects on the reconstruction of the neutrinos.

By performing this inclusive study (we do not care what other particles are producted) of K_S from B decays, we can improve our knowledge of K_S production and determine the extent to which the simulations and experiments agree. Adjustments can then be made to the K_S production rates and spectra in the simulation to bring the computer models into better agreement with the physical data.

MATERIALS AND METHODS

The $B\overline{B}$ Data Sample

For this analysis, we use data collected by the *BABAR* detector between 1996 and 2006 (runs 1-5) as well as data generated by Monte Carlo simulation[3]. Since we study K_S from B decays, the data set which we examine contains only those events in which one B-meson was fully reconstructed[4]. The B meson is reconstructed from purely hadronic decay modes: $B \rightarrow D^{(*)} + X$, where $X = n\pi + mK + rK^0_S + q\pi^0$ with $n + m + r + d < 6$. More than 1000 such modes are used, however many do not yield a high purity for B's. To reduce the probability of poorly reconstructed events polluting our sample, we require purity greater than 70% and in the case of multiple tag-B candidates, we choose the one with the highest purity.

In order to be able to compare the amount of K_S from B decays produced in data with those in Monte Carlo, we must determine the number of $B\overline{B}$ events in the data and simulation. This can be done by fitting a special function to the reconstructed mass spectrum of the tagged B meson. The B mass is reconstructed as $m_{ES} = \sqrt{(\frac{\sqrt{s}}{2})^2 - \overrightarrow{p_B}^2}$, where the B energy has been substituted by $\frac{\sqrt{s}}{2}$ and $\sqrt{s}$ is the center-of-mass energy of the e^+e^- collision. The subscript "ES" stands for "energy substituted". The function that we use to fit the m_{ES} spectrum is the sum of an Argus and a Crystal Ball function:

$$f_{Bmass}(x) = f_{Argus}(x) + f_{CrystalBall}(x; \alpha, n, \bar{x}, \sigma),$$

where

$$f_{Argus}(x; S, m_0, c, p, \Delta x) = S \cdot (x - \Delta x) \cdot (1 - \tfrac{x}{m_0}^2)^p \cdot e^{c(1-\frac{x}{m_0}^2)},$$

and

$$f_{CrystalBall}(x; N, \alpha, n, \bar{x}, \sigma) = N \cdot \begin{cases} exp(-\frac{(x-\bar{x})^2}{2\sigma^2}) & \text{for } \left|\frac{x-\bar{x}}{\sigma}\right| < \alpha \\ A \cdot (B - \frac{x-\bar{x}}{\sigma})^{-n} & \text{for } \left|\frac{x-\bar{x}}{\sigma}\right| \geq \alpha \end{cases}$$

with

$$A = (\tfrac{n}{|\alpha|})^n \cdot exp(-\tfrac{|\alpha|^2}{2}) \quad \text{and} \quad B = \tfrac{n}{|\alpha|} - |\alpha|\,.$$

The Crystal Ball function[5] represents the events with a well-reconstructed tagged B meson. The Argus function[6] represents the remaining background from non-$B\overline{B}$ events (continuum events from processes $e^+e^- \rightarrow q\bar{q}$ where q=u,d,s,c) and to some extent the combinatorial background, which comes from $B\overline{B}$ events where particles are incorrectly matched together to produce something that looks like a B meson. By summing them together we get a function which models both the well-reconstructed $B\overline{B}$ and background events.

Figure 1 shows the result of the m_{ES} fits for data and Monte Carlo. The χ^2 per degree of freedom for the data nd MC fits are 17.1 and 48.8 respectively. Since the ideal case would have a χ^2 of 1, our goodness of fit in these cases is poor. It is known that in order to improve the χ^2, for example, an additional contribution to the fit function is necessary to more accurately model the combinatorial background. However, this complicated fit is out of the scope of this study and the accuracy achieved by the present fit is sufficient for this analysis. To determine the total number of events with a well-reconstructed B ($N_{B\overline{B}}$), we define a signal region in m_{ES}: $5.275 < m_{ES} < 5.284$ MeV/c^2. $N_{B\overline{B}}$ can then be determined in two different ways:

- $N_{B\overline{B}} = \int_{SignalRegion} CrystalBall$

– by integration of the Crystal Ball function over the m_{ES} signal region.

- $N_{B\overline{B}} = \int_{SignalRegion} m_{ES}Spectrum - \int_{SignalRegion} Argus$
  – by subtracting from the number of events in the signal region of the m_{ES} spectrum the integral of the Argus function over the m_{ES} signal region.

We choose to use the first method for our analysis and will later assign the difference between the two methods as systematic error on $N_{B\overline{B}}$.

Because there are more well-reconstructed events in the simulation than in the data, due to the fact that more events have been generated in the simulation, it will be necessary when comparing K_S spectra, and to determine the K_S production rate in data and MC, to scale the simulation histograms down to match the size of the data sample for a meaningful comparison. This scale factor can be found by taking the ratio of the determines number of $B\overline{B}$ events in both samples. The number of $B\overline{B}$ events and the scale factor are given in Table 1.

K_S *Selection*

The K_S candidates are reconstructed in the decay channel $K_S \to \pi^+\pi^-$. This decay channel has a large branching fraction of $(68.95 \pm 0.14)\%$ and is experimentally easy to reconstruct. These two pions from the K_S decay are reconstructed from charged tracks in the detector that do not come from the reconstructed B which we tagged earlier. To ensure that our sample of K_S is as clean as possible we apply additional selection criteria using the following variables:

- d_{3D}: The flight length is the distance from the primary vertex (e^+e^- interaction point) to the vertex where the pions are found to have originated from. This is how far the K_S particle travelled in 3 dimensions. In calculating d_{3D}, we can ignore the flight length of the B meson from the primary vertex because it is on the order of 500μm and thus nominal compared to the K_S flight length.

  - Insist that $d_{3D} > 2$mm.

- α_{xy}: The angle between the reconstructed momentum vector of the K_S and the flight length vector in the xy-plane.

  - Insist that $\mathrm{Cos}(\alpha_{xy}) > 0.9992$.

- $VtxProb$: The vertex probability is the probability that the vertex the pions originate from is correctly reconstructed, or more precisely, the χ^2 probability of the vertex fit.

  - Insist that $VtxProb > 10^{-6}$

- $m_{\pi\pi}$: The reconstructed $\pi^+\pi^-$ invariant mass.

  - This cut is discussed in the following section.

Figure 2 shows how cutting on the first three quantities changes the $m_{\pi\pi}$ distribution.

With this sample we can begin to make comparisons between K_S production rates and spectra for data and simulation by inspecting the following six kinematic variables for the K_S:

- p^*: The momentum of the K_S in the rest frame of the $\Upsilon(4S)$.

- $Cos(\theta)$: The cosine of the angle (θ) between the K_S direction and the electron beam as seen from the $\Upsilon(4S)$ rest frame.

- d_{3D}: the 3-dimensional distance between the interaction point and the decay vertex in the lab frame.

- d_{xy}: the 2-dimensional distance between the interaction point and the decay vertex in the lab frame.

- The time that it takes for the K_S to decay in the lab frame, $\tau = \frac{d_{3D} \cdot m}{p_{lab}}$, where:

  - m = the mass of the K_S (0.4976 GeV/c^2)[2];

– p_{lab} = the momentum of the K_S in the lab frame;

- The corrected K_S decay time, $\Delta\tau = (d_{3D} - d_{min}) \cdot \frac{m}{p_{lab}}$ where $d_{min} = 2$ mm.

Since we want to study the production of K_S in data and MC, we need to correct for known differences in the reconstruction efficiencies for $K_S \to \pi\pi$ decays between data and MC. The efficiency correction factors (recommended by the *BABAR* collaboration[7]) in Table 2 are applied as weights to the reconstructed K_S candidates in simulation. Upon the spectra of these variables after correction for reconstruction efficiencies, we perform two background subtractions: one from the background in the B mass distribution and the other from the background in the K_S mass distribution.

K_S *Background Subtraction*

First we perform a sideband subtraction based on the reconstructed $\pi^+\pi^-$ invariant mass, $m_{\pi\pi}$, to remove fake and wrongly reconstructed K_S candidates. We define a $m_{\pi\pi}$ signal region with a full-width of 8 MeV/c^2 which is centered around the mass peak as determined by the Particle Data Group[2]. The sidebands are chosen to lie equidistant from the peak and themselves each have a width of 40 MeV/c^2. A 10 MeV/c^2 gap is left on both sides between the signal and sideband regions so that any tails from the mass distribution of true K_S do not penetrate into the sidebands (Figure 3). The factor by which we weight the sidebands to subtract the contribution of fake K_S in the signal region is simply defined as:

$wtSide = \frac{SignalWidth}{TotalSideWidth} = 0.1$.

To perform the actual subtraction for any given kinematic variable, we take the spectrum in the signal region and subtract from it the spectrum of the sideband region multiplied by the scaling factor of $wtSide$. The kinematic variables before and after sideband subtraction are shown in Figure 4. All following distributions will be shown for the K_S signal region after sideband subtraction.

B *Background Subtraction*

Since we only study K_S from B decays, we need to remove the remaining non-$B\overline{B}$ background and the combinatorial background caused by wrongly reconstructed tag-B mesons. We again make a fit of the reconstructed tag-B mass distribution with a function comprised of an Argus and Crystal Ball sum. Unlike before where we fit the tagged B mass of the entire sample, here we use the sample after the K_S sideband subtraction. The range of the m_{ES} signal region was chosen earler and contains the peak of the $CrystalBall$ ($5.275 < m_{ES} < 5.284$ GeV/c^2). The sideband is chosen far away from the signal region where only the $Argus$ function contributes to the fit ($5.22 < m_{ES} < 5.25$ GeV/c^2). The result of the fits is shown in Figure 5. The scale factor for the sidebands is defined as:

$wt_{mES} = \frac{\int_{signalregion} Argus}{\int_{sidebandregion} Argus}$.

As with the previous sideband subtraction, we plot the signal region minus the sidebands that are scaled down by the factor wt_{mES} (Figure 6). This produces spectra that are representative of the spectra for well-reconstructed K_S from B decays. All future plots will employ this sideband subtraction as well as the K_S subtraction.

RESULTS

In order to compare the data and MC spectra, the MC spectra must first be scaled down according to the number of $B\overline{B}$ events found in the data. The scale factor for this was computed in Table 1 and found to be $wt_{MC} = 0.321314$. Figures 7 and 8 compare the spectra of the data against those of the scaled MC. We observe that the total production rate of K_S is overestimated in simulation by 17.2%. Please note that the flight length distributions in Figure 8 are cut off at 5 cm, which means that about 25% of the total rate is not shown. The discrepancy between data and MC is shown to be less in this region than for the total rate, we infer then that the rate discrepancy between data and MC gets larger for longer flight distances.

The ratios for both the regular and corrected decay times are relatively flat. The shape of the center-of-mass momentum spectra in the intermediate momentum range is rather similar in data and MC. However, both the high and low momentum regions show disagreement. The ratio of $Cos(\theta)$ is also relatively flat until $Cos(\theta) \rightarrow 1$, where MC shows a higher production than data.

We can calculate the efficiencies of the K_S selection as a function of the studied kinematic variables by taking the ratio of the reconstructed and fully subtracted MC spectra to the generated m_{ES} subtracted MCtruth spectra. The efficiency plots for the center-of-mass K_S momentum and polar angle are shown in Figure 9. The average efficiency is 0.249 (indicated as red line). From the efficiency spectra, we can calculate the efficiency-corrected spectra. These are found by dividing the reconstructed and fully subtracted data spectra by the efficiency spectra obtained from simulation. Figure 10 shows the efficiency-corrected data spectra for the center-of-mass K_S momentum and polar angle.

DISCUSSION AND CONCLUSIONS

We find the K_S production rate as the number of K_S detected divided by the number of $B\overline{B}$ events. The results are shown in Table 4, where the uncertainties quoted are statistical, taken from the error of the Crystal Ball fit. The sytematic uncertainty can be assigned as the difference between the yield calculated from the Crystal Ball fit and the yield calculated from the Argus-subtracted integral. I find this systematic uncertainty to be 0.03% absolute for data and less than 0.02% absolute for Monte Carlo. The table of relative yield in K_S production rate confirms what we noted earlier: that MC has a higher rate of production than data.

Besides the overall rate difference, the MC overestimates the K_S yield in data especially for low and high momentum regions. We divide the momentum spectra into three regions and find the average of the ratio of data and MC yields in each region (Table 5). We

suggest to use these averages as correction factors in their respective regions to bring the MC momentum spectra into better agreement with the data.

Compared to a previous study in *BABAR* [8], this study uses a larger K_S data sample and thus has a better statistical precision and makes use of the latest improvements in the *BABAR* reconstruction software. Another improvement over the previous study is that known differences in the K_S reconstruction efficiency have properly been accounted for. The results obtained in this study will be useful for many future *BABAR* analyses that depend on a reliable simulation of K_S production.

ACKNOWLEDGMENTS

I would like to thank my mentor Jochen Dingfelder, as well as Wells Wulsin for all of their help and guidance. I would also like to thank Vera Luth for her guidance. I am also grateful to SULI and the DOE for funding my research.

REFERENCES

[1] B. Aubert *et al.* (*BABAR* Coll.), Nucl. Inst. Meth. **A479**, 1 (2002).

[2] W.-M. Yao *et al.* (Particle Data Group), J. Phys. G **33**, 1 (2006).

[3] S. Agostinelli *et al.* (GEANT4 Coll.), Nucl. Instrum. Methods Phys Res. Sect. A **506**, 250 (2003).

[4] D. del Re, S. Grancagnolo, R. Faccini, A. Sarti, G. Denardo, *Semi-Exclusive B reconstruction* BAD #271 *BABAR* Internal Analysis Document (2001).

[5] Crystal Ball Collaboration, T. Skwarnicki, Report No. DESY F31-86-02 (unpublished).

[6] ARGUS Collaboration, H. Albrecht *et al.*, Z. Phys. C **48**, 543 (1990).

[7] K_s Reconstruction Efficiency Study, http://www.slac.stanford.edu/BFROOT/www/Physics/TrackEff
2006.html

[8] W. Wulsin and J. Dingfelder, K_s *Production Spectra* BAD #1642 *BABAR* Internal Analysis Document (2006).

FIGURES

Figure 1: m_{ES} distribution in data and MC.
The red points with error bars indicate simulated events in data or MC. The vertical red lines indicate the chosen m_{ES} signal region.

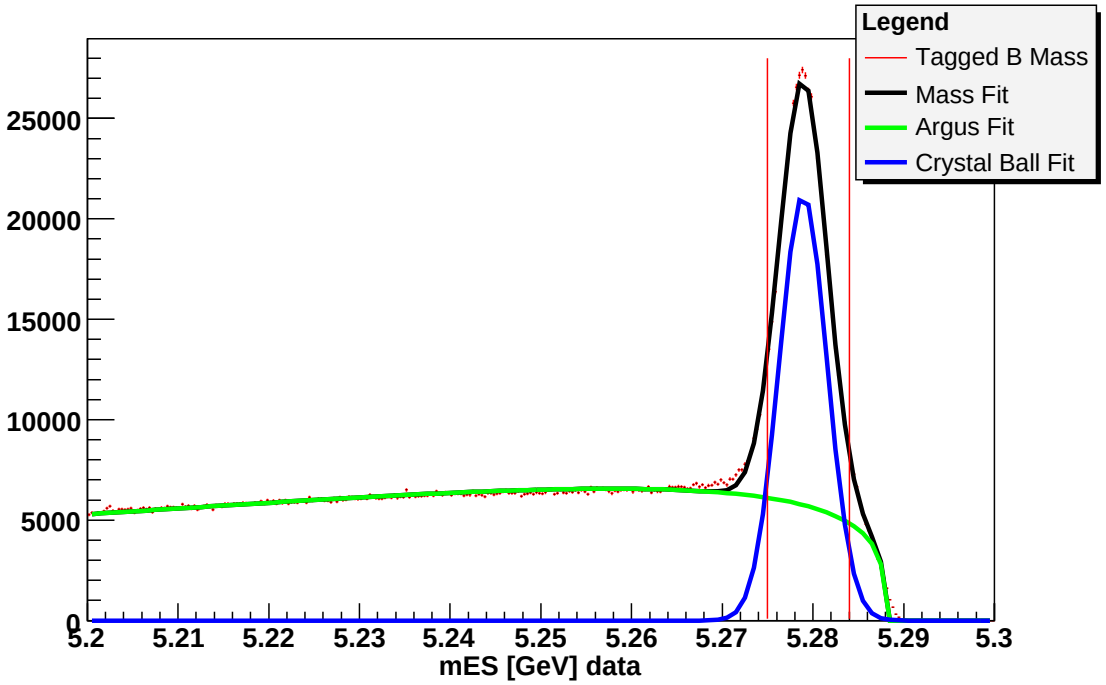

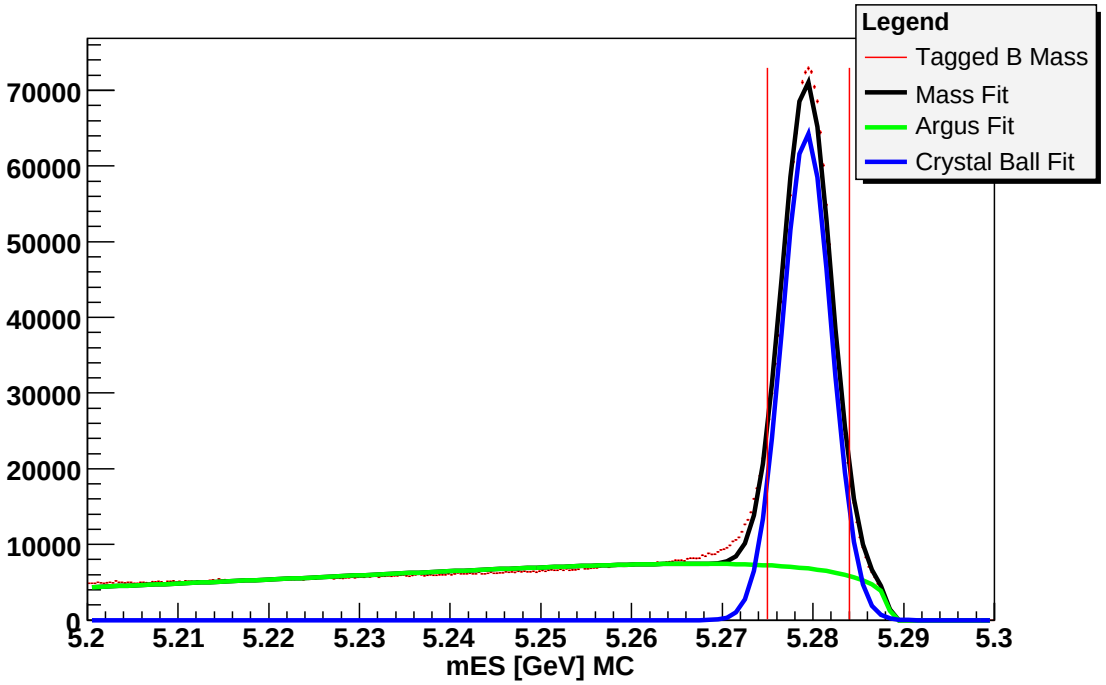

Figure 2: $M_{\pi\pi}$ distribution in MC demonstrating K_S cuts.
(top) d_{3D} cut only, (middle) d_{3D} and $VtxProb$ cuts, (bottom) all three cuts

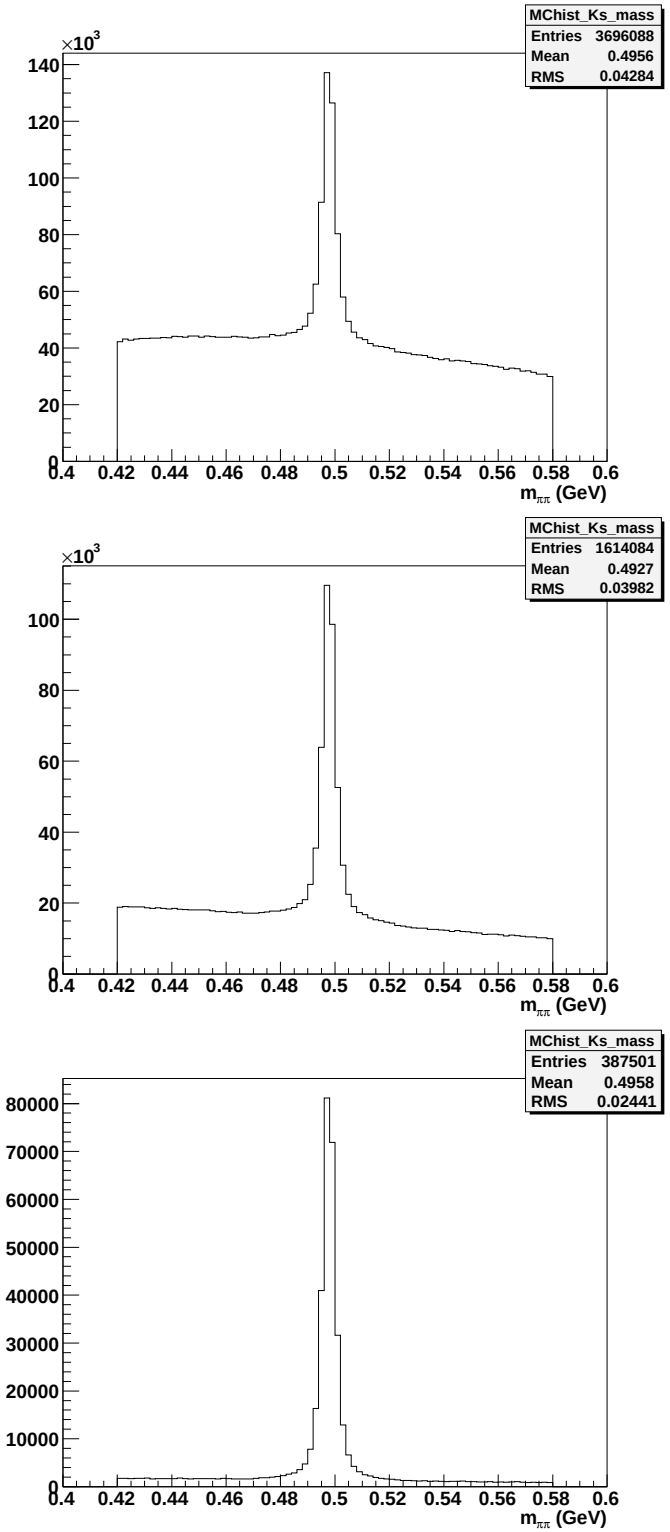

Figure 3: $M_{\pi\pi}$ Distribution In Data And MC.

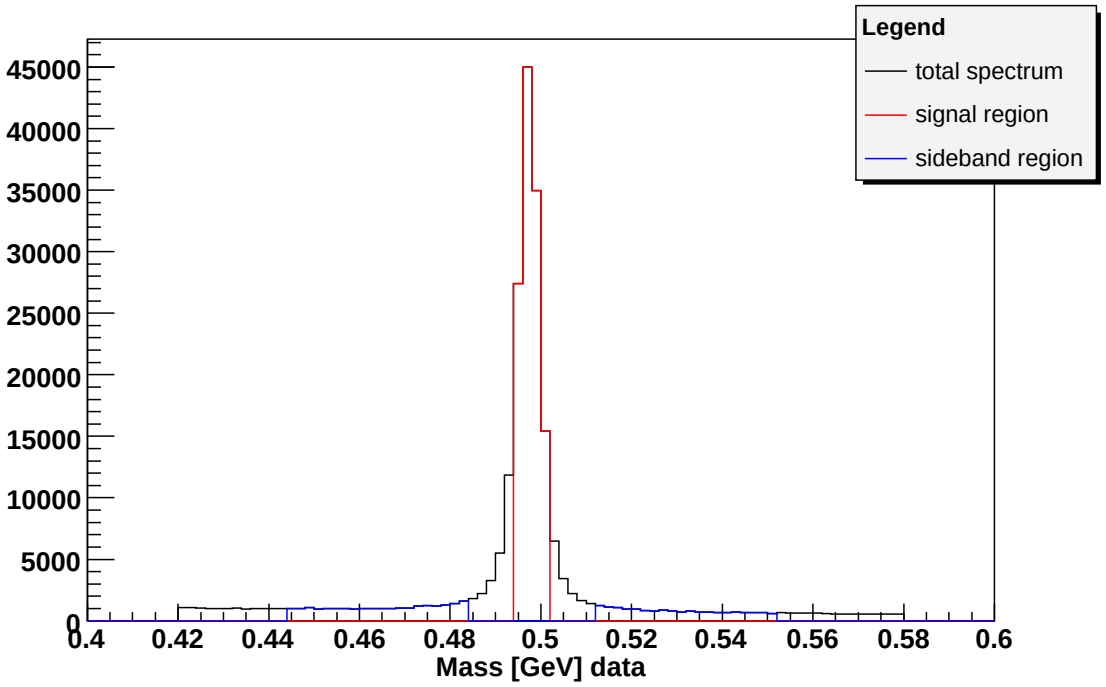

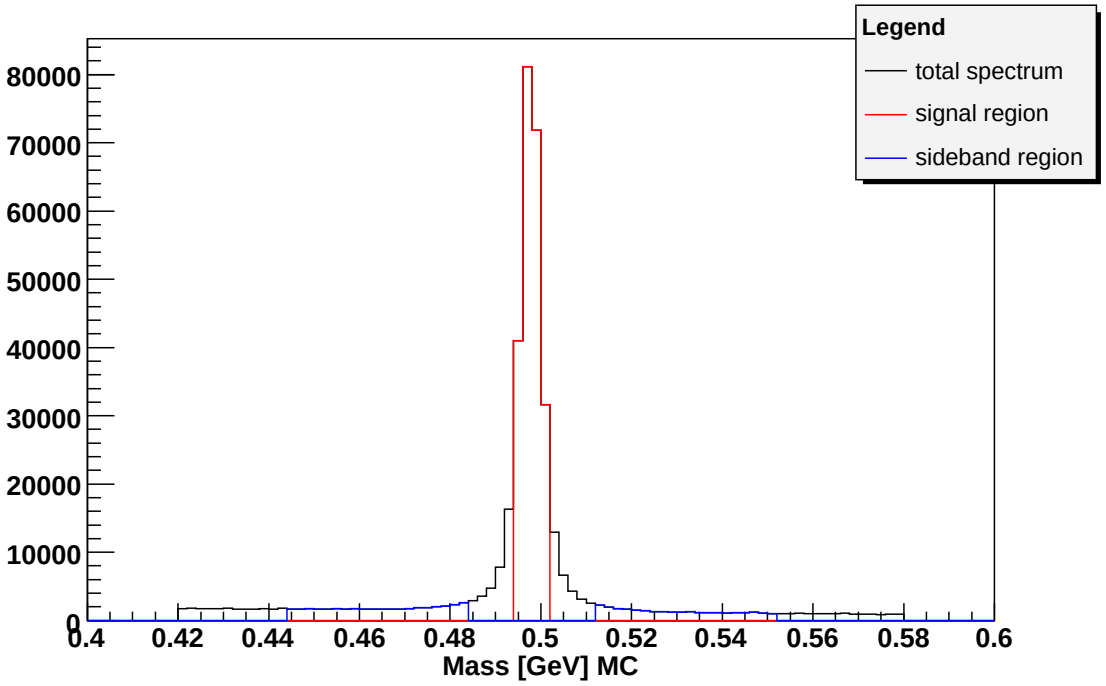

Figure 4: Kinematic Spectra demonstrating K_S sideband subtraction

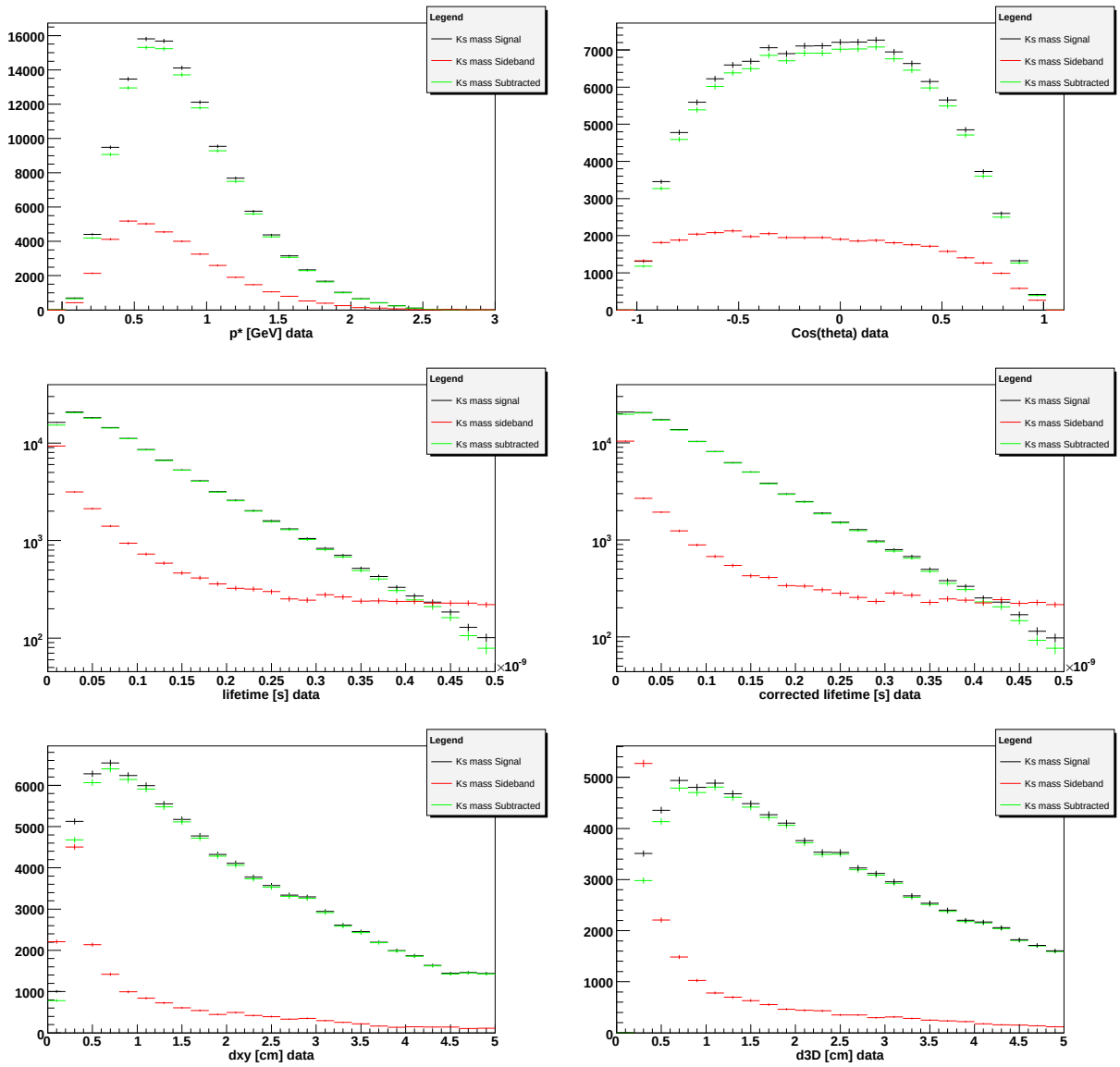

Figure 5: K_S sideband-subtracted m_{ES} distribution in data and MC
The red points with error bars indicate simulated events in data or MC. The vertical red lines indicate the chosen m_{ES} signal region. The vertical black lines indicate the chosen sideband region.

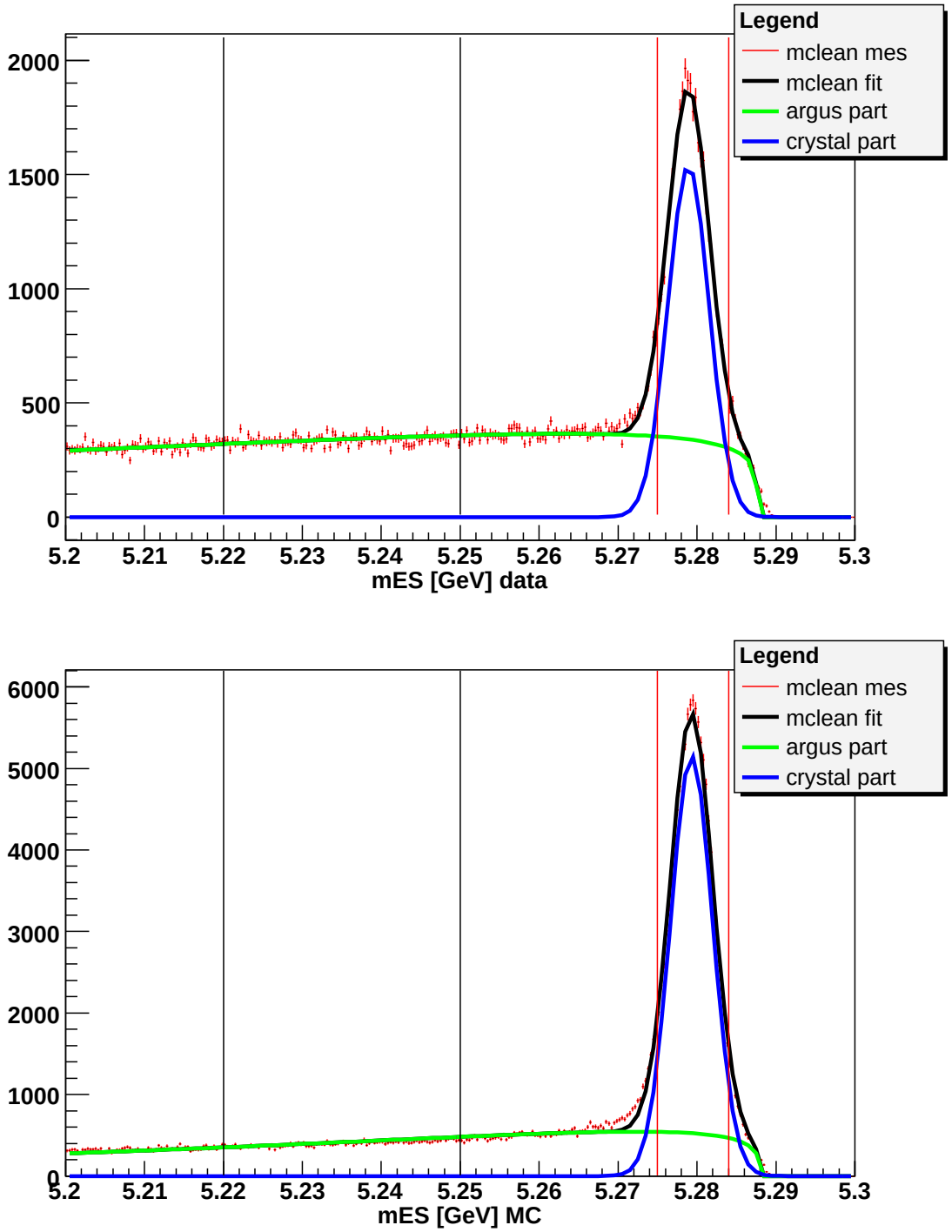

Figure 6: Kinematic Spectra demonstrating B sideband subtraction

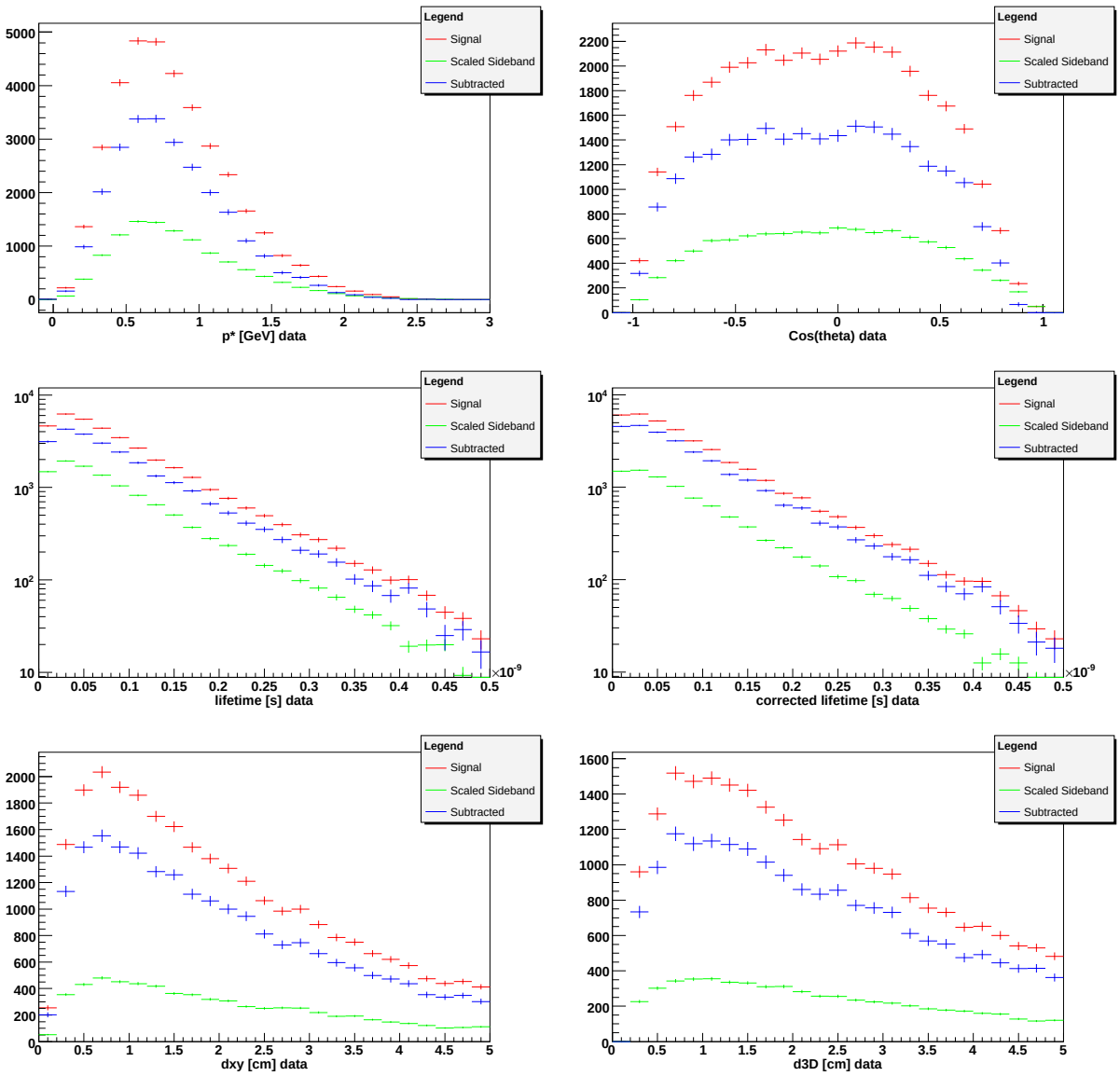

Figure 7: Comparing data and MC
Kinematic Spectra (left) and data over MC ratio plots (right)

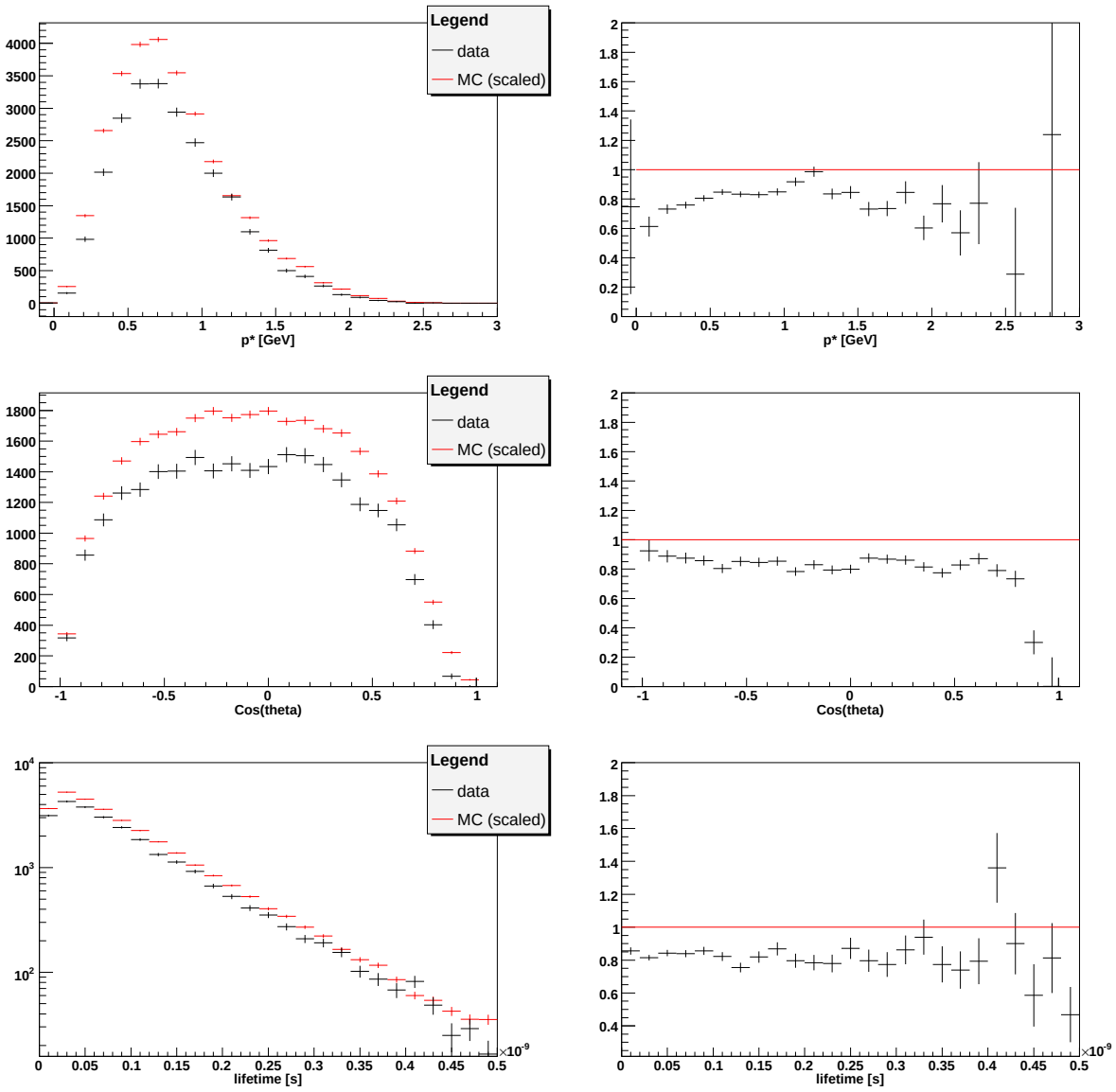

Figure 8: Comparing data and MC
Kinematic Spectra (left) and data over MC ratio plots (right)

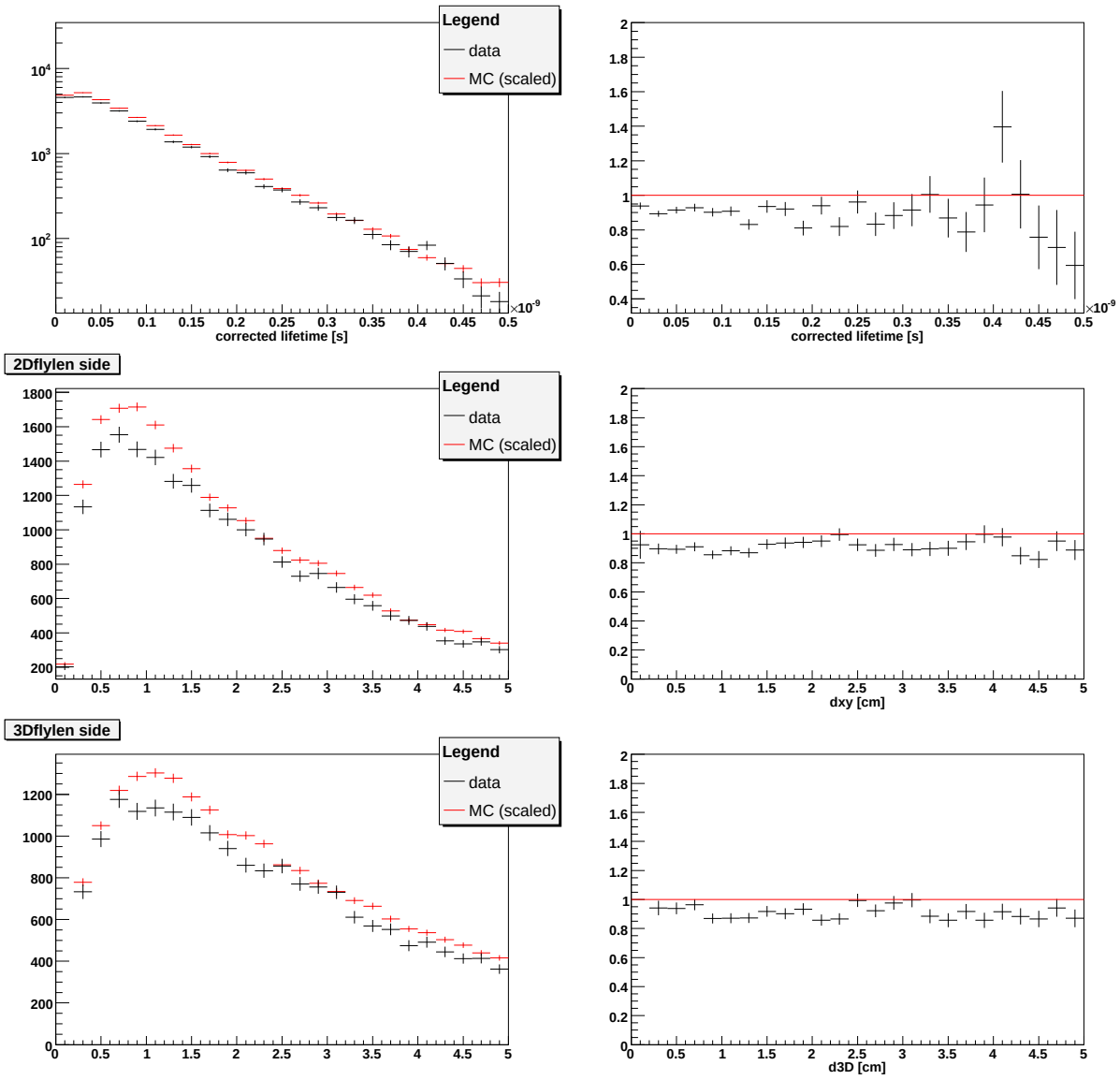

Figure 9: Efficiency Plots
Center-of-mass momentum (left) and cos(θ) (right)

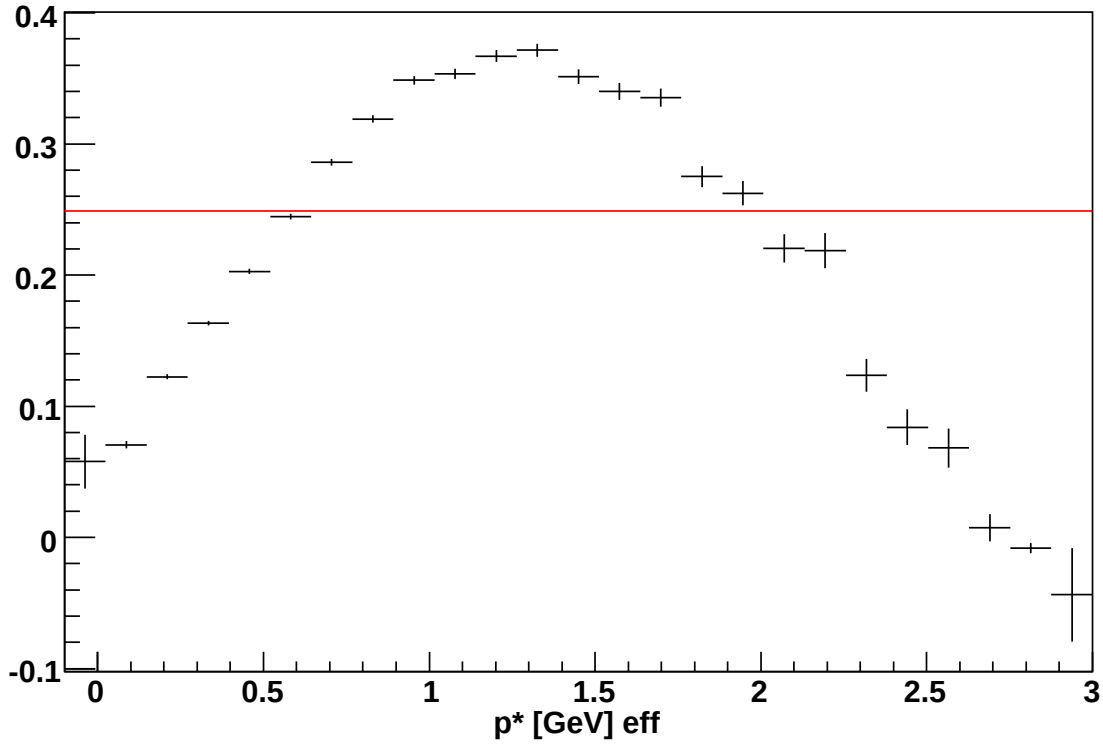

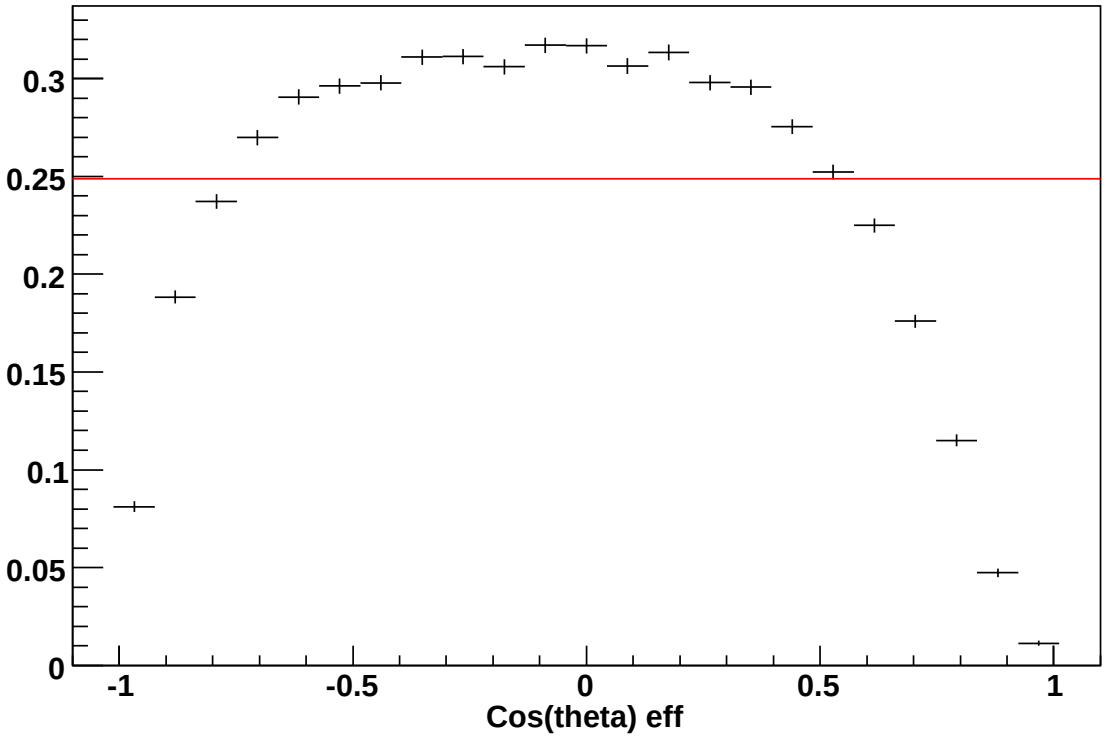

Figure 10: Efficiency-Corrected Plots
Center-of-mass momentum (left) and cos(θ) (right)

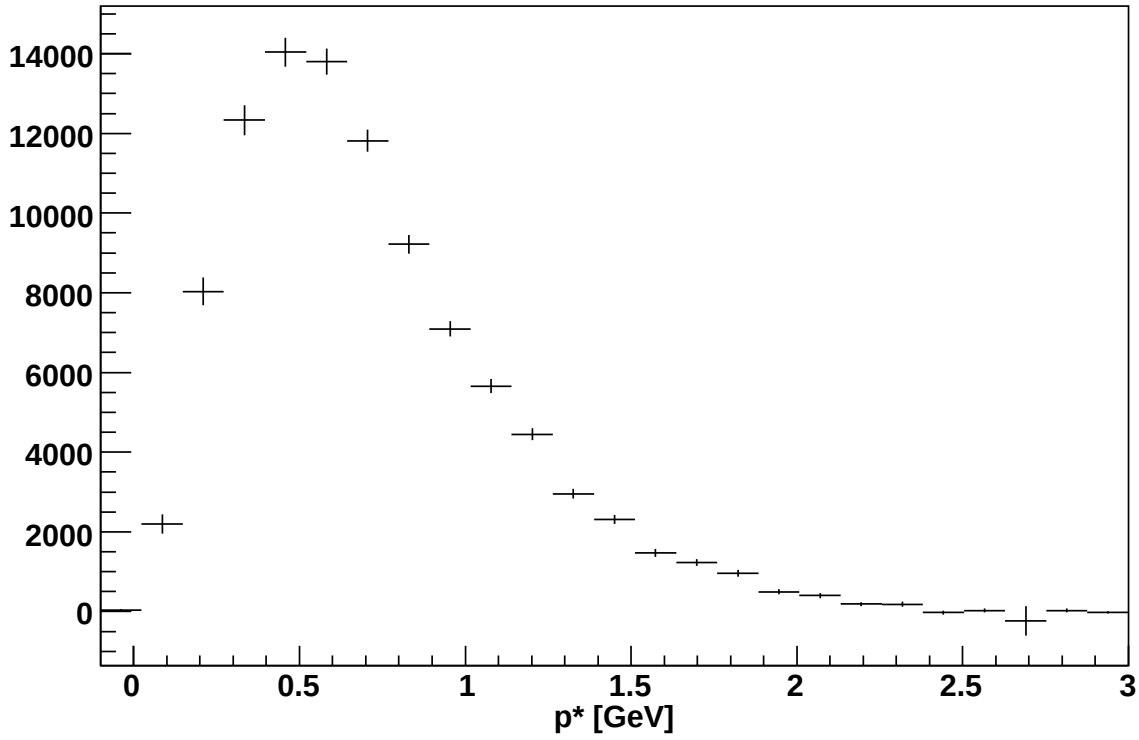

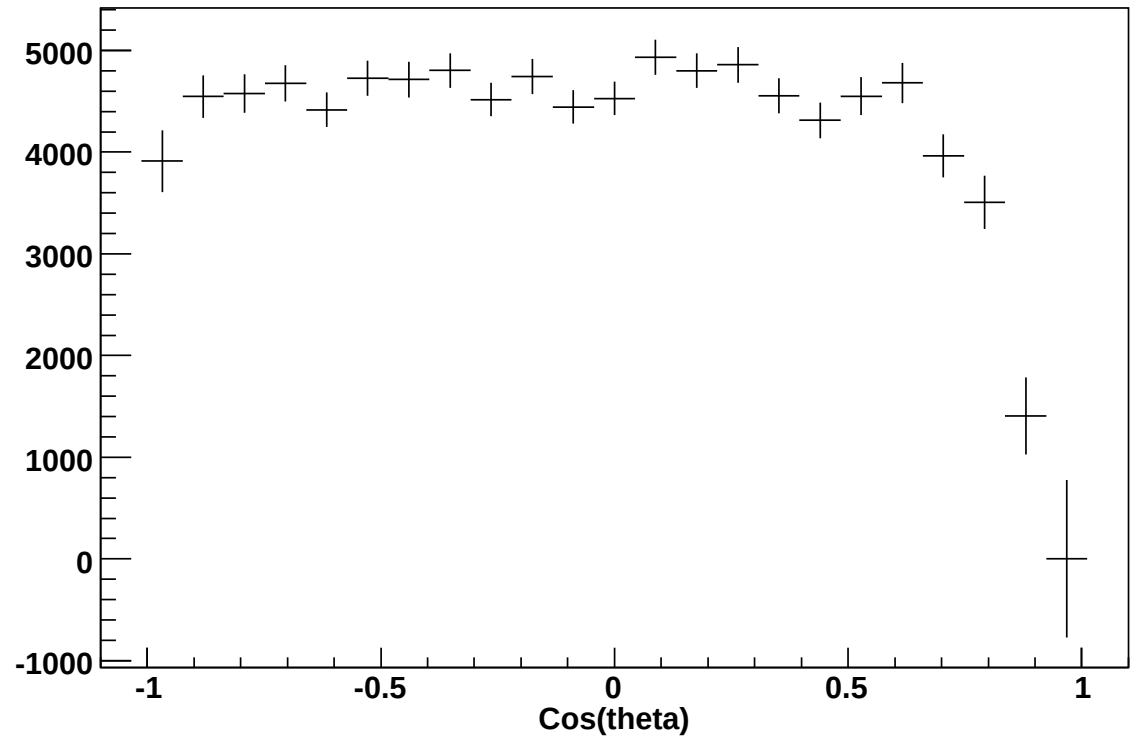

TABLES

Table 1: Number of $B\overline{B}$ events before K_S selection

	A	B	C	D
$N_{B\overline{B}} =$	$\int_{m_{ES}sig} CrystalBall$	$\int_{m_{ES}sig} m_{ES}Spectrum$	$\int_{m_{ES}sig} Argus$	B - C
Data	382664	532716	152149	380567
MC	1190930	1363830	182549	1181281
wt_{MC} = D/MC	0.321314	–	–	0.322164

Table 2: Correction Factors for K_S reconstruction, applied to K_S in simulation

	Correction for K_S reconstruction efficiency	Correction for signal window cut	Total Correction (Product)
Run1	1.004 ± 0.025	1.000	1.004
Run2	1.009 ± 0.038	0.970	0.979
Run3	1.001 ± 0.018	0.974	0.975
Run4	0.983 ± 0.012	0.961	0.945
Run5	0.994 ± 0.011	0.950	0.944

Table 3: Number of K_S Candidates

	A	B	C	D = B/C
$N_{K_S} =$	$\int_{signal} CrystalBall$	$\int_{signal} Argus$	$\int_{sideband} Argus$	wt_{mES}
m_{ES} interval	$5.275 < m_{ES} < 5.284$	$5.275 < m_{ES} < 5.284$	$5.22 < m_{ES} < 5.25$	
Data	27669	9100	30848	0.294996
MC	94878	14069	37678	0.373399

Table 4: Relative yield of K_S from B decays

$N_{B\overline{B}} = \int_{m_{ES}sig}$	$CrystalBall$	$m_{ES}Spectrum - Argus$
Data	(7.23 ± .06)%	(7.20 ± 0.06)%
MC	(7.97 ± 0.04)%	(7.95 ± 0.04)%

Table 5: Correction Factors
Average Correction Factors for K_S MC production in three K_S momentum intervals.

Region of p^*	Yield ratio = data/MC
$0.0 < p^* < 0.4$ GeV/c^2	77.05%
$0.4 < p^* < 1.5$ GeV/c^2	85.13%
$1.5 < p^* < 3.0$ GeV/c^2	76.55%

SLAC-TN-07-013
August 2007

Simulation of Neutron Backgrounds from the ILC Extraction Line Beam Dump

Siva Darbha

Office of Science, SULI Program

University of Toronto

Stanford Linear Accelerator Center

Menlo Park, California

August 17, 2007

Prepared in partial fulfillment of the requirements of the Office of Science, U.S. Department of Energy Science Undergraduate Laboratory Internship (SULI) Program under the direction of Dr. Takashi Maruyama and Dr. Lewis Keller in the International Linear Collider (ILC) Division at the Stanford Linear Accelerator Center (SLAC).

Participant: _____
Signature

Research Advisors: _____
Signature

_____
Signature

Work supported in part by US Department of Energy contract DE-AC02-76SF00515

Table of Contents

ABSTRACT

Simulation of Neutron Backgrounds from the ILC Extraction Line Beam Dump. SIVA DARBHA (University of Toronto, Toronto, ON M5S 1A1) LEWIS KELLER (Stanford Linear Accelerator Center, Menlo Park, CA 94025) TAKASHI MARUYAMA (Stanford Linear Accelerator Center, Menlo Park, CA 94025)

The operation of the International Linear Collider (ILC) as a precision measurement machine is dependent upon the quality of the charge-coupled device (CCD) silicon vertex detector. A neutron flux of 10^{10} neutrons/cm^2 incident upon the vertex detector will degrade its performance by causing displacement damage in the silicon. One source of a neutron background arises from the dumping of the spent electron and positron beams into the extraction line beam dumps. The Monte Carlo program FLUKA was used to simulate the collision of the electron beam with the dump and to determine the resulting neutron fluence at the interaction point (IP). A collimator and tunnel were added and their effect on the fluence was analyzed. A neutron source was then generated and directed along the extraction line towards a model of the BeamCal, vertex detector, and beampipe to determine the neutron fluence in the silicon layers of the detector. Scattering in the BeamCal and beampipe was studied by manipulating the composition of the BeamCal. The fluence in the first silicon layer for the current tungsten BeamCal geometry was corrected according to a 1 MeV equivalent silicon displacement damage to obtain a comparable value for the damage done to the CCD vertex detector. The IP fluence was determined to be $3.65*10^{10}$ +/- $2.34*10^{10}$ neutrons/cm^2/year when the tunnel and collimator were in place, with no appreciable increase in statistics when the tunnel was removed. The BeamCal was discovered to act as a collimator by significantly impeding the flow of neutrons towards the detector. The

majority of damage done to the first layer of the detector was found to come from neutrons with a direct line of sight from the quadrupole, with only a small fraction scattering off of the beampipe and into the detector. The 1 MeV equivalent neutron fluence was determined to be $1.85*10^9$ neutrons/cm^2/year when the positron beam was considered, or $9.27*10^8$ neutrons/cm^2/year by one beam alone, which contributes 18.5% of the threshold value in one year. Future work will improve the detector model by adding the endcap sections of the silicon detector, and will study in detail the neutron scattering off of the tunnel walls. Other sources of neutron backgrounds will also be analyzed, including electron-positron pairs, Beamstrahlung photons, and radiative Bhabha scattering, in order to obtain a complete picture of the overall neutron damage done to the vertex detector.

INTRODUCTION

The Large Hadron Collider (LHC) operating at CERN will probe a new energy scale using 14 TeV center of mass energy proton-proton collisions, and will produce a wealth of new physics, including searches for the Higgs boson and Supersymmetry [1]. The International Linear Collider (ILC) is a proposed linear electron-positron collider that will be 31 km in length and will have a center of mass energy of 500 GeV. It will have a cleaner signal to noise ratio than the LHC and will provide precision measurements for some of the physics discovered there. The electron and positron beams in the ILC will have $2*10^{10}$ particles per bunch and a bunch separation of 370 ns, with 2625 bunches in 1 ms trains at a repetition rate of 5 Hz; they will come into collision at the interaction point (IP) at a 14 mrad crossing angle [2].

The Beam Delivery System (BDS) in the ILC is responsible for transporting the electron and positron beams from the main linacs, colliding them at the IP, and discarding the spent beams to the extraction line beam dumps. The extraction line is shown in Figure 1. The beam dumps are stainless steel cylindrical containers, of 75 cm radius and 7.5 m length, with a titanium window, of 15 cm radius and 1 mm thickness, through which the beams enter; the dumps contain water at a pressure of 10 bar [3]. Water was used in the dumps since its high specific heat capacity makes it ideal to dissipate the energy of the beams. Only a minute fraction of the particles in any bunch crossing will interact, leaving the high energy electron and positron beams to be extracted from the IP in their near entirety and discarded in the water dump. The dumps are designed to absorb 17 MW of beam power at a 500 GeV center of mass energy [3].

The extracted beams will interact with the H_2O molecules in the dump, leading to EMF showering that will produce a flux of neutrons, most of which are forward directed. Some of this ‘gas’ of secondary particles is backward directed and will reach the detector, creating unwanted

backgrounds in the tracking devices and calorimeters that will obscure the physics processes observed from actual collisions. The flux of neutrons may even cause displacement damage in the silicon atoms in the charge-coupled device (CCD) vertex detector, which is the innermost tracking system in the SiD detector model, if it reaches a value higher than 10^{10} neutrons/cm^2, leading to charge traps [4], [5]. The traps would degrade the performance of the detector by reducing the charge transfer along the CCD and by causing junction leakage [4], [5]. Such degradation would hinder the performance of the ILC as a precision machine and would require frequent repairs, which should be minimized to allow continuous and robust recording of data.

This paper investigates the neutron detector backgrounds from the extraction line beam dump through Monte Carlo simulations. The program FLUKA was used for the simulations due to its robustness with low energy neutron cross sections. Only the electron beam was used for the analysis, with the positron beam having symmetric and analogous results. The neutron fluences at the dump and at the detector were studied first without material near the beam line to provide a benchmark estimate. Concrete tunnel walls and a concrete collimator were then added to the simulation and their effect on the fluences was studied. Information gathered on neutron distributions during this work was used to simulate an isotropic and uniformly distributed neutron source located in the bore of the extraction line quadrupole and incident upon the beryllium beampipe and the five layers of the CCD silicon vertex detector central barrel to obtain an estimate of the real neutron fluence at the vertex detector. Particle biasing techniques were used to increase statistics on the simulated events, and the effectiveness of each bias was studied.

MATERIALS AND METHODS

The Monte Carlo program FLUKA was used for the simulations. The spent electron beam was given an initial position at the origin and was directed in the positive z-direction with

an energy of 250 GeV. The beam was collided into the water dump, which was placed at z = 300 m and was modeled by a circular cylinder of water with a radius of 75 cm and a length of 5 m (see Figure 2). The stainless steel container and Ti window were ignored since they would not impede an outward flux of neutrons from inside the dump and would increase the computation time.

The neutron fluence decays exponentially as a function of $\cos\theta$ for neutrons leaving the water dump in the negative z-direction, where θ is the polar angle with respect to the z-axis. The distributions were measured on the surface of the dump at A-A' in Figure 2, binned over small ranges of $\cos\theta$, and treated as isotropic in each bin (see Figure 3). The fluence was assumed to be isotropic in the range of $-1 < \cos\theta < -0.99$, which corresponds to an 8.1^{o} spread around the negative z-direction from the surface of the water dump and a circle of radius 42.7 m at z = 0.

The relevant fluence value was that measured in a circle of 1.5 cm radius at z = 0, concentric with the z-axis and parallel to the xy-plane, which is the IP fluence. The neutrons that reach this circle are the ones that will reach the vertex detector, since they have passed through the extraction line quadrupole bore and have not been impeded by collimators, magnets, or the tunnel. However, due to insufficient statistics from a scoring plane 1.5 cm in radius, a circular scoring plane 2 m in radius at z = 0 was used. The fluence calculated, per square centimeter, with this scoring plane would be the same as that measured with a 1.5 cm radius circle after a sufficiently long time due to the isotropic fluence.

As a primary benchmark estimate, 10^4 electrons were collided into the water dump and the IP fluence was measured with no material in the beamline. A concrete collimator and a concrete tunnel wall were then added to the simulation, as shown in Figure 2, and the IP fluence was measured with $5*10^4$ incident electrons. Finally, the tunnel was removed, the collimator was

kept in place, and the IP fluence was measured with $5*10^4$ incident electrons to study neutrons which scatter off of the tunnel walls and towards the detector.

In order to increase the statistics on the fluence scoring, three biasing techniques were used. Firstly, leading particle biasing was activated for electrons, positrons, and photons with energy below 2.5 GeV. Since simulating a full electromagnetic shower requires long computation time, leading particle biasing traces only the most energetic secondary created by the electrons, positrons, or photons below 2.5 GeV and eliminates all others, adjusting the 'weight' of the most energetic particle accordingly. Secondly, the interaction cross section for neutron production by photonuclear interactions was increased by a factor of 50, and the 'weight' associated with each neutron produced this way was decreased by a factor of 50 to preserve particle multiplicity. Finally, the cylindrical water dump was divided into 10 adjacent regions as in Figure 3. The region at the back of the dump was given an 'importance' of 1.0, and each region progressively closer to z = 0 was given a factor of 2.0 larger importance. As photons produced in the water dump passed from one region to another, their multiplicity was increased or decreased on average by the ratio of importances on either side of the boundary. Those passing from a region of lower importance to a region of higher importance were split on average by a factor of 2.0, and if traveling in the opposite direction were terminated or transported according to Russian Roulette [6]. FLUKA adjusted the 'weight' associated with biased particles to conserve particle multiplicity when the biases were applied. The computation time and effectiveness were studied for each type of bias with 6000 incident electrons.

Production and transport cutoffs were activated to decrease simulation time. A 50 MeV cutff on both was applied to electrons and positrons, and a 10 keV cutoff on both was applied to photons. A transport cutoff of $1.0332*10^{-5}$ GeV was applied to neutrons, which in FLUKA

corresponds to all low energy neutron groups with group number greater than or equal to 48. This value was chosen from Non-Ionizing Energy Loss (NIEL) scaling studies which show that neutrons below 10 keV do not have sufficient energy to create displacement damage, which are mostly from point defects and defect clusters, in the silicon bulk of the vertex detector [7]. The NIEL stopping power for neutrons in silicon also decreases with decreasing kinetic energy, and consequently neutrons below 10 keV were not a concern [8].

Once the neutron fluence at the IP was determined, the real neutron fluence at the CCD silicon vertex detector was studied, since the neutrons that reach the IP do not necessarily collide with the detector elements. The central barrel beryllium beampipe and the five layers of the Si barrel vertex detector were placed around the IP, as shown in Figure 4, and were based on the geometry specified at the Snowmass conference [9]. Figure 5 shows the full model of the detector and the nearest section of the extraction line, which consists of the quadrupole and the BeamCal. The BeamCal was modeled by a 12.5 cm thick slab of tungsten; the Si layers in it were ignored since they have a low probability of scattering the incident neutrons.

The neutron energy and 'weight' distributions at A-A' in Figure 2 were recorded from the previous simulations and were sampled from and used to generate a neutron source. Figure 6 shows the energy distribution. The initial positions of the neutrons in the source were generated randomly in the quadrupole bore at D-D' in Figure 5 in a circle of 1.5 cm radius centered at x = -2.1 cm and y = 0 cm. This starting point modeled the neutrons from the water dump that would reach the surface of the first extraction line quadrupole from the dump without being blocked by collimators, magnets, or other material. All neutrons in the source were given a 7 mrad trajectory from the z-axis.

The resulting neutron fluence at the five layers of the CCD silicon vertex detector was measured. This value was combined with the IP fluence, when the tunnel and collimator were in place, to provide an estimate of the total fluence at the vertex detector. The measurement was performed twice more, when the BeamCal was removed and when it was replaced with an infinitely absorbing material, in order to give an estimate of the BeamCal scattering. The tungsten was then returned, and the fluence as a function of the BeamCal aperture radius was studied. Finally, since the amount of displacement damage done to CCD silicon detectors by neutrons is proportional to neutron energy, a correction was applied to the fluence at the first layer of the detector, with the tungsten BeamCal in place, by scaling it to a 1 MeV equivalent silicon displacement damage (see Figure 7) [10]. This provided a normalized and comparable value for the amount of damage done to the vertex detector by neutron backscattering from the water dump. The other fluence values were left uncorrected, but could be corrected by the same method.

RESULTS

The IP fluence with no objects in the extraction line was measured to be $8.33*10^{10}$ +/- $1.50*10^{10}$ neutrons/cm^2/year. When the tunnel and collimator were added for a more accurate estimate, the fluence dropped to $3.65*10^{10}$ +/- $2.34*10^{10}$ neutrons/cm^2/year. When the tunnel was removed, there was no appreciable change in the fluence given the current level of statistics, as it remained at $3.73*10^{10}$ +/- $3.34*10^{10}$ neutrons/cm^2/year. The computation time and effectiveness of the biasing techniques used in the IP fluence scoring are shown in Table 1.

Figure 8 shows the fluence at the five layers of the inner detector for the three different modifications of the BeamCal. For the first layer, there was over an order of magnitude difference between the tungsten and no BeamCal cases, the former having a fluence of $1.79*10^{10}$

neutrons/cm^2/year and latter having one of 4.28*10^8 neutrons/cm^2/year. There was a similar difference between the tungsten and black BeamCal cases, the latter having a fluence of 2.21*10^7 neutrons/cm^2/year. In all three cases, the fluence in layers two to five dropped far below that in layer 1, implying that the first layer experiences the bulk of the neutron damage. The neutron fluence of 4.28*10^8 neutrons/cm^2/year at the first layer when the tungsten BeamCal was in place is of particular importance, since it was found for the current status of the extraction line for the first layer, and is shown circled in Figure 8. This neutron fluence at the detector is 1.2% of the fluence that reaches the IP, with the rest of the neutrons passing through the empty space in the detector or scattering off of the Be beampipe harmlessly (see Figure 4).

The energy distribution of the neutrons that contribute to this fluence shows a large number of neutrons with energy greater than 10 MeV, implying that the current nominal fluence underestimates the displacement damage power (see Figure 9). This distribution corrected with the information from Figure 8 gives the 1 MeV damage equivalent neutron fluence, which was calculated to be 9.27*10^8 neutrons/cm^2/year, more than a factor of two larger than the uncorrected value. The symmetric positron beam contributes the same amount of displacement damage, meaning the final corrected fluence is 1.85*10^9 neutrons/cm^2/year. In one year, this amounts to 18.5% of the 10^{10} neutrons/cm^2 flux that would degrade the vertex detector to the point of repair or replacement.

Figure 10 shows the fluence at the five layers of the detector as the BeamCal aperture was expanded; the fluence increases as the aperture is opened.

DISCUSSION AND CONCLUSIONS

The neutron fluence at the IP when there is no material in the extraction line, which was 8.33*10^{10} +/- 1.50*10^{10} neutrons/cm^2/year, is the highest level of background that is possible at

the detector from backscattering from the beam dump if one assumes that every particle that reaches the IP will damage the vertex detector. The collimator in front of the dump blocked roughly half of this flux, since the fluence decreased by a factor of two to $3.73*10^{10}$ +/- $3.34*10^{10}$ neutrons/cm^2/year when the collimator was added. There was no appreciable increase in fluence when the tunnel was added given the current level of statistics, as it remained at $3.65*10^{10}$ +/- $2.34*10^{10}$ neutrons/cm^2/year. This should not be interpreted to mean that there is no scattering off of the tunnel walls, as the root-mean-square (RMS) deviation in the fluences once the collimator was added was more than 50% of the fluence itself. The amount of scattering is an important value to know when looking for potential solutions to reduce the backscattering problem. One solution being considered is to move the water dump out of a direct line of sight from the detector and to place a dipole immediately before the collimator to bend the trajectory of the beam towards the dump. If neutrons do not scatter off of the tunnel walls, this would be an effective solution. However, if the neutrons do scatter off of the tunnel walls and act like a gas of particles moving back towards the detector, as suspected, then bending the beam would not reduce this background source. A further study of neutron scattering is being conducted.

The computation time and effectiveness of the biasing techniques for 6000 incident electrons are shown in Table 1. As columns 6 and 7 show, that statistics increased by a factor of 203 at the surface of the dump and by a factor of 59 at the IP. This allowed the estimation of a more stable IP fluence and provided a large distribution from which to sample in order to produce the neutron source. The total ‘weight’ of the neutrons recorded at z = 300 m and z = 0 m, shown in columns 4 and 5, was preserved as the different biases were applied, meaning that the biases did not obscure the underlying physics when improving the statistics. This validated the use of these biases with 10^4 and $5*10^4$ incident electrons when estimating the IP fluence.

The sharp drop in the fluence at layer 1 of the vertex detector from $1.79*10^{10}$ to $4.28*10^{8}$ neutrons/cm^2/year, shown in Figure 8, implies that the BeamCal acts like a collimator and impedes the flow of neutrons through it by 97.6%. Since this large amount of collimation is not the intent of the BeamCal, the effect of the fluence on its tungsten and silicon layers are being studied in further detail. When the black BeamCal is in place, there is no direct line of sight from the quadrupole bore to the detector, and the only neutrons that can hit the detector are those that scatter off of the beryllium beampipe. Thus, the further drop in the fluence to $2.21*10^{7}$ neutrons/cm^2/year for the black BeamCal gives the estimate that 5.16% of the neutrons that hit the detector have scattered off of the beampipe, and the rest have hit it along their direct line of sight. Furthermore, the order of magnitude drop in the fluence between layer 1 and layers 2 to 5 of the silicon detector show that the outer layers are well shielded from the neutron fluence and are not a concern; attention should be focused on the innermost layer which takes the bulk of the displacement damage. The endcap sections of the silicon detector are being added and their effect on the fluence at all of the layers is being studied.

The neutron energy at the vertex detector is more heavily distributed above 10 MeV, as shown in Figure 9, which implies that the damage to the detector is greater than the nominal fluence. The corrected 1 MeV equivalent neutron fluence of $9.27*10^{8}$ neutrons/cm^2/year is properly normalized and can be compared to the threshold value of 10^{10} neutrons/cm^2. When the positron beam is considered and the fluence doubles to $1.85*10^{9}$ neutrons/cm^2/year, the neutron backscattering from the dump contributes 18.5% of the threshold value in one year. Even if this was the only background, the detector would degrade within 6 years; a longer lifetime is desired.

Although the current background level is not overwhelming, the relationship in Figure 10 is an important consideration when analyzing the effect of other neutron backgrounds in the

detector. Two particularly important neutron backgrounds arise from electron-positron pairs produced from beam-beam interactions and synchrotron radiation produced from the quadrupoles used to focus the beams immediately before the IP; both products can hit the BeamCal and produce a neutrons through electromagnetic showers [11]. This is the dominant source of neutron background, as the neutrons produced at the BeamCal are immediately by the vertex detector and cannot be shielded. A simple method to reduce this flux would be to open the BeamCal aperture to prevent interactions. However, as Figure 10 shows, a tradeoff exists, since doing so would increase the neutron background from the extraction line beam dump. In the extreme case, the BeamCal could be opened up larger than the extraction line quadrupole aperture, and the dump background would equal $2.09*10^{10}$ neutrons/cm^2/year, which would require the vertex detector to be replaced every six months.

These results have directed our further studies towards analyzing the main sources of neutron backgrounds, including electron-positron pairs, Beamstrahlung photons, and radiative Bhabha scattering, in order to obtain a complete picture of the overall neutron damage done to the vertex detector and to understand the tradeoffs that exist in attempting to suppress it. The detector model will also be improved, and the effect of the neutron flux on the endcap tracking chambers and other elements will be studied. The neutron damage in the CCD silicon detector must be minimized in order to ensure detector longevity as well as minimal repairs of the detector components, allowing the ILC to effectively perform measurements and discover new fundamental physics.

ACKNOWLEDGEMENTS

This research was conducted at the Stanford Linear Accelerator Center, located in Menlo Park, California, USA. I would like to thank the Department of Energy for giving me with the

opportunity to participate in the SULI program. Most importantly, I would like to thank my two supervisors, Dr. Takashi Maruyama and Dr. Lewis Keller, whose knowledge, enthusiasm, and dedication made the work and the experience both exciting and rewarding. I would also like to acknowledge Mario Santana for his help resolving problems with FLUKA and Dr. Nan Phinney for presenting me with this research opportunity. Finally, I would like to thank Dr. Tom Markiewicz and Nicholas Arias for their help throughout the summer.

REFERENCES

[1] ATLAS Collaboration, "ATLAS Detector and Physics Performance Technical Design Report," ATLAS TDR 14, CERN/LHCC 99-14, Vol. 1, pp. 3, 25 May 1999.

[2] G. Aarons *et al.*, "International Linear Collider Reference Design Report," ILC Global Design Effort and World Wide Study, Vol. 3: Accelerator, pp. 2.1-1 to 2.1-5, August 2007.

[3] G. Aarons *et al.*, "International Linear Collider Reference Design Report," ILC Global Design Effort and World Wide Study, Vol. 3: Accelerator, pp. 2.7-1 to 2.7-18, August 2007.

[4] W. R. Dawes, Jr., "Overview of Radiation Hardening for Semiconductor Detectors," *Nuclear Instruments and Methods in Physics Research*, A 288, pp. 54-61, 1990.

[5] J. E. Brau and N. Sinev, "Operation of a CCD Particle Detector in the Presence of Bulk Neutron Damage," *IEEE Transactions on Nuclear Science*, vol. 47, no. 6, pp. 1898-1901, December 2000.

[6] The FLUKA team, *Online FLUKA manual*, INFN and CERN, version 2006.3b, March 2007.

[7] G. Lindstrom, "Radiation damage in silicon detectors," *Nuclear Instruments and Methods in Physics Research*, A 512, pp. 30-43, 2003.

[8] A. Chilingarov, J. S. Meyer, and T. Sloan, "Radiation damage due to NIEL in GaAs particle detectors," *Nuclear Instruments and Methods in Physics Research*, A 395, pp. 35-44, 1997.

[9] N. Graf, SLAC Confluence, sidaug05, July 23, 2005,

http://confluence.slac.stanford.edu/display/ilc/sidaug05

[10] T. M. Flanders and M. H. Sparks, “Monte Carlo calculations of the neutron environment produced by the White Sands Missile Range Fast Burst Reactor,” *Nuclear Science and Engineering*, vol. 103, pp. 265 – 275, 1989.

[11] T. Abe *et al.*, “SiD Detector Outline Document,” pp. 30, 19 May 2006.

Figures

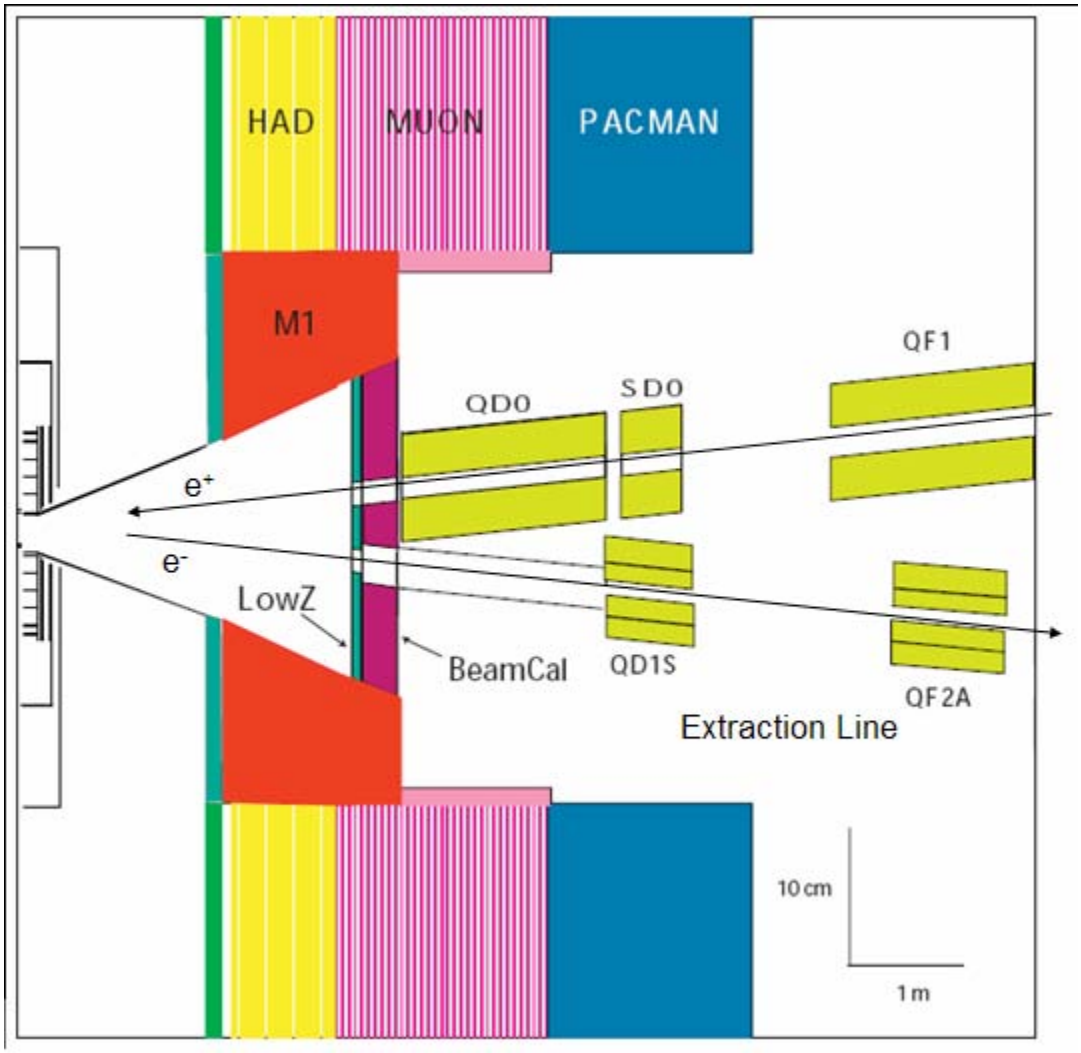

Figure 1. A Geant4 model of the extraction line. The light green indicates quadrupoles, and the water dump is located 300 m down the extraction line.

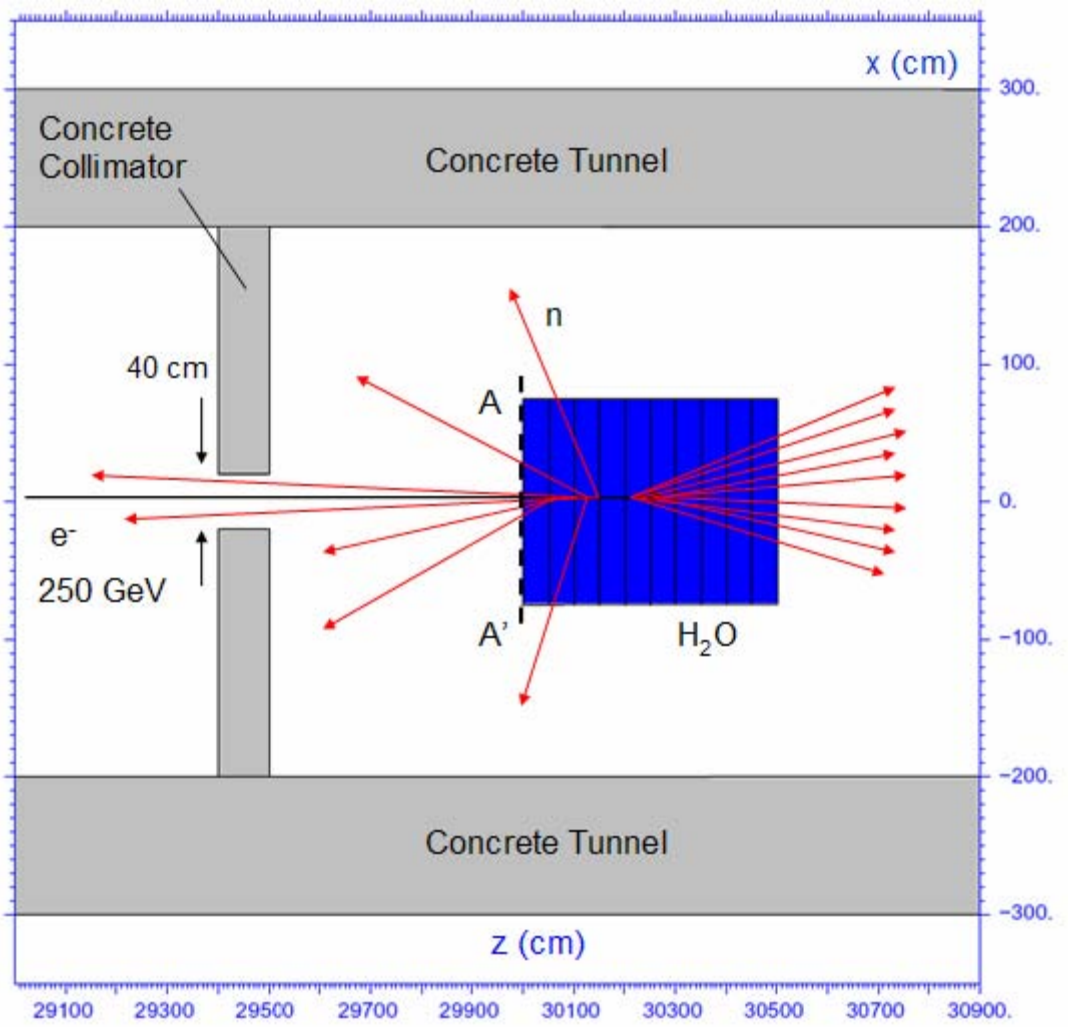

Figure 2. The FLUKA model of the beam dump with a concrete collimator and concrete tunnel in place. The 250 GeV input electron beam acts as a line source in the water dump, and the red arrows symbolize possible trajectories of the neutrons produced in the dump along that source.

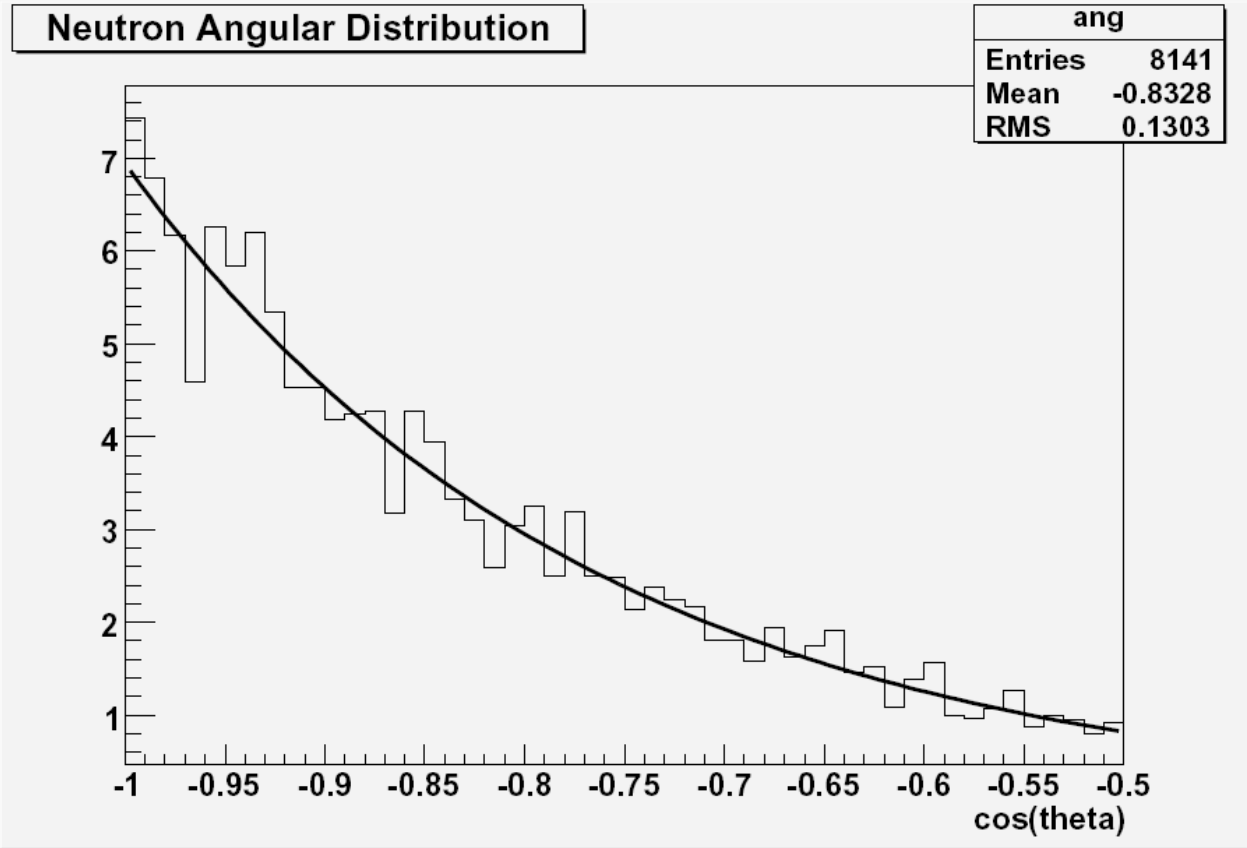

Figure 3. The neutron angular distribution at A-A' in Figure 2. The neutron fluence can be treated as isotropic in each bin. The fluence was scored at z = 0 m with a 2 m radius scoring plane with the assumption of the isotropy in the first bin ($-1 < \cos\theta < -0.99$).

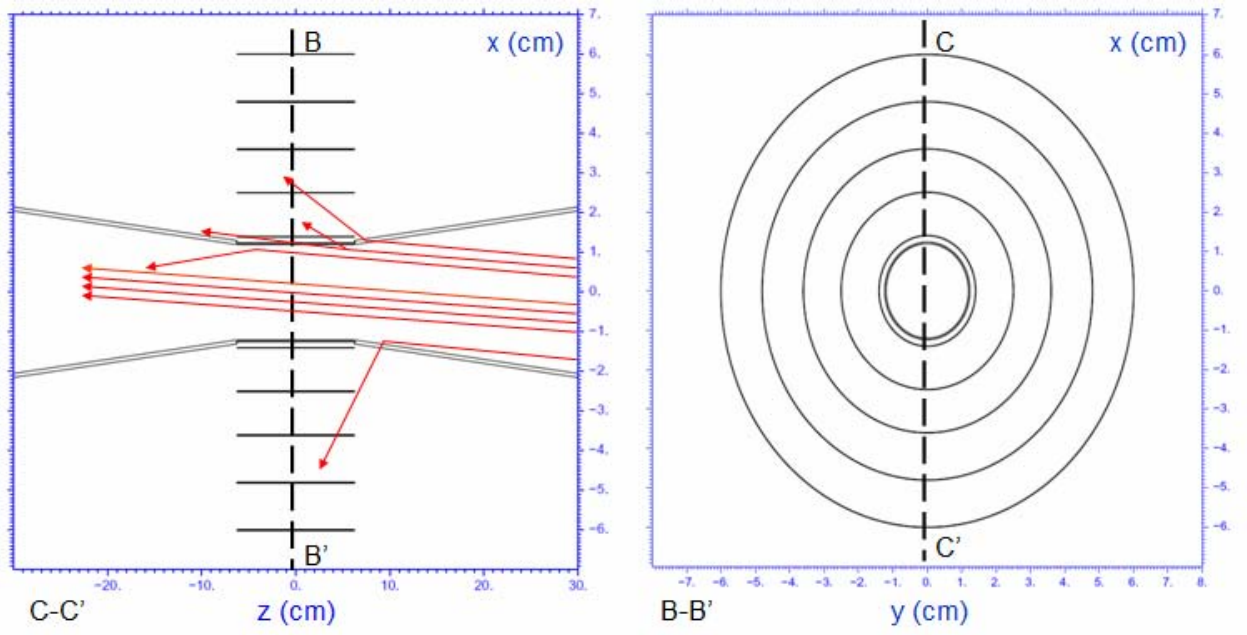

Figure 4. The CCD silicon vertex detector in the SiD detector model and the beryllium beampipe. The five layers of the detector were modeled by concentric cylinders, each 0.01 cm

thick. The beampipe barrel was made 0.04 cm thick and the conical section was made 0.1 cm thick. The left and right conical sections of the beampipe extend outward to -167.9 cm and +167.9 cm respectively, but have been truncated here at -30 cm and +30 cm [9].

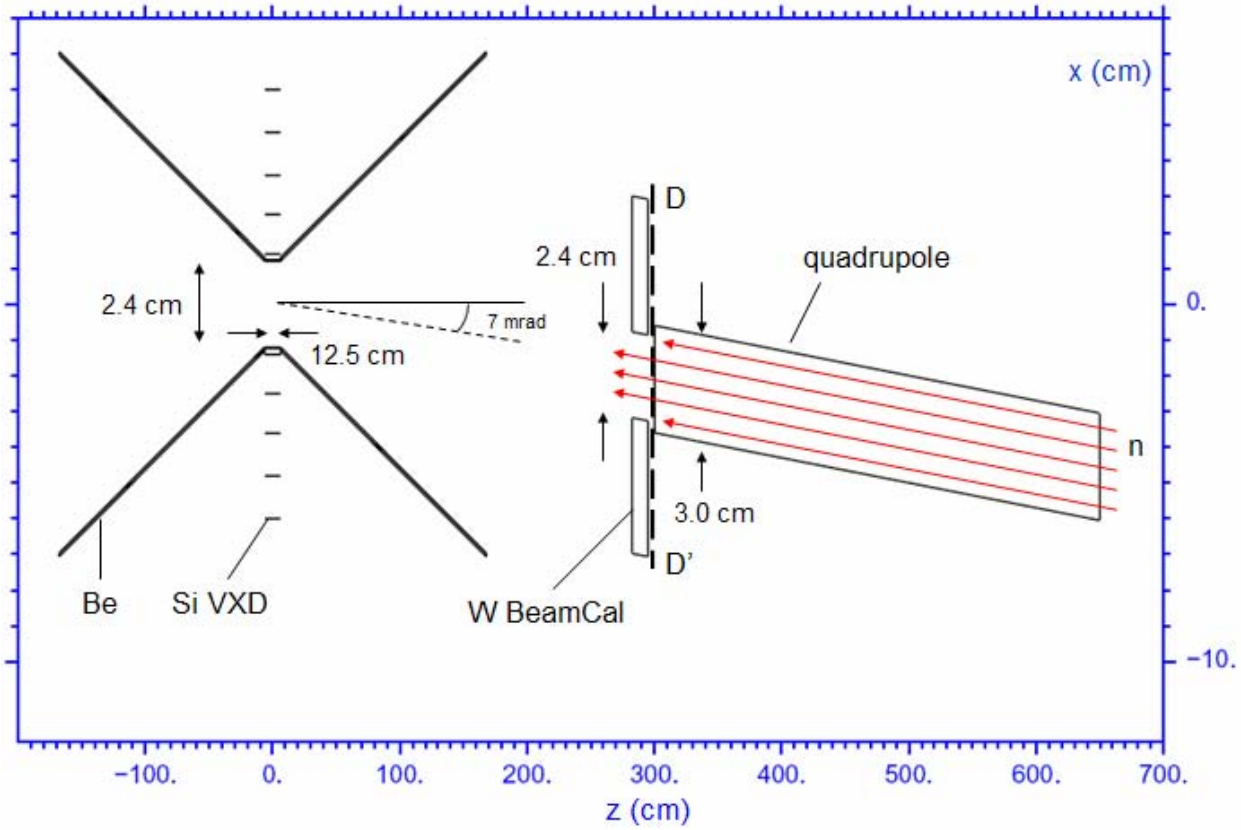

Figure 5. The full model of the extraction line. The BeamCal was modeled by a 12.5 cm thick slab of tungsten. The neutron source was evenly distribution on the surface of the quadrupole at D-D' and the neutrons were given a trajectory of 7 mrad towards the detector.

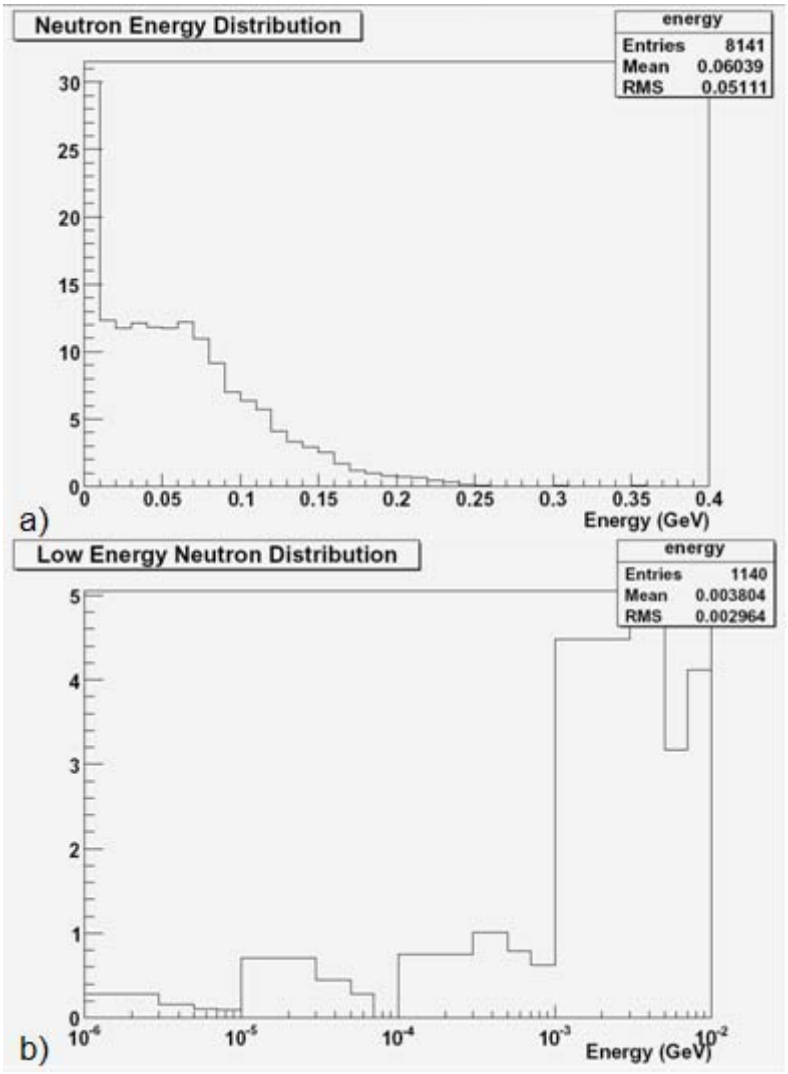

Figure 6. a) The neutron energy distribution collected at A-A' in Figure 2. b) The low energy neutron distribution for neutrons in the first bin in Figure 6a).

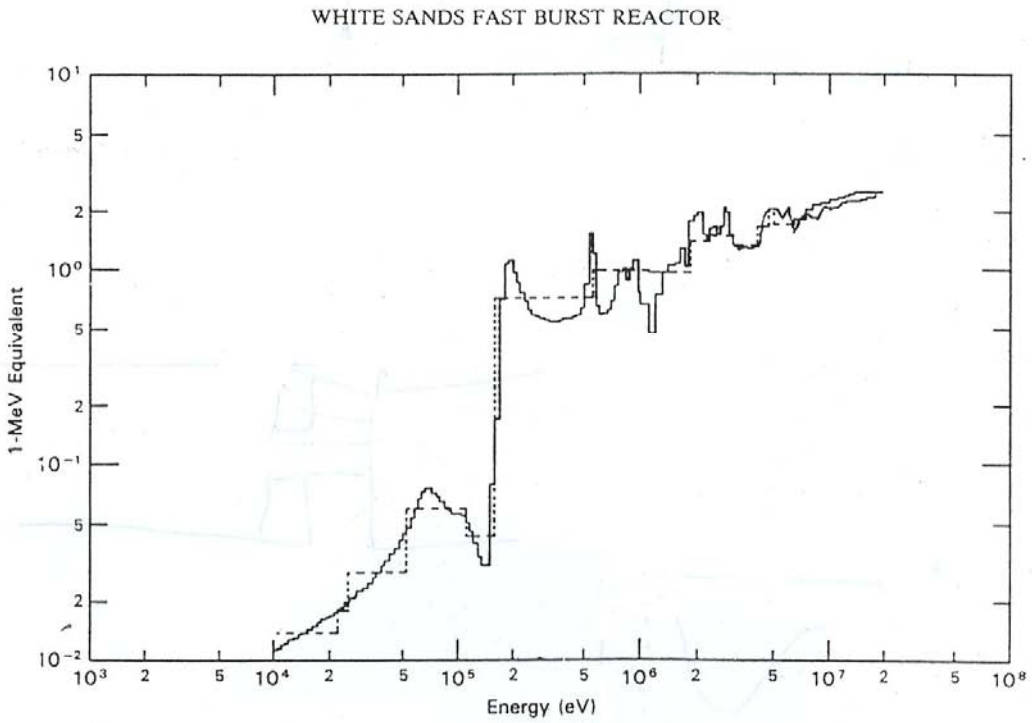

Figure 7. Silicon displacement as a function of energy. Figure was made by T. M. Flanders and M. H. Sparks [10].

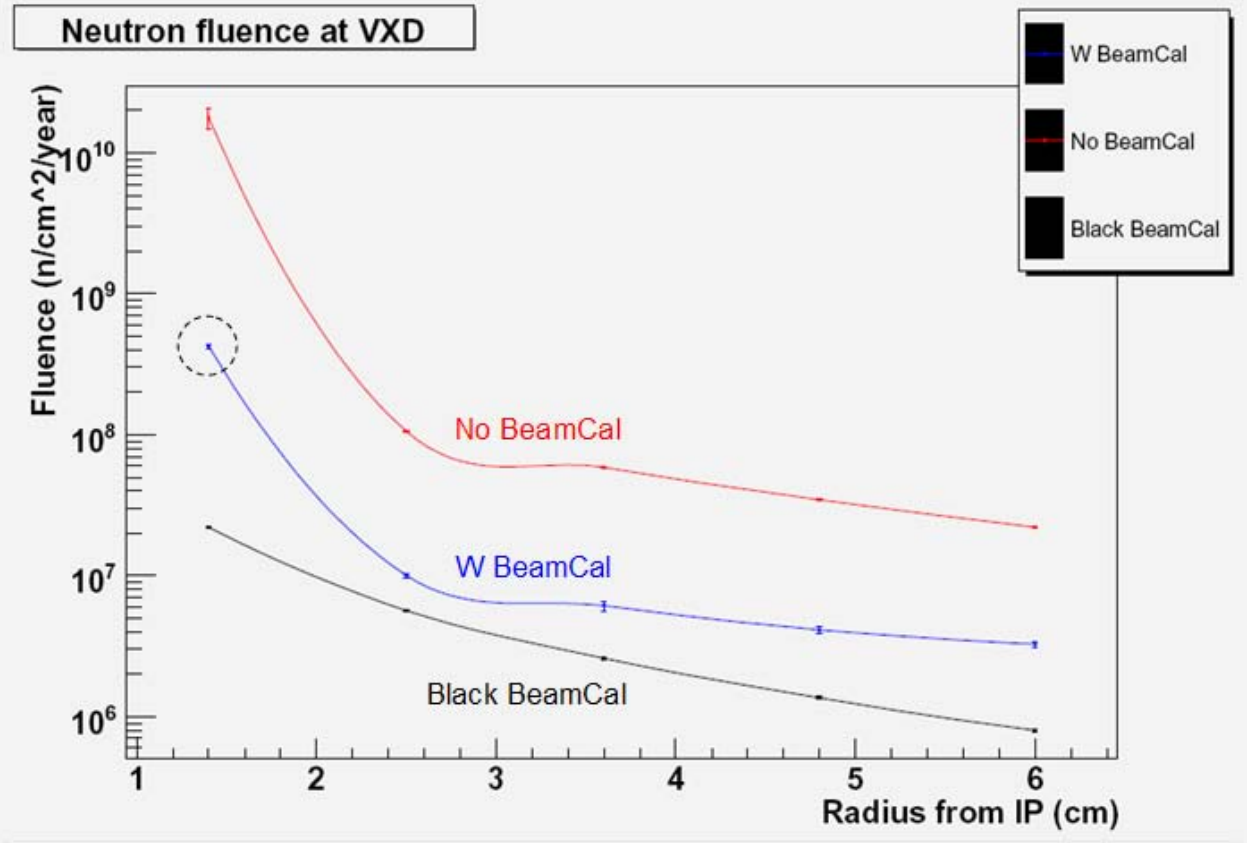

Figure 8. The fluence as a function of radius from the IP for three different modifications of the BeamCal. The circled value, $4.28*10^8$ neutrons/cm^2/year, is of particular importance, since it corresponds to the current BeamCal type and aperture radius.

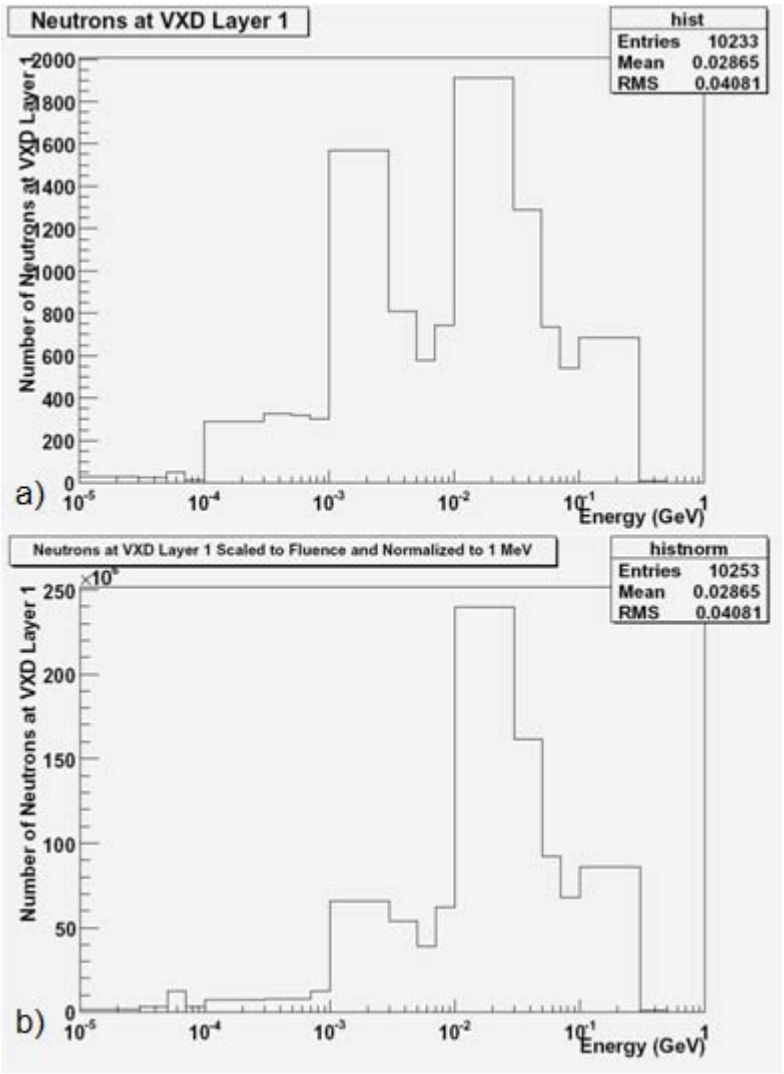

Figure 9. a) The neutron energy distribution for the flux that reaches the first layer of the silicon detector. b) The neutron energy distribution scaled to 1 MeV equivalent neutron displacement damage to CCD silicon detectors.

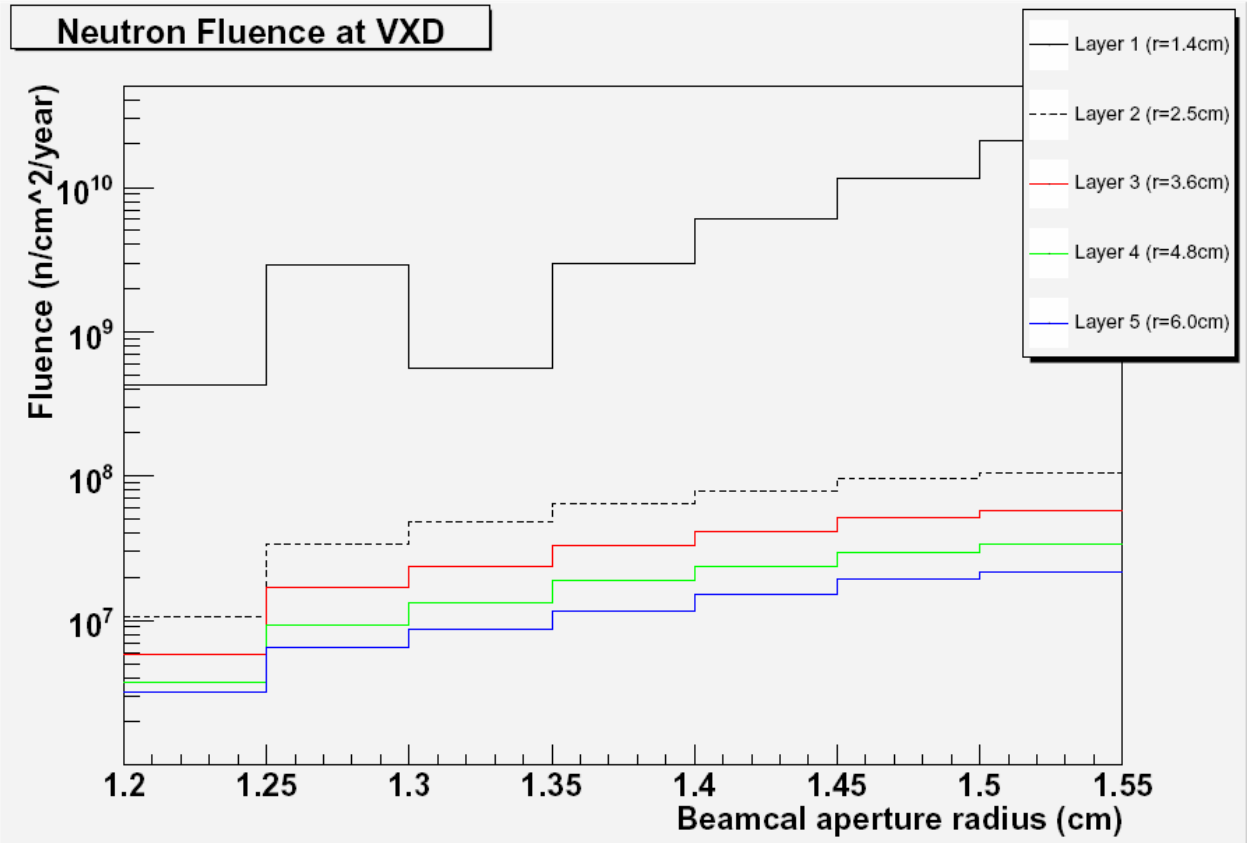

Figure 10. The neutron fluence at the five layers of the vertex detector as the aperture radius of the BeamCal is expanded. At a radius of 1.5 cm, the BeamCal does not block any of the incident neutrons.

Tables

			Neutron total 'weight'		Neutron total number	
Run Number	Type of Bias	Computation Time	At z = 300 m	At z = 0	At z = 300 m	At z = 0
1	No biasing	23 hours 35 min	82	2	82	2
2	Leading particle biasing activated for EMF particles (for e^-,e^+ < 2.5 GeV and γ < 2.5 GeV)	1 hour 36 min	103	0	87	0
3	Decay length biasing activated for photonuclear interactions (biasing factor = 0.020)	6 hours 46 min	103	0.781	5008	49
4	Splitting in waterdump activated for photons	6 hours 22 min	96.4	1.09	16619	117

	(10 regions in waterdump, factor of 2 for each region boundary)					

Table 1. Computation time and effectiveness of each bias. All runs were made with 6000 electrons incident on the water dump and each run contains the biases of all previous runs.

SLAC-TN-07-015
August 2007

Definition of a Twelve-Point Polygonal SAA Boundary for the GLAST Mission

Sabra I. Djomehri

Office of Science, SULI Program 2007

University of California, Santa Cruz

Stanford Linear Accelerator Center

Menlo Park, California

August 24, 2007

Prepared in fulfillment of the requirement of the Office of Science, Department of Energy's Science Undergraduate Laboratory Internship under the direction of Markus M. Ackermann at the Kavli Institute for Particle Astrophysics at Stanford Linear Accelerator Center.

Participant: _____
Signature

Research Advisor: _____
Signature

Work supported in part by US Department of Energy contract DE-AC02-76SF00515

TABLE OF CONTENTS

I. ABSTRACT

Definition of a Twelve-Point Polygonal SAA Boundary for the GLAST Mission. SABRA I. DJOMEHRI (University of California, Santa Cruz, CA 95064) MARKUS M. ACKERMANN (Stanford Linear Accelerator Center, Menlo Park, CA 94025).

The Gamma-Ray Large Area Space Telescope (GLAST), set to launch in early 2008, detects gamma rays within a huge energy range of 100 MeV – 300 GeV. Background cosmic radiation interferes with such detection resulting in confusion over distinguishing cosmic from gamma rays encountered. This quandary is resolved by encasing GLAST's Large Area Telescope (LAT) with an Anti-Coincidence Detector (ACD), a device which identifies and vetoes charged particles. The ACD accomplishes this through plastic scintillator tiles; when cosmic rays strike, photons produced induce currents in Photomulitplier Tubes (PMTs) attached to these tiles. However, as GLAST orbits Earth at altitudes ~550km and latitudes between -26° and 26°, it will confront the South Atlantic Anomaly (SAA), a region of high particle flux caused by trapped radiation in the geomagnetic field. Since the SAA flux would degrade the sensitivity of the ACD's PMTs over time, a determined boundary enclosing this region need be attained, signaling when to lower the voltage on the PMTs as a protective measure. The operational constraints on such a boundary require a convex SAA polygon with twelve edges, whose area is minimal ensuring GLAST has maximum observation time. The AP8 and PSB97 models describing the behavior of trapped radiation were used in analyzing the SAA and defining a convex SAA boundary of twelve sides. The smallest possible boundary was found to cover 14.58% of GLAST's observation time. Further analysis of defining a boundary safety margin to account for inaccuracies in the models reveals if the total SAA

hull area is increased by ~20%, the loss of total observational area is < 5%. These twelve coordinates defining the SAA flux region are ready for implementation by the GLAST satellite.

II. INTRODUCTION

The universe contains a myriad of exotic entities, some able to produce enormous amounts of energy. Gamma-ray radiation, generated by such objects as black holes, neutron stars, and relativistic hot gas, is the most energetic form of radiation. The Gamma-ray Large Area Space Telescope (GLAST) seeks to unravel mysteries behind such extraordinary phenomena in order to better understand the high-energy world and how it affects the behavior of the universe. Set to launch in early 2008, the GLAST satellite is highly sensitive to gamma rays within an approximate energy range of 100MeV-300GeV [1]. Being 30-100 times more sensitive than any previous gamma ray telescope, GLAST aims at locating gamma ray sources throughout the universe and studying their properties [1].

A key component of GLAST is its outer detector layer, called the Anti-Coincidence Detector (ACD), whose purpose is to efficiently identify and disregard incident charged particles. In order to maximize its veto capabilities, the ACD consists of 89 plastic scintillator tiles, for which signals produced in them are read out by Photomultiplier Tubes (PMTs) [2]. When the scintillators encounter an influx of charged particles, photons are produced which pass into the PMT. Upon entering, the photons encounter the photocathode, causing electrons to be ejected via the photoelectric effect. These electrons proceed towards an increasingly positive series of dynodes, generating a

cascade of electrons [3]. This amplification of electrons generates a measurable current which indicates when an "unwanted" particle has been received by the ACD. About its orbit, GLAST will encounter many such charged particles; the particles of greatest concern to GLAST are those that have been captured by the geomagnetic field.

Earth's magnetic field acts as a shield from solar and cosmic particles, either by deflecting or trapping them. When such energetically charged particles become trapped, their movement is controlled by the magnetospheric magnetic field and the aggregate of particles forms regions above Earth known as the inner and outer Van Allen radiation belts. The trajectory of a trapped particle residing in these belts is described by gyration along magnetic field lines and gradual longitudinal drifts westward or eastward (for ions or electrons, respectively) [4]. The toroidal surfaces generated from this kind of motion are called drift shells. In order to describe the behavior of trapped radiation, the McIlwain coordinate system for dipole/non-dipole situations can be applied. This system identifies the coordinates (B,L) , for which B represents the relative magnetic field intensity with respect to the magnetic equator, and L signifies the equatorial radius of a drift shell [4]. It is important to note that a particle always remains on the same drift shell, which is different than a magnetic shell. A unique effect of the characteristic properties of the geomagnetic field is a phenomenon called the South Atlantic Anomaly (SAA), a portion of the inner Van Allen radiation belt that approaches closest to the Earth’s surface.

A common problem affecting satellites (and in particular GLAST's ACD) occurs when their orbit crosses the SAA. At this altitude, the flux of radiation is significantly higher than anywhere else due to both the offset center of the geomagnetic field and its tilt from Earth’s axis [5]. Passing through this high radiation environment degrades the

sensitivity and thus performance of the ACD by inducing high currents in the PMTs. To prevent this, the ACD must be turned off from survey mode when it encounters the SAA zone, which contributes to lost observation time. In order to maximize GLAST's period of observation, precision is necessary in determining the smallest possible polygonal boundary of the SAA region.

III. MATERIALS AND METHODS

a) Models

To determine the SAA boundary region for GLAST, models of trapped radiation are applied. The standard models of radiation belt energetic particles are the AP-8 and AE-8 models, for protons and electrons, respectively. These models produce omnidirectional fluxes as functions of the geomagnetic coordinates, B/B_o and L, where $B_o = 0.311653/L^3$ [6]. They map fluxes in the energy range 0.04 MeV - 7 MeV for electrons and 0.1 MeV - 400 MeV for protons. Being able to cover this energy range is a significant improvement from older AP models (i.e. AP-1,5,6, and 7), which contain large discrepancies in the energy spectra [7]. Another feature of this model is that it can describe solar maximum/minimum cycles; however, time variations beyond solar cycles are not considered. All data is taken from nearly two dozen satellites from the sixties and seventies [7].

In addition to the standard model, the PSB97 model is also used. This model specifically maps low altitude proton fluxes in the energy range between 18 MeV - 500 MeV, and is restricted to fluxes during solar minimum conditions [8]. Data for this model is taken from the SAMPEX satellite. Geomagnetic field models are necessary to translate

geographical coordinates of fluxes into geomagnetic coordinates. For that purpose, the IGRF-10 is used throughout this work [9]. However, since the population of high-energy charged particles (> 10 MeV) stably trapped by the geomagnetic field mainly consists of protons, most of the energy acquired by GLAST's ACD is due to protons. Therefore, the following investigation is restricted to SAA proton fluxes.

b) Operational Constraints

As such models can be used to provide visuals of the approximate boundary of the SAA, they do not actually calculate a boundary of the type required by GLAST. The GLAST requires all enclosing edges of this boundary region to be convex to prevent passing through the SAA more than once per orbit. In order to do this, one must calculate the convex hull of the SAA region. A convex hull is the smallest convex set that includes a given set of points [10]. Figure 1 represents a 3D convex hull, where the overall shape is determined by the extreme (or outer) points in the set [11]. For the purpose of attaining the SAA boundary, simply finding a 2D hull of the SAA is necessary. Python scripts evaluate all points in a grid of latitudes (-26°, 26°) and longitudes (-180°, 180°) that have fluxes larger than 1 particle/(cm^2 s), and places these points in a set for determining the convex hull. In addition to being convex, another technical requirement for this polygon is that it must have twelve edges.

c) The Algorithm

Various convex hull algorithms have been produced, some faster than others. Examples of some well known algorithms include Graham Scan (in O($n$log$n$) time), QuickHull (in O(nk) time), and Brute Force (in O(n^4) time) [12]. The time described here represents the number of operations utilized by an algorithm to solve the given problem,

with *n* being the number of points in the input set, and *k* being the number of vertices on the output hull. The less factors existing, the shorter the runtime resulting in a faster algorithm. The fairly quick and simplistic algorithm, QuickHull, is used in this work to determine the SAA's convex hull. Its basic procedure is generating a full hull by first calculating an upper and lower hull. QuickHull does this by using triangulation; it starts by finding the leftmost highest and rightmost lowest extreme points (*a*,*b*), finds a third extreme point *c* farthest away from *ab* (in the orthogonal direction), discards all points inside Δ*abc*, and then recurses on the sides (a,c) and (c,b). Figure 2 is a representation of this procedure [12].

IV. RESULTS

Before the actual convex hull is attained, it is necessary to test the accuracy of the two available models (AP8 and PSB97). Figure 3 shows two possible versions of the SAA flux region as defined by both models in the year 2008; the gray contour representing the AP8 SAA and the blue contour lines describing the PSB97 SAA. In all following contour graphs presented, only protons with energies larger than 20 MeV are considered, and all fluxes (shown by the colorbars) given in particles/(cm^2 s) correspond to a logarithmic scale of base 10. Since both SAA representations are valid, the determined SAA boundary should encompass both resulting in a type of combined hull.

Two concerns that must be considered when defining this boundary are the disparities at solar maximum/minimum conditions and those that arise after extended time periods. Figure 4 compares changes in the SAA at solar minimum and solar maximum using the AP8 model, with the gray contour representing solar minimum

conditions and the blue contour lines defining the solar maximum situation. At solar maximum, the size of the SAA is predicted to decrease due to increased particle interaction with the Earth's upper atmosphere. These interactions cause erosion of the SAA's outer edges, whose effects are verified by Figure 4. Since the flux region at solar maximum never expands past the solar minimum flux region, this factor is ignored in defining the SAA boundary and thus is no longer a concern.

Another potential concern regards shifts in the SAA over large temporal intervals. As mentioned above, protons have a slow longitudinal westward drift, which is a ~0.3° shift per year [4]. Figure 5 verifies this shift, and reveals how slight the shift actually is even over the course of a decade. The gray contour represents the AP8 model in the year 2000, while the blue contour lines describe the AP8 model in the year 2010. Since this westward shift is relatively unsubstantial, it can also be ignored when defining the SAA hull (assuming periodic updates of the boundary's coordinates are implemented).

The next three figures, Figures 6-8, exemplify the evolution of the defined SAA boundary from an *n*-sided polygon to the desired 12-sided polygon. To account for uncertainties in the models, each point with a flux > 1 particle/(cm^2 s) in either the two models is considered inside the SAA. Each point on a densely spaced grid of latitudes and longitudes is classified based on this condition as lying inside or outside the SAA and the convex hull enclosing all inner points is calculated by the QuickHull algorithm.

Figure 6 shows an attained *n*-sided polygon defined by the blue line, which encloses the green region containing all points in the SAA with fluxes > 1 particle/(cm^2 s). Figure 7 compares the previously attained *n*-sided convex hull from Figure 6 with the reduced 12-sided convex polygon. To achieve this reduction, the area loss is < 0.01%,

which signifies that the technical requirement of the GLAST to be bounded by a 12-edge polygon does not decrease GLAST's total observational time by any substantial amount. Figure 8 compares the newly attained 12-edge convex SAA boundary with the original SAA flux regions of both models, where the red line is the defined boundary, the gray contour represents fluxes corresponding to the AP8 model, and the blue contour lines once again show fluxes corresponding to the PSB97 model. The figure verifies that the determined SAA hull actually envelopes both models' SAA representations, and displays twelve coordinate points which accurately define the vertices of the SAA polygon. (See Table 1 for exact coordinates).

One safety measure that can be applied to account for uncertainties in these models' predictions is determining a suitable margin of error for this boundary. Again, python scripts were used in developing scaled versions of the SAA polygon. An example can be seen in Figure 9, which shows the possibility of an SAA hull expanded in all directions (except the hull's base) by 3°. Table 1 compares the twelve unscaled vertices of the SAA polygon with the twelve SAA vertices scaled by 1°, 3°, and 5°. The impact of having such a safety margin can be further analyzed from Table 2, which gives a range of scaled amounts, from 0.5° – 5°. For example, if the SAA polygon were actually to be scaled by 3°, this would account for an increase in SAA area by ~13%, but the total loss in observational time (measured by the loss in observational area) would be roughly 2.25%. Even if the SAA boundary were scaled by 5°, which would increase the area by ~22%, the loss of observational time is still comfortably < 5%.

V. DISCUSSION AND CONCLUSIONS

The objective of this project was to meticulously define a 12-edge convex SAA polygonal boundary of minimum area in order to ensure maximum observational time for GLAST. The vertices defining this polygon are noted in Table 1. By utilizing these coordinates in its software, GLAST will know when to lower the voltages of the ACD and thus when it should be shut off from survey mode during the time spent crossing over the SAA high flux zone. This will ensure lasting efficiency of the ACD, which itself strives to protect and support efficiency of GLAST's ability to take data.

Coordinates revealed above were derived based on the operational constraints of GLAST to have a polygonal boundary with twelve sides, be convex, and only consider latitudes of (-26°, 26°) and longitudes of (-180°, 180°). Conditions at solar maximum did not affect the definition of this boundary, nor did large spans of time; these concerns were left behind when the convex hull was actually determined. After an *n*-sided SAA polygon was defined using the AP8/PSB97 trapped radiation models and the QuickHull algorithm, a concern arose regarding a potentially considerable loss in observational area when the hull is reduced from *n* sides to twelve. However, this concern is quelled by the fact that twelve edges can be almost directly drawn on top of the *n*-edged polygon, resulting in a total observational area loss of < 0.01%. The determined SAA boundary of minimum area was found to cover 14.58% of GLAST's observation time. Further analysis entails deciding an appropriate safety margin for the SAA boundary due to possible errors within the models. Results show that scaling the SAA polygon by 0.5° – 5° can increase polygonal area in a range between ~ 2% - 22%. However, for this range of scaling,

GLAST's total observational time decreases by < 5%, or more specifically by ~ 0.35% - 3.8%.

VI. ACKNOWLEDGMENTS

This research was supported by the Kavli Institute for Particle Astrophysics at Stanford Linear Accelerator Center, Department of Energy, Office of Science. I would like to thank my mentor Markus Ackermann, Greg Madejski, and Doug Applegate for all their support and assistance throughout the term of my internship. Also, I would like to thank the Department of Energy, the Office of Science, and the SULI Program for providing my participation in this sublime internship experience.

VII. REFERENCES

[1] Michelson, P.F. "Instrumentation for the Gamma-ray Large Area Space Telescope (GLAST) mission," X-Ray and Gamma-Ray Telescopes and Instruments for Astronomy, vol. 4851, pp. 1144-1150, 2003.

[2] Moiseev, A.A., Hartman, R.C., Johnson, T.E., Ormes, J.F., Thompson, D.J., "Design and Characteristics of the Anticoincidence Detector for the GLASTE Large Area Telescope," Proceedings of the 29th ICRC, Pune, India, 2005.

[3] Tissue, B.M., "Photomultiplier Tube", [Online document], 1996 Feb 21, [cited 2007 July 3], Available http: http://elchem.kaist.ac.kr/vt/chem-ed/optics/detector/pmt.htm

[4] McIlwain, C. E., Coordinates for Mapping the Distribution of Magnetically Trapped Particles, *J. Geophys. Res., 66*, 3681-3691, 1961.

[5] Daly, E.J., "The Radiation Belts", in Radiation Physics and Chemistry, 43, 1, pp.1-18 (in Special Issue on Space Radiation Environment and Effects), 1994.

[6] Hess, W.N., The Radiation Belt and Magnetosphere, Blaisdell Publ. Co., 1968.

[7] Heynderickx, D., J. Lemaire, E. J. Daly, and H. D. R. Evans, Calculating Low-Altitude Trapped Particle Fluxes With the NASA Models AP-8 and AE-8, *Radiat. Meas., 26*, 947-952, 1996b.

[8] Heynderickx, D., M. Kruglanski, V. Pierrard, J. Lemaire, M. D. Looper, and J. B. Blake, A Low Altitude Trapped Proton Model for Solar Minimum Conditions Based on SAMPEX/PET Data, *IEEE Trans. Nucl. Sci., 46*, 1475, 1999.

[9] The International Association of Geomagnetism and Aeronomy, IAGA, "The International Geomagnetic Reference Field (IGRF)", [Online reference guide], 2007, [cited 2007 July 23], Available http: www.iugg.org/IAGA/iaga_pages/pubs_prods/**igrf**.htm

[10] Computer Science Dept., Stony Brook Univ., "Convex Hull", [Online Resource], 2001 Mar 7, [cited 2007 July 18], Available http: www.cs.sunysb.edu/~algorith/files/**convex-hull**.shtml

[11] xCellerator, ConvexHull, California Institute of Technology, 2005, [cited 2007 July 23], Available http: http://xlr8r.info/mPower/pages/convexHull.html

[12] O'Rourke, J. Computational Geometry in C. 2nd Ed., Cambridge University Press, 1998.

VIII. FIGURES

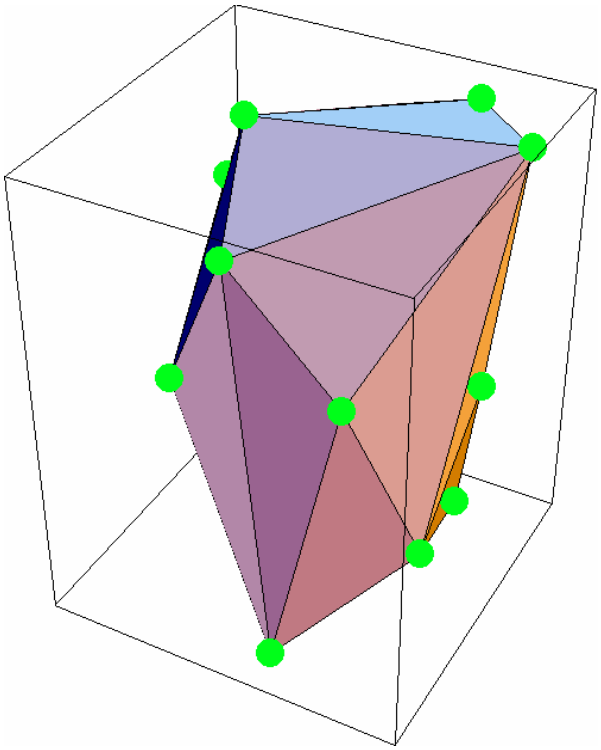

Figure 1. Three-dimensional representation of a convex hull.

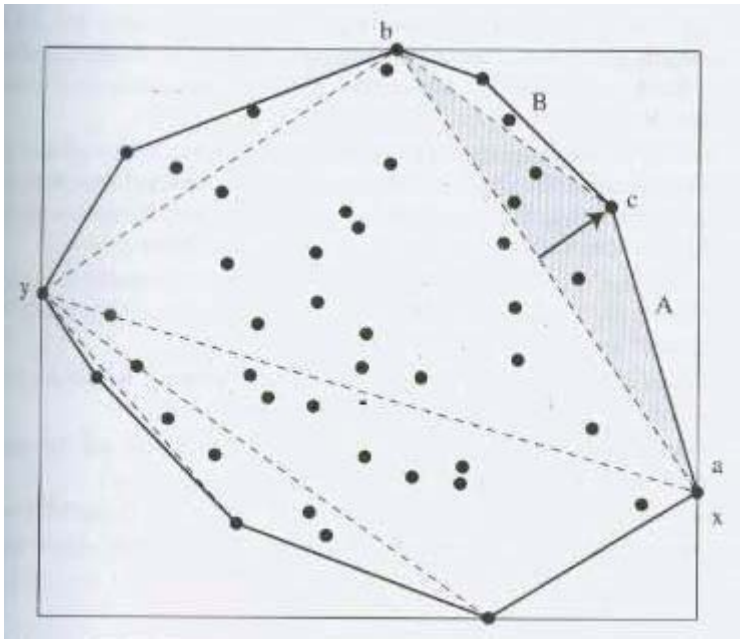

Figure 2. Visual representation of the QuickHull algorithm. To find the entire hull, QuickHull first finds the upper and lower hull using triangulation. The procedure starts with identification of two extreme points (a,b), then a third extreme point c is found directly to the right of ab, and all points inside ∆abc are discarded. The algorithm then recurses on the sides A and B.

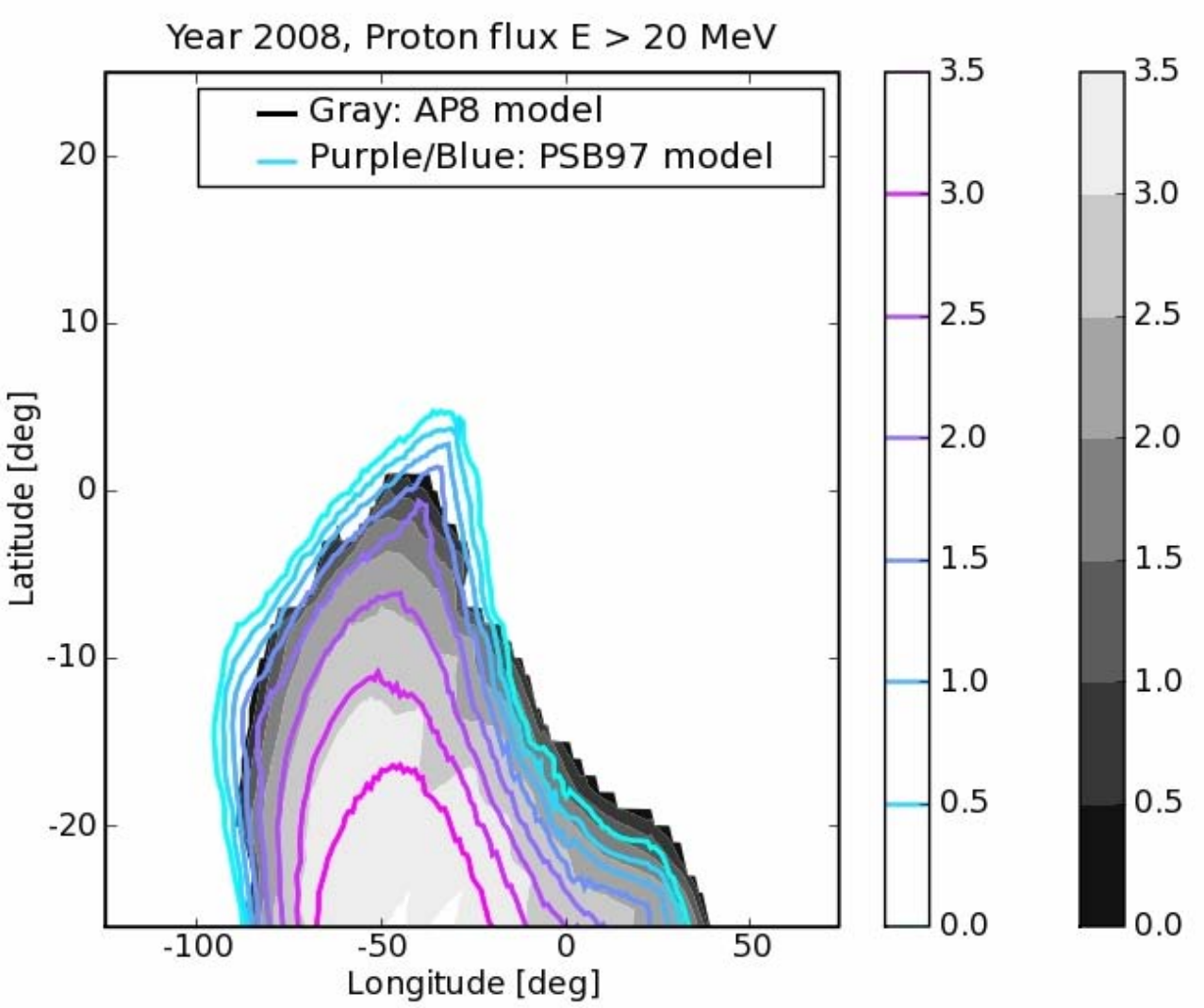

Figure 3. Flux contours for protons with energies E > 20 MeV. The gray shaded region describes proton fluxes as calculated by the AP8 model, the purple/blue contour lines define proton fluxes as attained by the PSB97 model; both show predicted fluxes in 2008. The colorbars on the right side show the mapping between contour lines with $\log_{10}$ flux/ (particles/cm^2 s).

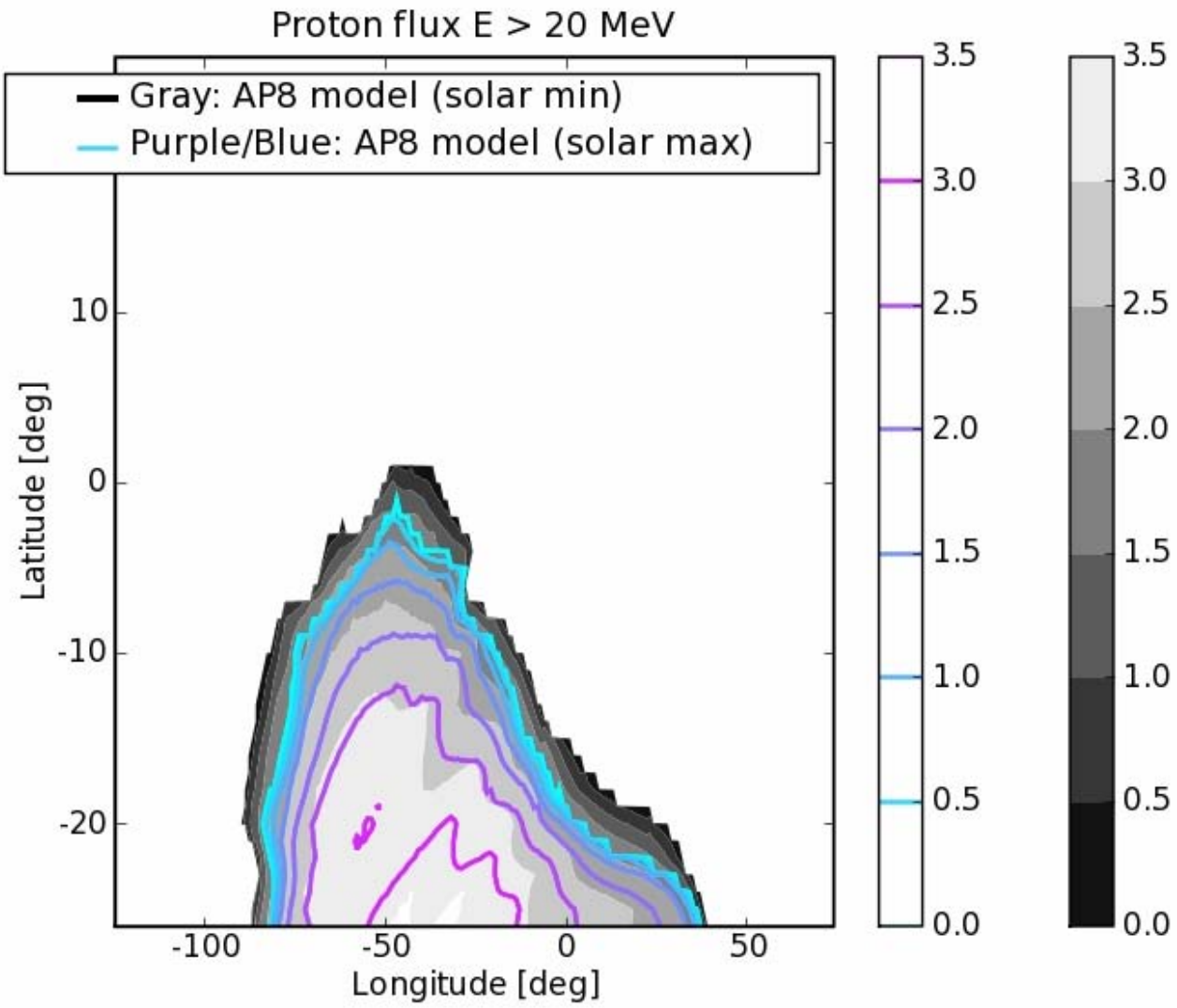

Figure 4. Flux contours for protons with energies E > 20 MeV. The gray shaded region describes proton fluxes of the AP8 model at solar minimum; purple/blue contour lines represent proton fluxes of the AP8 model at solar maximum. The colorbars on the right side show the mapping between contour lines with log_{10} flux /(particles/cm^2 s).

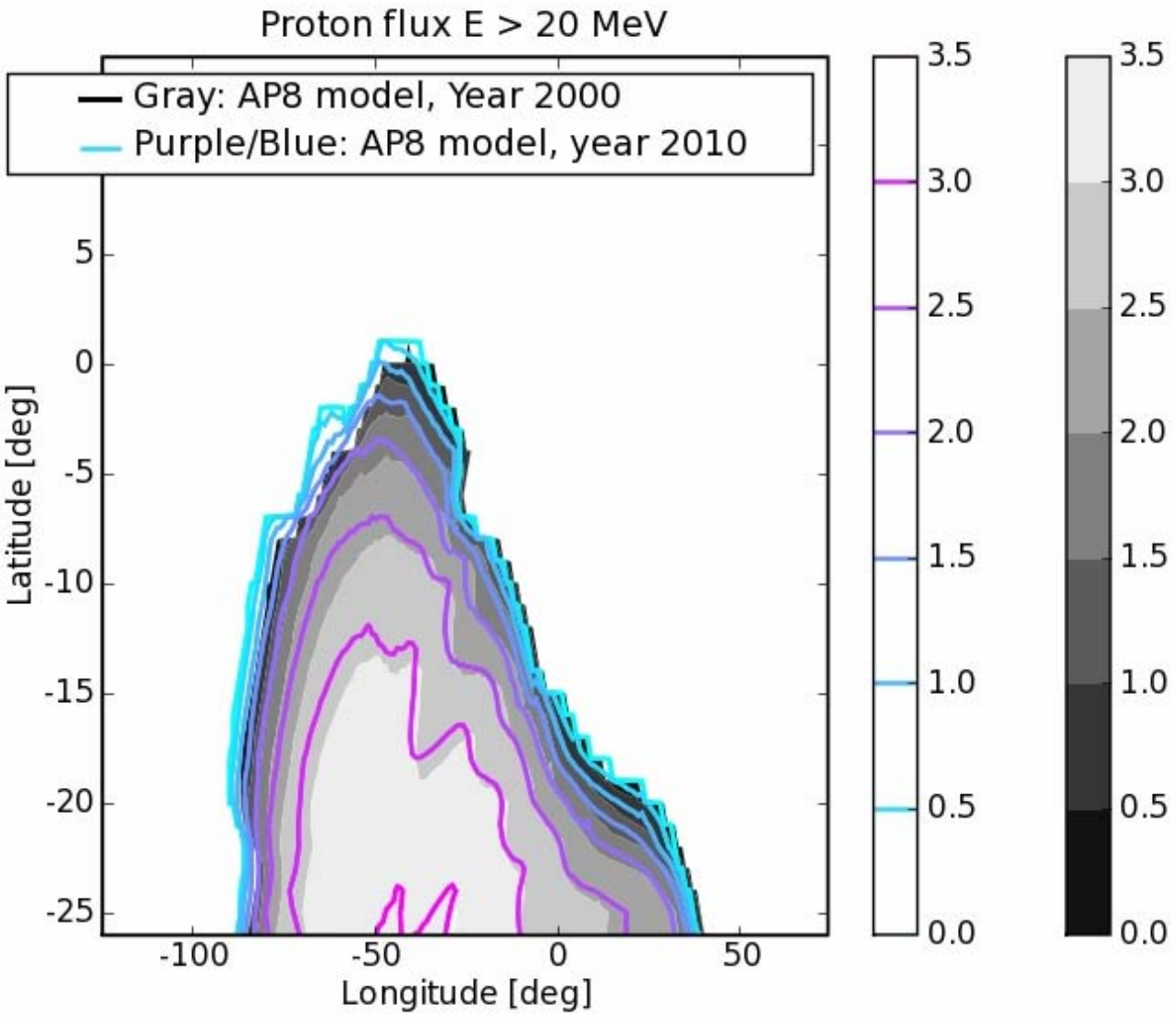

Figure 5. Flux contours for protons with energies E > 20 MeV. The gray shaded region describes proton fluxes of the AP8 model in the year 2000; purple/blue contour lines define proton fluxes of the AP8 model in 2010. The colorbars on the right side show the mapping between contour lines with $\log_{10}$ flux /(particles/cm^2 s).

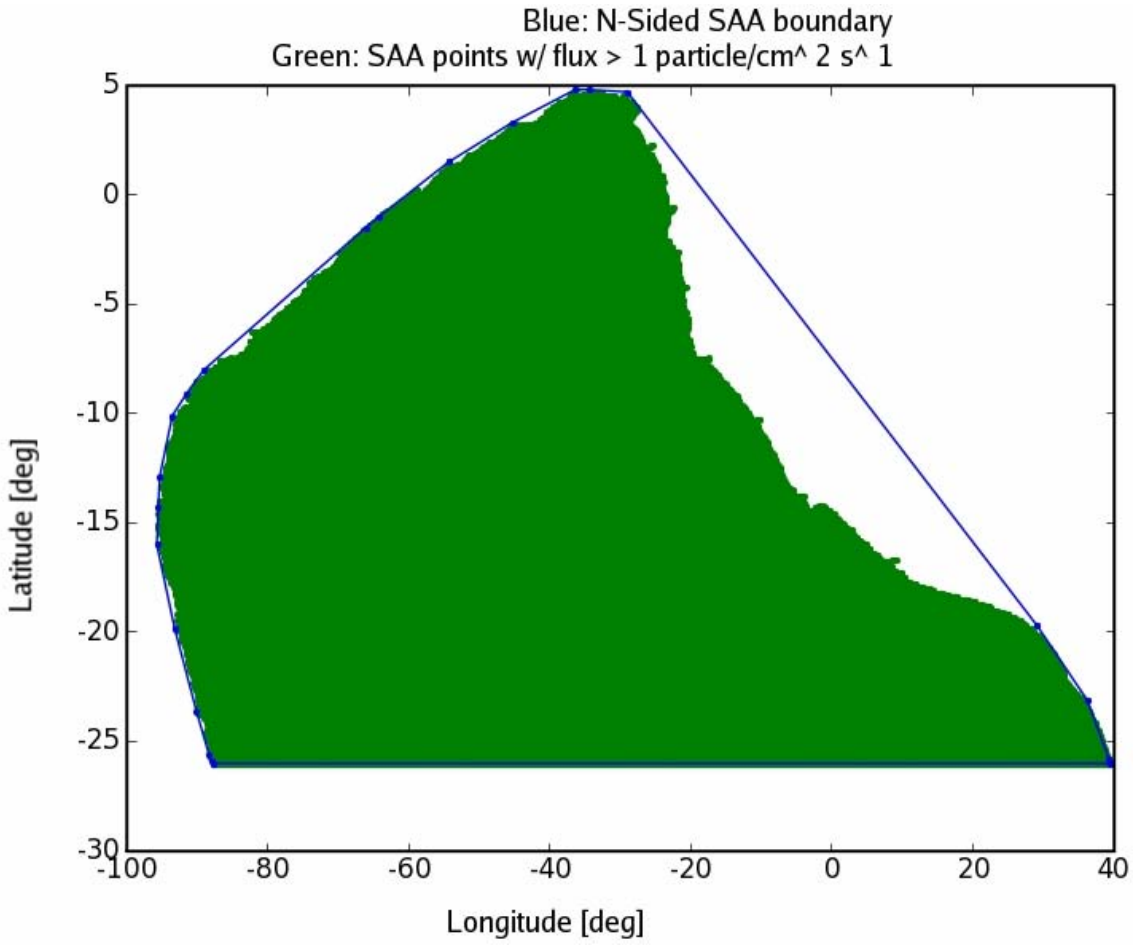

Figure 6. The SAA convex hull with n sides encompassing proton fluxes from both the AP8 and PSB97 models. The green region contains all points where proton fluxes larger than 1 particle/cm^2 s are evaluated on a grid of longitudes and latitudes with 0.1 degree spacing. The blue line shows the convex hull enclosing these points; it is a polygon with 22 edges.

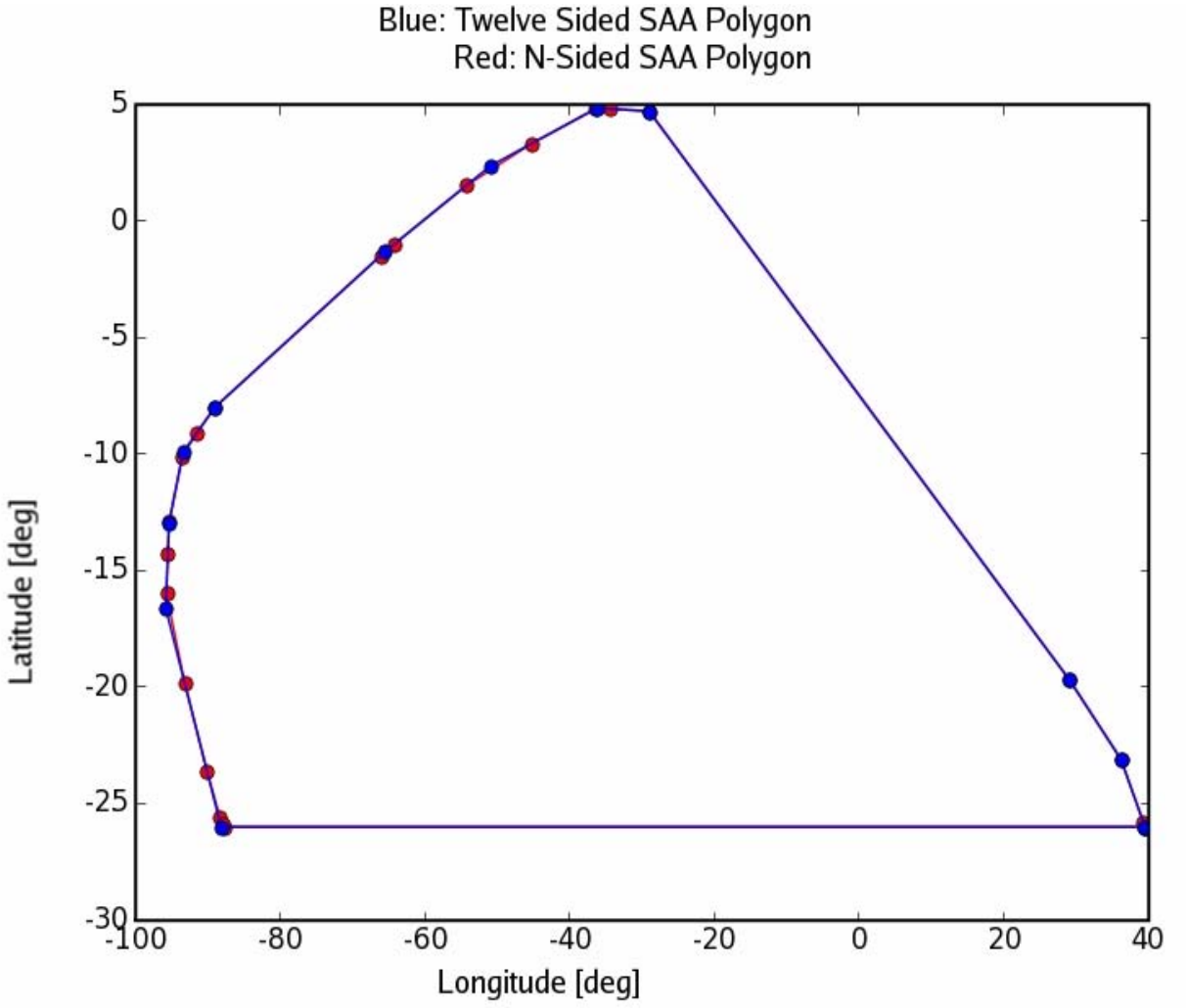

Figure 7. Comparison of the previously attained 22-sided SAA hull with the reduced convex hull of twelve edges. The red boundary is the 22-sided hull, and the blue line defines the minimum area for an SAA polygonal boundary with twelve sides.

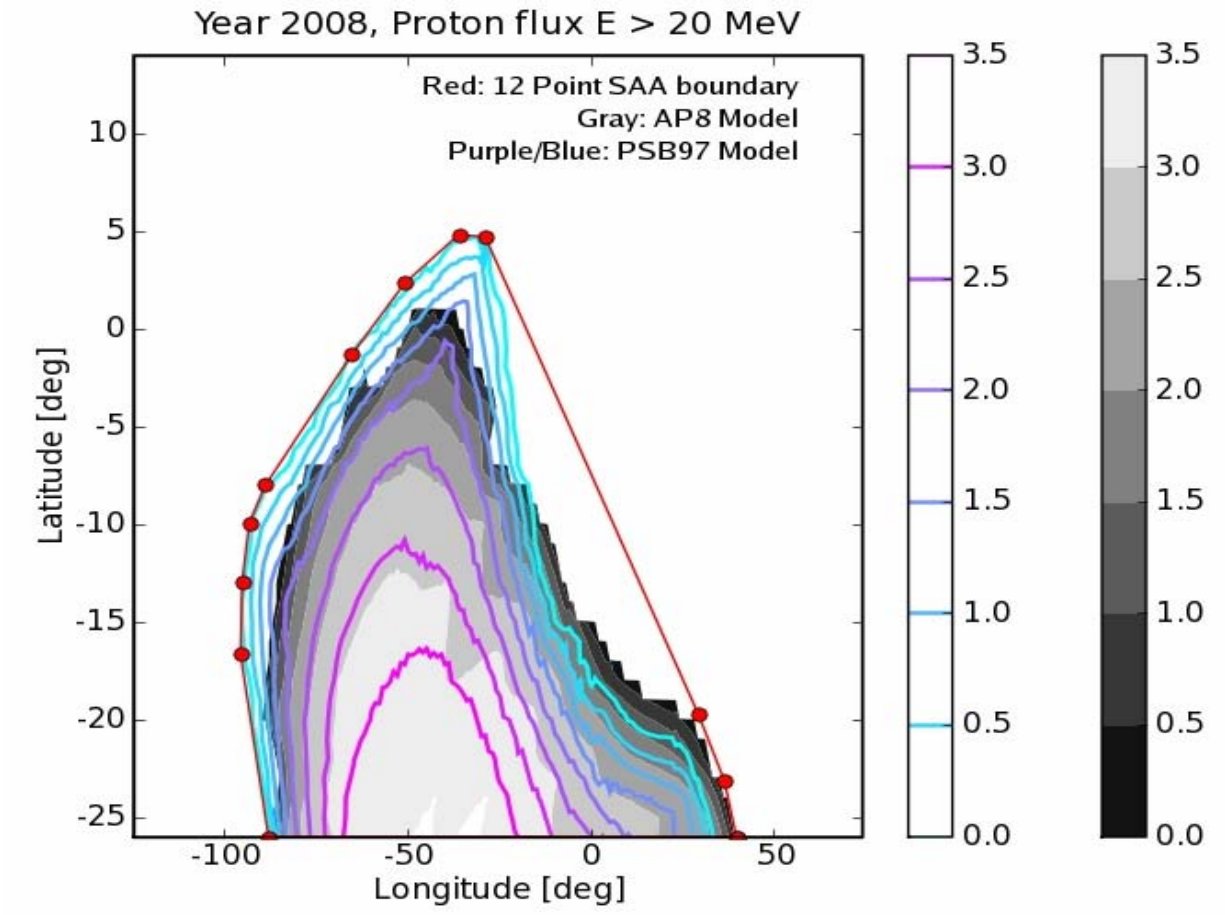

Figure 8. Comparison of the twelve edge SAA boundary with flux contours for protons with energies E > 20 MeV. The gray shaded region describes proton fluxes of the AP8 model, the purple/blue contour lines define proton fluxes of the PSB97 model; both as defined in the year 2008. The colorbars on the right side show the mapping between contour lines with log_{10} flux /(particles/cm^2 s). The red line shows the twelve sided SAA polygonal boundary of minimal area.

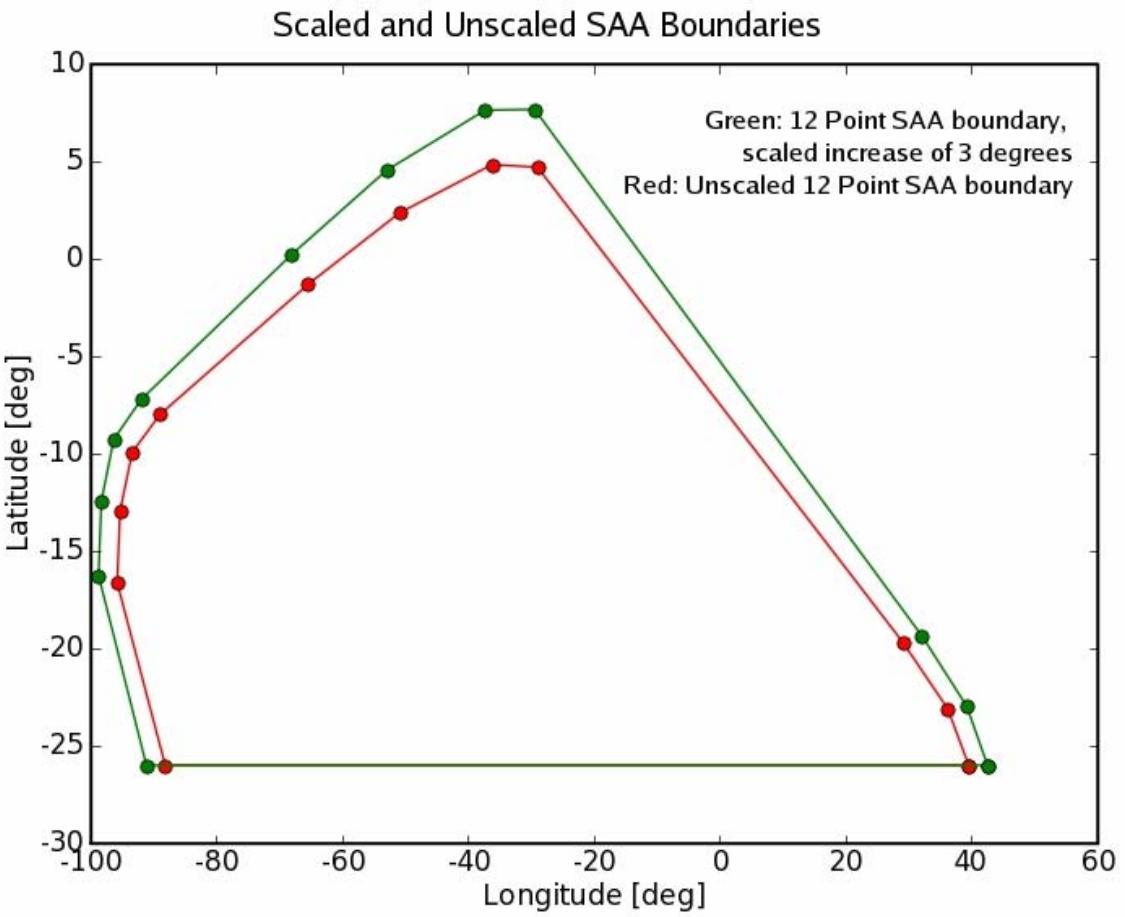

Figure 9. The unscaled twelve sided SAA boundary drawn with a twelve sided boundary scaled with a 3° increase. The red line shows the unscaled boundary, while the green line shows the scaled boundary. The increased hull area represents a safety margin for the twelve sided SAA polygon.

IX. TABLES

Point #	SAA Hull Coordinates	SAA Hull Coordinates (scaled by 1 degree)	SAA Hull Coordinates (scaled by 3 degrees)	SAA Hull Coordinates (scaled by 5 degrees)
1	(39.53, -26.0)	(40.53, -26.0)	(42.53, -26.0)	(44.53, -26.0)
2	(36.19, -23.09)	(37.19, -23.05)	(39.19, -22.96)	(41.19, -22.86)
3	(29.09, -19.69)	(30.09, -19.58)	(32.08, -19.35)	(34.06, -19.11)
4	(-29.00, 4.70)	(-29.15, 5.69)	(-29.45, 7.67)	(-29.76, 9.64)
5	(-36.21, 4.83)	(-36.58, 5.76)	(-37.29, 7.63)	(-38.02, 9.49)
6	(-50.93, 2.35)	(-51.61, 3.08)	(-52.98, 4.54)	(-54.35, 5.99)
7	(-65.45, -1.32)	(-66.31, -0.80)	(-68.03, 0.23)	(-69.7, 1.26)
8	(-89.00, -7.99)	(-89.96, -7.73)	(-91.89, -7.19)	(-93.82, -6.66)
9	(-93.39, -9.93)	(-94.37, -9.71)	(-96.31, -9.25)	(-98.26, -8.79)
10	(-95.34, -12.97)	(-96.33, -12.79)	(-98.29, -12.43)	(-100.26, -12.06)
11	(-95.78, -16.64)	(-96.77, -16.51)	(-98.75, -16.25)	(-100.73, -15.99)
12	(-88.14, -26.0)	(-89.14, -26.0)	(-91.14, -26.0)	(-93.14, -26.0)

Table 1. Twelve coordinate points defining the SAA hull, including coordinates of the SAA hull scaled by an increase of 1°, 3°, and 5°.

Scaled Amount (deg)	Percentage of Lost Observational Area (%)	Percentage of SAA Area Increase (%)
0.5	0.36	2.13
1	0.73	4.29
1.5	1.1	6.47
2	1.48	8.67
2.5	1.86	10.89
3	2.24	13.14
3.5	2.63	15.41
4	3.02	17.7
4.5	3.42	20.02
5	3.82	22.36

Table 2. The percentage of lost observational area and of SAA area increase (with respect to the unscaled area) at various scaling sizes.

Structure of ZnO Nanorods using X-Ray Diffraction

Marci Howdyshell

Office of Science, Science Undergraduate Laboratory Internship

Albion College

Stanford Linear Accelerator Center

Stanford, California

10 August 2007

Prepared in partial fulfillment of the requirements of the Office of Science, U.S. Department of Energy's Science Undergraduate Laboratory Internship (SULI) Program under the direction of Michael Toney and Bridget Ingham at the Stanford Synchrotron Radiation Laboratory of the Stanford Linear Accelerator Center in Palo Alto, CA.

Participant: _____

Research Advisor: _____

Work supported in part by US Department of Energy contract DE-AC02-76SF00515

TABLE OF CONTENTS

ABSTRACT

Many properties of zinc oxide, including wide bandgap semiconductivity, photoconductivity, and chemical sensing, make it a very promising material for areas such as optoelectronics and sensors. This research involves analysis of the formation, or nucleation, of zinc oxide by electrochemical deposition in order to gain a better understanding of the effect of different controlled parameters on the subsequently formed nanostructures. Electrochemical deposition involves the application of a potential to an electrolytic solution containing the species of interest, which causes the ions within to precipitate on one of the electrodes. While there are other ways of forming zinc oxide, this particular process is done at relatively low temperatures, and with the high amount of x-ray flux available at SSRL it is possible to observe such nucleation *in situ*. Additionally, several parameters can be controlled using the x-ray synchrotron; the concentration of Zn^{2+} and the potential applied were controlled during this project.

The research involved both gathering the X-ray diffraction data on SSRL beamline 11-3, and analyzing it using fit2d, Origin 6.0 and Microsoft Excel. A time series showed that both the in-plane and out-of-plane components of the ZnO nanorods grew steadily at approximately the same rate throughout deposition. Additionally, analysis of post-scans showed that as potential goes from less negative to more negative, the resulting nanostructures become more oriented.

INTRODUCTION

In recent years, zinc oxide has become a popular subject of research due to its applications in the areas of sensors [1], optoelectronic devices [2] and piezoelectric devices [3]. Wide bandgap semiconductivity, photoconductivity, and chemical sensing are just a few examples of the properties that make ZnO so useful [4]. To better understand these bulk ZnO properties, it is advantageous to create and analyze its nanostructures, which have a high surface to volume ratio and therefore enhance bulk characteristics. Several techniques have been established to form such nanostructures, including thermal evaporation of ZnO powder in the presence of a carrying gas both with a catalyst [5] and without a catalyst [6], sol-gel [7], anodic aluminum oxide templating [8], metal-organic chemical vapor deposition [9], molecular beam epitaxy [10], pulsed laser deposition [11], and electrochemical deposition [12].

Electrochemical deposition has distinct advantages for the study of nanostructures because it is more cost-effective and easier than other techniques. During the process, a potential is applied to an electrolytic solution that contains the species of interest. The ions within the solution then precipitate on the electrode. It can be done at relatively low temperatures, making deposition possible on inexpensive substrates with low melting points, such as plastics. Additionally, a vacuum system is not necessary. Electrochemical deposition allows for complete control over several parameters, including temperature, pH, presence of surfactant, concentration of Zn^{2+} and potential applied. Lastly, it can be readily scaled for industrial production.

Although electrochemical deposition provides many benefits for the study of ZnO nanostructures, there are still many aspects of the deposition that are not fully understood. While the resulting nanostructures from the deposition can easily be observed and analyzed, nothing

from the final structures tells about what exactly happened during the deposition. It is unknown precisely how the orientation of the nuclei affects the final structure. This research allows for analysis the actual deposition process, as well as the resulting nanorods to investigate why the nanorods become oriented in the way that they do and how the degree of orientation is determined.

Using x-ray diffraction techniques, an x-ray beam is aimed at the crystal lattice such that the beam is reflected onto a detector. The result is a series of peaks in intensity that are due to constructive interference of waves from different layers in the lattice. The data from the diffraction experiments give details about the preferential structure; specifically, there are different orientations and shapes that may form, such as plates and rods [13]. These different outcomes depend directly upon the different parameters that are controlled during the experiment. The effects of initial concentration of Zn^{2+} and potential applied were examined because they are most significant in determination of the final structure. Ultimately, x-ray diffraction is an ideal tool for tracking crystallite orientation and an aid in the attempt to fully understand how the orientation of the rods develops from the nuclei to the final structure.

MATERIALS AND METHODS

A homemade electrochemical cell with heating capability, as illustrated in Figure 1, was used for the diffraction process. The samples are deposited on the working electrode, which is a quartz rod with 150 nm of gold deposited on it. This rod is inserted at the base of the cell such that x-rays may be directed at grazing incidence onto the film on top of the rod, where there is a

2 mm x-ray path length through the solution. The electrochemistry is controlled while x-ray diffraction patterns are recorded by the detector

The aqueous electrolytic solution within the cell had a controlled concentration of $Zn(NO_3)_2$ (Riedel DeHaën, 98%) varying from 1-50 mM, with a supporting electrolyte of 0.1 M KCl (BDH, 99%). The temperature of the solution was held between 60-65°C during the deposition. Also used was a Pt wire counter electrode, whose potential was regulated with the use of a potentiostat and varied from -970 mV to -370 mV with respect to an Ag/AgCl/KCl (3.5 M) reference electrode (+0.205 V vs. NHE). Oxygen was bubbled through the solution at a moderate rate.

The x-ray diffraction experiments were conducted using the area detector on beam line 11-3 of the Stanford Synchrotron Radiation Laboratory at the Stanford Linear Accelerator Center, California [14]. The area detector differs from a point detector in that it gives two-dimensional, rather than one-dimensional, results. The beam size was 0.15 mm by 0.05 mm and the wavelength was 0.9736 Å.

After gathering the data, the quartz rods were taken to Imperial College London, UK to obtain microstructure images of the resulting nanostructures with the use of LEO Gemini 1525 field emission microscope (FESEM).

RESULTS

X-ray diffraction on beam line 11-3 yielded a series of radial diffraction patterns such as Figure 2. This particular scan was taken after deposition occurred and solution was removed from Sample 04 (5 mM $Zn(NO_3)_2$, -370 mV). The diffraction pattern results from the interference of waves from different layers in the lattice, as described by Bragg's Law:

$$n\lambda = 2d\sin(\theta).$$

In this equation, λ is the wavelength, d is the separation between the parallel lattice planes, 2θ is the angle between the incident beam and the scattered beam, and n corresponds to the amount of shifting between the two waves. When n is an integer, i.e. the two waves are in phase, we see a bright spot of constructive interference, or, in this case, a bright arc.

Although the pattern is in real space, as defined by the scale of pixels along the horizontal and vertical directions, we can also read it radially using Q and χ. The angle χ completes an entire circle of 360°, with 0° at the vertical, but due to experimental limitations (the x-ray beam has a limited span it can cover before the cell obstructs it) only the region from -90° to 90° is useful for analysis. The scattering vector, Q (measured in $Å^{-1}$), increases radially outward. Q is related to the distance between parallel lattices ("d") as follows:

$$Q = 2\pi/d.$$

We can combine it with Bragg's Law, resulting in the following:

$$Q = (4\pi/\lambda)*\sin(\theta).$$

Each arc represents a specific orientation of either the ZnO crystals or the gold upon which it was deposited. The arcs of importance are labeled in Figure 2 as follows: ZnO (102), Au (200), Au (111), ZnO (101), and ZnO (002). By using the intensity color scale, one can see the relative intensities, measured in counts, of each orientation.

The program Fit2d was used to integrate Figure 2 in a process called caking to create the graph shown in Figure 3. This essentially changes the polar coordinates of χ and Q to Cartesian coordinates. The horizontal becomes the off-axis angle chi and the vertical is the magnitude of the scattering vector Q. Per the definition above, as Q increases on Figure 3, d decreases. Using

figure 3, one may see more easily the different diffraction peaks, which are once again labeled on the figure and are now horizontal lines.

Cuts were taken along the horizontal lines corresponding to the reflections of ZnO (102), ZnO (002), ZnO (101) and Au (111) of Figure 3 to create the four individual graphs shown in Figure 4. These graphs are now one-dimensional, with each one showing the intensity vs. chi for one specific orientation. They are offset for clarity.

The peaks in Figure 4 can be fitted with Gaussian curves to obtain the area, which corresponds to the degree of crystallinity along the different directions, the center, and FWHM (Full Width at Half Maximum), which tell us about the strength of the scattering and the variation in texture (preferential orientation).

DISCUSSION AND CONCLUSIONS

The different orientations that could be analyzed using the x-ray diffraction pattern of Figure 2 are ZnO (002), ZnO (102), ZnO (101), Au (111) and Au (200), which are all labeled in Figures 2 and 3. These orientations correspond to Miller Indices; each represents a combination of either in-plane or out-of-plane components. As shown in Figure 5, Au (111) is directed normal to the gold substrate, while ZnO (002) component of the hexagonal ZnO nanorod that is also perpendicular to the substrate. ZnO (100) gives a component entirely in the plane of the substrate. Lastly, ZnO (102) and ZnO (101) are combinations of the in-plane and out-of-plane components.

1. End-Scan Crystallinity

The first goal achieved during analysis was to look for correspondence between the potential applied and the degree of orientation of the full-grown nanostructures using the FWHM

of the end-scans for samples formed with $Zn(NO_3)_2$ concentration of 1 mM at potentials of -970 mV, -770 mV and -370 mV. The FWHM from the Gaussian fits for the ZnO (102) intensity peaks were used for this part of the analysis. Each FWHM corresponds with the amount of variation in crystallite (grain) direction about the midpoint. A greater width is the result of a larger distribution of grain orientation, i.e. less orientation of the grains. On the other hand, a very small width is caused by a highly oriented material. Figure 6 is a graph of the width of the ZnO (102) intensity peak (measured in degrees χ) vs. potential applied in mV for the three samples described above. When moving from less negative potential (-370 mV) to more negative potential (-970 mV), the width decreases, meaning the grains are more structurally ordered. These results are very encouraging in their strong suggestion that the degree of crystallinity of ZnO nanostructures can be controlled by the potential applied during electrochemical deposition. Further studies similar to this—possibly ones that that include more than four applied potentials—would be useful in providing more support for this conclusion.

2. Time-Series Analysis

A second aspect analyzed during this research project is a time series for one of the samples. For this analysis Gaussian fits were used for all 26 scans that took place during the deposition of the ZnO in a sample formed using 1 mM $Zn(NO_3)_2$ at -370 mV. The time scans allow one to look at each step of the growth process.

The ZnO (002) and the ZnO (101) peaks were used during this analysis. The areas of the peaks allowed comparison of the growth of the nanostructures normal to the substrate with the growth in the plane of the substrate. Figures 7 and 8 show the area ratio (the areas were scaled down for clarity) of the ZnO (002) and ZnO (101) peaks, respectively. A linear fit on each graph shows that they both are linearly increasing with time. In other words, Figures 7 and 8 show that

the nanostructures are growing steadily as time increases during deposition. Note that potential was applied starting at scan 5. Accordingly, the plots show no amount of substance until scan 6 (for ZnO (002)). Interpolation from the linear fit shows that the first point at which substance was detected is about halfway through scan 5. Each scan was about one minute long; therefore, nucleation time is approximately 30 seconds.

Note that there are a few small jumps in the data, specifically in the ZnO (101). These jumps are actually apparent in both orientations but more prominently so in the ZnO (101), which is likely to be due to the poor signal-to-noise ratio. The jumps may be caused by sudden increases in oxygen near the electrode. Further analysis of these jumps will be beneficial in the future.

Figure 9 combines Figures 7 and 8 to show that the rate of growth is nearly identical in both directions. The graphs correspond quite well with previous data collected during XANES analysis at Brookhaven National Laboratory [15, 16]. During deposition of ZnO using identical conditions, the XANES time series for the less negative potentials resulted in a nearly linear volume increase.

Future analysis will include doing time series for more of the samples from this experiment and comparing the results. It is expected that the time series of scans at more negative potentials will show more rapid growth than this one. Furthermore, it is predicted that at more negative potentials there will ultimately be more growth in the (002) orientation than the (101) orientation [15, 16]. Future research also includes obtaining the FESEM images from Imperial College London, UK, to use as a supplement to the above results and conclusions.

ACKNOWLEDGMENTS

There are several people who have helped me immensely during this project. I am most especially thankful for the intelligence, guidance and support provided by my mentors, Michael Toney and Bridget Ingham. Additional thanks to our collaborators Benoit Illy and Mary Ryan. I would also like to thank Apurva Mehta, for going out of his way to help out all of the SSRL interns. Lastly, I would like to thank the Office of Science, Department of Energy for funding the SULI program and all of the SULI coordinators at SLAC for making this experience possible.

REFERENCES

[1] Q. Wan, Q.H. Li, Y.J. Chen, T.H. Wang, X.L. He, J.P. Li and C.L. Lin, Appl. Phys. Lett. 84 (2004) 3654.
[2] M. Law, L.E. Greene, J.C. Johnson, R. Saykally and P.D. Yang, Nat. Mater. 4 (2005) 455.
[3] M. Kadota, T. Miura, Jpn. J. Appl. Phys. 41 (2002) 3281.
[4] B. Illy, B. A. Shollock, J.L. MacManus-Driscoll, M.P. Ryan, Nanotechnology 16 (2005) 320.
[5] X.Y. Kong, Y. Ding, R. Yang and Z.L. Wang, Science 303 (2004) 1348.
[6] Z.W. Pan, Z.R. Dai, and Z.L. Wang, Science 291 (2001) 1947.
[7] B.B. Lakshmi, P.K. Dorhout and C.R. Martin, Chem. Mater. 9 (1997) 857.
[8] Y. Li, G.W. Meng, L.D. Zhang and F. Philip, Appl. Phys. Lett. 76 (2000) 2011.
[9] J.Y. Park, D.J. Lee, Y.S. Yun, J.H. Moon, B.T. Lee and S.S. Kim, J. Cryst. Growth 276 (2005) 158.
[10] H. Kato, M. Sano, K. Miyamoto and T. Yao, J. Cryst. Growth 237-239 (2002) 538.
[11] T. Okada, B.H. Agung and Y. Nakata, Appl. Phys. A 79 (2004) 1417.
[12] M.H. Wong, A. Berenov, X. Qi, M.J. Kappers, Z.H. Barber, B. Illy, Z. Lockman, M.P. Ryan, J.L. MacManus-Driscoll, Nanotechnology 14 (2003) 968.
[13] Z. R. Tian, J.A. Voigt, J. Liu, B. Mckenzie, M.J. Mcdermott, M. A. Rodriguez, H. Konishi, H. Xu, Nat. Mater. 2 (2003) 821.
[14] RCSB Protein Data Bank, Structural Biology Synchrotron Users Organization, 2006, http://biosync.rcsb.org/ssrl/BL11-3.html
[15] B. Ingham, B. N. Illy, J. R. Mackay, S. P. White, S. C. Hendy, M. P. Ryan, Mat. Res. Soc. Symp. Proc. 1017 (2007) DD12.16
[16] B. Ingham, B. N. Illy and M. P. Ryan, J. Phys. Chem. C (submitted)

FIGURES

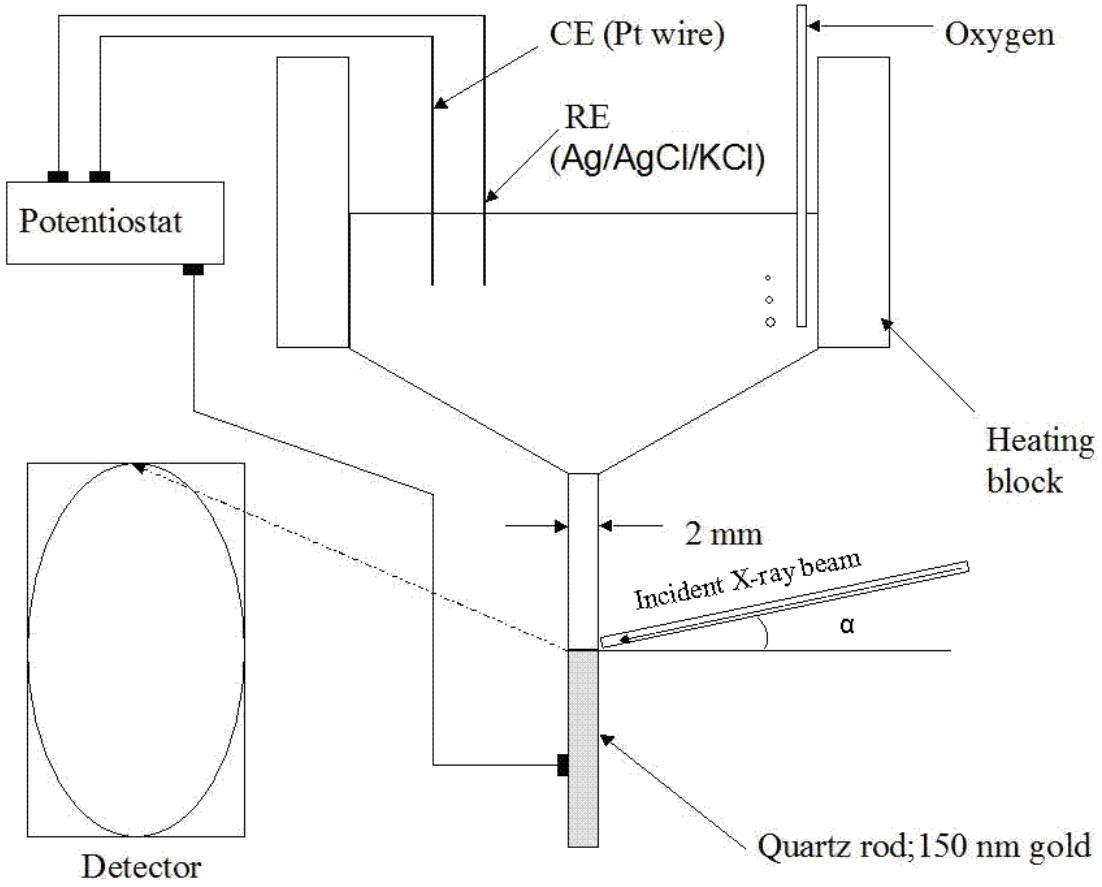

Figure 1: Schematic diagram of experimental setup. CE is counter electrode; RE is reference electrode. The electrochemistry is controlled as the x-ray beam reflects off the top of the quartz rod (working electrode) and onto the detector. The beam is directed at grazing incidence, meaning that the angle α is very small (~0.1°).

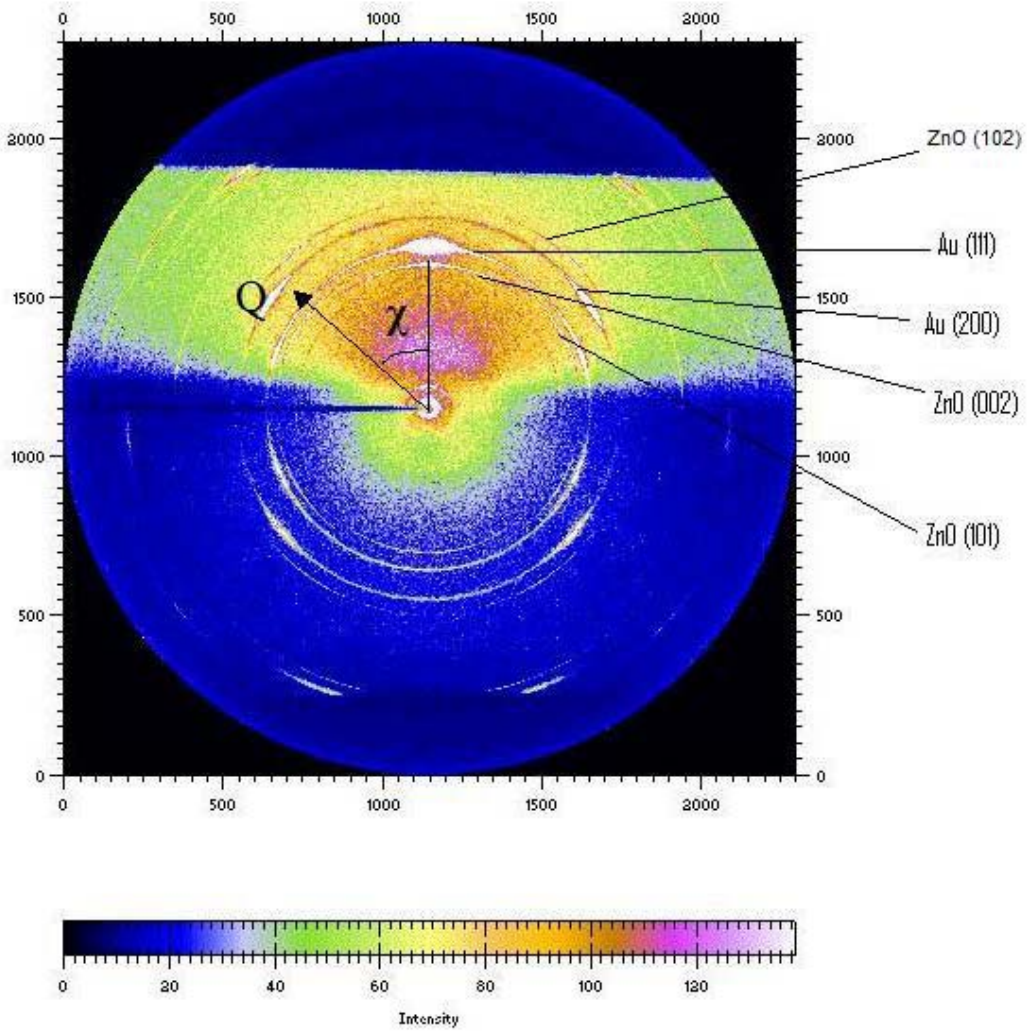

Figure 2: This is the diffraction pattern from an end scan (solution has been removed). Each intensity peak corresponds with a specific orientation of either ZnO or Au, as labeled. Areas colored blue were not used for analysis because the cell was in the way of the x-ray beam. The data can be read in polar coordinates by using the angle χ from the vertical and the scattering vector Q.

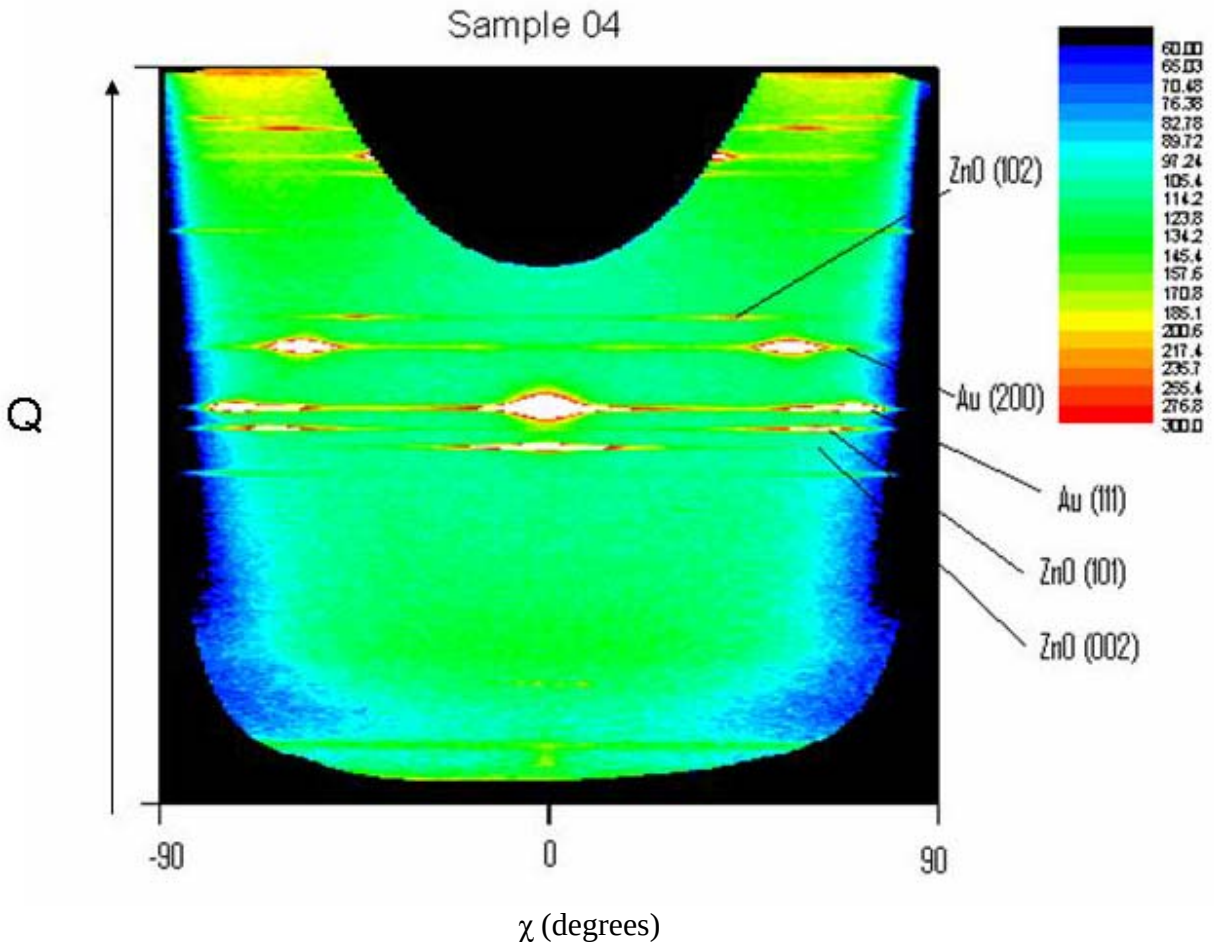

Figure 3: The raw data from Figure 2 has been caked in Fit2d to create this graph, in which χ is now the horizontal axis and Q is the vertical axis. The result is that the arcs containing the intensity peaks for the different orientations are now horizontal lines.

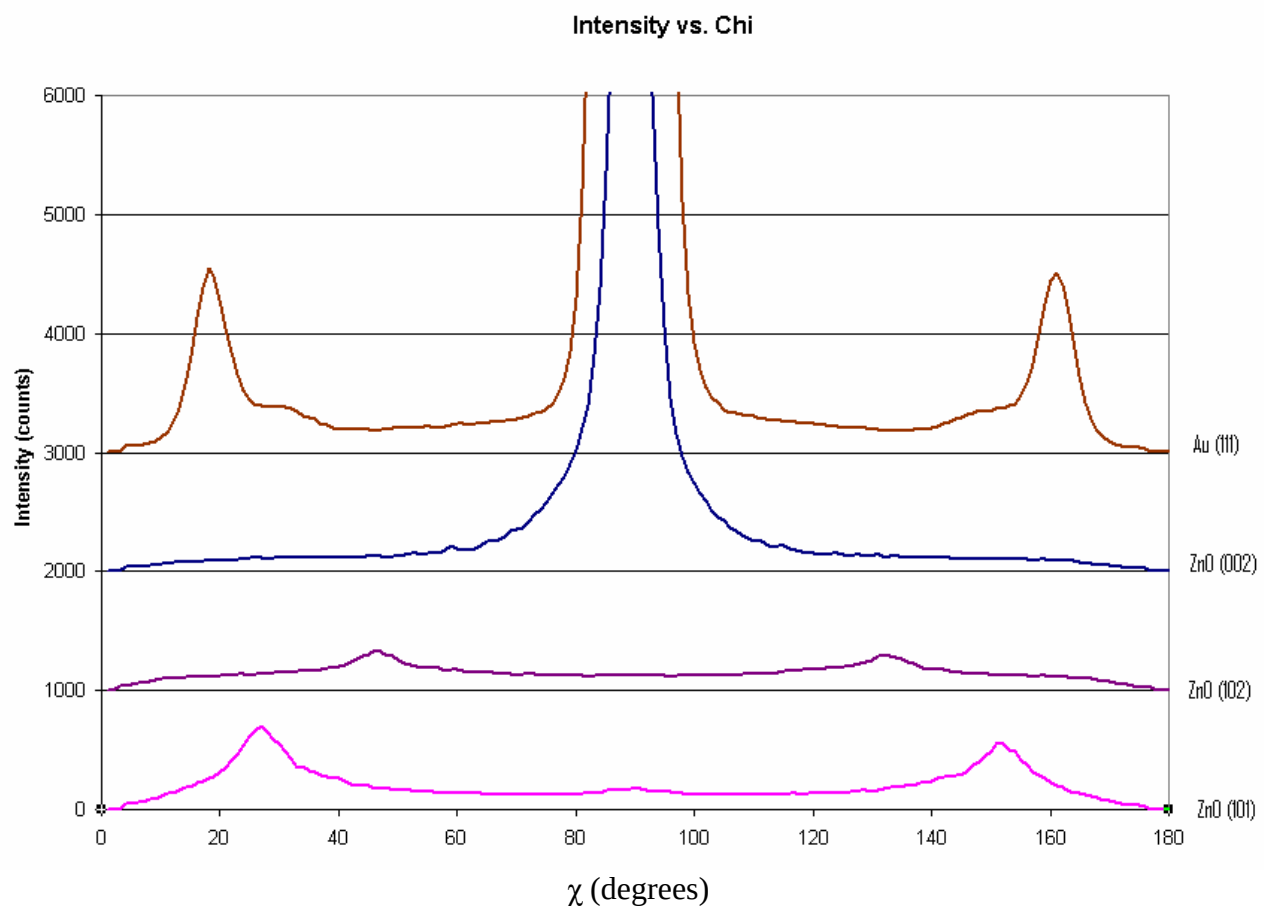

Figure 4: A cut was taken along the horizontal row of maximum intensity for each orientation of interest in the caked image of Figure 3. These cuts were used to create this graph of intensity vs. χ, which shows the individual intensity peaks for each orientation. The graph is offset for clarity.

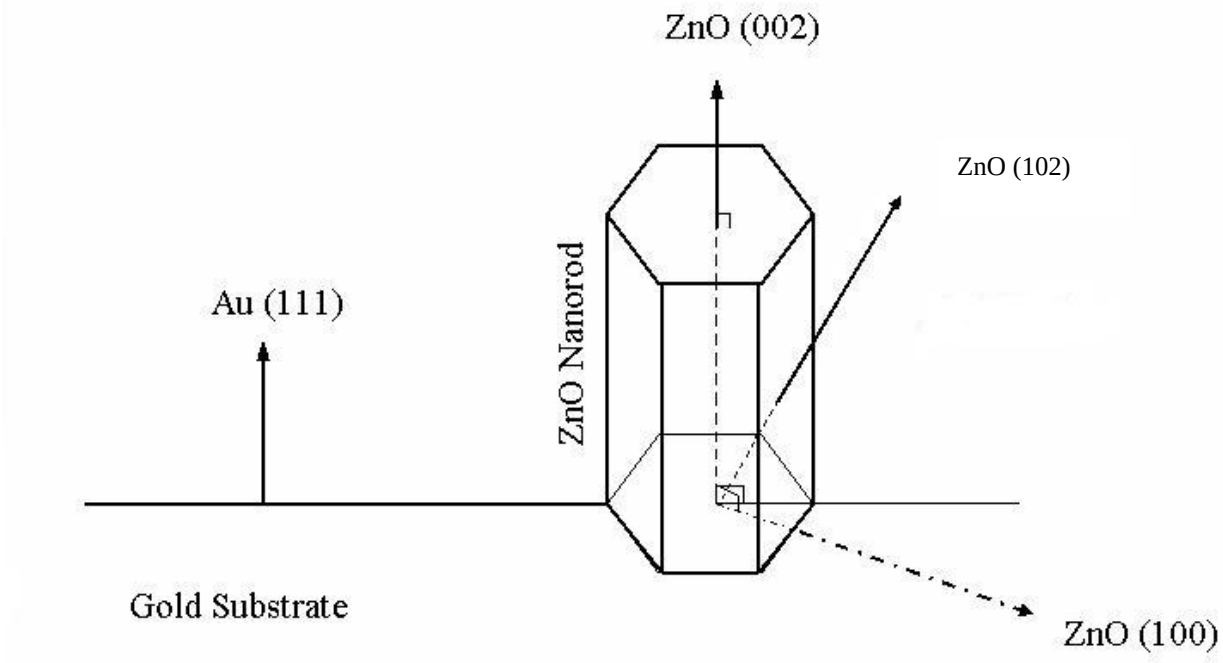

Figure 5: Several orientations are labeled in this diagram. The Au (111) orientation is straight off the substrate, while the different ZnO orientations correspond with in-plane and out-of-plane components of the hexagonal zinc oxide nanorods.

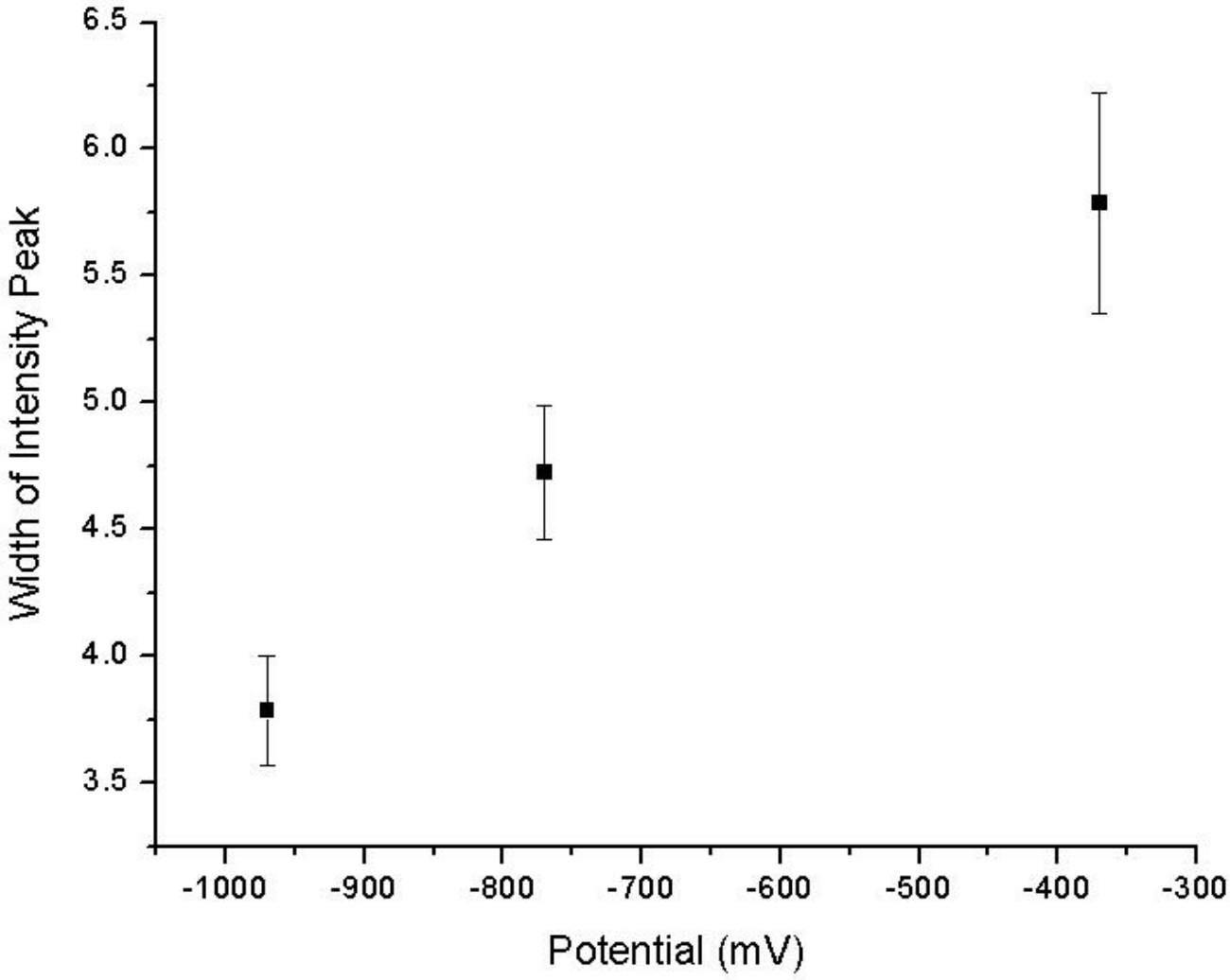

Figure 6: This is a plot of the width of the ZnO (102) intensity peak vs. the potential applied to the electrochemical solution. The width of the intensity peak (see Figure 4 for intensity peaks) is measured in degrees of χ.

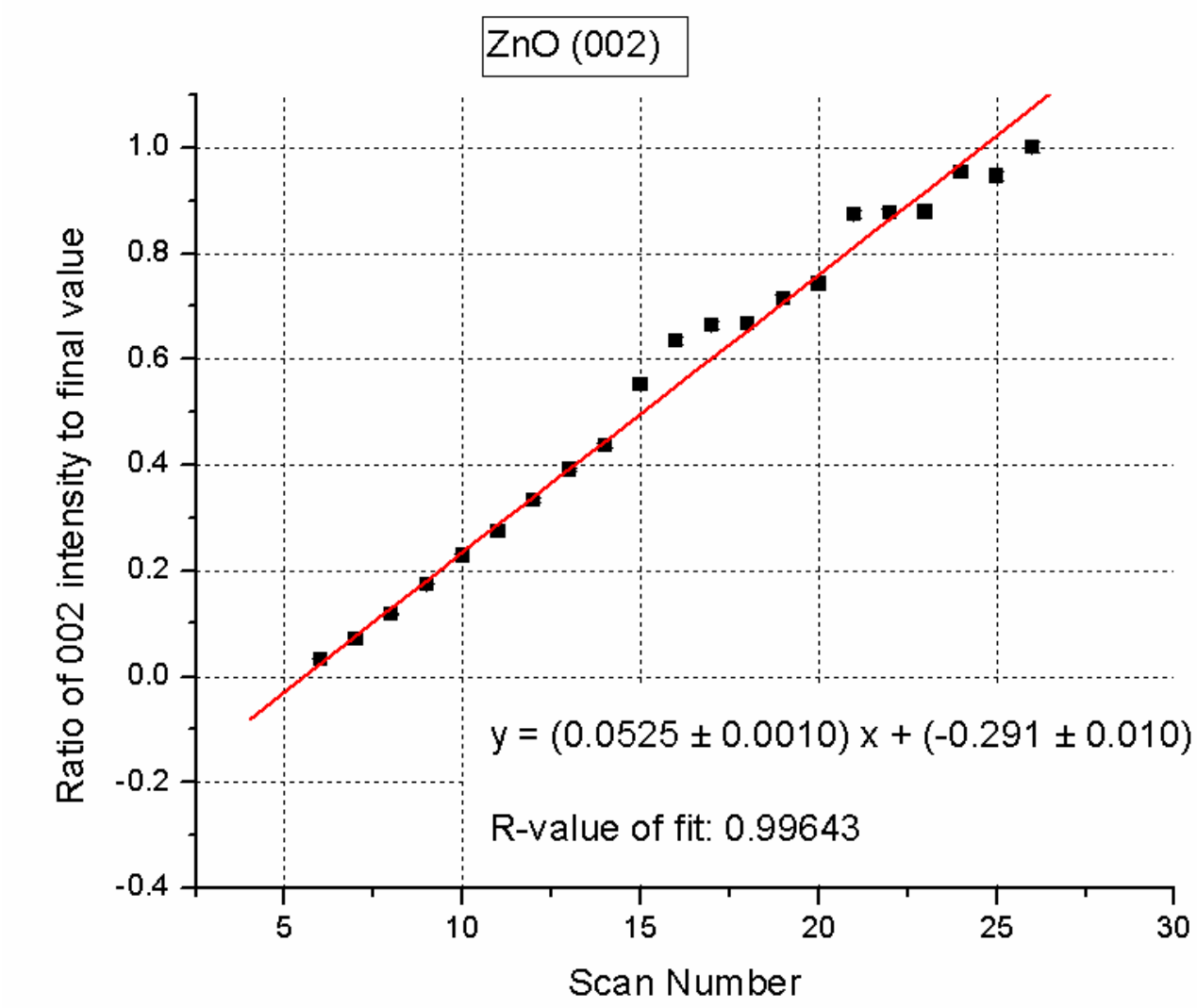

Figure 7: The area of the ZnO (002) intensity peak was divided by 48,789. The linear fit of the plot indicates steady growth over time.

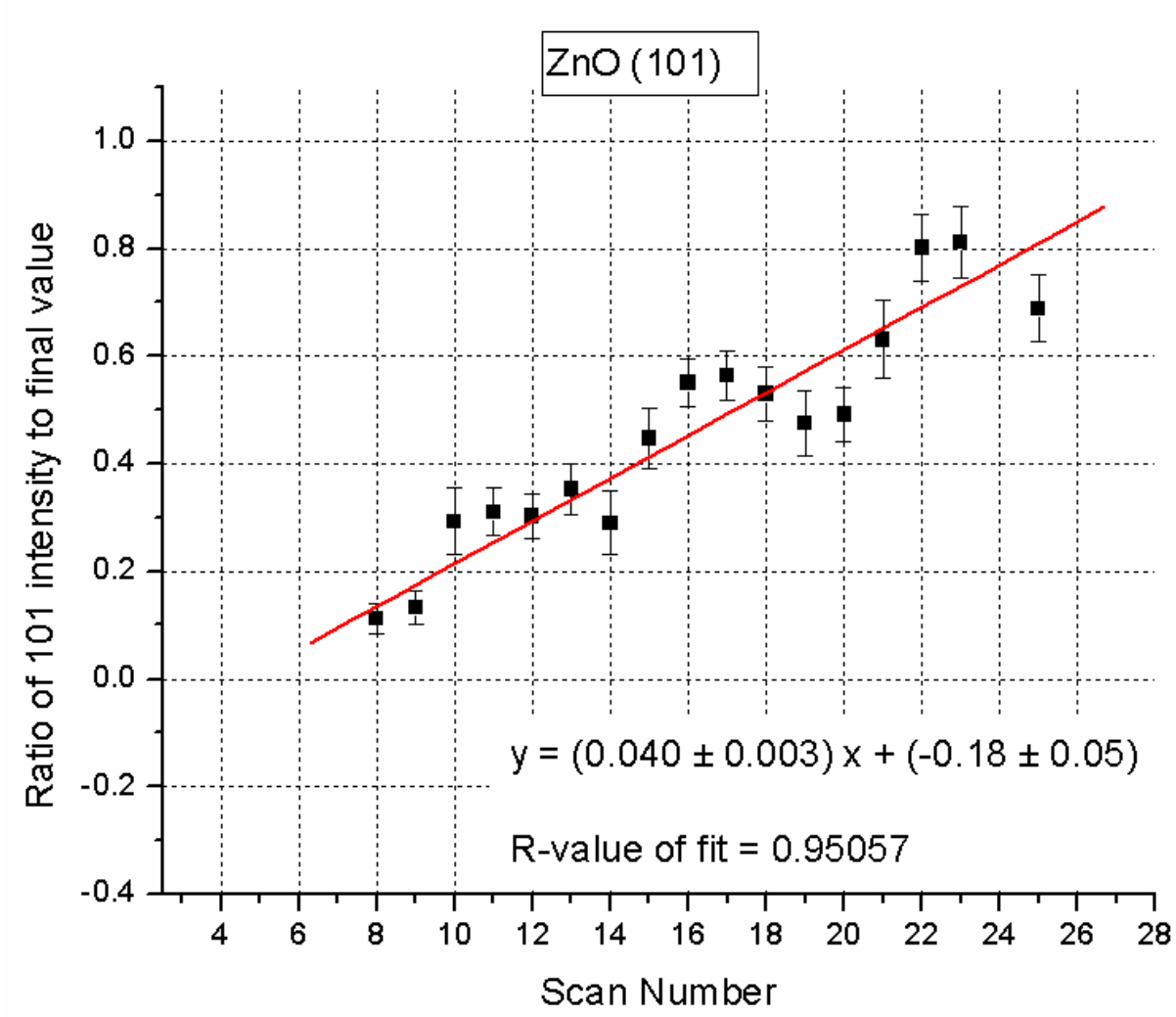

Figure 8: The area of the ZnO (101) intensity peak was divided by 1,600. The linear fit of the plot indicates steady growth over time.

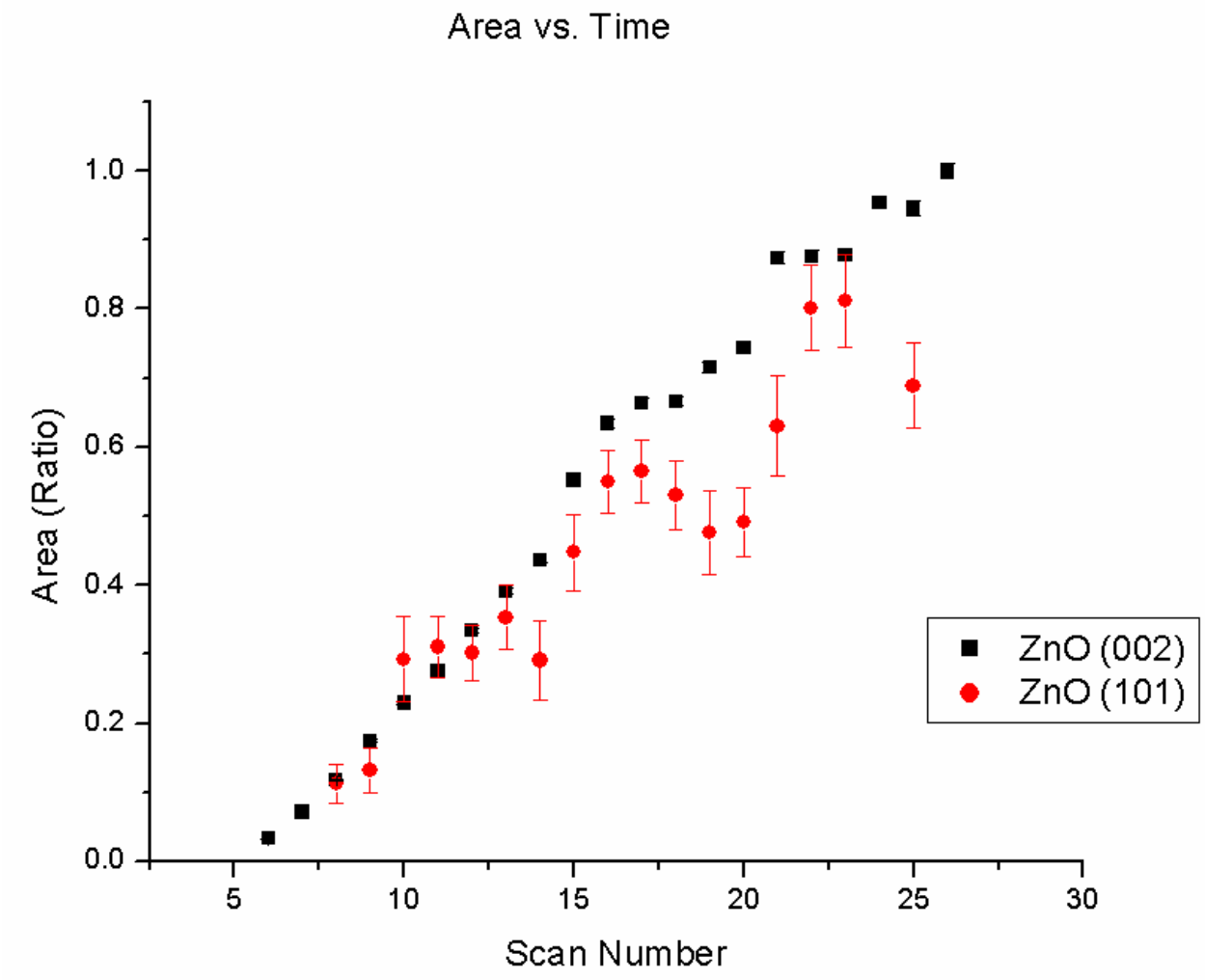

Figure 9: This area vs. scan number plot is merely a combination of Figures 7 and 8. It shows how the areas of both the ZnO (002) and the ZnO (101) change over time. Both orientations are scaled for clarity: ZnO (002) is scaled by a factor of 48,789 while ZnO (101) is scaled by a factor 1600.

SLAC-TN-07-025

Determining the Extent of Delocalization in Mixed-Valence Iron Dimers Using X-ray Absorption Spectroscopy

Alison Hoyt
Office of Science, Science Undergraduate Laboratory Internship Program

Yale University, New Haven

Stanford Linear Accelerator Center
Stanford, California

August 8, 2007

Prepared in partial fulfillment of the requirement of the Office of Science, Department of Energy's Science Undergraduate Laboratory Internship under the direction of Kelly Gaffney at the Stanford Synchrotron Radiation Laboratory at the Stanford Linear Accelerator Center.

Participant: _____

Research Advisor: _____

Work supported in part by US Department of Energy contract DE-AC02-76SF00515

TABLE OF CONTENTS

ABSRACT

Determining the Extent of Delocalization in Mixed-Valence Iron Dimers Using x-ray Absorption Spectroscopy. ALISON M. HOYT (Yale University, New Haven, CT 06520) KELLY GAFFNEY (Stanford Synchrotron Radiation Laboratory, Menlo Park, CA 94025).

This study examines the extent of charge delocalization in mixed valence compounds. Understanding the structure of charge delocalization is the first step in understanding the local dynamics of charge transfer. This insight has diverse applications such as the ability to mimic biological reactions and to enhance solar technology. Because of its fast time scale, synchrotron radiation was used to probe the iron K-edge for three organometallic systems. In these complexes, two bridged metal atoms share an effective charge of 5+. In a Robin-Day Class II compound, charge is localized and the two iron atoms have effective oxidation states of 2+ and 3+ respectively. For Class III delocalized compounds each metal center has an effective charge of 2.5+. Class II/III compounds exhibit characteristics of both localized and delocalized systems according to various optical spectroscopies. Synchrotron radiation was used to study charge distribution in these poorly-understood Class II/III intermediate systems. In the limit of absolute localization, spectra of the mixed valence species were expected to be a linear combination of the reduced and oxidized species. For the delocalized case, a linear combination was not expected. These two cases were used as calibration limits to determine the extent of delocalization in the unknown Class II/III compound. Results showed that synchrotron radiation classifies the Class II/III compound as localized. However, data also demonstrated that the linear combination model did not hold as expected and a revised model is necessary to better understand this phenomenon.

1. INTRODUCTION

X-ray absorption spectroscopy was used to study charge distribution in mixed valence organometallic complexes. These compounds consist of multiple metal atoms connected by a bridging ligand, a molecular structure that links the atoms together. A Robin-Day classification system classifies these mixed valence complexes based on the metal centers' electronic interaction [1]. Class II localized compounds consist of two metal centers with little electronic interaction. In the studied localized compound, the two iron atoms have effective oxidation states of 2+ and 3+ respectively. Class III compounds have a delocalized charge distribution with stronger electronic interaction between the two metal atoms. In this class, charge is shared between the two metal centers, which each have an effective charge of 2.5+. Many mixed valence compounds have been successfully characterized using UV/VIS and IR/NIR spectroscopy. However, an intermediate class of compounds has been discovered [2] which demonstrates characteristics of both class II and class III compounds [3]. This study examines charge distribution in poorly-understood Class II/III compounds using synchrotron based x-ray absorption spectroscopy.

Synchrotron radiation was selected because of its short time-scale. Faster than IR/NIR and UV/VIS spectroscopies because of the x-rays' shorter wavelength, x-ray absorption spectroscopy may be able to resolve processes that are time-averaged when probed with slower spectroscopic techniques. This experiment probes the transition as the Class II/III compound oscillates between a localized and delocalized state. Understanding and modeling this transition between electronic structures works toward the goal of understanding the local dynamics of

charge transfer. This insight has diverse applications such as the ability to mimic biological reactions and to enhance solar technology.

Synchrotron radiation is a useful tool in the examination of x-ray absorption as its high intensity, compared with other x-ray sources, allows for more precise measurements. This radiation is produced by a synchrotron, which uses electric and magnetic fields to accelerate charged particles around a ring. The magnetic field holds the particles in their circular path, while the electric field accelerates them. Both fields are synchronized to vary with the circulating particles, producing a narrow, tightly focused beam. As the particles are accelerated, they emit photons. At SSRL, the Stanford Synchrotron Radiation Laboratory, the narrow electron beam emits broadband x-ray radiation as it passes through an undulator or wiggler. These magnetic configurations cause the electron beam trajectory to oscillate and radiate x-rays. This intense radiation is used to perform a wide variety of experiments from protein crystallography to semiconductor material analysis.

This experiment uses synchrotron radiation to perform x-ray absorption spectroscopy (XAS). Absorption peaks provide information on the electronic orbitals and local structure surrounding a specific element in the compound. X-rays are absorbed if their energy is sufficient to excite the electron to a higher energy level or completely ionize the electron. This experiment probes the iron K-edge, where 1s core electrons are excited to higher unoccupied orbitals or into the continuum.

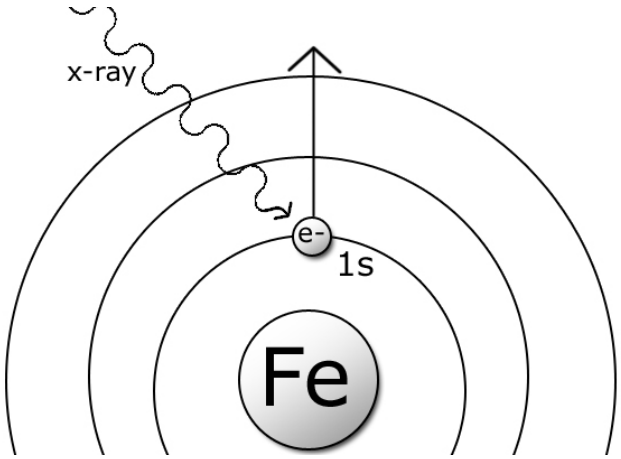

The pre-edge absorption signal

reflects electrons excited to the valence shell. This provides information on valence electron distribution and the extent of d-orbital splitting. Above the edge, the energy of the incoming x-ray is sufficient to excite a core electron into the continuum. The outgoing electron wave scatters off surrounding atoms and interferes with the incoming x-rays, altering the measured absorption signal. Structural information on nearest-neighbor surrounding atoms is extracted from these intensity fluctuations. This experiment will combine electronic and structural information from the pre-edge and edge regions to better understand electronic distribution in class II/III compounds.

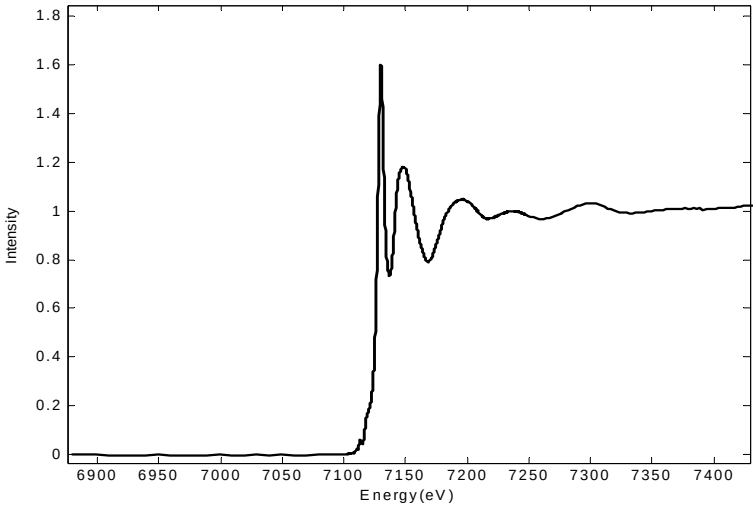

Figure. Shows the peak in absorption intensity at the edge (7125eV)

MATERIALS AND METHODS

i. Theoretical Model

Class II, III and II/III compounds were each prepared in three oxidation states: both metal centers reduced, both oxidized, and a mixed valence state. XAS Spectra were taken for each of these samples to determine the extent of delocalization in the Class II/III compound. (The Class II and III compounds were used for calibration.) In a theoretical localized charge system, there is no electronic interaction between the two metal centers. Under this assumption, the absorption contribution from one metal center is completely independent of the contribution of the second iron atom. If both iron atoms in the system are reduced (2+,2+), they contribute identical spectra due to the symmetry of the molecular environment surrounding the two iron atoms. In addition, two oxidized metal centers (3+,3+) will make identical but independent contributions. In the

localized mixed valence species (2+, 3+), the reduced and the oxidized iron atoms will contribute different and independent absorption spectra. The reduced iron atom will contribute an absorption spectra identical to the completely reduced system(2+,2+). The oxidized metal center will contribute an absorption spectra identical to the completely oxidized system (3+,3+). Thus, the localized mixed valence spectra (2+,3+) will be a linear combination of the fully reduced (2+,2+) and fully oxidized (3+,3+) systems. Conversely, a linear combination of the fully oxidized and reduced spectra is not expected for the delocalized mixed valence (2.5+, 2.5+) compound. Due to electronic interaction between metal centers, the absorption spectra contributed by one iron atom is not independent of the oxidation state of the second atom. A linear combination fit was used to test this model for our Class II and III compounds. Analysis of the Class II/III fit to determine delocalization was calibrated with respect to the fully localized and delocalized compounds.

ii. Sample Preparation

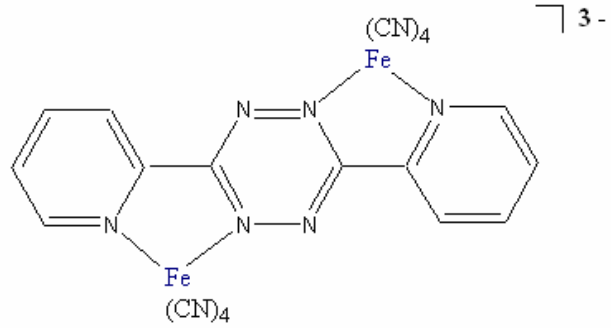

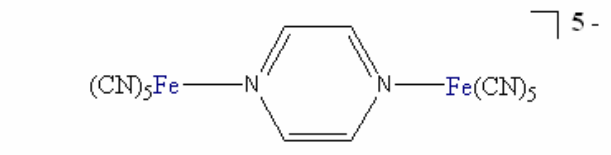

Iron based bimetallic compounds were chosen to span the Robin Day classification system. The pyrazine bridged decacyanodiiron(2+, 3+) ($(CN)_5Fe$-pz-$Fe(CN)_5^{5-}$) represented a class II system in water and a class II/III system in acetonitrile [4]. (Upper structure). The compound 3,6-bis-(2-pyridyl)-1,2,4,5-tetrazine (bptz) bridged octacyanodiiron(2+, 3+) ($(CN)_4Fe$-bptz-$Fe(CN)_4^{3-}$) in acetonitrile represented a class III system [5]. (Lower structure). The fully reduced forms (2+, 2+) of these molecules were

synthesized in an inert atmosphere according to published techniques in the Keith O. Hodgson Laboratory at the Stanford University Department of Chemistry. The fully oxidized states (3+, 3+) were obtained via electrochemical oxidation of the reduced (2+, 2+) state with bromine water. The mixed-valence compounds were prepared by mixing equi-molar amounts of the (2+, 2+) and the (3+, 3+) states.

iii. XAS Data Collection and Reduction

X-ray absorption spectra were recorded at the Stanford Synchrotron Radiation Laboratory (SSRL) on beamline 7-3. The broadband radiation at this beamline is produced by a 20-pole, 2-Tesla wiggler. Radiation was monochromatized using a Si(220), Phi = 0° double-crystal monochromator over an energy range of 6900eV to 7900eV. Absorption was measured at the iron K-edge, where absorbed x-rays excite 1s core electrons to higher energy levels. The sample was placed at a 45° angle to the incident x-ray beam, in order to use a fluorescence detection setup, necessary due to the dilute nature of the samples. This setup does not directly measure reductions in transmission as incident x-rays are absorbed, but rather photons emitted from the sample, called fluorescence. This process occurs as incident x-rays excite 1s core electrons to higher energy levels. When an electron relaxes into the remaining 1s core hole, its extra energy (the difference in energy levels) is emitted as a photon. This phenomenon allows us to monitor even small changes in absorption via fluorescence. Fluorescence was measured with a 30-element Germanium detector placed at a 90° angle to the incident x-ray beam. (See Appendix Figure 1). The dilute solutions were stored in air-tight sample cells with

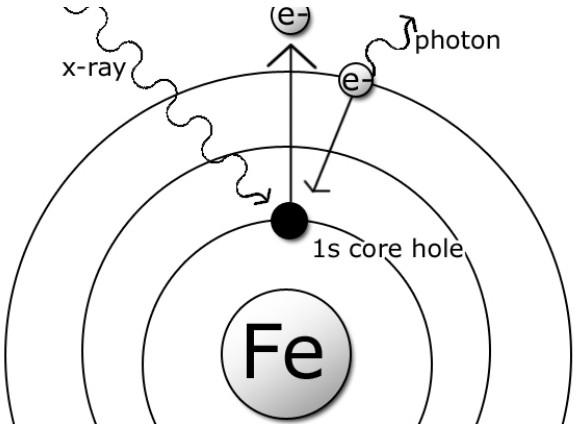

polyethylene windows at room temperature. Energies were calibrated to 7111.2eV (the first inflection point) using an iron foil standard. In general, eight scans were measured for each sample. EXAFSPAK was used to fit a smooth Gaussian to the pre-edge region of the averaged spectra. This fit was then subtracted from the full energy range to remove background. EXAFSPAK was also used to deglitch and spline the data. Athena used the spline to normalize all spectra intensities to 1 at 7350eV and to remove an upward sloping of the raw data at high energy.

3. RESULTS

All three compounds were compared to a linear combination of their oxidized and reduced spectra to determine the extent of delocalization. These linear combinations were not a perfect 50/50 ratio, but instead varied by compound. Optimal percentage fits were selected to minimize error between the linear combination fit and the experimental mixed valence spectra. Variation by compound was due to experimental constraints limiting precision in preparing the mixed valence species, which consisted of mixing the oxidized and reduced species. The Class II localized mixed valence experimental spectrum was fit with a 49.5% reduced (2+, 2+) and 50.5% oxidized (3+,3+) linear combination. The Class II/III mixed valence experimental spectrum was fit with a 59.0% reduced and 41.0% oxidized linear combination. The Class III spectrum was fit with a 42.3% reduced and 57.7% oxidized linear combination. The Class II mixed valence experimental spectrum was a reasonably good fit to its linear combination. There was an absolute error per point of ±0.00562nau (normalized absorption units) or ±1.4σ, where the standard deviation (σ) of the mixed valence spectra was ±0.004nau. (See Appendix Figures 2 and 3). As expected, the Class III was a poor fit to its linear combination, giving an absolute per point error twice as large at ±0.01466nau. The standard deviation also doubled to 0.009nau to

maintain a comparable error of ±1.6σ. (Fig. 6&7). The Class II/III data did not fall between the Class II and Class III spectra as expected. The linear combination fit experimental data better than anticipated. It had the lowest overall error and a comparable σ of ±0.004nau. The absolute error per point was ±0.00447nau or ±1.1σ. (Fig. 4&5).

Significant difference in error between the fit and the mixed valence spectra were seen for different energy ranges. Both the absolute error per point and the standard deviation of the mixed valence spectra were significantly lower in the pre-edge region (7109.5-7125eV) where detailed features were more finely resolved than in the edge (7125-7135eV). For example, the standard deviation value of ±0.002117 quadrupled to ±0.00840 from the pre-edge to the edge for the Class II compound. A change in scanning resolution from 0.05eV to 0.15eV at 7125eV may have contributed to this difference. The Class II compound seemed to fit relatively better in the edge (±0.857σ) than in the pre-edge (±2.17σ). The situation was reversed for the Class III compound with an error of ±2.0σ in the edge and ±1.1σ in the pre-edge region. The intermediate Class II/III compound fit well in both the edge (±0.919σ) and the pre-edge (±1.38σ). These unexpected results indicate that the intermediate compound fit the linear combination model slightly better than the Class II or III compounds.

4. DISCUSSION AND CONCLUSION

Both the absolute error and σ values vary significantly between energy regions. The error in terms of σ showed no strong trends between compounds or across energy regions. However, more valuable comparisons were made between absolute error values in similar energy regions (pre-edge vs. edge). When comparing by region and overall, the Class III compound had the largest absolute error per point, as expected. The Class II/III compound had the lowest overall error, the lowest absolute error in the pre-edge, and an absolute error comparable to that of the

Class II compound in the edge. The Class III compound has a consistently larger error in its linear combination fit than the Class II compound. This data provides evidence for a localized Class II compound and a delocalized Class III compound. These results also indicate that the Class II/III compound is marginally more localized than the Class II compound, which was expected to be the limit of localization. These trends were not revealed in the σ error values because of the uneven standard deviations between compounds. Low resolution for the more dilute Class III compound led σ error analysis to reflect an artificially good fit.

Additional error in fitting was introduced in determining the linear combination percentage. By optimizing the percentage, we unintentionally and unavoidably improved the fit for the Class III compound, even though a poor fit was expected. This error could be corrected in the future with the improved accuracy of a more precise procedure for creating the mixed valence compounds. Additional instrumental errors were considered and corrected for during data processing. This included fluctuations in the incident x-ray beam, corrected by normalizing all spectra to incident energy, and drift in the monochromator energy, corrected by calibrating the energy to an iron foil. These errors were negligible in comparison to the uncertainties generated in sample preparation.

The linear combination fit test indicated that Class III compounds are delocalized, while Class II and Class II/III compounds are localized. This localization analysis only holds if the assumed model of complete localization is applicable. This model provides a simple but insightful understanding of charge delocalization; however, analysis indicates that this simple model may not accurately explain this complex system. The linear combination model is valid in the extreme case of complete charge localization. However, even Class II compounds are rarely absolute localized systems, often maintaining some small electronic interaction between the two

metal centers. Difficulties arise with such deviations from the ideal case. An ideal molecule is necessary as initial calibration to understand how spectra deviate from an absolute linear combination with small increases in delocalization. The possibility that results may deviate from the model non-linearly makes it difficult to extrapolate from hypothetical calibration points. It is impossible to make conclusive statements about the extent of delocalization in the Class II/III compound without better understanding the Class II model calibration spectra. The differences between the Class II experimental spectra and its expected linear combination fit must be more closely probed. Further analysis of the Class II spectra may provide insight into this model of localization. However, it is clear that the Class II and Class II/III compounds fit the linear combination model significantly better than the Class III model, indicating that the x-ray absorption spectra of the Class II/III compound shares characteristics of a localized compound. This apparent localization may be due to the short time scale of the probing x-rays, which do not average over transitions on their time scale, but capture discrete states. Further experiments will allow more complete understanding of the timescales of this transition.

5. ACKNOWLEDGEMENTS

I would like to thank the Department of Energy, Office of Science and SLAC for this opportunity to participate in the SULI program. I would like to thank my mentors Kelly Gaffney, Jen Kaspar and Serena DeBeer-George as well as the rest of the Kelly Gaffney Group for their support and insight into my research.

6. REFERENCES

[1] M.B. Robin and P. Day, "Mixed Valence Chemistry- A Survey and Classification", *Advances In Inorganic Chemistry and Radiochemistry,* vol. 10, p. 247, 1967.

[2] K.D. Demadis, G.A. Neyhart, E.M. Kober, P.S. White, T.J. Meyer, "Intervalence Transfer at the Localized-to-Delocalized, Mixed-Valence Transition in Osmium Polypiridyl Complexes", *Inorganic Chemistry,* vol. 38, p. 5948, 1999.

[3] K.D. Demadis, C.M. Hartshorn, and T.J. Meyer, "The Localized-to-Delocalized Transition in Mixed-Valence Chemistry," *Chemical Reviews,* vol. 101, p. 2655, 2001.

[4] M.M. Ketterle, W. Kaim, J. Olabe, A. Parise, J. Fiedler, "Widely differing stabilities of molecule-bridged cyanodiiron(III, II) species in non-aqueous solvents," *Inorganica Chimica Acta,* vol. 291, p. 66, 1999.

[5] M.M. Glöckle and W. Kaim, N.E. Katz, M.G. Posse, E.H. Cutin, J. Fiedler, "The Fe^{III}/Fe^{II} vs. $Fe_2^{2.5}$ Formulation in Mixed-Valent Species $[(NC)_4Fe(BL)Fe(CN)_4]^{3-}$, BL=2,2'-Bipyrimidine and 3,6-Bis(2-pyridyl)-1,2,4,5-tetrazine. Distance and Size Do Not Always Matter," *Inorganic. Chemistry,* vol. 38, p.3270, 1999.

7. FIGURES

BL 7.3 Setup

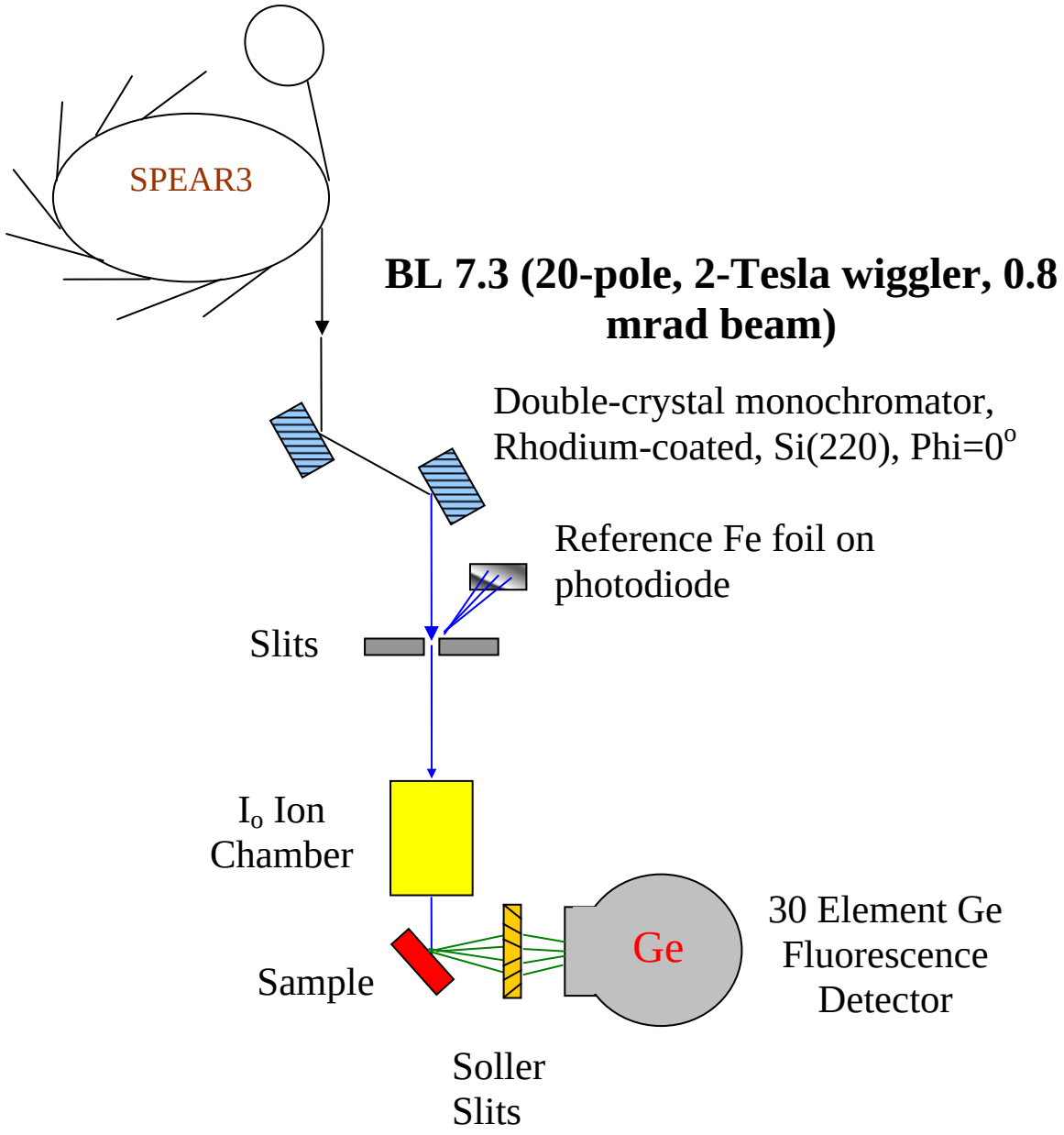

Figure 1. Diagram of the Fluorescence Detection Setup used to measure absorption.

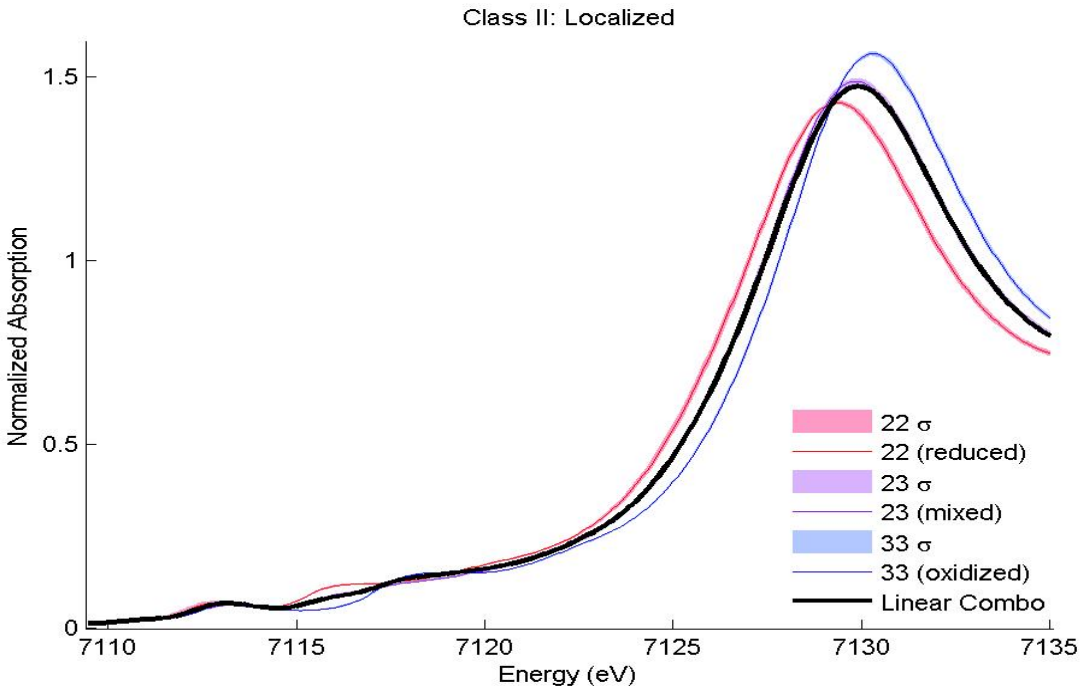

Figure 2. Absorption Spectra of the Class II localized compound. The mixed valence state (purple) was fit with a 49.5% reduced (red) and 50.5% oxidized (blue) linear combination fit.

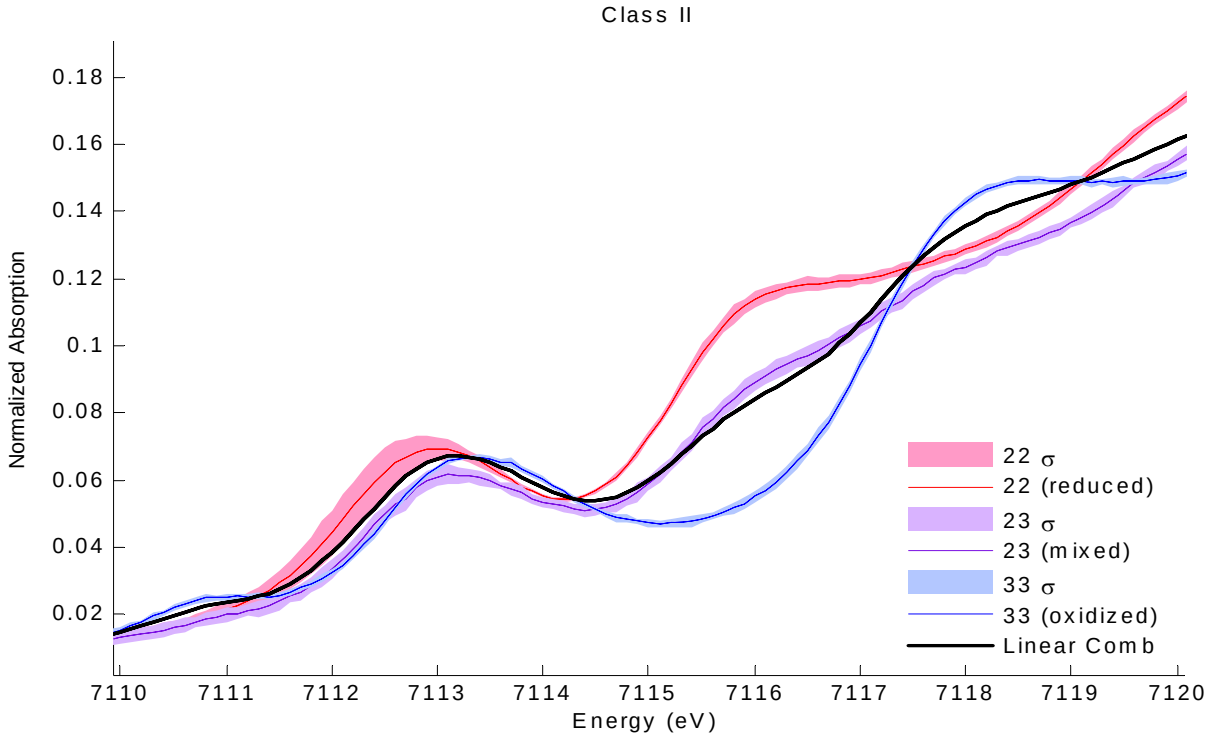

Figure 3. Absorption Spectra of the Class II localized compound zoomed in on the pre-edge energy range. The mixed valence state (purple) was fit with a 49.5% reduced (red) and 50.5% oxidized (blue) linear combination fit.

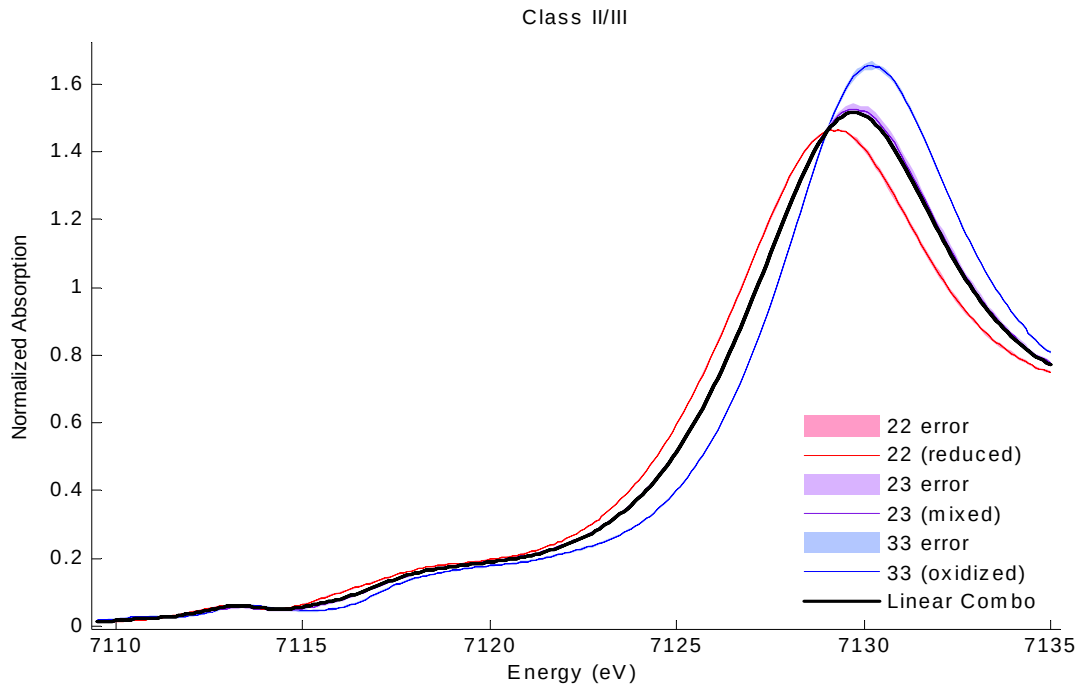

Figure 4. Absorption Spectra of the Class II/III unknown compound. The mixed valence state (purple) was fit with a 59.0% reduced (red) and 41.0% oxidized (blue) linear combination fit.

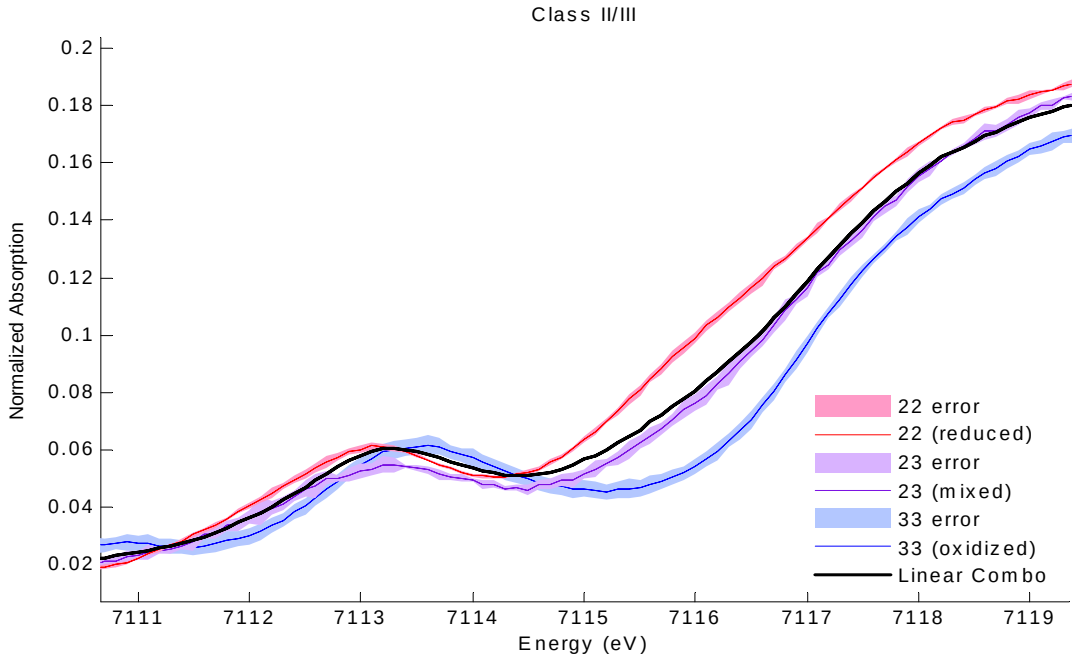

Figure 5. Absorption Spectra of the Class II/III unknown compound zoomed in on the pre-edge energy range. The mixed valence state (purple) was fit with a 59.0% reduced (red) and 41.0% oxidized (blue) linear combination fit.

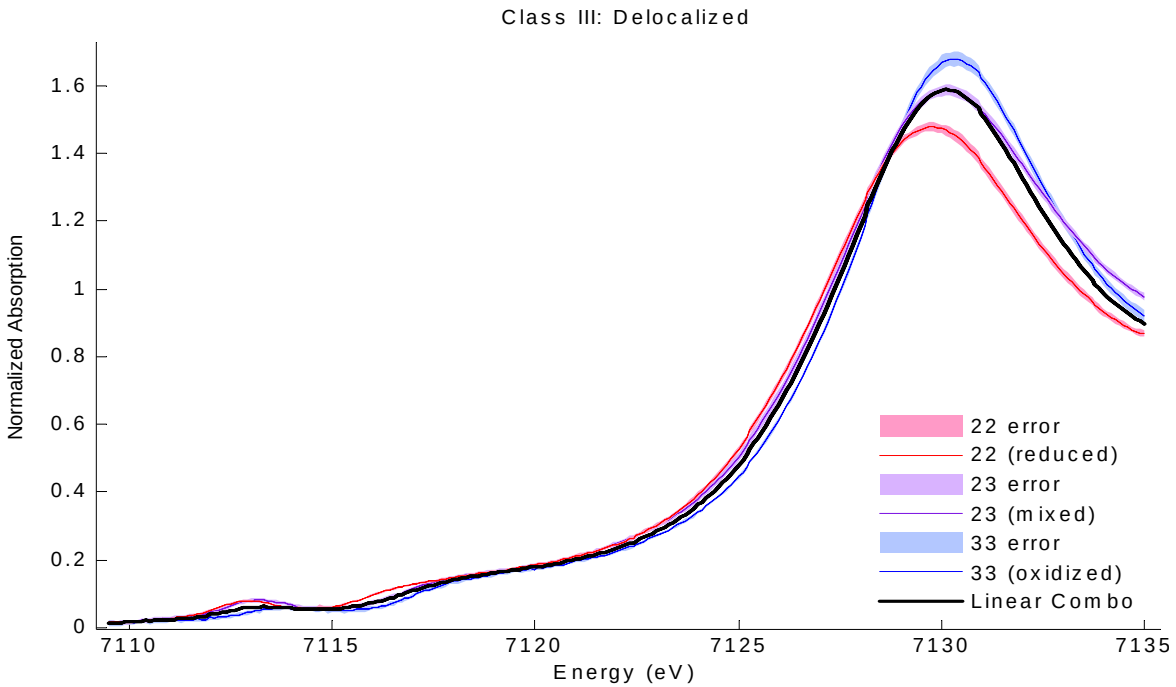

Figure 6. Absorption Spectra of the Class III delocalized compound. The mixed valence state (purple) was fit with a 42.3% reduced (red) and 57.7% oxidized (blue) linear combination fit.

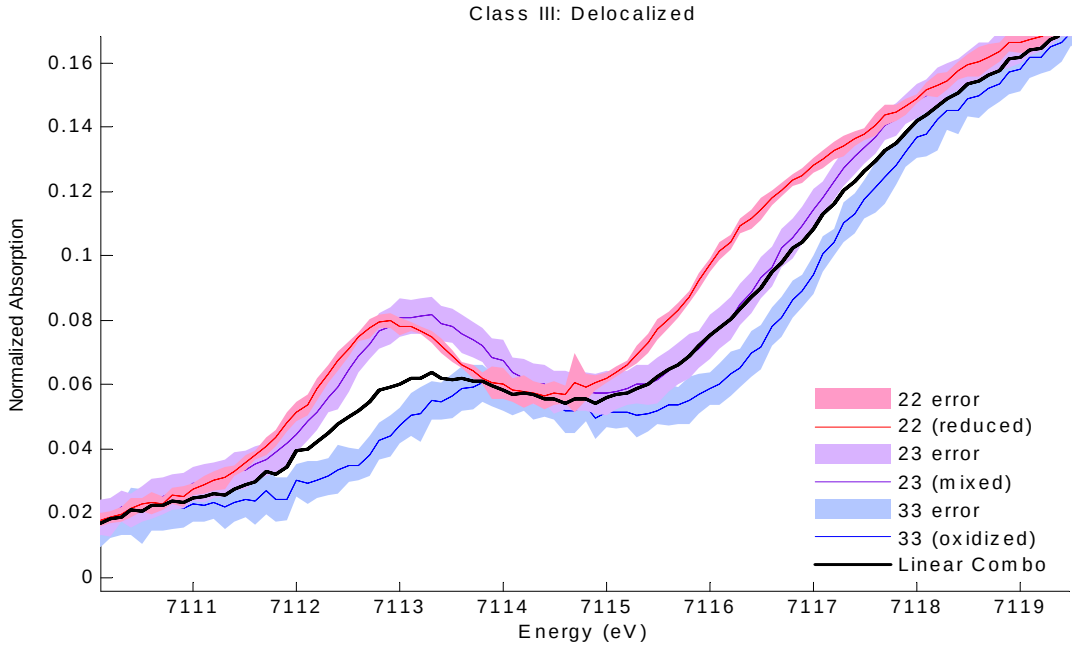

Figure 7. Absorption Spectra of the Class III delocalized compound zoomed in on the pre-edge energy range. The mixed valence state (purple) was fit with a 42.3% reduced (red) and 57.7% oxidized (blue) linear combination fit.

SLAC-TN-07-026

Introducing Defects in Photonic Band-Gap (PBG) Crystals

Elliott C. Johnson

Office of Science, Science Undergraduate Laboratory Internship (SULI)

North Dakota State University

Stanford Linear Accelerator Center

Stanford, CA

August 24, 2007

Prepared in partial fulfillment of the requirements of the Office of Science, Department of Energy's Science Undergraduate Laboratory Internship under the direction of Jim Spencer in the Advanced Acceleration Research Dept., Stanford Linear Accelerator Center.

Participant: _____

Signature

Research Advisor: _____

Signature

Work supported in part by US Department of Energy contract DE-AC02-76SF00515

TABLE OF CONTENTS

ABSTRACT

Introducing Defects in Photonic Band-Gap (PBG) Crystals. ELLIOTT C. JOHNSON (North Dakota State University, Fargo, ND, 58105) JIM SPENCER (Advanced Acceleration Research Dept., Stanford Linear Accelerator Center, Stanford, CA 94025)

Photonic Band-Gap (PBG) fibers are a periodic array of optical materials arranged in a lattice called a photonic crystal. The use of PBG fibers for particle acceleration is being studied by the Advanced Accelerator Research Department (AARD) at SLAC. By introducing defects in such fibers, e.g. removing one or more capillaries from a hexagonal lattice, spatially confined modes suitable for particle acceleration may be created. The AARD has acquired several test samples of PBG fiber arrays with varying refractive index, capillary size, and length from an external vendor for testing. The PBGs were inspected with a microscope and characteristics of the capillaries including radii, spacing, and errors in construction were determined. Transmission tests were performed on these samples using a broad-range spectrophotometer. In addition, detailed E-field simulations of different PBG configurations were done using the CUDOS and RSOFT codes. Several accelerating modes for different configurations were found and studied in detail.

I. INTRODUCTION

In order to study particle physics at smaller scales, higher accelerating gradients are needed. These can be created by using smaller structures, where larger field strengths should be generated. One such structure proposed by the Advanced Accelerator Research Department (AARD) at SLAC is a photonic band-gap (PBG) material with a hollow-core defect[1]. PBG crystals can be assembled by stacking glass capillary tubes in a tight lattice (see Fig. 1). It has been found that introducing central defects, e.g. eliminating one capillary spatially confines modes and equivalently longitudinal E-fields in the defect, creating an accelerator structure[1]. A particular configuration where the diameter of the central defect is 52% the spacing of outside capillaries is called the Lin configuration. The lowest accelerating mode for this configuration using a 1.3μ diameter defect has been studied in detail[1]. PBG fiber arrays can be constructed in very small sizes compared to the accelerator structures in current use, but none yet match the Lin configuration. Another potential benefit is their dielectric composition which allows control of phase velocity closer to the speed of light (SOL) and higher breakdown fields than metallic cavities.

To understand commercially available PBG crystals, samples formed with capillaries of varying wall thickness and radii were obtained from Incom, Inc[2]. With a microscope, the radii and spacing (pitch) of the capillary tubes were characterized for simulation to determine if accelerating modes will propagate in these samples. While PBG fibers are available from outside vendors, most commercial samples are primarily manufactured for telecom applications (TEM modes) and are not suitable for acceleration. For this reason, we are looking to assemble custom crystals based on the calculations and searches for available capillary tubes. This would provide a better means of understanding quality assurance, ease of making defects, and more efficient study of damage and coupling effects.

CUDOS MOF Utilities[3] and RSOFT's BandSOLVE[4] are two software codes used to simulate characteristics of PBG fibers. BandSOLVE is used to define the band gaps

for a given structure and to locate at which wavelengths the band gap overlaps the SOL line–a critical feature for particle acceleration. When the relevant wavelength regions are determined, CUDOS is used to find the precise frequencies of the accelerating modes, i.e. the TM_{0l}-like modes. Many parameters determine the allowed modes for acceleration, including the aforementioned radii and spacing, and also the refractive index of the material. With CUDOS, values for these parameters which lead to strong longitudinal E fields at unique wavelengths can be found–when they exist.

For our application, PBG crystals must be driven by a laser to achieve sufficiently-high gradients. The laser plays the role of the klystron in conventional RF accelerating cavities. The coupling of this field into the defect is a further major research problem. There is no commercial testing process available to us for this. To examine the transmission of our samples, we tested them with a spectrum of light, using a spectrophotometer.

II. MATERIALS AND METHODS

1. PBG Sample Characterization

The PBG crystal samples were inspected using a microscope with attached CCD camera and computer display. The sample was placed on a beam splitter. An external light illuminated the side of the beam splitter, which directed light upward through the sample and into the viewing lens. Several construction errors were photographed. For estimation of capillary diameter and spacing, segments of wires with known diameters were placed on the sample. Wires were also threaded into capillary tubes for further size approximation.

With the inner diameter of the capillaries and the pitch measured, the glass packing fraction (GPF), i.e. the ratio of the cross-sectional glass area to total area of the PBG sample was calculated. This was done by assuming the number of rings to be very large. Furthermore, Mathematica code was written to calculate the GPF for an arbitrary hexagonal configuration, by allowing the user to enter the inner and outer diameters of capillary tubes,

the number of rings removed constituting a defect, and the total number of rings.

A broad-range spectrophotometer[5] was used to measure the transmittance of each sample over the range 325 nm $\leq \lambda \leq$ 3000 nm. Baseline data was taken before adding the samples to quantify water impurities in the system, which absorb light in a frequency dependent way. Dry air was continuously pumped through the system to reduce such ambient effects and provide reproducibility.

2. PBG Mode Simulation

Table 1 shows a comparison of PBG configurations and our test samples (Incom A-D). Allowed bands for accelerating modes were found using RSoft's BandSOLVE[4]. BandSOLVE utilizes a CAD interface to construct fiber arrays. We constructed a 10-ring lattice (with no introduced defect) for the Lin configuration. We also made 10-ring lattices for the Incom B and D samples, scaled so that an introduced (single pulled tube) defect would be 5.0 μm in diameter. With each CAD lattice, a simulation was run that produced the set of band gaps for the configuration. A plot of the transition bands for the Lin fiber is given in Fig. 2 (with the SOL line also plotted for reference). The band gap diagrams for Incom Samples B and D are given in Fig. 3 and Fig. 4, respectively. Wavelengths that correlate to these bands were examined with CUDOS to search for acceptable accelerating modes.

Wavelengths corresponding to the SOL-crossing bands from the band diagram and the PBG parameters from Table 1 were entered into CUDOS MOF Utilities[3]. With these values and an effective index range, CUDOS uses the multipole method to find allowed modes[6]. For these simulations, the 6,8, or 8 ring cases were deemed adequate and saved time. Numerical information including the real and imaginary components of the effective index is given for found modes, as well as an executable for modal field visualization. The E_z field for the fundamental mode of the Lin fiber configuration[1] is shown in Fig. 5. By selecting a point on the mode cross-section, the relative intensity for that point of the mode

can be measured. The user is able to select viewing a Cartesian component of the Poynting vector, E or H field. The real, imaginary, or absolute part of the field can also be specified. In this way, the 2nd, 3rd, and 5th band gaps of the Lin configuration were studied, as well as the 2 lowest SOL-crossing bands for Incom samples B and D with a single pulled capillary defect.

III. RESULTS

1. PBG Sample Characterization

A comprehensive list of estimated parameters for the samples and other configurations is given in Table 1. The number of rings eliminated for the defect (N_{Def}) and the number of rings for calculation (N_{Rgs}) are unspecified for the Incom samples since these were to be determined in the study. Fig. 6 depicts an Incom PBG sample with a construction error that could be used as a single capillary defect. Other construction errors are shown in Fig. 7. A comparison of transmittance data for each sample as a function of wavelength is given in Fig. 8.

2. Found Modes

Five additional modes that may be suitable for acceleration were found for the Lin configuration. Fig. 9 shows a mode from Band Gap 3 (as shown in Fig. 2). Accelerating modes were found in the first and second SOL-crossing bands for Incom D, and these are shown in Figures 10 and 12. No defect modes were found for Incom B. One figure of merit is the ratio of maximum E_z in the core to the maximum of E_z in the glass. These ratios, the excitation wavelength, and the real and imaginary components of the effective index for each mode that was found are given in Table 2 for direct comparison with the lowest mode from the Lin configuration–referred to as the Lin mode[1].

IV. DISCUSSION AND CONCLUSIONS

1. PBG Characterization

Construction errors were observed on all Incom samples. The majority of these errors occurred along the boundary of a larger hexagonal lattice as shown in Fig. 7. This is likely due to a process of construction where groups of smaller hexagonal lattices are forced together to create a larger or super-lattice. The relative occurrence of errors corresponds to a construction "Quality" factor in Table 1. The Incom sample with significantly larger capillaries than the other samples showed very few construction errors, as expected.

Nearly all of the Incom samples had a smaller GPF (and thus larger % air) than the Lin configuration. This is a favorable result, as particle acceleration near c requires the overall refractive index of the lattice to be only slightly larger than 1. Unfortunately, it appears that on scales of capillary diameter $\leq$ 100 μm (Incom sample C excluded), there is a direct correspondence of lower GPF to construction errors due to manufacturing inexperience.

2. Transmission Test Data

The absorption by vibrational levels of water impurities is evident for all samples over the range $\lambda \geq$ 2700 nm as shown in Fig. 8. Absorption below $\lambda \approx 400$ nm for samples A and B implies borosilicate composition, because boron-induced defects in the silica absorb energy over this wavelength. For better quality glass without these impurities, e.g. the HC samples in Table 1, transmission down to 200 nm is common.

Samples A and B exhibit similar transmittance behavior, which is expected as a result of their similar % air and capillary size. Sample C shows increasing transmittance with wavelength increase outwards from the visible light region. This is also an expected result, as the sample appears black (in the visible) and is therefore likely to absorb less at longer

wavelengths. The transmission of sample D exhibits oscillatory behavior, and we anticipate that this is due to diffraction. The capillary size is very small compared to the other samples, and only about 1 order of magnitude larger than the operating wavelength. Consequently, slight misalignments of the sample with respect to the source during the test can lead to an effective aperture small enough to cause diffraction. The behavior is less pronounced as the wavelength decreases, which supports this speculation.

3. New Lin Modes Found

New modes suitable for acceleration were found in the 2nd, 3rd, and 5th band gaps for the Lin configuration shown in Fig. 2. Table 2 shows a comparison between these modes and the previously-found, lowest mode discussed in [1]. The real component of the effective index for each mode describes the amount of glass the mode "sees" as it propagates. The imaginary component of the effective index directly relates to mode leakage that should be minimized. As shown in Table 2, one new mode in band 3 has a significantly lower n_{im} value than the fundamental Lin mode.

Also displayed in Table 2 is the ratio of $E_{z,maxcore}$ to $E_{z,maxglass}$ for the 6, 7 and 8 ring cases of each Lin mode. This figure of merit, called $E_{z,n}$, is important because it describes the efficiency of the system or gradient capacity. The lowest mode has the highest value with 62%, and the ratio generally decreases with band increase. We estimate that the ratio from band 2 ($\approx$50%) is acceptable.

One way to decrease n_{im} for any configuration is to add rings, as demonstrated in Table 2. The decrease in n_{im} vs. number of rings was plotted for the Lin mode. This is shown in Fig. 15. A second-order polynomial fit was obtained by assuming a linear correction factor α and a quadratic correction factor β in the following two relations:

$$
\begin{aligned}
n_{i7} &= n_{i6} + \alpha + \beta \\
n_{i8} &= n_{i6} + 2\alpha + 4\beta
\end{aligned} \tag{1}
$$

For the Lin Mode, we calculated α and β to be $-1.28 \cdot 10^{-4}$ and $-1.22 \cdot 10^{-5}$, respectively. This suggests that there is very little gain in going beyond 7 or 8 rings.

The discovery of the higher-order accelerating modes in the Lin configuration has extensive implications. Most importantly, it has been shown that excitation wavelengths can vary significantly for a given fiber. For example, in Table 1, the Lin configuration has been shown to support acceleration modes over at least 450 nm $\leq\lambda\leq$ 1000 nm. This implies larger defects and capillary sizes may be practical to use. It also means that the type of laser used to excite the mode can vary. With a tunable laser source, different accelerating modes could be generated with minimal delay. Also, if a certain excitation wavelength were desired, several different (appropriately scaled) structures could be built specifically for that wavelength. For example, it should be noted that no fiber can currently be produced to the Lin specifications. Fabricating fibers with a defect radius of 2.5 μm is more realistic. By scaling the values to this design, we found that the center wavelength of the operational band is about 1.65 μm.

4. Incom Sample Mode Search

After several CUDOS trials, no modes suitable for acceleration were found in the first or second gaps for Incom B, even though the band gap diagram indicates that such modes may exist. More searches with smaller wavelength increments may result in useful modes. It is also possible that no accelerating modes exist in these bands, even though the bands cross the SOL line. This suggests that the likelihood of finding these modes is very sensitive to defect size in relation to the lattice. One goal is to develop a procedure for how to perturb such lattices to bring the required modes into these gaps.

Both the first and second bands of the diagram for Incom D were found to support defect modes, as shown in Figures 10 and 12. The effective index components and $E_{z,core}/E_{z,glass}$ ratios for these two modes are given in Table 3. The lowest mode strongly resembles the Lin mode, and this is reasonable. Incom D and the Lin configuration have very similar capillary radius to pitch ratios, as well as defect radius to pitch ratios. In fact, the lowest-order Incom D mode has comparable effective index values compared to the Lin mode, but also a slightly better E_z ratio. It's field distribution also compares favorably, as shown in the next figures (11, 13, 14).

For the Incom D case, the lowest-order mode shows TM_{01} nature in Fig. 11; it is uniform, radially symmetric over the defect region, and falls off smoothly with reduced amplitude outside. Alternatively, the second-band mode (shown in Fig. 12) shows very clear TM_{02} characteristics, with a uniform and radially symmetric field in the defect region, as well as a second peak of comparable amplitude in the lattice. It is important to note that these only show absolute E_z. Horizontal (x) and vertical (y) slices of E_z from the center outward for each of these modes are given in the figures. For comparison, a similar picture for the lowest-order Lin mode is given in Fig. 14. The outer edge of the defect is clearly shown in these plots. Note that Lin describes his mode as TM_{0l}-like. By comparison, it appears more TM_{03}-like.

5. Outlook

Although several types of PBG fibers are available, most are not suitable for a particle acceleration application. For example, telecom fibers are made for TEM mode applications. Very small capillaries in new PBG samples should allow us to work at wavelengths that were previously impossible.

In our application, one figure of merit for PBGs is the ratio of central defect size to operating wavelength. This value should be maximized to reduce damaging effects of high-energy electrons traveling down the fiber. The Lin configuration utilizes a wavelength on the order

of the defect size, which is impractical. A yet-to-be discovered configuration that employs a much larger defect size to wavelength is required for practical PBG fiber acceleration that does not compromise accelerating gradient. One avenue toward this goal is a more detailed tailoring of the outer periphery of the defect and near lattice in terms of shape and material.

VI. REFERENCES

[1] X.E. Lin. "Photonic band gap fiber accelerator," Physical Review Special Topics - Accelerators and Beams Vol. 4 051301 May 2001

[2] Several samples were provided to us by Jeffrey Solari of Incom, Inc. www.incomusa.com

[3] CUDOS Microstructured Optical Fiber Utilities http://www.physics.usyd.edu.au/cudos/mofsoftware/

[4] RSOFT BandSOLVE www.rsoftdesign

[5] Varian Inc. Cary 5000 NIR Spectrophotometer www.varianinc.com

[6] T.P. White, B.T. Kuhlmey, R.C. McPhedran, D. Maystre and G. Renversez, C. Martijn de Sterke, L.C. Botten. "Multipole method for microstructured optical fibers," J. Opt. Soc. Am. B, Vol. 19, No. 10, Oct. 2002

VII. ACKNOWLEDGMENTS

This research was conducted at Stanford Linear Accelerator Center. The author would like to recognize the U.S. Dept. of Energy, the Office of Science, and SLAC for organizing and funding the SULI program. Special thanks are extended to Bob Noble and Jim Spencer for their encouragement and guidance.

FIGURES

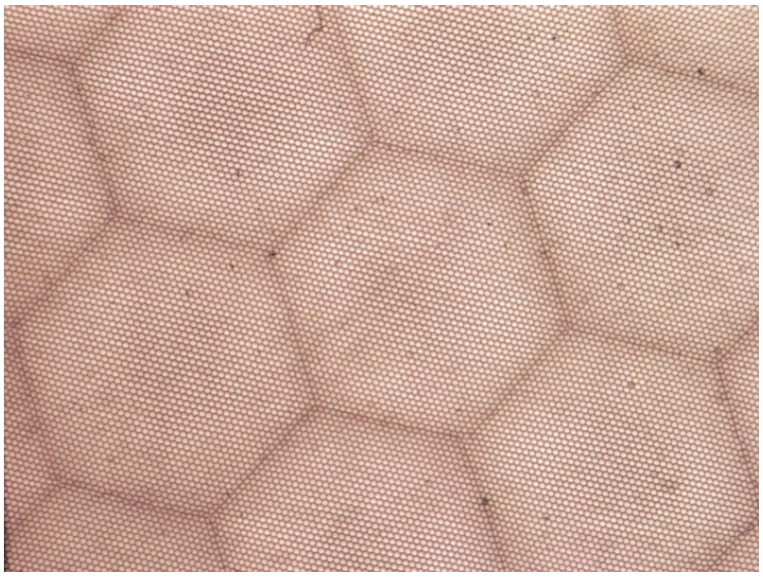

Figure 1: Incom sample D Photonic Band-Gap lattice.

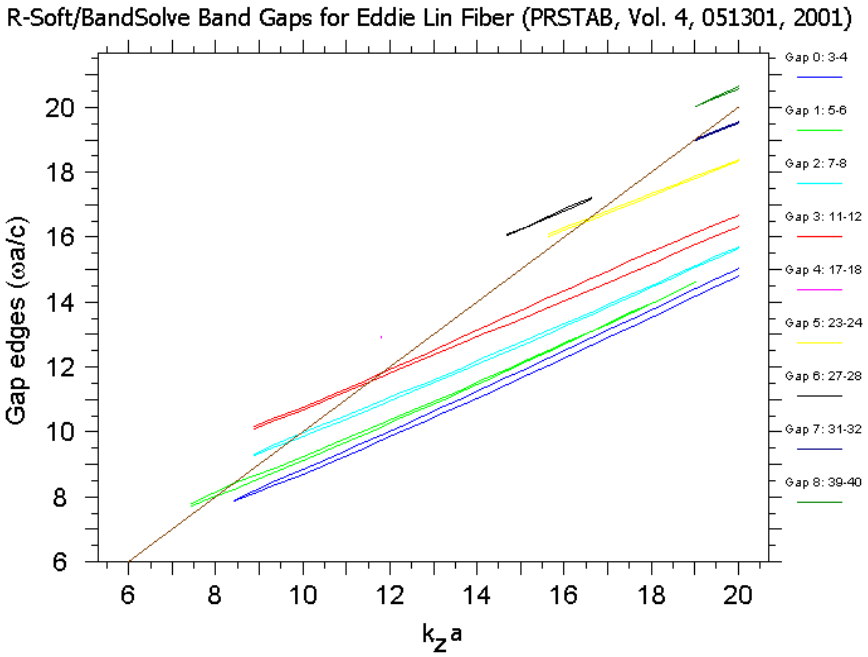

Figure 2: Complete band gaps for the Lin configuration (Table 1).

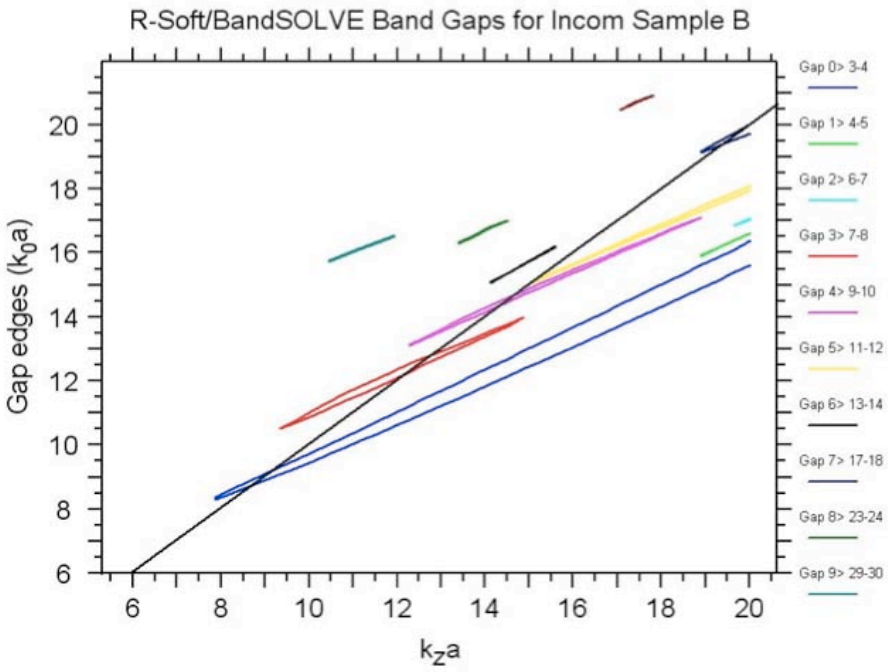

Figure 3: Unperturbed lattice band gaps of the Incom B PBG sample (Table 1).

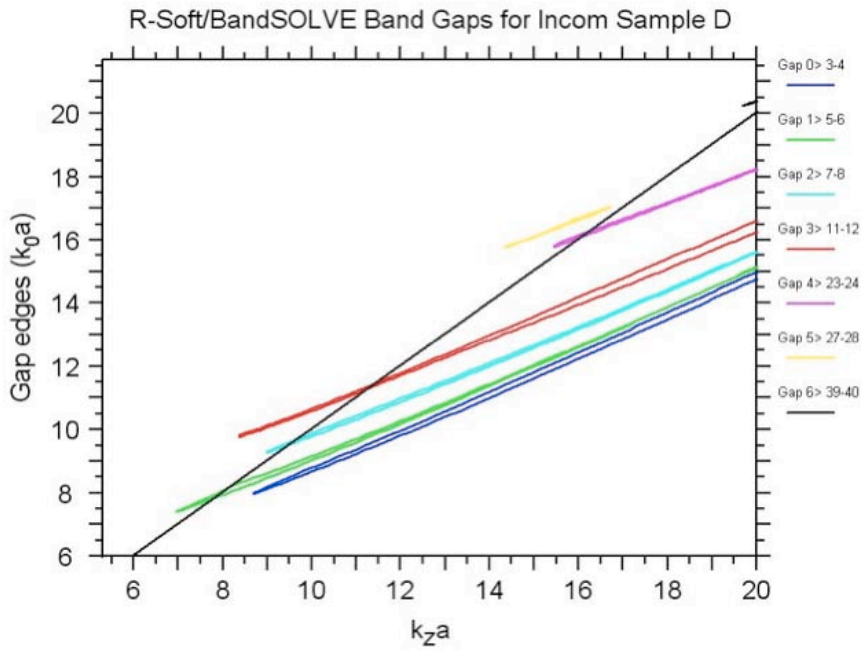

Figure 4: Unperturbed lattice band gaps of the Incom D PBG sample (Table 1).

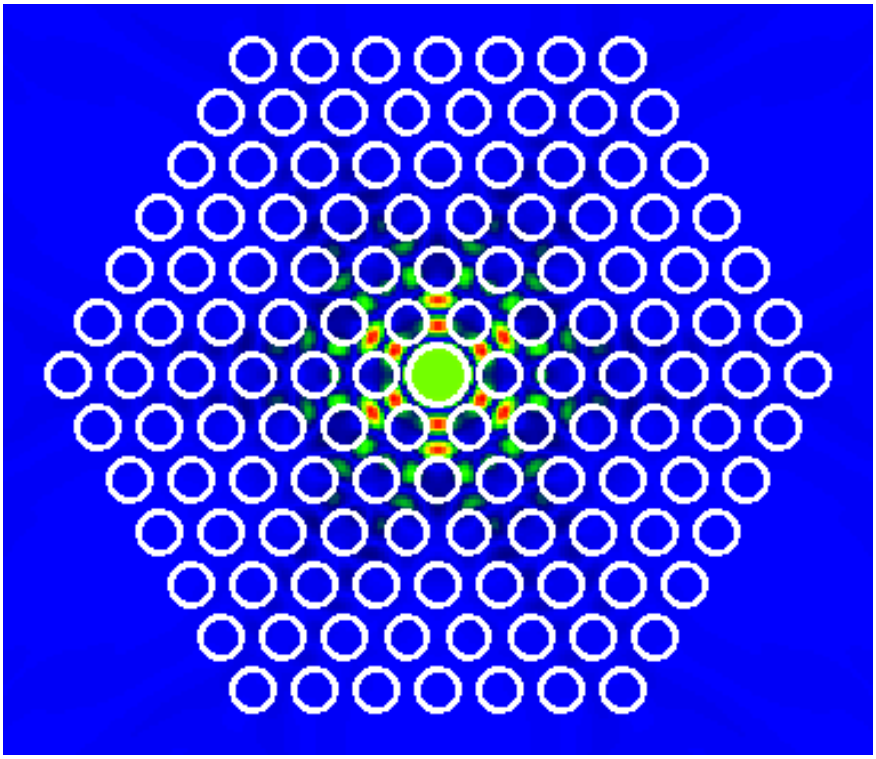

Figure 5: E_z for the lowest-order mode of the Lin configuration.

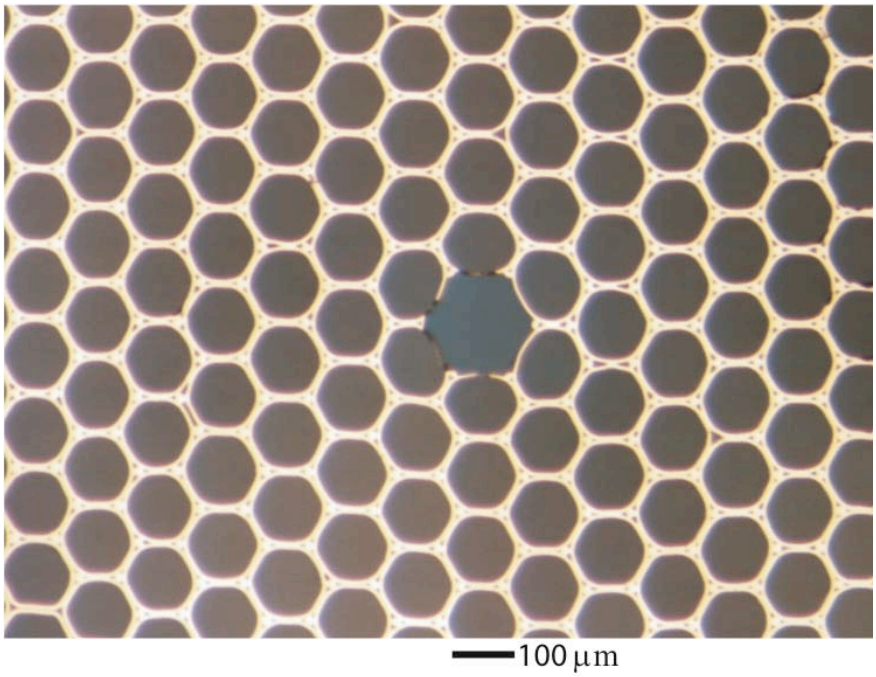

Figure 6: Photo of a 100μm PBG lattice (Incom B) with single capillary defect.

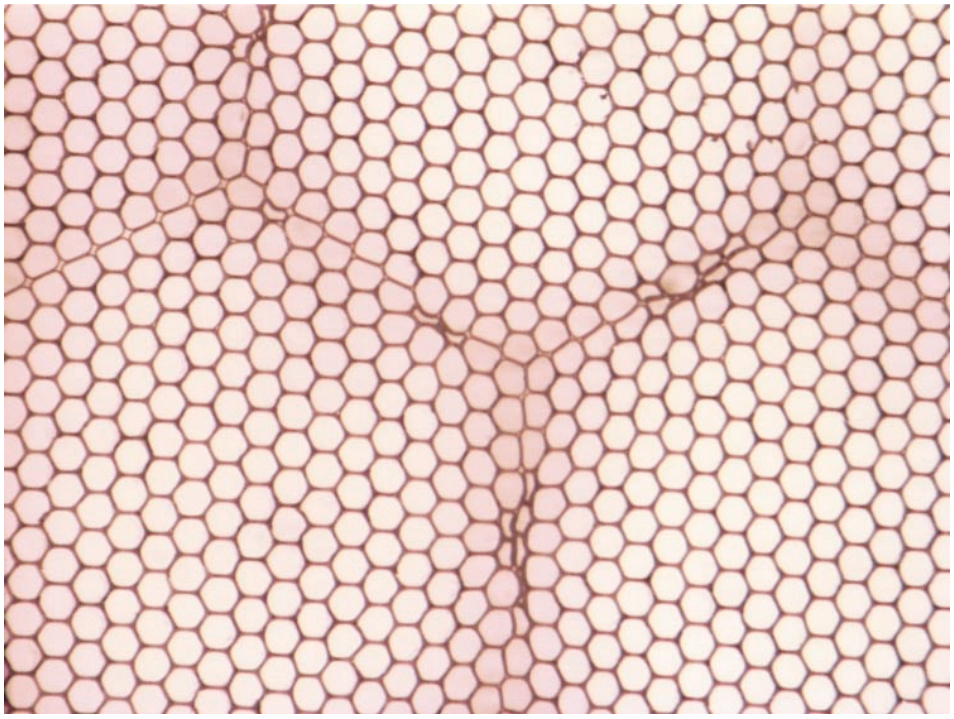

Figure 7: Construction errors along larger super-hexagonal lattice (Incom A).

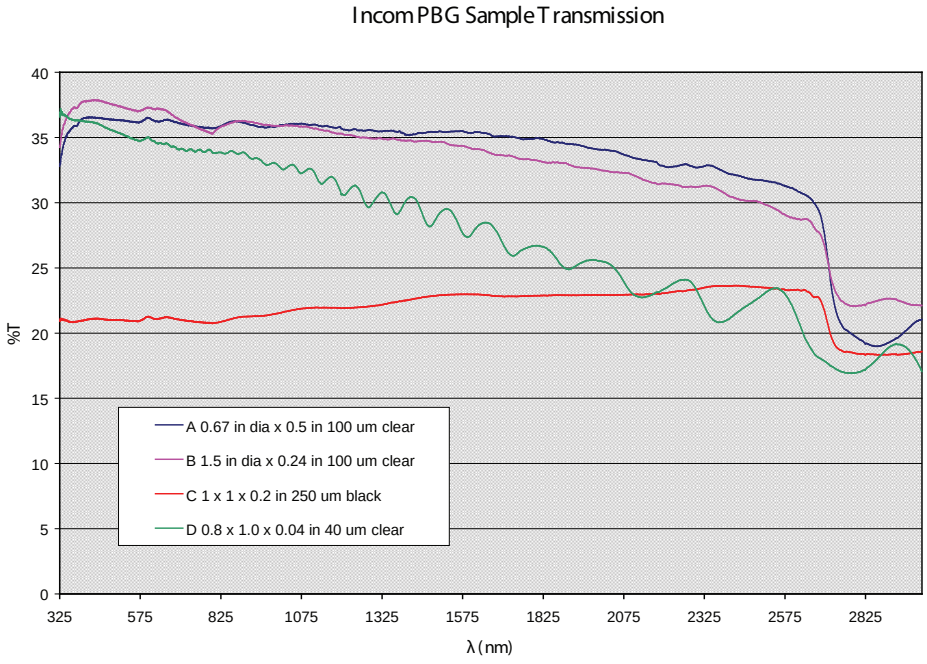

Figure 8: Transmittance data for the Incom samples.

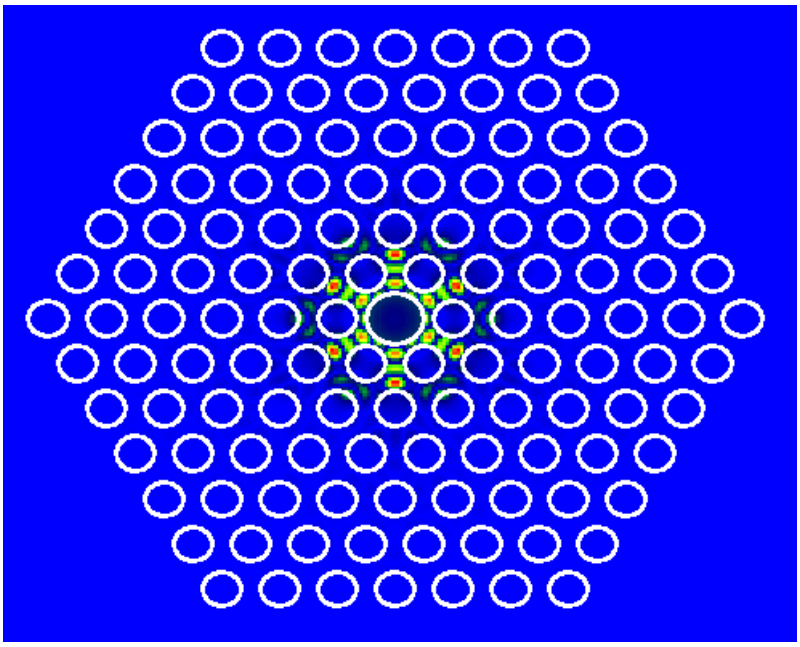

Figure 9: E_z for a third-band mode of the Lin configuration.

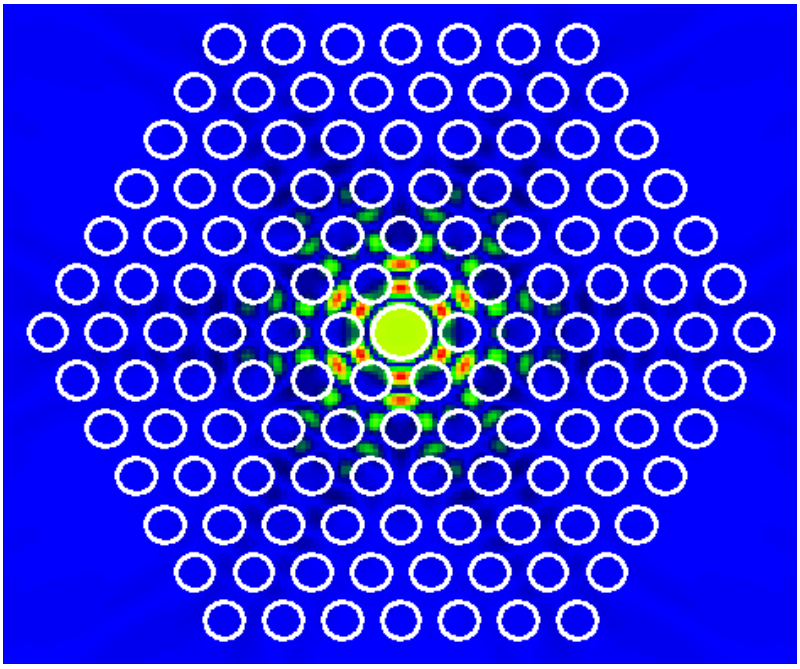

Figure 10: E_z for a first-band mode of the Incom D sample.

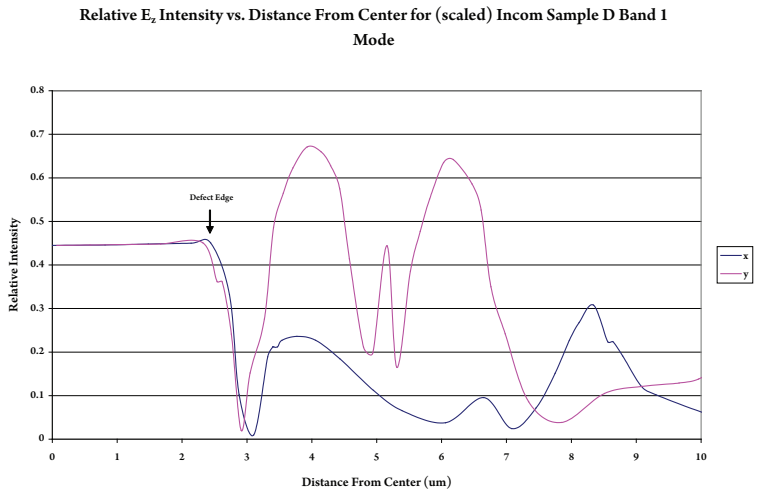

Figure 11: Intensity vs. distance from defect center for the Incom D Band 1 mode.

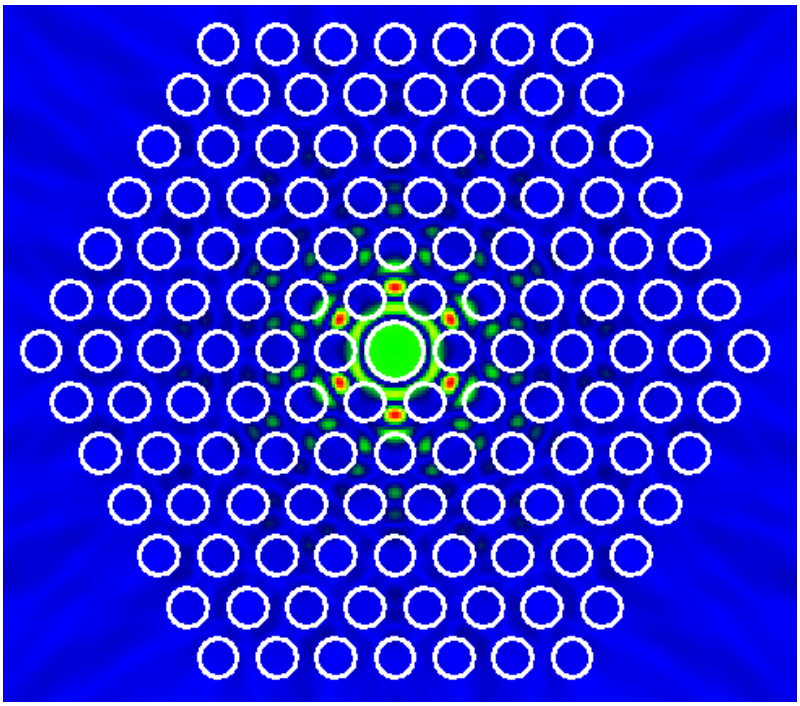

Figure 12: E_z for a second-band mode of the Incom D sample.

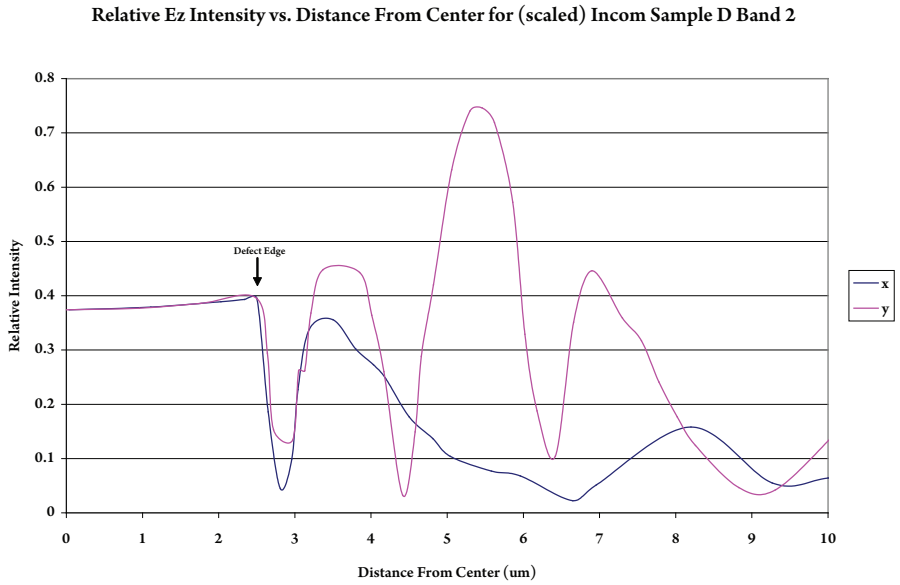

Figure 13: Intensity vs. distance from defect center for the Incom D Band 2 mode.

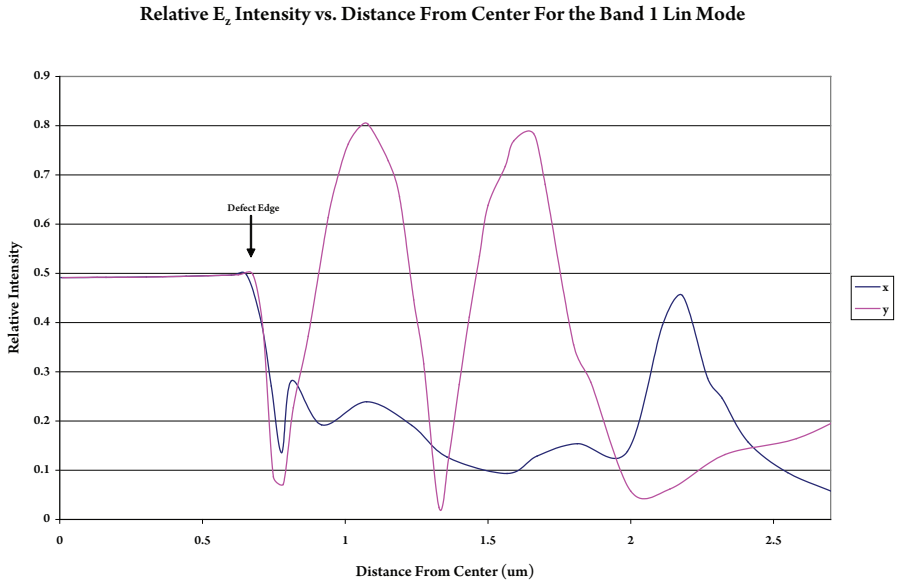

Figure 14: Intensity vs. distance from defect center for the lowest-order Lin mode.

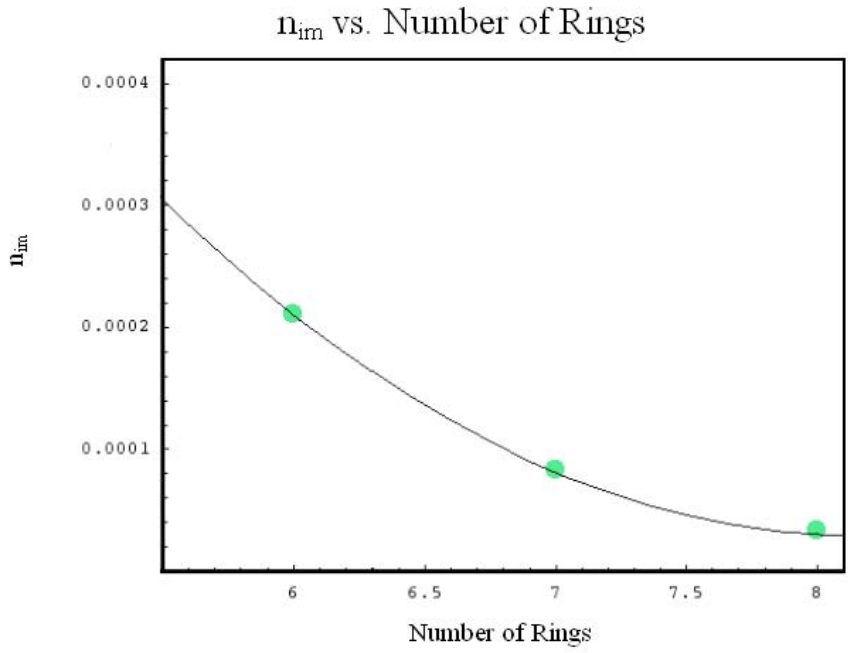

Figure 15: Imaginary effective index vs. ring number for the lowest-order Lin mode.

TABLES

TABLE 1. Representative examples and their characteristics for silica (ϵ=2.13) PBG fibers.

Parameter	$\mathbf{N}_{Def}$[1]	$\mathbf{N}_{Rgs}$[2]	**Wavelength** [nm]		**Pitch**	$\mathbf{R}_{Def}$	$\mathbf{R}_{Air}$	% **Air**	**Qual.**[3]
Designation	#	#	Center	Trans.Bd	μm	μm	μm	%	#
HC-1550-02[4]	7	9	1550	>200	3.8	5.45	–	>90[5]	1
HC19-1550-01	19	9	1550	>80	3.9	10±1	–	>90	2
HC-440-01	7	9	440	>60	1.44	2.45	–	>90	3
X.E. Lin[6]	1	6	1000	>20	1.31	0.68	0.46	65	–
Incom-A[7]	–	–	–	–	122.2	–	55	86.9	3
Incom-B	–	–	–	–	113.6	–	50	84.7	3
Incom-C	–	–	–	–	391.9	–	125	73.4	1
Incom-D	–	–	–	–	58.65	–	20	63.6	2

[1] Number of missing capillaries constituting the defect.
[2] Number of included capillary rings – excluding the single capillary for a perfect lattice.
[3] Qualitative measure of construction uniformity with "1" being best.
[4] www.blazephotonics.com for telecom apps based on amorphous, fused quartz (Suprasil).
[5] Excludes central defect core and outer ring of holes.
[6]X.E. Lin, "Photonic band gap fiber accelerator", Phys. Rev. ST Accel. 4(2001)051301. Calculated results.
[7] www.incomusa.com uses borosilicate "pyrex" and other glasses have very similar characteristics to a-SiO_2.

TABLE 2. Lin mode effective index comparison by number of rings. ($E_{z,n} = E^{max}_{z,Def}/E^{max}_{z,glass}$)

Mode	$\lambda(\mu$m)	$\mathbf{n}_{re,6}$	$\mathbf{n}_{im,6}$	$\mathbf{E}_{z,6}$	$\mathbf{n}_{re,7}$	$\mathbf{n}_{im,7}$	$\mathbf{E}_{z,7}$	$\mathbf{n}_{re,8}$	$\mathbf{n}_{im,8}$	$\mathbf{E}_{z,8}$
1, 1	1.008	1.001	$2.11 \cdot 10^{-4}$	0.62	1.001	$8.34 \cdot 10^{-5}$	0.64	1.001	$3.45 \cdot 10^{-5}$	0.64
2, 1	0.839	1.005	$1.69 \cdot 10^{-3}$	0.502	0.972	$1.05 \cdot 10^{-3}$	n/a	1.005	$7.48 \cdot 10^{-4}$	0.30
2, 2	0.839	1.005	$1.69 \cdot 10^{-3}$	0.502	1.005	$1.07 \cdot 10^{-3}$	0.503	1.005	$7.48 \cdot 10^{-4}$	0.50
3, 1	0.690	1.012	$5.72 \cdot 10^{-5}$	0.279	1.012	$3.41 \cdot 10^{-5}$	0.31	1.0012	$1.75 \cdot 10^{-5}$	0.30
3, 2	0.690	1.005	$7.26 \cdot 10^{-4}$	0.324	1.004	$4.52 \cdot 10^{-4}$	0.243	1.005	$4.31 \cdot 10^{-4}$	0.302
3, 3	0.690	1.007	$1.21 \cdot 10^{-3}$	0.34	1.006	$9.15 \cdot 10^{-4}$	0.299	1.007	$8.84 \cdot 10^{-4}$	n/a
5, 1	0.450	1.008	$3.69 \cdot 10^{-4}$	0.229	1.000	$2.50 \cdot 10^{-4}$	0.270	1.000	$2.66 \cdot 10^{-4}$	0.238

TABLE 3. Incom D Modes.

Band	$\lambda(\mu\mathrm{m})$	$\mathbf{n}_{re,6}$	$\mathbf{n}_{im,6}$	$\mathbf{E}_{z,6}$
1	3.93	1.0018	$3.223 \cdot 10^{-4}$	0.68
2	3.27	1.005	$2.25 \cdot 10^{-3}$	0.523

SLAC-TN-07-020

Improving LER Coupling and Increasing PEP-II Luminosity with Model-Independent Analysis

Lacey Kitch

Office of Science, Science Undergraduate Laboratory Internship (SULI)

Massachusetts Institute of Technology

Stanford Linear Accelerator Center

Menlo Park, CA

Prepared in partial fulfillment of the requirements of the Office of Science, Department of Energy's Science Undergraduate Laboratory Internship under the direction of Dr. Yiton Yan at the Accelerator Research Division of the Stanford Linear Accelerator Center

Participant: _____

Signature

Research Advisor: _____

Signature

Work supported in part by US Department of Energy contract DE-AC02-76SF00515

Contents

Abstract

Improving LER Coupling and PEP-II Luminosity with Model-Independent Analysis.
LACEY KITCH (Massachusetts Institute of Technology, Cambridge, MA 02139)
YITON YAN (Stanford Linear Accelerator Center, Menlo Park, CA 94025)

The PEP-II storage ring at SLAC houses electrons (in the High-Energy Ring, or HER) and positrons (in the Low-Energy Ring, or LER) for collision. The goal of this project was to improve the linear optics of the LER in order to decrease coupling, thereby decreasing emittance and increasing luminosity. To do this, we first took turn by turn BPM (Beam Position Monitor) data of a single positron bunch at two betatron resonance excitations, extracted orbits from this data using Model-Independent Analysis, and from these orbits formed a virtual model of the accelerator. We then took this virtual model and found an accelerator configuration which we predicted would, by creating vertical symmetric sextupole bumps and adjusting the strengths of several key quadrupole magnets, improve the coupling and decrease the emittance in the LER. We dialed this configuration into the LER and observed the coupling, emittance, and luminosity. Coupling immediately improved, as predicted, and the y emittance dropped by a dramatic 40%. After the HER was adjusted to match the LER at the Interaction Point (IP), we saw a 10% increase in luminosity, from $10.2x10^{33}cm^{-2}sec^{-1}$ to $11.2x10^{33}cm^{-2}sec^{-1}$, and achieved a record peak specific luminosity.

Introduction

The PEP-II storage ring at the Stanford Linear Accelerator Center is designed to store high-energy electrons and positrons for collision. The electrons circulate in the HER (High-Energy Ring) at 9 GeV and the positrons circulate in the LER (Low-Energy Ring) at 3.1 GeV. In order to maximize the likelihood of collisions between electrons and positrons at the Interaction Point (IP), PEP-II must have high luminosity. Luminosity is defined as the interaction rate per unit cross-section [6], and is proportional to the product of the intensities of the electron and positron beams over the cross-sectional area of the interaction region of the beams. Luminosity can be improved by increasing beam currents, improving LER-HER alignment, or decreasing emittance, the constant area in x or y phase space which the beam occupies. The latter was the goal of this project, and was accomplished by improving the linear optics (no higher-order corrections included) of the LER.

The linear optics of a beam can be fully characterized with ten parameters [6]. Four of these parameters have to do with coupling between x and y, or the degree to which the two transverse directions of beam motion are dependent. As a result of the fact that x emittance is typically much higher than y emittance, coupling causes y emittance to increase. The goal of this project was to decrease coupling in order to decrease emittance in the LER, and thus increase luminosity. Model-Independent Analysis (MIA) has previously been used to study the linear optics of the PEP-II beams [4], and we used MIA again here. From our MIA-derived orbits we derived Green's Functions and Phase Advances for use in fitting a virtual machine [5], which we would use to improve the linear optics of the LER. Usually, attempts to improve the linear optics of either of the PEP-II beams focus solely on adjusting the quadrupole magnets. This time, we attempted to also adjust the orbit corrector magnets in order to create symmetric Y sextupole bumps, which are pairs of nonlinear magnets used to produce linear effects by being separated from the beamline by a vertical symmetric 'bump' created by the orbit correctors.

The project consisted of four phases: obtaining beam data from the PEP-II LER and extracting four independent orbits with MIA, creating a virtual accelerator model which

fit the data, creating a solution which adjusted the strengths of several LER quadrupole magnets and orbit correctors in order to improve coupling in the LER, and then implementing the solution in the actual accelerator.

Materials and Methods

All steps in the procedure except for the dialing in of the final solution were done in MATLAB. The solution was dialed into PEP-II with a physical knob in the control room.

0.1 Taking BPM Data and Extracting Orbits

First, we took BPM data for a single LER positron bunch in order to measure the ten parameters which characterize the linear optics of the positron beam. In the PEP-II LER there are 319 BPM sites, some single-view in Y (measure displacement only along the Y axis), some single-view in X, and some double-view. We used MIA, which is capable of reducing noise by a factor of $\sqrt{N}$ or $\sqrt{M}$, whichever is larger, for M turns and N BPM measurements, to extract betatron oscillation modes from the BPM data. Unlike in a linac, where the beam jitter produces a signal which is extractable with MIA, in a storage ring the betatron motion is damped by synchrotron radiation and thus is difficult to measure. To aid in measurement, we excited the beam at the horizontal and then the vertical betatron eigentunes. For each excitation mode we collected a set of BPM data for 1024 consecutive turns. This produced four data matrices: a set of X data and a set of Y data for both the horizontal and vertical excitation modes. Each matrix was arranged such that a column contains the measurement data for a single BPM and a row contains the data for a single turn.

Since the position data at each BPM is strongly related to the data of its neighbors, we can use statistical methods to remove BPM data which is likely to be incorrect. We applied both strong and weak criterion to our data in order to find and discard unusable BPM columns.

Once we had isolated the good BPM data, we performed a Discrete Fourier Transform on each data set. The 0^{th} Fourier mode represents the self-consistent closed orbit; this is the path where the beam comes back to the same position after each turn. The other dominating mode is at the frequency of the resonance excitation. From this mode we can and did extract two independent orbits: a cosine-like orbit, represented by the real part of the mode coefficient, and a sine-like orbit, represented by the imaginary part. Since we could do this for both the horizontal and vertical excitation modes, we extracted four independent orbits (x_1, y_1), (x_2, y_2), $(x_3,\ y_3)$ and $(x_4,\ y_4)$ from the BPM data. These four orbits completely determine the transfer matrix, a matrix which operates on a phase space vector at one location to give the phase space vector at another location, between any two BPM positions.

0.2 Calculating Green's Functions and Phase Advances

In order to fit a virtual machine model to the measured data, we need measurement-derived quantities which we can use as fitting parameters in creating the virtual machine. One such quantity we can use are the betatron phase advances at each BPM location [5]. We extracted these phase advances by taking the arctangent of the ratio of the imaginary to the real part of the Fourier Transform mode at each BPM. Since we are taking a ratio, any BPM gains will cancel.

In addition to phase advances, we can use Green's functions to assist in fitting a virtual machine model to the data [5]. This is done by deriving relationships between machine invariants, our four calculated orbits, and calculable transfer matrices, of which the Green's functions are a part. From the four orbits we have already calculated, we can form, for each BPM 'a', a phase space matrix Z^a:

$$Z^a = \begin{pmatrix} x_1^a & x_2^a & x_3^a & x_4^a \\ x'^a_1 & x'^a_2 & x'^a_3 & x'^a_4 \\ y_1^a & y_2^a & y_3^a & y_4^a \\ y'^a_1 & y'^a_2 & y'^a_3 & y'^a_4 \end{pmatrix}$$

For any two adjacent BPMs there exists a symplectic transfer matrix $\mathcal{R}^{ab}$ such that $Z^b = \mathcal{R}^{ab} Z^a$. The symplectic condition on $\mathcal{R}$, $\mathcal{R}^T J \mathcal{R} = J$, implies that there exists an invariant antisymmetric matrix Q such that $Q = Z^{aT} J Z^a = Z^{bT} J Z^b$. While in general Q (being antisymmetric) would have six scalar invariants, the fact that the beam is excited along the eigentunes means that the coupling parameters are zero ($Q_{13} = Q_{14} = Q_{23} = Q_{24} = 0$) and thus that there are only two scalar invariants. While, due to individual BPM gains, we cannot directly calculate Q_{12} and Q_{34}, we can calculate their ratio. Taking the ratio of Q_{12} to Q_{34} cancels the BPM gain, and thus is an invariant.

Now, we can use the four orbits and the invariant ratio $\frac{Q_{12}}{Q_{34}}$ to determine the linear Green's functions between each pair of BPMs. Applying the symplectic condition and the relationship between phase space coordinates gives the following relationships between the four Green's functions, $\mathcal{R}_{12}$, $\mathcal{R}_{14}$, $\mathcal{R}_{32}$, $\mathcal{R}_{34}$; the four orbits; and Q_{12} and Q_{34}:

$$(x_1^a x_2^b - x_2^a x_1^b)/Q_{12} + (x_3^a x_4^b - x_4^a x_3^b)/Q_{34} = \mathcal{R}_{12}^{ab} \tag{1}$$
$$(x_1^a y_2^b - x_2^a y_1^b)/Q_{12} + (x_3^a y_4^b - x_4^a y_3^b)/Q_{34} = \mathcal{R}_{32}^{ab} \tag{2}$$
$$(y_1^a x_2^b - y_2^a x_1^b)/Q_{12} + (y_3^a x_4^b - y_4^a x_3^b)/Q_{34} = \mathcal{R}_{14}^{ab} \tag{3}$$
$$(y_1^a y_2^b - y_2^a y_1^b)/Q_{12} + (y_3^a y_4^b - y_4^a y_3^b)/Q_{34} = \mathcal{R}_{34}^{ab} \tag{4}$$

Since the BPMs are not perfect, we must take measurement error into account when we fit a virtual machine model to the measurement data. Thus we express the Green's functions in the BPM measurement frame, given by Eqs. 1-4, in terms of the Green's functions in the virtual machine frame, R_{ij}, the individual BPM gains, g_x and g_y, and the individual BPM cross-couplings, θ_{xy} and θ_{yx}:

$$\mathcal{R}_{12}^{ab} = g_x^b R_{12}^{ab} g_x^a + g_x^b R_{14}^{ab} \theta_{xy}^a + \theta_{xy}^b R_{32}^{ab} g_x^a + \theta_{xy}^b R_{34}^{ab} \theta_{xy}^a \tag{5}$$
$$\mathcal{R}_{32}^{ab} = g_y^b R_{32}^{ab} g_x^a + g_y^b R_{34}^{ab} \theta_{xy}^a + \theta_{yx}^b R_{12}^{ab} g_x^a + \theta_{yx}^b R_{14}^{ab} \theta_{xy}^a \tag{6}$$
$$\mathcal{R}_{14}^{ab} = g_x^b R_{14}^{ab} g_y^a + g_x^b R_{12}^{ab} \theta_{yx}^a + \theta_{xy}^b R_{34}^{ab} g_y^a + \theta_{xy}^b R_{32}^{ab} \theta_{yx}^a \tag{7}$$
$$\mathcal{R}_{34}^{ab} = g_y^b R_{34}^{ab} g_y^a + g_y^b R_{32}^{ab} \theta_{yx}^a + \theta_{yx}^b R_{14}^{ab} g_y^a + \theta_{yx}^b R_{12}^{ab} \theta_{yx}^a \tag{8}$$

With Eqns. 1-4 we calculated the Green's Functions in the BPM measurement frame, $\mathcal{R}_{ij}$. Then, using these results and Eqns. 5-8, we went on to fit a virtual model.

0.3 Fitting a Virtual Model to the Green's Functions and Phase Advances

To create a virtual machine model from the measured BPM data, we performed an SVD-enhanced least-squares fitting of the machine variables to the Green's functions and phase advances calculated from the BPM data. In order to do such a fitting, the measurement derived quantities, which are the Green's functions and phase advances, can be expressed as a vector, $\vec{Y}_m$. The fitted machine variables are then expressed as a vector, $\vec{Y}$, which is a function of the fitting variables $\vec{X}$, such as the BPM gains and cross-couplings.

To perform the fitting, we initialize $\vec{X}$ at a reasonable guess, such as a prior machine configuration, and call that $\vec{x}_0$. Then we try to find $\vec{x}$ such that:

$$\vec{Y}(\vec{x}_0 + \vec{x}) = \vec{Y}(\vec{x}_0) + M\vec{x} + \vartheta(\vec{x}^2) = \vec{Y}_m \tag{9}$$

Or, equivalently:

$$M\vec{x} = \vec{Y}_m - \vec{Y}(\vec{x}_0) = \vec{b} \tag{10}$$

where $M = \frac{\delta\vec{Y}}{\delta\vec{X}}|_{\vec{x}_0}$ and $\vartheta(\vec{x}^2)$ represents terms of second order or higher, which we disregard. The standard least-squares fitting solution is $\vec{x} = (M^T M)^{-1} M^T \vec{b}$. However, there may exist degeneracies which cause this solution to diverge, and so instead of using a standard least-squares fitting, we use an SVD-enhanced least-squares fitting [3]. The SVD-enhanced fitting solves eqn. 10 by using dominant SVD modes of M. After each iteration, we set $\vec{x}_0 = \vec{x}_0 + \vec{x}$, update the derivative matrix M, and begin again. After many iterations, the calculated Green's functions and phase advances, $\vec{Y}$, converge to the measured values, $\vec{Y}_m$, and we have obtained our virtual accelerator model. We used this process to fit a virtual accelerator to our four orbits.

0.4 Finding and Implementing a Wanted Model

Once we obtained a virtual accelerator model, we found a Wanted Model, or a solution which should improve the optics of the accelerator. To do this, we first selected a small number of magnets to use as variables. The magnets which we chose were the trombone quadrupoles, the global and local skew quadrupoles, and the symmetric Y sextupole

bumps. We then figured out, with MATLAB, a way to best vary these magnet strengths in order to improve certain linear optics parameters, which we weight according to their current importance to us. In this particular project, the goal was to improve the coupling in the LER, and so we heavily weighted the coupling parameters. We also assigned heavy weight to the tunes and beta functions at the interaction point, as we did not want to disturb the LER's current interaction point configuration. Disturbing this configuration would lead to different interaction with the HER, and so even if the LER had improved linear optics, it would not interact with the HER properly and thus we would not achieve high luminosity.

After we found the Wanted Model, we programmed our magnet strength adjustments into a physical knob which would dial the adjustments slowly into the real accelerator. We dialed the adjustments in and then measured the coupling, emittance, and luminosity. After dialing in our solution, the HER required some adjustment in order to match the new LER configuration at the IP, as some IP changes in the LER are unavoidable. We kept measuring luminosity as the HER was adjusted.

Results

After taking data from the PEP-II LER, we successfully created a virtual accelerator which fit the BPM gains and cross-coupling, as well as the betatron phase advances and even the coupling parameters, very well [See Figure 1 and Figure 3]. Surprisingly, we discovered a strange pattern in the BPM gains. A section of about 60 BPMs had a gain significantly lower than 1, as low as .6 and with an average of about .75, meaning that a very large section of BPMs was measuring with an average error of 25% [See Figure 2].

After finding the virtual machine and discerning that it was a good fit, we went on in search of a solution which would improve the coupling of the LER. We came up with three solutions which each had their various good and bad points. We compared the solutions based upon their predicted emittance, coupling, tune, and other factors [See Figure 4 for a comparison of emittance]. We wanted the solution to improve coupling

while not changing IP parameters. We picked our first solution, which improved the coupling greatly and also decreased emittance, while not changing any other parameters by too much [See Figure 5].

When we dialed this solution into the machine, the coupling decreased almost exactly as expected. This was a great success [See Figure 6]. Emittance also decreased, as predicted, by 40%. After adjusting the HER to match the LER and restoring its correct energy settings, luminosity increased by 10%, from $10.2x10^{33}cm^{-2}sec^{-1}$ to $11.2x10^{33}cm^{-2}sec^{-1}$. We also achieved a record peak specific luminosity, or luminosity divided by current [See Figure 7].

Discussion and Conclusion

One concern that arose during the modeling process was the section of BPMs with abnormally low gain. To discover whether these BPMs were actually measuring badly or whether our model was simply a bad fit, we tried removing this section of BPMs and even fitting with up to 300 Green's functions, and in both situations the virtual machine still fit very well [See Figure 1]. Also, since the coupling parameters of our virtual model fit the coupling parameters of the data well [See Figure 3], and coupling was not a fitting variable we used but a check of the model correctness, we had strong reason to believe that our virtual model was a good fit, and thus that the strange BPM gain patterns were real. When we measured the accelerator again after dialing in our solution, we found the same patterns, further supporting the claim that the BPM gains were not an effect of our virtual model.

When dialing our solution into the machine, we noticed that there was a large amount of improvement in the machine when only 50% of the planned magnet strength adjustment had been made. We did some quick calculation, and discovered that 50% of our solution still decreased emittance by a large amount. Staying at this 50% was also less risky, as it involved less magnet strength change. Based upon this, we decided to stop at 50% of the original solution. This may have sacrificed a small bit of emittance decrease, but with

much less risk of causing unpredicted changes in the machine.

At the end of this project, the decrease in emittance and large increase in luminosity showed that our procedure for improving coupling was a good one, and that we effectively altered the strengths of the symmetric Y sextupole bumps to achieve our goal, which had not been done before. After this success, a similar procedure will be done to improve the linear optics of the HER and possibly further increase luminosity.

Acknowledgements

This research was conducted at the Stanford Linear Accelerator Center. I'd like to thank the US Department of Energy, Office of Science, for giving me this wonderful opportunity. I'd especially like to thank my mentor, Yiton Yan, for all of his time, support, and teaching. Also, this would not have been possible without Franz-Josef Decker, Uli Wienands, Gerald Yocky, Martin Donald, Walter Wittmer, and Michael Sullivan, who did all the work in the control room, and Farah Rahbar, Mike Woods, and Steve Rock, who organized the SLAC SULI program.

References

[1] Y.T. Yan, Y. Cai, J. Inrwin, and M. Sullivan, "Linear Optics Verification for PEP-II using Model-Independent Analysis," SLAC-PUB-9368, August 2002

[2] Y.T. Yan, Y. Cai, "Precision Measurement of Coupling Ellipse Parameters in a Storage Ring," SLAC-PUB-10371, 2005

[3] Y.T. Yan, Y. Cai, "Precision PEP-II optics measurement with an SVD-enhanced Least-Square fitting" in Proceedings of the 8th International Computational Accelerator Physics Conference - ICAP 2004

[4] Y. Cai, J. Irwin, M. Sullivan, Y.T. Yan, Application of Model-Independent Analysis to PEP-II rings in Proceedings of the 2001 Particle Accelerator Conference

[5] Y.T. Yan, Y. Cai, F-J Decker, S. Ecklund, J. Irwin, J. Seeman, M. Sullivan, J. Turner, U. Wienands, Virtual Accelerator for Accelerator Optics Improvement, in Proceedings of the 2005 Particle Accelerator Conference, May 2005

[6] D.A. Edwards and M.J. Syphers, An Introduction to the Physics of High Energy Accelerators, Wiley Series in Beam Physics and Accelerator Technology, John Wiley and Sons, Inc., 1993

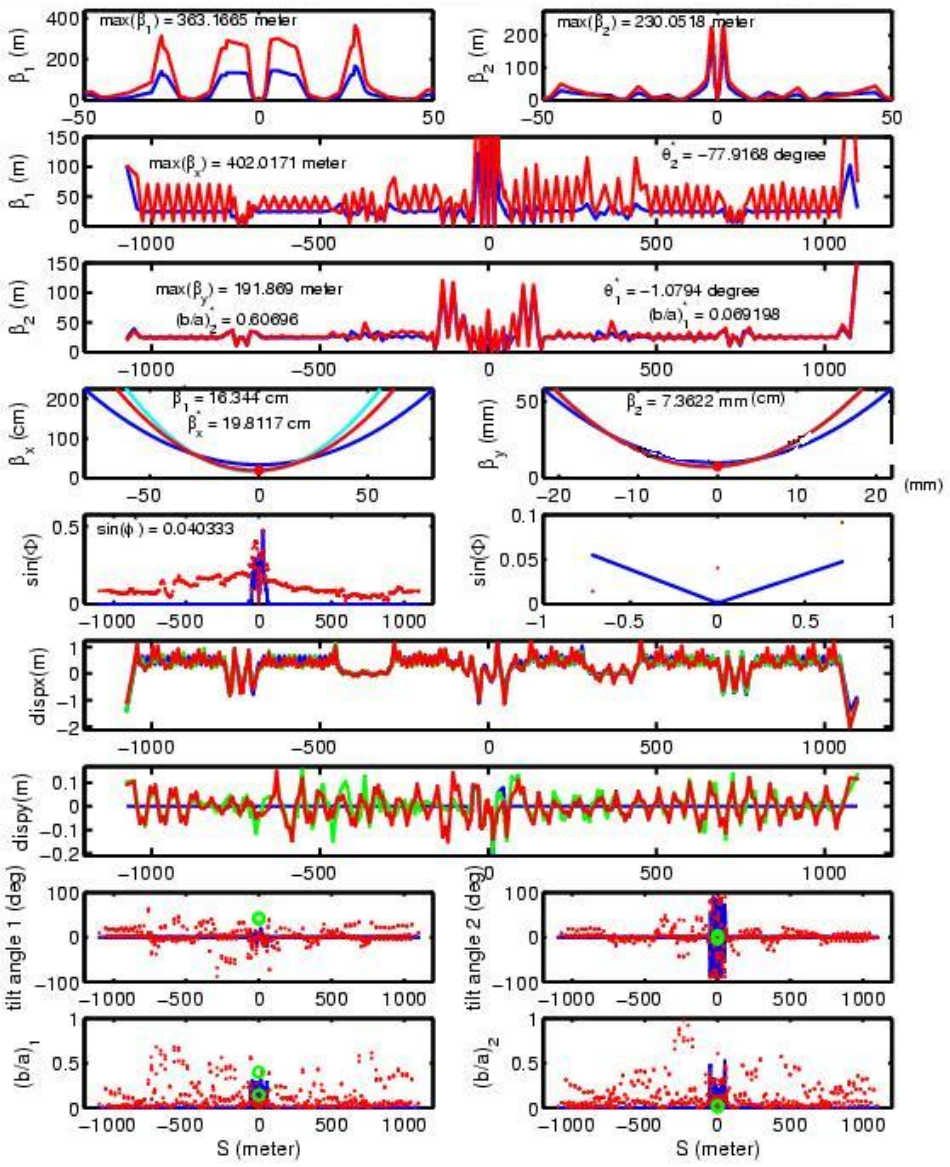

Figure 1: A plot showing linear optics parameters as a function of ring circumference in meters (unless otherwise indicated) for the LER data (green), the Virtual Machine created from the data (red), and the ideal lattice configuration (blue). The Virtual Machine is a good fit to the data but is far from the ideal lattice. Note especially the coupling, in the fifth row and first column, which is the target parameter to be fixed in this project.

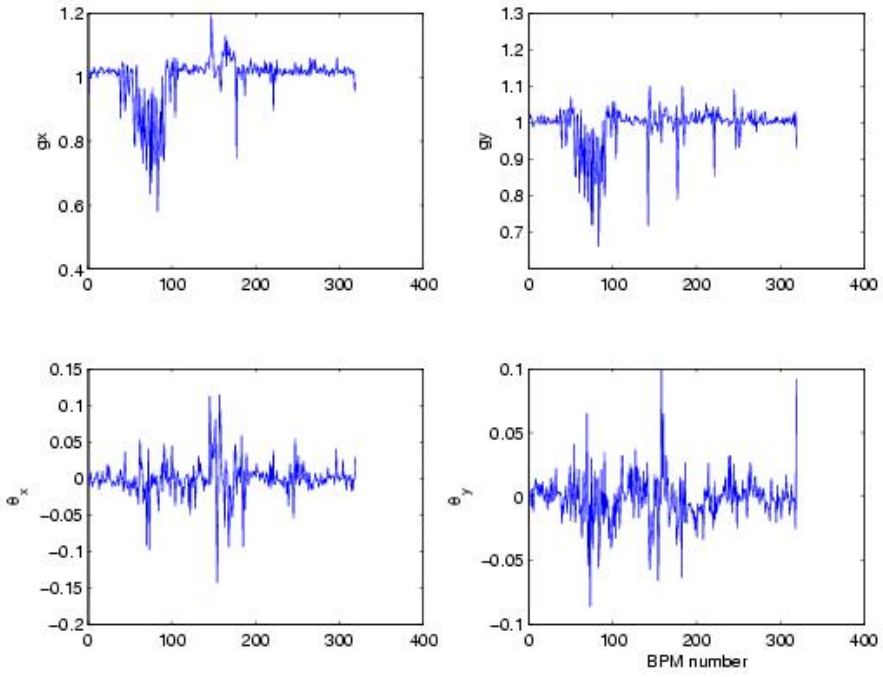

Figure 2: Top: BPM gain, for x and y measurements, as a function of BPM number. These gains are fitted from the BPM data. Bottom: BPM cross-coupling, for x and y measurements, as a function of BPM number. These are also fitted from the BPM data.

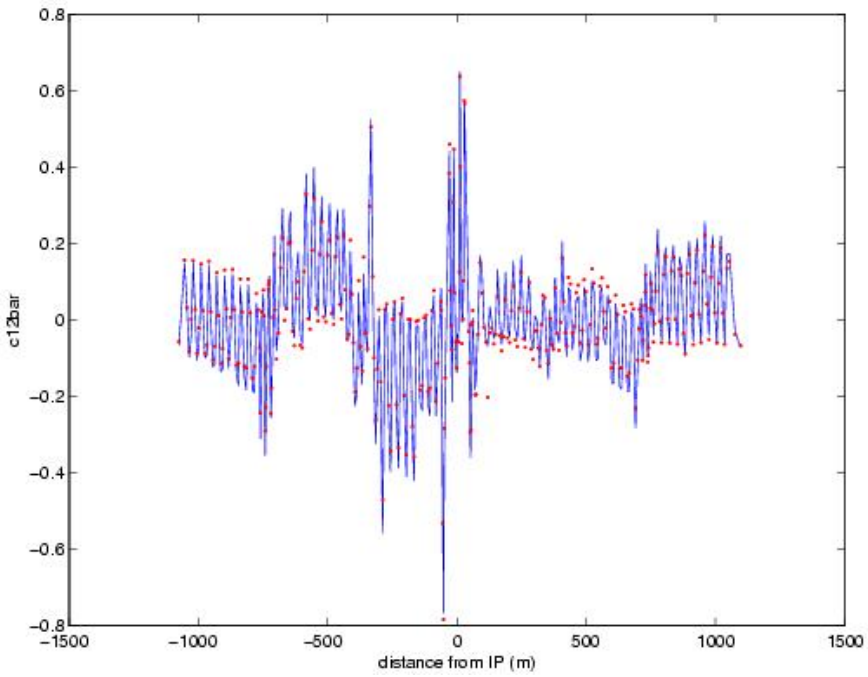

Figure 3: Coupling in our calculated Virtual Machine (blue) compared to the raw BPM data (red). The coupling fits very well, though we did not use coupling as a fitting parameter. This shows that our model is a good one.

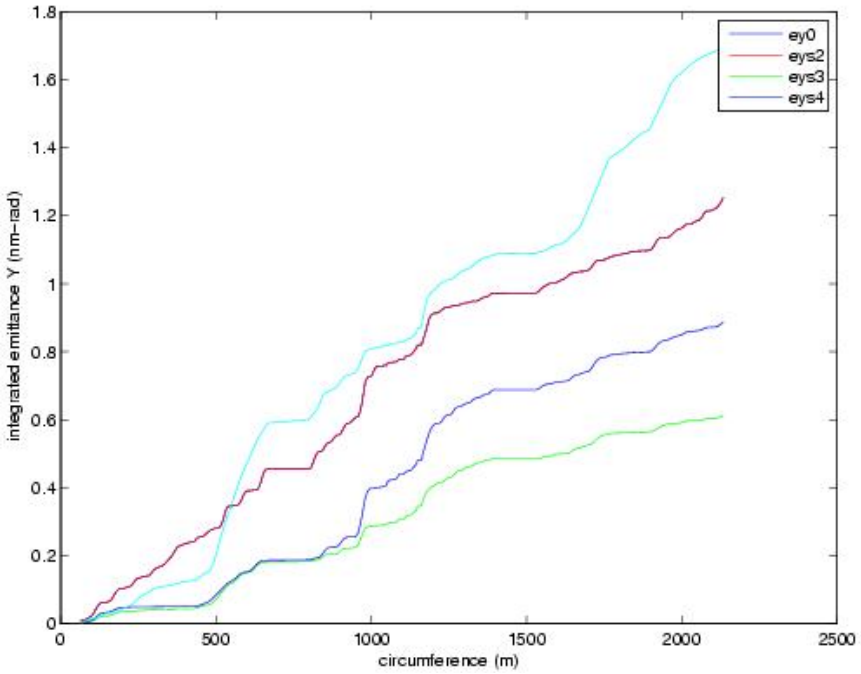

Figure 4: A comparison of the integrated Y emittance of the original virtual machine (red) and our three derived solutions (chosen solution in dark blue). X emittance, which is less important as it is generally much larger, is not shown and was similar for all three solutions.

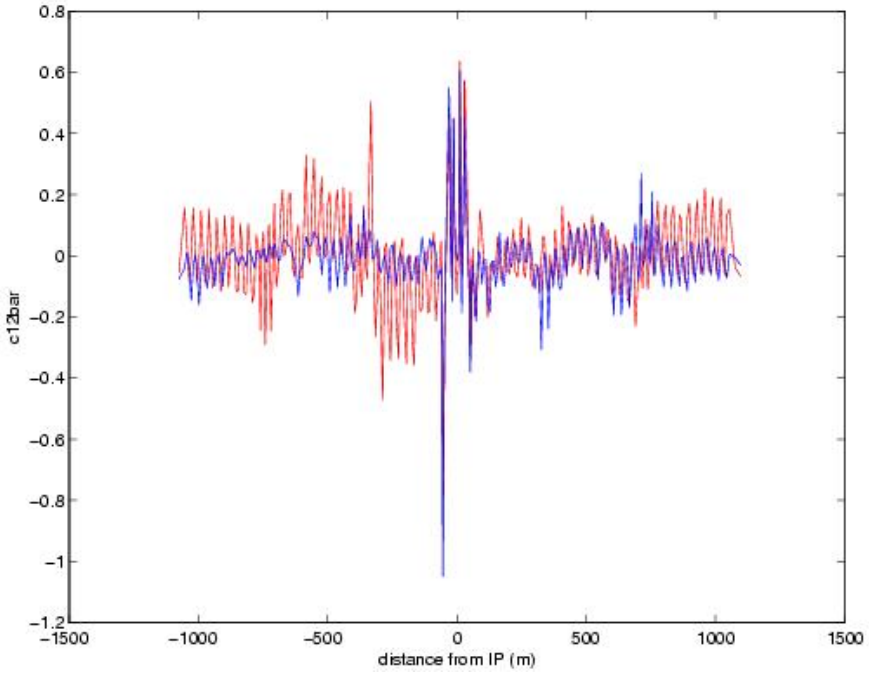

Figure 5: The coupling, as a function of distance from the Interaction Point, of the original virtual machine (red) and our chosen solution (blue). This predicts that coupling will improve with our solution, as the goal is for coupling to be smaller in magnitude.

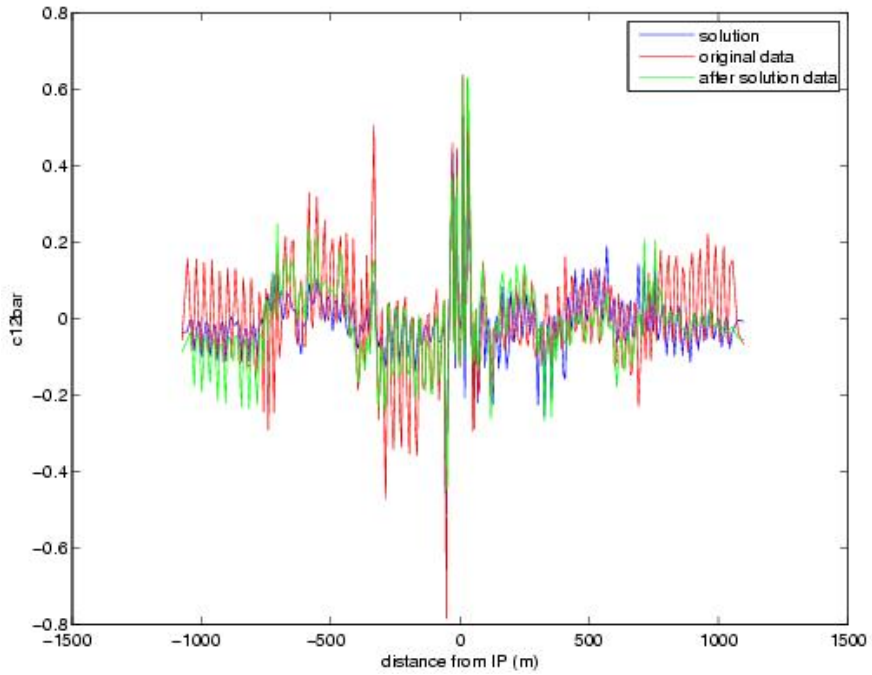

Figure 6: The coupling, as a function of distance from the IP, of the original virtual machine (red), as predicted for our solution (blue), and the machine after we implemented our solution (green). This shows that we succeeded in improving coupling, though we were not completely successful in some areas.

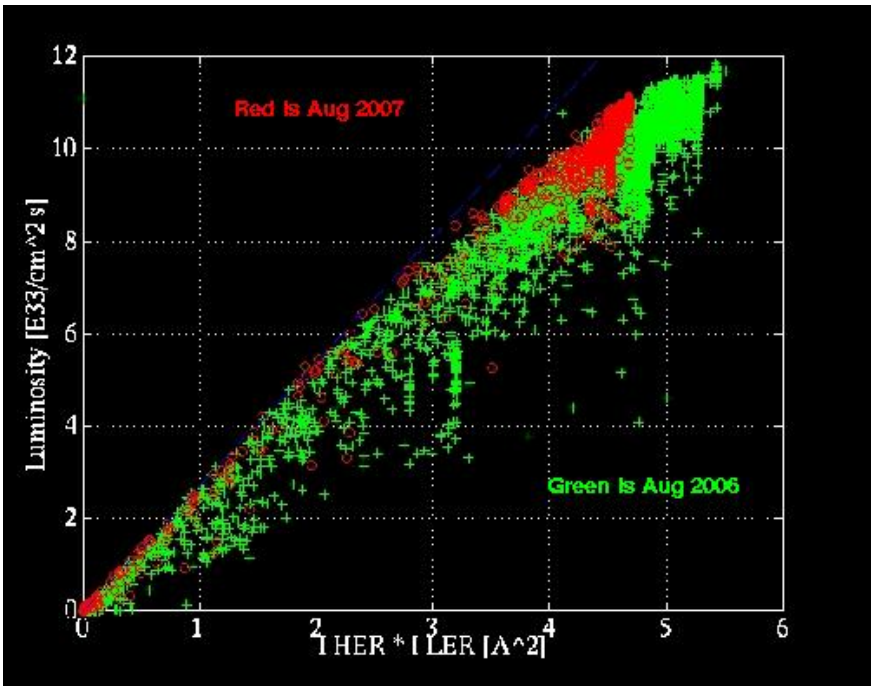

Figure 7: The Luminosity as a function of current. In red is the luminosity after our solution was applied. This shows a new record peak specific luminosity.

SLAC-TN-07-014
August 2007

ILC Electron Source Injector Simulations

Manu Lakshmanan
Office of Science, Science Undergraduate Laboratory Internship Program

Cornell University

Stanford Linear Accelerator Center
Menlo Park, CA

August 24, 2007

Prepared in partial fulfillment of the requirement of the Office of Science, Department of Energy's Science Undergraduate Laboratory Internship under the direction of Axel Brachmann in the Accelerator Department at the Stanford Linear Accelerator Center.

Participant: _____
Signature

Research Advisor: _____
Signature

Work supported in part by US Department of Energy contract DE-AC02-76SF00515

ILC Electron Source Injector Simulations

MANU LAKSHMANAN, AXEL BRACHMANN

ABSTRACT

As part of the global project aimed at proposing an efficient design for the ILC (International Linear Collider), we simulated possible setups for the electron source injector, which will provide insight into how the electron injector for the ILC should be designed in order to efficiently accelerate the electron beams through the bunching system. This study uses three types of software: E-Gun to simulate electron beam emission, Superfish to calculate solenoidal magnetic fields, and GPT (General Particle Tracer) to trace charged particles after emission through magnetic fields and subharmonic bunchers. We performed simulations of the electron source injector using various electron gun bias voltages (140kV – 200kV), emitted beam lengths (500ps – 1ns) and radii (7mm – 10mm), and electromagnetic field strengths of the first subharmonic buncher (5 – 20 MV/m). The results of the simulations show that for the current setup of the ILC, a modest electron gun bias voltage (~140kV) is sufficient to achieve the required bunching of the beam in the injector. Extensive simulations of parameters also involving the second subharmonic buncher should be performed in order to gain more insight into possible efficient designs for the ILC electron source injector.

Introduction

The International Linear Collider (ILC) is a proposed electron-positron collider planned to be built in the near future in hope that the data resulting from it will give insight into the physics of dark matter and dark energy. The global ILC collaboration

aims to improve the accelerator design for high efficiency. We study the design of the electron source injector, which produces, focuses and bunches the beam before it is injected into the damping ring and travels down the accelerator. The design of the injector is crucial for electron beams because it is much more effective to modify the distribution of particles in a beam before it reaches relativistic speeds, which for an electron beam happens almost immediately once in the accelerator. The electron beam is produced in the source injector by a photocathode electron DC gun which initially accelerates the electrons using a cathode voltage bias to the anode. After initial acceleration, charged particle beams are modified by space charge, the effect of the repulsive Coulomb force interactions among the particles within the beam that causes it to grow in cross section and length at a rapid rate [1]. Therefore, the beam is kept focused using a solenoidal field and longitudinally compressed or bunched using subharmonic bunchers (SHB). A SHB bunches the electron beam by applying an electromagnetic field that oscillates in time to modulate the velocities of the particles along the beam length.

The current design of the ILC electron source injector consists of a photocathode electron gun, a solenoidal magnetic field, and two SHB. The photocathode electron gun that will be used for the ILC is based on the design of the gun used for the SLC (Stanford Linear Collider), will have a bias voltage of 140 to 160 kV, and will be optimized to provide a space charge limited current, described by Child's Law:

$$I = K\sqrt{V^3} \tag{1}$$

where I is emitted current, K is the perveance, a physical parameter that depends on the geometry of the photocathode, and V the photocathode bias voltage. Because the desired

electron bunch charge is 3.2 nC at the collision point, the photocathode will emit an electron beam with charge 4.5 - 5nC to account for particle loss before collision. In the current design, the beam will be emitted as a 1 ns pulse, so the photocathode gun must produce a current of 4.5 – 5 A (or 4.5 – 5 nC/ns). The electron beam is focused in the injector using a solenoidal field. To compress or bunch the beam after emission, two SHB are placed just after photocathode gun, operating at frequencies of 216.7 MHz and 433.3 MHz respectively [2]. At SLAC, ILC injector simulations have been conducted using a 120-kV gun and a previous ILC model that consisted of two SHB at 108 MHz and 433.3 MHz respectively [4, 5]. The new setup with the first subharmonic buncher (SHB-I) operating at 216.7 MHz and possibly higher voltage electron guns need to be investigated.

In this work, we study a variety of electron gun and initial beam parameters, and buncher operating conditions that can be incorporated into the ILC electron source injector design described above. The injector design can only be optimized under the physical limitations of equipment available for the ILC by finding efficient combinations of the many parameters. Optimum bunching of an electron beam occurs for beams whose time length fits into the quarter period of the SHB. Therefore, the length of the beam when it reaches the first buncher should fit into the quarter period of the first buncher and the first buncher should compress the beam down to length that should just fit into the quarter period of second subharmonic buncher (SHB-II). We calculate this desired bunch length in the following way where ν_1 =216.7 MHz and ν_2 =433.3MHz are the frequencies of the two SHB, T_1 and T_2 their periods, and $tlen_1$ and $tlen_2$ the desired bunch lengths respectively.

$$T_i = \frac{1}{\nu_i} \tag{2}$$

$$tlen_i = \frac{1}{4} T_i = \frac{1}{4\nu_i} \tag{3}$$

Consequently, $tlen_1$=1.15 ns and $tlen_2$=577 ps. As a result, efficient bunching occurs for an electron beam that is 1.15 ns long when it reaches SHB-I and 577 ps when it reaches SHB-II. For the case of the ILC accelerator which has a driving frequency of 1.3 GHz, the efficient bunch length is 200 ps. This efficient bunch length for the accelerator means that the electron beam should be compressed by SHB-II down to 200 ps just before it is injected into the damping ring on its way to the accelerator.

After acquiring and analyzing the data of the electron beam in the various injector setups, we can draw conclusions about how the electron injector setup can be designed for the ILC for operational and cost efficiency.

Materials and Methods

The simulations of the ILC electron source were performed using three types of software: E-Gun [5], Superfish, and General Particle Tracer (GPT). E-Gun was used to simulate the electron beam as it is emitted by the electron gun, Superfish to calculate the magnetic fields resulting from different arrangements of electromagnets, and GPT to trace the particles in the beam after it is emitted from the electron gun. We performed simulations of the electron source injector using a range of electron gun bias voltages (140kV – 200kV), emitted beam lengths (500ps – 1ns) and radii (7mm – 10mm), and electromagnetic field strengths of the first subharmonic buncher (5 – 20 MV/m).

E-Gun

In E-Gun, a photocathode gun, as shown in Fig. 1, was specified by its bias

voltage *V*, the radius of the electron emitting area r_k and the perveance *K*, a physical quantity that depends on the geometry of the photocathode.

The three variables of interest defined in E-Gun were r_k, *V*, and the initial time pulse length of the electron beam Δt. The radius of the electron emitting area and the bias voltage can be input directly into the program, but the beam peak current is defined by the perveance (*K*). The reason for this is clear from the relationship between these parameters. Using eqn. 6 and the definition of current ($I \equiv \frac{dq}{dt}$):

$$I = K\sqrt{V^3} = \frac{Q}{\Delta t} \tag{7}$$

Rearranging eqn 7 gives:

$$\Delta t\sqrt{V^3} = \frac{Q}{K} \tag{8}$$

where *Q* is the current of the electron beam emitted by the gun over the time Δt. Taking into account that $Q=5nC$, eqn. 8 becomes:

$$\Delta t\sqrt{V^3} = \frac{5nC}{K} \tag{9}$$

where eqn. 9 now expresses the two variables of interest, Δt and *V*, as a function of the perveance *K*. Therefore, for a desired given input *V*, *K* was chosen to correspond to the desired Δt to be tested.

After calculating the emitted current using Child's Law and tracing the particles to the end of the gun, E-Gun presents information broken down to the individual rays making up the beam, each representing a macro particle of electrons. The number of rays used must be input. Because of space charge, the electron beam cannot be represented as a single body, but instead as several particles that act upon each other as the beam moves.

Therefore, the greater the number of rays used to represent the beam, the more realistic the problem and the more accurate the results. However, with a greater number of rays to account for, the required computation time increases. For each ray, the program presents the ray position, kinetic energy, current, and divergence angle for the beam at the end of the gun. The software gives the ray positions in the two dimensional r-z plane, where *z* is the direction of the current, orthogonal to the surface of the photocathode, and *r* the radial distance from the z-axis. Presenting position in 2-D is sufficient because the photocathode is cylindrically symmetric and consequently the emitted electron beam is also cylindrically symmetric. Another output value of interest from the program is the emittance of the beam at the end of the gun. The information about the rays at the end of the gun from E-Gun was then used to define the initial conditions of the particles in GPT. The position and kinetic energy coordinates for each ray must be transformed and input into GPT as phase space Cartesian coordinates $(x, y, z, \gamma\beta_x, \gamma\beta_y, \gamma\beta_z)$, where the product $\gamma\beta$ of the Lorentz factor γ and the relativistic β is known as the particle normalized momentum. Because the electron beam is cylindrically symmetric, an array of random azimuthal angles φ could be used to transform the *r* coordinates of the rays in E-Gun to (x,y) coordinates for use in GPT. The *r* and *z*-components of the particle normalized momentum $\gamma\beta_r$ and $\gamma\beta_z$ respectively for each ray was calculated from the kinetic energy *T* and divergence angle θ provided by E-Gun. Then the coordinates $\gamma\beta_x$ and $\gamma\beta_y$ were transformed from $\gamma\beta_r$ and φ using the following procedure:

$$\gamma = 1 + \frac{T}{m_e c^2} \tag{11}$$

$$\beta = \sqrt{1 - \frac{1}{\gamma^2}} \tag{12}$$

$$\gamma\beta_z = \gamma\beta\cos\theta \tag{13}$$

$$\gamma\beta_r = \gamma\beta\sin\theta \tag{14}$$

$$\gamma\beta_x = \gamma\beta_r\cos\varphi \tag{15}$$

$$\gamma\beta_y = \gamma\beta_r\sin\varphi \tag{16}$$

where m_e is the electron rest mass and *c* the speed of light. The last array of data needed for the initial conditions of the rays in GPT is the number of electrons that each ray represents *N*. The number of electrons N_j for a ray *j* is:

$$N_j = \frac{\Delta I_j}{I} \tag{17}$$

where ΔI_j is the amount of current of ray *j* and *I* is the total current of the electron beam.

Superfish

Different arrangements of solenoids, reflectors, Helmholtz coils were input into Superfish to calculate the resulting magnetic fields. We set the current in the coils of the electromagnets, the dimensions of the components, and the permittivity and permeability of the reflector material. Since the components are cylindrically symmetric about the beam, the program displays them in the r-z plane. The two data arrays taken from Superfish and imported into GPT describe the z-component of the magnetic field as a function of position along the accelerator $B_z(z)$. The arrangement of components in Superfish that we chose to use was one that resulted in the most symmetric, constant function for $B_z(z)$.

GPT

The electric fields due to the subharmonic bunchers were defined in GPT and were of the form:

$$E_z(r,z) = E_z(z)\cos(\omega t + \phi) \tag{18}$$

where $E_z(z)$ is the function representing the *z* component of the electric field as it varies in space within the bunching cavity, ω the angular frequency of the SHB, *t* the time variable, and ϕ the phase shift. The electric field in space $E_z(z)$, takes the shape of a Gaussian function with its peak at the location of the SHB, z=1.5m:

$$E_z(z) = E_0 e^{-\pi(z-1.5)^2} \tag{19}$$

where E_0 is a constant in place for the amplitude. GPT then simulates the electron beam imported from E-Gun in time by tracing the individual rays subject to space charge, external and self-induced magnetic and electric fields. The program then presents the beam trajectory in the r-z plane. One example of a beam trajectory at all times is shown in Fig. 2. From the trajectory, the program calculates the beam emittance, length, radius, and particle loss in time. A particle was considered lost if its *r* or *z* coordinate had a difference of more than three standard deviations from the average coordinates of the beam.

Data Analysis

The initial time pulse length of the electron beam Δt, the radius of the electron emitting area r_k and bias voltage *V* of the photocathode, the solenoidal field, and the phase shift ϕ and amplitude E_0 of the RF cavities were all varied in order to determine the behavior of the electron beam for different electron injector setups.

Using our data of resulting electron bunch length as a function of SHB-I electromagnetic field strength, we calculate the electromagnetic field strength of SHB-I needed to compress the bunch down to 577ps. This calculation was performed for beams of radius $r_k = 10mm$ at the photocathode.

Results and Discussion

The arrangement of the solenoids used to contain the beam and the corresponding magnetic filed is shown in Fig. 3 and 4, respectively. The required electromagnetic fields strengths for SHB-I needed in order to result in a 577 ps bunch length for the different sets of parameters are shown in Table 1.

Our results show that the beam will not grow longitudinally due to space charge beyond the quarter wave length of SHB I for all investigated initial pulse lengths and gun bias voltage cases. Moreover, a gun bias voltages of 140 kV is sufficient; thereby reducing the cost and risk associated with the gun. On the other hand, by using very high power electron gun (200 kV) and high electromagnetic field for SHB-I (15 MV/m), the need for SHB-II can be eliminated as SHB-I would be sufficient to compress the beam bunch length to 200 ps as demonstrated in one case of our simulations in which the electron gun and SHB-I compressed a 890 ps beam at the electron gun into a 222 ps long one.

Future work would involve including SHB-II in the simulations, further optimization of solenoidal fields, changing the z-location of SHB-I, and investigation of the possibility of using only one SHB in the injector. The electron source injector is crucial to the quality of the beam as it travels down the accelerator and collides at the

detector. An optimized electron injector design is of particular interest to the ILC as it is the source of all beams (including the positron beam) used throughout the injector.

Acknowledgements

I would like to thank the Department of Energy, Office of Science and the Stanford Linear Accelerator Center for making this research possible through the SULI program. I would especially like to thank Dr. Axel Brachmann for his time and patience in guiding me with this project.

References

[1] ILC Reference Design Report 2007. February 2007.

[2] S. Humphries Jr, Charged Particle Beams. New York: John Wiley and Sons, Inc., 1990.

[3] A.W. Chao and M. Tigner, Handbook of Accelerator Physics and Engineering. . Singapore: World Scientific Publishing Co., 1999.

[4] C. B. Haakonsen, A. Brachmann, "Simulations of the ILC Electron Gun and Electron Bunching System." SLAC-TN-06-027, August 2006.

[5] F. Zhou, *et al*., "Design of a High-Current Injector and Transport Optics for the ILC Electron Source." SLAC-PUB-12587, June 2007.

[6] W.B. Herrmannsfeldt, Egun – an Electron Optics and Gun Design Program. Stanford Linear Accelerator Center, Stanford University, Stanford, CA. SLAC – 331, Oct.

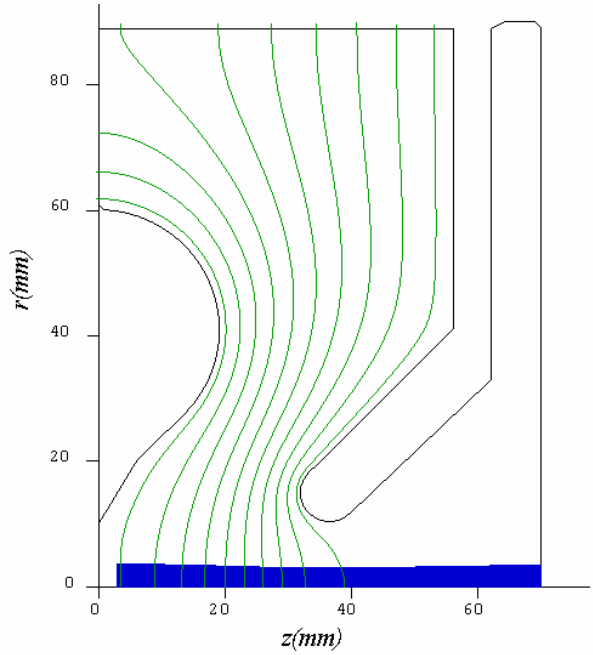

Figure 1. Electron gun in the r-z plane that was used to simulate emission of electron beam.

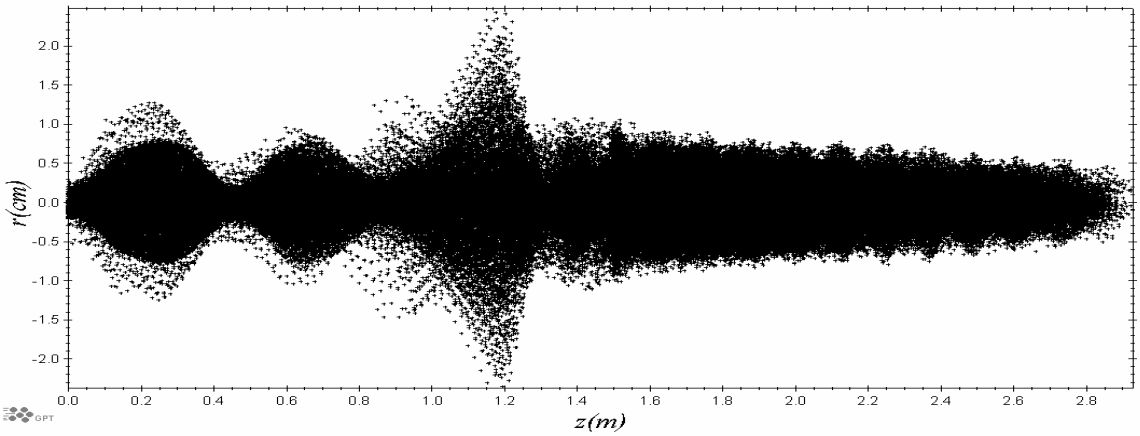

Figure 2. Example trajectory from GPT of electron beam taken at all times in the r-z plane.

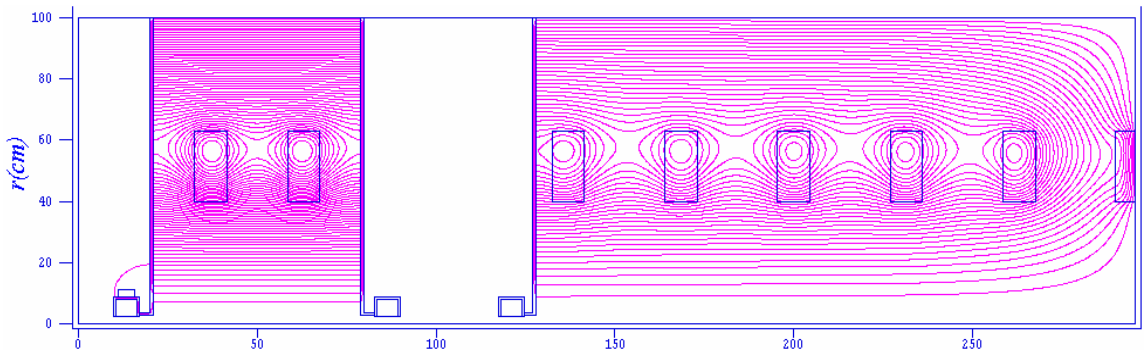

Figure 3. Arrangement of solenoids and reflectors in the r-z plane used in our injector setup to produce the magnetic field to focus the beam.

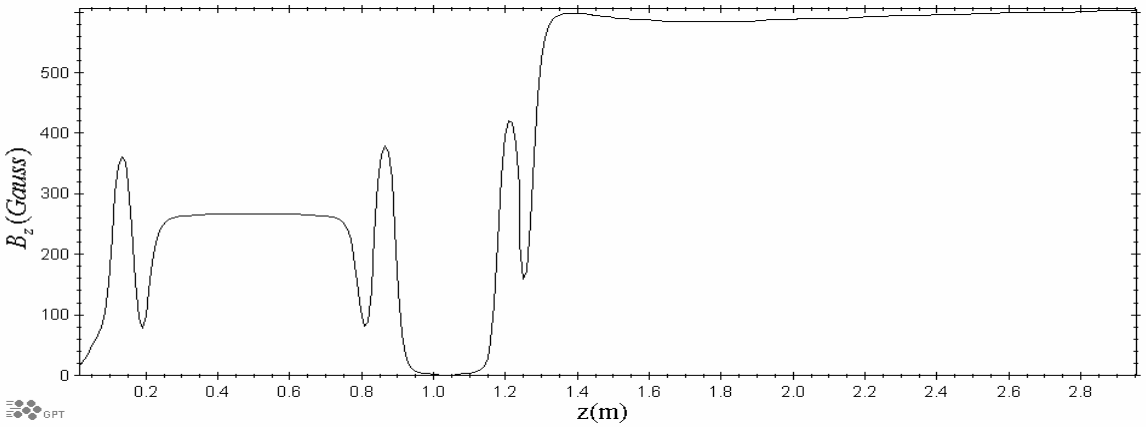

Figure 4. The magnetic field due to the arrangement of solenoids and reflectors shown in Fig. 3.

Initial time pulse length, $\Delta t(ps)$	Electron Gun Bias Voltage, $V(kV)$				
		140	**160**	**180**	**200**
	500	7.58	6.92	8.03	11.12
	630	7.46	8.19	8.36	12.06
	760	7.66	6.48	7.59	7.81
	890	7.20	9.28	7.03	8.69
	1020	5.64	6.04	6.83	8.17

Table 1. SHB-I field strength $E_z(MV/m)$ needed to compress bunch to 577 ps.

SLAC-TN-07-018

Building X-ray Diffraction Calibration Software

Joshua Lande

Office of Science, Science Undergraduate Laboratory Internship (SULI)

Marlboro College

Stanford Linear Accelerator Center

Stanford, CA

August 24, 2007

Prepared in partial fulfillment of the requirements of the Office of Science, Department of Energy's Science Undergraduate Laboratory Internship under the direction of Dr. Samuel Webb at the Stanford Synchrotron Radiation Laboratory at the Stanford Linear Accelerator Center.

Participant: _____

Signature

Research Advisor: _____

Signature

Work supported in part by US Department of Energy contract DE-AC02-76SF00515

TABLE OF CONTENTS

ABSTRACT

Building X-ray Diffraction Calibration Software. JOSHUA LANDE (Marlboro College, Marlboro, VT 05344) DR. SAMUEL WEBB (Stanford Synchrotron Radiation Laboratory at the Stanford Linear Accelerator Center, Stanford, CA 94025)

X-ray diffraction is a technique used to analyze the structure of crystals. It records the interference pattern created when x-rays travel through a crystal. Three dimensional structure can be inferred from these two dimensional diffraction patterns. Before the patterns can be analyzed, diffraction data must be precisely calibrated. Calibration is used to determine the experimental parameters of the particular experiment. This is done by fitting the experimental parameters to the diffraction pattern of a well understood crystal. Fit2D is a software package commonly used to do this calibration but it leaves much to be desired. In particular, it does not give very much control over the calibration of the data, requires a significant amount of manual input, does not allow for the calibration of highly tilted geometries, does not properly explain the assumptions that it is making, and cannot be modified. We build code to do this calibration while at the same time overcoming the limitations of Fit2D. This paper describes the development of the calibration software and the assumptions that are made in doing the calibration.

INTRODUCTION

A particularly good method for probing the structure of crystals is x-ray diffraction–the process where x-rays interact with a particular crystal of interest. Because x-rays have wave-like properties, they scatter, or diffract, as they interact with atoms. The x-rays leaving each atom in a crystal interfere constructively or deconstructively as a function of angle. Because crystals have very regular structure, the interference minima and maxima are very regular. These diffraction patterns are measured with a detector. By looking at them, we infer general properties of a diffracted crystal such as the distance between atomic bonds.

X-rays preferentially diffract at certain angles. Because diffraction experiments image many small crystals at different orientations, diffraction patterns have a radial symmetry about the incoming beam. If the beam diffracts preferentially at a particular angle in one direction normal to the incoming beam, it will also diffract at that same angle for any other direction normal to the beam. Because of this symmetry, cones of x-rays emanate from the sample. When we detect this pattern, we measure intensity with a flat detector. When the cone of x-rays intersect the plane of this detector, we detect conic sections of high intensity. When the detector is perpendicular to the incoming rays, we see circles of high intensity. When the detector is tilted slightly, we see ellipses of high intensity. With more extreme tilts, we can see parabolas and hyperbolas. A particular diffraction pattern is shown in figure 1.

Previous literature has determined a set of geometric transformations for dealing with experimental data taken with a detector at an arbitrary angle to the x-rays[1]. This theory is useful because it allows us to infer from these images physically meaningful properties of the sample.

By measuring the parameters of an x-ray diffraction experiment, such as the particular tilt, we can use these transformations to calculate the properties of the crystal that we are interested in. But often, the reverse of this process is desired. We often do not precisely know the parameters of a diffraction experiment. This happens because it is difficult to accurately

measure these parameters. A process of calibration can be used to precisely determine the experimental parameters. We first diffract a well understood sample. We then fit the experimental parameters to the diffraction pattern to figure out the precise experimental arrangement that was used. This process is done to calibrate other diffraction data. We first image a known crystal and use it to determine these experimental parameters. We then use the inferred experimental parameters to the analyze diffraction data that we are interested in.

This process of calibration must be done before any sample is analyzed. Fit2D is a program which is commonly used to do this sort of calibration. It has many limitations. In particular, the software's curve fitting algorithm requires a lot of time for manual entry. Furthermore, it gives very little control over how the fitting is done. In particular, it cannot ignore overlapping diffraction rings. It can't account for highly tilted geometries. Also, Fit2D is a black box. We don't know what assumptions it is using to do the calibration, we don't know what type of calculations it is doing, and we cannot modify it. Because of these issues, we built a program to properly calibrating these diffraction images. Our new software is particularly useful because it can overcome the limitations of Fit2D and allow for better and more reliable calibration.

THEORY

Figure 2 shows the general setup of a diffraction experiment. Here, x-rays enter the sample from the left and diffract with various angles. Quantum theory predicts that most of the intensity of the outgoing beam would be found in discrete cones of light.[2] One particular cone is shown in the diagram. It is clear from the diagram that if the detector is perpendicular to the incoming x-ray source, then the detector will record a series of rings. The detector in a diffraction experiment is often placed at an angle to the incoming beam. This is sometimes caused by experimental error and is sometimes done deliberately to record diffraction

patterns at higher scattering angles. Figure 3 shows geometrically how this works.

Previous literature has derived geometric transforms to deal with this complication[1]. I will summarize and then use their results.[1] The wavelength is denoted by λ. Suppose that our detector is at an angle to the incoming beam. We can characterize any tilting of the detector as two orthogonal rotations. We will call the rotation along the x axis α and the rotation along the y axis β. Figure 4 and 5 illustrate these rotations.

Our detector is made up of many pixels. Each pixel is addressed by a unique pair of coordinates. We will call the pixel location of some point of interest on the detector (x_d, y_d). We will call the pixel location where the x-rays would hit if they went straight through the sample as (x_c, y_c). The distance between the sample and this center is d. Figure 6 illustrates the situation. We will call the pixel scale of the image ps. This is the distance between each pixel (e.g. 1000 mm / pixel). Finally, we will call (x'',y'') the distance from the center of the image to our point of interest. It is easy to convert from pixel values to distances using the formula

$$x'' = (x_d - x_c) \times ps \qquad\qquad y'' = (y_d - y_c) \times ps. \tag{1}$$

(x'',y'') are easy to measure but do not directly tell us anything that is physically meaningful. We must use a transformation to get at physically meaningful quantities.

We can imagine another detector set up the same distance away from the detector. This new detector is perpendicular to the incoming beam as is shown in figure 7. We are interested in where the same x-rays that were detected at (x'',y'') would have been detected on this imaginary detector. We will call this new point (x,y).

[1]Note that I will stray from convention by labeling what literature calls γ by α. This is done to keep a more consistent notation.

The transform that we are interested in is taken from [1]:

$$x = \frac{dx'' \cos(\beta)}{d + y'' \sin(\alpha) + x'' \sin(\beta)} \qquad y = \frac{dy'' \cos(\alpha)}{d + y'' \sin(\alpha) + x'' \sin(\beta)}. \tag{2}$$

We can invert these formula:

$$x'' = \frac{yd}{d\cos(\beta) - x\sin(\beta) - y\cos(\beta)\tan(\alpha)} \quad y'' = \frac{xd\cos(\beta)/\cos(\alpha)}{d\cos(\beta) - x\sin(\beta) - y\cos(\beta)\tan(\alpha)}. \tag{3}$$

Physicists are interested angles instead of distances because they do not depend on detector placement. First, we define 2θ. It is the angle of scattering of the incoming beam. Refer to Figure 8. We define it as follows:

$$\tan(2\theta) = \frac{r}{d} \text{ with } r^2 = x^2 + y^2. \tag{4}$$

Physicists mainly care about the quantity Q and χ:

$$Q = \frac{4\pi \sin(2\theta/2)}{\lambda} \qquad \tan(\chi) = \frac{y}{x}. \tag{5}$$

χ is the azimuthal angle around the incoming beam. Q is particularly interesting because it is proportional to the change in momentum of the photons that arrive at the detector. Both theory and experiment have shown that the Q values for diffraction peaks are a material constant.

Suppose that we now consider a pixel value (x_d,y_d), we can use equation 1 to convert it to (x'',y''). We can use equation 2 to calculate (x,y) and then equation 5 to calculate Q and χ. There are 7 parameters used in this transformation. The pixel scale is fixed by the detector but the other six parameters are free to vary from experiment to experiment. The free parameters are x_c, y_c, α, β, d, and λ. They characterize a particular diffraction

experiment. A common procedure when analyzing diffraction data is to take a diffraction pattern and calculate the Q values for each ring. Once the experimental parameters are known, these formulas give a straightforward way to do the calculations.

HANDLING DIFFRACTION DATA

Our calibration program is written in Python, which is particularly adept for building scientific applications. It is a high level languages which makes it robust, flexible, and easy to write. Python has many packages for handling scientific data. These packages allow for fast array operations and include powerful mathematical functions. It also has a powerful library for creating platform independent GUIs. Furthermore, Python acts as a powerful glue language which can interface well with code written in many other languages. This turned out to be very useful. The only practical drawback to Python is performance. It tends to run slower then other programming languages. We decided that our program would have an acceptable performance and we used several strategies to speed up our program.

In order to calibrate diffraction data, we first had to read the data into our program. The diffraction experiment at Stanford Linear Accelerator Center captures diffraction images using the Mar345 Image Plate Detector System. The Mar345 detector generates .mar3450 data files. A Mar diffraction file is made up of three sections as is specified by [3]. The first section is the header. It is a set of two column ascii. The header contains general information about the image, e.g. the *ps* value, the time that the experiment ran for, an estimate for the wavelength of the incoming x-rays, the pixel center of the image and the distance from the detector. The second section is a list of intensity values that were too high to store inside of the data array. This data is stored as uncompressed packed binary. The image itself is finally stored as compressed packed binary. The data is compressed using the lossless "pck" compression algorithm developed by Jan P. Abrahams. The algorithm was developed specifically to compress x-ray diffraction data. It is particularly efficient because

it exploits radial symmetry in the images. It achieves close to 70 percent compression. Code to decompress this format can be found at [4]. As far as I can tell, this is the only implementation of the decompression algorithm that has been written. It is written in the C programming language. To use the algorithm, we wrote a Python wrapper around the C code. Wrapping the C code was decidedly non-trivial but proved to be an elegant solution.

THE CALIBRATION ALGORITHM

Calibration is used to precisely determine the experimental parameters (x_c, y_c, d, λ, α, and β) of a particular diffraction experiment. These parameters can then be used to accurately and precisely analyze other diffraction data. It is easiest to first imagine an experiment where one already knows precisely the experimental parameters. If you collected a diffraction pattern, you can calculate Q and χ for any of the rings. We can do this procedure in reverse. Many crystals have well measured Q values. So, for any set of experimental parameters, we can use equations 1, 3, and 5 to calculate exactly what should show up on the detector. It should be easy to compute this with what is actually recorded. To calibrate an image, we vary the experimental parameters until the output image closely resembles the expected image. Calibration is a large fitting procedure. We fit the experimental parameters to the observed data. Presumably, the experimental parameters that fit best the observed data are the real experimental parameters.

The whola point of this process is to image a standard crystal before imaging important samples. The standard crystal gives you enough information to figure out how the experiment is set up. We can then use this information to precisely and accurately analize the rest of the data.

My calibration algorithm works as follows. It begins by finding a list of peaks around the image of maximum intensity (corresponding to the peaks on the diffraction rings). To get this list of peaks, the code needs a decent initial guess at what the experimental parameters

should be. It also needs a list of the true Q value for the image. Furthermore, it requires a ranges dQ for all the Q values. These ranges do not tell where the true Q should be, but instead where in the image to look for the Q values. The program makes the assumption that when the the initial guess is good enough the Q ranges will entirely contain the acutal peak while at the same time not contaning any other peaks. With this assumption, the code picks a large number of χ values. For each χ slice and for each Q value, the code moves along the straight line from $Q - dQ$ to $Q + dQ$ and records all of the intensity values along the way. It uses a linear interpolation to get intensity values between real pixels. After it has recored all the intensity values, it fits a Gaussian curve to the peak. The center of the Gaussian becomes the Q value at the peak. The code converts this Q and χ pair into pixel values to generate a list of all of the pixel values where there were peaks. Figure 9 gives a general sense of how this works.

Once the code has calculated the peak list, it then defines a goodness of fit function as follows. For any set of experimental parameters, it takes the entire peak list and converts that list into Q_{fit} and χ_{fit} values. The particular Q and χ values will depend upon the experimental parameters. We know the true Q value for the peak also since that was one of the user inputs. Presumably, once we picked the true experimental parameters, these Q values should be exactly the same. We can quantify how close these experimental parameters are to the true values as follows:

$$\text{Residual}(x_c,y_c,d,\lambda,\alpha,\beta) = \sum_{All\ \ pairs} (Q_{fit} - Q_{real})^2. \tag{6}$$

The closer the experimental parameters are to the true parameters, the lower a residual. Ideally, the residual should be 0 for a perfect fit. I had my code numerically minimized this function of 6 variables. To do so, I used an existing non-linear minimization package called levmar[5]. levmar performs the Levenberg-Marquardt least-squares minimization procedure to minimize an arbitrary function of n dimensions. By minimizing the residual function, my

code will calibrate x-ray diffraction data.

FUTURE WORK

There is quite a bit of work to be done on this project. Ideally, this program could develop into a full fledged x-ray diffraction data reduction package. It could be able to handle all of the standard diffraction computations. In this respect, there are many fetures which can be added to the program. A more refined graphical user interface could then be developed to make the program easy to use.

ACKNOWLEDGMENTS

I would like to acknowledge the U. S. Department of Energy, Office of Science for creating, organizing, and funding the SULI program. I would like to thank the Stanford Linear Acceleartor Center for hosting me this summer. I would like to thank David Bronfenbrenner and Dr. Apurva Mehta for their suggestions, help, and support of my project. Most importantly, I would like to personally thank my mentor Dr. Samuel Webb. Sam's vision and insight propelled this project forward and and his guidance challenged me to excel in the research.

REFERENCES

[1] A. Kumar, "Analysis Strategy of Powder Diffraction Data with 2-D detector," Office of Science, SULI Program, Stanford Linear Accelerator Center, Menlo Park, CA, Tech. Rep., Dec. 2005.

[2] B. Warren, *X-Ray Diffraction*. New York: Dover Publications, Inc., 1990.

[3] *mar345_formats*, X-ray Research G.m.b.H. Std. 1, 1997. [Online]. Available: http://www.mar-usa.com/support/downloads/mar345_formats.pdf

[4] D. C. Klein. (1995, Oct.) pck.c. [Online]. Available: http://www.ccp4.ac.uk/ccp4bin/viewcvs/ccp4/lib/DiffractionImage/MAR/pck.c

[5] M. Lourakis. (2006, June) levmar: Levenberg-marquardt nonlinear least squares algorithms in c/c++. [Online]. Available: http://www.ics.forth.gr/~lourakis/levmar/

FIGURES AND TABLES

FIGURES

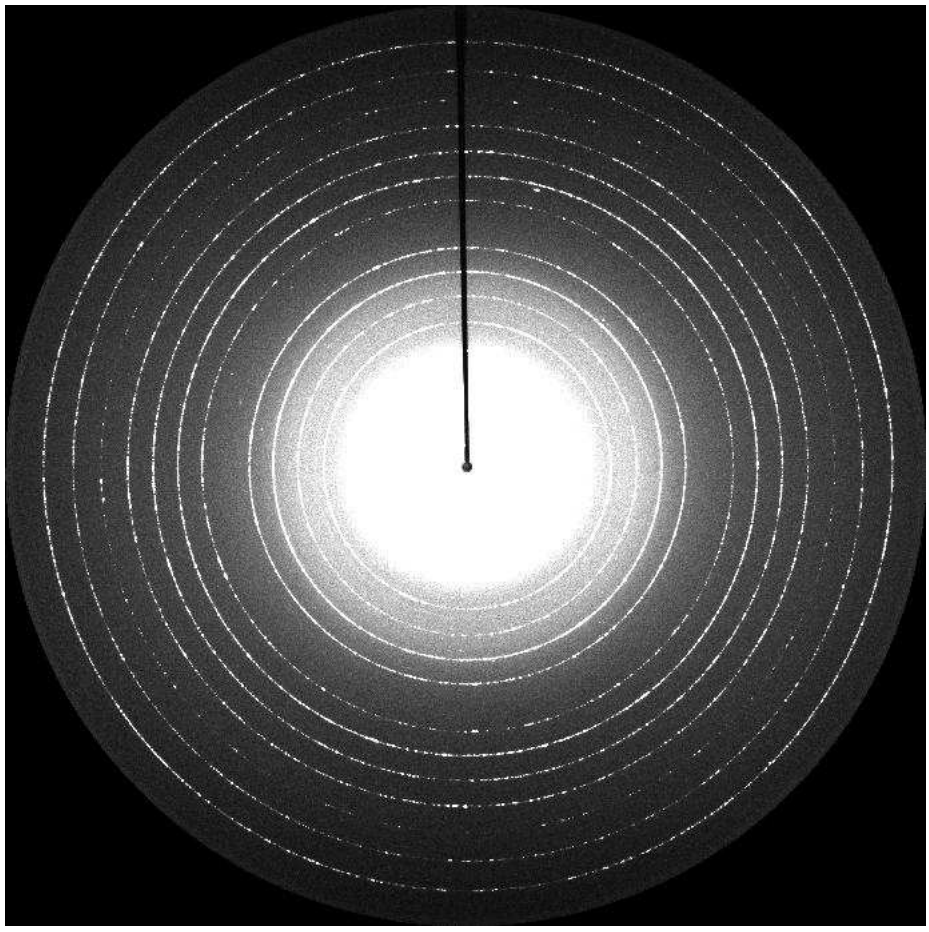

Figure 1: Here is a diffraction pattern of Lanthanum Hexaboride. it is commonly used to calibrate diffraction experiments. Notice the discrete diffraction rings.

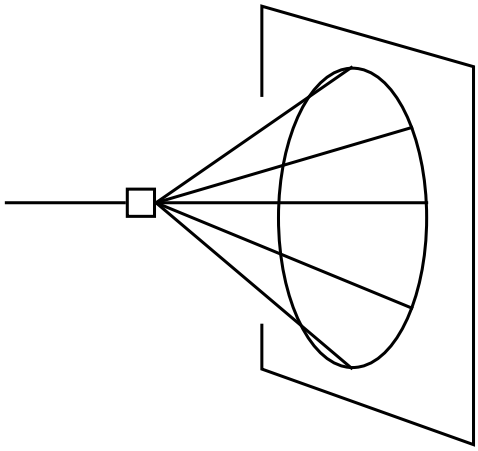

Figure 2: An X-Ray diffraction setup. X-rays scatter from a 3-D sample and are captured by a 2-D detector.

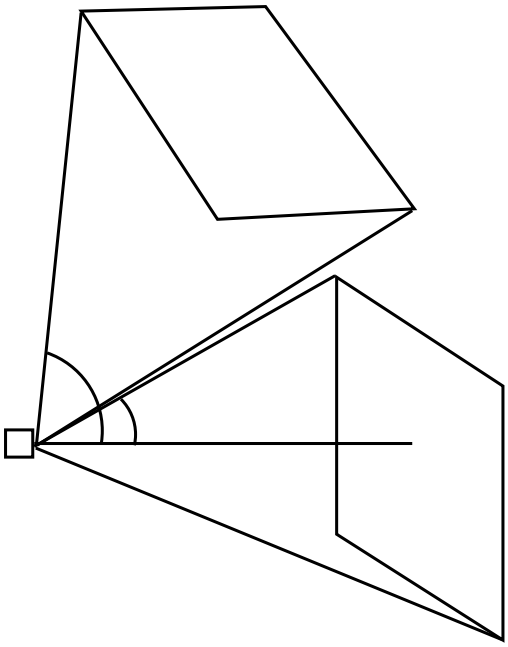

Figure 3: This diagram illustrates how tilted geometries allow for the collection of diffraction data at more extreme angles without the need for a larger detector.

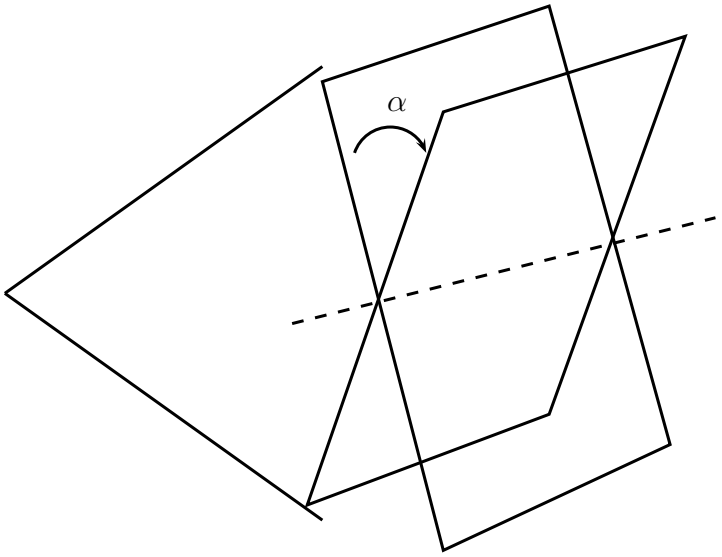

Figure 4: The rotation angle α.

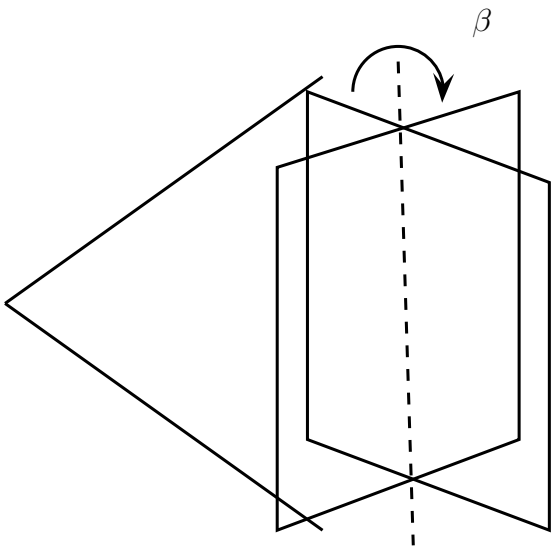

Figure 5: The rotation angle β. Any detector rotation can be characterized as a rotation by both α and β.

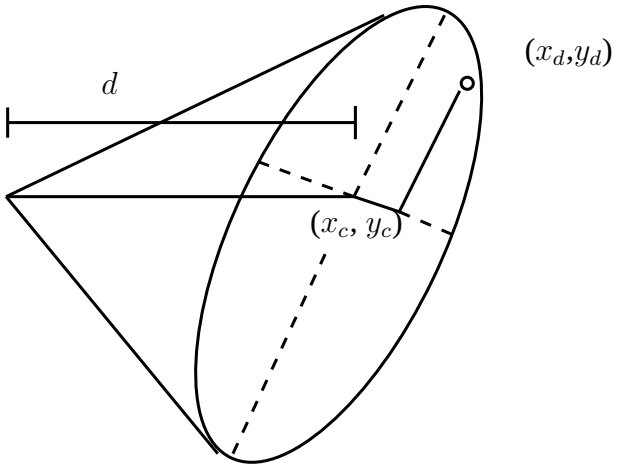

Figure 6: The setup of the experiment. Here, the detector is titled by an angle with respect to the experiment. The image that is recorded on the detector will therefore look distorted.

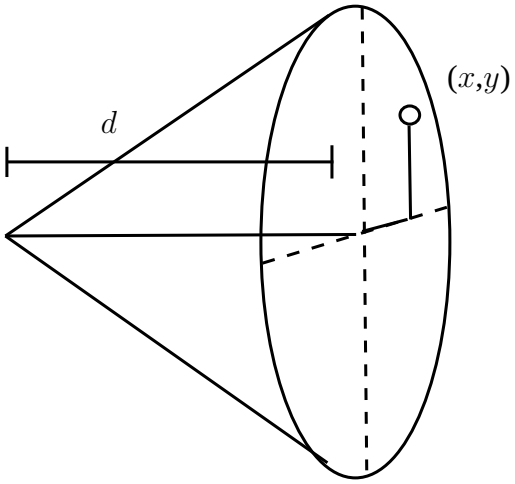

Figure 7: One can imagine another diffraction experiment where the detector is perpendicular to the experiment. (x,y) is the point that the x-ray that arrived at (x'',y'') would have landed at if it arrived at this detector instead.

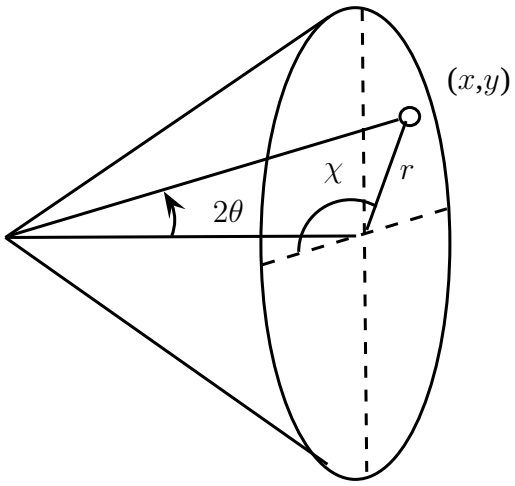

Figure 8: Above is the angle 2θ for a particular point (x,y). 2θ is the angle of scattering of the beam. χ is the azimuthal angle.

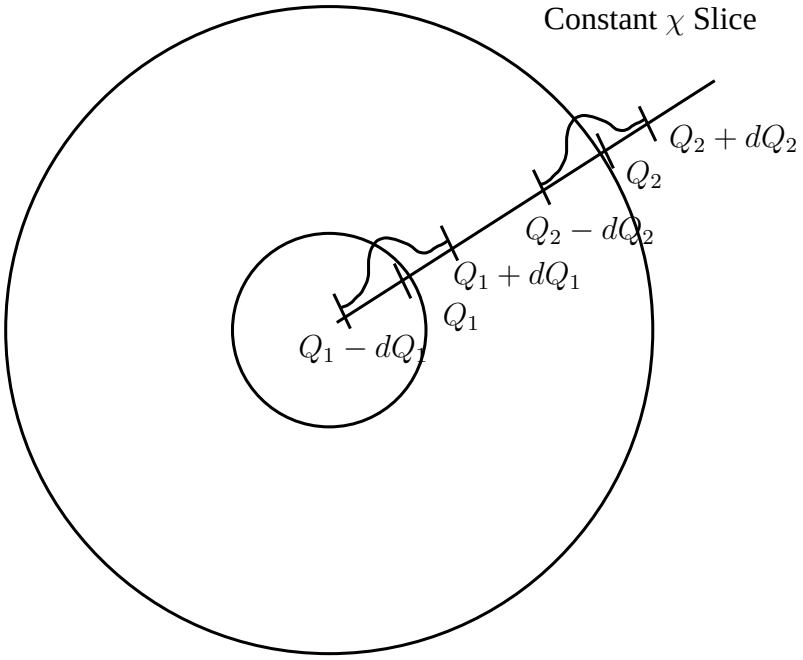

Figure 9: Here is a schematic diagram of the peak finding algorithm. For a particular χ slice, my code fits Gaussians along the line to find the peaks.

SLAC-TN-07-027

Bunch by Bunch Profiling with a Rotating X-Ray Mask

Christopher J. Lee

Office of Science, Science Undergraduate Laboratory Internship Program

University of California – San Diego

San Diego, California

Stanford Linear Accelerator Center

Stanford, California

August 22, 2007

Prepared in partial fulfillment of the requirement of the Office of Science, Department of Energy's Science Undergraduate Laboratory Internship under the direction of Dr. Alan Fisher in the Accelerator System Division of the Stanford Linear Accelerator Center.

Participant: _____

Signature

Research Advisor: _____

Signature

Work supported in part by US Department of Energy contract DE-AC02-76SF00515

Table of Contents

Abstract

Bunch by Bunch Profiling with a Rotating X-Ray Mask. CHRISTOPHER J. LEE (University of California – San Diego, San Diego, CA 92037) ALAN S. FISHER (Stanford Linear Accelerator Center, Stanford, CA 94025)

It is desirable to monitor the cross sections of each positron bunch in the Low Energy Ring (LER) storage rings of the Positron Electron Project II (PEP-II) located at the Stanford Linear Accelerator Center. One method is to pass the x-rays given off by each bunch through a scintillator, thereby studying a visible image. A rotating x-ray mask with three slots scans the beam image in three different orientations, allowing us to mechanically collect data to characterize and profile each image. Progress was made in designing the x-ray mask, researching and procuring parts, as well as advancing project plans. However, due to time constraints and difficulties in procuring special parts, the full system was not completed. A simpler setup was built to test the hardware as well as the feasibility of characterizing a circular image with a rotating mask. A blinking green light emitting diode (LED) simulated a single positron bunch stored in the LER ring. The selected hardware handled this simulation setup well and produced data that led to a reasonable estimation of the LED image diameter.

Bunch by Bunch Profiling with a Rotating X-Ray Mask

Introduction

High energy particles collide and obliterate each other at the Stanford Linear Accelerator Center (SLAC). Electrons and positrons accelerate down a two mile long linear accelerator to be stored inside two 2.2 km circumference rings of the Positron Electron Project (PEP-II). The low energy ring (LER) stores circulating positrons in more than 1700 distinct groups called 'bunches,' while the high energy ring (HER) stores electron bunches. Eventually, these two particle types collide at the interaction point (IP) within the BABAR detector. The more collisions there are in one pass, the more useful data SLAC scientists can work with. A key parameter determining the luminosity (collision rate) is the size of each beam at the IP, which in turn is related by the focusing magnets to the size elsewhere in the ring. Thus, it's of interest to somehow monitor the beam cross sections.

One way of doing this is by imaging the bunches. A charged particle moving near the speed of light radiates photons when an external force changes the trajectory. This synchrotron radiation is largely emitted as x-rays. And by passing the x-rays through a scintillator, a crystal that converts radiation to visible light, we can see the bunches. Currently the LER has a live feed x-ray pinhole camera, which monitors the *overall* cross sectional beam size; we cannot yet observe *each* bunch's size with this.

The goal is to determine individual bunch sizes. The difficulty lies in measuring 1700 bunches - with only 4.2 nanoseconds between each bunch. The nontrivial solution is to set up a camera to take a series of snapshots; however this requires putting a very costly camera, with an image intensifier and a high-speed electronic gate, into the damaging radiation environment of

the tunnel. Moreover, this camera can only take 2 images per second, requiring 14 minutes to measure all the bunches.

The proposed solution builds upon *measuring* projections of the beam image; *no* snapshots are taken. It turns out the particles distribute as a Gaussian, forming an elliptical beam cross section. Mathematically we represent an ellipse in three variables: semi-major and minor axes, and the angle of inclination. By determining these three unknowns, we can construct an accurate beam image and determine the size of the beam.

We solve for the three unknowns by measuring the projection of the beam intensity along three axes. The concept is to scan the beam cross section with a disc shaped x-ray mask that is opaque to the x-rays except for three narrow slots. As the disc rotates at 1 Hz, the slots sequentially approach the beam at different orientations. X-rays passing through each slot strike a fast scintillator, and the brightness of the resulting visible light is measured with a fast photomultiplier tube (PMT). While the bunches take 7.3 microseconds to run around the ring and return to the pinhole camera, the slots barely move in comparison. But the PMT produces a pulse for each bunch passing by. By digitizing and sorting these pulses, one gets a set of points for each bunch and for each slot. These points, the intensity as a function of slot position, are fitted to a Gaussian curve. Repeating this procedure gives three Gaussian equations, which solve for the three ellipse quantities.

During the course of the project, progress was made in designing this system, but there wasn't enough time to gather materials, build, and implement the final product. Instead, to test the project concept of profiling an image with a rotating mask, we built a similar and much simpler setup: A *two* slit wheel scanning the image of a blinking green light emitting diode (LED). The blinking simulated pulses from a single bunch passing by, allowing us to collect data

with an oscilloscope rather than the fast electronics required for sorting the actual beam's 1700 bunches.

Materials and Methods

The primary components of the final system are the photomultiplier tube, a scintillator, x-ray mask wheel, a motor, and an angular encoder. As for the simulation setup, the major components are a LED, an optical lens and a two slot mask wheel. Details and selection of these components are discussed below.

A. Photomultiplier Tube And Scintillator

There are only about 4.2 nanoseconds between consecutive bunches. To collect data within this tiny window, the scintillator's emission plus the PMT's response time must add to less than 4.2 ns. This demands a small and fast PMT, plus an unusually fast scintillator. The Hamamatsu R7400P is a suitable PMT with about a 1.5 ns rise time. As for a scintillator to convert the bunch peak's 7 keV x-rays to visible light we are investigating $LiBaF_3$ (0.8 ns), $KMgF_3$ (1.3 ns), and $KCaF_3$ (2 ns).

B. X-ray Mask Wheel

The design and construction of the x-ray mask disc poses a special problem. The wheel will have a 10 cm radius, with three slots located 8.5 cm from the center and spread 15 degrees apart. The slot length will be 15 mm, and the ideal slot width would be 20 microns. Using the best x-ray absorber, platinum, the thinnest we can make the mask is 200 microns. Now, at that aspect ratio, the thickness of the slot poses a problem; the depth is longer than the width, and the slot looks like a deep tunnel. Ideally x-rays fly through a perfectly aligned 20 micron slot, and avoid hitting the walls of the tunnel. But in practice the slot will be misaligned, either from imperfectly making the slots (since machining a perfect tunnel is difficult) or the mask not being perpendicular to the x-rays. When incoming x-rays hit the walls of the tunnel, they are scattered and absorbed, reducing the x-rays reaching the scintillator. Making the slot material as thin as

possible minimizes the tunnel death effect, which is why we chose the densest x-ray absorber: platinum. As for how thick to make the platinum slots, Figure 1 shows our x-ray power spectrum, and Figure 2 shows that a 200 micron platinum plate masks out almost all our x-rays.

A solid platinum wheel sounds ideal, but would be very expensive, so we took a couple of steps to minimize costs. The beam strikes only a circular portion of the wheel, so only an annular section needs to be x-ray opaque. A small platinum plate with three slots makes up a portion of this ring, and the rest consisting of 1.59 mm thick stainless steel. This x-ray opaque loop is placed on a solid aluminum circle. We expect this wheel to weight about 227 grams.

C. Motor And Angular Encoder

A New Focus Model 3501 optical chopper will rotate the wheel at a precise rate of 1 Hz. The chopper has an optical sensor to indicate the passage of each slot coupled with a controller that allows precise control of the rotation rate. We tested the motor by constructing a test wheel that had the same moment of inertia, and about 4 times the mass as the final wheel. To relieve radial load on the motor, the motor was placed face-up so the load could be placed on top, axially. The motor was able to speed up and maintain a steady 1 Hz with this test wheel, so it should be able to output enough torque for the final wheel.

To track the precise angular position of the wheel, we will attach an angular encoder to the shaft of the wheel. An angular encoder is a device that looks like a motor that outputs a digital signal corresponding to the position of the shaft. The Accucoder Model 958 is an encoder that has an angular resolution of 4096 discrete points per turn (about .09 degrees). We wrote a Labview program to observe the encoder output as a meaningful angle. Since we will read the encoder once per PEP ring turn, (the 7.3-μs time for a particle to go around the ring, giving 136,000 encoder readings in one turn of the wheel), the accuracy can be further increased by

assuming that the wheel is turning at a steady rate between increments of the encoder and interpolating the position of the wheel in between each point.

D. Simulation Apparatus And Methodology

For the simulation setup, a 5 volt green LED blinking every 7.3 microseconds emulates the light pulses of a single bunch going around the PEP-II rings. Note that this LED is not an ideal Gaussian light source, but we're not too concerned since this is meant to be a rough simulation. A 100 mm focal length lens focuses this LED as a 6 mm circular image, located 49.2 mm from the center of a two-slit chopper wheel rotating at 2 Hz. The slots are 1 mm wide, set 180 degrees apart, and set to scan the image up vertically, staying parallel to the x-axis. With two slots on a wheel turning at 2 Hz, a slot scans the LED image every quarter second. A PMT, placed behind the wheel, measures the brightness of the horizontal slices of the image. With each blink, the PMT outputs a signal proportional to the brightness of the light strip. This setup is built on a 18'' optical breadboard and placed inside a 24'' black box.

For data collection, an oscilloscope is sufficient for observing the PMT output, whereas for the final project, (signal every 4.2 ns, and 1700 bunches to keep track of), a fast electronics system is needed.

Results

The results of the simulation setup are presented in Figs. 3 to 6, with each subsequent plot zooming in on features of Fig. 3. The "Slot Signal" (Fig. 3) shows the PMT blips produced each time a slot passes over the PMT (every quarter second). The peaks are negative because the PMT we're using uses a negative voltage input, hence the PMT amplifies negatively. Zooming into one peak reveals a nearly Gaussian cluster (Fig. 3) from scanning a circular image that is a Gaussian approximation. Focusing in on the details of each point we can see the contribution

from the individual LED blinks (Figure 4). Again, the data from this test setup differs from the final setup since we aren't getting perfectly Gaussian peaks. But for now we will approximate our simulation clusters as Gaussian and perform a fit on them for a quick check.

Discussion

In Fig. 4, the noisy datapoints that do not follow the peak arise from the oscilloscope writing data even when the LED is off. Figure 6 compares the cleaned up data to a Gaussian Fit:

$$y = A*e^{(-0.5*(x - B)^2/S^2)} +B$$

"A" is the amplitude of the peak, "B" is the vertical offset, and "S" is the standard deviation; values are stated in Table 1. Taking the width of the Gaussian fit to be the full width at half maximum, which is approximately 2.355 times the standard deviation, we get a value of .0075 second. For an approximation, we imagine a point located at the image sweeping an arc. The length of this arc is:

0.007536*2 Hz *2 Slots ***PI***49.2 mm ~ **4.66 mm**

Since the LED image was a rather uniform circle instead of Gaussian, we expected a value smaller than the image diameter of 6.3 mm, which our calculations show. Again, this simulation run was only meant to demonstrate the feasibility of using a rotating mask to determine the diameter of a Gaussian image; we aren't too concerned here how accurate the diameter results are.

Future Work

Our chief concern is to continue investigating for a sub-nanosecond scintillator that can work with our low photon energies. Also we'll need to implement and program an angular encoder into our setup.

References

[1] A. Fisher. (2007, August). LER Synchrotron-Light Power for the X-Ray Monitor. [Online]. Available: http://www.slac.stanford.edu/~afisher/XRay/XrayPower/XrayPower.pdf

Acknowledgments

This project was conducted during a Summer Undergraduate Laboratory Internship (SULI) at the Accelerator Systems Division of the Stanford Linear Accelerator Center. I am grateful to the U. S. Department of Energy, Office of Science for funding the program, making it possible for me to have a wonderful and fun learning experience. Great thanks to my mentor Alan Fisher for his constant help, patience, and inspiration. I would also like to thank Nick Reeck for his consultation on the mechanical design of the x-ray wheel.

Tables

Parameters	Names	Values
A	amplitude	-0.05176
B	Baseline/Offset	-0.005
S	standard deviation (sec)	0.003129

Table 1. Fitting parameters

Figures

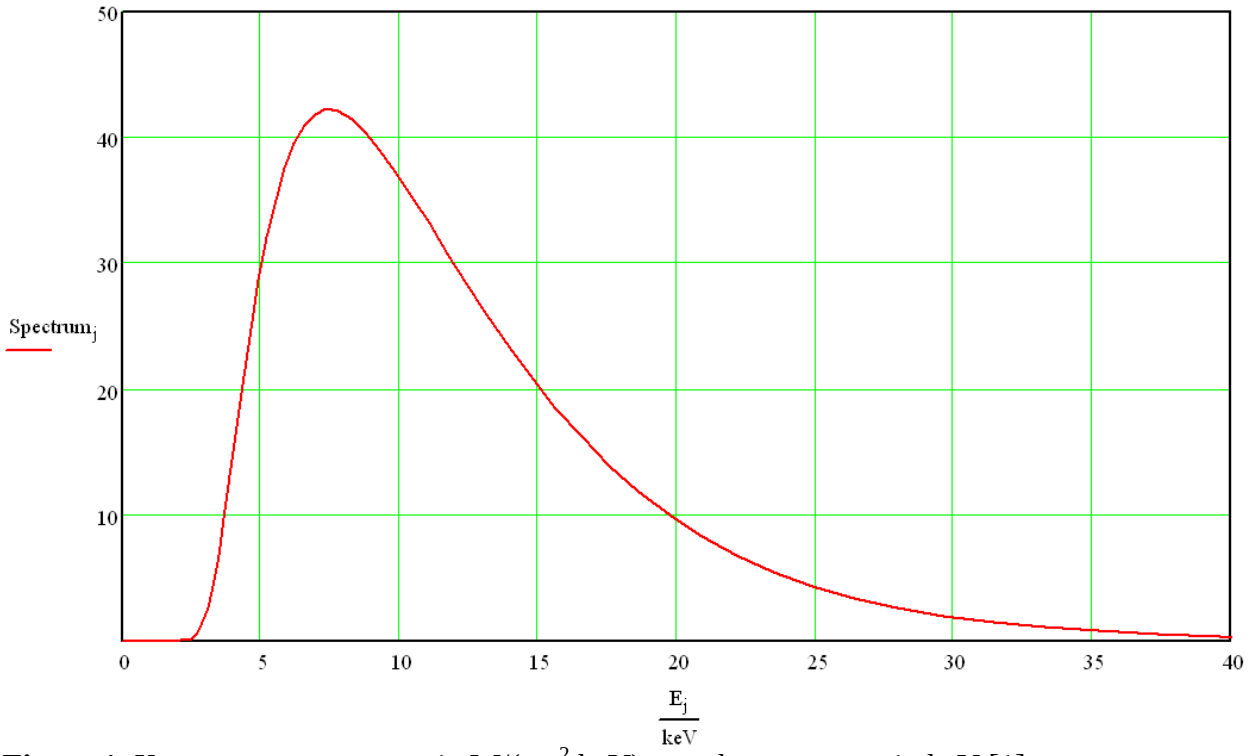

Figure 1. X-ray power spectrum, in W/(cm^2·keV), vs. photon energy in keV [1].

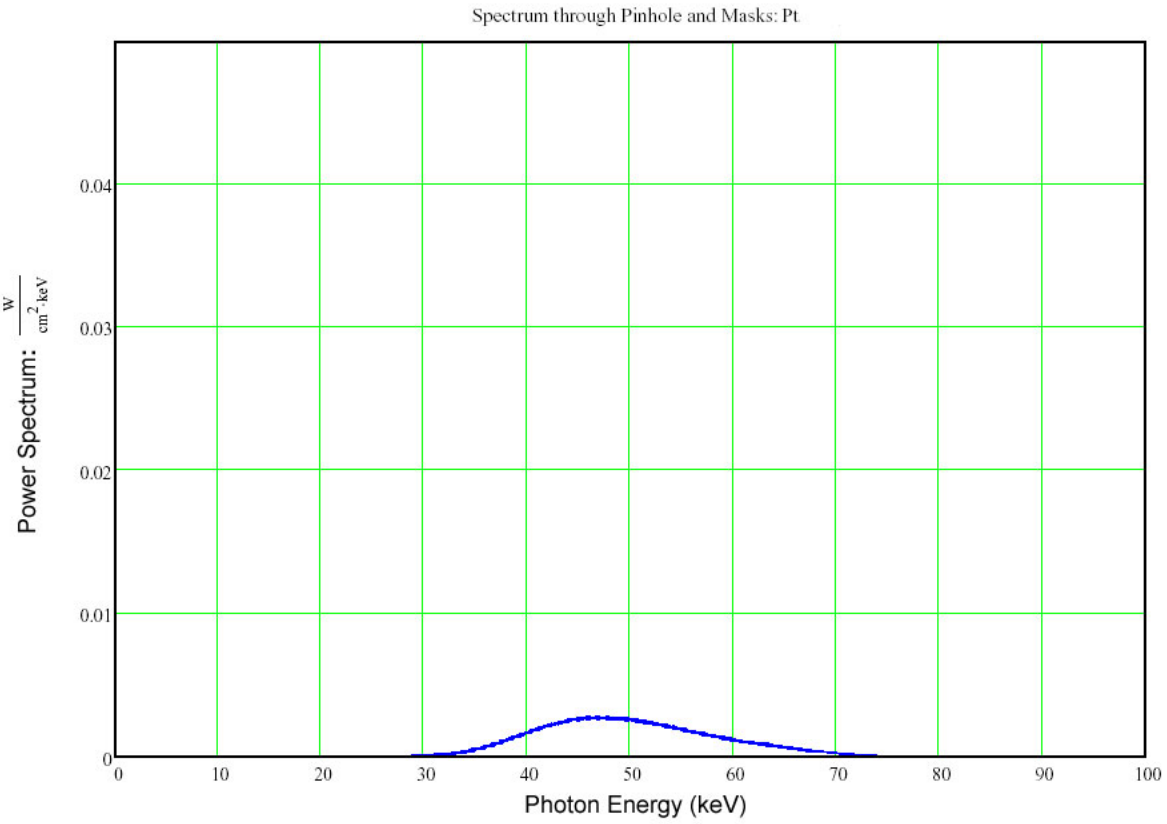

Figure 2. X-ray energy leakage through 200 micron platinum mask [1].

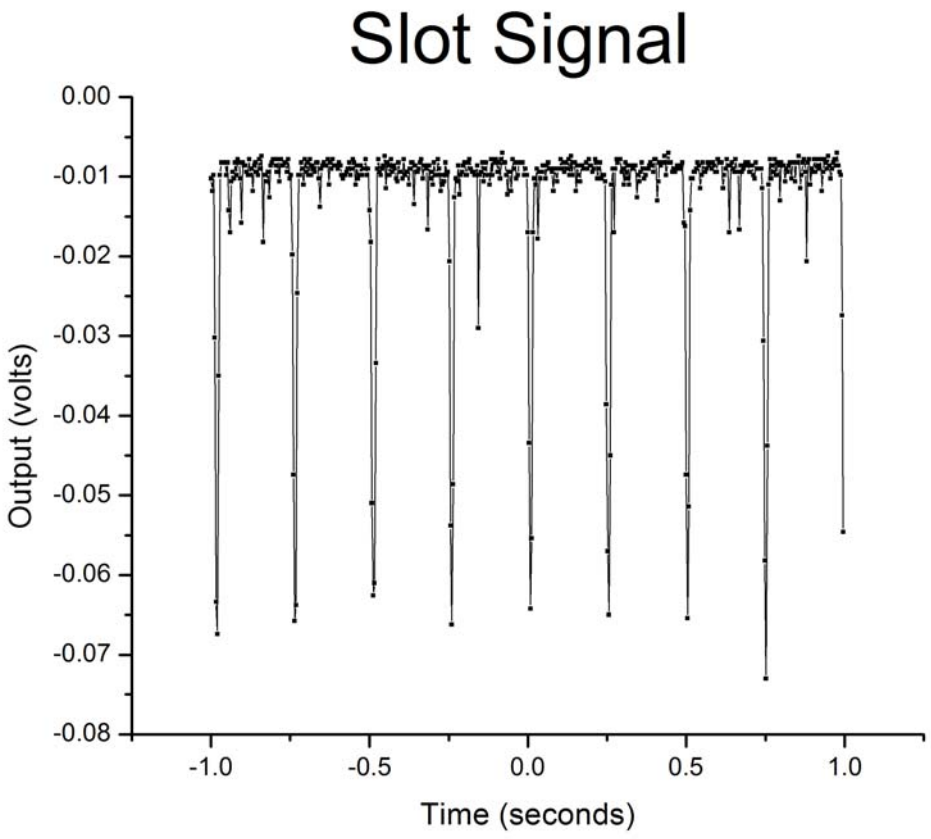

Figure 3. Photomultiplier signal as the slots pass in front of the PMT.

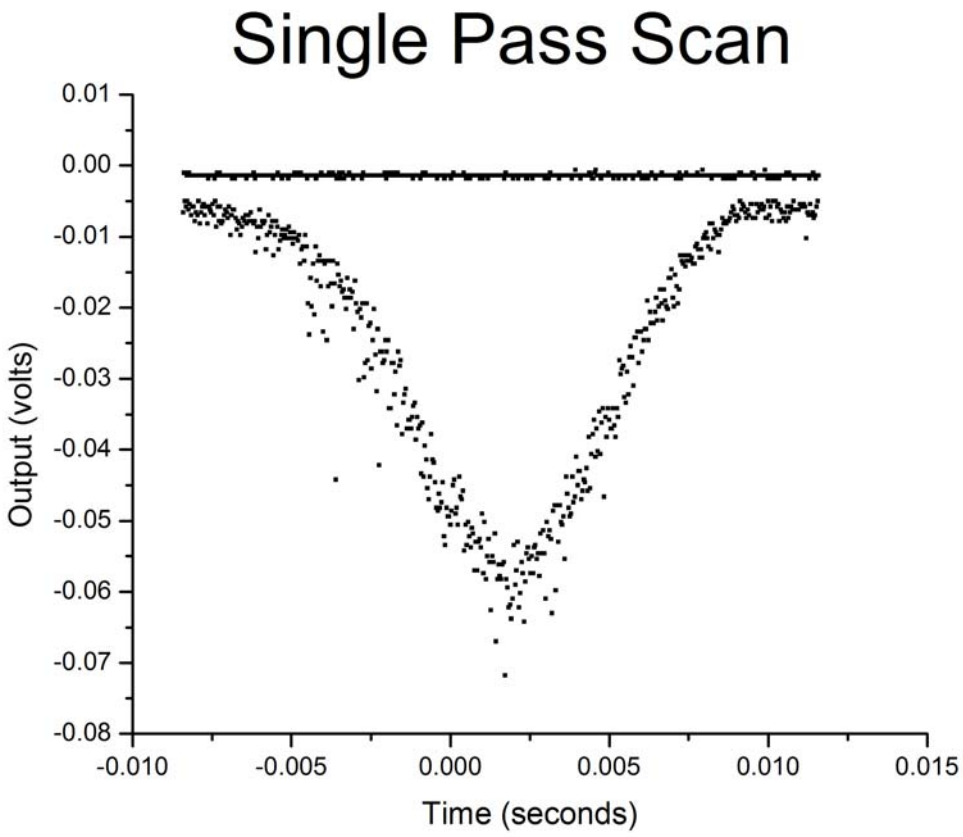

Figure 4. Photomultiplier output from a single pass slot scan of the LED image.

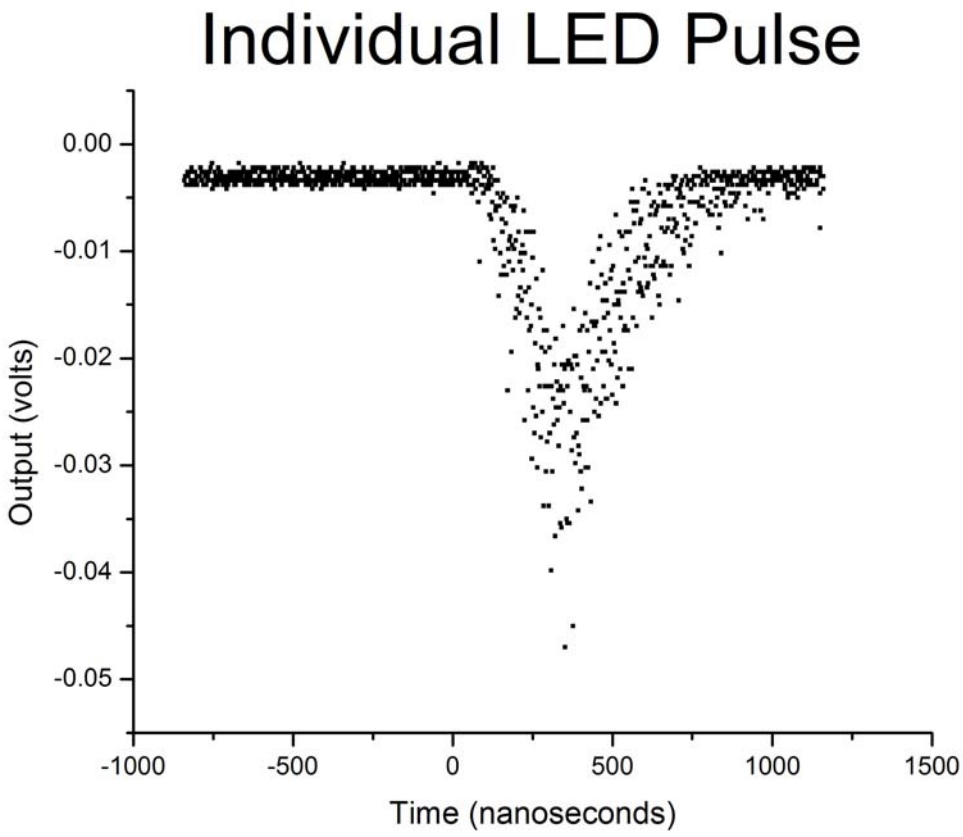

Figure 5. Pulses from each LED blink (every 7.3 microseconds).

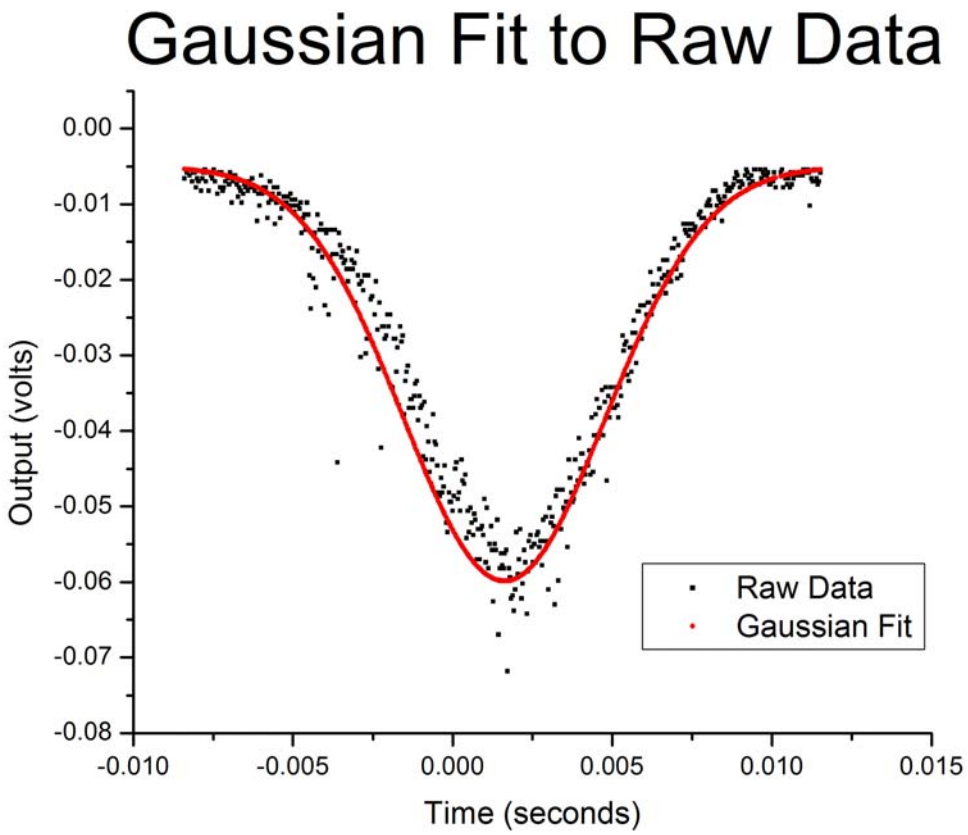

Figure 6. Gaussian fit applied to single scan. (Excluding points taken when LED was off)

SLAC-TN-07-011

What the Formation of the First Stars Left in its Wake

Christene Lynch

Office of Science, Science Undergraduate Laboratory Internship (SULI)

Gettysburg College

Stanford Linear Accelerator Center

Stanford, CA

August 15, 2007

Prepared in partial fulfillment of the requirements of the Office of Science, Department of Energy's Science Undergraduate Laboratory Internship under the direction of Marcelo Alvarez at the Kavli Institute for Particle Astrophysics and Cosmology, Stanford Linear Accelerator Center.

Participant: _____

Signature

Research Advisor: _____

Signature

Work supported in part by US Department of Energy contract DE-AC02-76SF00515

Table of Contents

1 Abstract

What the Formation of the First Stars Left in its Wake. CHRISTENE LYNCH (Gettysburg College, Gettysburg, PA 17325) MARCELO ALVAREZ (Kavli Institute for Particle Astrophysics and Cosmology, Stanford Linear Accelerator Center, Stanford, CA 94025)

The formation of the first stars marked a crucial transition in the formation of structure in the universe. Through their feedback effects, which include ionization by their radiation and the supernovae or black holes formed at the end of their lives, they were able to influence the evolution of their surroundings. In this paper we present a new visualization and use analytical calculations in order to study the influence of these first stars. The visualization was created using both Enzo, a simulation program that uses adaptive mesh refinement, and Amira, a 3D volume rendering program. This visualization allows for a better understanding of the impact these stars had on their surroundings and conveys the importance of these stars to a broader audience. The analytical calculations used investigate the possibility that black holes left by the first stars could be seeds for the 10^9 $M_\odot$ black holes seen as quasars at redshift $z\sim6$. We find that if a remnant black hole was to begin Eddington accretion at $z\sim20$, then it would be able to form a 10^9 $M_\odot$ black hole by $z\sim6$, but that there is likely to be a delay in the onset of accretion onto the seed black hole because of the radiative feedback of its progenitor. Future, more detailed, numerical calculations will be necessary to understand whether the black holes left by the first stars could possibly be seeds for quasar formation.

2 Introduction

In the beginning our universe was uniform and simple; however, today it is very complex. To understand how this transition occurred, the earliest stages of structure formation in the universe are being examined.

Only a few minutes after the big bang, the universe consisted of a very hot, dense, ionized plasma which was coupled to the radiation field through continuous scattering of photons with ions and electrons. The end of this era was marked by the epoch of recombination, about 400,000 years after the big bang, roughly a redshift $z{\sim}1000$. By this time, the universe had expanded and cooled enough that matter became decoupled from radiation, and electrons and ions combined to form neutral atoms [1]. The Cosmic Microwave Background (CMB) is the radiation from these last interactions of photons with matter. What followed is a period of darkness called the cosmic dark ages [2].

During the dark ages, matter began to cluster as the universe grew in complexity. Since baryonic matter was coupled to radiation before the epoch of recombination, any fluctuations in density also occurred in the temperature of the radiation, and this was recorded in the CMB. It has been found that these fluctuations cannot lead to the structure observed in the universe today [1]. The leading explanation for how the universe grew in complexity is that, before the epoch of recombination, dark matter density fluctuations were able to increase, because unlike the baryonic matter, dark matter was not coupled to radiation. Thus when baryonic matter became decoupled, it was influenced by the gravity of higher density regions of dark matter. The dark matter halos that formed could have led to the collapsing of the baryonic gas clouds and the formation of structures like stars and galaxies.

The end of the dark ages most likely occurred about 100 million years after the big bang when the first stars formed and began to emit radiation [3]. These stars, named Population III stars, formed in collapsing clouds of atomic hydrogen, helium and small amounts of molecular hydrogen. These stars were probably different from stars forming today: they

were likely to be very massive and composed of only hydrogen and helium [4]. Their UV radiation ionized surrounding gas by propagating an ionization front (I-front) leaving behind an "H II" region. This marked the beginning of the reionization epoch. Using the spectra of distant quasars, astronomers have estimated that this reionization period ended at a redshift $z \sim 6$, about a billion years after the big bang [5].

It is important to study these stars because they affected the universe we see today. Through their feedback effects, which include re-ionizing the universe and supernova explosions or black holes formed at the end of their lives, they influenced the formation of subsequent structure in the universe. To model formation, evolution, and feedback effects of Pop III stars, numerical simulations as well as analytical calculations are being used. Both are important in understanding these stars and will be used in this paper. This paper will discuss the influence of the first stars on the structure of the universe and presents a new visualization of a PopIII star forming, creating an HII region, and dying as a supernova. This visualization will differ from existing visualizations in that the perspective will not be limited to one point. It will not only revolve around the star but will also fly in toward it as the star begins to shine. If these first stars had masses less than 140 $M_{\odot}$ or greater than 260 $M_{\odot}$, they would have collapsed directly to a black hole [6]. We will also be investigating the fate of such remnant black holes and will be taking a detailed look at the Bondi-Hoyle and Eddington accretion rates in order to reach some preliminary conclusions about the relevance of these first black holes to the z~6 quasars.

3 Materials and Methods

In this section we will first describe our visualization techniques used and then give an overview of the physical models which describe black hole accretion in the early universe.

3.1 First Star Visualization

To create our visualization we use two different programs; one called Enzo, which calculates the progress of several physical processes as the star forms and evolves, and another called Amira, which visualizes this process. Enzo simulates the evolution of baryonic and dark matter through the use of different numerical algorithms. These algorithms include the physical processes of gravity, hydrodynamics, and radiation transport. One must first supply Enzo with appropriate initial conditions, after which it uses its algorithms to calculate changes in these conditions as time evolves. Enzo uses adaptive mesh refinement (AMR), which simultaneously resolves a large range of length scales to accurately model physical phenomena. AMR is vital, since structures studied in these simulations occur on a wide range of length scales and the simulation has to be able to resolve both the larger structures, from several hundreds of thousands of light years, to smaller structures of several light hours [7]. AMR refines the simulation by first covering the computational domain with a set of coarse structured grids and then, during the computation, using local error estimators to find areas that may need more resolution. These areas are then covered by subgrids and the equations are advanced.

The AMR data was visualized using Amira's AMRvolren module, which creates a 3D image of the data by a photorealistic rendering technique. This technique assigns a color, brightness, and opacity to the temperature and density fields. To do this, the black body spectrum of the gas being visualized is convolved with a choice of 3 filters which correspond to RGB values. Absorption is taken into account using Rayleigh's law, which states that the intensity of the scattered light is proportional to the product of density and λ^{-4}. Lastly the emission is scaled using the normalized gas density present at the voxel location [7]

In order to orchestrate the visualization, we used an IDL routine written by Tom Abel, which allowed us to manipulate position and orientation of the camera interactively. This eliminated the need for an algorithm that creates the path, and allowed us to specify control

data points of distance, time and rotation as a function of frame number, smoothly interpolated with cubic spline functions. We then created a tcl script within Amira that enabled it to read in the camerapath from the IDL routine program. Once the path of the camera was specified, frames were taken for each time and viewpoint, and finally compiled together to create an animation of our visualization.

3.2 Accretion onto remnant Black Holes

In 1939, Hoyle and Lyttleton investigated accretion onto an object of mass M, moving at a steady speed, v_∞, through an infinite gas cloud of uniform density, ρ_∞. They assumed that the pressure of the gas was negligible and derived the equation $\dot{M}= 4\pi G^2 M^2 \rho_\infty / v_\infty^3$ for the accretion rate, where G is the gravitational constant [8]. Later, Bondi took into account the pressure of the gas when determining the accretion rate of such an object. He assumed the object to be at rest in a uniform cloud of gas which is at rest at infinity and has a uniform density and pressure at infinity. The motion of the gas cloud was assumed to be spherically symmetric and steady and the increase in mass of the object was neglected, so that the force field is unchanging. Bondi found that the maximum accretion rate of such an object is $\dot{M}= 4\pi\lambda_c\ G^2 M^2 \rho_\infty / c_\infty^3$, where λ_c is a non-dimensional parameter of order unity, and c_∞ is the sound speed of the gas [9]. These two accretion rates were combined to obtain the accretion rate of an object moving through an infinite gas cloud,

$$\dot{M}_{\rm BH} = \frac{2\pi G^2 M^2 \rho_\infty}{(c_\infty^2 + v_\infty^2)^{3/2}}, \tag{1}$$

which is called the Bondi-Hoyle accretion rate [10]. From this point onward we will be assuming that v_∞ is zero so that $\dot{M}_{\rm BH}= 2\pi G^2 M^2 \rho_\infty / c_\infty^3$.

The accretion rate is limited by the Eddington rate of accretion, which is given by

$$\dot{M}_{\rm Edd} = \frac{4\pi G M m_p}{\sigma_T c} \left(\frac{1-\epsilon}{\epsilon} \right), \tag{2}$$

where ϵ is the radiative efficiency of the gas, σ_T is the Thomson scattering cross section, and c is the speed of light. The Eddington accretion rate is the largest rate of accretion an object can have without reaching the Eddington limit, at which point the radiation pressure supplied by matter accreting into the object is equal to the the gravitational force supplied by this object, and it can no longer accrete. Accreting at the Eddington rate requires that the Bondi-Hoyle accretion rate to be greater than or equal to the Eddington rate. Using the equation for sound speed, $c_s^2{=}\gamma p/\rho$, and the pressure equation $p{=}nk_BT$, where number density is given by $n{=}\rho/\mu m_p$, we can rewrite the Bondi-Hoyle accretion rate as $\dot{M}_{\rm BH}{=}\,(4\pi G^2\rho)/m_p[(\gamma k_B)\,/\,(\mu m_p)]^{-3/2}M^2T^{-3/2}$. Assuming that the black hole accretes at the Bondi-Hoyle rate we can find we can find what fraction this accretion is of the Eddington rate by dividing the rewritten Bondi-Hoyle accretion rate by equation (2). We obtain

$$\frac{\dot{M}_{\rm BH}}{\dot{M}_{\rm Edd}} = \frac{G\sigma_T c}{m_p}\left(\frac{\epsilon}{1-\epsilon}\right)\left(\frac{\gamma k_B}{\mu m_P}\right)^{-3/2}\frac{M\rho}{T^{3/2}}. \tag{3}$$

If the black hole's Bondi-Hoyle accretion rate is equal to the Eddington rate, then $\dot{M}_{\rm BH}/\dot{M}_{\rm Edd}{=}1$. By solving for the mass of the black hole versus redshift, we will be able to determine whether the black hole grows from its initial mass to the mass of the quasars at $z{\sim}\ 6$.

4 Results

4.1 First Star Visualization

The visualization that has been created gives a rotating view of the first star as it begins its life and eventually dies in a pair-instability supernova. The top grid of this visualization has a grid resolution of 128^3 within a 250 cubic co-moving kpc volume. A subgrid is used with a higher resolution and 92^3 grid cells [11]. We begin the visualization by zooming in on the gas cloud in which the star forms. We come to a stop when the star begins to form, at about $z{\sim}20.4$. We slowly zoom out while the ionization front escapes from the shock, about

1 Myr after the star begins forming, which allows us to get a better view of this process. The visualization zooms out just after the supernova begins, at about 2.7 Myr after formation. The visualization ends with a full view of the star which gives the full impression that these stars formed individually (see figure 1). The IDL routine written by Tom Abel was extremely helpful in creating this visualization. It allowed us to use actual data points to trace out the camera path that we wanted to take and allowed us to make quick changes to this path in order to make it more accurately fit the evolution of the star. If further research is to be done with these simulations, however, it will be necessary for a faster data format to be developed to read in the data.

4.2 Accretion onto remnant Black Holes

In attempting to understand the possible accretion rates of black holes left by the first stars, we first considered the situation where the black hole accretes at the Eddington rate. Assuming that a typical first star would leave behind a black hole of 100 $M_{\odot}$, the resulting Eddington rate of this black hole would be

$$\dot{M}_{\rm Edd} = 2 \times 10^{-6}\ M_{\odot}{\rm yr}^{-1} \left(\frac{\rm M}{100\ {\rm M}_{\odot}}\right) \left(\frac{1-\epsilon}{9\epsilon}\right). \tag{4}$$

Equation (4) can be rewritten as $\dot{M}_{\rm Edd}$=$M/t_{\rm sal}$, where $t_{\rm sal}$ is the time it takes the black hole to increase its mass by a factor of e and is given by $t_{\rm sal}$=5×10^{7} $(9\epsilon/\left(1-\epsilon\right))$ yr. This implies a simple differential equation that can be solved using separation of parts:

$$\ln\left(M_f/M_i\right) = \left(t_f - t_i\right)/t_{\rm sal}. \tag{5}$$

We can obtain an expression for the initial redshift, z_i, which Eddington accretion must begin at to create the 10^9 $M_{\odot}$ quasars at $z$$\sim$6, by using the relation between the age of the universe and the redshift, t=$2/[3H(z)]$. In this relation, $H(z)$ is the Hubble parameter,

which is given by $H(z)=H_o\Omega_m^{1/2}(1+z)^{3/2}$, where H_0 is the present value, and $\Omega_m=\rho/\rho_{\rm crit}$ is the density in units of the critical density for closure. Substituting equation $H(z)$ into equation (5), we obtain $t_i=t_f[(1+z_i)\,/\,(1+z_f)]^{3/2}$. Solving for z_i we obtain

$$z_i = (1+z_f)\,(1-\ln{(M_f/M_i)}\,t_{\rm sal}/t_f)^{-3/2} - 1. \tag{6}$$

Using equation (6) for a 100 $M_\odot$ black hole accreting at the Eddington rate, we find the redshift that this black hole must start accreting matter to be $z\simeq 20$. It is reasonable for black holes from the first stars to be formed by this time since it has been estimated that the first stars were formed at around a $z\sim 20$ [5]. Nevertheless, when these black holes form there is very little cold gas to be accreted, which prevents accretion at the Eddington rate. However, these black holes may soon come into contact with large cold gas clouds and be able to accrete at the Eddington rate. Given this possibility, it would be valuable to know the density necessary for accretion at this rate.

To solve for the density enhancement necessary for Eddington accretion, we first need to find the density of the universe as it depends on redshift. Since we are only interested in the density of the matter that can be accreted by the black hole we will only consider the baryonic matter density of the universe. Given that mass is conserved as the universe expands, the change in density of the universe depends on the change in its volume. To find the volume of the universe, the scale factor, which indicates how much the universe has expanded, can be used. The scale factor is inversely proportional to $(1+z)$, so if the universe expands by a scale factor of a_1 then the volume increases by a_1^3 or $(1+z_1)^{-3}$. We can now write the density in terms of the redshift,

$$\rho_{b,z} = \rho_{b,0}\,[(1+z)\,/\,(1+z_0)]^3\,. \tag{7}$$

To find $\rho_{b,0}$ we will assume that the initial redshift is $z_0=0$ and set ρ_i equal to the baryonic

density of the universe today.

The baryonic density parameter gives the ratio of the current baryonic density to the critical density of the universe, Ω_b=$\rho_{b,0}/\rho_{\rm crit}$, where $\rho_{\rm crit}$= $3H_0^2/(8\pi G)$. Consequently, if we multiply the baryonic density parameter by $\rho_{\rm crit}$ we will have the current baryonic density of the universe, giving $\rho_{b,0}$=$\Omega_b\rho_{\rm crit}$. If we define h=$H_0/(100$ km/s/Mpc) then $\rho_{\rm crit}$=$3h^2(10^4$ km/s/Mpc)$/(8\pi G)$, which is equivalent to $\rho_{\rm crit}$= 1.88×10^{-29} h^2 g cm^{-3}, which implies $\rho_{b,0}$=1.88×10^{-29} g cm$^{-3}\Omega_b h^2$. Using the latest constraints from the WMAP satellite [12], $\Omega_b h^2$=2.23×10^{-2}, the baryonic density in the universe today is $\rho_{b,0}$= 4.2×10^{-31} g cm^{-3}. We can now substitute it into equation (7) to obtain the baryonic density of the universe as a function of redshift,

$$\rho_{b,z} = 4.2 \times 10^{-31}{\rm gcm}^{-3}\,(1+{\rm z})^3\,. \tag{8}$$

Now what is necessary is an expression for the density that allows for accretion at the Eddington rate. Assuming a certain temperature and resulting mass we can use equation (3) and specify that $\dot{M}_{\rm BH}/\dot{M}_{\rm Edd}$=1, meaning that the Bondi-Hoyle accretion rate is equivalent to the Eddington rate, and find the density necessary for this situation. In this case we see that the density required, $\rho_{\rm BH}$, is inversely proportional to the mass of the final object and directly proportional to the temperature of the gas to the 3/2 power, so $\rho_{\rm BH}\propto M^{-1}T^{3/2}$. Let us assume that a black hole left by a first star is radiating with an efficiency of 0.1, is accreting at the Eddington rate at z∼6 to form the $10^9 M_\odot$ quasars, and the temperature of the gas is 10^4 K. Using equation (3) we find that the density necessary for this situation is ρ_{BH}=6.774×10^{-27} g cm^{-3}. By substituting into equation (8), we can determine by how much the density of a gas cloud required for Eddington accretion is greater than the actual density of the universe at this redshift. For a redshift z=6, the density of the universe is $\rho_{b,6}$=1.44×10^{-28} g cm^{-3}, meaning that the density of a gas cloud required for Eddington rate accretion is $\rho_{\rm BH}/\rho_{b,6}$ ≃(47) times greater than the actual density of the universe. Using the above ratio we can generalize it for all redshifts z as follows. The density of the universe is now given by

$\rho_{b,z}$=1.44×10^{-28}[(1 + z) /7]^3 and the density required for accretion at the Eddington rate is given by $\rho_{\rm BH}$=6.8×10^{-27}(M/10$^9 M_\odot$)$^{-1}$(T/10^{4}K)$^{3/2}$((1 − ϵ) /9ϵ). The overdensity required is

$$\frac{\rho_{\rm BH}}{\rho_{b,z}} = 1 + \delta_{\rm BH} \simeq (47) \left(\frac{(1+z)}{7}\right)^{-3} \left(\frac{M}{10^9 M_\odot}\right)^{-1} \left(\frac{T}{10^4 {\rm K}}\right)^{3/2} \left(\frac{(1-\epsilon)}{9\epsilon}\right), \qquad (9)$$

and will tell us by how much the density of a gas cloud is greater than the density of the universe if a black hole is to accrete it at the Eddington accretion rate. For a 100 $M_\odot$ black hole at z≃20, the overdensity is 1.7×10^7. At the center of a halo before cooling occurs, the overdensity is about 10^4, which implies that if a black hole of this size is to accrete at the Eddington rate a sufficient amount of cooling must occur before hand.

5 Discussion and Conclusions

The visualizations created to study the first stars are important tools. They allow for predictions about the influence these stars had on the evolution of the universe to be made and using these predictions it is possible to search for evidence that these stars existed. Using future telescopes, like the James Webb Space Telescope scheduled for launch in 2013, we can search for objects like the oldest Pop II star or the first galaxies and study their spectra to find their heavy element patterns. We can then compare these patterns to the predicted patterns generated by the first stars to decide whether these stars could have lead to the metal enrichment of the universe. We can also look for the radiation that would be emitted from the pair-instability supernovae created at the end of these stars' lives. [13]. These visualizations are also useful in communicating to the public the importance of understanding these stars and educating them about recent advances made in research about them.

From inspecting the accretion rates of the possible black holes left by the first stars we have found that if these black holes had a mass of 100 $M_\odot$ and were able to accrete at the Eddington rate at redshift z∼20 they would be able to form the quasars we see at z∼6. Yet

it is not likely that these black holes will come into contact with clouds of gas, which are dense enough to allow for accretion at the Eddington rate, at $z\sim20$. We have determined an expression (equation 9), which indicates how much denser gas clouds must be than the universe if the black hole is to accrete them at the Eddington rate for a given redshift, temperature and mass. If the rate of accumulation of clouds of gas in the relic H II regions of the first stars is better understood then we will be able to use this equation to determine at what redshift these clouds are dense enough to allow for accretion at the Eddington rate. To understand when such densities can can reached, more detailed numerical calculations, on the evolution of these black holes between their formation and $z\sim6$, will be necessary.

6 Acknowledgments

This research was conducted at the Stanford Linear Accelerator Center in Menlo Park, California. I would like to thank the Department of Energy, Office of Science and SLAC for providing me this opportunity to participate in the SULI program and the National Science Foundation for helping to sponsor such great program. I would especially like to thank my mentor, Marcelo Alvarez, for his patience and willingness to help me understand the physics behind my project and for always being available when problems arose. I also owe thanks to Tom Abel for his enormous amount of help in programming and writing the IDL routine used.

References

[1] T. Padamanabhan, *After the First Three Minutes, The Story of Our Universe.* Cambridge, UK: Cambridge University Press, 1998.

[2] M.Rees, "The Hubble telescope and the high redshift universe," presented at the 37th Herstmonceux Conference at Cambridge, UK, N. Tanvir *et al.*, Eds., 1997.

[3] A. Loeb, "The dark ages of the universe," *Scientific American*, vol. 295, pp. 46–53, Nov. 2006.

[4] T. Abel *et al.*, "The formation of the first stars," *Science*, vol. 295, pp. 93–98, 2002.

[5] V. Bromm and R. Larson, "The first stars," *Annual Review of Astronomy and Astrophysics*, vol. 42, pp. 79–118, Sept. 2004.

[6] A. Heger *et al.*, "The final stages of the most massive stars," presented at the The Fate of the Most Massive Stars, Asp Conference Series, 2005.

[7] R. Kaehler *et al.*, "A framework for interactive, high-qualit voluem rendering of cosmological simulations," presented at the Proc. Int. Workshop on Volume Graphics, 2006.

[8] F. Hoyle and R. Lyttleton, "The effect of interstellar matter on climactic variation," *Proc. Cam. Phil. Soc.*, vol. 35, p. 405, 1939.

[9] H. Bondi, "On spherically symmetical accretion," *Monthly Notices of the Royal Astronomical Society*, vol. 112, p. 195, 1952.

[10] R. Edgar, "A review of Bondi-Hoyle-Lyttleton accretion," *New Astronomy Reviews*, vol. 48, pp. 843–859, Sept. 2004.

[11] T. Abel *et al.*, "The HII region of a primordial star," *The Astrophysical Journal*, vol. 659, pp. L87–L90, Apr. 2007.

[12] D. Spergel *et al.*, "Three-year Wilkinson Microwave Anisotropy Probe (WMAP) observations: Impliacations for cosmology," *The Astrophysical Journal Supplement Series*, vol. 170, pp. 377–408, June 2007.

[13] J. Wise and T. Abel, "The number of supernovae for primordial stars in the universe," *The Astrophysical Journal*, vol. 629, pp. 614–624, Aug. 2005.

Figures

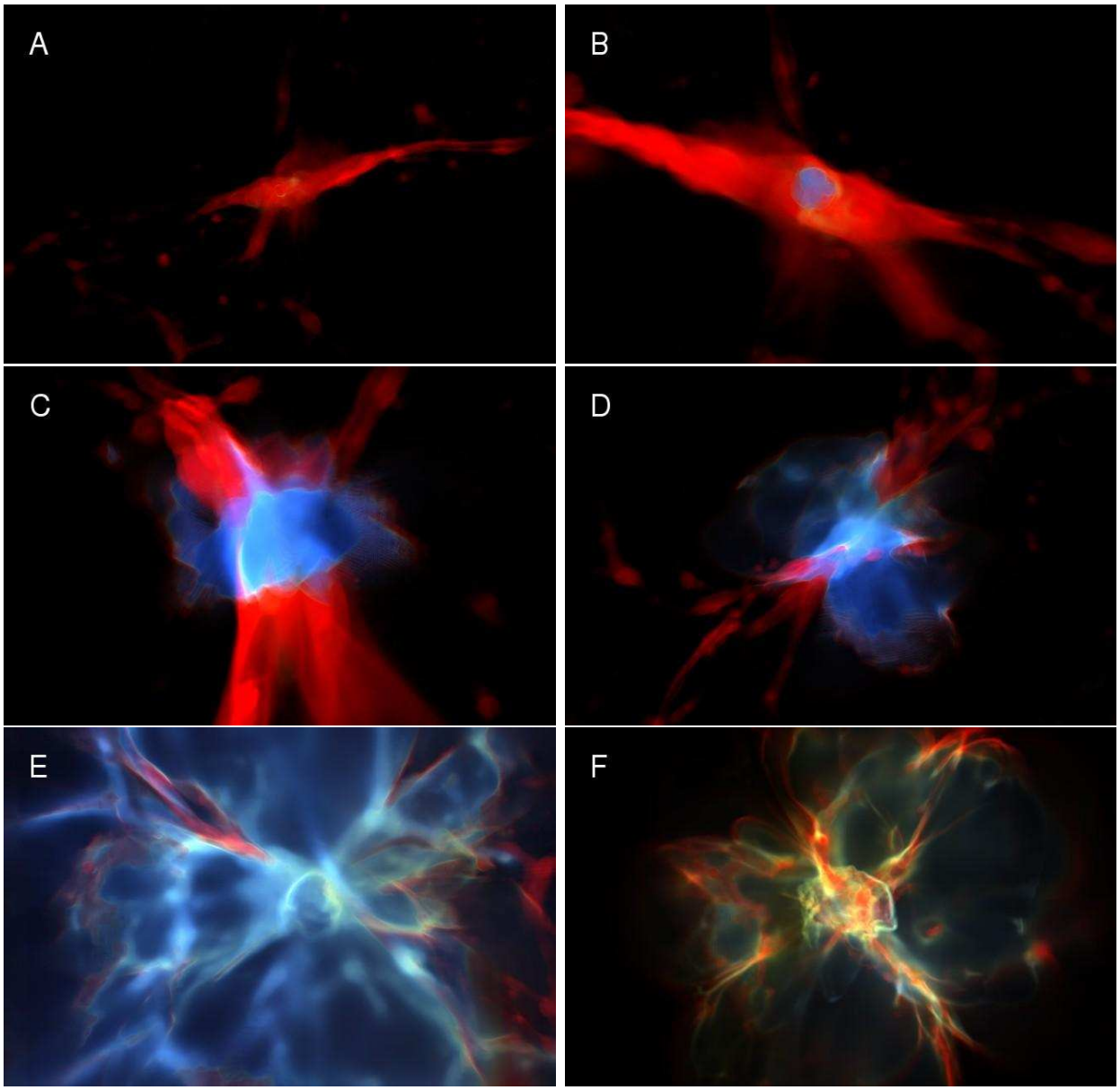

Figure 1: The first stars are formed in dense cold clouds of hydrogen and helium, which formed during the dark ages (A). When these clouds collapsed to form the first stars a shock was formed which propagated through the rest of the cloud. In the beginning of formation the ionization front is trapped behind the shock. (B). If the star is massive enough the ionization front will eventually break away from the shock and quickly ionize the rest of the gas cloud (C, D, and E). If these stars have a mass between 140 $M_{\odot}$ and 260 $M_{\odot}$ they will end their lives in a pair-instability supernova, about 2.7 Myr after they are formed (F).

SLAC-TN-07-007
August 2007

Determining the Local Structure of Platinum Streptidine using X-Ray Absorption Spectroscopy

Michaëlle Mayalu

Office of Science, SULI Program

Massachusetts Institute of Technology

Stanford Linear Accelerator Center

Stanford, CA

August 17, 2007

Prepared in partial fulfillment of the requirements of the Office of Science, U.S. Department of Energy Science Undergraduate Laboratory Internship (SULI) Program under the direction of Stephen Rock in the Linear Collider Detector Department at Stanford Linear Accelerator Center.

Participant: _____

Signature

Research Advisor: _____

Signature

Work supported in part by US Department of Energy contract DE-AC02-76SF00515

Table of Contents

ABSTRACT

Determining the Local Structure of Platinum Streptidine using X-Ray Absorption Spectroscopy. MICHAËLLE MAYALU (Massachusetts Institute of Technology Cambridge, MA 0213-4307) SERENA DEBEER GEORGE (Stanford Linear Accelerator Center Stanford, CA 94025)

X-Ray absorption spectroscopy (XAS) is a technique that utilizes high energy X-rays commonly obtained from synchrotron radiation to determine the structure of known and unknown substances and materials. By examining the absorption vs. energy pattern, one can determine the local structure surrounding the absorbing atom. Analysis of a region of the absorption vs. energy graph called extended x-ray absorption fine structure (EXAFS) leads to information about the identity of the atoms surrounding the absorber, the number of atoms surrounding the absorber, and the distances between the absorber and neighboring atoms. Using XAS, structural descriptions of platinum streptidine, a newly synthesized platinum anti-cancer agent, have been obtained. The results show that the platinum is in fact coordinated to the streptidine, which was the main question that needed to be answered about the drug.

I. INTRODUCTION

The discovery of platinum anti-cancer agents has lead to extensive research into the mechanisms by which these complexes succeed in inhibiting cell division. It is believed that the platinum complex may bind to a certain site in the DNA thus preventing further division of the cell. Although the discovery of platinum anti-cancer drugs has made considerable advances in the treating certain cancers, many mysteries regarding these drugs still remain.

It is not known what the mechanisms are that lead to the drug being taken up by the cell membrane and integrated into the DNA, and why the drug is successful in treating some types of cancers but ineffectual in treating other types. Also, the platinum has been found to be very toxic causing nephrotoxity, neuropathy, ototoxicity, hematological toxicity, neuropathology and seizures [1]. A fair amount of research has been directed at developing agents that will reduce the toxicity of the platinum, as well as synthesizing new platinum complexes that may have less toxic side effects.

Cisplatin is one of the most successful platinum anti-cancer agents and is very effective in treating testicular and ovarian cancers [2]. Although the drug is quite efficient, it is still highly toxic and only is successful in certain types of cancers. Also, some cancers develop resistance to the drug after the first treatment[2]. Consequently, the search for improved platinum drugs that treat a wider range of cancers and display fewer toxic side effects continues.

Many other drugs are being synthesized including a Platinum-Streptidine complex [3]. Although several analytical methods have been performed on this drug, such as elemental analysis and nuclear magnetic resonance (see Figure i), much is still unknown

about the solid state structure, and even more importantly the solution state structure of the Platinum-Streptidine complex. Because the structure and coordination of the drug is essential to understanding how the drug interacts with molecules in the body, X-ray absorption spectroscopy (XAS) is a powerful tool for determining the structure of this newly developed drug.

X-Ray absorption spectroscopy is a technique that utilizes high energy X-rays commonly obtained from synchrotron radiation to determine the structure of known and unknown substances and materials. The X-rays are absorbed into the atom of a sample with detectors mounted at the front and back of the sample. Relative absorbance is measured by taking the log of the currents in each detector [4] .Another way of measuring the absorbance is to measure the fluorescence intensity. The graph of the fluorescence intensity vs. the energy is equivalent to the graph of the absorbance vs. energy[4]. By examining the absorption vs. energy pattern, one can determine the local structure surrounding the atom as well as in some cases the angle between the atom and the absorber.

At a certain energy, the absorption vs. energy graph shows an abrupt increase in absorption which signifies the release of an electron from the atoms core shells. This jump is referred to as the absorption edge. Beyond the edge, at higher energies, is a region called the extended x-ray absorption fine structure or EXAFS. The oscillatory behavior in this region is due to the interactions between the photoelectron wave generated by the absorbing atom and the backscattering of the wave from atoms nearby. This interaction causes constructive and destructive interference which leads to the sinusoidal curves that characterize the EXAFS[4] (see Figure ii). Analysis of the EXAFS

region leads to information about the identity of the atoms surrounding the absorber, the number of atoms surrounding the absorber, and the distances between the absorber and neighboring atoms.

Since obtaining useful data on dilute samples is only possible using synchrotron radiation, this type of radiation is essential to the Platinum Streptidine experiment because dilute Platinum Streptidine is a better representative of how the complex will operate *in vivo* [4]. The main questions to be answered by analysis of XAS data measured with XAS are: Is it the Pt coordinated to the Streptidine? And if this is the case, through which atoms? [3]

II. MATERIALS AND METHODS

XAS measurements and data analysis were conducted at the Stanford Synchrotron Radiation Laboratory (SSRL). Pt L_3-edge data were measured on beam-line 9-3 on solid and solution samples in transmission and fluorescence mode, respectively. The energy was calibrated using a platinum foil and assigning the first inflection point to 11563.0 eV. The data scan range was 11330-12690eV.The flux was ~ $2*10^{12}$ photons per second at 100 mA with a 1 (vertical) by 4 (horizontal) mm spot size. The data represent 3- and 11-scan averages (scan time, 30 min per scan) for the solid and solution, respectively. Samples were monitored for radiation damage throughout the procedure. It should be noted that the platinum streptidine was dissolved in dimethyl-sulfoxide. The final concentration was ~2mM in Pt.

Analysis of the data was conducted with the programs EXAFSPAK [5] and FEFF[6,7]. Also, the Cambridge Structural Database was used as a reference of known complexes [8].

The pre-edge region of the data was subtracted by fitting it with a first order polynomial and then subtracting the polynomial so it lied flat. The smooth background due to atomic interference was eliminated by fitting the region above the edge with a three region cubic spline that was then subtracted [5]. The EXAFS was then k^3-weighted to enhance the oscillations at high k.

Several theoretical models of the EXAFS were produced using FEFF for the calculation of the single scattering phase and amplitude parameters and EXAFSPAK for the fitting. The data were fitted with a k-range of 2-15$Å^{-1}$ and 2-12 $Å^{-1}$ for the solid and solution data respectively. Parameters such as the bond length(R), the mean square displacement (σ^2) and the experimental energy threshold (E_0) were allowed to float while the coordination number (N) was changed systematically with every fit. It should be noted that the energy threshold (E_0) was constrained to the same value for all paths. In working with the EXAFS and FEFF software it must be noted that although the approximations might make sense mathematically, they may not be of physical or chemical relevance. Therefore a balance must be reached between both mathematical and physical significance. The Cambridge Structural Database was therefore used as a reference to compare similar known structures with the fits generated in EXAFSPAK.

III.RESULTS AND ANALYSIS

i. Comparison: Solid vs. Solution (Figure 1, 2,3)

Figure 1 shows a comparison of the normalized Pt L_3-edge data of platinum tetrachloride (K_2PtCl_4) to solid platinum streptidine complex ($C_8H_{18}N_6O_7Cl_4Pt$). As can been seen from the graph, significant differences exist between the two edges. The platinum tetrachloride edge is to a lower energy indicating that it is more reduced than

the platinum streptidine. The difference in white-line intensities for the platinum tetrachloride and solid platinum streptidine should also be noted. Also the initial EXAFS oscillations of the two complexes are out of phase. These differences indicate that the solid platinum streptidine is not merely a simple platinum tetrachloride complex, as could have been inferred through other analysis methods (i.e. on the basis of elemental analysis). The results indicate that the streptidine must interact with the platinum in a significant enough way to alter the structure, yielding a complex distinct from $[PtCl_4]^{2-}$.

A comparison of the solid and solution Pt L_3 edges is shown in Figure 2. As can be seen, the rising edge positions of the solid and solution data are at different energies, the solution edge being at a slightly higher energy than the solid edge. This is consistent with the elements present in the solid structure being replaced with lighter atoms in the solution structure (see EXAFS analysis, vide infra).

The k^3-weighted EXAFS for the Pt-Std solid and solution data are shown in figure 3(a). As can be seen, the amplitude of the EXAFS decreases slightly on going from the solid to the solution, while the frequency is essentially the same. The decrease in amplitude may indicate a decrease in coordination number or may also be indicative of heavier atoms in the solid being replaced by lighter atoms in solution. This agrees with the conclusions drawn from the edge data. Because the frequencies of the Pt EXAFS are relatively the same in solid and solution, it may be that the same element or one of similar weights surrounds the absorber in both solid and solution.

The corresponding Fourier Transforms for the Pt-Std solid and solution EXAFS are shown in figure 3(b). As can be seen from the graph the peak intensity greatly decreases from solid to solution. Similar to the decrease in EXAFS amplitude, the

decrease in peak intensity indicates a decrease in coordination number and/or lighter atoms ligated to the Platinum. The relative distances of the peak from the absorber however remains constant and therefore supports the previous assumption that same element or one of similar weight surrounds the atom in both solid and solution.

ii. Solid Fit (Figure 4, Table 2)

The k^3-weighted data and fits for the solid form of Pt-Std with the corresponding Fourier Transforms (k=2-15 $Å^{-1}$) are shown in Figure 4. FEFF-based fits were preformed, and the data were best fit by 4 Pt-Cl at 2.30 Å and 1 Pt-N at 2.02 Å (Figure 4b). The fit for 4 Pt-Cl at 2.30 Å (Figure 4a) was also reasonable. But, as previously discussed, evidence suggests that the solid Pt-Std is not merely a platinum tetrachloride complex. Also as can be seen from Table 1 there was a decrease in the normalized error when a nitrogen atom was added to the platinum tetrachloride, which indicates that the 4 Pt-Cl with 1 Pt-N is the more likely structure of the solid Pt-Std.

iii. Solution Fit (Figure 5, Table 2)

The k^3-weighted data and fits with the corresponding Fourier transforms for the dilute form of Pt-Std are shown in Figure 5. However, it should be noted that the EXAFS were only usable out to k=12 $Å^{-1}$, which greatly reduced the resolution. Therefore, because sulfur and chlorine are so close in atomic number, the fits for Pt-Cl or Pt-S vectors were indistinguishable. The structure is most likely a mixture of Pt-Cl and Pt-S with Pt-N because, as previously noted, the intensity of the Fourier transform from solid to solution decreased indicating the replacement of chlorine for a lighter atom.

The best fit was obtained by inclusion of 4 Pt-S/Cl at 2.30 Å and 1 Pt-N at 2.03 Å (Figure 5c). A very similar fit resulted in the inclusion of 3 Pt-S/Cl at 2.31 Å and 2 Pt-N at 2.08 Å (Figure 5a). Although the error for 4 Pt-S/Cl with 1 Pt-N is slightly lower (as shown in Table 2) it is less likely that this is the correct structure of dilute Pt-Std since previous examinations of the solid and solution Pt-Std edges and EXAFS indicated lighter atoms present in the solution. Another possibility, however is that the nitrogen is only loosely associated with the Pt which could account for the dilute Pt-Std edge being at a slightly higher energy than the solid.

Another very similar fit was obtained by 2 Pt-Cl/S at 2.33 Å and 3 Pt-N at 2.12 Å (Figure 5b). It should be noted however that coordination to the streptidine ligand via 3 nitrogens would be sterically quite hindered, and thus it is possible that one of the light atom interaction may be attributed to an oxygen atom from H_2O. Also, it should be emphasized that there not enough evidence to distinguish between the three possible structures. The three fits are far too similar.

IV.CONCLUSION

The results of this study show that the solid Pt-Std ($C_8H_{18}N_6O_7Cl_4Pt$) is not merely a platinum tetrachloride . This is demonstrated by the comparison of Pt L_3-edge XAS results of the Pt-Std and $PtCl_4$ which shows a significant difference between the two complexes. EXAFS data on the solid and solution Pt-Std show that the Pt-Std undergoes a change from solid to solution. More specifically, there are lighter atoms present in the solution Pt-Std. This is supported by examining the corresponding Fourier Transforms which also indicate lighter atoms in solution.

Furthermore, it can be concluded that Platinum is in fact coordinated to the streptidine through a bond with nitrogen. In the solid, the streptidine is coordinated to the Pt by one nitrogen at 2.02 Å. In the solution the streptidine could be coordinated to 1-3 nitrogens. This is shown by analysis and fitting of the EXAFS data of the solid and solution Pt-Std.

Future work should include the determination of how many chlorine and sulfur atoms are ligated in the solution structure and also the determination of how many nitrogens are coordinated to the dilute Pt-Std. This can be done by further XAS experiments to obtain Pt L_3 edge data at higher k. Data obtained to higher k would give an increased resolution rendering a better distinction between the sulfur and chlorine atoms. Another alternative would be to examine the edge of another element in the complex, such as chlorine. This would give additional information about the structure of the complex.

V.ACKNOWLEDGMENTS

This research was conducted at the Stanford Synchrotron Radiation Laboratory at the Stanford Linear Accelerator Center. I thank the U. S. Department of Energy, Office of Science for giving me the opportunity to participate in the SULI program and giving me this wonderful learning experience. Special thanks go to my mentor Serena DeBeer George for her patience and guidance. I also thank Apruva Metha for his stimulating lectures. And last, but definitely not least, I would also thank Martin George, who fixed my laptop computer! ☺

VI.REFERENCES

1. Reedijk, Jan. “Why Does Cisplatin Reach Guanine-N7 with Competing S-Donor Ligands Available in the Cell?” Chemistry Review (Aug. 1999): 2499-2510.
2. Wong, Ernest, and Christen Giandomenico. “Current Status of Platinum-Based Antitumor Drugs.” Chemisty Review (Aug. 1999): 2451-2466.
3. Aliaga-Alcalde, N, and Jan Reedijk. “Pt-Std (Platinum-Streptidine Complexes).” Scientific Paper. U of Leiden, Netherlands.
4. Cramer, Stephen P, and Keith O Hodgson. “X-Ray Absorption Spectroscopy: A New Structural Method and Its Applications to Bioinorganic Chemistry.” Progress in Organic Chemistry. Ed. Stephen J Lippard. Vol. 25. N.p.: John Wiley & Sons, 1979. 7-37.
5. George, G.N. EXAFSPAK; Stanford Synchrotron Radiation Laboratory, Standard Linear Accelerator Center, Stanford University, Stanford CA 94309.
6. Mustre de Leon, J.; Rehr, J.J.; Zabinsky, S. I.; Albers, R.C. *Phys. Rev. B* **1991**, *44*, 4146-4156.
7. Rehr, J.J.; Mustre de Leon, J.; Zabinsky, S. I.; Albers, R.C. *J. Am. Chem. Soc.* **1991**, *113*, 5135-5140
8. The Cambridge Structural Database. CD-ROM. Vers. 1.9. 2007.
9. George, Serena DeBeer, et al. “Spectroscopic Investigation of Stellacyanin Mutants: Axial Ligand Interactions at the Blue Copper Site.” Journal of American Chemical Society (Aug. 2003): 11314-11328. 25 July 2007 <http://www.pubs.acs.org>.

10. Scott, Robert A. “X-Ray Absorption Spectroscopy of Metallobiomolecules.” CMS. Fall 2007. Rpt. in EXAFS.

TABLES

Fits	Component	CN	R(A)	$\sigma^2(A^2)$	E_0(eV)	Normalized Error(χ^2) F/(No.pts)	Reduced Error(χ^2) F/(No.pts-No.Vars)
Fit 1	Pt-Cl	4	2.304907	0.002451	-5.996988	0.567001	0.574148
Fit 2	Pt-Cl Pt-N	4 1	2.303149 2.018205	0.002311 0.006925	-6.960680	0.547486	0.558014
Fit 3	Pt-Cl Pt-N	4 2	2.303241 2.020574	0.002332 0.013314	-7.083107	0.556331	0.567029
Fit 4	Pt-Cl	3	2.304137	0.001301	-6.346557	0.657848	0.670499
Fit 5	Pt-Cl Pt-N	3 1	2.314112 2.143173	0.001308 0.000541	-4.339458	0.657848	0.670499
Fit 6	Pt-Cl Pt-N	3 2	2.316230 2.157105	0.001471 0.002038	-3.440386	0.626655	0.638706

Table 1: Fit Results for the solid Pt L3 XAS Data

Fits	Component	CN	R(A)	$\sigma^2(A^2)$	E_0(eV)	Normalized Error(χ^2) F/(No.pts)	Reduced Error(χ^2) F/(No.pts-No.Vars)
Fit 1	Pt-S/Cl	4	2.297600	0.005870	-4.376000	0.420567	0.426844
Fit 2	Pt-S/Cl Pt-N	4 1	2.297591 2.026988	0.005589 0.005848	-5.306335	0.358606	0.367616
Fit 3	Pt-S/Cl Pt-N	3 1	2.308216 2.065793	0.003563 0.000716	-3.874737	0.388795	0.398564
Fit 4	Pt-S/Cl Pt-N	3 2	2.310000 2.082000	0.004120 0.005820	-3.467305	0.362555	0.371664
Fit 5	Pt-S/Cl Pt-N	3 3	2.307600 2.095000	0.004480 0.010780	-3.301708	0.371329	0.380658
Fit 6	Pt-S/Cl Pt-N	2 2	2.328183 2.103048	0.001509 0.000891	-1.346530	0.415886	0.426335
Fit 7	Pt-S/Cl Pt-N	2 3	2.327185 2.113151	0.002211 0.004120	-1.088723	0.388843	0.398613

Table 2: Fit Results for the solution Pt L3 XAS Data

FIGURES

(a)

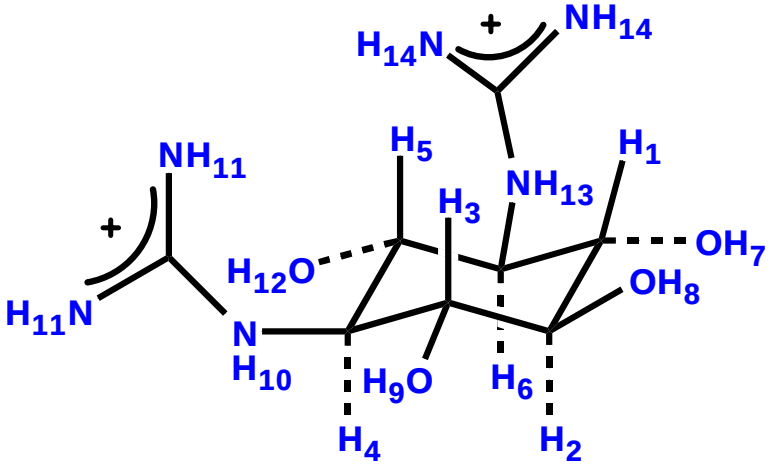

(b)

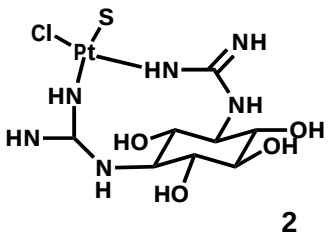

(c)

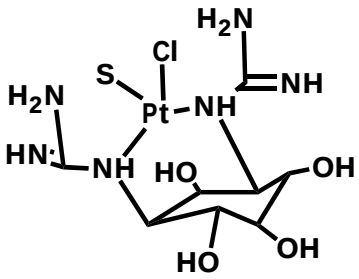

Figure i: (a) Diagram of Streptidine[1] (b), (c) Putative structures[1]

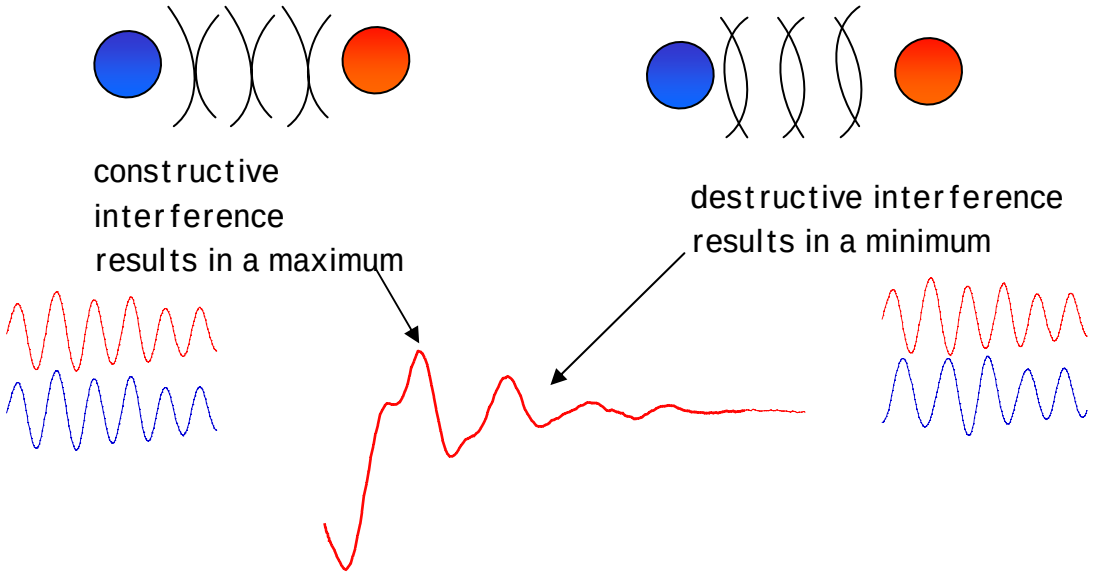

Figure ii: Diagram of EXAFS: constructive interference between the photoelectron wave and the backscatter wave results in a local maximum in the while destructive interference results in a local minim.

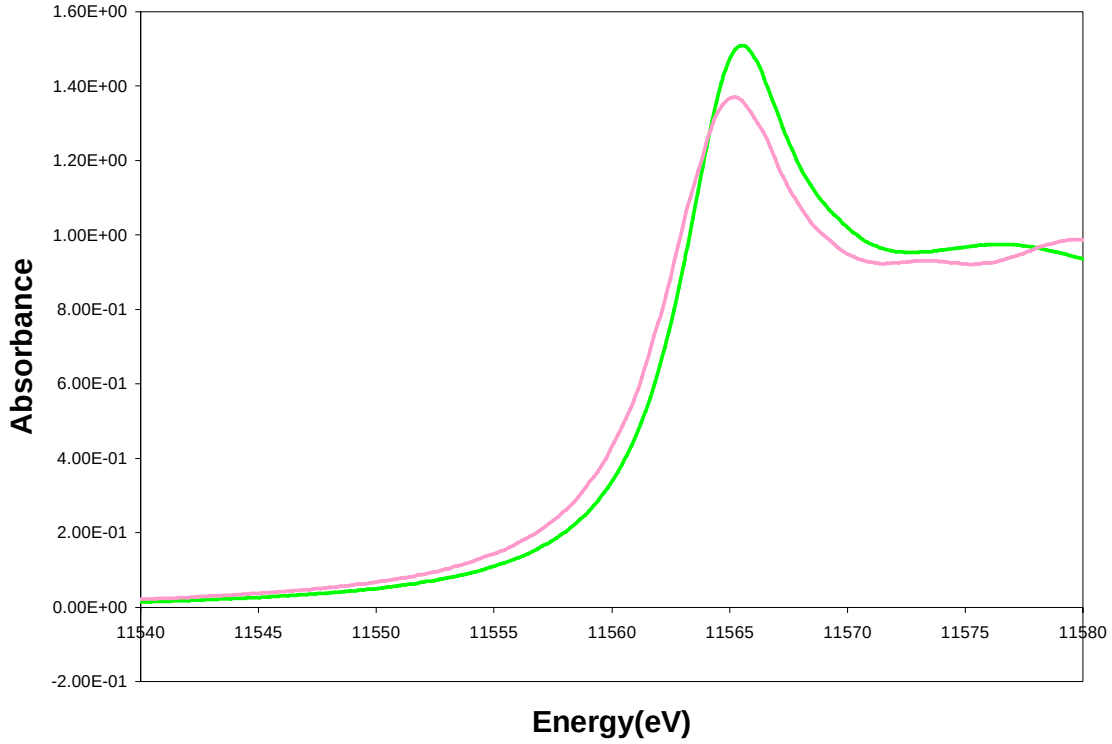

Figure 1: Comparison of the Pt L3-edge spectra of Solid Pt-Std ($C_8H_{18}N_6O_7Cl_4Pt$) (—) and platinum tetrachloride (K_2PtCl_4) (—).

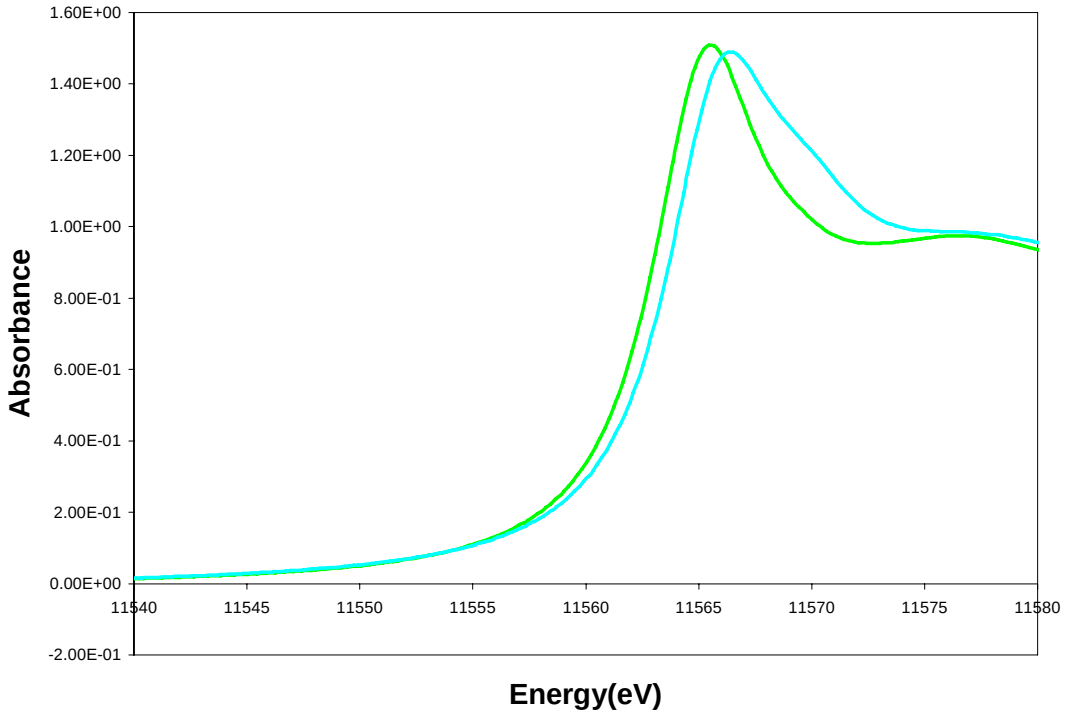

Figure 2: Comparison of the Pt L3-edge spectra of Solid (—) and Solution (—) Pt-Std

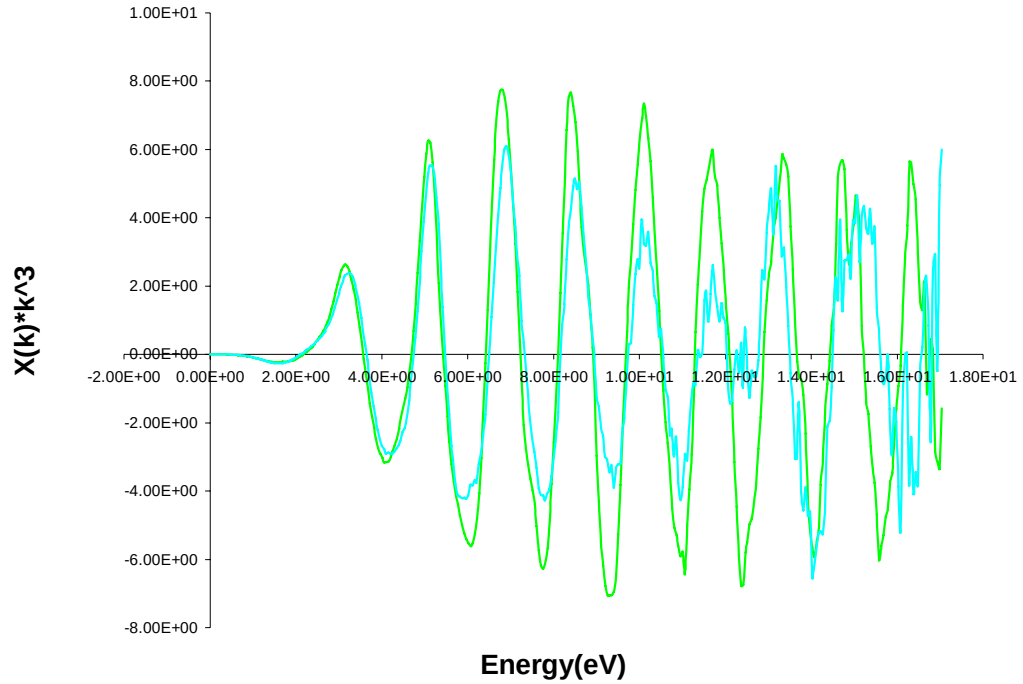

(a)

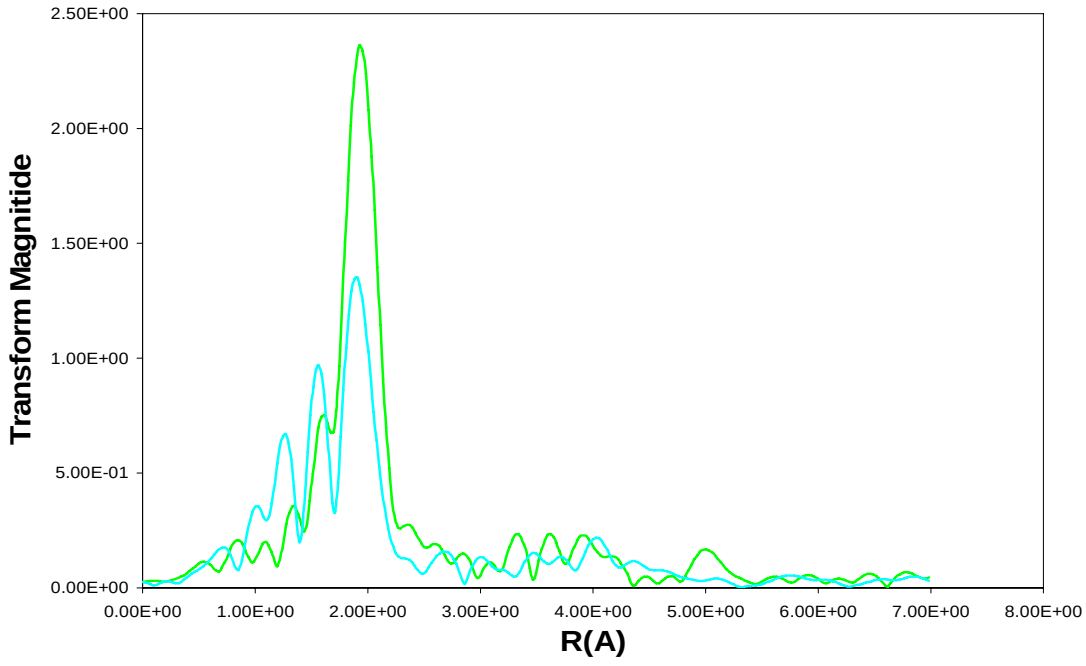

(b)

Figure 3: (a) Experimental EXASFS data for solid (—) and solution (—) Pt-Std (b) non-phase-shift corrected Fourier Transforms

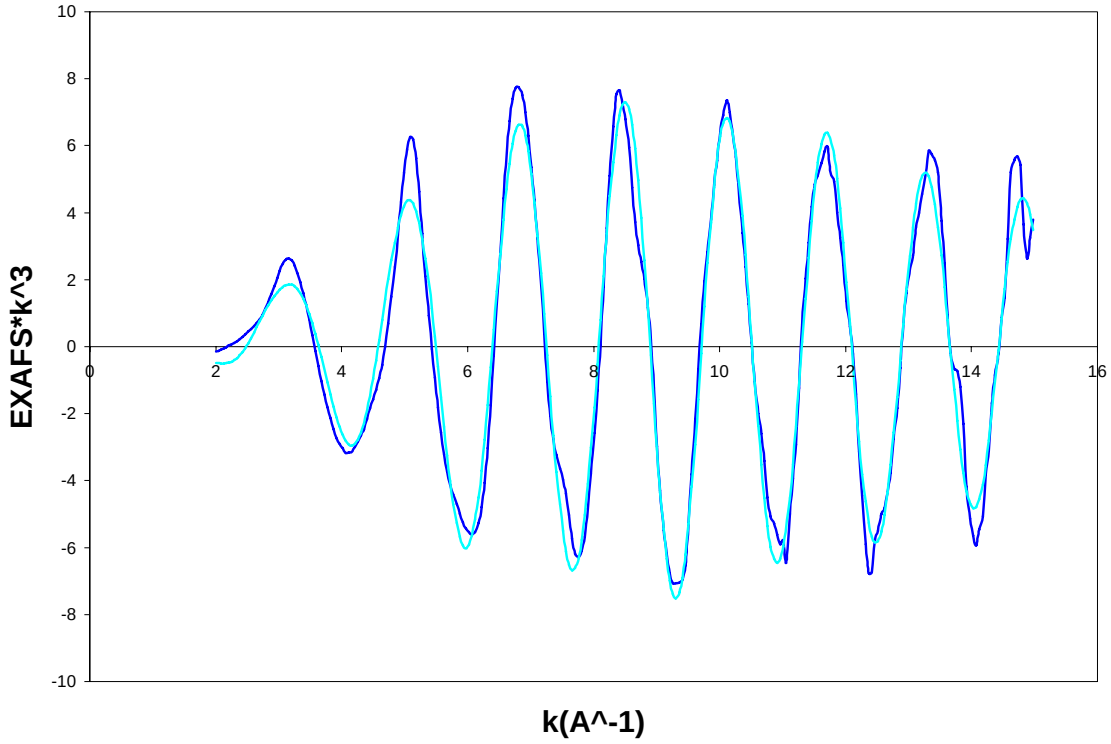
EXAFS*k^3
k(A^-1)
10
8
6
4
2
0
-2
-4
-6
-8
-10
0
2
4
6
8
10
12
14
16

(a)

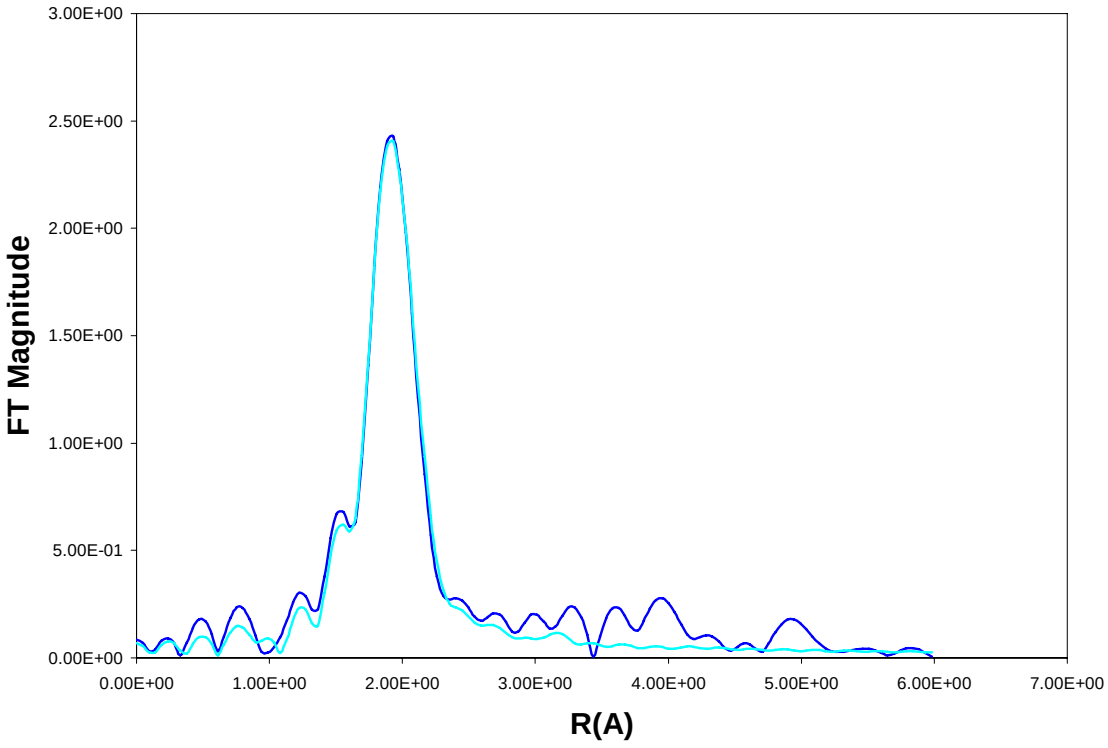
FT Magnitude
R(A)
3.00E+00
2.50E+00
2.00E+00
1.50E+00
1.00E+00
5.00E-01
0.00E+00
0.00E+00
1.00E+00
2.00E+00
3.00E+00
4.00E+00
5.00E+00
6.00E+00
7.00E+00

(b)

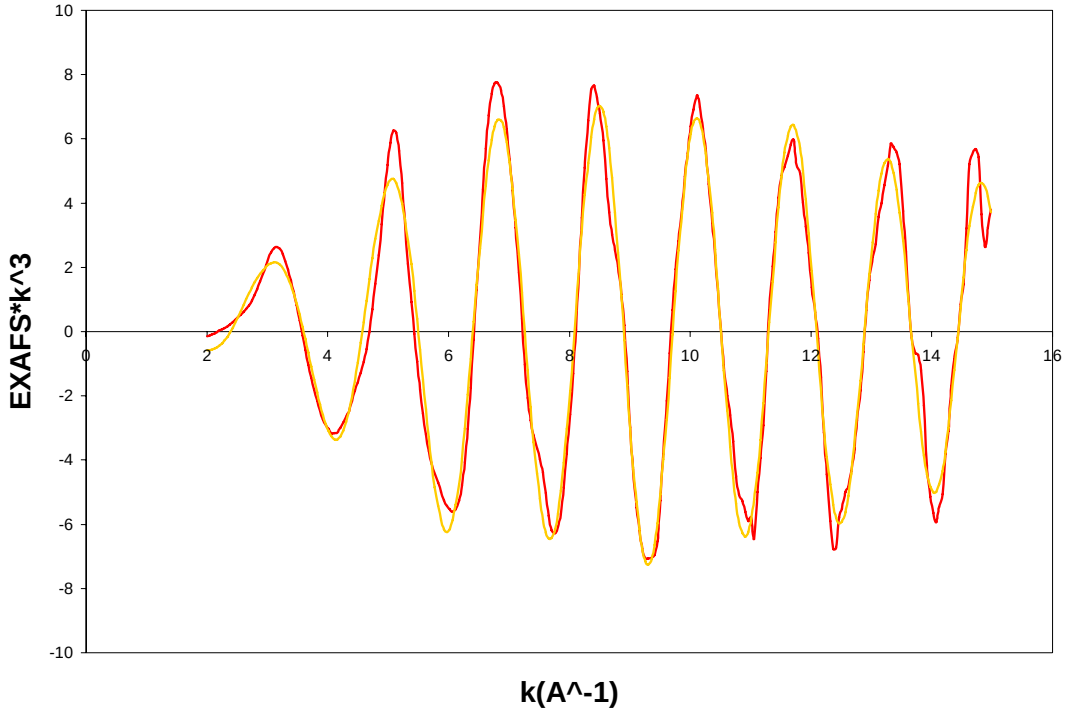

(c)

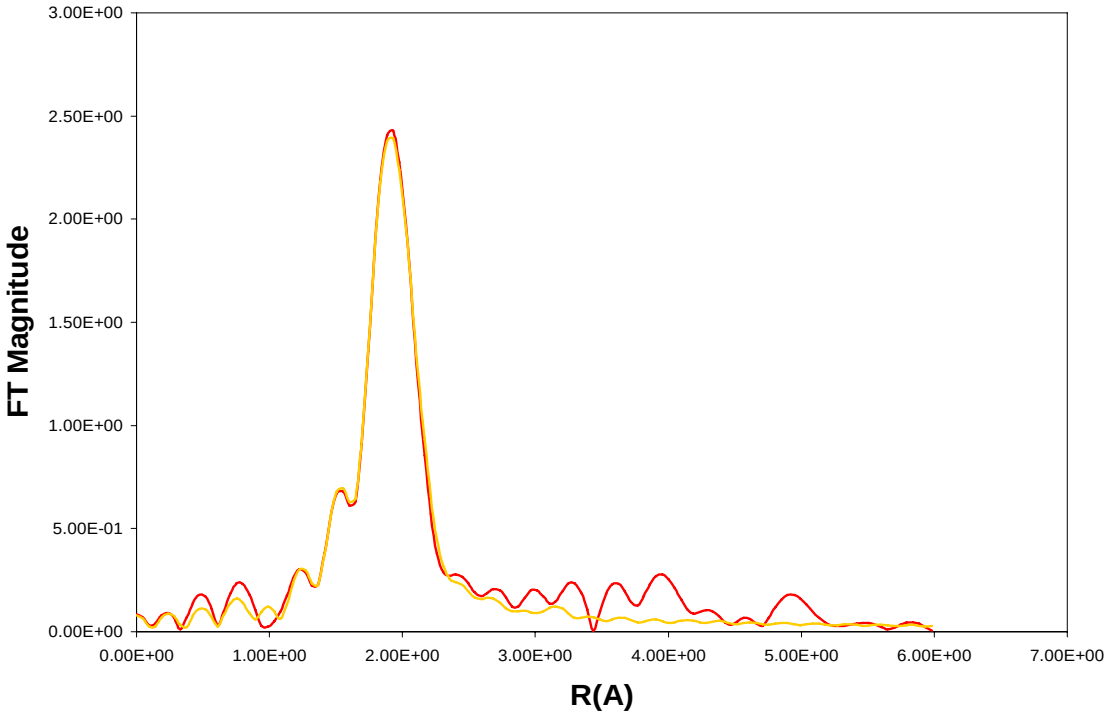

(d)

Figure 4: (a) Experimental EXASFS data(—) and fits(—) for the solid Pt-Std, Fit 1: 4 Pt-Cl at 2.30 Å (b) corresponding Fourier Transforms and fit, Fit 1 (c) EXASFS data(—) and fits(—) for the solid Pt-Std, Fit 2: 4 Pt-Cl at 2.30 Å and 1 Pt-N at 2.02 Å (d) corresponding Fourier Transforms and fit, Fit 2

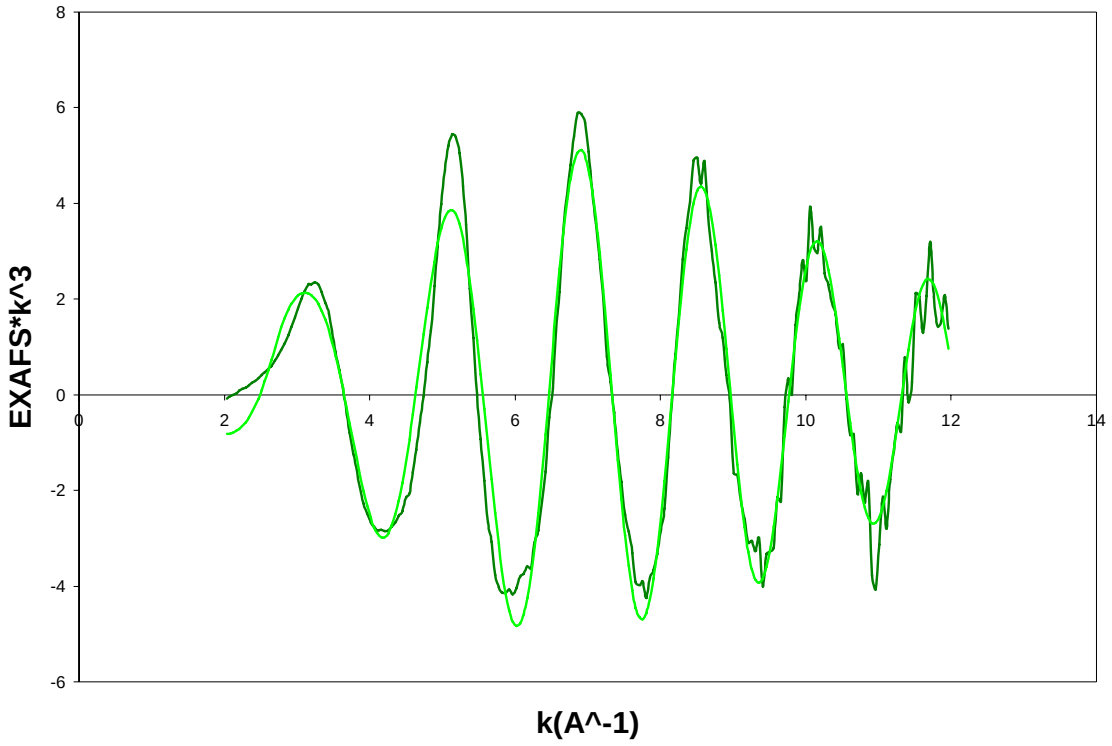
EXAFS*k^3
k(A^-1)
8
6
4
2
0
-2
-4
-6
0
2
4
6
8
10
12
14

(a)

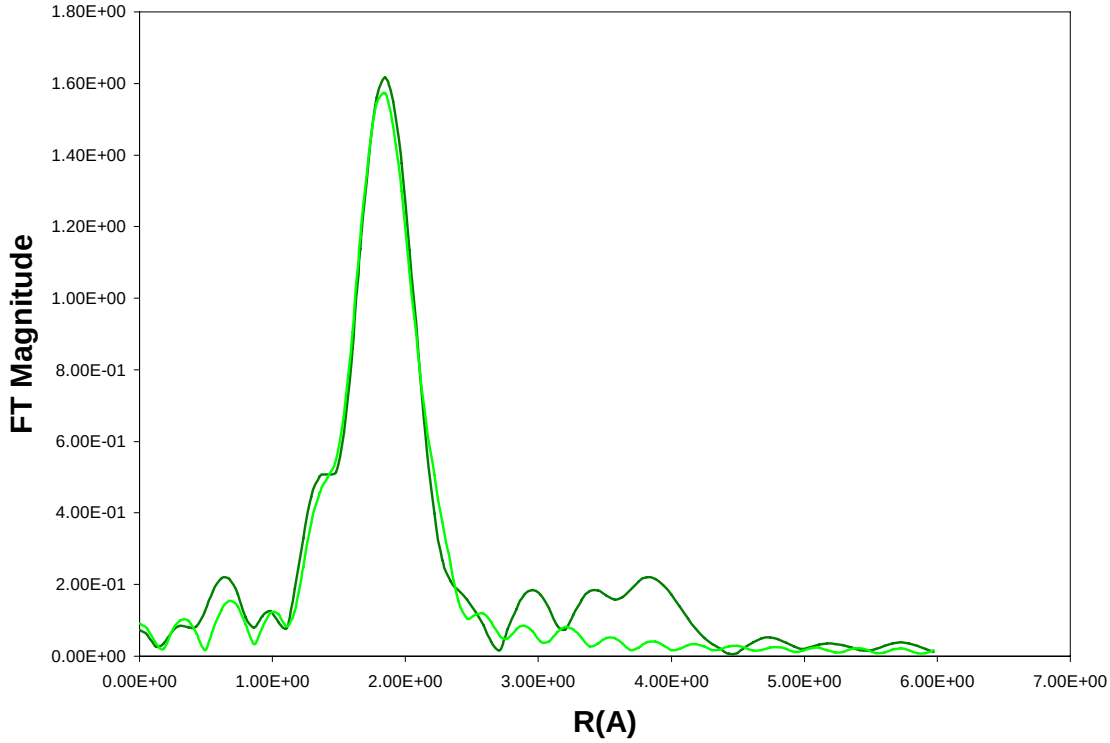
FT Magnitude
R(A)
1.80E+00
1.60E+00
1.40E+00
1.20E+00
1.00E+00
8.00E-01
6.00E-01
4.00E-01
2.00E-01
0.00E+00
0.00E+00
1.00E+00
2.00E+00
3.00E+00
4.00E+00
5.00E+00
6.00E+00
7.00E+00

(b)

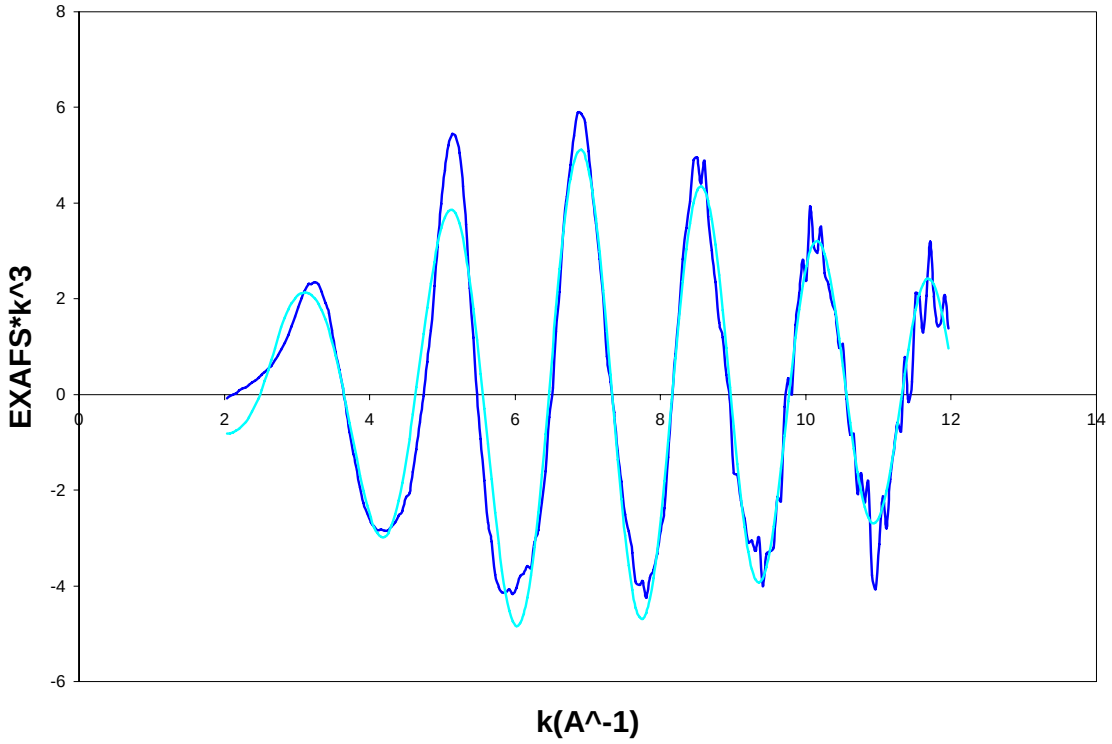
EXAFS*k^3
k(A^-1)
8
6
4
2
0
-2
-4
-6
0
2
4
6
8
10
12
14

(c)

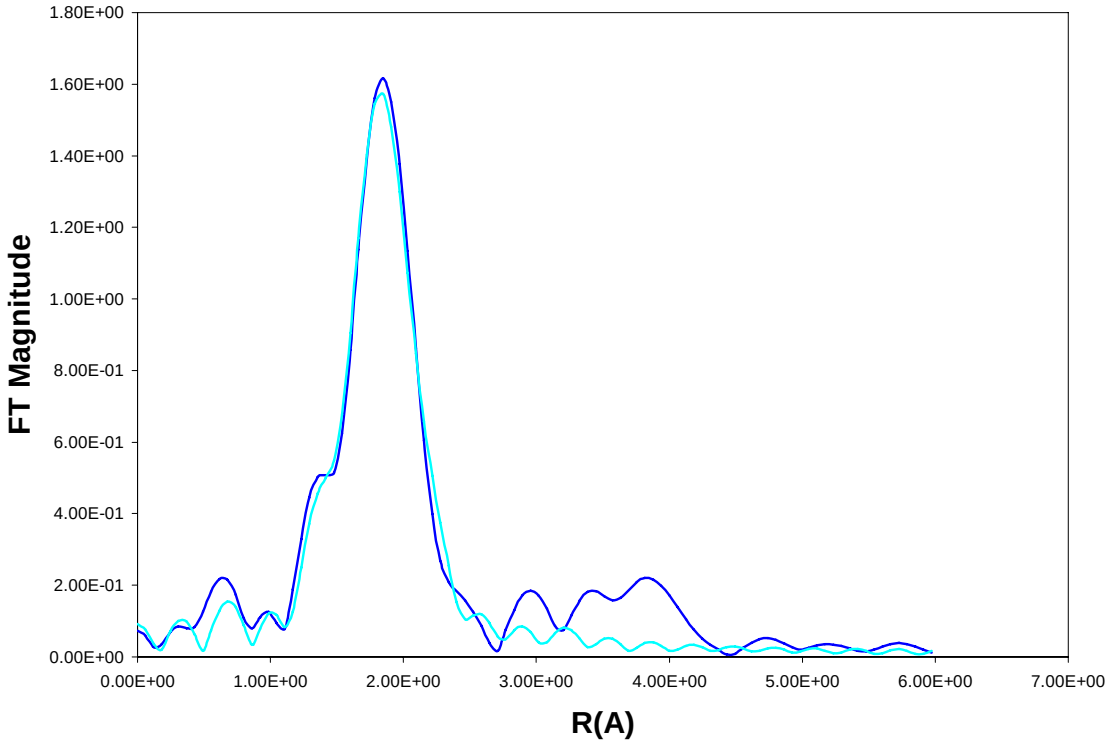
FT Magnitude
R(A)
1.80E+00
1.60E+00
1.40E+00
1.20E+00
1.00E+00
8.00E-01
6.00E-01
4.00E-01
2.00E-01
0.00E+00
0.00E+00
1.00E+00
2.00E+00
3.00E+00
4.00E+00
5.00E+00
6.00E+00
7.00E+00

(d)

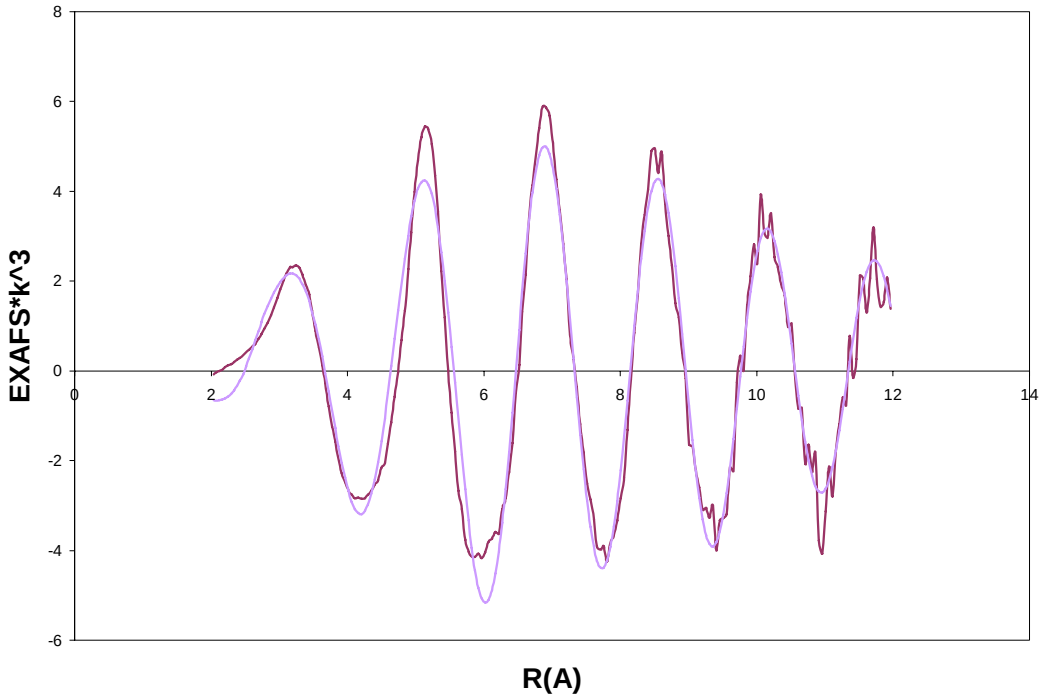

(e)

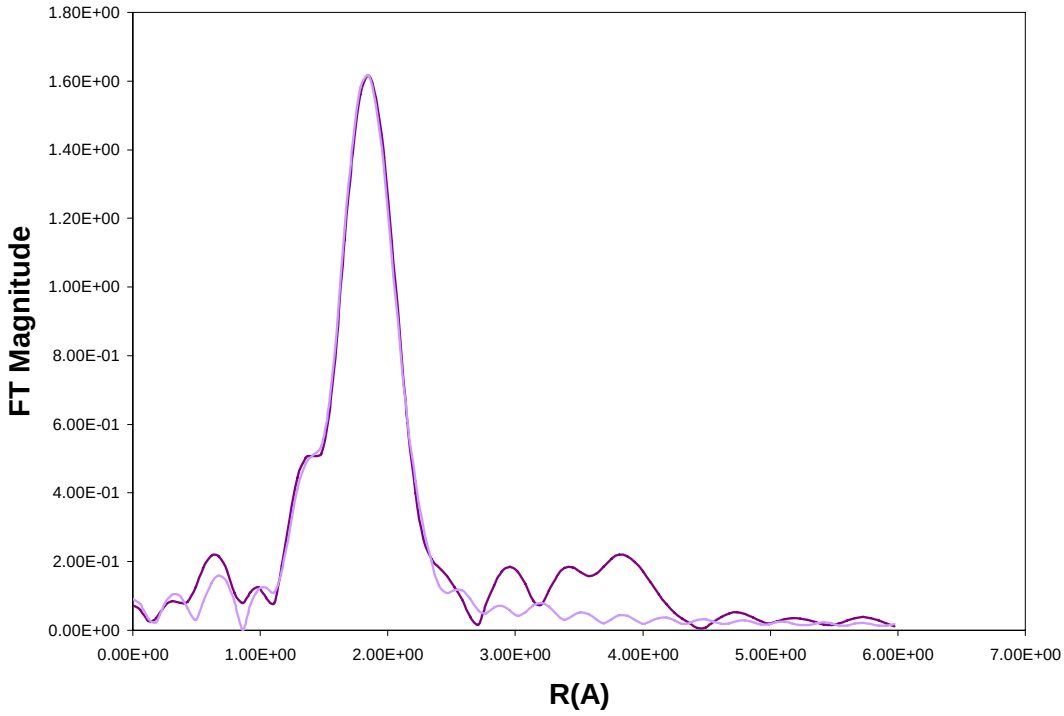

(f)

Figure 5: (a) Experimental EXASFS data (—) and fits (—) for the solution Pt-Std, Fit 4: 3 Pt-S/Cl at 2.31 Å and 2 Pt-N at 2.08 Å. (b) corresponding Fourier Transforms and fit, Fit 4 (c) EXASFS data (—) and fits (—)for the solid Pt-Std, Fit 7: 2 Pt-Cl/S at 2.33 Å and 3 Pt-N at 2.12 Å (d) corresponding Fourier Transforms and fit, Fit 7 (e) Experimental EXASFS data(—) and fits(—) for the solution Pt-Std, Fit 2: 4 Pt-S/Cl at 2.30 Å and 1 Pt-N at 2.03 Å (f) corresponding Fourier Transforms and fit, Fit 2

SLAC-TN-07-016
August 2007

Long-term X-ray Variability of NGC 4945

Amara Miller

Science Undergraduate Laboratory Internship Program

University of California, Davis

Stanford Linear Accelerator Center (SLAC)

Stanford, CA

August, 2007

Prepared in partial fulfillment of the requirement of the Office of Science, Department of Energy's Science Undergraduate Laboratory Internship under the direction of Grzegorz Madejski, a member of the Kavli Institute at the Stanford Linear Accelerator Center.

Participant: _____
Signature

Research Advisor: _____
Signature

Work supported in part by US Department of Energy contract DE-AC02-76SF00515

Table of Contents

Abstract

Long-term X-ray Variability of NGC 4945. AMARA MILLER (University of California Davis, Davis, CA 95616) GRZEGORZ MADEJSKI (Stanford Linear Accelerator Center, Stanford, CA, 94305).

Though short-term X-ray variability has been studied for the active galaxy NGC 4945, long-term studies promise to contribute to our understanding of the processes involved in accretion onto supermassive black holes. In order to understand the relationship between black hole mass and breaks in the power spectral density (PSD), the long-term X-ray variability of NGC 4945 was studied over the energy range 8-30 keV. Observations occurred over the year 2006 using the *Rossi X-ray Timing Explorer*. The data was reduced using the package FTOOLS, most notably the scripts Rex and **faxbary**. Light curves were produced and a PSD was obtained using a Fast Fourier Transform algorithm. Preliminary studies of the light curve show greater X-ray variability at higher frequencies. This result complements previous studies of NGC 4945 by Martin Mueller. However, the PSD produced must go through further study before accurate results can be obtained. A way to account for the window function of the PSD must be found before the behavior at lower frequencies can be studied with accuracy and the relationship between black hole mass and the break in NGC 4945's PSD can be better understood. Further work includes exploration into ways to subtract the window function from the PSD, as well as a closer analysis of the PSD produced by averaging the data into logarithmic bins. The possibility of a better way to bin the data should be considered so that the window function would be minimized.

1. Introduction

Most galaxies in the universe show little activity beyond what would be expected for a collection of stars and gas. However, a small percentage of observed galaxies (called active galaxies) show extreme activity well above what is considered normal. The accepted theory today is that an active galaxy is powered by accretion of galactic gases onto a supermassive black hole [1], giving it the name of an active galactic nucleus (AGN) [2]. By using Hubble's law in conjunction with the measured redshift, the distance can be obtained and it is clear the luminosity of these objects is unusually high. The mass of the black hole can be constrained from the luminosity and thus the Eddington limit. The rapid variability of X-ray radiation implies that the size of the nucleus is extremely small for the amount of mass present, supporting the theory of black hole accretion. The mass of a black hole is expressed in units of solar mass. One solar mass is equivalent to the mass of the sun, $\sim 2 \times 10^{30}\ kg$, and is expressed by the symbol $M_{\odot}$. Compared to a smaller black hole of mass $1.0 - 3.0\ M_{\odot}$ (such as those inferred to exist in the binary systems of the galaxy), a supermassive black hole can be as large as $10^9\ M_{\odot}$.

According to the model of an accreting supermassive black hole, instabilities within the material orbiting the galaxy begin to redistribute angular momentum and cause matter to spiral inward, forming an accretion disk about the nucleus. The energy released in this process can be emitted as electromagnetic radiation within a wide band range, including X-ray wavelengths. The current model of this process explains the presence of X-ray emission through inverse Compton scattering. This occurs when lower energy photons are scattered to higher energies when they interact with nearly-relativistic electrons in the hot gaseous material of the accretion disk. The cold material farther from the nucleus radiates as emission lines. Taking into account these effects, the observed broad-

band spectrum from AGNs can be explained. However, the exact processes involved are not fully understood, and the black hole model is not yet completely confirmed. Despite difficulty in understanding AGN, they display strong cosmological evolution which furthers the study of the early universe. Most of the knowledge we have about the intergalactic medium comes from the study of absorption lines in the spectra of distant quasars [2], one class of AGNs.

Both light curves and spectra are used to study AGNs. A light curve is a graph of the light intensity of an observed object as a function of time. In this project the term spectrum refers to a power spectral density (PSD), a graph of the variability amplitude of the light curve plotted against the frequency of variability. This amplitude often takes the shape of a powerlaw. However, at a certain point this powerlaw must break into a different structure since a single power law is divergent mathematically. According to [3] and [4], there is a strong correlation between the black hole mass of an AGN and its associated PSD break amplitude. The break amplitute is where the single power law description is no longer applicable to the data. This relationship is not fully understood, and it is the goal of this paper to explore this correlation using data obtained for NGC 4945.

NGC 4945 is a nearby, edge-on starburst galaxy with an active nucleus of the Seyfert type 2 classification. In the first few X-ray studies, the data revealed a heavily obscured, strong, hard X-ray source above 10 keV. Because the circum-nuclear material is partially optically thick to electron scattering, the absorbing column is one of the largest ($\sim 10^{24}$ cm^{-2}) that still allows a direct view of the nucleus at hard x-ray energies (see Figures 4 & 5). NGC 4945 is a megamaser source, implying the edge-on geometry mentioned previously. It is one of only a few AGNs for which the black hole mass can

be constrained (at $\sim 1.4 \times 10^6\ M_\odot$) from detailed mapping of the megamaser spots [5]. It has been determined that this object has a high variability on short time scales, but in order to determine the properties of this active galaxy more accurately, the variability on longer time scales is studied below using data collected by the *Rossi X-ray Timing Explorer (RXTE)*. This project will supplement data that has been obtained and studied in previous experiments. Because of the unique position of knowing the black hole's mass reliably, the data collected will further our understanding of the relationship between the break in the PSD of an AGN and it's black hole mass [6]. It will also contribute to the study of the structure of AGNs, as well as our understanding of how and why X-ray radiation is produced.

The low-earth orbit satellite *RXTE* features unprecedented time resolution combined with a moderate spectral resolution and broad-band X-ray sensitivity, making it ideal for studying the variability of cosmic X-ray sources. It carries two instruments, both of which will be used in this study: the Proportional Counter Array (PCA) and the High Energy X-ray Timing Experiment (HEXTE) [7]. More about the data collected from the *Rossi XTE* is discussed at greater length below.

2. Materials and Methods

In order to fully analyze the data from *RXTE*, light curves and spectra had to be produced. However, a PSD of all the observations of NGC 4945 was not immediately available from the data collected by *RXTE*, so various reduction processes took place prior to the final analysis. In addition, there are inherent limitations associated with the duration and sampling rate of the observation that restrict the range of frequencies that can be analyzed using a Fast Fourier Transform (FFT) algorithm on the spectrum. Data

reduction scripts used were obtained from the HEASARC website, including the packages FTOOLS (a data analysis package for astronomical applications) and XANADU (a suite of spectral, timing, and image analysis programs). The file format used was the HEASARC standard Flexible Image Transport System (FITS).

Every four days over the course of the year 2006 NGC 4945 was observed for ∼40 minutes. In this project both PCA and HEXTE data were used to study the energy range from 8-30 keV. The PCA on *RXTE* contains five proportional counters referred to as PCUs 0-4, each with one propane layer and 4 Xenon layers operating within an energy range of 2-60 keV [7]. PCUs 0, 3, and 4 were not on during the entire observation, and as of December 25, 2006, PCU 1 developed a leak in it's propane layer. Because the background data for PCU 1 would not be accurate for all the data collected, as well as the fact that it was on for only a minimal amount of time during data collection, PCU 1 data was not used in the analysis. For these reasons it was necessary to ignore data from PCUs 0-1 and 3-4 and only use PCU 2 to extract light curves and spectra from NGC 4945.

HEXTE consists of two clusters of 4NaI/CsI phoswich scintillation detectors that are sensitive to X-rays from 15- 250 keV [8]. Because this energy range does not cover the lower energy X-rays within our desired data set, HEXTE was mainly used to check the data and the reduction process. Data from cluster 1 of the HEXTE system was used when producing light curves and spectra.

PCA data were reduced according to the restrictions discussed above using standard *RXTE* analysis tools, most notably Rex, a component of FTOOLS. Rex is script designed to run through the basic data reduction of PCA and HEXTE for multiple observations. Rex initially read the index files in the database structure and proceeded to filter the

data. After the filtering process was complete, the program then produced a model background file which was subtracted from the results [9]. The background file used in analysis of PCA data was the most recent available from the HEASARC website for faint sources, pca_bkg_cmfaint17_eMv20051128.mdl. The energy channels analyzed were 18-73, the equivalent of 8-30 keV (the energy range desired in this study). Rex was then run on the Cluster 1 HEXTE data for the 7-41 channel range, corresponding to ∼12-100 keV. There were ∼ 150 different observations of NGC 4945 over the course of 2006, and Rex produced a combined light curve and raw spectrum for all observations. These light curves and spectra were then analyzed with the tools **lcurve** and **xspec** to check the data for accuracy (i.e., no obvious spikes or instabilities).

Because the observations of NGC 4945 occurred over such a long time frame, it was necessary to consider the revolution of the earth about the sun. This revolution places the satellite at a greater distance from the source half the year, and the additional light travel time must be accounted for in the results. The correction is often called the Barycenter Correction, a procedure that has been built into a tool called **faxbary**, part of the HEARSARC software FTOOLS. Before running **faxbary**, a list file was created containing all orbit files that covered the entire length of the observation (Days 4450 to 4875). **Faxbary** was then applied to both HEXTE and PCA data using the most accurate clock corrections in the file tcd.dat. After running the script, a copy of the original light curve file with an additional column, BARYTIME, was created. This additional column contained the corrected timing data for the observation.

In order to produce a PSD using a Fast Fourier Transform algorithm, it was necessary to place the timing data into consecutive time bins. The desired result would bin the data collected from each day into an individual "newbin." Because the satellite only

collected data on NGC 4945 approximately every 4 days, and on each of those days had multiple 16 s observations, this binning took three steps. Initially, a basic C program was written using the FITSIO library of C subroutines for reading and writing data files in FITS data format. This program took the barycentric corrected times and subtracted the initial time of the observations from each value. It then divided the resulting value by 16 s and rounded the remainder to the nearest integer, creating a list of the equivalent 16 s binned times.

Another C program was written to output the start and end row/bin numbers, as well as the number of 16 s observations and the gap size between observations that occurred every 4 days. This table was analyzed and a new rebinning time of 16200 s (and offset of 137) was determined. This new rebinning time was able to place observations that were obtained on the same day into the same interval. A program was written to place the 16 s bins calculated in the previous step into these larger bins corresponding to the sampling which took place $\sim 3-4$ days. The larger bins were intervals within which the count rates were averaged. The error for the count rate was also calculated, using the formula

$$c = \frac{1}{N}\sqrt{\sum_{i}^{N}(a_i)^2}$$

where c is the averaged error for a newbin, N is the number of data entries averaged, and a_i is the i^{th} data entry for the error. Thus the output of the final rebinning was a fits file containing three rows: the averaged count rate per newbin, the error per newbin, and the time corresponding to the newbin. The time was calculated using $t_n = n\Delta$, where Δ is the time step (the rebinning time 16200 s multiplied by 16 s) between each n^{th} entry.

A Fast Fourier Transform algorithm was run on the final rebinned data and used to create a PSD for NGC 4945. A physical process can be described as some quantity

as a function of time, $h(t)$, or as the process's amplitude as a function of frequency, $H(f)$. A Fourier Transform is a mathematical expression relating these two different representations of the same process. The equations for a Fourier Transform are

$$H(f) = \int_{-\infty}^{\infty} h(t) e^{2\pi i f t} \, \mathrm{d}t$$
$$h(t) = \int_{-\infty}^{\infty} H(f) e^{-2\pi i f t} \, \mathrm{d}f \tag{1}$$

In a process involving complex values (such as a wave function) $H(f)$ would differ throughout the frequency range of $-\infty < f < \infty$. Because the discrete values dealt with in this project, $H(f) < 0$ is a reflection about the y axis of $H(f) > 0$. The algorithm called *realft* found in Numerical Recipes [10] was used, since the data analyzed was both discrete and real. This algorithm took the averaged count rate for the rebinned times and produced as output the transformed power values. These values corresponded to both the real and imaginary components for a corresponding frequency. To obtain the amplitude, which was the desired result, the program then squared both the real and complex components and added them together.

As stated previously, there are inherent limitations associated with the sampling rate of the observation that restrict the range of frequencies that can be analyzed using a Fast Fourier Transform (FFT) method on the spectrum. A window function is a set of data which has the same sampling as the data used to obtain the desired PSD, and so is able to show the inherent limitations associated with the specific sampling process. To check the results of the PSD, a window function of the rebinned data was produced by creating a parallel set of data that had gaps in the same locations as the PCA count rates and the value one in every location that a value existed in the actual data set. This correlated set

of values was then run through an FFT to produce a new fits file that was used to graph a "blank" PSD showing the inherent errors in a PSD with the same data sequence.

3. Results

As described above, after running Rex the light curves and spectra were then analyzed with the tools **lcurve** and **xspec** to check if the data appeared accurate. Figure 1 and Figure 2 show the two light curves produced for PCA and HEXTE data using **lcurve**. Both have a newbin time of 86400 seconds. The average count rate for data collected by the PCA is 1.19 counts/s. The average count rate for data collected by HEXTE is slightly smaller at 1.02 counts/s. The count rates of both the PCA and HEXTE data do not vary significantly from the average count rate over the course of the year. There is a data gap after the first three data points up to $\sim 6 \times 10^6$ s. The data are then continuous, though there are regular, periodic, linear increases in the count rate in Figure 1. These periodic increases are harder to see in Figure 2. The error for the HEXTE data (Figure 2) is greater than that seen on the PCA data (Figure 1).

Figure 3 compares the two light curves for PCA and HEXTE data. Plotting one against the other, the mean line nearly has a slope of one, indicating that the two sets of data correlate, paralleling each other in shape. Errors on this graph are not included, but are $\sim 0.1 - 0.2$, or 10%. With errors included, it is possible the two sets of data correlate better than shown. The fact that they correlate in Figure 3 implies that the data reduction process was sucessful and that there were no unexpected jumps or discontinuities.

The raw data obtained from Rex was also analyzed with **xspec** to see if the energy spectrum was consistent with previous observations of NGC 4945. The model used was

a powerlaw, plus a Gaussian emission line (due to the presence of iron, commonly seen in AGN), plus a photoelectric absorption to which there was added another powerlaw (to account for nearby weak x-ray sources that were also included in the field of view). This was run on both the PCA and HEXTE data, as shown in Figures 4 and 5. This model was very rough with a chi-squared was 367.83 for 82 bins, or the reduced chi-squared was 4.9706 for 74 degrees of freedom. The large chi-squared is most likely due to the poorly modeled low energy region, in which there are fluctuations outside of the predicted model.

Figure 4 shows the modeled data along with the residuals of the model. The PCA data is the first unbroken line of data covering the range 3-30 keV. The second line in the graph from 30-80 keV is of the HEXTE data, which observes at higher energies. Most of the residuals are within the 3 to 7 keV range where there are fluctuations in the data. These low energy residuals are probably due to inadequately modeling of the host galaxy, but are not relevant to the study of NGC 4945 since we are interested in higher energies. Figure 5 is graphed in a logarithmic space. It is clear from this graph that the HEXTE and PCA data closely follows the model, with no obvious breaks at energies higher than 7 keV. As touched on earlier, there are minor fluctuations in the low energy range of 3 to 7 keV.

Figure 6 shows the PSD obtained from the FFT transform. It is graphed on a logarithmic scale with power and as a function of frequency. From the beginning of the graph to $5 \times 10^{-7} Hz$ the power jumps up and down, starting very large and oscillating in sharp peaks. From $5 \times 10^{-7} Hz$ to the end of the graph the data also fluctuates up and down in spikes, but it is less sporadic and there is a clear linear increase with a slope of ~ 1. Figure 7 shows the Window Function for the PSD in Figure 6. The window function

shows similar jumps in the data from the beginning of the graph to $\sim 5 \times 10^{-7} Hz$, after which the oscillations begin to level off and show a constant average for the remainder of the graph. This behavior is unusually sporadic. It was expected that the data set would begin large, drop suddenly after the initial data points, and then oscillate in a series of jumps until it reached zero. Such a graph would accurately represent what would appear should the sampling be a gap followed by a large block of data. This window function is unexpected, with uneven jumps and no sudden drop.

4. Discussion and Conclusion

According to Figure 1, the average count rate does not change significantly over the course of the observation, implying that there is little variability on long time scales. There does appear to be variability on smaller time scales of approximately several weeks to a month as indicated by the linear increases in count rate at periodic intervals. This is promising, for it would imply the data collected correlates with previous studies. However, looking at Figure 6 there is little indication of variability at shorter time scales. Though there is a linear increase at higher frequencies, it is on the order of f^1, which is an unexpected result. It is expected that the PSD should portray a f^{-1} decrease, or no rise at all. When comparing Figure 6 to its window function in Figure 7, it is possible that the uneven power at lower frequencies is being reflected onto higher frequencies, and thus causing a linear increase to appear. The window function also shows similar jumps in power at lower frequencies, implying that these unusual attributes of the PSD are also a product of the way the data set is sampled. This makes it impossible to analyze the PSD until a way can be developed to account for the window function.

Because the PCA and HEXTE data correlate (shown in Figure 3), it is inferred that

the variability of NGC 4945 is intrinsic rather than extrinsic. PCA and HEXTE detectors work within different energy ranges, and if the light curves correspond to each other it implies that the energy spectrum does not change appreciably, even over large changes in the intensity of the source. Unlike intrinsic variability, extrinsic variability would be caused by some object, such as a cloud of gas, interfering with the light coming from the active galaxy NGC 4945 and mimicking a variability intrinsic to the source. Were this the case, if there was an energy change the intensity of HEXTE and PCA would not necessarily correlate. Because it is shown that they do, it can be inferred that it is much more likely for the variability to be intrinsic to the source.

Studying time scales up to the full year of the observation proved to be more difficult than expected since the window function for the data was too rough to enable an accurate study of variability at lower frequencies. Further study will not be possible until a way is discovered to account for the window function and subtract it from the data. At present, work is being done to look into this possibility and analyze the window function more thoroughly. Further work should include a closer analysis of the PSD produced by averaging the data into logarithmic bins. The possibility of a better way to bin the data should be considered so that the window function would be minimized. This could include multiplying the light curve by a window function before implementing a FFT, as was done in [11]. Finally, if it is possible to obtain clearer results, a comparison between the long-term and short-term variability of NGC 4945 should take place so that the PSD break can be determined more accurately. With this knowledge, it will be possible to investigate the relationship between the PSD break of NGC 4945 and the black hole mass.

Acknowledgments

This research was conducted at the Stanford Linear Accelerator Center (SLAC), in Menlo Park, CA. I would like to thank my mentor, Greg Madejski, for his patience at my constant questions as well as for his wonderful advice and support. Special thanks go to Martin Mueller, who helped me understand the sequence of steps needed as well as directed me to various programming resources and excellent advice. Special thanks goes to all those involved at the SULI program at SLAC, especially Program Administrator Farah Rahbar and Program Director Steve Rock. Lastly, I would like to thank the Department of Energy for the opportunity to participate in this research program and the incredible learning experience I have had.

References

[1] Frank H. Shu,The Physical Universe: An Introduction to Astronomy, Mill Valley: University Science Books, 1982.

[2] Julian H. Krolik, Active Galactic Nuclei: From the Central Black Hole to the Galactic Environment, Princeton University Press, 1999.

[3] Philip Uttley and Ian McHardy, "A Brief Review of Long-term X-ray and Optical Variability in Radio-quiet AGN." Feb. 2004.

[4] A. Markowitz et. all, "X-ray Fluctuation Power Spectral Densities of Seyfert 1 Galaxies." *The Astrophysical Journal*, March 2003.

[5] Greg Madejski et. all, "Structure of the Circumnuclear Region of Seyfert 2 Galaxies

Revealed by *Rossi X-ray Timing Explorer* Hard X-ray Observations of NGC 4945." *The Astrophysical Journal*, May 2000.

[6] Martin Mueller et. all, "The X-ray Variability of NGC 4945." Dec. 2003.

[7] RXTE Guest Observer Facility, "The Rossi X-ray Timing Explorer Mission." 2007, Available at HTTP: http://rxte.gsfc.nasa.gov/docs/xte/xtegof.html.

[8] Philip Blanco, "The High Energy X-ray Timing Experiment." 1996, Available at HTTP: http://rxte.gsfc.nasa.gov/docs/xte/HEXTE.html.

[9] RXTE Guest Observer Facility, The RXTE Cook Book. 2007, Available at HTTP: http://heasarc.gsfc.nasa.gov/docs/xte/recipes/cook_book.html.

[10] William H. Press et. all, Numerical Recipes: The Art of Scientific Computing, New York: Cambridge University Press, 2007.

[11] Rick Edelson and Kirpal Nandra, "A Cutoff in the X-ray Fluctuation Power Density Spectrum of the Seyfert 1 Galaxy NGC 3516." *The Astrophysical Journal*, April 1999.

Figures

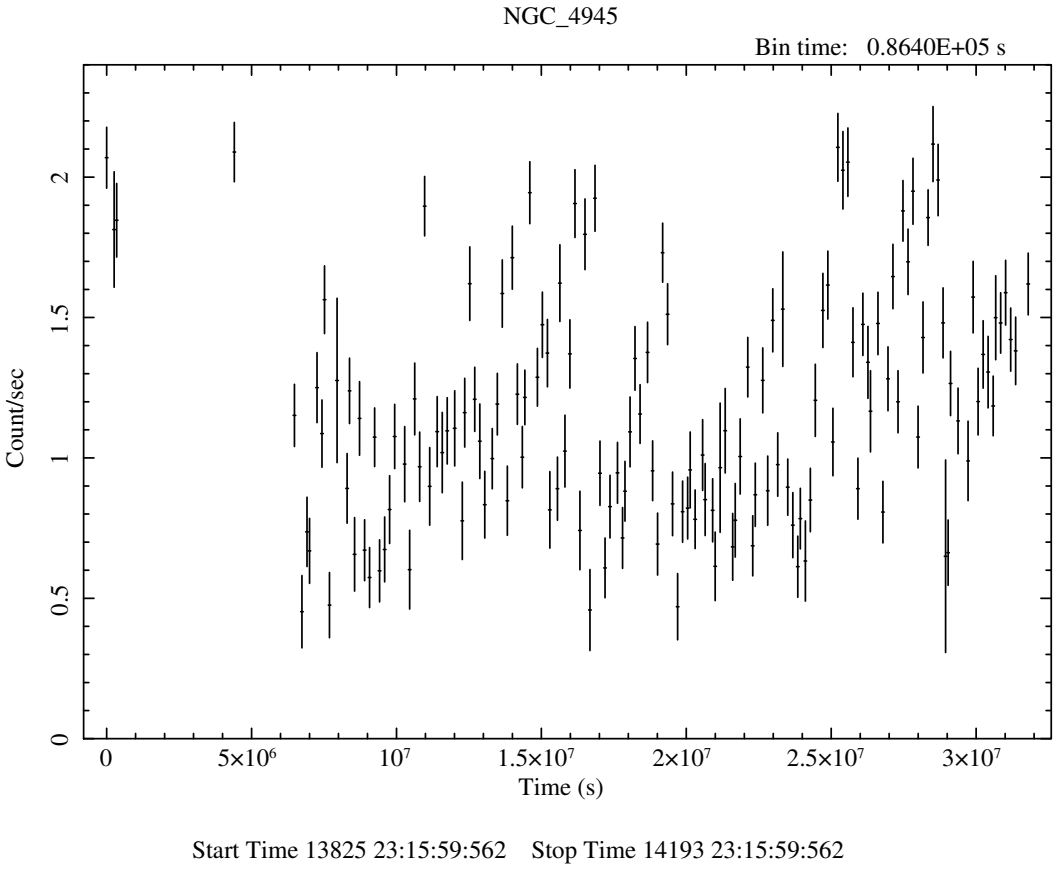

Figure 1: *RXTE* light curve for NGC 4945 in the 8-30 keV band produced using PCA data. This graph was created using **lcurve** with a newbin time was 86400 s. Error bars are shown.

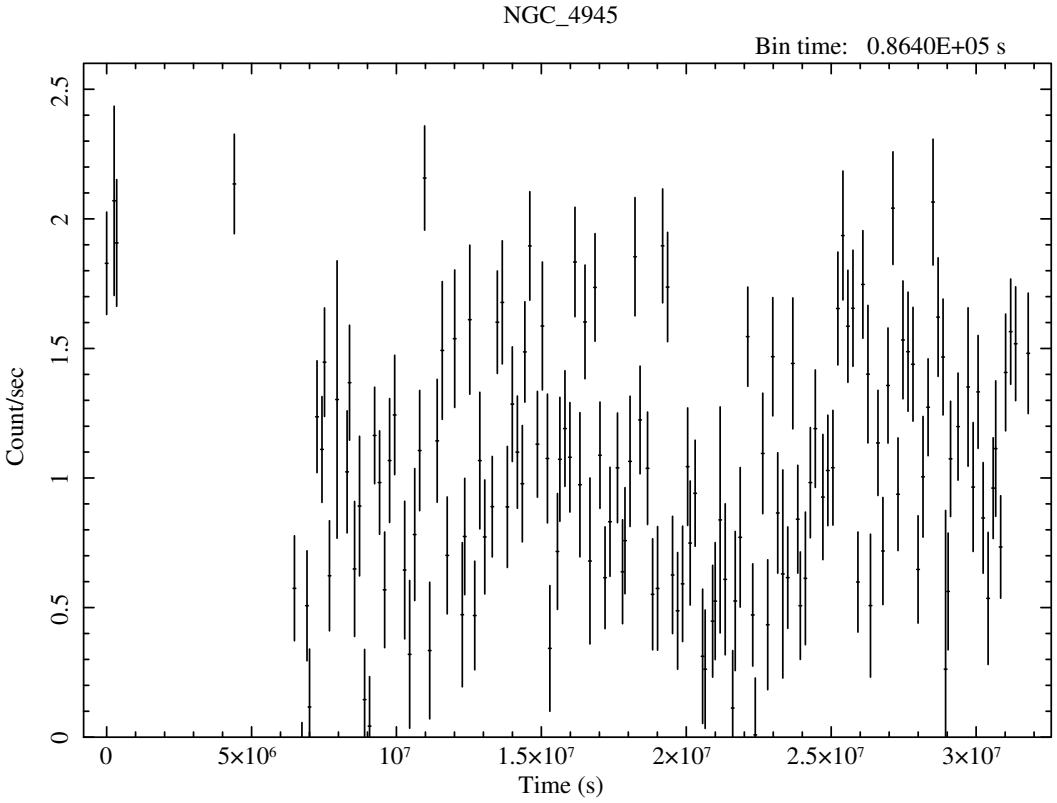

Figure 2: *RXTE* light curve for NGC 4945 in the 12-100 keV range produced from HEXTE data. This graph was also created using **lcurve** with a newbin time of 86400 s. Note that the shape of the HEXTE light curve reflects that of the PCA light curve.

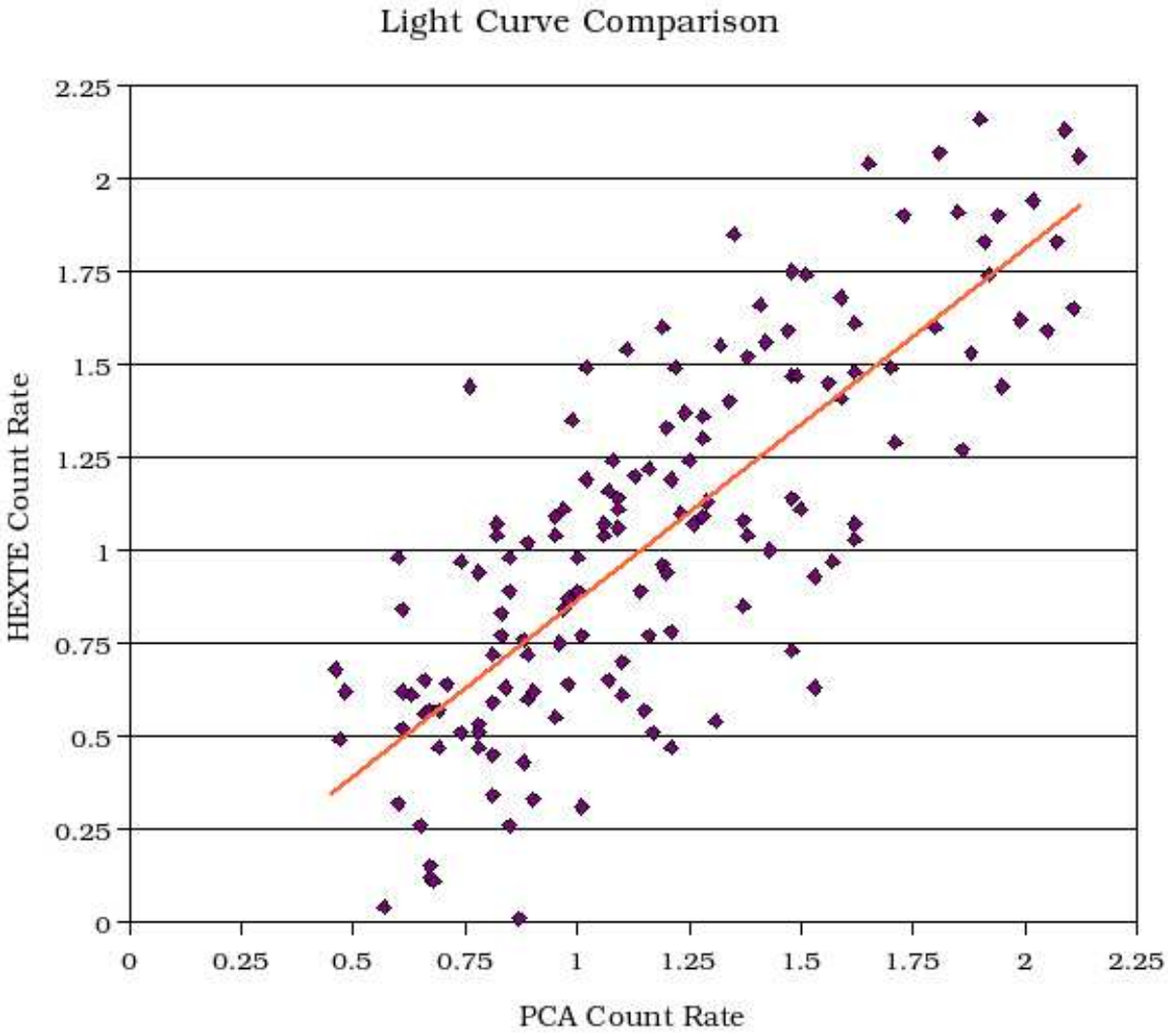

Figure 3: This graph plots the PCA count rate against the HEXTE count rate for the observed object, NGC 4945. Both count rates were obtained from light curves produced by the script Rex, part of FTOOLS. The mean line has a linear slope, indicating that the PCA and HEXTE data closely parallel each other in shape.

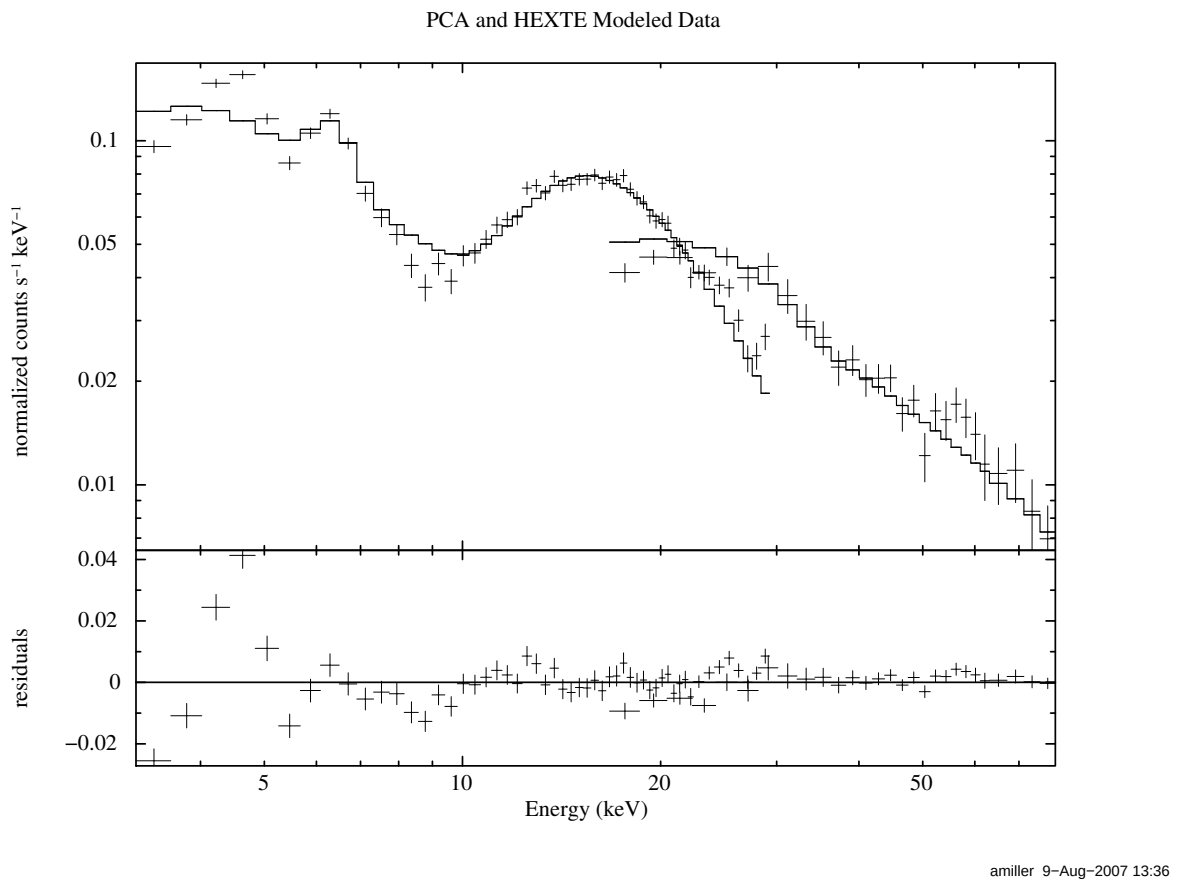

Figure 4: Both PCA and HEXTE data shown with residuals corresponding to the model applied. The solid black line is the model while the crosses are data points (error bars included). The first unbroken segment in the energy range of 3-30 keV is from the PCA data, while the second segment in the energy range of $\sim 15-70$ keV is from the HEXTE data. The specifics of the model are discussed in the Results section.

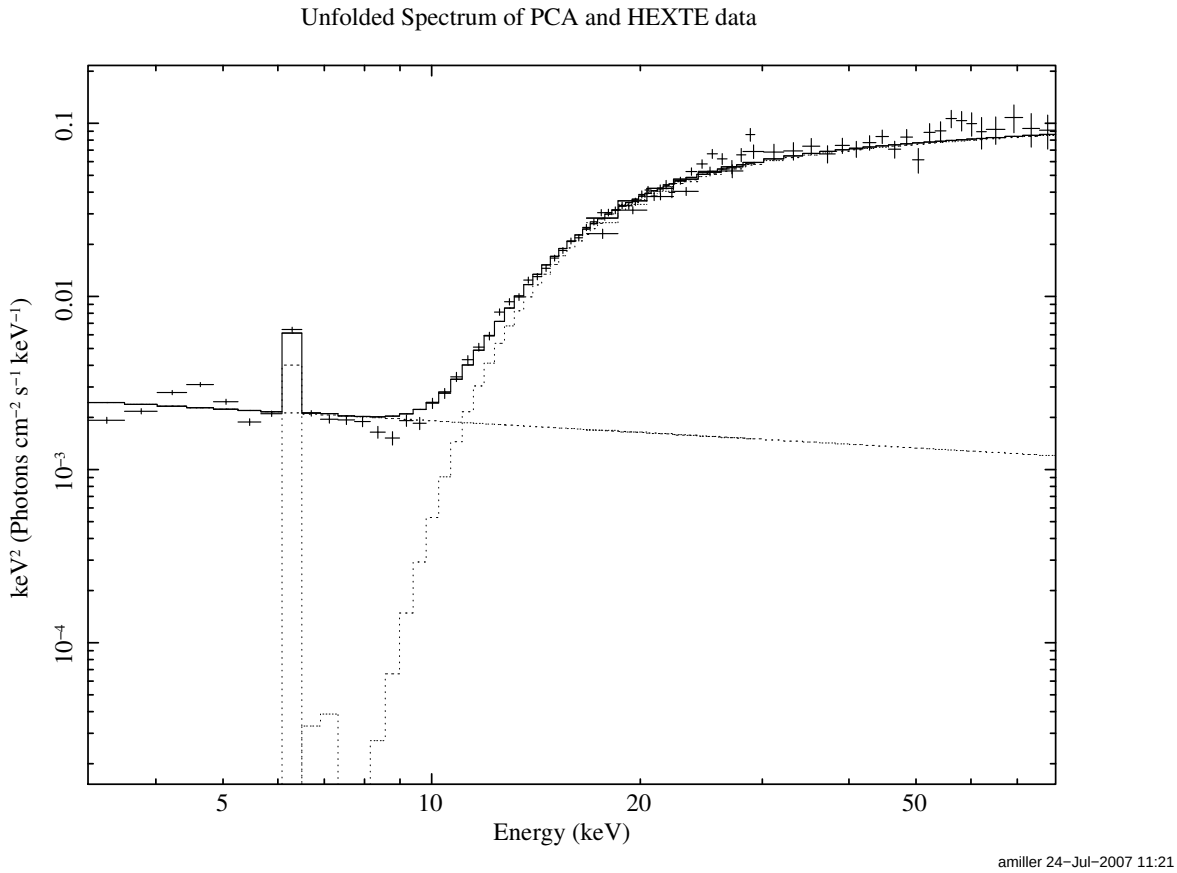

Figure 5: PCA and HEXTE data on a logarithmic scale with the model used in Figure 4 (described in the Results section). The model is again the solid black line, while the crosses are data points (error bars included). The PCA data ranges from 3-30 keV, while the HEXTE data ranges from $\sim 15 - 80$ keV. The HEXTE data and PCA correspond nicely to the model, with not obvious jumps or gaps, implying the data reduction process was successful.

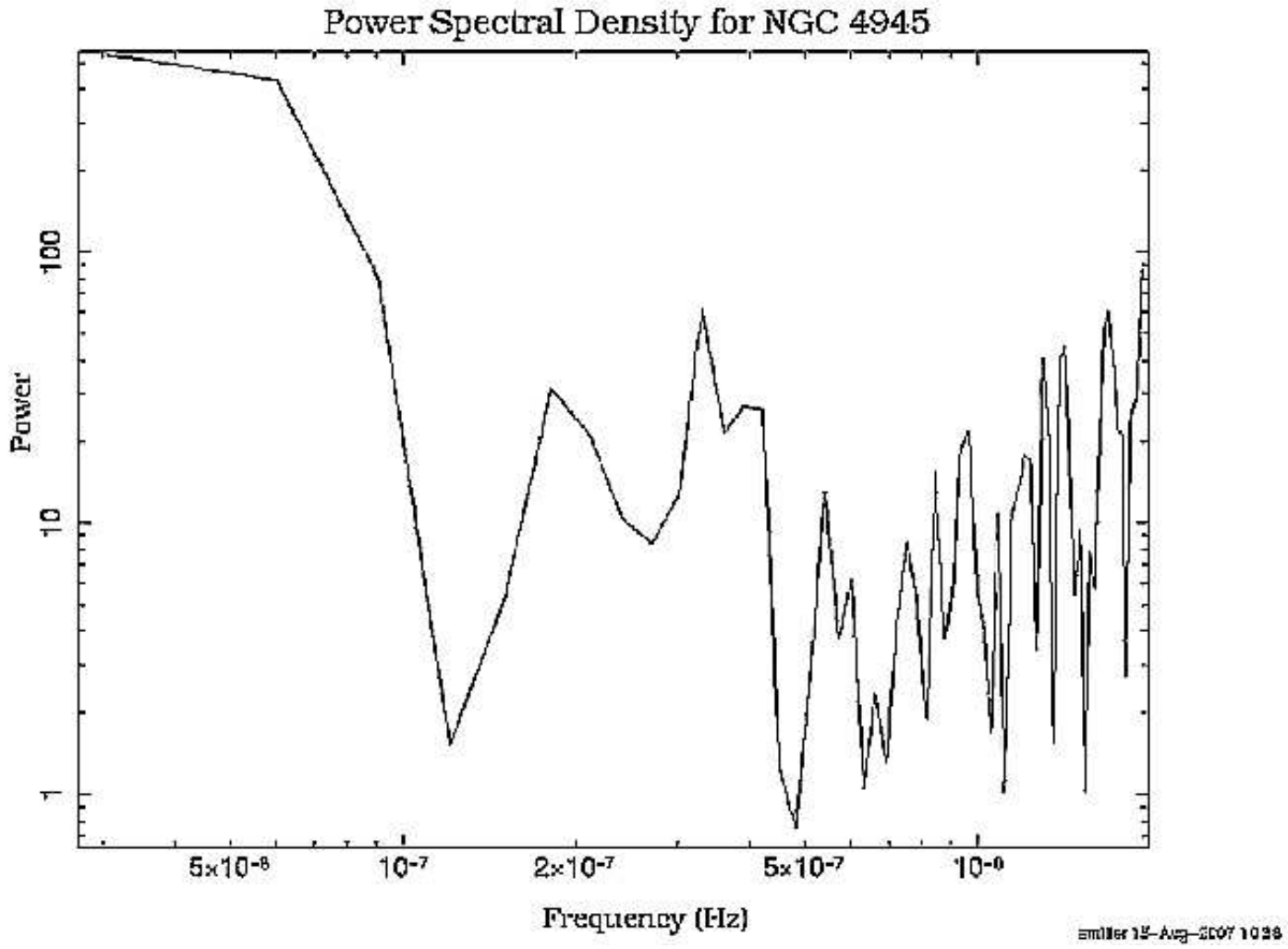

Figure 6: A PSD produced from PCA data. The scale is logarithmic, with Power as a function of Frequency.

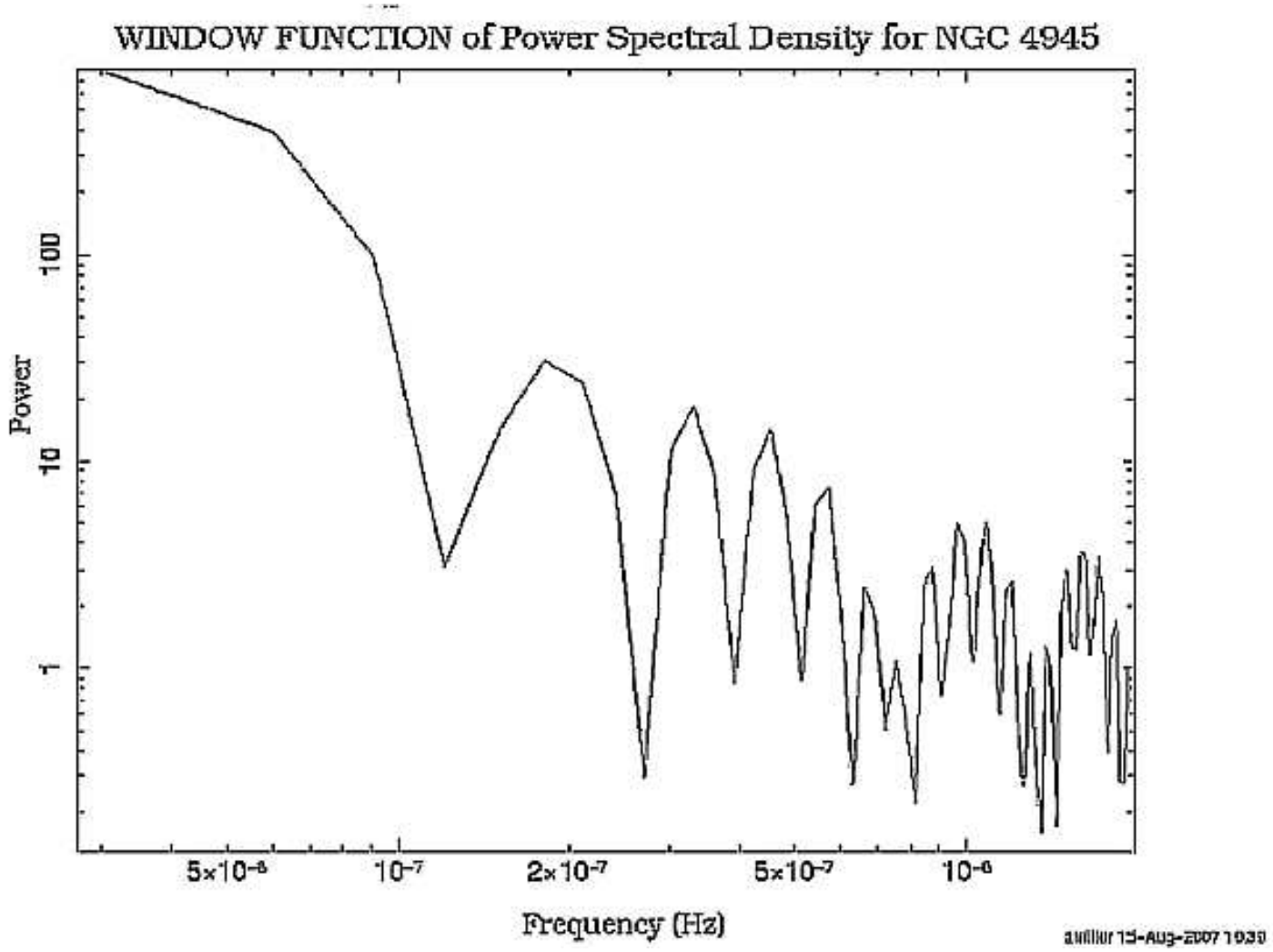

Figure 7: The Window Function for the PSD in Figure 6. The Window Function can be thought of as the intrinsic error of the FFT. The PCA data used in the FFT was analyzed and a blank copy of the pattern of that data was reproduced and run through an FFT, producing a "control" PSD to compare to the real PSD. The scale is also logarithmic.

SLAC-TN-07-009
August 2007

Calibration of the Camera of the LSST

Andy Scacco

Office of Science, Science Undergraduate Laboratory Internship (SULI)

University of Colorado, Boulder

Stanford Linear Accelerator Center

Menlo Park, California

August 7, 2007

Prepared in partial fulfillment of the requirements of the Office of Science, Department of Energy's Science Undergraduate Laboratory Internship under the direction of David Burke in the Particle Physics and Astrophysics Division at Stanford Linear Accelerator Center.

Participant: _____
Signature

Research Advisor: _____
Signature

Work supported in part by US Department of Energy contract DE-AC02-76SF00515

Table of Contents

ABSTRACT

Calibration of the Camera of the LSST. ANDY SCACCO (University of Colorado, Boulder, CO 80309) DAVID BURKE (Stanford Linear Accelerator Center, Menlo Park, CA 94025).

The camera of the Large Synoptic Survey Telescope (LSST) is analyzed theoretically using the ZEMAX optical design software. The purpose of this analysis is to have a theoretical model for the testing and calibration of the optics before they are installed in the telescope. The most effective way to perform this testing and calibration is also investigated. The calibration of the lenses and sensors in the telescope will be performed using either a highly focused laser beam or a filtered quartz lamp with a monochromator, enabling very precise measurements to be made. The image the light source produces on the focal plane of the camera will be compared to the image predicted by the ZEMAX software and the optics and sensors for the camera will be adjusted until the desired agreement is reached. The minimal size of the spot produced by the light source is determined for a large sampling of angles and locations on the focal plane. A spot size that matches the spot size of the point spread function (PSF) of the telescope can be produced for light that strikes the focal plane at its center or for light that strikes the focal plane parallel to the optical axis of the camera, but not for light that strikes the focal plane off center at a significant angle. This work is a starting point for the testing and calibration of the LSST camera, which will be implemented and modified as necessary as the camera is built, assembled and tested.

INTRODUCTION

The large synoptic survey telescope (LSST) is a proposed, ground based telescope that is scheduled to be become operational in 2014 in Cerro Pachón, Chile. It will be able to observe stars, galaxies, planets, and other celestial objects down to 24th magnitude in brightness [1]. The LSST consists of three mirrors to focus starlight and a centrally positioned CCD camera. The LSST's mirror design (See Figure 1) focuses light onto the focal plane of the telescope at which the CCD array is placed. Incoming rays of light from an individual star are very nearly parallel to each other and all will be focused to a very small spot on the focal plane where they strike the CCD detector. Thus, each CCD corresponds to a specific angular position in the sky where a star is. The LSST camera consists of three lenses and a filter (See Figure 1). There are 6 different filters that can be placed one at a time inside the camera (Figure 2) by a carousel mechanism. These filters are used in the telescope to observe light in the visible spectrum from 320 to 1050 nm in wavelength (Figure 3) [1].

The LSST will have an extremely large étendue, which is equal to the product of the area of the 8.4 meter diameter aperture and the 3.5 degree camera field of view and is a measure of how much data the telescope is capable of obtaining. It will survey the entire night sky every three days, and in greater depth than any previous large scale sky survey [1]. This will enable it to record approximately 30 terabits of data per night [1]. This large amount of data will allow new scientific investigations, especially in areas of statistical astrophysics. This data will also be open to the public so that any scientist can access it at any time. The LSST will investigate the nature of dark energy, be able to detect potentially hazardous asteroids and probe the remote

solar system, study astronomical phenomena with transient time scales, and investigate the formation of our galaxy [1].

A telescope camera receives information about a celestial object from the light that it receives. The charged coupled devices (CCD's) on the camera record the position of the star along with its brightness. Therefore it is essential that the CCD's on the camera be calibrated perfectly so that the information they provide to scientists is correct. To calibrate the camera, we will use a Gaussian beam to mimic light from a distant star. We will measure the properties of the beam independently before it is positioned to shine on the camera. When the beam shines on the camera, we will use a splitter mirror and photodiode to monitor the laser beam as tests are being performed [2]. When the beam strikes the CCD array, electrons in the CCD semiconductor will absorb these photons and be collected by the read-out electronics. The total charge is then recorded by a computer which reconstructs the images using this data combined with the knowledge of where the telescope is pointing and atmospheric corrections [2].

When a telescope camera views a star, the light from the star comes in parallel because the light is so far away and so a star is very nearly a point source. This light would ideally be focused to a single point; however, the combined influence of aberrations in the telescope optics and the atmosphere turn this point into a larger spot [2]. This spot is described by the point spread function (PSF), which is a graph of the overall spatial distribution of the intensity of light that hits the telescope detector [3]. Thus the point spread function (PSF) of the telescope should reflect the image produced when the LSST views a star. In the case of a large ground based telescope such as the LSST, the PSF is dominated by astronomical seeing as a result of uneven air layers in the atmosphere [4]. The telescope's contribution to seeing is usually approximately three times smaller than the atmosphere's [2] (See Figure 4). Telescope PSF's are approximately

Gaussian distributions and are measured by the full width at half maximum (FWHM), which is a measure of the width of the distribution when the profile drops to half of its maximum value [5]. The FWHM of the LSST PSF is 30 microns under good quality observing conditions [2]. This means that in order to best model a star with a light source, the FWHM of that light source should be approximately 30 microns when it hits the focal plane detector.

Because the LSST has such a large field of view, it means that light rays are more sharply convergent at the focal plane and come in from greater angles. For optical systems, the paraxial approximation is used, which assume that all light rays travel through the center of the optical system, and all travel parallel to the optical axis. Deviating for that ideal central 0 degree light rays causes lens aberrations to play a much greater role in defocusing the image. Because such a large field of view telescope has never been made before to such a high degree of precision, it is necessary to make sure that the LSST performs in the desired fashion. Additionally, we need to be able to generate a schematic for testing and calibrating the camera and demonstrate that this schematic actually will work. Furthermore, we are limited by not having the telescope to test on, which was designed so that it would generate optimal images when combined with the camera. The telescope and camera assembly's PSF is very small because aberrations in the telescope's mirrors are cancelled out by aberrations in the lenses of the camera. Thus when either is isolated on its own, it will have significant aberration. Our proposed method of shining a Gaussian beam directly at the camera does not take advantage of the focusing properties of the telescope which aid in the generation of a small PSF. This means that it is possible for the Gaussian beam to generate a spot that is too large but for the telescope and camera together to still be able to image points of light to a spot size that is much smaller. Because we are adopting a testing routine that does not have the telescope for assistance, we must be able to generate the desired small spot in

enough locations to perform the desired tests on the LSST camera and to calibrate its sensors, but we should not necessarily expect to generate the extremely small spot size from every angle and every position on the detector.

Each individual detector on the camera is approximately 10 microns by 10 microns across [2]; therefore we will need to generate a very small spot of light on the detector so that we can calibrate the CCD array as precisely as possible (See Figure 5). A 30 micron by 30 micron spot should be sufficient to calibrate the CCD's in bunches of about 9 at a time. This calibration would give the telescope the required precision to carry out all its scientific tasks. The laser to be used in this task must be one that can be focused to the desired size. We must also be able to produce light in each of the 6 LSST filter band passes, so multiple wavelengths of laser light are needed.

MATERIALS AND METHODS

To achieve the goal of creating a very small (30 microns in diameter) spot on the focal plane of the CCD detector of the camera, we need a collimated, monochromatic source of light. The intensity distribution of this light source also has to be a Gaussian distribution, or very close to a Gaussian. The reason for this is that a Gaussian distribution of incoming light produces a Gaussian distribution of out coming light after it is passed through a lens [6]. We can produce this with a laser which is by nature a Gaussian beam or with a quartz lamp and a monochromator. A collimated monochromatic light beam is very nearly Gaussian, so it functions for our purposes in much the same way that a laser beam would, and is also much less expensive. For the monochromator, we can use a variety of filters to select light of the desired wavelength.

Then the light is passed through a pinhole. After the pinhole it is possible to use a collimating lens so all the light is traveling in a parallel beam. Then the light is passed through another lens, which focuses the light through another pinhole [7]. To show that this design works, we must lay down the physics of its operation.

The light source will be placed far enough away from the pinhole that the light can be approximated as a plane wave when it passes through the pinhole, so that it comes out in a Frauenhofer diffraction pattern. Frauenhofer diffraction produces an intensity distribution known as the Airy disk, which is very similar to a Gaussian if the part of the distribution outside of the central peak is cut off [8]. To cut off the outside part of the Airy disk, another pinhole must be used with a size that is adjusted so that the light that is outside the central peak does not pass through, but the entire central peak does. After the light passes through both pinholes, it must then be focused to the desired waist size of 30 microns and sent through the optics of the camera. We must also make sure that the intensity of the light beam that actually hits the CCD is not intense enough to damage it but is strong enough that it can be detected. For actual astronomical observations the light the telescope receives will be very faint, therefore it is not much of a problem if we throw away the vast majority of the light, which makes the monochromator option viable.

The calculations relating to Gaussian beams propagating through the camera lenses were performed using the computer software program ZEMAX. It is a ray-tracing program with the necessary functionality of being capable of analyzing the propagation of a Gaussian beam through an optical system. The specifications of the lenses in the camera are included in figure 6.

The LSST telescope is designed to have a 3.5 degree field of view. This means that it will be able to detect incoming light from any angle between -1.75 and 1.75 degrees. If light from the

aperture of the telescope propagates at angles between -1.75 and 1.75 degrees, the telescope focuses that light onto the focal plane, with each of the extremes in angle corresponding to each of the extremes in focal plane position. Also, the angle of the incoming light when it reaches the camera varies from 14 to 23.6 degrees [1] (See Figure 7). Therefore we must analyze Gaussian beams propagating with angles in the range from 14-23.6 degrees.

Gaussian beams were propagated from a variety of locations and at a variety of angles. A diagram showing how we sampled various angles and locations is shown in Figure 8, which forms the basis for the coordinate and angle system used in Figures 9-13. We analyzed a Gaussian beam aimed at the center of the focal plane at varying angles and wavelength (Figure 9). We also tested a Gaussian beam angled directly perpendicular to the focal plane at varying distances out from the center (Figures 10, 11). Additionally we tested Gaussian beams at an angle and at a distance from the center of the focal plane (Figures 12, 13).

Any beam of light that does not travel along the optical axis of a rotationally symmetric system will suffer from astigmatism [9]. This means that Gaussian beams will have waists at different locations in both the sagittal and transverse directions (Figure 14). As such, the Gaussian beam can be focused either in the sagittal direction or in the transverse direction, but not in both directions simultaneously. Thus when the beam is focused in the transverse direction, the transverse component of the beam size is equal to the size of the waist projected onto the transverse plane. Data presented in Figures 9-13 records the spot size in the transverse direction when the beam is focused in the sagittal direction, and the spot size in the sagittal direction when the beam is focused in the transverse direction (Figure 14). In Figures 9, 12, 13, the radial component is the same as the transverse and or tangential component and the azimuthal component is the same as the sagittal component.

RESULTS

We obtained a data set consisting of a table of spot sizes predicted with the ZEMAX software program for incoming Gaussian beams. The results from shining a Gaussian beam at the center of the focal plane with light of varying wavelength and of varying angle is shown in Figure 9. The results from shining a Gaussian beam vertically downward at varying distance from the center of the focal plane are shown in Figures 10 and 11. The results from shining a Gaussian beam at an angle and not at the center of the focal plane are shown in Figures 12 and 13.

Figure 9 shows the dependence of spot size on wavelength for light aimed at the center of the focal plane. It is easy to tell which wavelengths correspond to which filters from the groupings of 5 data points that go together and then the jumps in the graph between them. There is a general trend that an increase in wavelength corresponds to an increase in spot size, especially at greater angles. However, the greater effect is that the spot size increases greatly at larger angles. The overall maximum spot radius for all angles and all wavelengths is 17.1 microns.

In Figures 10 and 11, a Gaussian beam is aimed straight downward through the optical system so that it would intersect the focal plane at a varying distance from the center. These graphs show the spot size as a function of wavelength and as a function of distance from the center of the focal plane respectively. Spot size increases slowly with wavelength and as a function of distance from the center. Spot size increases with distance outward from the center. It begins to become a noticeable difference around a distance of 100 mm and then increases

rapidly. The maximum spot radius for all positions on the focal plane and all wavelengths is 18.7 microns.

Figures 12 and 13 show the effect of tilted, off axis beams on the spot size at the focal plane. Figure 12 is for a low wavelength Gaussian beam and shows a much smaller spot size than Figure 13 for a large wavelength Gaussian beam. The radial spot size increases drastically as the distance from the center of the focal plane increases. Also, the angle at which the beam comes in has a very large effect on the beam size. At large angles, the spot size increases more rapidly with distance out from the center of the focal plane. Also, when the beam is originating from a more central location and is angled outward to strike the focal plane at a more distant location from the center, the spot size is larger than for a beam that hits the focal plane in the same spot, originates much farther out and is angled inward. Only at close distance to the center or at very low angle or both does the spot size remain low.

DISCUSSION AND CONCLUSION

From the data we analyzed, an acceptable spot size is generated by Gaussian beams either entering the optical system parallel to the optical axis or intersecting the center of the focal plane. For Gaussian beams intersecting the focal plane off center and at an angle, an acceptable spot size cannot be generated due to astigmatism in the camera.

We can use the data from the beams entering parallel to the optical axis (Figures 10, 11) to hit every sensor on the CCD array with light. Gaussian beams directed parallel to the optical axis can be made to generate a 30 micron spot on the focal plane; therefore we can then make sure all the CCD's on the focal plane function properly by checking them in groups of

approximately nine at a time. Though this data is extremely useful for testing the function of the CCD's and basic properties of the optics, this information does not actually reflect what will occur when the telescope looks at a star once it is fully assembled because the telescope's mirrors focus light to angles between 14 and 23.6 degrees by the time it reaches the camera.

Light from a star hits the primary mirror of the telescope with all rays traveling parallel to each other. All these rays will travel with the same angle with respect to the optical system. This angle determines where on the focal plane they are focused to and thus tells the location on the sky of that star. The location at which one of these rays strikes the primary mirror determines at which angle the beam of light travels when it converges to a focus at the focal plane with all the other rays from the same star that were initially parallel to it. We can analyze how this happens when the star is in the center of the telescope's field of view by the simulation of Gaussian beams that intersect the center of the focal plane (Figure 9). Stars at other locations not in the center of the field of view should behave similarly.

Light from these stars is focused to an off center location on the focal plane and comes in at varying angles. We modeled this situation with Gaussian beams (Figures 12, 13), but the Gaussian beams that do not travel parallel to the optical axis and do not intersect the focal plane suffer from too much astigmatism to be focused to a small enough spot to be very useful for calibrating the camera. For stars in this category, the focusing properties of the telescope mirrors are needed to correct the astigmatism generated by the camera. Using a Gaussian beam that is not focused to correct for this will retain the astigmatism of the camera, which results in a spot size that is too large. We can still do this test and compare the theoretical spot size with the actual spot size as a check that the optics were made to the correct specifications. If we take a measurement of the focus in two separate measurements in the sagittal and transverse directions

independently, we use both of them together to test the camera much better than a single measurement as well. However, precision measuring with the CCD's in this setup is a difficult task.

In this research, we have developed a plan for the testing and calibration of the LSST camera. As the camera is being built, this plan will be used in the testing and calibration of the LSST and any necessary adjustments to the camera will be made. Further research will be able to use this testing design to measure the quantum efficiency of photon absorption as a function of wavelength for the LSST to test the filter design of the camera. Additionally, the effect of camera elements shifting position will need to be analyzed to determine the tolerance of the optical system and how precise we need to be in manufacturing and positioning the parts of the camera so that the telescope will still image the sky correctly. Further analysis could also analyze the LSST camera for ghosting, a process which occurs due to a small amount of reflection instead of refraction at the surface of the lenses and creates faint extra images on the focal plane. This design for testing the camera of the LSST will contribute to the successful construction and calibration of the LSST. After it is successfully constructed, the LSST will help researchers investigate the nature of dark energy, be able to detect potentially hazardous asteroids and probe the remote solar system, study astronomical phenomena with transient time scales, and investigate the formation of our galaxy [1].

ACKNOWLEDGEMENTS

This research was performed at the Stanford Linear Accelerator Center in the summer of 2007. I would like to thank the Department of Energy, Office of Science for providing me with this opportunity and for organizing and funding the program, my mentor, David Burke, for guidance and knowledge in helping me with this project, and Stanford Linear Accelerator Center for hosting me and for being able to work in this excellent research facility.

REFERENCES

[1] "Large Synoptic Survey Telescope", Available at http://www.lsst.org (2007 August 9).

[2] D. Burke, private communication (2007).

[3] "Point Spread Function", Available at http://en.wikipedia.org (2007 August 6).

[4] "Astronomical Seeing", Available at http://en.wikipedia.org (2007 August 3).

[5] "Full Width at Half Maximum", Available at http://www.noao.edu/image_gallery/text/fwhm.html (2007 August 6).

[6] "Gaussian Beam", Available at http://en.wikipedia.org (2007 July 25).

[7] A. Sonnenfeld, private communication (2007).

[8] "Airy Disk", Available at http://scienceworld.wolfram.com/physics/ (2007 July 25).

[9] "Astigmatism", Available at http://en.wikipedia.org/wiki/Astigmatism (2007 July 25).

[10] "Aberrations", Available at http://grus.berkeley.edu/~jrg/Aberrations/ (2007 July 25).

TABLES AND FIGURES

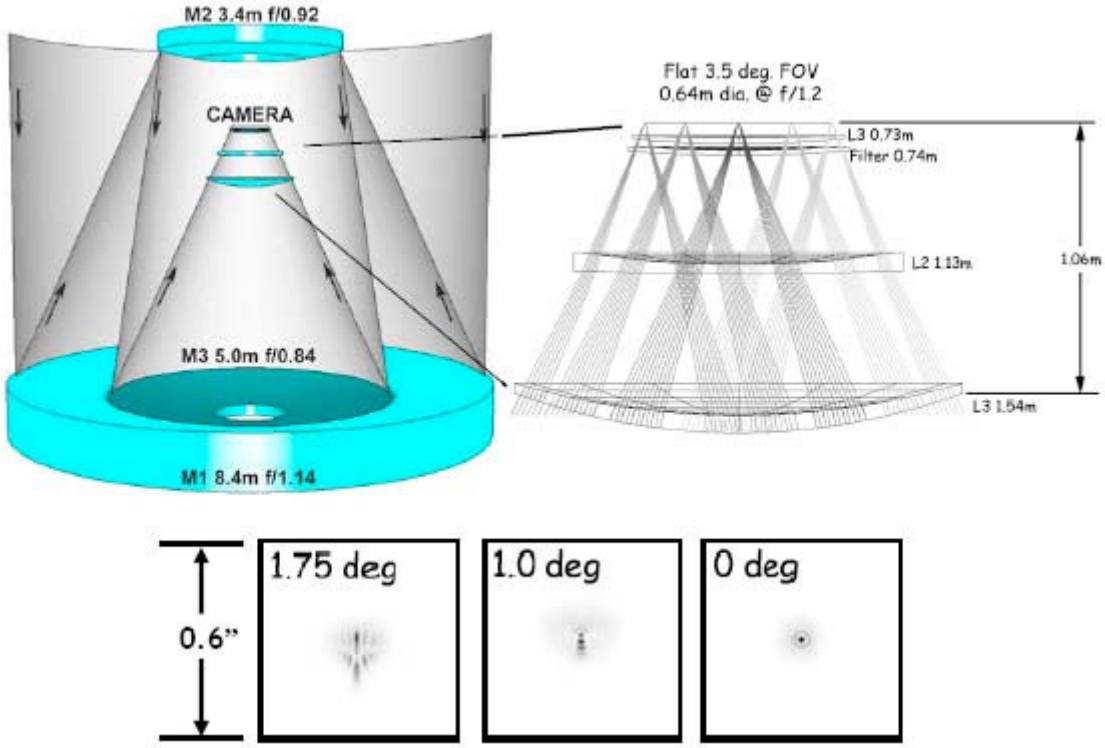

Figure 1. LSST optics and PSF for varying angles of incoming light [1]. Note that the total FOV is 2*1.75 = 3.5 degrees.

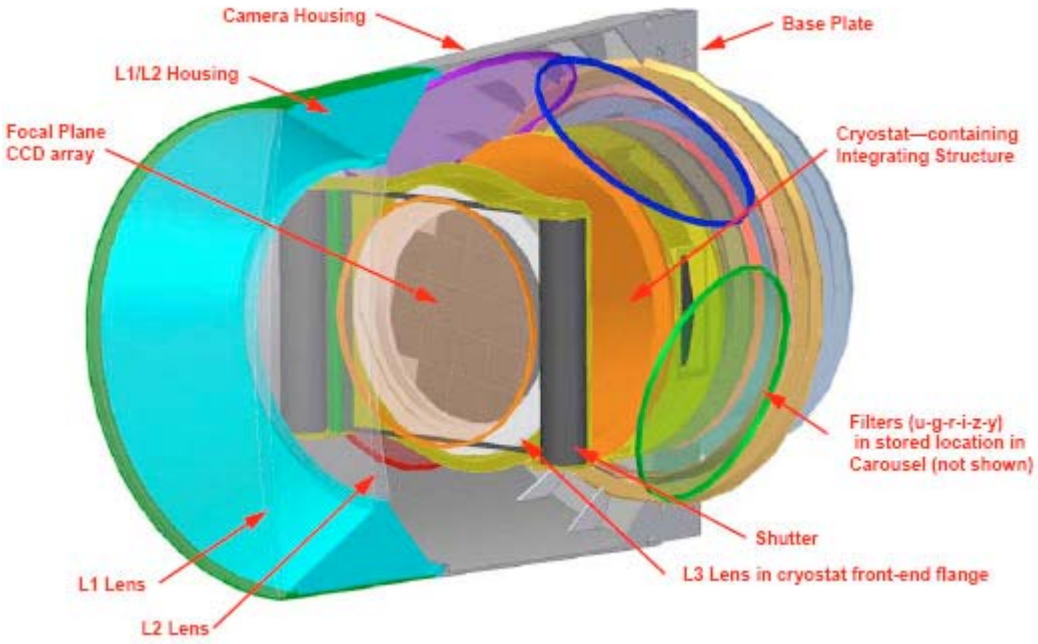

Figure 2. LSST camera design [1]. Filters can be interchanged via the carousel.

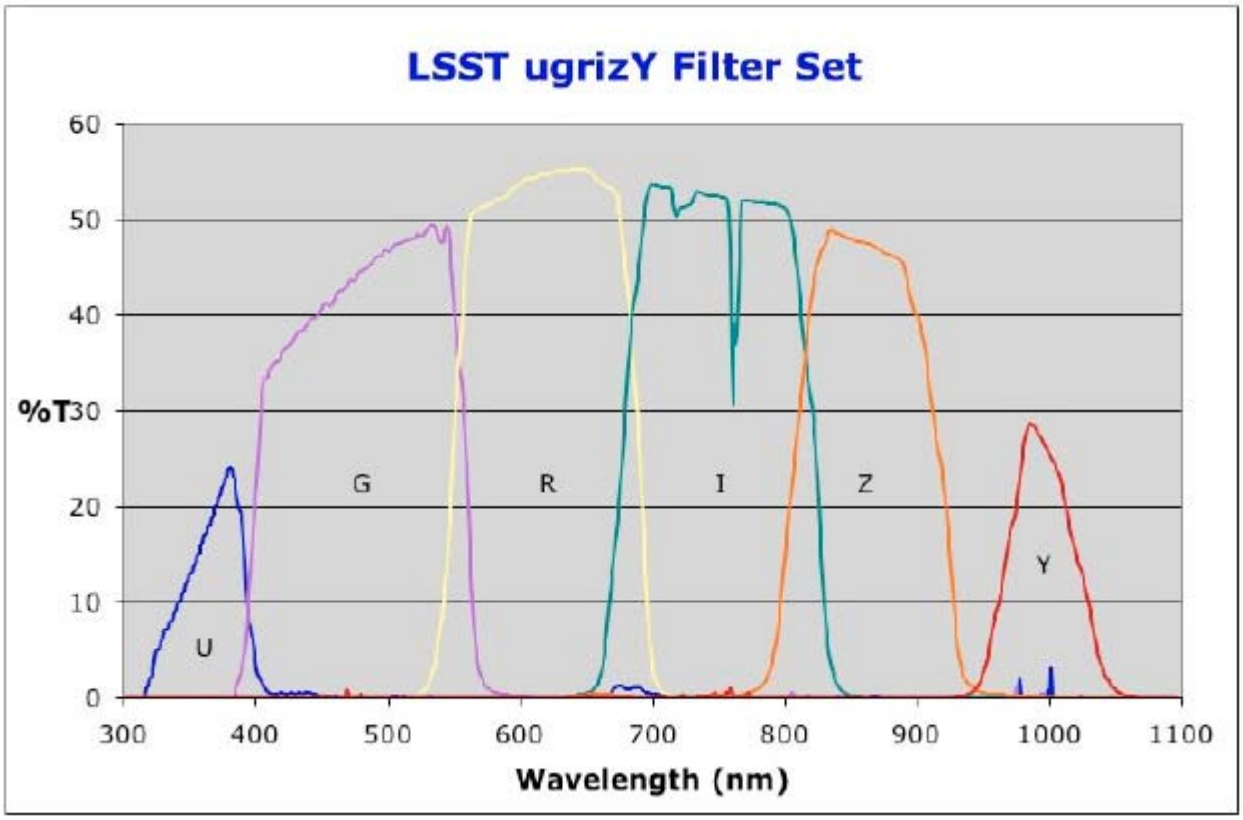

Figure 3. LSST filter set showing the wavelengths that each operates at and their respective percentage transmittances [1].

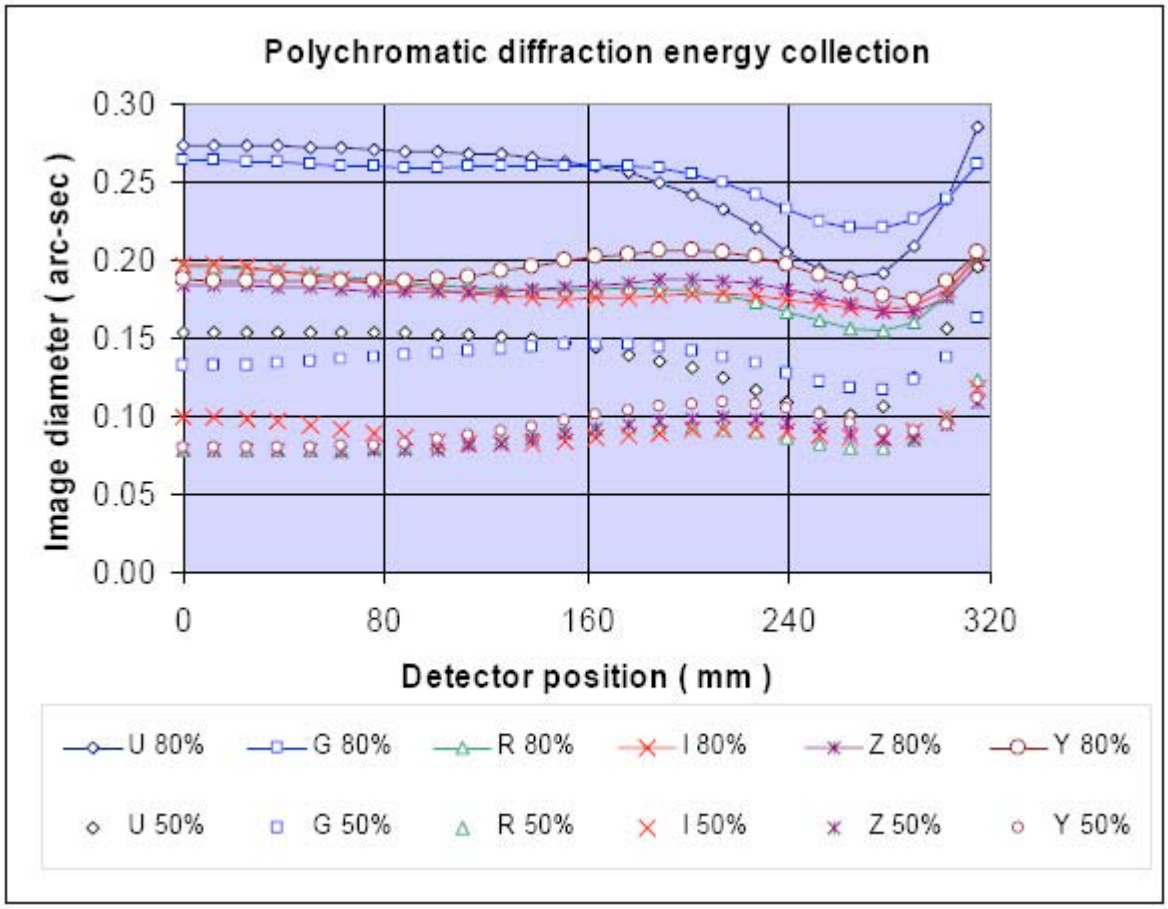

Figure 4. Energy from light encircled within a given image diameter for each of the filter bands and at each position on the focal plane of the detector [1]. Note: 0.6 arc-secs correspond to 30 microns for the LSST. The atmosphere also contributes to the PSF, making its FWHM larger than shown in this graph.

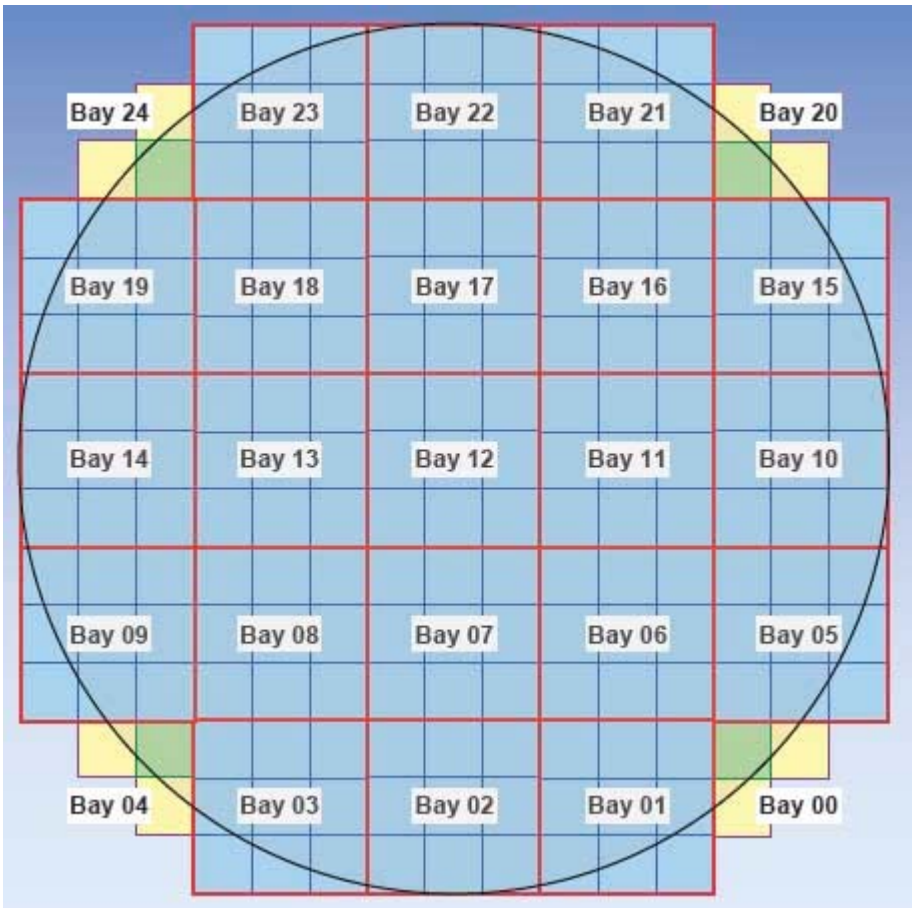

Figure 5. LSST CCD array. Each 3 by 3 array is composed of 10 micron CCD wells [1].

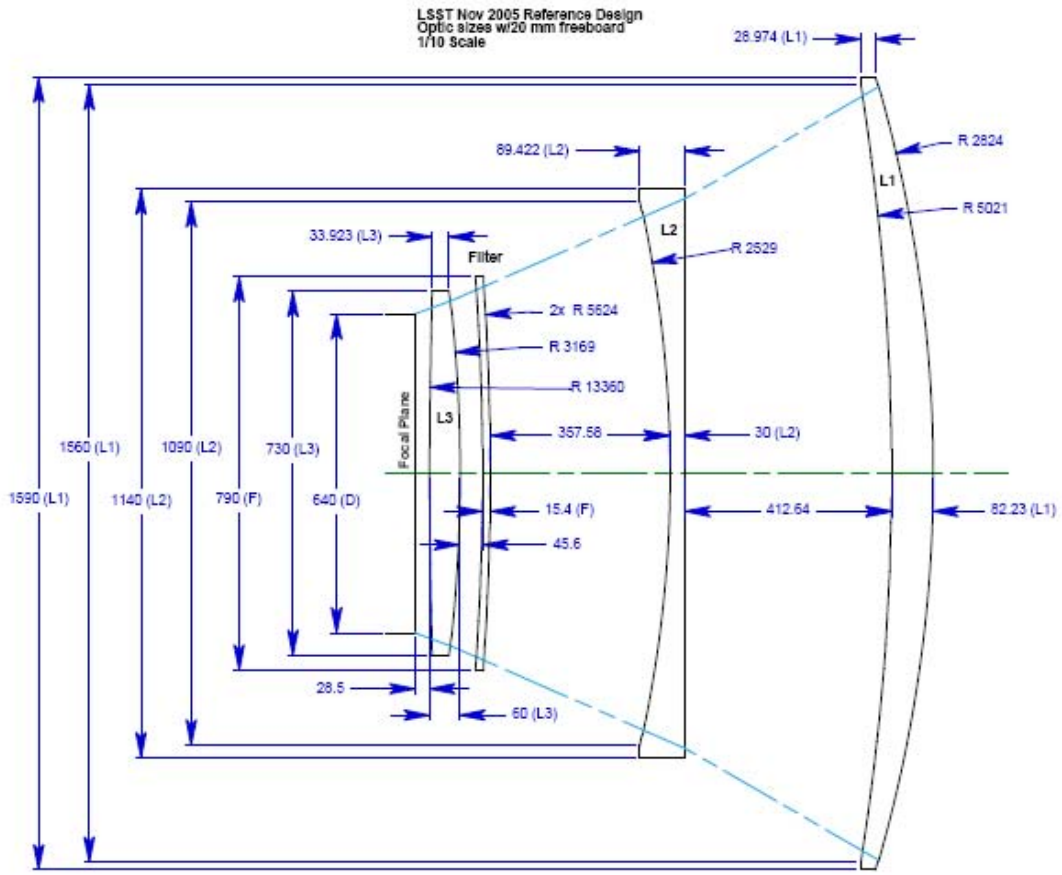

Figure 6. LSST camera layout with dimensions and radii of curvature for lenses [2].

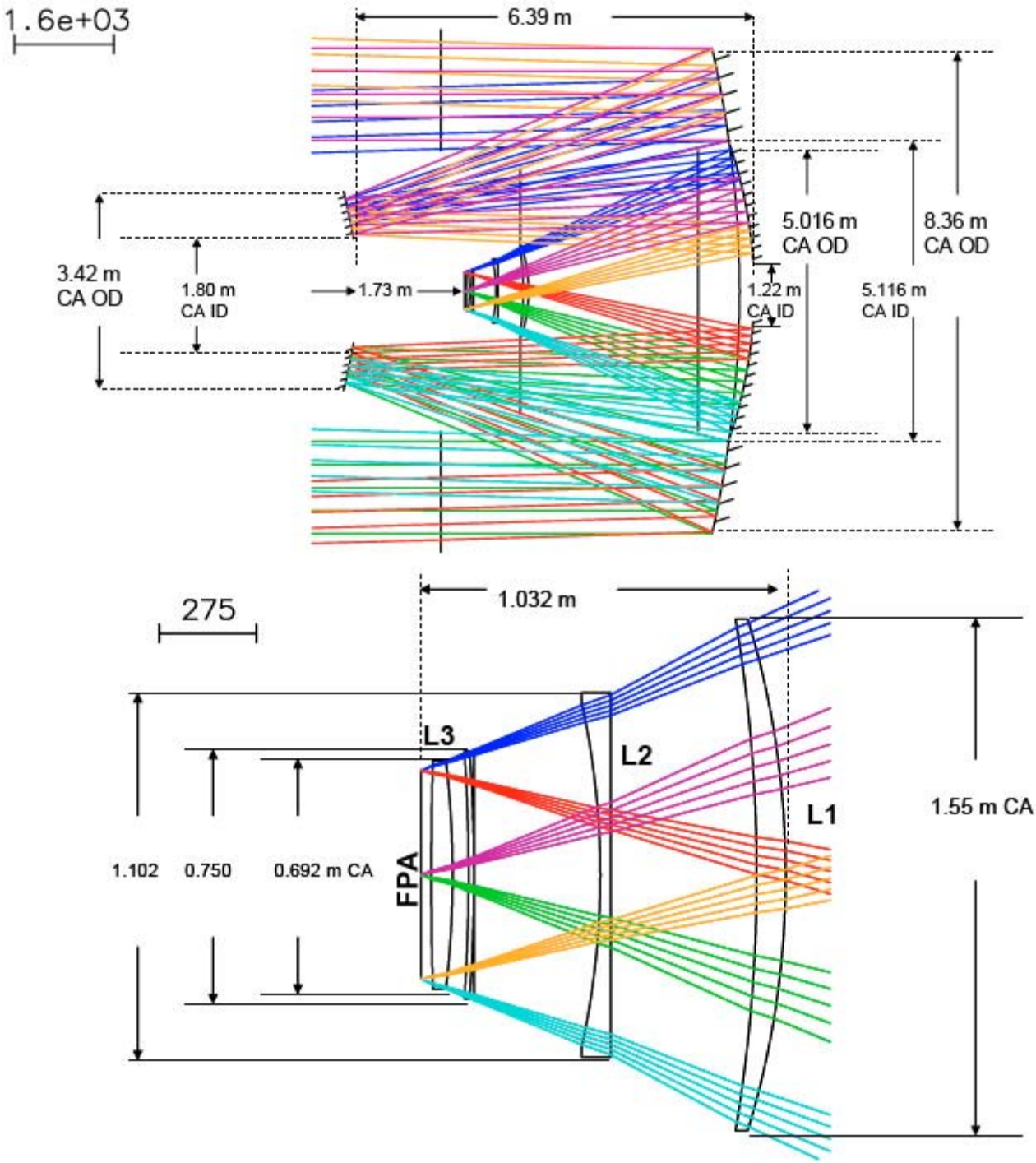

Figure 7. Diagram showing the rays of light that would enter the LSST telescope along with a zoomed in view of the camera itself [1].

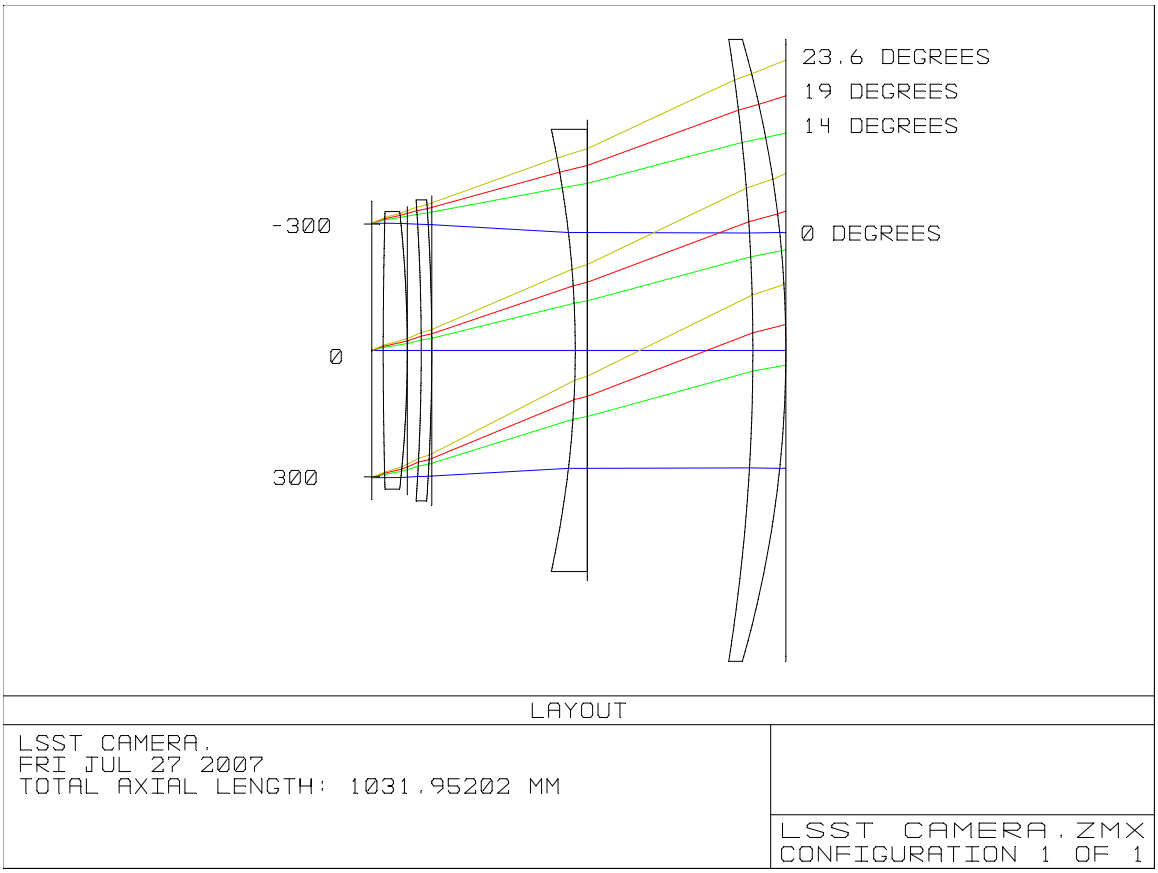

Figure 8. Diagram showing how locations and angles specified in graphs correspond to locations and angles on the camera optics itself.

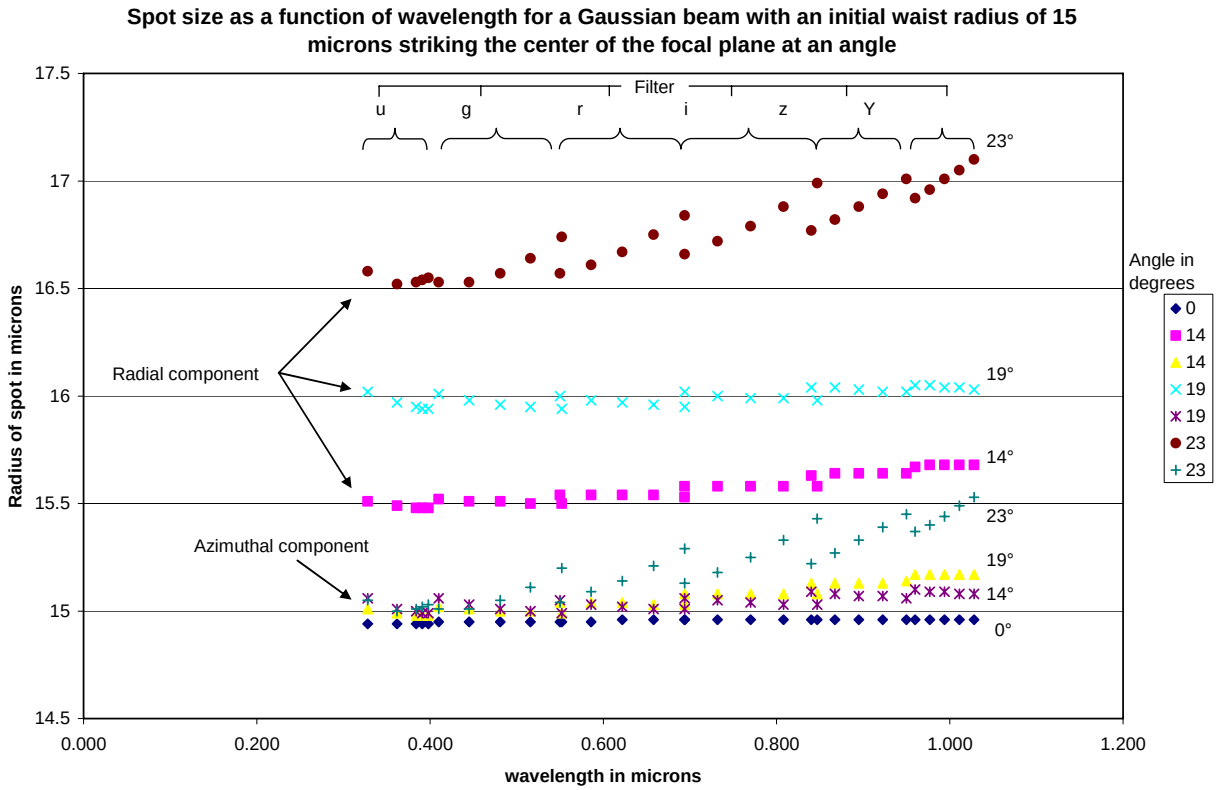

Figure 9. Graph of the radius of a spot formed by a Gaussian beam striking the focal plane in the exact center at an angle as a function of wavelength.

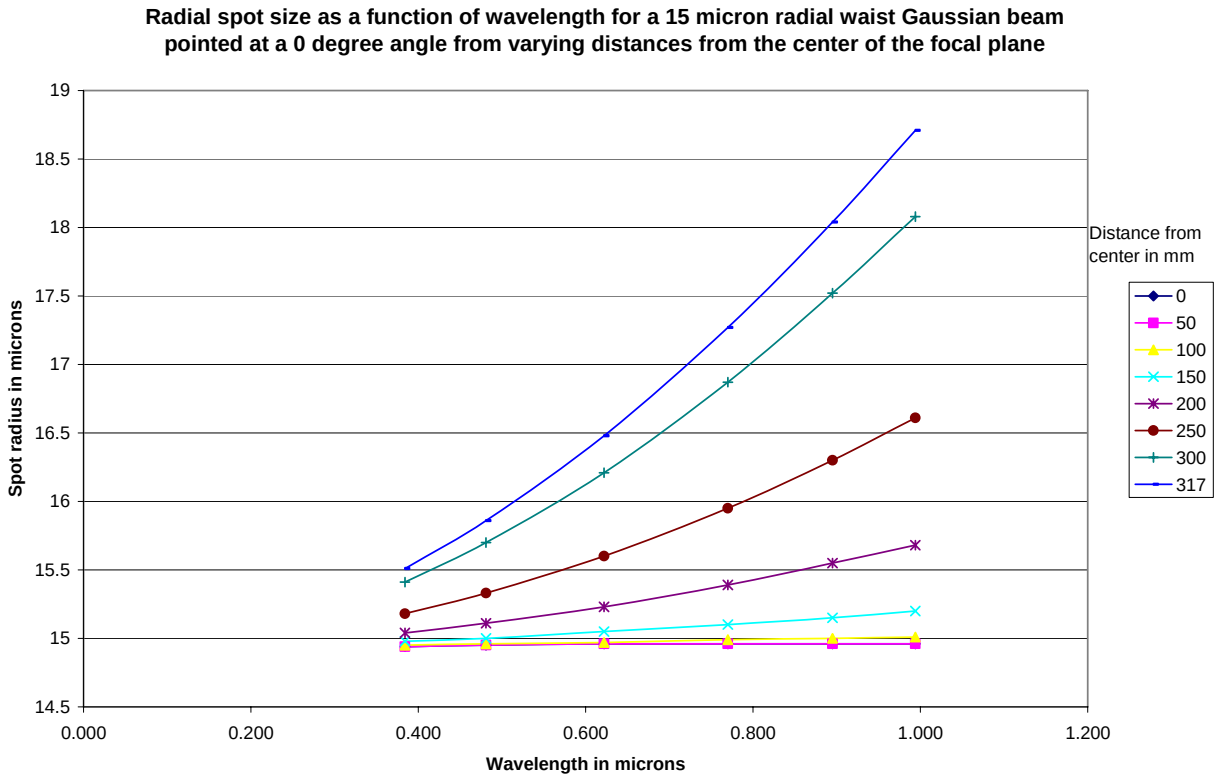

Figure 10. Graph of the radius of a spot formed by a Gaussian beam aimed straight downward as a function of wavelength.

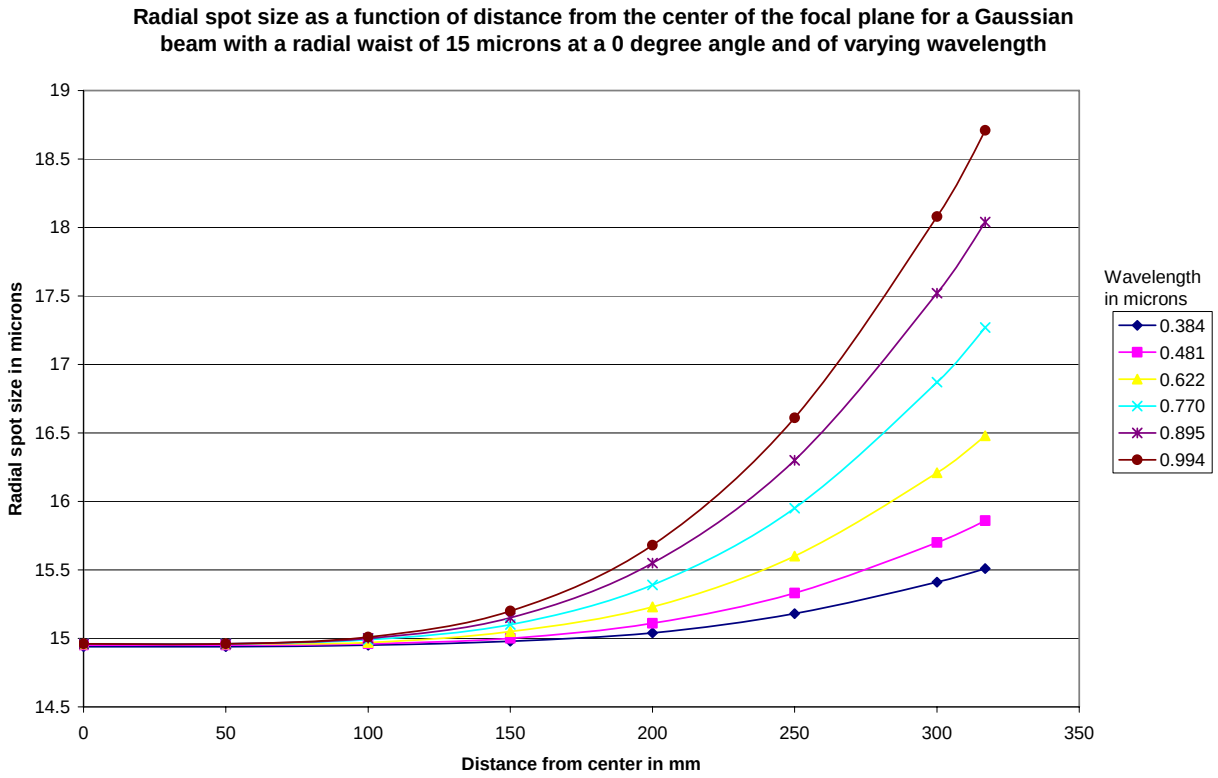

Figure 11. Graph of the radius of a spot formed by a Gaussian beam aimed straight downward as a function of location on the focal plane.

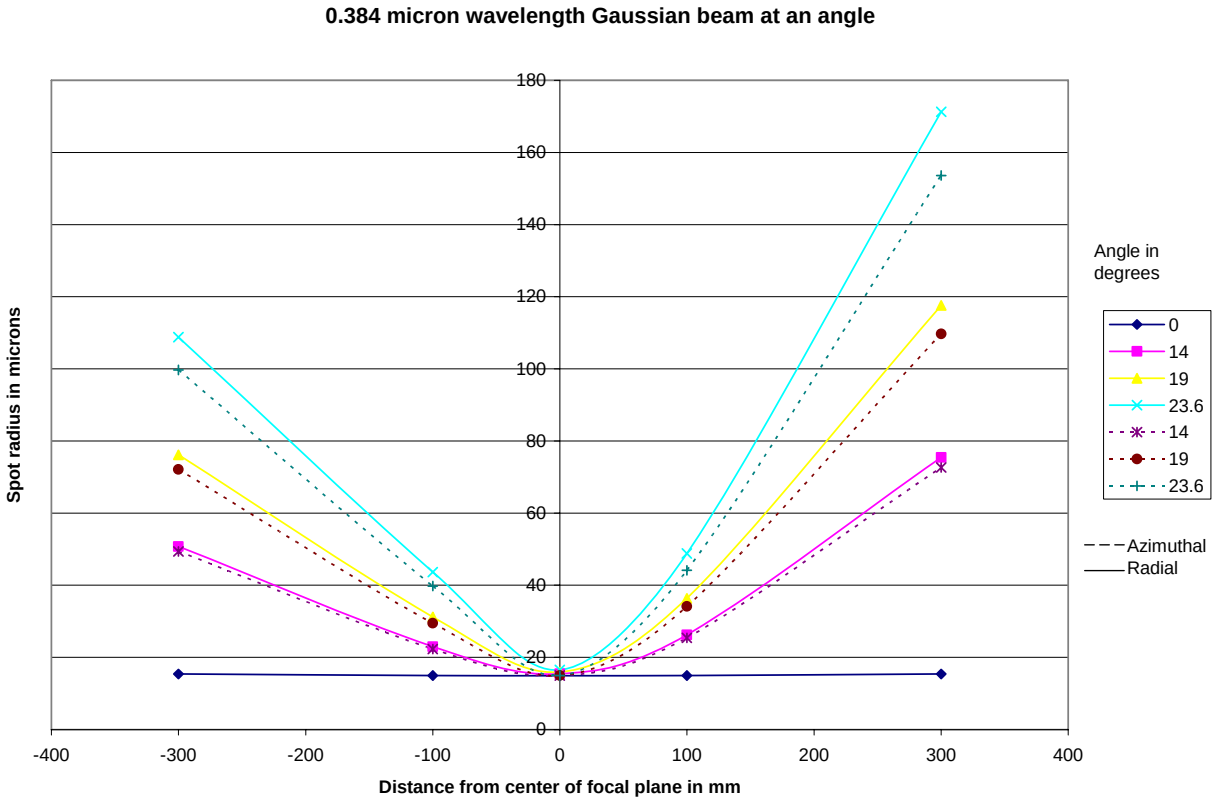

Figure 12. Graph of the radius of a spot formed by a Gaussian beam of 0.384 micron wavelength as a function of angle and location on the focal plane.

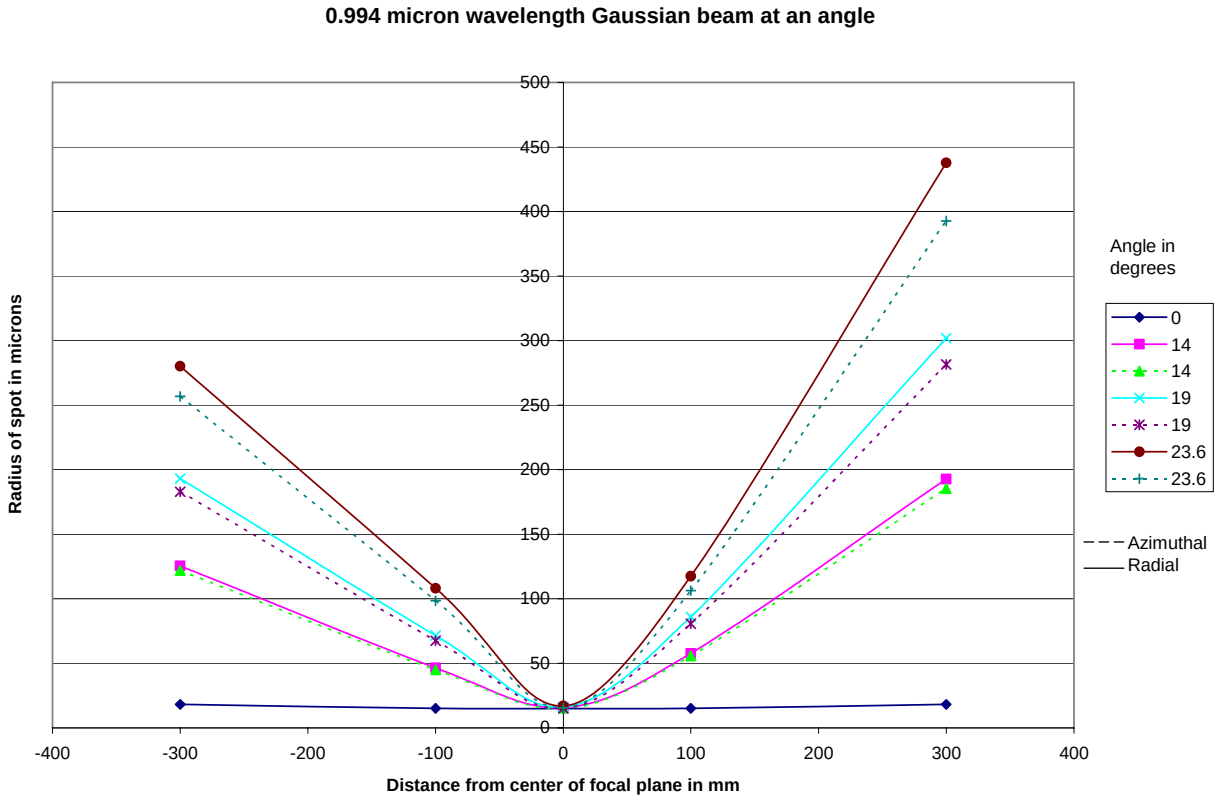

Figure 13. Graph of the radius of a spot formed by a Gaussian beam of 0.994 micron wavelength as a function of angle and location on the focal plane.

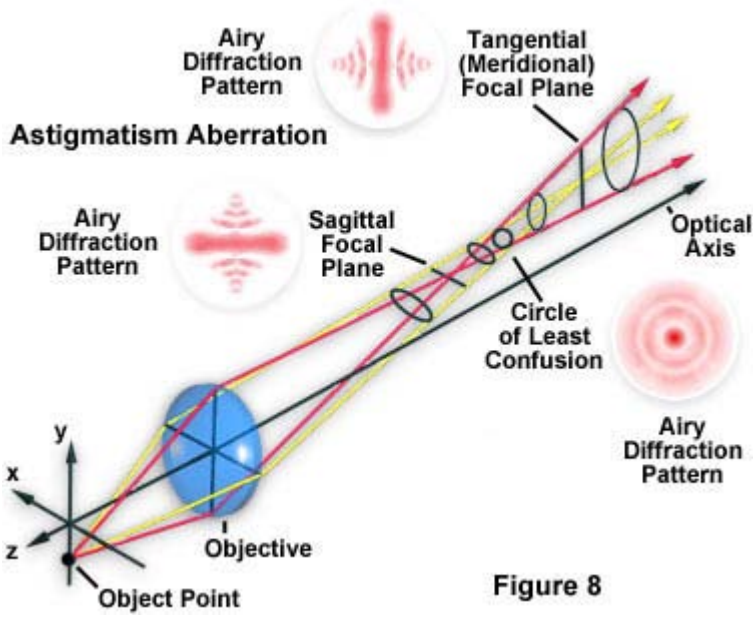

Figure 14. Diagram showing the two different foci and the effect of astigmatism [10].

SLAC-TN-07-017
August 2007

Characterization of the Structure of Cation-Doped Bacteriogenic Uranium Oxides using X-Ray Diffraction

Jonathan M. Stahlman
Office of Science, Science Undergraduate Laboratory Internship Program

Carnegie Mellon University, Pittsburgh

Stanford Linear Accelerator Center
Menlo Park, California

August 25, 2007

Prepared in fulfillment of the requirement of the Office of Science, Department of Energy's Science Undergraduate Laboratory Internship under the direction of Dr. John Bargar and Dr. Eleanor Schofield in the Environmental Remediation Science group at the Stanford Synchrotron Radiation Laboratory at the Stanford Linear Accelerator Center.

Participant: _____
Signature

Research Advisor: _____
Signature

Work supported in part by US Department of Energy contract DE-AC02-76SF00515

Table of Contents

Abstract

Characterization of the Structure of Cation-Doped Bacteriogenic Uranium Oxides using X-Ray Diffraction. JONATHAN M. STAHLMAN (Carnegie Mellon University, Pittsburgh, PA 15289) JOHN BARGAR (Stanford Linear Accelerator Center, Menlo Park, CA 94025)

Remediation of uranium contamination in subsurface groundwater has become imperative as previous research and manufacturing involving radionuclides has led to contamination of groundwater sources. A possible *in situ* solution for sequestration of uranium is a bacterial process in which *Shewanella oneidensis* MR-1 reduces the soluble (and thus mobile) U(VI) oxidation state into the less mobile UO_2 crystalline phase. However, the long term stability of the UO_2 compound must be studied as oxidative conditions could return it back into the U(VI) state. Incorporation of other cations into the structure during manufacture of the UO_2 could alter the dissolution behavior. A wide angle x-ray scattering (WAXS) experiment was performed to determine whether or not calcium, manganese, and magnesium are incorporated into this structure. If so, the substituted atoms would cause a contraction or expansion in the lattice because of their differing size, causing the lattice constant to be altered. After several stages of data reduction, the WAXS diffraction peaks were fit using the Le Bail fit method in order to determine the lattice constant. Initial results suggest that there may be incorporation of manganese into the UO_2 structure due to a .03 Å decrease in lattice constant, but more data is needed to confirm this. The calcium and magnesium doped samples showed little to no change in the lattice constant, indicating no significant incorporation into the structure. Most importantly, this experiment revealed an artifact of the cleaning process used to remove the bacteria from the sample. It appears the NaOH used to clean the samples is contracting the lattice also by ~ .03 Å, but no physical explanation is offered as of yet.

Introduction

Research in the remediation of uranium contamination in subsurface groundwater is imperative as the Department of Energy (DOE) has many sites in which previous research and manufacturing involving radionuclides has led to contamination of local groundwater sources. The total estimated volume of groundwater contaminated with radionuclides is over 1.7 trillion gallons in over 5,700 plumes [1]. Because of this enormous reserve, leaching of uranium into groundwater could pose a continuing environmental and health risk for countless years.

Steps have been taken to combat this problem. Due to the enormity of the contamination, extraction would prove not only to be prohibitively expensive but almost impossible in practice [1]. Thus, a search for an efficient method of *in situ* sequestration has been undertaken. A possible solution for uranium sequestration is the stimulation of *Shewanella oneidensis* MR-1, a bacterial strain which can reduce the soluble (and thus mobile) U(VI) oxidation state into the less mobile U(IV) state[2]. Once in this state, the uranium will precipitate out as nanoparticulate crystalline UO_2. Stimulation of this process is easily accomplished, but the long term stability of this solution is unknown. If the bacteriogenic UO_2 were to be exposed to oxidative conditions, it could then return to its mobile U(VI) state and once more pose a risk.

Along with collaborators, the Environmental Remediation Science group at the Stanford Synchrotron Radiation Laboratory (SSRL) is investigating the long term stability of the UO_2 compound. Because the actual sequestration of the uranium will occur in the subsurface, a thorough study of the environmental effects must be done. The goal of this project is to determine if the presence of cations, such as Ca^{2+}, during the bacterial process alters the basic structure of the UO_2 crystal, leading to changes in the solubility of the compound.

Samples for the study are prepared at the Ecole Polytechnique Federale de Lausanne (EPFL). The synchrotron facilities at SSRL allow for characterization of both the long range and local structure of the bacteriogenic UO_2 compounds using a variety of x-ray scattering and spectroscopy techniques. Simultaneously, collaborators at Washington University in St. Louis are analyzing the solubility and dissolution rates of the various compounds. Putting these results together produces an overall understanding of the structure and behavior of bacteriogenic UO_2 in subsurface conditions.

In this paper, we will analyze the results of a wide angle x-ray scattering (WAXS) experiment on various cation-doped bacteriogenic UO_2 compounds. Specifically, we analyze samples in which Ca, Mn, and Mg cations have been added. These cations were chosen as they are normally present in groundwater. After several stages of data reduction, we are able to extract the lattice constant of the UO_2. To determine the lattice constant, we use the technique of Le Bail fitting, a derivative of the Rietveld Refinement method. If the cations had been incorporated into the crystal, we predict that the crystal lattice should contract or expand due to the difference in atomic sizes of the cations compared to the uranium, resulting in a measurably different lattice constant.

Materials & Methods

An array of uranium oxide samples were prepared by collaborators at EPFL. Each was prepared under a unique set of conditions, which include the concentration of dopant, pH, and cleaning agent used. A summary of these samples and their characteristics is seen in Tables 1 and 2. A cleaning agent is used to remove the bacterial cells from the samples in order to reduce background noise in the diffraction patterns.

Once at SSRL, the wet samples were loaded into 0.2 mm glass capillary tubes in an anaerobic chamber. The sample capillaries were then mounted in sealed containers with a constant flow of nitrogen in order to preserve the anaerobic conditions. Sealed kapton windows were added to the containers in order for the x-ray beam to pass through the container without adding background noise.

A diagram of the experimental setup can be seen in Figure 1. Diffraction measurements were taken at beamline 7-2 at the SSRL facility using a Huber 6-circle diffractometer. Intensity measurements were taken using a vortex detector before and after the beam strikes the sample. The second detector, labeled I_1, scanned over a range of Q values from 0.8 $Å^{-1}$ to 14.5 $Å^{-1}$ in .02 increments. As in most diffraction experiments, Q is defined as :

$$Q = \frac{4\pi \sin(2\theta/2)}{\lambda}$$

where λ is x-ray wavelength and 2θ is the angle between the diffracted beam and the unscattered beam. This was all done with a monochromatic x-ray beam of 0.7696 Å. The UO_2 is nanoparticulate, so the experiment is one of powder diffraction. Thus, the diffraction pattern will be cylindrically symmetric around the axis of the beam. Therefore, it was only necessary to scan over one slice of this diffraction pattern in 2θ space.

At each Q value, the energy spectrum of the signal was recorded. This will later be used to subtract out the inelastically scattered x-rays. Three to four scans over the 2θ range were taken of each sample and then directly summed together. LaB6, a diffraction standard, was used to determine the wavelength of the x-ray beam. In addition to our samples, an empty capillary was also scanned for later background subtraction.

First, the inelastic scattered x-ray signal (or Compton scattered) was subtracted from the data. The Compton scattered x-rays must be subtracted because the Le Bail analysis does not take this phenomenon into account. The wavelength of the Compton scattered x-rays goes as:

$$\lambda' = \lambda + \frac{h}{m_e c}\left(1 - \cos(2\theta/2)\right)$$

where λ' is the scattered wavelength and $h/m_e c$ is known as the Compton wavelength, equal to 2.43×10^{-2} Å. Because the Compton wavelength is small relative to the initial x-ray wavelength, there is not much difference in wavelength between Compton scattered and elastic scattered x-rays at small 2θ. Therefore, separating the elastic signal from the Compton signal at this angle will be quite difficult. However, for our setup, above $2\theta = 80°$, the two peaks are easily discernible, as seen in Figure 2.

To separate the elastic signal from the Compton signal, the energy spectrum scans with Q > 10.78 are first fit with a pair of Gaussian peaks, using the peak center, peak width, and peak area as the parameters for the fit. This initial fit gave three pieces of information about the two peaks. The elastic peak energy theoretically should not change, so the peak center was averaged from this first fit. As well, both peak widths appeared to be constant, so these were averaged. These three average values were then used as constants in fits over all Q and more accurate fits were thus achieved at lower Q values. The area of the elastic peak was then used to determine the ratio of elastic counts to total counts for each Q value. This ratio was then used to scale the summed data to extract the elastic signal.

Background subtraction of the capillary reflections was accomplished using the software package XRD-BS [4]. Scaling of the capillary data for subtraction from the diffraction data was

done by visual inspection for each sample for accuracy. In addition, the program can also account for absorption corrections for cylindrical geometries given a value of μL, the absorption coefficient multiplied by the total length traversed by the x-ray beam. This quantity depends on the physical makeup of the sample as well as its geometry. It appears in the equation:

$$I = I_0 e^{-\mu L}$$

where I is the observed intensity and I_0 is the initial intensity. μL was estimated experimentally by measuring the intensity of the beam with and without the sample in the path of the beam. The negative natural log of the ratio I/I_0 then gives a value of μL for each sample. Values of μL for our samples ranged from 0.3 to 1.5.

The diffraction data was then analyzed using the General Structure Analysis System (GSAS) software package along with EXPGUI [3,4]. Specifically, we used the Le Bail fitting method, a derivative of the Rietveld Refinement. Unlike a Rietveld Refinement, a Le Bail fit takes the observed intensities as arbitrary unknowns and uses the space group, lattice constants, and other parameters to fit the diffraction data without taking into consideration the locations of the atoms within the unit cell. This method is ideal for extracting the lattice constant, though some care must be taken in assuring the fit makes physical sense[6]. UO_2 exists in a face-centered cubic structure, thus making the analysis much simpler, as only one lattice constant must be determined from the fit.

A pseudo Voigt profile was chosen to model the peaks. This profile mixes Gaussian and Lorentzian functions to fit the diffraction peak. Most importantly, the profile function is used to describe the broadening of the peaks. This may be caused by several things: microstrain, experiment instrumentation, and particle size. Examining our LaB6 calibration data, we see very

little broadening (compared to the raw data), so we can assume that instrumental broadening is negligible. Thus, only two profile parameters were used to fit the data: a Lorentzian particle broadening term and a Gaussian strain broadening term. This combination tended to give the best fits. In addition, several parameters to model a broad background and a zero offset in Q space were added in order to further improve the Le Bail fits. A good fit is determined by examining the value of reduced X^2 for the fit.

After a good fit is attained, the parameters of the fit provide the value of the lattice constant. In addition, GSAS provides an estimate of the uncertainty on the given value of the lattice constant. Theoretically, the particle size could also be inferred from the Le Bail fits. However, this is not always the most reliable method as peak broadening could be caused by microstrain or particle size. Thus, separation of the two with a Le Bail fit can be somewhat unreliable [6].

Results

A plot of the raw data can be seen in Figure 3. The first nine peaks have been labeled with the appropriate Miller indices. Notice the very broad peaks. This is due to the nanoparticulate nature of the UO_2 crystals.

Figure 4 plots peak center as a function of Q from the Compton fitting before and after the constants have been determined for one of the samples. In addition, the lighter colors represent the width of the peak. Figure 5 shows a plot of the diffraction data before and after Compton subtraction. A sample background subtraction can be seen in Figure 6.

A sample Le Bail fit is shown in Figure 7. Table 1 presents the lattice constants of all of the doped samples while Table 2 summarizes the results of the undoped samples. All uncertainties were generated using GSAS.

Discussion

Examining Figure 4, this shows that fixing the three variables mentioned earlier results in much better fitting for later Compton subtraction. Theoretically, the Compton peak center should intersect the elastic center at Q=0. This does not happen with our fitting, but the correction is still a good approximation. In addition, the Compton subtraction isn't entirely vital to extracting the lattice constants using a Le Bail fit. This occurs because the value of the lattice constant is adjusted according to the location in Q space of the peak and does not rely heavily on the intensity or width of the peak. The Compton correction is a broad spectrum effect and does not significantly change the shape of the diffraction data (Figure 5). Still, it is important to do this correction in anticipation of a more rigorous analysis, such as a Rietveld Refinement, which is planned for the future.

The background subtraction of the capillary signal is also shown to be adequate. Though minor, this is still an important consideration and significantly improved our data.

The results of the Le Bail fitting are somewhat surprising. The Ca^{2+} cation is slightly larger than the U^{4+}, while Mg^{2+} is slightly smaller. However, examining Table 1, we see that the calcium and magnesium showed little difference in their lattice constants. Also, we were only able to process one sample for each of these dopants. More samples would confirm whether a real trend actually exists. If the lattice constants truly haven't changed, then we must infer that these elements are not being incorporated into the UO_2 structure.

The manganese samples gave mixed results. The .1 mM sample and the 5 mM sample both showed lattice contractions of ~.03 Å. Mn^{2+} has an atomic radius of .93 Å while U^{4+} has a radius of 1.0 Å. Thus, the lattice contraction we measure for these two samples is of the right order of magnitude to be consistent with our prediction that manganese is being substituted into

the structure in place of the uranium. However, the 1 mM sample showed no lattice contraction. This is quite puzzling as this completely goes against the trend. To clarify this, we hope to reexamine the data and possibly repeat the experiment for better confirmation.

One very unpredicted result was the result presented in Table 2. Here, we discover that the cleaning method employing NaOH seems to be changing the lattice constant of the UO_2. Physically, we are unable at the moment to explain the reasoning why this cleaning process would be changing the UO_2 structure. This is quite unexpected and must be taken care of immediately before any other experiments can be done. The Lysozyme cleaning does not seem to have this effect on the structure, so it may become the cleaning method of choice.

We have analyzed the results of a WAXS experiment on cation doped bacteriogenic UO_2 and found several interesting features. The Mn doped samples show a likely lattice contraction, but mixed results have caused doubt as to whether this is true or not. More importantly we have discovered that our cleaning method is affecting the structure of that which we are studying. Thus, we must change our methods of sample preparation. Future work will include a more rigorous analysis of the data, most likely using the Rietveld Refinement method. This analysis will produce information about the structure such as atomic positions and particle size. Overall, this experiment has helped to characterize the structure of doped bacteriogenic UO_2.

Acknowledgments

We would like to acknowledge the Department of Energy and the SULI program for funding this research. We would also like to thank Apurva Mehta as an invaluable source of information during this research. Finally, we would like to express our gratitude to our mentors John Bargar and Eleanor Schofield for all of their guidance and help in completing this research.

References

[1] U.S. Department of Energy. Office of Science. Office of Biological Research. Bioremediation of Metal and Radionuclides... What It is and How It Works. 2nd. 2003.

[2] Chongxuan Liu, Yuri A. Gorby, John M. Zachara, Jim K. Fredrickson, Christopher F. Brown, " Reduction kinetics of Fe(III), Co(III), U(VI), Cr(VI), and Tc(VII) in cultures of dissimilatory metal-reducing bacteria," Biotechnology and Bioengineering, vol. 80, no. 6, pp. 637-649, 2002.

[3] A.C. Larson and R.B. Von Dreele, "General Structure Analysis System (GSAS)", Los Alamos National Laboratory Report LAUR 86-748 (2000).

[4] B. H. Toby, EXPGUI, a graphical user interface for GSAS, Journal of Applied Crystallography, vol. 34, 210-213, 2001.

[5] S. Webb. XRD-BS, Stanford Linear Accelerator Center. (2006).

[6] D. Balzar, et al., " Size–strain line-broadening analysis of the ceria round-robin sample ," Journal of Applied Crystallography, vol. 37, pp. 911-924, 2004.

[7] "A Profile Refinement Method for Nuclear and Magnetic Structures." Rietveld, H.M., Journal of Applied Crystallography, vol. 2, pp. 65-71, 1969.

Fit Lattice Constants of Doped Bacteriogenic UO_2 Samples			
	Calcium (pH=6.0)	**Magnesium (pH=8.0)**	**Magnesium (pH=6.3)**
Undoped	5.4437 ± .0029 Å	5.4307 ± .0016 Å	5.4331 ± .0016 Å
.1 mM	-	-	5.3956 ± .0061 Å
1 mM	-	-	5.4387 ± .0016 Å
5 mM	-	-	5.4018 ± .0022 Å
10 mM	5.4353 ± .0022 Å	5.4405 ± .0045 Å	-

Table 1. Summary of Doped Samples - All were cleaned using NaOH

Fit Lattice Constants of Undoped Bacteriogenic UO_2 Samples			
Cleaning Method	**None**	**NaOH**	**Lysozyme**
pH = 8	5.4753 ± .0025 Å	5.4307 ± .0016 Å	5.4702 ±.0016 Å
pH = 6.3	-	5.4331 ± .0016 Å	5.4643 ±.0017 Å
pH = 6	-	5.4437 ± .0029 Å	-

Table 2. Summary of Undoped Samples

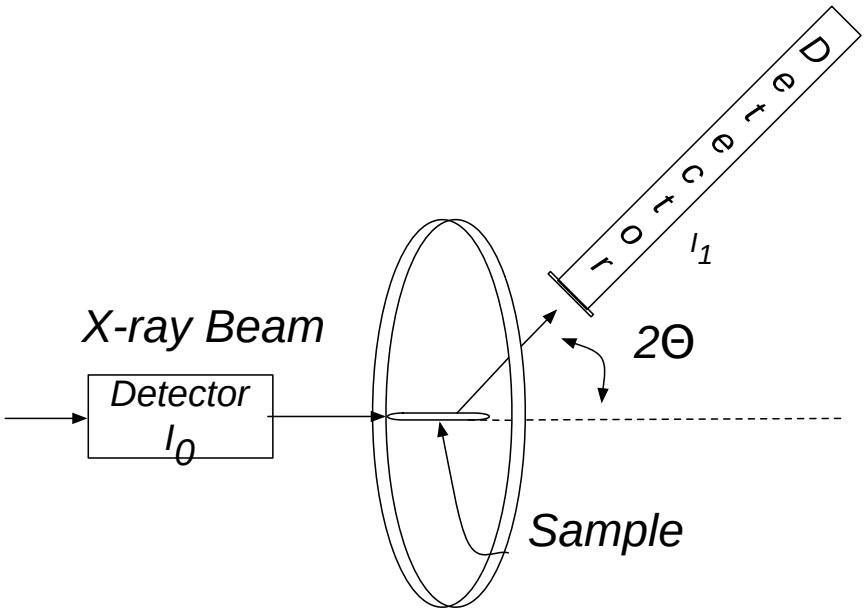

Figure 1. Diagram of Experimental Setup

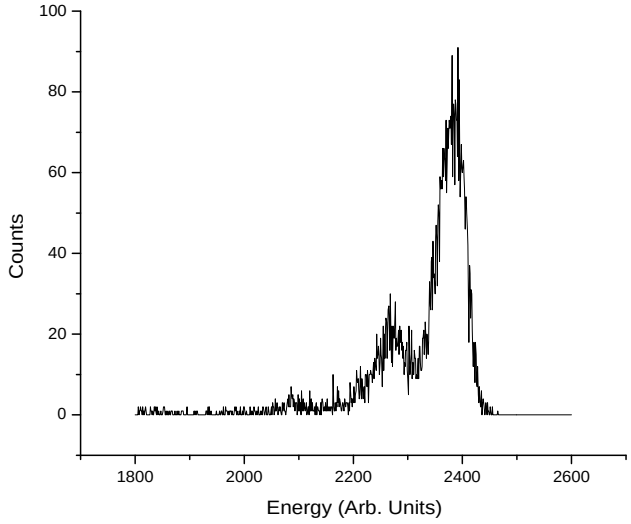

Figure 2. Energy Spectrum at High Q

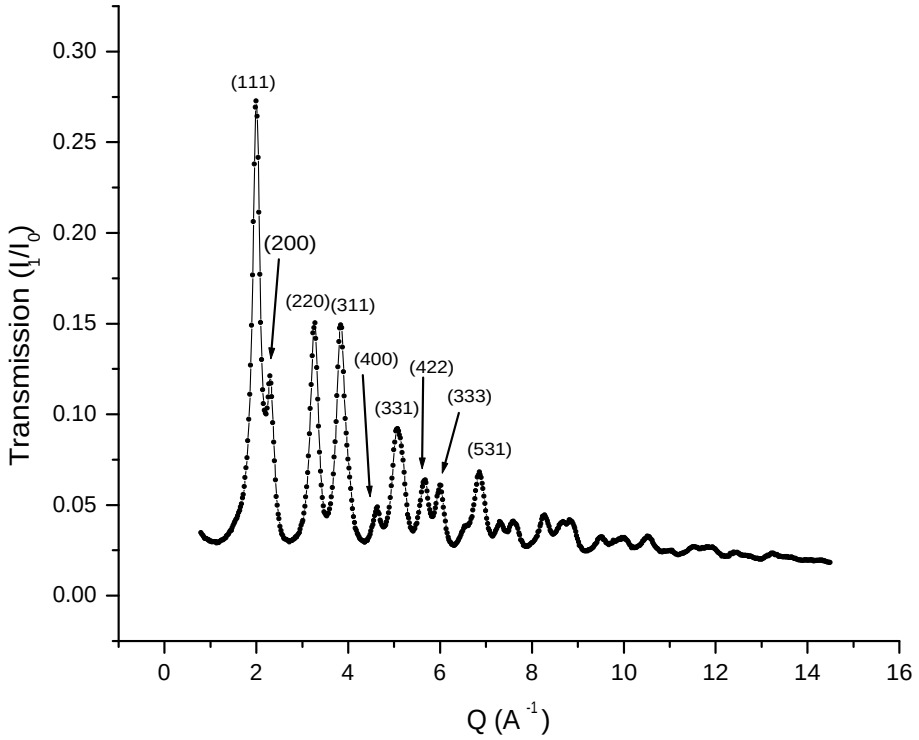

Figure 3. Raw data with first nine peaks labeled with Miller Indices

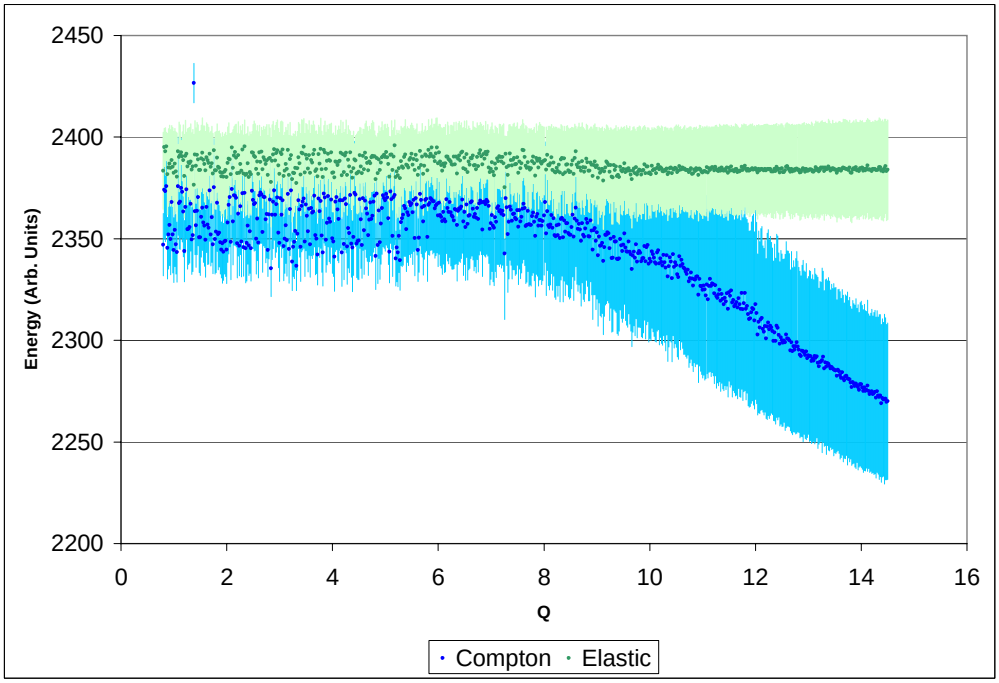

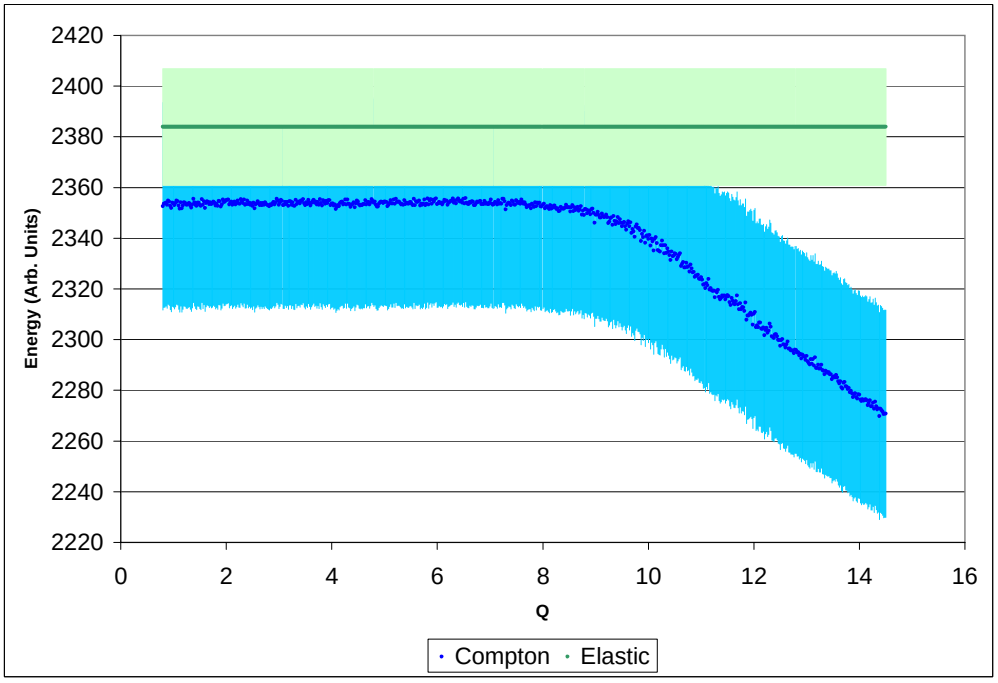

Figure 4. Top - Initial Compton Fittting

Bottom- Final Compton Fit - Elastic peak position and width, and Compton width held constant

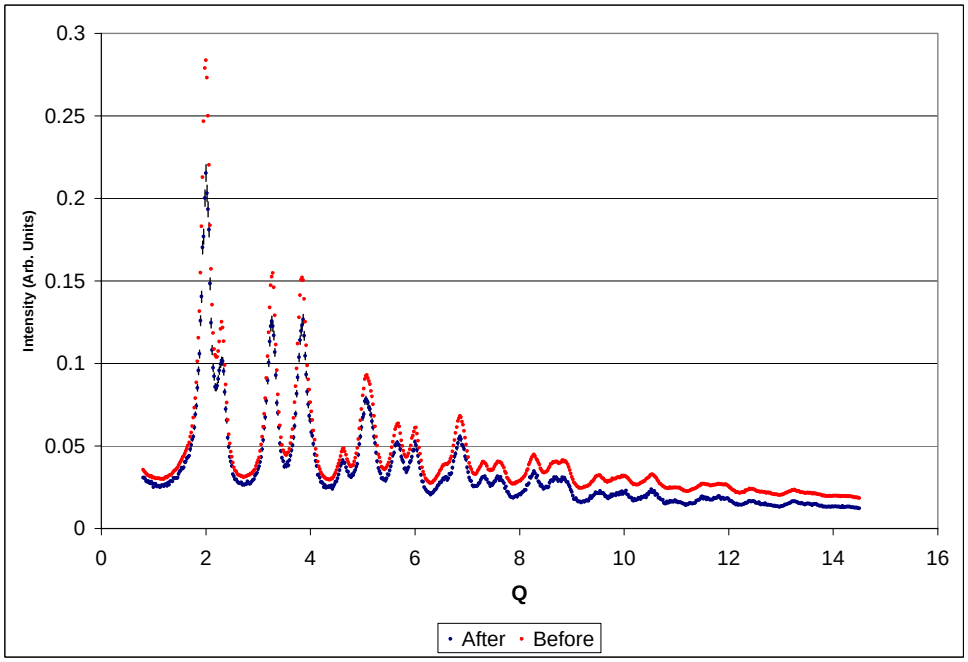

Figure 5. Sample Compton Subtraction

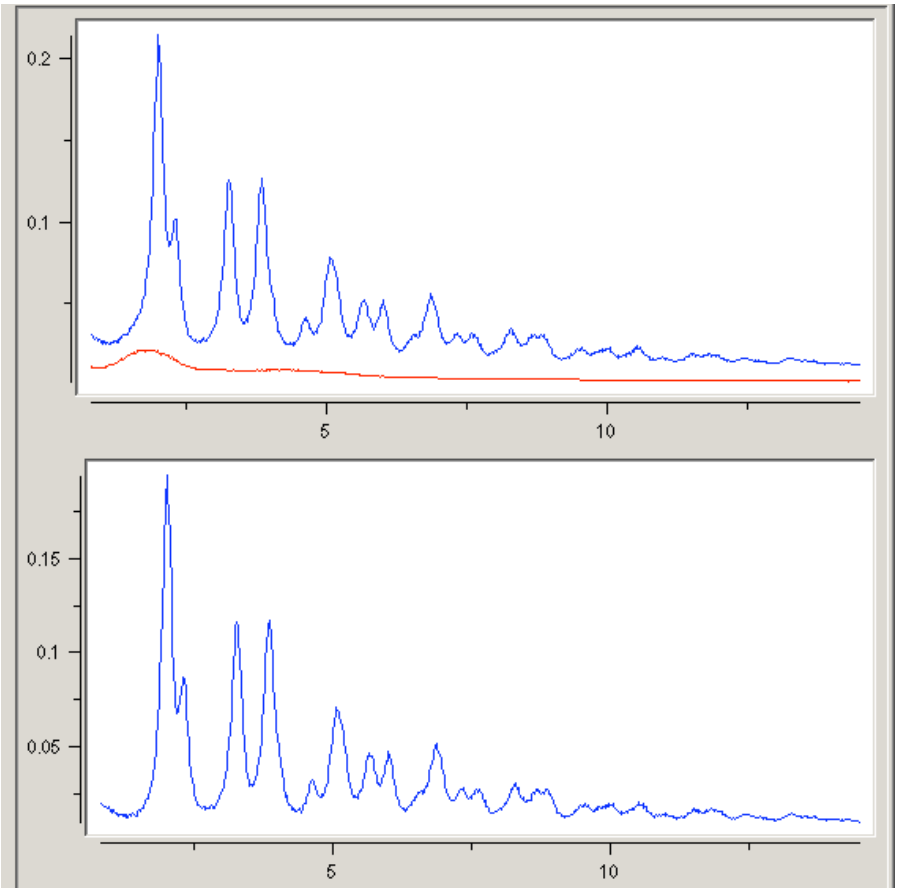

Figure 6. Background Subtraction of Capillary Signal.

Blue Line = Sample Data ; Red Line = Capillary Data

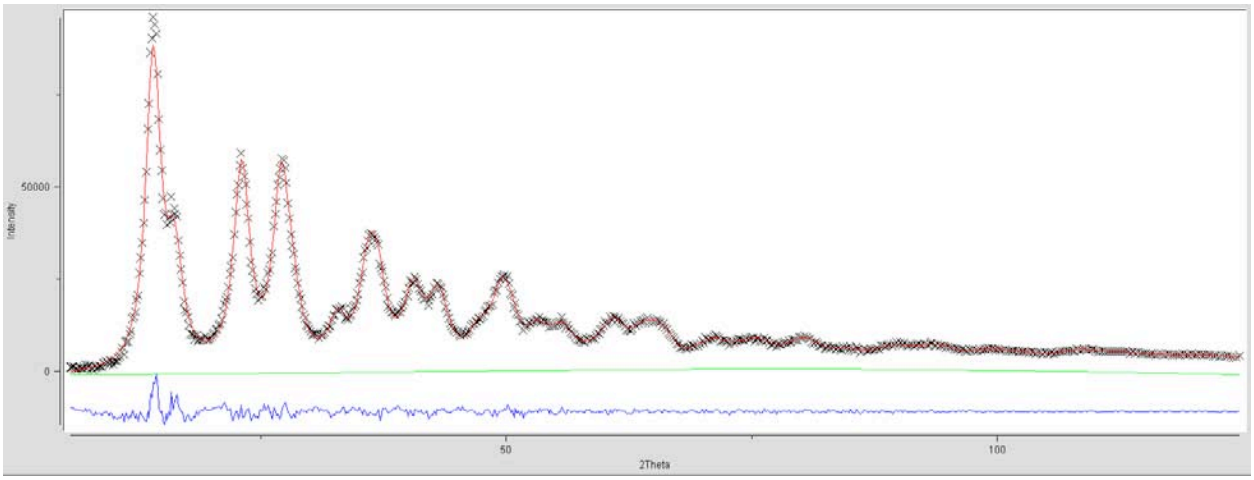

Figure 7. Sample Le Bail Fit

Red Line - Fit Line; Green Line - Background; Blue Line - Error in Fitting

SLAC-TN-07-028

Measurements of High-Field THz Induced Photocurrents in Semiconductors

Michael Wiczer

Office of Science, SULI Program

University of Illinois – Urbana-Champaign

Stanford Linear Accelerator Center

Stanford, CA

August 24, 2007

Prepared in partial fulfillment of the requirements of the Office of Science, Department of Energy's Science Undergraduate Laboratory Internship under the direction of A. M. Lindenberg in the Stanford Synchrotron Radiation Laboratory at the Stanford Linear Accelerator Center.

Participant: _____
Signature

Research Advisor: _____
Signature

Work supported in part by US Department of Energy contract DE-AC02-76SF00515

Table of Contents

Abstract

Measurements of High-Field THz Induced Photocurrents in Semiconductors. MICHAEL WICZER (University of Illinois – Urbana-Champaign, Urbana, IL 61801) AARON LINDENBERG (Stanford Linear Accelerator Center, Menlo Park, CA 94025).

THz pulses have provided a useful tool for probing, with time resolution, the free carriers in a system. The development of methods to produce intense THz radiation has been slow since spectroscopists and condensed matter physicists first began probing materials with THz pulses. We have developed a method for producing intense ultra-short THz pulses, which have full width half maximum of 300 fs – approximately a half cycle of THz radiation. These intense half cycle pulses (HCPs) allow us to use THz radiation not only as a probe of the free carriers in a system but also as a source of excitation to alter a system in some way. In particular, HPCs perturb free carriers considerably in short time scales but show minimal effect to individual free carriers over long time. By exposing the semiconductor indium antimonide (InSb) to our intense THz HCP radiation, we have observed non-linear optical effects which suggest the generation of new free carriers by below band-gap THz photons. This generation of free carriers appears to be caused by an avalanche multiplication process, which should amplify the number of free carriers already in the system and then induce a current in the timescale of our THz pulse. This amplification on such a short timescale suggests the possibility of an ultra-fast detector of weak above band-gap radiation. We constructed a device which detects these currents by painting an electrode structure on the surface of the semiconductor. The currents induced across the electrodes by this avalanche multiplication process were measured and compared with other measurements of this non-linear optical process. We successfully measured THz induced currents in InSb, which indicate promise towards the development of an ultra-fast detector, and

we gain insight into a possible physical explanation of the THz induced free carriers we observe in InSb.

Introduction

Ultra-fast THz (10^{12} Hz) radiation has proved tremendously useful for probing time-resolved dynamics in a variety of systems [1]. Traditionally, a sample is excited or set into motion in some way (i.e. by a "pump" such as an IR-laser pulse or synchrotron radiation pulse) and at various times following this excitation, a THz pulse passes through the sample and "probes" its state at that instant. THz radiation is an extremely good probe of systems because each THz photon has very low energy (1 THz photon ~ 4 meV). Thus, the radiation is absorbed by free electrons in the system (a detectable effect), but the small increase in the energy of the free electron has no discernible effect on the system. Although this has been a powerful tool for studying dynamics for some time, we are beginning to learn that – at high enough intensity – THz radiation can act as a valuable source of excitation ("pump") of a system.

New techniques have provided for the generation of THz radiation by optical rectification [2] not limited in intensity by a threshold for damaging a non-linear optical crystal. We have developed an experimental setup which uses a plasma in air as a nonlinear optical element. For our purposes, the THz radiation generated by this method is only limited by the intensity of incident 800 nm and 400 nm laser light. With this tool available, we can begin to study ultra-fast dynamics using THz radiation as a pump.

One such experiment employing this high intensity THz radiation studies its interaction with semiconductors. Indium antimonide (InSb) was placed in the path of the THz beam and absorption was measured. Since the photons had much lower energy than the band-gap of the semiconductor (4 meV << .17 eV), one would not expect the THz radiation to increase the

number of free carriers in the semiconductor. Instead, the THz absorption should provide a measure of the number of free carriers currently present in the semiconductor (due to thermal excitation). However, we have observed that THz radiation at high enough intensity generates new free carriers. We measure this phenomenon by using the THz pulse as a probe of its own interactions and by observing current generated by the new free carriers.

Our THz radiation is short enough (~300 fs FWHM) to be considered a half-cycle pulse [3]. In this case, the integral of electric (or magnetic) field over all time is 0, but one half-cycle of the electric field is much stronger than all others (Figure 1). Thus, for short times, the THz pulse can act as a positive field. If this field is strong enough, it can accelerate existing free carriers in the conduction band of the semiconductor. Once accelerated, these free electrons can collide with valence electrons, and, if there is enough energy, create new electron-hole pairs. The new conduction band electrons can now feel the electric field and accelerate into valence electrons to produce even more electron-hole pairs [4-6]. Upon investigating this process – avalanche multiplication – we observe that the ultra-fast, high intensity THz radiation provides for an experiment which isolates certain physical processes extremely well. While in bulk systems, electron-electron collisions in the conduction band and electron-phonon coupling prove significant, both of these processes occur on much longer time-scales than our experiment. Furthermore, fields this intense are generally unable to penetrate the surface of the semiconductor material, which breaks down at much lower fields. The ultra-fast nature of the pulse once again allows for the pulse to excite the sample before it breaks down, and the field is not screened.

This setup may assist the development of an ultra-fast detector. Our THz radiation can multiply the number of free carriers in the semiconductor and produce a current in very short

timescales. This amplification can be harnessed by the construction of a photoconductive dipole antenna [7-8]. By placing two electrodes on the surface of the sample with the polarization of the THz beam pointing across the electrodes, the THz beam will sweep and multiply any newly generated free carriers (i.e. by an above band-gap photon). This device, which generally uses a known pulsed laser to detect small THz signals, can use a known THz signal to detect small laser signals with high gain and very fast response – as fast as the THz pulse length. As yet, no detection method this fast exists.

Materials and Methods

We generate high-intensity THz pulses with a Ti:Sapphire laser system. A mode-locked Ti:Sapphire oscillator produces weak, 25 fs pulses, which are then sent to a regenerative amplifier to be amplified using chirped pulse amplification (CPA) [9]. The final laser pulses have total energy of approximately 1 mJ, pulse length of 50 fs, wavelength centered at 800 nm (full width half maximum spanning from about 775-825 nm), and a repetition rate of 1 KHz. These laser pulses are then passed through a β-barium borate (BBO) frequency-doubling crystal to produce 400 nm light collinear with the original 800 nm light. As described by Bartel et al, if this beam is focused to a small enough waist to ionize air – and has an appropriate divergence angle for optimal phase matching – a 3-rd order non-linear optical effect will produce a quasi-DC electromagnetic field. Since the pulse duration for the incoming laser beams are so short, this quasi-DC field takes the form of an ultra-short THz pulse [10].

A sample photoconductive antenna is constructed in order to test both the physics of the interaction between intense THz radiation and semiconductor samples as well as the potential development of an ultra-fast photoconductive switch. Using silver paste two vertical electrodes, approximately 5 mm in length and separated by 500 μm, were painted onto the InSb sample.

Although InSb is a semiconductor, its extremely narrow band-gap allows for a high density of free carriers even at room temperature ($2\times10^{16}\ cm^{-3}$). Thus, it has a relatively low resistivity, and the resistance across the two electrodes was measured to be approximately 50 Ω. Since the heat of a soldering iron damages the semiconductor material, wires were attached to the surface of the semiconductor with epoxy, and electrical contact with the electrodes was ensured with additional silver paste. In order to minimize the amplification of ambient electrical noise, wire directly from a coaxial cable was mounted to the sample and cable length was minimized (Figure 2). The current across these electrodes was input into a current amplifier (Stanford Research Systems SR570) set to a gain of 1 pA/V. This was the most sensitive gain setting on the current amplifier, and thus the output from the amplifier was slow (output time constant of 3.5 s). An optical shutter (Thorlabs SH05 shutter with Thorlabs SC10 controller) modulated the beam at .2 Hz. A reference signal from this shutter and the output of the current amplifier were synchronized using a lock-in amplifier (SR830) acquiring with a time constant of 100 s.

This type of device has been used extensively in the past to detect THz radiation [7]. When used with a semiconductor with carrier lifetimes of approximately or less than the width of the THz pulse, the current induced across the electrodes increases linearly with electric field amplitude for low fields. If the carrier lifetimes are much longer than the width of the THz pulse (as in InSb) and no new free carriers are induced, a free carrier feels the electric field of the THz pulse for a very long time, and the current across the electrodes is approximately zero. If, however, new free carriers are induced, then the average conduction band electron loses energy at every collision. The electron no longer feels the electric field uninterrupted for the entire width of the pulse. Rather during the positive portion of the pulse, the energy decreases. The now slower free carrier then feels the rest of the field, which reduces its velocity further until the net

velocity of free carriers is in the direction opposite the direction the charge was accelerated during the THz pulse. This results in a net current indicative only of the free carriers generated during the positive portion of the THz pulse (Figure 3). The expectation at high THz intensity is that, once the field reaches an impact-ionization threshold, additional free carriers will be generated, and a current will form. We measure the dependence of current on incident electric field by focusing our THz beam to a small waist and translating the sample along the direction of propagation of the THz beam. At the beam waist, the electric field amplitude will be greatest and as the sample is translated away from the waist, the amplitude decreases.

The intention is that we acquire data as the photoconductive antenna translates along the propagation axis of the focusing THz beam. This data then needs to be calibrated to be expressed against peak electric field instead of position. To this end, we mapped the THz beam as it propagates. We use a bolometer, which measures the total THz intensity incident on the detector. Spatial resolution is provided by blocking all THz radiation except that which passes through a narrow slit (Figure 4). The slit is open to a small portion of the THz beam's longitudinal profile at a particular propagation distance; the THz intensity incident on the bolometer is a measure of the THz intensity at the position of the slit.

Results

Modeling:

In order to characterize the physical processes involved in our experiment, we must produce a model which predicts a signature of the suspected physical process, which might be measurable. We produce a simple "order-of-magnitude" model for the current generated by avalanche multiplication induced by THz radiation in InSb. Since the THz wavelength is so long and the pulses so intense, it is an accurate picture to consider the effect of the bulk electric field

created by the THz radiation as opposed to multi-photon absorption – which is a much more complex description of the process. The traditional treatment of semiconductors exposed to fields as high as the peak field of the THz HCP we generate (approximately 200 KV/cm) is to suggest that a free electron reaches a saturation velocity because of the increased number of collisions at fields this high. Furthermore, avalanche breakdown will occur, the semiconductor will become a conductor, and fields will be screened. However, the THz pulses we generate are short enough that relatively few collisions occur. Hence, the electron can – for this short duration – transport through the semiconductor at velocities much greater than the saturation velocity, and fields much greater than the breakdown field of the semiconductor can penetrate the sample. Thus, a "hot-electron" transport model – one where the electron has a fixed energy incident on the material – appears more appropriate than a high-field transport model – one where the electron starts at rest and then is accelerated. Kane developed a model for the rate of impact ionization collisions – collisions with valence electrons which create new electron-hole pairs – as a function of a hot electron's kinetic energy [4]. Based on Kane's "random-k" approximation, we find that – if the hole effective mass is much greater than the free carrier effective mass – the collision rate, ω(E), is related to the following integral expression [4]:

$$\omega(E_1) \propto \int_{E_g}^{E_1-E_g} \int_{E_g}^{E_1-E_3} \varphi_c(E_2)\varphi_c(E_3)\varphi_v(E_4)dE_2dE_3$$

Where E_1 is the energy of the initial hot electron and E_4 is the energy of the valence electron which interacts with the initial hot electron. Once the hot electron interacts with the valence electron, the hot electron loses energy and the valence electron gains enough energy to enter the conduction band. This produces two final electrons in the conduction band with energies E_2 and E_3. The conservation of energy condition is that $E_1=E_2+E_3-E_4$. All energies are measured from

the valence band edge, and the band gap energy is E_g (E_g = 0.17 eV for InSb (E_4<0; E_1,E_2,E_3>E_g). φ_c is the density of states function of the conduction band and φ_v is the density of states for the valence band. If we assume a parabolic band structure, these functions become

$$\varphi_c(E) = \frac{1}{2\pi^2}\left(\frac{2m_c}{\hbar^2}\right)^{3/2}\sqrt{E-E_g}\,,\ \varphi_v(E) = \frac{1}{2\pi^2}\left(\frac{2m_v}{\hbar^2}\right)^{3/2}\sqrt{-E}$$

Where m_c is the effective mass of a free electron (0.014 m_e in InSb) and m_v is the effective mass of a hole (0.43 m_e in InSb). This integral was evaluated and the constant of proportionality was determined by calibrating our results to previous Monte-Carlo calculations of low-energy impact ionization rates in InSb [5]. The calculated collision rate is given in Figure 5.

Using this, we must now consider that the electron, in fact, starts at rest and is accelerated. The instantaneous collision probability per unit time, P(t), must satisfy

$$P(t) = \left(1 - \int_{t_0}^{t} P(s)ds\right)\omega\big(E(t)\big)$$

Where t_0 is the time for the electron to accelerate to the threshold energy and E(t), under a constant field, is given by $E(t) = \frac{1}{2m^*}\big(qFt\big)^2$. For various field strengths, P(t) and, in turn, the average times for the first ionizing collision were calculated. The dependence of collision time on applied field (assuming a constant field) τ(F) was found to be given by $\tau(F) \propto (F - F_t)^{-0.9}$ (Figure 6), where F_t is the threshold field for impact ionization. If we approximate our THz pulse as a square wave, we can generate an approximation for the multiplication factor:

$$M(F) = 2^{t_p/\tau(F)}$$

where t_p is the width of the pulse. It is important to note that many assumption have been made which cause considerable inaccuracies in the multiplication factor. We believe that the given

expression for the multiplication factor is nevertheless useful in understanding qualitative trends and achieving order-of-magnitude approximations.

Experiment:

Using slits to provide spatial resolution to our bolometer measurement (as described in Materials and Methods section), we acquired a map of the intensity profile of the THz beam as it propagates (Figure 7). After extracting the intensity peak at each position along the propagation axis (and then taking the square root of intensity) we were able to extract the relative peak electric field as a function of position along the propagation axis (Figure 8).

Once the THz beam profile was achieved, the electrode structure (Figure 2) was placed at the focus of the THz beam. Current was measured where the electrodes were placed at various longitudinal positions along the beam profile (Figure 9). The width of the current profile was approximately 750 μm FWHM, which is comparable to the width of the THz intensity profile at the focus. This suggests that the current measured is, in fact, induced by the THz beam. We then placed the electrode structure at various positions along the propagation axis of the THz beam (Figure 10). The current profile was much broader than the intensity profile of the THz beam. Some current was found when no THz radiation was generated but 800 nm IR radiation was incident on the electrode gap. This suggests that the current profile of the THz beam may have been broadened by scattered IR radiation.

Discussion and Conclusions

We have tentatively observed THz induced photocurrents on 300 fs timescales. The mere existence of this photocurrent is valuable as it shows promise as an ultra-fast, high gain photoconductive switch – a fast detector of weak above-band-gap radiation. Although these data have not yet been related to similar absorptions measurements, we expect that after repeating our

photocurrent measurements with improved scattered light cancellation the absorption and photocurrent measurements will relate in interesting ways.

It is valuable here to speculate about frequency dependences. The frequency response of the bolometer that was used for absorption measurements favors higher frequencies. Furthermore, in low-intensity conditions, InSb absorbs low frequency THz radiation considerably more than higher frequency THz. This suggests that our absorption measurements, which indicate an increase in free carriers, are mostly providing insight in the response of InSb to higher frequency THz radiation. Based on the impact ionization model, we understand that the width of the HCP is extremely significant to the gain generated by avalanche multiplication. Lower frequency components help to broaden the HCP. Our understanding of the photoconductive antenna, on the other hand, suggests that it can provide insight into the response of InSb to low as well as high THz frequencies. This is because the electrodes are on the surface of the sample, so absorption effects through the depth of the sample are insignificant. Furthermore, our understanding of the mechanism which generates photocurrents suggests that the current is much more sensitive to the properties of the electric field of the THz pulse as a function of time as opposed to the frequency components. The lack of frequency discrimination in the photoconductive antenna and the observation that the effects of impact ionization are amplified by the present of low frequency THz radiation suggest that the photoconductive antenna should be more sensitive to these non-linear effects than the absorption measurements. Thus, currents should begin to develop at lower peak intensity than increased absorption began. This seems to support our tentative results that the current profile is broader than the absorption profile of the THz beam. It does not change the fact that scattered IR light may have played a significant role in broadening the current profile, but a broader profile is expected nevertheless.

Necessary further investigation includes the repetition of our measurement of the photocurrent profile with the effects of scattered IR light being reduced. Furthermore, we would like to repeat our measurements at low temperatures. This will provide direct evidence for whether the non-linear effects we observe are produced by conduction band electrons or valence band electrons since, as the conduction band electrons are reduced, the effect will be either enhanced or reduced. Finally, we should refine our photoconductive antenna design for use as an ultra-fast photoconductive detector.

Acknowledgments

This research was conducted at the Stanford Linear Accelerator Center (SLAC). I thank my mentor, Professor Aaron Lindenberg, and his post-doctoral associate Haidan Wen for their direction and discussions which guided this project. I also thank the Department of Energy, Office of Science for funding my research and for organizing the Science Undergraduate Laboratory Internships (SULI) program. Finally, I would like to thank the organizers of the SULI program at SLAC.

References:

[1] C.A. Schmuttenmaer, “Exploring Dynamics in the Far-Infrared with Terahertz Spectroscopy,” in Chemical Reviews, Vol. 104, 2004, pp. 1759-1779.

[2] T.J. Carrig, G. Rodriguez, T.S. Clement, A.J. Taylor, and K.R. Stewart, “Scaling of Terahertz Radiation Via Optical Rectification in Electrooptic Crystals,” in Applied Physics Letters, Vol. 66, 1995, pp. 121-123.

[3] T. Bartel, P. Gall, K. Reimann, M. Woerner, and T. Elsaesser, “Generation of single-cycle THz transients with high electric-field amplitudes,” in Optics Letters, Vol. 30, 2005, pp. 2805-2807.

[4] E.O. Kane, “Electron Scattering by Pair Production in Silicon”, in Physical Review, Vol. 159, 1967, pp. 624-631.

[5] R.C. Curby and D.K. Ferry, “Impact Ionization in Narrow Gap Semiconductor”, in Physica Status Solidi (a), Vol. 15, pp. 319-328.

[6] S.A. Jamison and A.V. Nurmikko, “Avalanche formation and high-intensity infrared transmission limit in InAs, InSb, and $Hg_{1-x}Cd_xTe$”, in Physical Review B, Vol. 19, 5185-5193.

[7] P.R. Smith, D.H. Auston, and M.C. Nuss, “Subpicosecond Photoconducting Dipole Antennas” in IEEE Journal of Quantum Electronics, Vol. 24, 1988, pp. 255-260.

[8] M. van Exter, C. Fattinger, and D. Grischkowsky, “High-brightness terahertz beams characterized with an ultrafast detector”, in Applied Physics Letters, Vol. 55, 1989, pp. 337-339.

[9] U. Keller, G. W 'tHooft* W H. Knox, and J. E. Cunningham, “Femtosecond pulses from a continuously self-starting passively mode-locked Ti:sapphire laser” in Optics Letters, Vol. 16, 1991, pp. 1022-1024.

[10] T. Bartel, P. Gall, K. Reimann, M. Woerner, and T. Elsaesser, “Generation of single-cycle THz transients with high electric-field amplitudes” in Optics Letters, Vol. 30, 2005, pp. 2805-2807.

Figures

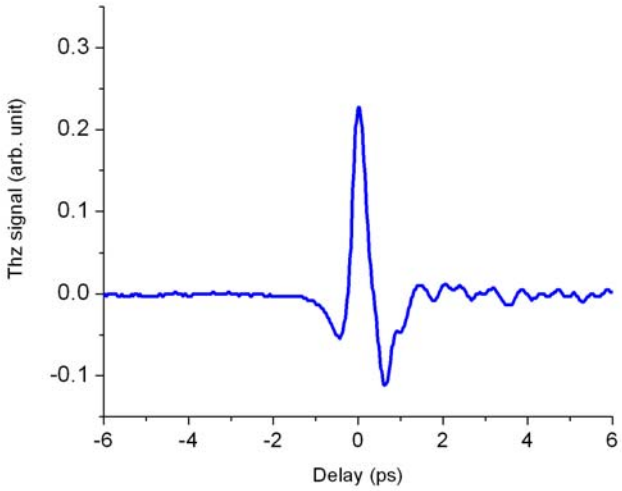

Figure 1. A half-cycle pulse of THz radiation acts as a directional electric field for short times.

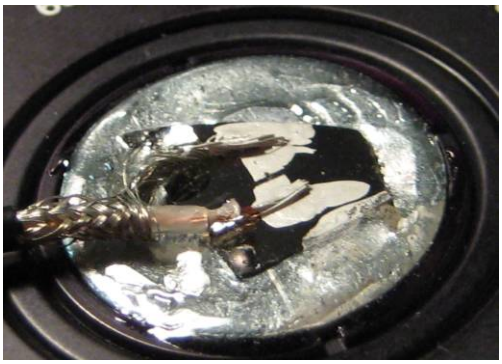

Figure 2. Electrodes attached to InSb surface with silver paint and epoxy glue.

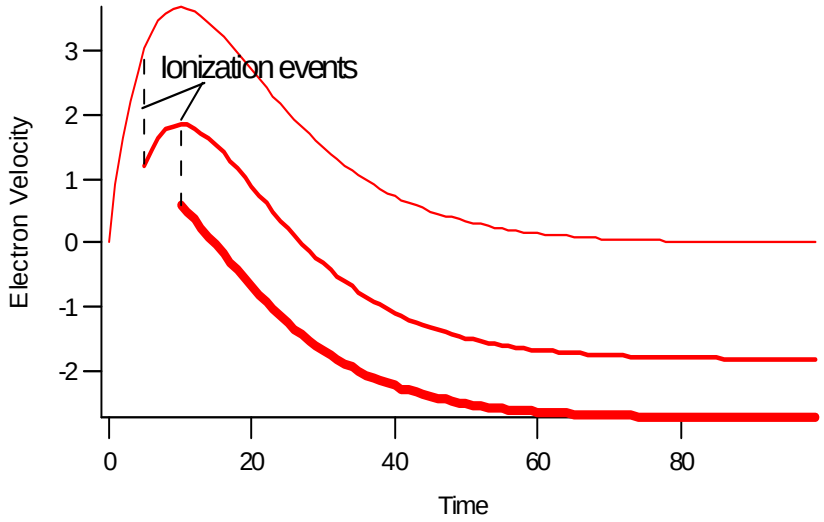

Figure 3. A free electron which is subject to a THz HCP for long times has velocity qualitatively depicted in thee top trace. For every ionization event, not only are total free carriers doubled, but the net velocity after long times becomes non-zero (bottom two traces).

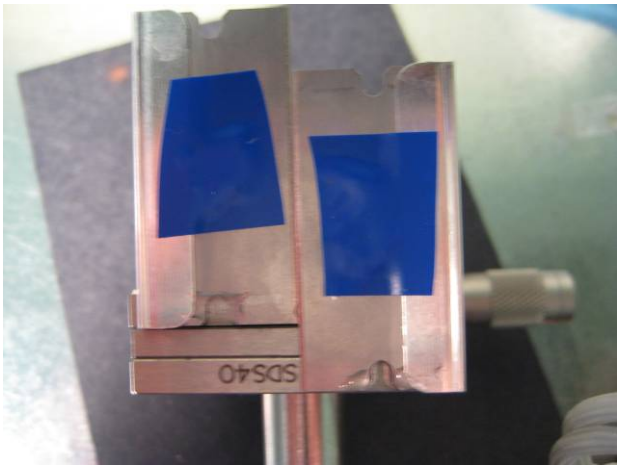

Figure 4. Width between narrow slits is adjusted by micrometer position. Only THz radiation at a specified position reaches the bolometer when the slits are positioned in front of the THz beam.

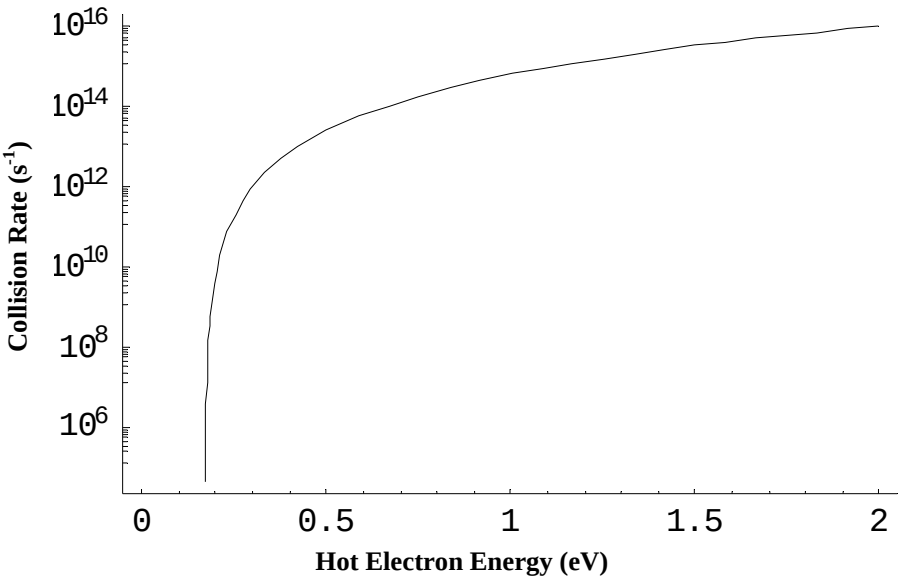

Figure 5. Probability of ionizing collision per unit time vs. electron kinetic energy.

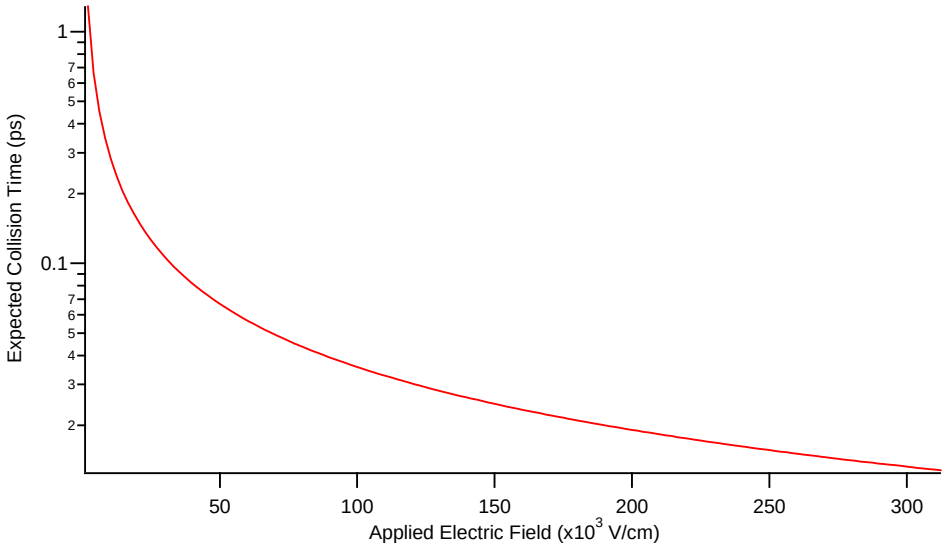

Figure 6. Expected time for first ionizing collision vs. applied field.

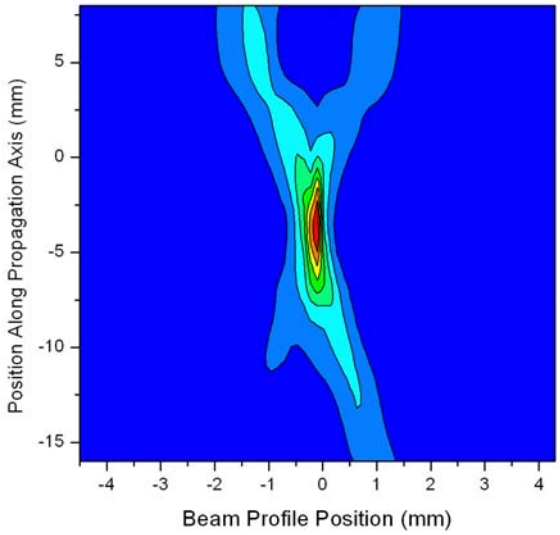

Figure 7. THz beam intensity contour plot.

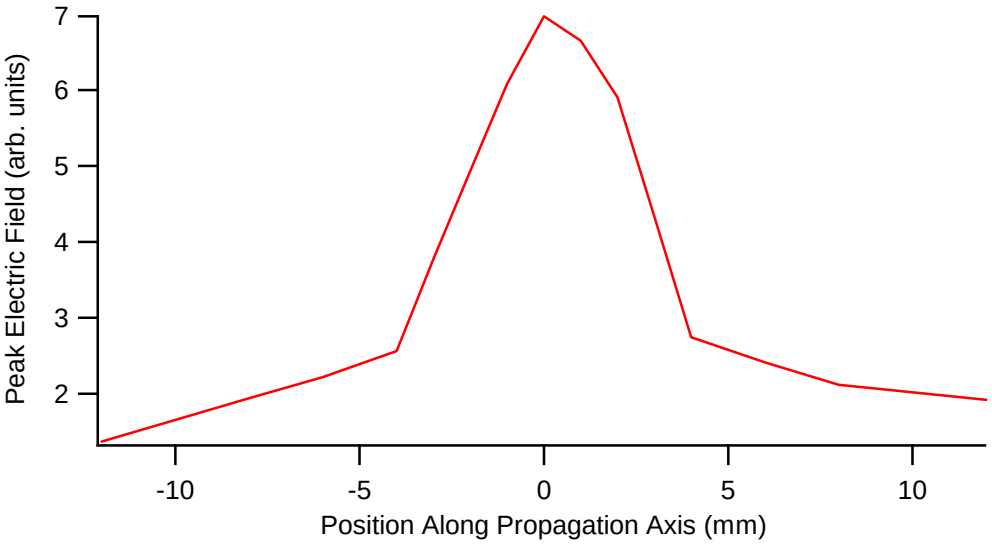

Figure 8. Peak THz electric field vs. propagation distance as beam is focused.

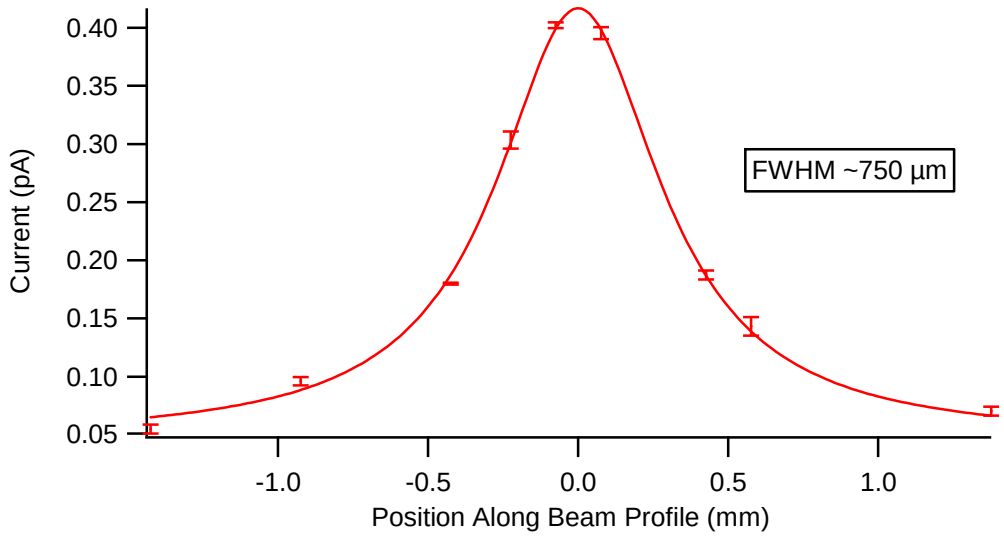

Figure 9. THz induced current vs. position along beam profile at focus of THz beam.

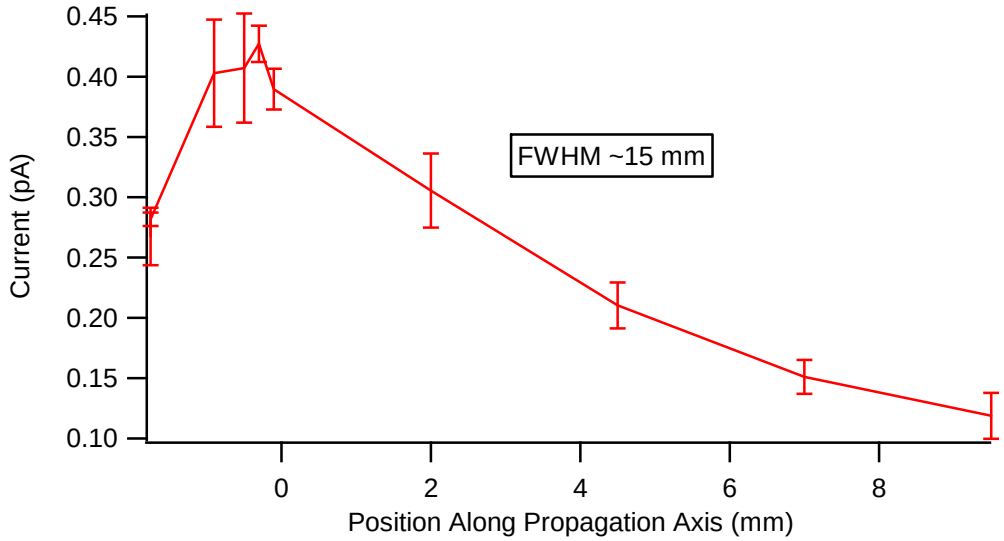

Figure 10. THz induced current vs. propagation distance as beam is focused. This trace is about twice as broad as the non-linear features observed in absorption measurements.